

Fig. 21.40 Apodized aperture. Apodization is used to limit the side-lobes of the ultrasound beam pattern. Transducers near the edge of the aperture are excited with a low voltage during transmit compared to the central transducers and are amplified with a lower gain compared to the central transducers during receive. The drawing on the right shows the image line corresponding to the beam pattern with the superficial and deep echoes plus the mark on the right, indicating the focal depth

every 20 μs, advancing the focus 15 mm each time along with the corresponding aperture. This focal adjustment is called dynamic focusing and is similar in concept to time-gain compensation. It is also possible to acquire data along the ultrasound line using several pulse-echo cycles, each with a transmit burst that is focused at a different depth. Although dynamic receive focusing takes no more time than static focusing, using double transmit focusing to further improve the lateral resolution of the image at a greater range of depths does reduce the frame rate by half. The location of the transmit focus is indicated by a carrot on the right of the image.

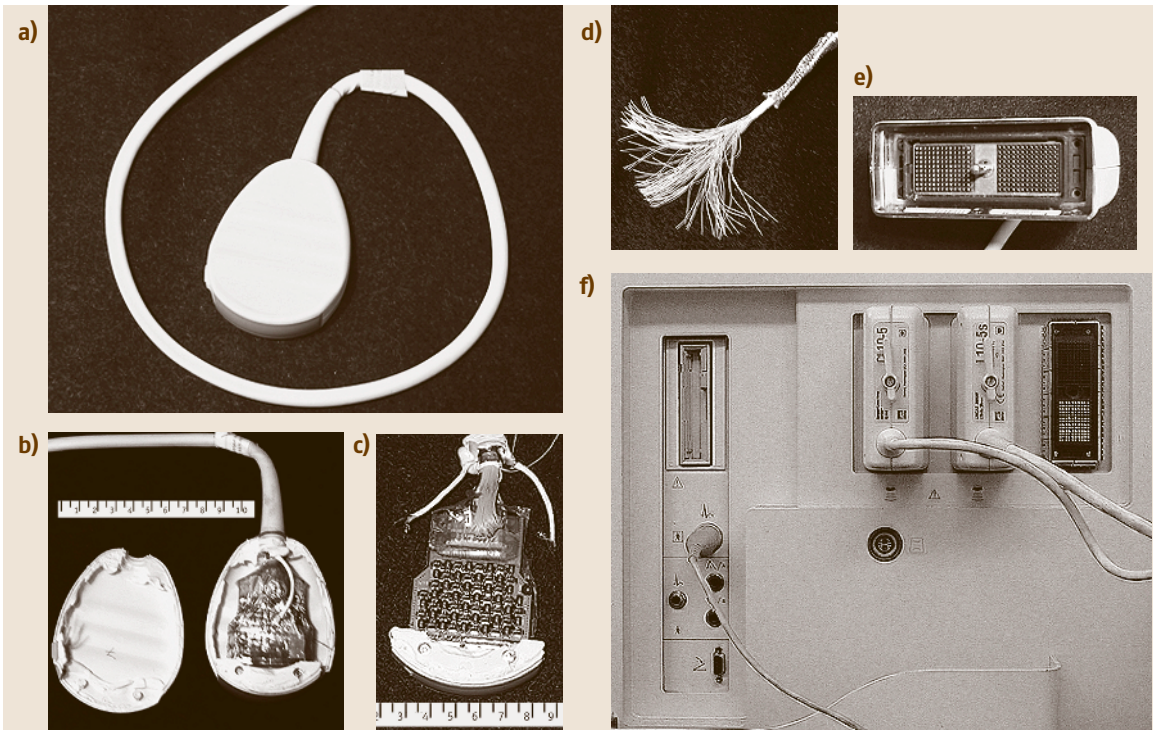


Fig. 21.41a–f Scan head details. This curved linear-array scan head consists of an array of 128 transducer elements cut from a single block of PZT piezoelectric ceramic. The array block is 64 mm long and 5 mm wide, cut into elements 0.4 mm long and 5 mm wide with a 0.1 mm kerf between. The block is curved to form a curved linear array. **(a)** Transducer in housing with cable; **(b)** Transducer housing removed showing the copper foil shielding over the internal electronics; **(c)** Shielding removed to show the 64 electronic matching circuits on this side of the circuit board; **(d)** 128 individual coaxial cables housed in the ultrasound scan head cable; **(e)** Scan head plug showing the connector electrodes for the 128 coaxial cables; **(f)** Front panel of the ultrasound scanner showing the sockets for the scan head connections. The front panel also shows connectors for other instruments including: electrocardiograph, plethysmograph, phonocardiograph microphone and computer disk drive for data exchange

Amazon EX1014 Page 873

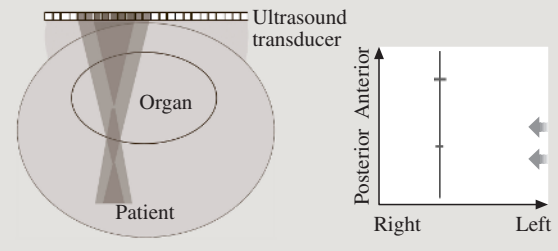


Fig. 21.42 Adjustable focus with large aperture. Using a high = density linear array to generate a large aperture allows electronic adjustment of the focal depth by adjusting the electronic delay of the transmit and receive signals so that the signal at the center transducers is delayed more than the signal at the edge transducers in both transmit and receive. Dual transmit focal depths, indicated by the pair of *arrows* on the right of the image, require that separate transmit pulses be sent into tissue for each of the two focal depths. On receive, the focus can be changed between the time that shallow echoes are received and the time that deep echoes are received

Because a linear array can steer the ultrasound beam, it is possible to form an image of each voxel in the tissue plane from different views, combining the results into a compound image (Fig. 21.43). The algorithm for combining the data from different angles is important in creating a pleasing image.

Phased Array Transducers. By applying a selected time delay to each transducer in an array, the ultrasound beam can be focused or tilted as desired (Fig. 21.39). Phased array transducers (Fig. 21.44) form the ultrasound image by tilting the ultrasound beam using selected delays on each transducer on transmit and receive to achieve the desired tilt. A scanhead with a transducer array of width

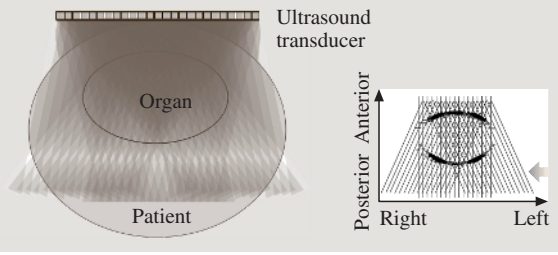


Fig. 21.43 Compound real-time imaging. By tilting the beam patterns to cross during acquisition of the image plane, system can take advantage of the specular backscatter of planar reflectors in the tissue

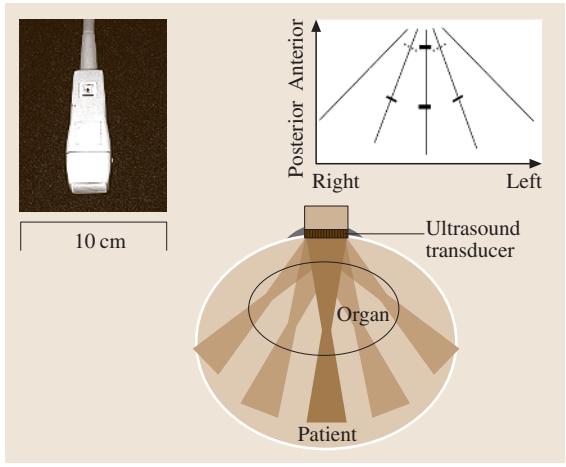


Fig. 21.44 Phased-array scan head. A phased-array scan head is able to use the same aperture for all ultrasound scan line beam patterns, directing the beam along different lines by adjusting the relative phase of the signals to the transducers

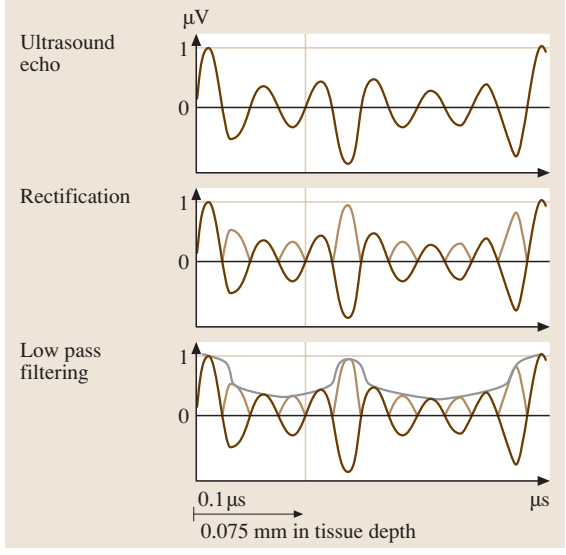


Fig. 21.45 Amplitude demodulation. To create a B-mode image of tissue anatomy, the strength or amplitude of the received ultrasound echo is determined as a function of depth. The RF echo is rectified (converting 5 MHz to 10 MHz) and low-pass-filtered with a 1 MHz cutoff to yield a depth resolution of 0.75 mm. That is effective if the ultrasound transmit burst is shorter than 1 μs. Amplitude demodulation requires one pulse-echo cycle along each ultrasound beam pattern line

Amazon EX1014 Page 874

D can tilt an ultrasound beam to an angle θ in tissue with an ultrasound velocity of c by applying a time delay gradient along the transducer of

$$\frac{tc}{D} = \sin\theta \,. \tag{21.11}$$

The time t is often represented as a function of the phase of the ultrasound ϕ for the ultrasound frequency f_{us}

$$t = \frac{\frac{\phi}{2\pi}}{f_{us}} \,. \tag{21.12}$$

To allow the ultrasound beam to tilt to θ degrees, the width of each transducer element must be less than $\lambda/2$ but the pitch (w = center to center spacing of the elements) must be $\lambda/4$ in order that, at the maximum deflection angle, a single beam pattern is defined when ultrasound intersects the array at angle θ

$$w < \frac{\lambda}{4\sin\theta} = \frac{c}{4 f_{us}\sin\theta} \,. \tag{21.13}$$

A 3 MHz scan head tilting the ultrasound beam 30° to the left and to the right requires a transducer element pitch of 0.3 mm.

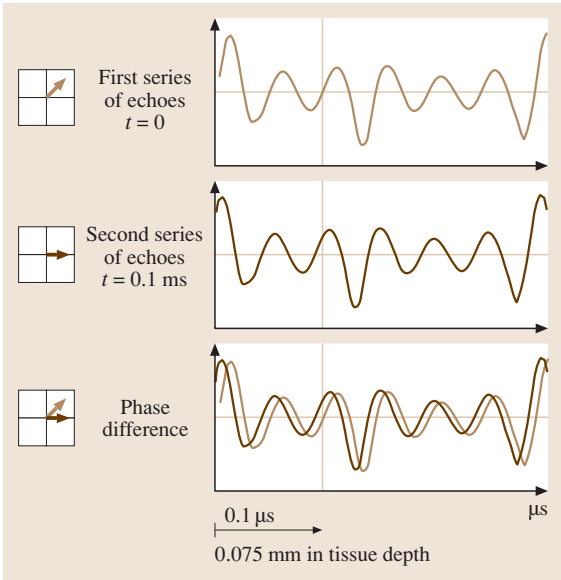


Fig. 21.46 Phase demodulation. To measure blood velocity, or tissue displacement or strain, the change in phase (or echo displacement) between successive pulse-echo cycles at a particular depth must be determined. In this case, a phase change of $\pi/4$ of 5 MHz ultrasound represents an echo time shift of 0.05 μs/8 = 0.006 25 μs, which is equivalent to a displacement of the scatterers toward the transducer of 0.006 25 μs × 0.75 mm/μs = 0.0047 mm in the time between pulse-echo cycles or 0.1 ms, yielding a velocity of 0.047 mm/ms or 0.047 m/s. The Doppler equation, time-domain velocimetry and strain imaging are all based on this computation. In Doppler demodulation, the phase and amplitude of the echo at any depth can be represented as a vector on a phase diagram. These vectors can be represented as complex numbers if the vertical direction is represented as the "imaginary" ($\sqrt{-1}$) direction and the horizontal direction represents the "real" direction

Pulsed Doppler [21.57]

The series of echoes from a single ultrasound transmit pulse provides information about the echogenicity of the tissue along the ultrasound beam pattern at various depths. The echogenicity of the tissue at each depth is determined by amplitude demodulation (Fig. 21.45). The measurement of the velocity of blood or tissue requires pairs of echoes from two (or more) ultrasound transmit pulses along the same beam pattern line, separated by a short time (0.1 ms). By comparing a second echo series from the same transducer beam pattern from a later time to the echo series from the first pulse, motion of the echogenic tissue along the beam pattern can be detected and measured. If the second echo series is identical to the first echo series, then none of the tissue along the ultrasound beam pattern has moved or changed during the period. However, if the second echo series is different, then the tissue has moved or changed. Motion in the direction of ultrasound propagation causes a simple time shift in the echo series, lateral motion or a change in tissue properties results in a loss of coherence between the echoes.

If the tissue has moved toward the ultrasound transducer, then the second echo pattern will arrive earlier after the transmit pulse compared to the first (Fig. 21.46). If the difference is detected by Doppler processing, then the echoes from each region of tissue are characterized by a vector in a complex plane (Fig. 21.46). One rotation of the vector is equivalent to the reflector moving toward the transducer to shorten the round-trip path by one wavelength of the ultrasound. If the ultrasound is 5 MHz, then the wavelength is 320 μm so one rotation represents a shortening of the round trip ultrasound travel distance of 320 μm, or 160 μm each way. A phase rotation of one quarter of a cycle ($\pi/2$ rad) represents 40 μm of motion. Doppler processing cannot tell the difference between 20 and 180 μm of motion because the vector is pointed in the same direction after the 160 μm displacement. This is called aliasing and is responsible for a waveform with the highest forward velocities incorrectly shown as reverse velocities (Fig. 21.47). Doppler

Amazon EX1014 Page 875

systems cannot tell the difference between displacements of 100 μm toward the transducer and 60 μm away from the transducer, because both are represented by the same phase shift. A motion of 20 μm will result in a rotation of the phase vector by 45° ($\pi/4$ rad). Often the interval between the first echo and the second echo is 0.1 ms. The velocity of the tissue in this case is $20/0.1\,\mu m/ms = 200\,mm/s = 20\,cm/s = 0.2\,m/s$.

The Doppler frequency is the phase change of the echo in cycles during the pulse interval divided by the pulse interval. In this case the phase change is 1/8 cycle, so the Doppler frequency is $0.125/0.1\,ms = 1250\,cy/s = 1.25\,kHz$.

Usually, pulsed Doppler systems are used to measure blood velocity. Unfortunately, it is rarely convenient to align the ultrasound beam pattern along the axis of a blood vessel so typically the angle between the ultrasound beam pattern and the vessel axis is 60°. This is called the Doppler angle. The ultrasound system can only measure the projection of the blood velocity vector along the ultrasound beam. That projection is the cosine of the angle between the velocity vector and the ultrasound beam. The Doppler equation relating velocity to the ultrasound echo is:

$$f = \frac{2 v_f f_{us} \cos\theta_D}{c} \quad \text{or} \quad v_f = c\frac{\frac{f}{f_{us}}}{2\cos\theta_D} . \qquad (21.14)$$

where f is the Doppler frequency that you hear, the factor of 2 accounts for the round-trip of the ultrasound, v_f is the velocity of the blood, f_{us} is the ultrasound frequency, θ_D is the angle between the blood velocity and the ultrasound beam, and c is the speed of ultrasound in tissue. The form

$$\frac{v_f}{c} = \frac{\frac{f}{f_{us}}}{2\cos\theta_D} \qquad (21.15)$$

emphasizes the relationship between the ratio of the blood velocity to the ultrasound velocity and the Doppler frequency to the ultrasound frequency. Since the ultrasound wavelength $\lambda = c/f_{us}$,

$$v_f = \frac{f\lambda}{2\cos\theta_D} . \qquad (21.16)$$

To provide a measurement of blood velocity, ultrasound instruments have a cursor on the screen to align with the axis of the vessel under examination (Fig. 21.48). The associated Doppler data, here represented as a spectral waveform, is provided with a scale showing the angle-adjusted velocity based on the projection of the measured velocity onto the vessel axis. Although this adjustment is theoretically justified by the geometry, unfortunately, it does not provide a useful velocity value. If a Doppler angle of zero degrees is used, then the value is correct, however, if other angles between the ultrasound beam and the presumed velocity vector are used, then the value of the velocity is not correct. The reason is that blood velocity vectors are rarely aligned with the axis of the artery. Instead, blood velocities form helical patterns along the artery [21.58–60]. Angle-adjusted Doppler velocity measurements are systematically higher as the Doppler angle increases from zero to 70 degrees or more. Although at a Doppler angle of zero, velocities are accurately used to determine both the volume flow rate and the Bernoulli pressure drop, neither result is correct when Doppler angles other than zero are used [21.61–63].

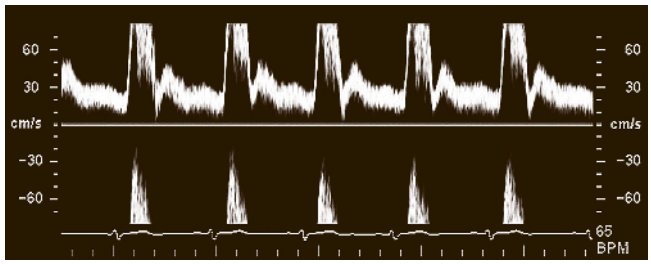


Fig. 21.47 Aliasing. Blood velocities that cause high phase shifts (greater than 180° or π radians) between pairs of pulsed Doppler echoes cause the Doppler system to mistake high-velocity forward flow for reverse flow. Continuity in blood flow allows the examiner to detect this error

Pulsed Doppler Range of Measurement. The highest Doppler frequency shift that can be measured with pulsed Doppler occurs when the phase change of the echoes during the interval between echo acquisitions [pulse repetition interval (PRI)] is 180° (half a cycle). The Doppler frequency at that condition is half of the pulse repetition frequency (PRF, the Doppler sampling frequency). This is called the Nyquist limit, after Harry Nyquist. This establishes the highest velocity that the Doppler can detect, although since the signal is analyzed as a complex number with twice the data (half as a "real" number and half as an "imaginary" number) Doppler frequencies between $+0.5$ PRF and -0.5 PRF are reported. As long as there is no reverse flow the range of Doppler frequencies available is equal to the PRF. If the phase vector is characterized by a 2 bit complex number into four values, then the smallest phase change that can be classified is 1/4 cycle. So, a 5 MHz Doppler system with the data recorded as 2 bits, and a PRF of 10 kHz, can only report four Doppler frequency ranges,

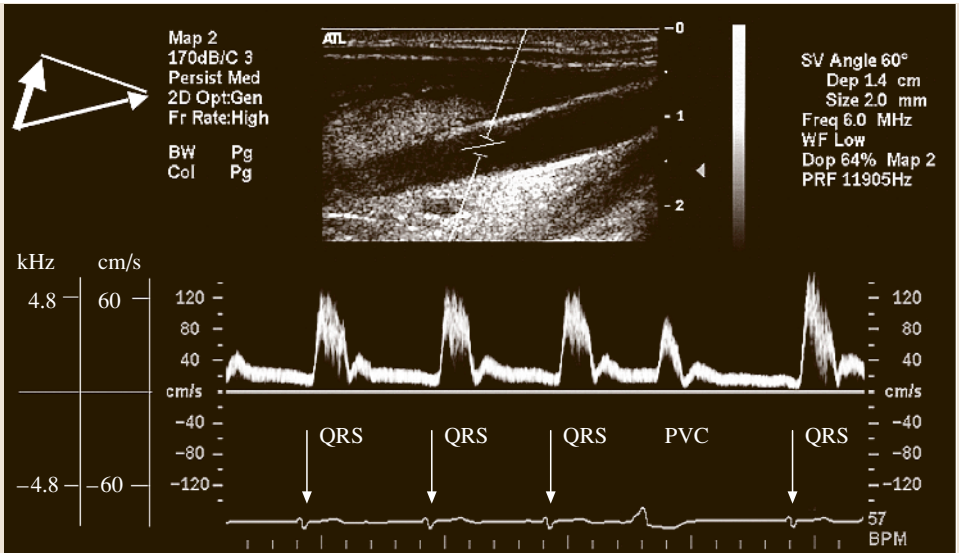


Fig. 21.48 Duplex Doppler image and waveform of a carotid artery. The axis of the ultrasound beam pattern used for Doppler is shown crossing the artery at an angle of 60° to the vessel axis. A cursor is aligned parallel to the vessel axis to provide θ_D for the Doppler equation. The Doppler frequency, which is produced by the speakers of the instrument, is shown by a scale drawn on the *left*. The scale showing the speed at which the blood is approaching the transducer is drawn adjacent to the frequency scale. The instrument computes the scale on the screen by dividing the cosine of the Doppler angle into the approach speed. Along the lower edge of the image is the electrocardiograph tracing (ECG) showing the "QRS complex" (small up and down) indicating the onset of ventricular contraction in each cardiac cycle. The lump in the trace 200 ms later is the T wave indication the end of ventricular contraction. The fourth beat is too early and the QRS has an odd shape. This is a premature ventricular contraction (PVC) originating from an abnormal spot on the ventricle. The PVC causes the ventricle to contract before filling is complete, producing a low-volume contraction, and low systolic blood velocities. The ventricle overfills before the next normal contraction, causing elevated systolic velocities

-1.25 to $+1.25$ kHz, $+1.25$ to $+3.75$ kHz, $+3.75$ to $+6.25$ kHz, and $+6.25$ to $+8.75$ kHz. -1.25 kHz is equal to $+8.75$ kHz. Such a Doppler system would probably classify -1.25 to $+1.25$ kHz as no motion. By increasing the number of bits in the digitizers representing the phase vector, the resolution of the phase shift is increased, and the number of possible measured velocities is increased. This does not increase the Nyquist limit.

Another way to increase the number of velocities that can be measured is to increase the number of pulse-echo cycles or Doppler phase samples that are gathered. The number of samples used to resolve the velocity is called the ensemble length or packet length. In a typical spectral waveform pulsed Doppler system, Doppler samples will be gathered from a voxel at a PRF of 12.8 kHz for 10 ms to provide 128 Doppler samples for frequency analysis. The Nyquist limit (upper frequency limit) is 6.4 kHz. The lowest frequency that can be detected is 100 Hz, one full Doppler cycle in the 10 ms acquisition period. If the signals are digitized into 2 bit complex numbers, then each of the 128 possible frequencies can be tested to see whether each is present or absent, but no information is available about the strength of each frequency signal. To determine the strength of each frequency, the signals must be digitized into numbers with more binary bits. Spectral waveform analysis assumes that there are many Doppler frequencies present in the Doppler signal from the voxel of interest.

Pulsed Doppler Pulse-Pair analysis. The Doppler frequency shift can be measured from just two echo samples separated by a known time. The assumption is that only a single Doppler frequency is present in the signal. The phase change divided by the sample interval time provides the Doppler frequency. The upper limit of the Doppler frequency is the Nyquist limit. To resolve the Doppler frequency, the phase angle change must be resolved. Representing the phase angle by a two bit complex number only resolves the phase angle into four divisions. For 5 MHz ultrasound, displacements of

Amazon EX1014 Page 877

40 μm can be resolved. For a 10 kHz PRF sample frequency, this allows a velocity of ±40 cm/s (±0.4 m/s) to be detected. However, if the phases are represented by 10 bit complex numbers, the phase angles can be resolved into 1000 divisions and the displacement and velocities can also be resolved. With 10 bit quadrature digitizers, velocities between plus and minus 80 cm/s can be measured with a resolution of 0.8 cm/s, equivalent to displacements of 80 nm during the pulse interval.

Pulsed Doppler Wall/Clutter Filtering. The measurement of blood velocity with ultrasound is complicated by the containment in vascular walls. The echogenicity of the blood is 60 dB less than the echogenicity of the walls at 5 MHz. The blood cells are Rayleigh scatterers because they are smaller (7 μm) than the wavelength of ultrasound (300 μm for 5 MHz). The strength of the echo from blood increases with the fourth power of the frequency. However, frequency-dependent attenuation of the ultrasound by overlying tissues limits most Doppler ultrasound studies to frequencies of 2–6 MHz. 5 MHz produces the strongest echoes for vessels under 2 cm of tissue, deeper vessels, and those behind the skull require 2 MHz ultrasound waves to penetrate these tissues [21.64–66].

In many examinations, Doppler measurements from blood adjacent to the wall are desired, so Doppler echoes from the voxel next to the wall will include strong wall echoes as well as weak echoes from the adjacent blood. Unfortunately, vascular walls move with velocities near 2 mm/10 ms or 0.2 m/s (20 cm/s). The strong echoes from these moving walls must be rejected to reveal the adjacent blood velocity, which may be only slightly higher than 20 cm/s. The strong echoes from the wall are called clutter. 10 bits of the system dynamic range are required to handle the clutter and the blood echoes must be resolved above that, so most ultrasound systems now utilize a 14–16 bit dynamic range, which is achieved by combining the outputs of separate digitizers (one for each transducer) and digitizing faster than the required four times the ultrasound center frequency, then filtering the result for processing.

Pulsed Doppler Spectral Analysis. To measure the Doppler frequency shift, any method of frequency analysis can be used. Zero-crossing rate meters and zero-crossing time interval histograms have been replaced with real-time spectrum analyzers. Although the time-compression analyzer produces identical results, the popular fast Fourier transform (FFT) analyzer is used to produce spectral waveforms of Doppler signals

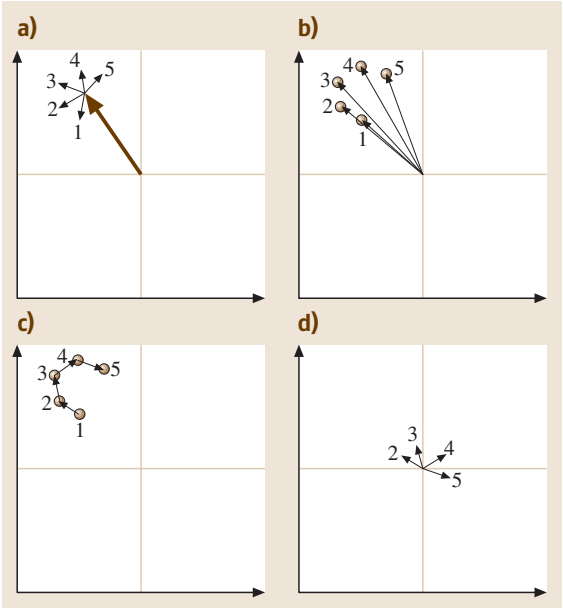


Fig. 21.49a–d Autocorrelation clutter (high-pass) filter. By representing each pulse-echo from a particular depth as a point on a phase diagram, the trajectory of the echo phase in time can be plotted. **(a)** The Doppler echo comes from two types of reflectors, strong reflecting stationary structures (*clutter*) and weak reflecting moving blood cells. In each of the five pulse-echo cycles (ensemble or packet of 5), the contribution from the strong reflectors is the same. The moving blood cells reflect the same amplitude (vector length) but a different phase during each pulse-echo cycle. **(b)** The ultrasound receiver cannot differentiate the clutter contributed by the stationary structures from the signal contributed by the moving blood cells. High-pass filter. **(c)** By taking the difference between successive results, the effect of the clutter is eliminated. **(d)** By centering the resultant vectors on a new phase diagram, the phase angle change between each pulse-echo cycle can be used to compute the blood velocity

(Figs. 21.47, 21.48). The FFT analyzer is coupled to the pulsed Doppler so that the FFT analyzer receives a quadrature pair of data from the depth of interest for each pulse-echo cycle. The advantage of the spectral analysis is that if the voxel contains several flow velocities, the FFT spectrum will display the Doppler frequency for each velocity. Unfortunately, in blood flow, eddy oscillation frequencies up to 500 Hz occur; the typical FFT length of 10 ms (100 spectra per second) is only capable of resolving eddies of 50 Hz or lower. When a voxel contains higher-frequency eddies, the re-

sult appears as spectral broadening or as harmonics on the spectral waveform.

Pulsed Doppler Autocorrelation. Autocorrelation is a frequency analysis method which is an extension of pulse-pair analysis. Autocorrelation analysis assumes that there is only one valid Doppler frequency in the blood flow. Autocorrelation analysis identifies that frequency. However, to reject the stationary and slow moving strong echoes of the wall, a clutter filter must be applied. Clutter is a stationary echo superimposed on the changing Doppler echo. The analysis is based on an ensemble of N echoes, usually eight echoes. The difference between adjacent pairs of echoes n and $n-1$ (for $n=2,\ N$) creates a new group of $N-1$ vectors (Fig. 21.49). By taking the average of the change in angles, a Doppler velocity can be obtained. Sometimes two filtering steps are required rather than one. Such filters are called finite impulse response (FIR) and infinite impulse response (IIR) filters.

Time–Domain Velocimetry. The Doppler equation contains the Doppler frequency and the phase angle. Doppler signals are subject to aliasing when the between-pulse phase angle change ($\Delta\phi$, a circular variable) has a value greater than π. In addition, echoes from deep tissues have a lower center frequency than echoes from shallow tissues, causing confusion about the correct value of the ultrasound frequency f_{us} to use in the equation.

$$\frac{v_f}{c} = \frac{\frac{\Delta\phi}{\Delta t}}{f_{us}\, 2\cos\theta_D}\,. \qquad (21.17)$$

Of course, the center frequency of deep echoes is still within the bandwidth of the transmitted ultrasound; the center frequency is depressed because of the greater attenuation of the higher-frequency portions of the transmitted bandwidth.

Since bandwidth is inversely proportional to pulse duration and pulse duration is related to spatial resolution, it is desirable to have a short pulse duration so that spatial resolution is as small as possible. This means broadband pulses, permitting depression of the center frequency of the echo. The desire for improved resolution and the desire to avoid aliasing combine in the use of time-domain velocimetry as an alternative to Doppler.

$$\frac{v_f}{c} = \frac{\frac{\Delta\tau}{\Delta t}}{2\cos\theta_D}\,. \qquad (21.18)$$

In time-domain velocimetry, two successive ultrasound echoes are compared to see if a time shift ($\Delta\tau$) has occurred in the echo in the intervening time (Δt), which indicates tissue motion. By measuring the time shift, the velocity can be calculated. Of course, clutter from solid tissue in the voxel may provide a substantial stationary echo superimposed on the small shifted echo. To remove the clutter echo, subtraction of adjacent pairs

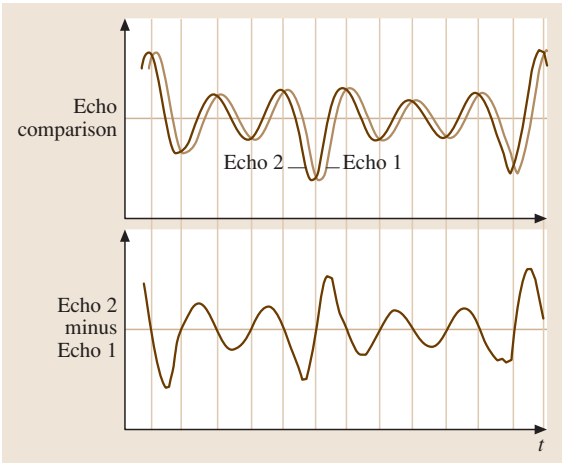


Fig. 21.50 Time-domain demodulation removing clutter. To remove clutter in time-domain demodulation, the RF echo signal from each pulse-echo cycle is subtracted from the preceding RF echo signal to yield the residual due to tissue motion

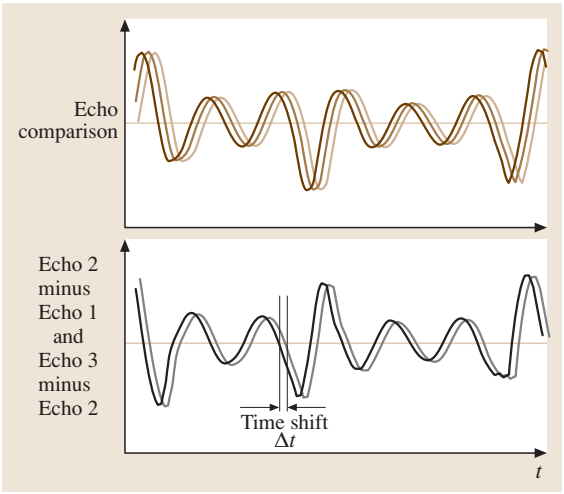


Fig. 21.51 Time-domain demodulation measuring the velocity component. By measuring the time shift between successive echo pairs, multiplying by half the ultrasound velocity and dividing by the pulse repetition interval time, the velocity of the tissue along the ultrasound beam results

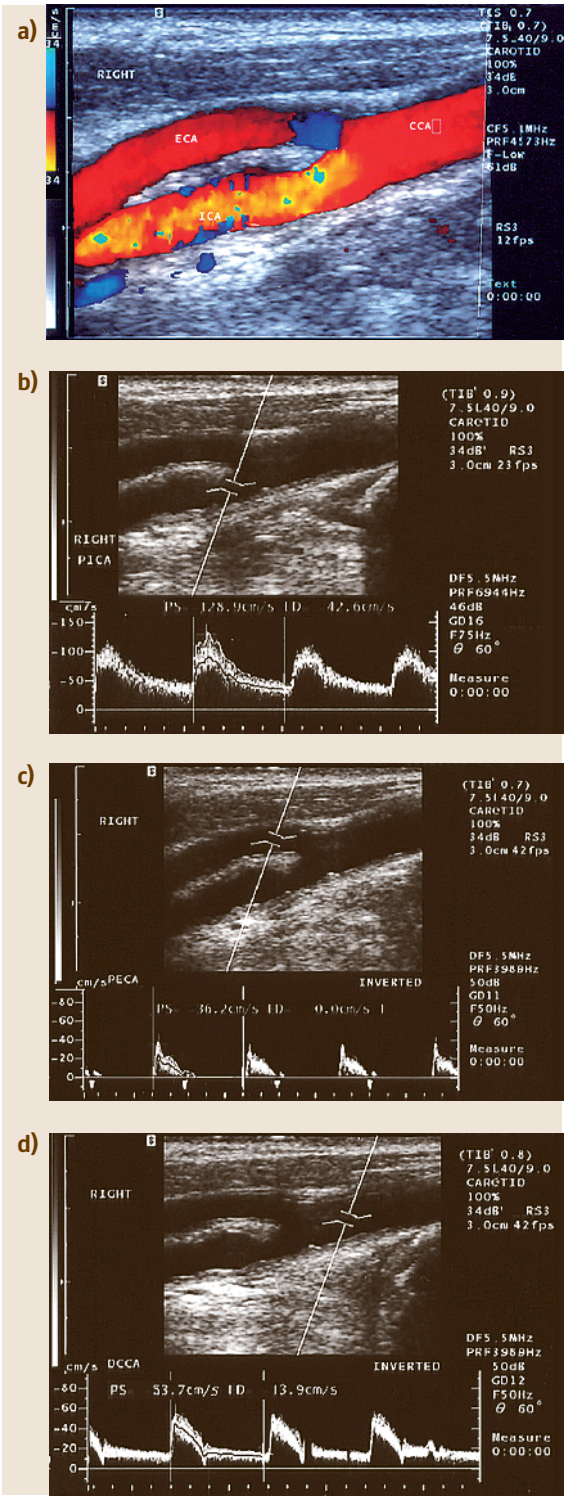


Fig. 21.52a–d Ultrasound images from a conventional carotid artery Doppler examination in the neck [21.67]. *Orientation*: a linear array transducer located at the top of each image acquires the 128 vertical scan lines in sequence across the 35 mm-wide image. Two of the monochrome B-mode images **(c)** and **(d)** were acquired in 24 ms (42 frames per second) so the scan lines progress across the image at a speed of (35/24) 1.46 m/s, a speed similar to blood velocity. The color flow image **(a)** was acquired at 12 fps; the other monochrome image **(b)** was acquired at 23 fps. *Anatomy*: **(a)** ECA external carotid artery supplying the face, ICA internal carotid artery supplying the brain, CCA common carotid artery from the heart via the Brachiocephalic trunk. **(a)** Color Doppler image of the carotid bifurcation. The color scale on the left of the image shows that forward flow is shown as *red* and reverse flow is shown as *blue*. The flow directions are with respect to the transducer array at the top of the image rather than with respect to the heart to the right of the image. The blue region at the origin of the external carotid artery shows that the vertical component of the velocity vector is pointing toward the ultrasound transducer rather than showing that flow is reversed toward the heart. Notice that this region is bounded by black bands indicating *zero* velocity toward the transducer. The *blue spots* in the lumen of the internal carotid artery are aliasing (Fig. 21.47). Notice that each of those regions is surrounded by an *orange* color indicating high blood velocity components with respect to the transducer. *Doppler waveform orientation*: each of the three Doppler waveforms is acquired from an ultrasound beam pattern that is tilted at an angle with respect to the transducer, selected by the examiner to form an angle of 60° with respect to the artery axis. **(b)** *lower* Normal Doppler spectral waveform from the internal carotid artery with high diastolic flow. Because the brain continuously requires 10% (10 ml/s) of the cardiac output (100 ml/s), the peripheral resistance is low so blood flows to the brain during systole and diastole. **(c)** *lower* Normal Doppler spectral waveform from the external carotid artery with low diastolic flow. Because the face at rest requires little blood flow but when active (chewing, blushing) requires more blood flow, at rest the arteriolar sphincters are constricted, only accepting blood flow during systole. When the arteriolar resistance decreases, the external carotid also has flow during diastole. **(d)** *lower* Normal Doppler spectral waveform from the common carotid artery which has the combined internal and external flow waveform. A pulsatility index showing the ratio between the diastolic and systolic velocities is sometimes used to classify waveforms

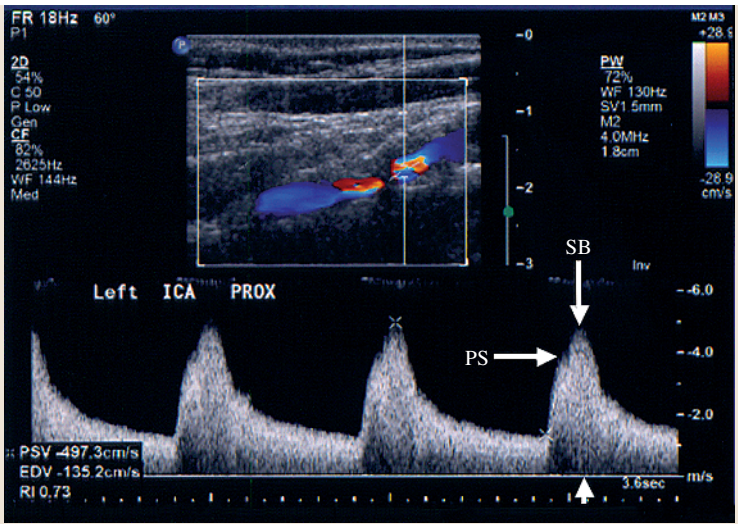


Fig. 21.53 Stenotic internal carotid artery. Even after 25 years of exploring the meaning of carotid artery spectral waveforms, there is no agreement on how the data should be interpreted. Although this color Doppler image shows an interruption in the color flow image of the lumen, the interruption is not due to an arterial occlusion, but to a local region of high ultrasound attenuation which causes the color Doppler signal to drop out. Thus, the diameter of the color Doppler streak cannot be used to assess the lumen. In this case, the vessel walls cannot be easily seen. A stenosis is present at the Doppler sample volume as indicated by the high velocity. The spectral waveform is confusing. The highest Doppler frequency shift which was measured by the examiner 220 ms after the onset of systole at 497.3 cm/s is probably not accurate because the measurement is at the time of greatest spectral broadening (SB), indicating eddies in the flow. Use of the Doppler equation is not appropriate for these eddy velocities because the heading of the vectors is not known. The true peak systolic (PS) velocity probably occurs 100 ms after the onset of systole where the measurement is near 4 m/s and the Doppler equation is probably accurate if the velocity vector is assumed to be parallel to the artery axis. An appreciating of the difference between the believed accuracy of 497.3 cm/s versus 'about 4 m/s' is important because of the clinical decisions that result. The PSV is used to decide whether a patient with symptoms of mini-stroke should have surgery. In this case, the end diastolic velocity (EDV) is measured at 135.2 cm/s. An EDV value exceeding 140 cm/s in a single measurement would cause a vascular surgeon to schedule the patient for carotid endarterectomy surgery even if the patient has no symptoms

of echoes (Fig. 21.50) provides the difference waveform containing the motion information. Then the time shift between difference waveforms can be measured (Fig. 21.51).

A comparison between the time-domain equation and the Doppler equation shows that $\Delta\tau = \Delta\phi / f_{us}$. This indicates that it is the demodulator frequency, not the frequency of the echo, that is relevant for the Doppler equation; the former must be close (and is usually equal) to the transmitted center frequency, i. e., the frequency required in the Doppler equation. There are substantial differences between the Doppler and time-domain systems. First the time-domain system usually transmits a broadband, short ultrasound pulse. The signal-to-noise ratio of the echo is determined by the transmit pulse energy. To achieve the same energy in a short pulse, the temporal peak power must be high, leading to a high acoustic pressure. When analyzing the time shift between the echoes, it is easiest to test for the time-lagged correlation by stepping one digitizing interval at a time. So, if the echo is digitized at a rate of 20 MHz, the digitizing interval is 50 ns ($\Delta\tau$), equivalent to a tissue displacement of 0.0375 mm. If the pulse repetition frequency is 10 kHz, so the inter-pulse interval is 100 µs (Δt), the velocity resolution is 38 cm/s (0.4 m/s). Time-domain systems usually digitize at a higher frequency and usually interpolate the wave between the measurements to improve velocity resolution. For large time shifts, when noise is present, the time domain system usually has trouble with peak hopping, associating the wrong cycles in the wave when determining the time shift. This results in a measurement error identical to

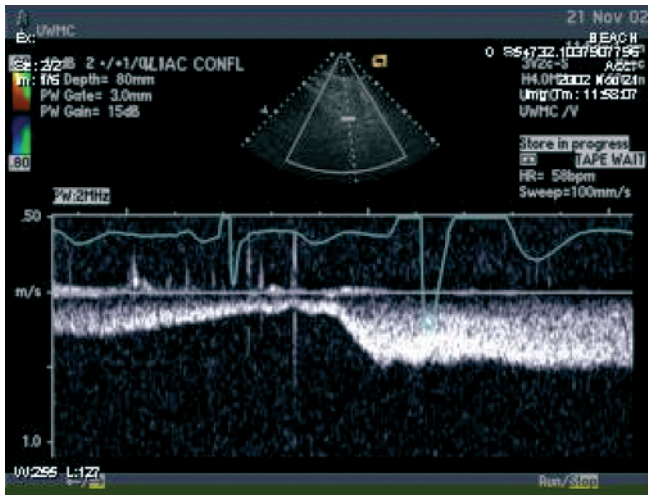


Fig. 21.54 Doppler spectral waveform signals from the inferior vena cava showing augmented flow. Doppler spectral waveforms show velocity (*vertical axis*) versus time (*horizontal axis*). In addition to the difference in flow direction, venous flow is differentiated from cardiac flow because the venous flow varies with respiration and with manual compressions of the tissues. Here the sudden increase in venous flow in the distal inferior vena cava was created by releasing an occlusion of the venous outflow from the legs. ECG tracing (*green*) shows cardiac timing. The heart beat to the right of center is due to a premature ventricular contraction, an abnormal heart rhythm which does not affect the venous flow

aliasing. So, the advantages of time-domain processing over Doppler processing, while promising, have not been fulfilled.

Clinical Applications of Ultrasound Velocimetry

The most common application of pulse Doppler ultrasound spectral waveform analysis is the examination of the carotid arteries [21.68] for stenoses that might lead to stroke (Figs. 21.52, 21.53). The measurement of high systolic (> 125 cm/s) carotid blood velocity is associated with a 20% chance of stroke in two years in a patient reporting stroke-like symptoms

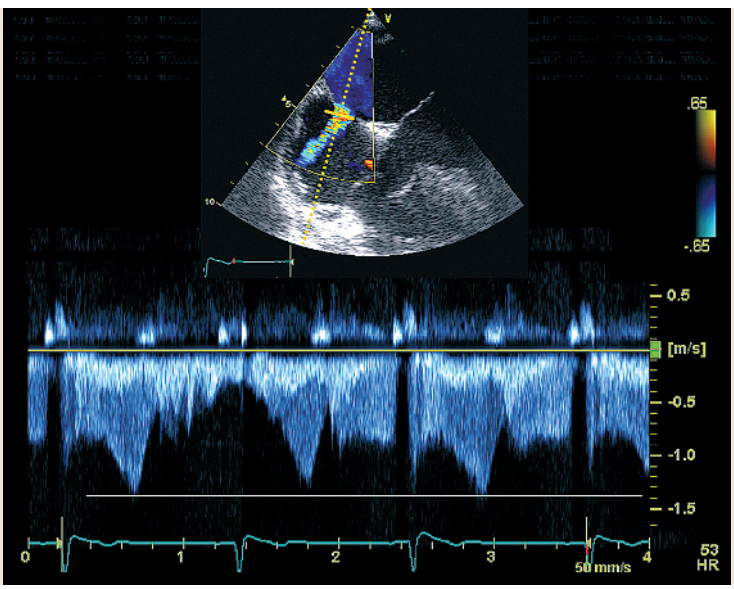


Fig. 21.55 Duplex echocardiogram of a heart with an atrial septal defect. The jet of blood from the left atrium to the right atrium can easily be seen on the color flow image. The Doppler spectral waveform taken at the center of the jet orifice at a Doppler angle of 25° to the jet shows velocities as high as 1.4 m/s when the inter-atrial pressure difference is the greatest. Correcting the velocity for the Doppler angle ($\cos 25 = 0.906$) increases the velocity value to 1.54 m/s. Cardiologists usually attempt to orient the Doppler transducer to align the jet with the Doppler ultrasound beam to achieve a *zero* Doppler angle. The pressure difference between the chambers can be computed using the Bernoulli equation for blood velocity $\Delta p[\text{mmHg}] = 4\,[\text{mmHg}/(\text{m/s})^2]\,\text{V}^2$. The pressure difference here is near 9 mmHg (courtesy Frances DeRook and Keith Comess)

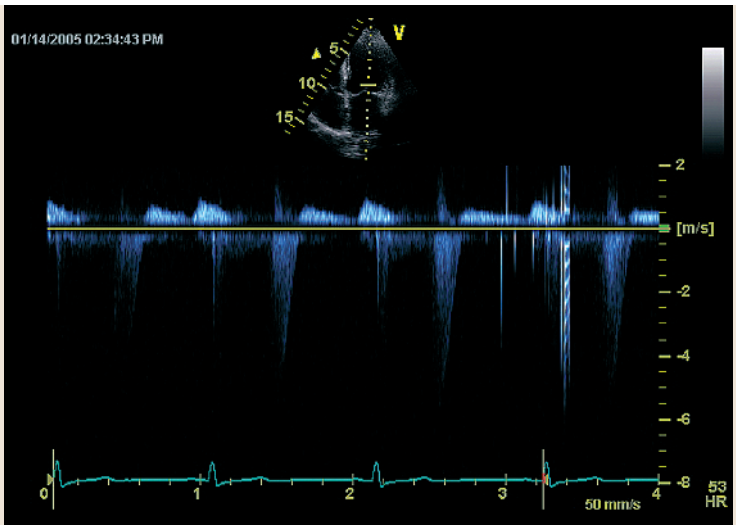


Fig. 21.56 Vibration from the mitral valve. Signals from blood flow are mixed with signals from solid tissue motion. Here, the signal of solid tissue motion is suppressed by the wall filter, which suppresses clutter at frequencies below 400 Hz. However, in this case with the Doppler sample volume in the mitral orifice, as the mitral valve closes for the fourth time, the valve vibrates at a frequency of 2 kHz for a period of 8 ms causing the harmonic (Bessel function) spectral pattern with seven harmonic terms, indicating that the amplitude of the vibration is high (courtesy Frances DeRook and Keith Comess)

(TIA = transient ischemic attack, RIND = reversible ischemic neurological deficit). The measurement of a high-end diastolic velocity (> 140 cm/s) in any patient is associated with a 20% chance of stroke in two years from emboli released from the carotid stenosis. Such findings, by themselves, can direct a patient to treatment that will prevent devastating disability.

Examination of the veins of the legs with Doppler for the detection of deep venous thrombosis (DVT) is another popular examination that can lead to life sav-

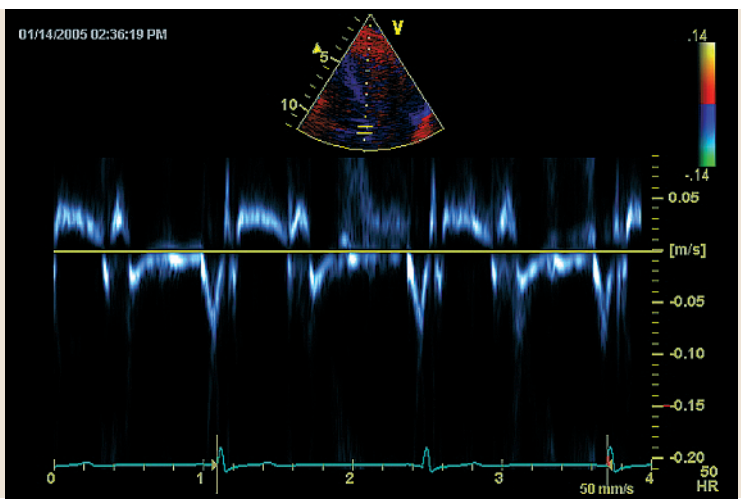


Fig. 21.57 Duplex echocardiogram tissue Doppler of myocardium. Like velocity measurements from blood flow, velocities of solid tissues can also be measured. Low velocities of the intra-ventricular septum of the heart indicates abnormal muscle contraction (courtesy Frances DeRook and Keith Comess)

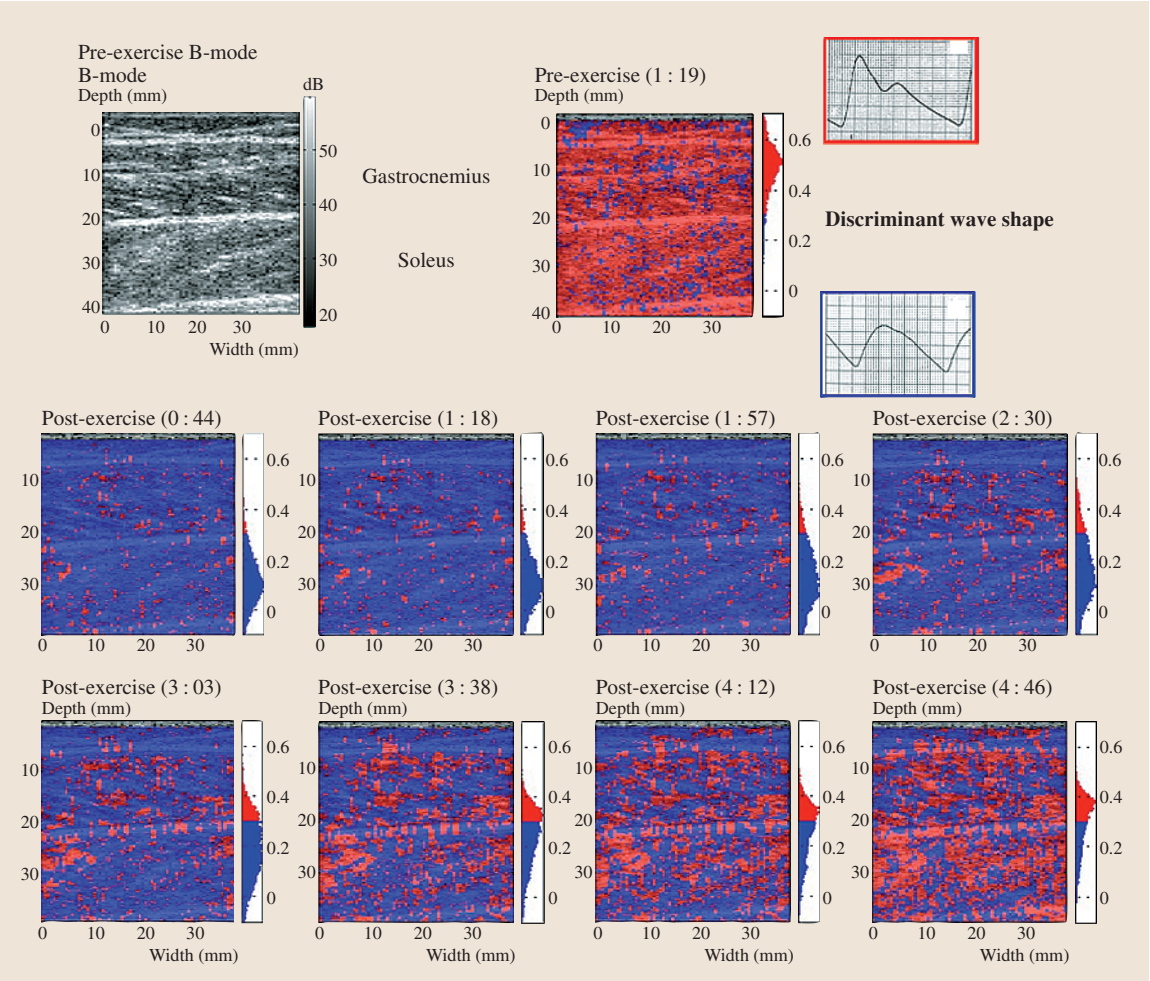


Fig. 21.58 Tissue strain in calf muscles. During tissue perfusion, different strain waveforms indicate resting perfusion (red) with high peripheral (arteriolar) resistance or hyperemic perfusion (blue) with low peripheral resistance. In this case, the calf muscle was imaged at rest, and then at intervals for a period of 5 min following a toe stand exercise. Immediately after exercise, the peripheral resistance is low to make up for the metabolic oxygen deficit after exercise. Five minutes after exercise, most of the muscle tissue has returned to the resting state (Courtesy John Kucewicz)

ing therapy. Because venous pressures are near 5 mmHg in the supine patient, normal venous flow is associated with respiration and minor local compression rather than pulsatile with the cardiac cycle (Fig. 21.54). Pulmonary embolus from venous emboli released from a DVT may account for one-third of sudden cardiac death cases [21.69]. A venous Doppler examination failing to show spontaneous venous flow with respiration indicates a venous obstruction that may be a DVT that could progress to threaten life if not treated with anticoagulation.

Cardiac Doppler examinations for blood flow are perfectly suited to characterize narrow holes between the cardiovascular structures in the chest (Fig. 21.55). By measuring the velocity of blood flow jets and applying the Bernoulli equation, the instantaneous pressure difference between the associated chambers of the heart can be measured. This works for all heart valves and wall defects so the method can be used to identify pulmonary artery hypertension as well as cardiac valve failure.

Although blood velocity through valves can be measured (Fig. 21.56), the dynamics of solid structures such

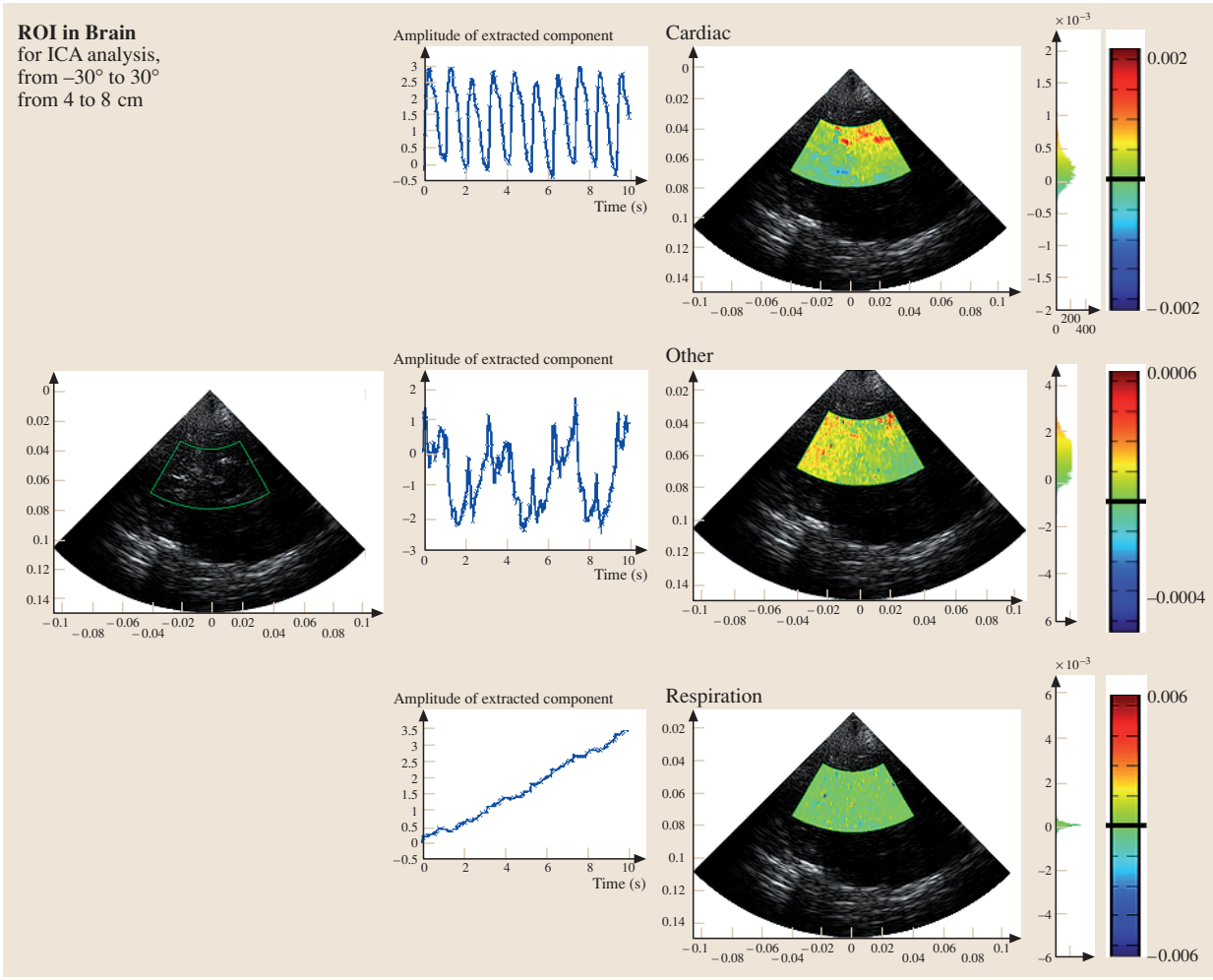


Fig. 21.59 Tissue pulsations in brain measured with ultrasonic phase gradient demodulation. Using ultrasound to measure tissue displacement over time with a resolution of 0.05 μm and differentiating motion with depth to measure strain, perfusion waveforms can be obtained. Independent component analysis of the brain perfusion signal reveals the cardiac and respiration contributions to the natural tissue strain (Courtesy Lingyun Huang)

as valve vibration, can also be characterized. By measuring the velocity of the cardiac wall, regions of poor myocardial function can be identified (Fig. 21.57).

Tissue Strain Imaging

A number of laboratories are exploring the ultrasound measurement of tissue strain [21.70] for diagnostic purposes. The most popular examinations involve the measurement of tissue response to externally applied vibration or pressure. These methods are called elastography or elastometry. During ultrasound examination, the ultrasound scan head or a nearby device is pressed on the tissue to induce a strain of several percent, either static or vibrating. By monitoring the relative motions of the tissues in response to the applied strain using Doppler or time-domain methods, the relative elastic properties of the tissues can be determined. The computation simply takes the derivative of the motion as a function of depth. To achieve 10% resolution on a 1% applied strain in 1 mm voxels requires that the ultrasound motion detection system resolve 1 μm tissue displacements. This requires a 1 GHz digitizing rate for a time-domain system without interpolation. A Doppler system with 6 bits

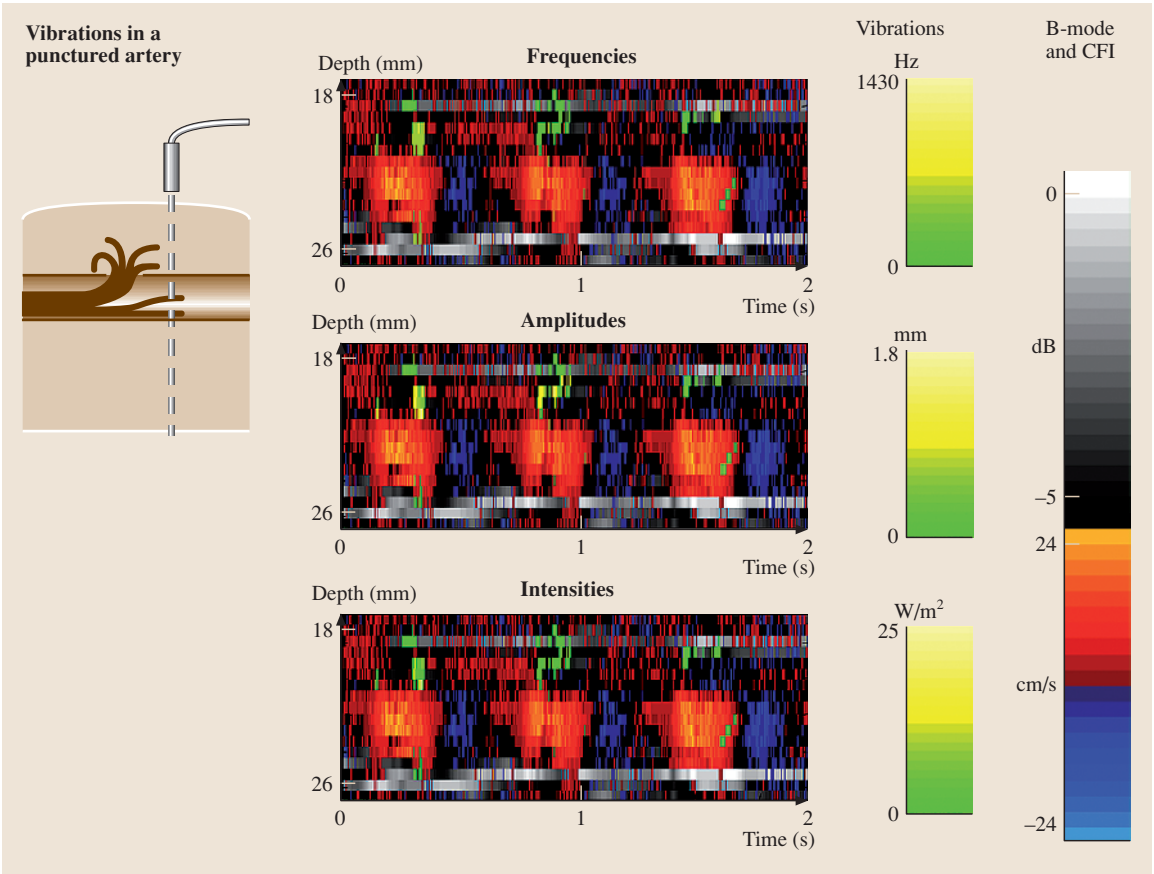
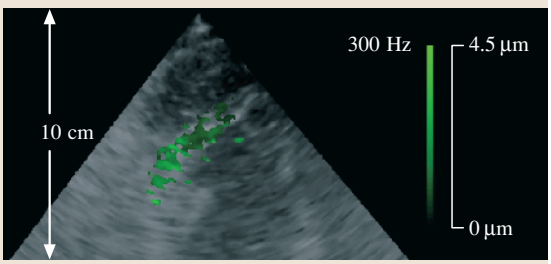


Fig. 21.60 Tissue vibrations of a punctured artery. Flow through any small orifice which results in a pressure drop can cause vibrations. Arterial bleeding can be detected by searching Doppler signals for such vibrations. (Courtesy M. Paun, M. Plett)

of dynamic range can achieve a 1 μm displacement resolution.

60 – 70% focal stenosis in top third of RCA
Apical view



Center frequency: 2 MHz; PRF = 1 kHz; ensemble = 10

Image Computing Systems Laboratory, Electrical Engineering

More challenging is to examine the natural tissue strain that occurs as the tissue fills and empties of blood each cardiac contraction and each respiratory cycle. Normal tissue strain for arteriolar filling is 0.1%. To resolve 0.1% strain with 10% resolution in 1 mm voxels requires the resolution of 0.1 μm displacements. This requires Doppler demodulation of a 5 MHz echo with at least 9 bits of dynamic range. Ultrasound pulsatil-

Fig. 21.61 Vibration of a coronary artery stenosis. Flow through any small orifice which results in a pressure drop can cause vibrations. Flow though a stenosis causes a bruit (Fig. 21.2), or murmur which can be detected and measured with ultrasound. These 4.5 μm-amplitude 300 Hz vibrations on the surface of the heart at the location of a stenosis in the right coronary artery occur only in diastole when the coronary flow rates are the highest. (Courtesy S. Sikdar, T. Zwink, S. Goldberg)

ity images can be made of most body tissues including muscle (Fig. 21.58) showing physiological responses to stresses, and brain [21.71] (Fig. 21.59) showing the separate effects of pulse and respiration.

Tissue Vibration Imaging

Several pathological conditions are associated with the presence of tissue vibrations. These were discussed at the beginning of the chapter where the detection of the vibrations with a stethoscope was described. Of particular interest are vibrations associated with arterial stenosis and vibrations and motions associated with internal bleeding [21.72]. Using the same Doppler demodulation methods, but filtering for the cyclic motions of the highly echogenic solid tissues rather than the continuous motions of the poorly echogenic blood, vibrations can be detected and rendered as an image showing pathologies such as arterial bleeding (Fig. 21.60). The amplitude and frequency of the vibrations are characteristic of the rate of bleeding. Arterial stenoses including stenoses of the coronary arteries (Fig. 21.61) can be demonstrated in vibration images.

Modern Ultrasound Scanners

Real-time diagnostic ultrasound scanners changed little on the outside between 1975 and 2000; they are narrow enough to fit through a doorway (Fig. 21.62) and draw less than 1.5 kW of electrical power from a standard power outlet in the hospital wall. However, inside the systems have evolved from analogue devices to digital devices (Fig. 21.63), with the conversion to digital processing determined by cutting-edge computer technology. Now an ultrasound scanner with a full array of functions is constructed from software, using a Windows laptop computer (Fig. 21.64) or a custom box. Ultrasound systems can be produced inexpensively and can obtain the diagnostic results automatically, so that a patient can use the system for self-management of some conditions (Fig. 21.64).



Fig. 21.62 Modern ultrasound imaging system. During the quarter century between 1975 and 2000, ultrasound systems retained the same exterior design, mounted on wheels, narrow enough to fit through a doorway, light enough that a sonographer could push the system, short enough so that a sonographer could see over the top and powered by a 1.5 kW outlet. To the right is the key to good ultrasound diagnosis, the well-trained, certified, experienced ultrasound examiner

21.5 Medical Contrast Agents

Contrast agents are used in medical imaging to make invisible structures visible. Contrast agents can be classified by anatomic/application: intraluminal/intracavity, excretory, diffusional, and chemotactic. Contrast mechanisms include reflection, absorption, fluorescence, emission and nuclear resonance frequency shift.

Intraluminal/intracavity agents are used to visualize the cardiovascular system, gastrointestinal system, reproductive system, body cavities, and other spaces. The contrast agent is injected into the space, where it spreads throughout the structure of interest. Excretory systems are used to visualize the renal system [excretory urogram or intravenous pyelogram (IVP)] or gall bladder and bile duct (cholangiopancreaticogram). The contrast agent is injected into the venous system and is excreted in concentrated form by the target organ. Because of the concentrating action of the kidney, a contrast agent in the urine will be 100 times more concentrated than in the blood. Diffusional agents are injected into the venous system and diffuse into the interstitial space through leaky capillaries. Newly formed capillaries are leaky, and such diffusion may mark local angiogenic factors secreted by tumors or retinopathy. Contrast magnetic resonance imaging (MRI) for breast tumor detection and fluorescene angiography of the retina are examples of diffusional agents. Chemotactic agents are injected into

Amazon EX1014 Page 887

the veins and diffuse into the interstitial space through normal capillaries, where they bind to tissues of interest such as tumor cells. The time between the injection of a chemotactic contrast agent and the imaging study is several hours. This method is common in nuclear medicine imaging.

Ultrasound contrast agents cause increased backscatter of ultrasound and often cause the generation of harmonics. X-ray contrast agents contain heavy nuclei which absorb X-rays to provide contrast. Fluorescene, indocyanine green and other dyes are activated by high-energy (short-wavelength) photons and emit longer-wavelength photons, which are detected by optical camera systems. Chemotactic chemicals prepared with short-half-life (hours) nuclear isotopes are prepared and injected within a few hours. After allowing time for the agents to accumulate in the tissues of interest, the sources of radiation are imaged with pinhole or collimation nuclear radiation cameras. Gadolinium is used as a contrast agent in nuclear magnetic resonance imaging. The paramagnetism of gadolinium decreases the T_1 and T_2 relaxation times, which are displayed in the MR image.

21.5.1 Ultrasound Contrast Agents

The first intravenous ultrasound contrast agents [21.73] were large bubbles generated by intravenous injection of indocyanine green [21.74], other injectable liquids including saline and blood [21.75–77], and finally agitated saline [21.78]. These bubbles were so large that they would not pass through capillaries, so appearance in the left heart or arteries was proof of a shunt bypassing the lungs. These bubbles were generated inadvertently or deliberately by flow-induced cavitation. The bubbles contained air that was dissolved in the blood. These bubbles generated strong ultrasound reflections because of the large difference in ultrasound impedance between the body (water) and the air in the bubbles. Small bubbles were not stable, so only large bubbles survived.

Currently, most commercial ultrasound contrast agents are small bubbles or particles, which are able to pass through the capillaries of the lungs but are confined to the vascular system. Some ultrasound contrast agents are solid particles smaller than a micron in diameter. These are Rayleigh scatters of ultrasound at the fundamental frequency. Most ultrasound contrast agents are bubbles about 3 μm in diameter (Fig. 21.65) so that they will pass through pulmonary capillaries and recirculate in the cardiovascular system. They are also Rayleigh scatters, but because they oscillate, they convert the fundamental ultrasound frequency into harmonics because of the nonlinear properties of their oscillation.

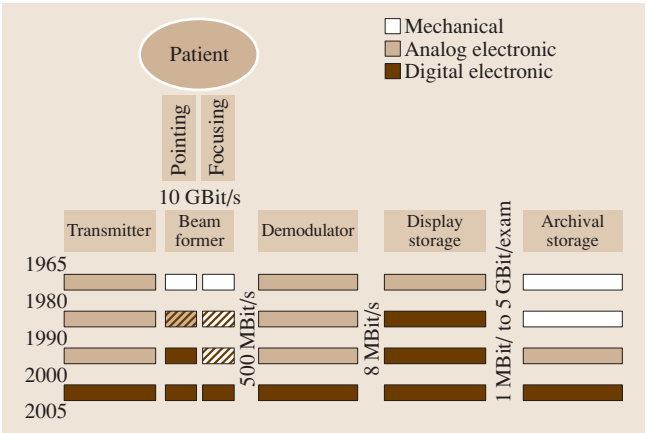


Fig. 21.63 Diagnostic ultrasound signal processing history. The amount of data transferred between the stages of the ultrasound signal-processing chain is a minimum around the display, the display systems were converted to digital processing during the early years of digital technology development. Beam forming occurs in two directions: in the plane of the image, where the evolution from mechanical to analog to digital proceeded with time, and perpendicular to the plane of the image, where mechanical focusing was replaced by digital electronic focusing and then steering with the advent of transducers segmented into two-dimensional arrays. Pointing of the ultrasound beam between 1980 and 1990 was done digitally in linear array raster scans by switching on selected transducers in the array, but in phased-array sector scans the direction of the beam was determined by adjusting the phase delay with nanosecond resolution on each transducer. Because analog signals have a continuum of possible signal levels, small differences in analog signals can be extracted as long as the differences are greater than the noise in the signal. Once a signal is digitized, no noise is added to the signal by processing. The 10 GBit/s data rate on the receiving path is based on the assumption that the transducer is divided into an array

21.5.2 Stability of Large Bubbles

The size of stable bubbles can be estimated from physical principles. The gas inside a stable bubble of radius r (Fig. 21.65) is under a pressure equal to the sum of the ambient atmospheric pressure plus the fluid pressure (1 atm = 10 m of water), and the pressure generated by the surface tension of the interface between the contained gas and the external fluid (water). In the body and in carbonated beverages, the depth of the bubbles is

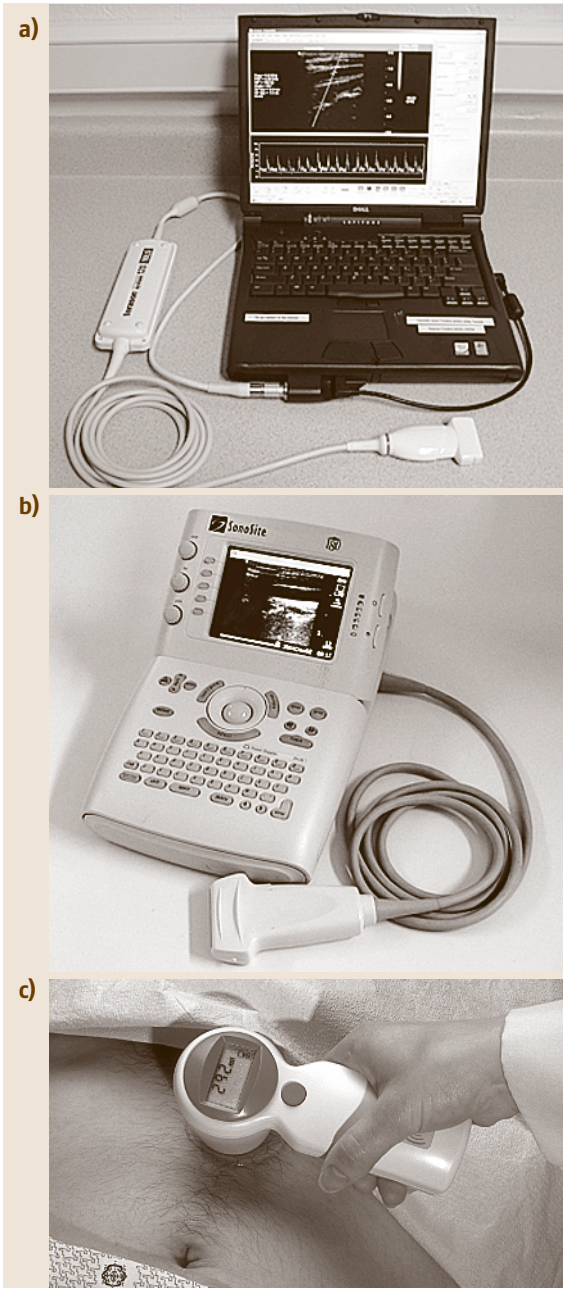


Fig. 21.64a–c Two small ultrasound imaging systems, based on the request of the Defense Advanced Research Project Administration for general-purpose handheld systems with full function **(a)** and **(b)** and an application-specific imaging system. **(a)** Terason scanner using a laptop computer; **(b)** SonoSite scanner using custom electronics; **(c)** Application-specific ultrasound scanners (BladderScan) are palm-sized and fully automatic. This instrument shows no image, but displays the volume of urine in the bladder as a number or an alarm, depending on the application

small compared to 10 m of water, so the pressure added because of the depth of the fluid can be ignored compared to atmospheric pressure. A force balance on the equator of the bubble equates the pressure force $P\pi r^2$ to the surface tension force $\sigma 2\pi r$. Thus the pressure in the bubble above the ambient pressure is $P = 2\sigma/r$. In the absence of a surfactant, the surface tension of water is 70 d/cm. When $r = 1.4\,\mu$m, $P = 1$ atm; this is a huge chemical potential to drive the contained gas into solution. If a bubble is 0.14 mm in diameter, too large to pass through a capillary (red blood cells are 8 μm in diameter), then the pressure elevation in the bubble caused by surface tension is 0.01 atm and the gas contained in the bubble has a low driving force to diffuse into solution. So, large bubbles are more stable than small bubbles. If the surface tension is reduced by applying a surfactant (shell) to the bubble, then small bubbles become stable. If the gas contained in the bubble is less soluble in blood and/or has a low diffusion constant, then the bubble has a longer life.

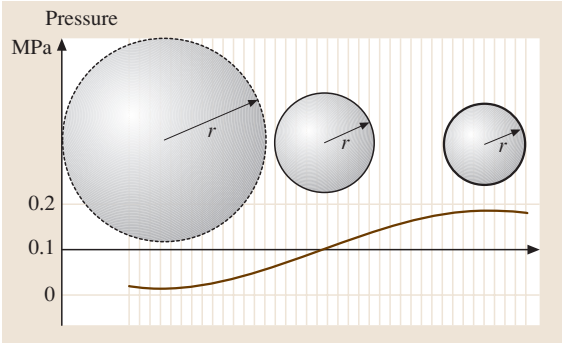


Fig. 21.65 Contrast agent bubble. An ultrasound contrast bubble is a system consisting of a gas inside the bubble, a surfactant, a surrounding liquid, and solutes including gases and surfactants in the liquid solvent. Thermodynamics and the transport of heat and of the dissolved gasses and dissolved surfactant materials all contribute to the response of a bubble to ultrasound exposure. Interactions between bubbles are also important factors in contrast agent dynamics. Here are the expected sizes for a bubble based on an isothermal ideal gas model without considering surface tension for an ultrasound intensity of 87.5 kPa

Amazon EX1014 Page 889

21.5.3 Agitated Saline and Patent Foramen Ovale (PFO)

Agitated saline contrast bubbles are generated by forcing fluid rapidly through a small orifice, such as an injection needle. They have an important diagnostic application: to determine whether there is a shunt from the right heart to the left heart, bypassing the lungs. The most common of these shunts is the *patent foramen ovale* (PFO). PFO may be a cardiovascular defect of considerable medical importance. If a person under the age of 50 has a stroke due to occluded vessels in the brain (ischemic stroke), the most likely cause is a PFO. One affected group is divers, who return from great depths with large amounts of gas dissolved in their body tissues, especially in fat. Bubbles which form in the low-pressure venous system as the gas is transported toward the lungs, might pass through a PFO during a cough, releasing these large bubbles into the arterial system where they cause occlusion of arteries and ischemia of the tissues that were supplied by the arteries. Ischemia of some tissues might be unnoticed. Ischemia of other tissues might cause pain that is ignored. Ischemia of some portions of the brain might result in undetected changes in personality or memory. Only ischemia of the motor and sensory cortices of the brain causes loss of sensory and motor function that are recognized as stroke symptoms. In divers, these symptoms are called neurological symptoms of the bends, in others they are called transient ischemic attacks (TIA) or stroke, depending on whether the symptoms last less than 24 h or longer than 24 h, respectively.

The foramen ovale is a normal structure before birth, along with the ductus arteriosus, allowing the blood to circulate in parallel through the fetal body, lungs and placenta. At birth, with the muscular constriction of the ductus arteriosus to obliterate the lumen, pressure shifts cause the flap valve of the foramen ovale to close and over time it will seal in most people. However, in some people the foramen ovale does not seal, opening occasionally when the person coughs or strains. The prevalence of PFO in the general population is 30% at age 20 and 10% at age 70. The reason for the decline in prevalence is either because in some people the foramen seals after age 20 or because these people suffer repeated embolic events from the venous to the arterial circulation, which progressively damage body organs leading to failure and death. In the absence of PFO, such venous emboli pass to the lungs where they temporarily occlude portions of the lung, but resolve over time.

The importance of the diagnosis of PFO is currently disputed, but two factors may make testing for PFO a part of every physical examination:

1. the cost of the contrast agent is only the 2 min that it takes to handle off-the-shelf saline and
2. recently catheter methods of sealing a PFO have been released for testing, avoiding the need for open-chest heart surgery to seal the defect. If 2/3 of the

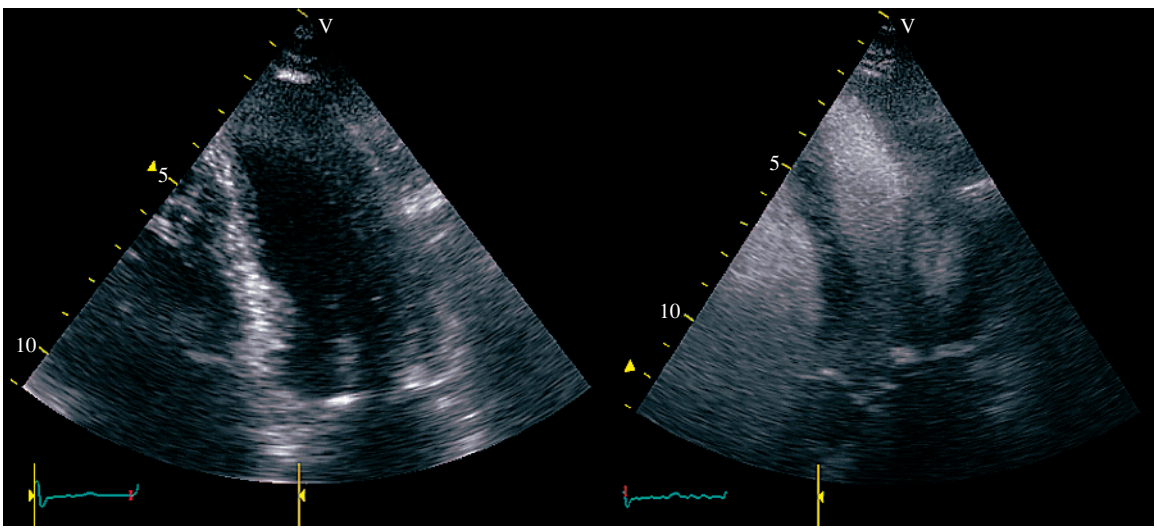


Fig. 21.66 Two-dimensional B-mode real-time echocardiogram of the left ventricle. *Left*: left ventricle without ultrasound contrast agent. *Right*: left ventricle with intravenously infused Optison ultrasound contrast agent (courtesy Frances DeRook and Keith Comess)

Amazon EX1014 Page 890

people with PFO at age 20 die before the age of 70, this diagnosis would be an issue of considerable importance.

21.5.4 Ultrasound Contrast Agent Motivation

The case for the development of stable ultrasound contrast bubbles small enough to pass through the capillaries of the lungs and appear in the systemic arteries is based on the wide use of ultrasound in medical imaging. Over half of all medical imaging is done with ultrasound, so there are many potential applications for contrast agents. Because these mechanical agents are confined to the vascular space, they cannot provide contrast in excretory, diffusional or extravascular chemotactic applications. Blood is a poor reflector of ultrasound, generating echoes 60 dB below the echoes from vascular walls. Contrast agents increase the backscatter. In most cases, the detection of blood flow is easy by Doppler methods which can reject the high-intensity stationary echoes from vascular walls and detect the moving echoes of blood using Doppler methods. However, in cases where the blood is moving slowly, these methods are more difficult and there is an advantage from the increased echo signals produced by contrast agents. Thus, in identifying the exact location of endocardium (Fig. 21.66), in regions deep within strong attenuators (such as skull) and for blood flow in capillaries, contrast agents promise to provide important additional diagnostic information.

21.5.5 Ultrasound Contrast Agent Development

Ultrasound microbubble contrast agents have been under development for a quarter century [21.79]. The first task in the development of microbubble contrast agents was to make stable bubbles small enough so that they could pass through the capillaries of the lungs (about 3 μm in diameter) after injection into the venous system, and stable enough to survive long enough to be useful (more than 1 min, preferably 30 min). Three strategies are available to stabilize the microbubbles:

1. lower the surface tension,
2. form bubbles of a gas with low solubility or diffusivity in water/blood and
3. produce a gas-impermeable barrier at the gas–liquid interface.

Surfactants lower surface tension; fluorocarbons have low solubility in water/blood; polymeric shells can be impermeable to gas diffusion. A series of contrast agents have been developed based on various combinations of surfactant, contained gas and method of formation.

The behavior of ultrasound contrast agent microbubbles is complicated and can easily consume an entire career. Only a few factors will be mentioned here. A microbubble consists of three phases: the contained gas, the surfactant, and the surrounding fluid. The size distribution of the bubbles is determined by the method of formation. Air-filled albumin-coated microspheres can be formed by whipping a mixture of albumin and water in a blender. This forms a broad distribution of microspheres. The desired size can be selected by centrifugation or flotation. A more nearly uniform microbubble size can be achieved by metering the relative volume of surfactant and gas through a calibrated nozzle orifice. The relative amounts of gas and surfactant are determined by the desired surface to volume ratio. The speed of bubble extrusion is crucial to the formation of bubbles of stable size. If prepared for medical use, in addition to a sterile preparation, formed using Food and Drug Administration (FDA)-approved good manufacturing practice, the agent must have sufficient stability and shelf life to permit distribution, storage and timely preparation for use.

When released into blood, the contained gas is usually not at equilibrium with the dissolved gases in the blood. A microbubble filled with fluorocarbon will take up nitrogen, oxygen and carbon dioxide without releasing much fluorocarbon, so the microbubble will swell after injection. The amount of swelling will depend, in part, on the amount and properties of the surfactant. If the bubble swells so that the surface area begins to exceed the available surfactant, the surface tension rises. This may favor bubble coalescence. As the microbubble passes through the lungs, some of the contained fluorocarbon will be released. Gas exchange between the microbubble and the dissolved gas in the blood is continuous during the life of the bubble. Some surfactants and some contained gases have chemical or physical affinities for the interior surfaces of the cardiovascular system of the lungs, arteries, capillaries or veins. The bubbles may become specifically adsorbed to the endoluminal surfaces of these vessels. This can be accidental or deliberate, and can become part of the functionality of the contrast agent. When specifically adsorbed, the surfactant may migrate to the vascular surface or may take on molecules from the vascular surface or surroundings. Of course, the contrast agent might be taken up by cells,

Amazon EX1014 Page 891

transported by those cells and/or retained in particular tissues or organs.

21.5.6 Interactions Between Ultrasound and Microbubbles

When exposed to ultrasound at diagnostic frequencies (1–20 MHz), the contrast bubbles will oscillate at the driving frequency of the ultrasound, emitting the fundamental frequency as well as harmonics of the fundamental frequency. Microbubbles have a natural resonance frequency, primarily determined by their size, surface tension, shell rigidity (if any) and the density of surrounding material. If stimulated at a frequency near the resonant frequency, the amplitude of oscillations will be greater. The pressure of the interior gas varies with volume according to the rules of adiabatic compression and expansion, at least to the extent that the process is too fast for heat transfer. Although the waveform of the oscillation is primarily determined by the waveform of the driving ultrasound, the surfactant forces also play a great role in this process. When the ultrasound pressure is high (for 0.3 μs) the gas compresses, the temperature raises, the water vapor pressure increases as does the pressure of other gases. The gas pressures rise above the surrounding partial pressures of gas, providing a driving force to move gas out of the bubble into solution. Because the bubble is small, the surface area available for heat and mass transfer is small, and the amount of loss of heat and gas is small. Alternatively, when the ultrasound pressure is low (the subsequent 0.3 μs), the pressures and temperature drops, providing driving forces for heat and gas to enter the bubble. Now the surface area is large and it is easy for transport into the bubble, leading to rectified diffusion of gas and heat into the bubble.

At the body temperature of 37 °C, the vapor pressure of water is 6.2 kPa, 6% of atmospheric pressure. An acoustic wave of 285 mW/cm^2 SPTP (spatial peak temporal peak) intensity drops the pressure in a bubble below the vapor pressure of water (ignoring surface tension) which will cause the water to vaporize, filling the bubble with water vapor in addition to the other contained gasses. The latent heat of evaporation lowers the temperature of the bubble. On compression, the recondensing of the water adds heat to the bubble. When the ultrasound is compressing the bubble, the surfactant acts as a stable skin. The skin may even exhibit negative surface tension. Like the hull of a submarine deep in the ocean, the surfactant may hold the bubble gas pressure lower than the surrounding pressure. Similarly, when the ultrasound pressure has dropped below ambient, and the bubble expands to form a larger surface area, the surfactant, which is often a monolayer of molecules on the surface, will change in configuration, become patchy and result in increased surface tension, holding the internal gas pressure higher than expected from the surrounding pressure. As there is a driving force for the gaseous contents of the microbubble to experience rectified diffusion, there is also a driving force for the surface phase to experience rectified diffusion, changing the composition of the surface. A stable molecular monolayer on the surface of the bubble at one bubble volume will become compressed when the bubble becomes small, providing a driving chemical potential to both change the phase of the monolayer to a multilayer and to drive some of the surfactant into solution. The monolayer will be expanded when the bubble becomes large, providing a driving chemical potential to draw surfactant from solution. The solution my provide surfactant materials that are similar to or different from the original surfactant on the microbubble. Unless the concentration of potential surfactants in solution is high, this process is too slow to affect bubble behavior. In experimental solutions, such concentrations may be low, but the complex mixture of complex molecules in blood may favor such a process.

21.5.7 Bubble Destruction

The first experiments with microbubble contrast agents were disappointing. Contrast agents did not produce reflections as bright as expected. Increasing the transmit intensity did not improve the strength of the echoes coming from the agents. In an effort to improve the signal strength, broadband ultrasound transducers were used to form harmonic images. An ultrasound transducer oscillates at a resonant fundamental frequency determined by the thickness. The transducer has no efficiency or sensitivity at double the frequency, although it does have one-third the efficiency and sensitivity at triple the frequency. By damping the transducer, a transducer with a center resonant frequency of 3 MHz can be made to operate at frequenciesof 1.9–4.1 MHz. In harmonic imaging to detect contrast bubbles, a 2 MHz transmit burst is applied to this broadband transducer and the receiver is tuned to 4 MHz. Echoes from tissue are expected at 2 MHz, echoes from contrast microbubbles are expected at 2 MHz and 4 MHz. By selecting only echoes at 4 MHz, clear visualization of the contrast bubbles was expected. Unfortunately, for this application, because ultrasound transmit intensities are so high, ultrasound transmission in tissue is nonlinear, generating

Amazon EX1014 Page 892

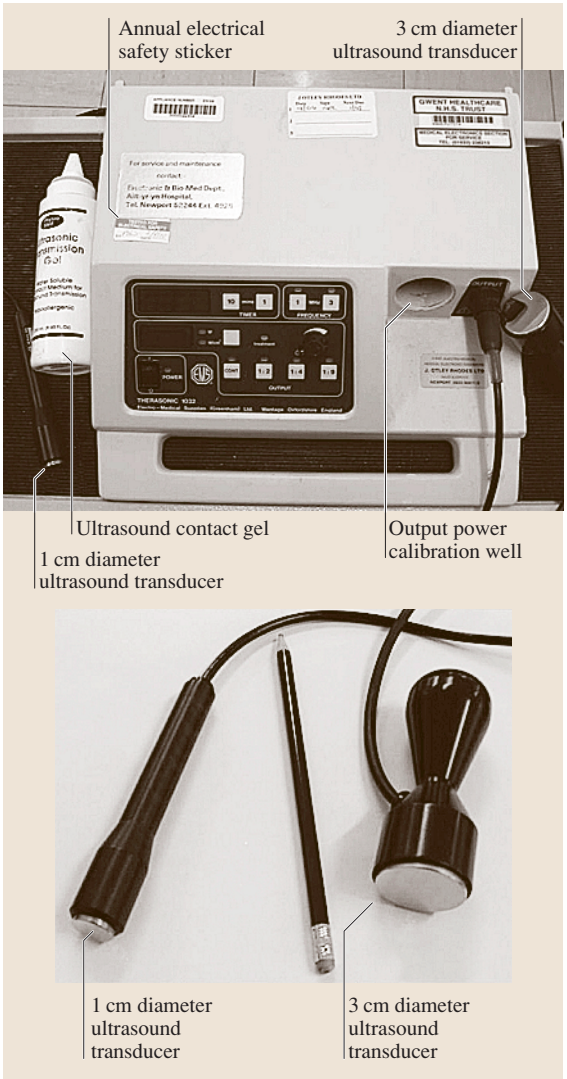


Fig. 21.67 Ultrasound therapy system

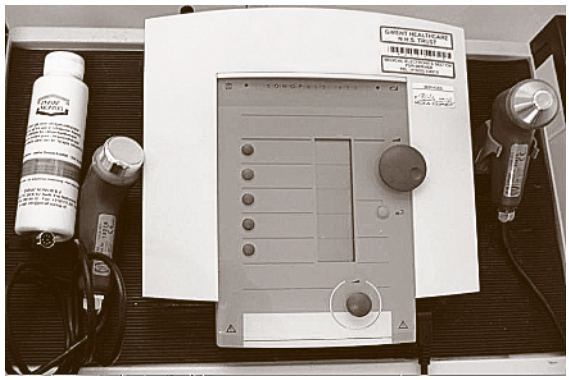


Fig. 21.68 Combined ultrasound diathermy and electrotherapy system. Deep heating of tissue can be achieved by using ultrasound or by using radio-frequency electric currents. This system is capable of delivering both kinds of heating. The two transducers shown are for ultrasound, but since the metallic surface is in contact with the patient, either can also apply RF diathermy when used with a counter-electrode

harmonics in the transmit beam on the way to the reflectors. So even without contrast microbubbles, tissue echoes contain 4 MHz, 6 MHz and 8 MHz components when exposed to 2 MHz transmit pulses. Even more disturbing, real-time B-mode images still did not show brighter echoes from contrast-filled blood spaces than from the same spaces before the introduction of the contrast agent. The reason for this puzzling result is that the transmitted ultrasound pulse destroys the echogenic bubbles, bleaching the contrast effect. Only bubbles of a particular size are bleached by the particular incident ultrasound frequency used, some becoming larger by coalescence and some dividing into smaller sizes, so they are not strongly echogenic at the incident frequency. The process of bubble destruction takes several milliseconds after exposure to a single ultrasound transmit burst. This provided the basis for two new methods of imaging with ultrasound contrast microbubbles: interrupted imaging and color Doppler imaging. If 2-D real-time B-mode imaging is used at a typical frame rate of 30 images per second, the interval between one pulse-echo cycle along an image line and the next is 33 ms, so the echogenic bubbles are gone after the first frame, and any new echogenic bubbles that enter the image field are destroyed as the imaging continues. This led to interrupted imaging of the heart muscle. In interrupted imaging, a series of ECG-triggered images is recorded for later analysis. Each image is acquired at the same time during the cardiac cycle so that successive images are separated by at least one cycle. During the sequence of ECG-triggered acquisition of images from a single plane, an initial image is obtained (i0), after an interval of five cardiac cycles a second image is obtained (i5), after the next interval of four cardiac cycles the next image is obtained (i4), then after three cycles (i3) and after two cycles (i2) and finally after an interval of one cycle the final image is obtained (i1). In theory, the prior image bleaches all of the contrast while acquiring the image. For contrast to appear in the next image, perfusion must carry the contrast bubbles into the image. By subtracting i5 from i0, all regions with significant

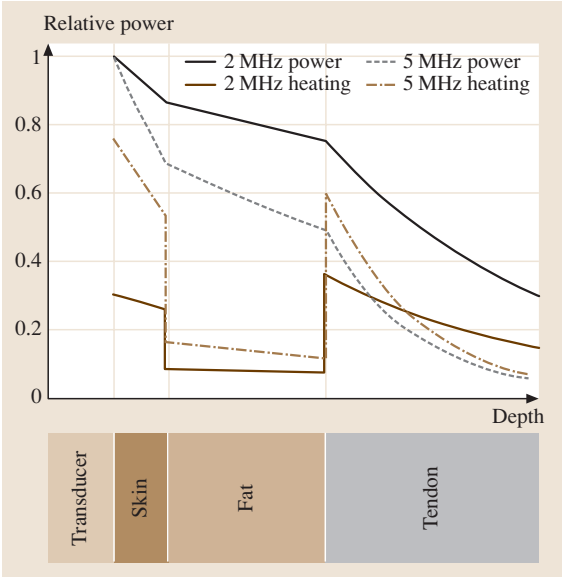


Fig. 21.69 5 MHz ultrasound is attenuated more in a short distance than 2 MHz ultrasound (*upper lines*). At shallow depths 5 MHz ultrasound delivers more heat because of greater absorption (*lower interrupted line*), but at the deepest depths, 2 MHz ultrasound provides greater heating (*lower solid line*). Because of the low absorption of ultrasound by fat, little heating occurs in fat

perfusion are dark. By subtracting i1 from i2, only the regions that are filled with contrast within a second are dark, those that fill during the time between 1 and 2 s are bright. By subtracting i4 from i5, the bright regions showing contrast bubbles in the image i5 that are not present in i4 show the regions that are filling slowly with blood.

During a color Doppler or color power angiography ultrasound examination, the ultrasound system sends an ensemble of eight transmit bursts at intervals of 0.2 ms along the ultrasound beam pattern to measure the changes in phase of the ultrasound echoes. In that 1.6 ms period, the contrast bubbles will begin and complete the process of vanishing. Thus there will be a large change in the echoes received from each depth during the period of the ensemble. This will be interpreted by the ultrasound system as a Doppler signal and displayed as color in the image.

The exact role of ultrasound contrast agents in medical diagnosis remains to be developed. However, there are a number of efforts to develop nanoparticles for useful applications. These nanoparticles are the same size as ultrasound contrast agents and may contain gas as well as liquid. The National Cancer Institute Unconventional Innovations Program supports some of this work for the diagnosis, treatment and monitoring of cancer. Nanoparticles can act as machines, using ultrasound energy as the supply to do useful work. This can be achieved using protein mechanics. Protein folding confirmations can change in nanoseconds, the molecular volume is different for each conformation and the energy states of folding change under high and low pressure, so ultrasound can be used to drive proteins from one conformational state to another. Nanoparticles can be used to deliver drugs [21.80] to target tissues, with ultrasound serving to trigger the release of the drug at desired times.

21.6 Ultrasound Hyperthermia in Physical Therapy

One of the earliest medical applications of ultrasound was the therapeutic heating of deep tissue because absorption of ultrasound by tissue results in the conversion of ultrasound energy into heat. In common practice, an ultrasound transducer 3 cm in diameter transmitting 20 W at a frequency of 3 MHz is applied to the skin (Figs. 21.67, 21.68).

As a rule, the size of the treatment area should be less than twice the surface area of the transducer. Because of diffraction effects, the ultrasound field has a complex pattern of peaks and valleys. The best transducers have a beam nonuniformity ratio (BNR) of 2 : 1 in intensity. A BNR of 6 : 1 is clinically acceptable. Some instruments have a BNR of 8 : 1.

The ultrasound passes through skin and subcutaneous fat to the muscles and connective tissues below. Because the attenuation of ultrasound in tendon is 10 times the attenuation in fat, the majority of the heating is in the tendon (Fig. 21.69). Heating is more superficial when a higher ultrasound frequency is used.

The attenuation in muscle and tendon is higher than in fat, favoring the heating of these tissues even when they are covered by fat. However, the attenuation of skin is quite variable; some reports show skin attenuation higher than tendon. The variability of the attenuation in skin results from two factors, the thin and nonuniform character of skin, and the variable air content of

the stratum corneum, the outermost layer of skin. With careful application of ultrasonic gel, the air can be removed from the stratum corneum layer, lowering the attenuation.

Although ultrasound diathermy as well as other diathermy methods are often used in physical therapy, the effectiveness of the treatments beyond the placebo effect is questioned by some.

21.7 High-Intensity Focused Ultrasound (HIFU) in Surgery

Starting in 1950, William J. Fry and colleagues at the University of Illinois, Urbana, developed an ultrasound method to heat small volumes of deep tissue to high temperatures. Using a 10 cm-diameter transducer operating at 2 MHz focused at a depth of 10 cm, tissue the size of a grain of rice can be heated at 25 °C per second, causing the tissue to boil in 2.5 s. This method allowed Fry to create thermal lesions in the brain for the treatment of brain tumors and other neurological conditions.

The technology is still in evolution, but holds promise of allowing the cautery of deep tissue without damaging the overlying superficial tissue. A 35 mm-diameter 5 MHz concave ultrasound transducer focused at a depth of 35 mm (Fig. 21.70) delivering 30 W of acoustic power to a treatment volume 1 mm in diameter and 10 mm long can deliver an intensity of 3 kW/cm^2 (30 MW/m^2) to form a lesion (Fig. 21.71). At such intensities the nonlinearity of the tissue causes much of the ultrasound to be converted to higher harmonics (Fig. 21.72), increasing the fraction of the incident power absorbed in the treatment volume. During HIFU treatment, ultrasound images of the treatment volume show a spot of increased echogenicity caused by bubbles filled with water vapor (boiling) or with gas coming out of solution. When the HIFU treatment stops, the hyper-echogenic zone quickly becomes anechoic. During treatment, the bubbles may act as a shield, restricting the delivery of ultrasound to deeper tissues (Figs. 21.73, 21.74).

HIFU treatment can coagulate blood to stop bleeding or to render tissue ischemic, causing necrosis. The method holds promise for:

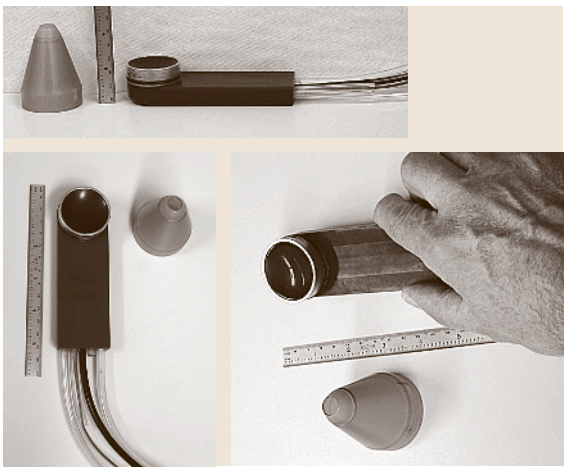


Fig. 21.70 3.5 MHz HIFU transducer used in abdominal surgery research. Notice that the black transducer face is concave (the reflection of the fluorescent light fixture is curved). The transducer is fitted with a signal cable (*black*), a pair of tubes to deliver and return cooling water (*clear*), and a thermocouple cable (*thin*) to monitor the temperature of the transducer. A plastic cone filled with water fits on the front of the transducer to conduct the sound to the tissue

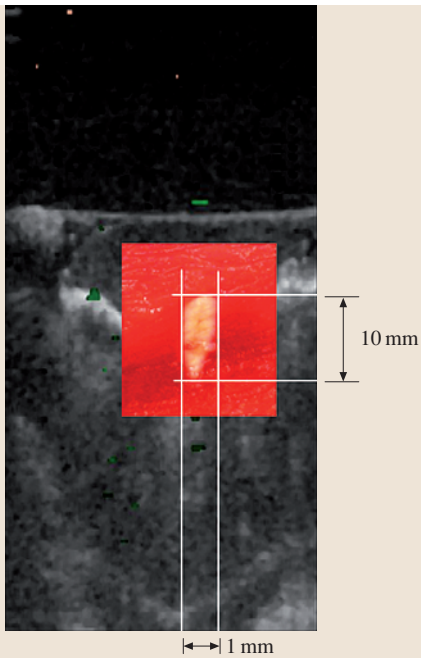


Fig. 21.71 Histology of a HIFU lesion overlaid onto the ultrasound image. 5 s high-intensity focused ultrasound cautry at a depth of 5 cm under tissue in porcine spleen. Typical lesions are 10 mm long (in depth from the transducer) and 1 mm in diameter

Amazon EX1014 Page 895

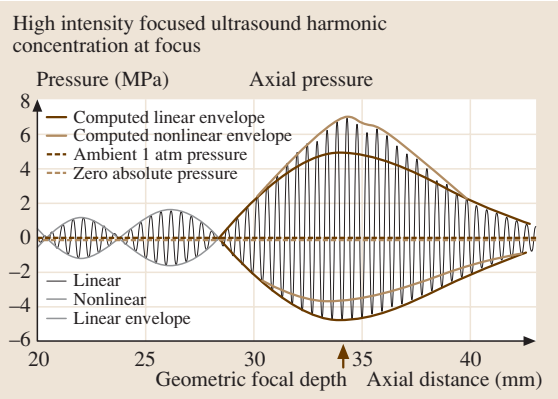


Fig. 21.72 Computed central beam instantaneous pressures from a HIFU transducer. The high acoustic pressures in the focal zone create nonlinear effects that generate harmonics in the transmitted ultrasound beam (courtesy F. Curra)

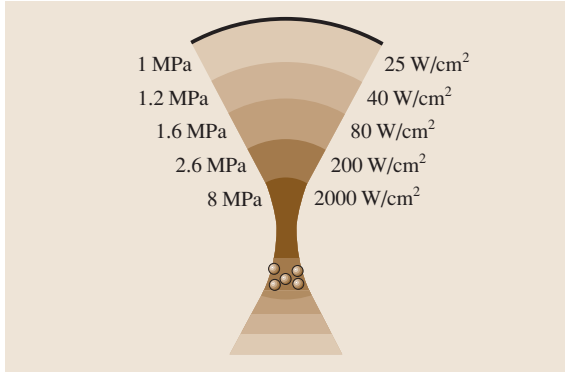


Fig. 21.73 Typical HIFU ultrasound beam profile. High-intensity focused ultrasound beam profile showing increase in beam intensity, not accounting for attenuation. The small circles post focus represent bubbles formed by a combination of mechanical-index-induced cavitation boiling. They are pushed into the post-focus zone by radiation pressure. As the exposure continues, more bubbles will be formed at shallower depths. Post-focal bubbles may provide a safety shield, preventing HIFU exposure of deeper, healthy tissue

1. stopping internal bleeding of the liver or spleen,
2. stopping bleeding due to catheter procedures,
3. reducing the size of tissues such as uterine fibroids and prostate hypertrophy,
4. destroying cancer cells and tumors,
5. birth-control procedures such as vasectomy and tubal ligation,
6. tissue welding, and
7. pushing tissues using radiation force to stretch or compress them.

Thermal dose is one way to summarize hyperthermia treatment conditions. Thermal dose implies that tissue changes occur above 43 °C, and that the effect is increased with increasing time and increasing temperature. One empirical formula for thermal dose has been given [21.81] as:

$$D = \int_{t_1}^{t_2} n(T)^{(T-43)}\,\mathrm{d}t\,,$$

where t_1 and t_2 are the initial and final times of the heating profile, respectively, and $n(T)$ is 4 for $T < 43\,^{\circ}\mathrm{C}$ and 2 for $T > 43\,^{\circ}\mathrm{C}$. The temperature is determined by the rate of heat delivery per tissue volume, which is the product of the intensity times the attenuation minus the rate at which heat is removed from the tissue by conduction through tissues, and convection via the blood.

The most difficult issue with HIFU is the small treatment volume versus the relatively large access window. Under ideal conditions, the treatment of a single volume of tissue 10 mm^3 takes about 2 s. A cubic region 50 mm on a side has a volume of 125 000 mm^3 and requires nearly 4 h to treat. These long treatment times present a considerable economic problem for the adoption of the technology.

21.8 Lithotripsy of Kidney Stones

Explosive ultrasound can be used to fracture kidney stones in the renal pelvis where the urine is collected from the kidney and directed down the ureter to the bladder. Stones which form in the renal pelvis from solutes in the urine are very painful. The pain occurs because urine is moved down the ureter by peristaltic action, and the peristalsis cannot handle a bolus the size of a stone. One type of ultrasound lithotripter uses a 10 cm-diameter concave reflector with a spark gap at the source focus. The elliptical curvature forms a target focus 12 cm from the face of the reflector. Equally intense ultrasound pulses can be formed using focused piezoelectric transducers or electromagnetically driven membranes with the ultrasound focused using an acoustic lens.

A water path is used to couple the reflector to the skin nearest the affected kidney so that the target focus can be positioned on the kidney stone. By firing the spark gap in the water at the source focus, pressures of +100 MPa followed by −10 MPa are achieved at the target focus. Treatment of a kidney stone may require 3000 shocks delivered over an hour. The object of the treatment is to break a large stone (≥ 1 cm in diameter) into smaller pieces (≤ 2 mm diameter) that the ureter can carry to the bladder. The mechanism of stone destruction includes erosion, spallation, fatigue, shear and circumferential compression associated with the primary shock wave or resulting cavitation. Erosion is caused by cavitation. Spallation is the ejection of the distal portion of the stone, resulting from a decompression wave reflected from the distal portion of the stone. Unfortunately, lithotripsy is often associated with injury to the kidney parenchyma [21.82].

21.9 Thrombolysis

A new therapeutic application of ultrasound is the destruction of blood clots occluding vessels. Two mechanical methods may contribute to clot destruction [21.83–85]: the formation of microbubbles in the clot (cavitation) and differential radiation force on the clot squeezing and expanding the clot like a sponge to take up thrombolytic drugs. There are research reports of successful thrombolysis in coronary arteries [21.86], intracranial arteries [21.87, 88] and vascular access shunts for dialysis. The ultrasound intensities required for thrombolysis are similar to those used in diagnostic ultrasound. The mechanisms include streaming and disaggregation of the clot [21.89].

21.10 Lower-Frequency Therapies

Lower-frequency ultrasound is used for tissue disruption and cleaning purposes. To remove an opacified lens (cataract) from the eye through a small incision, a needle oscillating at 25–60 kHz is used to emulsify the lens (phacoemulsification), which is then removed by aspiration (suction).

Dental scaling is performed with a similar instrument operating at frequencies of 18–30 kHz and applied power of 30 W. Cavitation is an important mechanism in the cleaning process. Chemical additives such as toothpaste can suppress cavitation and degrade the cleaning efficiency.

21.11 Ultrasound Safety

Undoubtedly, ultrasound is safe. In over a half century of widespread use of diagnostic ultrasound, there are no currently accepted reports of harm to patients or examiners from the use of diagnostic ultrasound. However, in 1950, unamplified X-ray fluoroscopic imaging was considered so safe that it was used for shoe fitting in nearly all shoe stores, and for the entertainment of children waiting to be served. In 1950, smoking was considered to be so beneficial to health that nearly all doctors smoked. Although there are reports that ultrasound examination in pregnancy is associated with increased birth complications in retrospective studies where ultrasound was applied to high-risk pregnancies, a causative effect is unlikely. Fewer complications were found in pregnancies randomized to ultrasound examination compared to those with conventional care [21.90] because of the increased knowledge of physicians about the expected date of delivery. In one discussion of the safety of Doppler ultrasound examination of the ophthalmic artery through the eye, an experienced investigator stated “If the patient doesn’t see flashes of light, I figure that the exam is safe”. Still today, diagnostic ultrasound is considered so safe that, although there are occasional disclaimers such as “to be used only under the supervision of a physician”, ultrasound examinations are performed for educational purposes on students, demonstrated on hired actors at trade shows, available for home use, and advertised

Amazon EX1014 Page 897

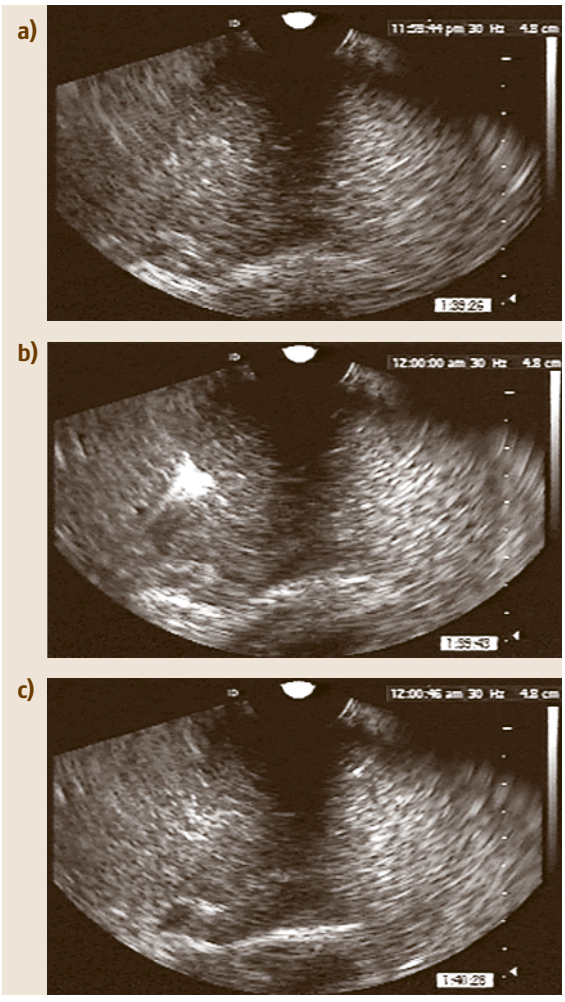


Fig. 21.74a–c B-mode imaging of high-intensity focused ultrasound lesion formation. Focal intensity 1000 W/cm2. **(a)** B-mode image of tissue before HIFU therapy. **(b)** Echogenic region at HIFU treatment zone after 15 s of exposure. **(c)** Echogenicity vanishes with time after cessation of HIFU exposure

for entertainment purposes. One prominent ultrasound safety expert warned that driving to the examination carried more risk than the risk associated with ultrasound examination.

In 1976, the United States congress passed the Medical Device Amendments providing that the Food and Drug Administration should have authority over medical devices [21.91]. At that time, any medical device in clinical use, in the absence of evidence of hazard, was considered safe. Any new medical device that was substantially equivalent to a pre-enactment device could be approved for distribution in interstate commerce and use by filing a 510k application showing equivalence. Devices that were not substantially equivalent required pre-market approval (PMA) as an investigational device. This started a search for existing ultrasound systems that had been sold across state lines so that the ultrasound output levels could be measured. These old systems are called pre-enactment systems. New ultrasound devices that had similar or lower acoustic outputs were considered equivalent and could be approved by the FDA under a 510k application, which was simpler and far less costly than the PMA process.

In 1976, continuous-wave (CW) Doppler systems were in use, pulsed Doppler systems were in use, M-mode, 2-D static B-mode and 2-D real-time B-mode systems were also in use. One CW Doppler system at the time caused red spots on the skin that were called *Doppler hickies*, but were still considered safe because there were no complaints.

The task was to characterize the equivalent acoustic output. Over the quarter century since enactment, various methods have been developed to describe the effect of ultrasound on tissue, to establish equivalence. Because of the common use of therapeutic ultrasound to create tissue hyperthermia, the first consideration was the heating effect of the ultrasound; later mechanical effects were included in the analysis.

The heating of tissue is governed by the bioheat equation. This equation relates the increase in tissue temperature to the rate of heat deposit minus the rate of heat removal divided by the heat capacity of the tissue. The rate of heat deposit is proportional to the incoming ultrasound power minus the outgoing ultrasound power, per unit mass. In a simple computation, the heat capacity of tissue is the same as water, 1 cal/gm or $4.2\,\mathrm{J/gm\,^{\circ}C} = 4.2\,\mathrm{J/cm^3\,^{\circ}C} = 4.2\,\mathrm{W\,s/cm^3\,^{\circ}C}$. So, if ultrasound at an intensity of $4.2\,\mathrm{W/cm^2}$ is completely absorbed by a layer of tissue (water) that is 1 cm thick, the temperature will rise 1 °C per second, if no heat is carried away. $42\,\mathrm{mW/cm^2}$ ($420\,\mathrm{W/m^2}$) will raise the temperature by only 0.01 °C per second, allowing 100 s of exposure to raise the temperature from the normal body temperature of 37 °C to 38 °C, well below fever temperature considered safe by most people. Since at 4 MHz, only half of the ultrasound power is converted to heat in one cm, the heating rate is half of the values above.

Until 1985, ultrasound exposure levels were quoted in terms of $\mathrm{W/cm^2}$ related to tissue heating. Based on pre-enactment levels, diagnostic ultrasound systems had

Amazon EX1014 Page 898

a temporal average (TA) acoustic intensity at the transducer focal zone measured in a water-filled test tank of 100 mW/cm^2 (1 kW/m^2) or less. The major exception was ultrasound systems for the examination of the eye, which had pre-enactment intensities of 7 mW/cm^2 (70 W/m^2). So, the generally accepted temporal average allowable intensities became: 7 mW/cm^2 (70 W/m^2) for the eye and 100 mW/cm^2 (1 kW/m^2) for all other diagnostic applications. The maximum intensity of sunlight is about 50 mW/cm^2 (500 W/m^2), but the attenuation of sunlight at the skin is near 100%. Acceptable physical therapy ultrasound intensities were about 30 times higher: 3 W/cm^2 (30 kW/m^2).

Ultrasound beam patterns are not uniform, especially in the Fresnel zone (near field). The intensities at the focus in diagnostic ultrasound beams are often three times higher than the average intensities. Because of this, ultrasound intensities were reported as spatial peak (SP) intensities, to indicate the variations, or spatial average (SA) intensities.

With pulsed-echo ultrasound imaging, the transmitted ultrasound is on for less than 0.5 μs every millisecond along the same ultrasound beam pattern in M-mode examination; thus the ultrasound was on only 1/2000 of the time (duty factor or duty cycle of 0.05%). For a spatial peak temporal average intensity of 100 mW/cm^2, (1 kW/m^2) the pulse average (PA) was 2000 times as great or 200 W/cm^2 (2 kW/m^2) (SP PA) and the temporal peak (TP) intensity was twice that value (SPTP, Fig. 21.23, broadband pulse). A conventional pulsed Doppler examination with a 1 μs transmit burst every 50 μs has a duty factor of 2% and an SPTP intensity of 5 W/cm^2 (50 kW/m^2). In both M-mode and Doppler examinations, the ultrasound beam pattern is held stationary for several seconds. But in real-time 2-D B-mode imaging, each successive beam axis is along a different line. Typically, the ultrasound is directed along the same line at the frame rate, about 30 times per second.

Over the next decade, the guidelines for ultrasound intensities in different applications became more sophisticated, separating application-specific output levels into four categories: general, cardiac, vascular, and ophthalmic. The motivation was to allow higher intensity levels to be used for Doppler blood velocity measurements because the echoes returned by blood were 0.000 001 (60 dB) lower than those from tissue. Rather than accepting the intensities measured at the focal zone in a water tank, the intensities were derated by computing the expected intensity if the water were replaced by attenuating tissue with an attenuation rate of 0.3 dB/(MHz cm). Derating allows a 3 MHz cardiac Doppler system focused at a depth of 11 cm to derate the intensity by 10 dB, thus allowing a tenfold increase in transmit power. The derated SPTA limits were: fetal, neonatal and other general-purpose applications −94 mW/cm^2; cardiac −430 mW/cm^2; peripheral vascular −720 mW/cm^2; ophthalmic −17 mW/cm^2; the SPPA limits were 190 W/cm^2 for the first three categories and 28 W/cm^2 for ophthalmic exams.

Working together, the US Food and Drug Administration (FDA), National Electronic Manufacturers Association (NEMA) and the American Institute of Ultrasound in Medicine (AIUM) began to agreed on output display standards (ODS) for ultrasound instruments, including the thermal index (TI, the intensity required to raise the temperature of tissue by 1 °C) predictive of tissue heating, and the mechanical index (MI) predictive of cavitation and interactions with ultrasound contrast agents. The TI was further divided into subcategories for soft tissue (TIS), bone near the focus (TIB) and cranial bone near the skin (TIC) based on the expected absorption of ultrasound in the tissue. These values also include the fact that the ultrasound beam is scanning across the tissue in 2-D imaging. The computation of MI is based on the SPTP intensity values, includes attenuation derating but not the scanning of the ultrasound beam.

To better understand the MI values, refer to Fig. 21.5 which indicates that the amplitude of the pressure fluctuation for a 0.3 W/cm^2 wave is 1 atm, or 100 kPa = 100 kN/m^2. The pressure increases by the square root of intensity, for a linear system (which this cannot be). So, for the M-mode SPTP intensity of 200 W/cm^2, (2 MW/m^2) the pressure amplitude is 26 atm, making the peak positive pressure 27 atm (2.7 MPa) and the peak negative pressure (below zero) −25 atm (−2.5 MPa). The MI is defined as the negative pressure amplitude [MPa] divided by the square root of the ultrasound frequency [MHz]. This provides a basis for the estimation of the chance of an adverse nonthermal event. At 3 MHz, the MI for this case is 1.5. An MI less than 1.9 is acceptable for obstetrical examinations in the absence of ultrasound contrast agents our other sources of gas bubbles.

In 1991, the FDA released its 510k guidance [21.92], establishing a new track for approval of non-PMA devices, regulatory track 3. This permitted increased outputs for devices implementing the output display standard developed jointly by the AIUM and NEMA [21.93]. This standard recognized two general classes of mechanisms by ultrasound could adversely affect biological tissue, thermal and mechanical, and

provided simple metrics for the likelihood of such effects, the thermal index (TI) and mechanical index (MI).

Similar standards have been addressed in other countries by organizations and agencies including Health Canada, the European Committee for Medical Ultrasound Safety (ECMUS), the British Medical Ultrasound Society (BMUS), the European Federation of Societies for Ultrasound in Medicine and Biology (EFSUMB), the Australasian Society for Ultrasound in Medicine (ASUM), the Asian Federation for Societies of Ultrasound in Medicine and Biology (AFSUMB), the Latin American Federation of Ultrasound in Medicine and Biology (FLAUS), the Mediterranean and African Society of Ultrasound (MASU), and the World Federation for Ultrasound in Medicine and Biology (WFUMB).

In spite of the confidence that ultrasound is absolutely safe, all ultrasound agencies subscribe to the policy of using ultrasound exposure levels that are as low as reasonably achievable (ALARA) for diagnostic ultrasound examinations.

In the presence of ultrasound contrast agents or gas in the lungs or gut, there is a risk of damaging capillaries and creating interstitial hemorrhaging in tissues when high-MI examinations are performed.

However, there are some other considerations. In addition to heating tissue and the compression/decompression mechanical factors related to mechanical index, an ultrasound wave exerts radiation pressure on tissue as it passes through. The radiation pressure is proportional to intensity. Radiation force is used in the measurement of acoustic output. The body force is equal to the [power entering a region minus the power transmitted through and exiting the region] divided by the speed of sound. At a pulsed Doppler focus in the examination of the fetus, a temporal peak radiation pressure of 1700 Pa can be generated at a frequency equal to the pulse repetition frequency (PRF) of 5 kHz, which is well within the hearing range. If the ultrasound beam pattern is directed to intersect the ear, the radiation pressure oscillation can be heard by the fetus and cause increased fetal activity [21.94].

Of more serious concern is the increase in permeability in cell membranes and other biologic barriers to small and large molecules that can be induced by ultrasound [21.95]. This may prove useful for the delivery of therapeutic drugs through the skin (sonoporation) and genes across membranes including the placental barrier and the blood–brain barrier, but it might also allow the inadvertent transfer of pathogens. The effect is enhanced in the presence of gas and ultrasound contrast agents. It is possible that such effects have escaped detection by current monitoring methods.

The conceptual simplicity of the pulse-echo system has allowed instrument engineers to devote all efforts toward lowering the cost and improving the diagnostic utility of these instruments. Unlike most other medical imaging methods, ultrasound is low-cost, portable, real-time, and considered safe in most applications.

Further Reading

Please find a complete compilation of citations from Ultrasound in Medicine and Biology which list the thousands of articles on medical acoustics written prior to 1987: http://www.ncbi.nlm.nih.gov/entrez/query.fcgi?CMD=Display&DB=pubmed

References

21.1 G.E. Horn, J.M. Mynors: Recording the bowel sounds, Med. Biol. Eng. **4**(2), 205–208 (1966)

21.2 T. Tomomasa, A. Morikawa, R.H. Sandler, H.A. Mansy, H. Koneko, T. Masahiko, P.E. Hyman, Z. Itoh: Gastrointestinal sounds and migrating motor complex in fasted humans, Am. J. Gastroenterol. **94**(2), 374–381 (1999)

21.3 C. Leknius, B.J. Kenyon: Simple instrument for auscultation of temporomandibular joint sounds, J. Prosthet. Dent. **92**(6), 604 (2004)

21.4 S.E. Widmalm, W.J. Williams, D. Djurdjanovic, D.C. McKay: The frequency range of TMJ sounds, J. Oral. Rehabil. **30**(4), 335–346 (2003)

21.5 C. Oster, R.W. Katzberg, R.H. Tallents, T.W. Morris, J. Bartholomew, T.L. Miller, K. Hayakawa: Characterization of temporomandibular joint sounds. A preliminary investigation with arthrographic correlation, Oral Surg. Oral Med. Oral Pathol. **58**(1), 10–16 (1984)

21.6 A. Peylan: Direct auscultation of the joints; Preliminary clinical observations, Rheumatism **9**(4), 77–81 (1953)

21.7 E.P. McCutcheon, R.F. Rushmer: Korotkoff sounds. An experimental critique, Circ. Res. **20**(2), 149–161 (1967)

21.8 J.E. Meisner, R.F. Rushmer: Production of sounds in distensible tubes, Circ. Res. **12**, 651–658 (1963)

21.9 S. Jarcho: The young stethoscopist (H. I. Bowditch, 1846), Am. J. Cardiol. **13**, 808–819 (1964)

21.10 R.F. Rushmer, R.S. Bark, R.M. Ellis: Direct-writing heart-sound recorder (The sonvelograph), Ama. Am. J. Dis. Child **83**(6), 733–739 (1952)

Amazon EX1014 Page 900

21.11 M.A. Chizner: The diagnosis of heart disease by clinical assessment alone, Curr. Probl. Cardiol. **26**(5), 285–379 (2001)

21.12 M.A. Chizner: The diagnosis of heart disease by clinical assessment alone, Dis. Mon. **48**(1), 7–98 (2002)

21.13 A.E. Aubert, B.G. Denys, F. Meno, P.S. Reddy: Investigation of genesis of gallop sounds in dogs by quantitative phonocardiography and digital frequency analysis, Circulation **71**, 987–993 (1985)

21.14 R.F. Rushmer, C. Morgan: Meaning of murmurs, Am. J. Cardiol. **21**(5), 722–730 (1968)

21.15 J.E. Foreman, K.J. Hutchison: Arterial wall vibration distal to stenoses in isolated arteries, J. Physiol. **205**(2), 30–31 (1969)

21.16 J.E. Foreman, K.J. Hutchison: Arterial wall vibration distal to stenoses in isolated arteries of dog and man, Circ. Res. **26**(5), 583–590 (1970)

21.17 A.M. Khalifa, D.P. Giddens: Characterization and evolution poststenotic flow disturbances, J. Biomech. **14**(5), 279–296 (1981)

21.18 G.W. Duncan, J.O. Gruber, C.F. Dewey, G.S. Myers, R.S. Lees: Evaluation of carotid stenosis by phonoangiography, N. Engl. J. Med. **293**(22), 1124–1128 (1975)

21.19 J.P. Kistler, R.S. Lees, J. Friedman, M. Pressin, J.P. Mohr, G.S. Roberson, R.G. Ojemann: The bruit of carotid stenosis versus radiated basal heart murmurs. Differentiation by phonoangiography, Circulation **57**(5), 975–981 (1978)

21.20 J.P. Kistler, R.S. Lees, A. Miller, R.M. Crowell, G. Roberson: Correlation of spectral phonoangiography and carotid angiography with gross pathology in carotid stenosis, N. Engl. J. Med. **305**(8), 417–419 (1981)

21.21 R. Knox, P. Breslau, D.E. Strandness Jr.: Quantitative carotid phonoangiography, Stroke **12**, 798–803 (1981)

21.22 R.S. Lees: Phonoangiography: qualitative and quantitative, Ann. Biomed. Eng. **12**(1), 55–62 (1984)

21.23 R.S. Lees, C.F. Dewey Jr.: Phonoangiography: a new noninvasive diagnostic method for studying arterial disease, Proc. Natl. Acad. Sci. USA **67**, 935–942 (1970)

21.24 A. Miller, R.S. Lees, J.P. Kistler, W.M. Abbott: Spectral analysis of arterial bruits (phonoangiography): Experimental validation, Circulation **61**(3), 515–520 (1980)

21.25 A. Miller, R.S. Lees, J.P. Kistler, W.M. Abbott: Effects of surrounding tissue on the sound spectrum of arterial bruits in vivo, Stroke **11**(4), 394–398 (1980)

21.26 D. Smith, T. Ishimitsu, E. Craige: Mechanical vibration transmission characteristics of the left ventricle: implications with regard to auscultation and phonocardiography, J. Am. Coll. Cardiol. **4**, 517–521 (1984)

21.27 D. Smith, T. Ishimitsu, E. Craige: Abnormal diastolic mechanical vibration transmission characteristics of the left ventricle, J. Cardiogr. **15**, 507–512 (1985)

21.28 J.P. Murgo: Systolic ejection murmurs in the era of modern cardiology: What do we really know?, J. Am. Coll. Cardiol. **32**, 1596–1602 (1998)

21.29 H. Nygaard, L. Thuesen, J.M. Hasenkam, E.M. Pedersen, P.K. Paulsen: Assessing the severity of aortic valve stenosis by spectral analysis of cardiac murmurs (spectral vibrocardiography). Part I: Technical aspects, J. Heart Valve Dis. **2**, 454–467 (1993)

21.30 Z. Sun, K.K. Poh, L.H. Ling, G.S. Hong, C.H. Chew: Acoustic diagnosis of aortic stenosis, J. Heart Valve Dis. **14**, 186–194 (2005)

21.31 D.J. Doyle, D.M. Mandell, R.M. Richardson: Monitoring hemodialysis vascular access by digital phonoangiography, Ann. Biomed. Eng. **30**(7), 982 (2002)

21.32 C. Clark: Turbulent wall pressure measurements in a model of aortic stenosis, J. Biomech. **10**(8), 461–472 (1977)

21.33 M.B. Rappoport, H.B. Sprague: Physiologic and physical laws that govern auscultation and their clinical application, Am. Heart J. **21**, 257 (1941)

21.34 R. Tidwell, R. Rushmer, R. Polley: The office diagnosis of operable congenital heart lesions, Northwest Med. **52**(7), 546 (1953)

21.35 R. Tidwell, R. Rushmer, R. Polley: The office diagnosis of operable congenital heart lesions, Northwest Med. **52**(8), 635 (1953)

21.36 R. Tidwell, R. Rushmer, R. Polley: The office diagnosis of operable congenital heart lesions; coarctation of the aorta, Northwest Med. **52**(11), 927 (1953)

21.37 F.D. Fielder, P. Pocock: Foetal blood flow detector, Ultrasonics **6**(4), 240–241 (1968)

21.38 W.L. Johnson, H.F. Stegall, J.N. Lein, R.F. Rushmer: Detection of fetal life in early pregnancy with an ultrasonic doppler flowmeter, Obstet. Gynecol. **26**, 305–307 (1965)

21.39 R.F. Rushmer, C.L. Morgan, D.C. Harding: Electronic aids to auscultation, Med. Res. Eng. **7**(4), 28–36 (1968)

21.40 R.F. Rushmer, D.R. Sparkman, R.F. Polley, E.E. Bryan, R.R. Bruce, G.B. Welch, W.C. Bridges: Variability in detection and interpretation of heart murmurs; A comparison of auscultation and stethography, AMA Am. J. Dis. Child **83**(6), 740–754 (1952)

21.41 R.F. Rushmer, R.A. Tidwell, R.M. Ellis: Sonvelographic recording of murmurs during acute myocarditis, Am. Heart J. **48**(6), 835–846 (1954)

21.42 P.N.T. Wells: Review, absorption and dispersion of ultrasound in biological tissue, Ultrasound Med. Biol. **1**, 369–376 (1975)

21.43 M.A. Allison, J. Tiefenbrun, R.D. Langer, C.M. Wright: Atherosclerotic calcification and intimal medial

Amazon EX1014 Page 901

thickness of the carotid arteries, Int. J. Cardiol. **103**(1), 98–104 (2005)
21.44 J.A. Jensen: FIELD (1997) http://www.es.oersted.dtu.dk/staff/jaj/field/index.html; http://www.es.oersted.dtu.dk/staff/jaj/old_field/
21.45 R.F. Rushmer, D.W. Baker, H.F. Stegall: Transcutaneous doppler flow detection as a nondestructive technique, J. Appl. Physiol. **21**(2), 554–566 (1966)
21.46 D.L. Franklin, W. Schlegel, R.F. Rushmer: Blood flow measured by doppler frequency shift of back-scattered ultrasound, Science **134**, 564–565 (1961)
21.47 H.F. Stegall, R.F. Rushmer, D.W. Baker: A transcutaneous ultrasonic blood-velocity meter, J. Appl. Physiol. **21**(2), 707–711 (1966)
21.48 D.E. Strandness Jr., E.P. McCutcheon, R.F. Rushmer: Application of a transcutaneous doppler flowmeter in evaluation of occlusive arterial disease, Surg. Gynecol. Obstet. **122**(5), 1039–1045 (1966)
21.49 D.E. Strandness Jr., R.D. Schultz, D.S. Sumner, R.F. Rushmer: Ultrasonic flow detection. A useful technic in the evaluation of peripheral vascular disease, Am. J. Surg. **113**(3), 311–320 (1967)
21.50 R.F. Rushmer, D.W. Baker, W.L. Johnson, D.E. Strandness: Clinical applications of a transcutaneous ultrasonic flow detector, JAMA **199**(5), 326–328 (1967)
21.51 C.R. Hill: Medical ultrasonics: an historical review, Br. J. Radiol. **46**(550), 899–905 (1973)
21.52 A.H. Crawford: Ultrasonic medical equipment, Ultrasonics **8**(2), 105–111 (1970)
21.53 B. Buttery, G. Davison: The ghost artifact, J. Ultras. Med. **3**, 49–52 (1984)
21.54 R.M. Ellis, D.L. Franklin, R.F. Rushmer: Left ventricular dimensions recorded by sonocardiometry, Circ. Res. **4**(6), 684–688 (1956)
21.55 R.F. Rushmer: Continuous measurements of left ventricular dimensions in intact, unanesthetized dogs, Circ. Res. **2**(1), 14–21 (1954)
21.56 J.C. Somer: Electronic Sector Scanning fo Ultrasonic Diagnosis, Ultrasonics **6**(3), 153–159 (1968)
21.57 F.E. Barber, D.W. Baker, A.W. Nation, D.E. Strandness Jr., J.M. Reid: Ultrasonic duplex-echo doppler scanner, IEEE Trans. Biomed. Eng. vBME **21**(2), 109–113 (1974)
21.58 D.N. Ku, D.P. Giddens: Pulsatile flow in a model carotid bifurcation, Arteriosclerosis **3**(1), 31–39 (1983)
21.59 T.L. Yearwood, K.B. Chandran: Experimental investigation of steady flow through a model of the human aortic arch, J. Biomech. **13**(12), 1075–1088 (1980)
21.60 T.L. Yearwood, K.B. Chandran: Physiological pulsatile flow experiments in a model of the human aortic arch, J. Biomech. **15**(9), 683–704 (1982)
21.61 D.E. Strandness Jr.: *Duplex Scanning in Vascular Disorders*, 3rd edn. (Lippincott Williams Wilkins, Philadelphia 2002)
21.62 G. Papanicolaou, K.W. Beach, R.E. Zierler, D.E. Strandness Jr.: The relationship between arm-ankle pressure difference and peak systolic velocity in patients with stenotic lower extremity vein grafts, Ann. Vasc. Surg. **9**(6), 554–560 (1995)
21.63 T.R. Kohler, S.C. Nicholls, R.E. Zierler, K.W. Beach, P.J. Schubert, D.E. Strandness Jr.: Assessment of pressure gradient by Doppler ultrasound: experimental and clinical observations, J. Vasc. Surg. **6**(5), 460–469 (1987)
21.64 D.N. White, J.M. Clark, M.N. White: Studies in ultrasonic echoencephalography. 7. General principles of recording information in ultrasonic B- and C-scanning and the effects of scatter, reflection and refraction by cadaver skull on this information, Med. Biol. Eng. **5**(1), 3–14 (1967)
21.65 D.N. White, J.M. Clark, M.N. White: Studies in ultrasonic echoencephalography. 8. The effects on resolution of irregularities in attenuation of an ultrasonic beam traversing cadaver skull, Med. Biol. Eng. **5**(1), 15–23 (1967)
21.66 D.N. White: Ultrasonic encephalography, Acta Radiol. Diagn.(Stockh.) **9**, 671–674 (1969)
21.67 D.N. Ku, D.P. Giddens, D.J. Phillips, D.E. Strandness Jr.: Hemodynamics of the normal human carotid bifurcation: in vitro and in vivo studies, Ultrasound Med. Biol. **11**(1), 13–26 (1985)
21.68 W.M. Blackshear Jr., D.J. Phillips, B.L. Thiele, J.H. Hirsch, P.M. Chikos, M.R. Marinelli, K.J. Ward, D.E. Strandness Jr.: Detection of carotid occlusive disease by ultrasonic imaging and pulsed doppler spectrum analysis, Surgery **86**(5), 698–706 (1979)
21.69 K.A. Comess, F.A. DeRook, M.L. Russell, T.A. Tognazzi-Evans, K.W. Beach: The incidence of pulmonary embolism in unexplained sudden cardiac arrest with pulseless electrical activity, Am. J. Med. **109**(5), 351–356 (2000)
21.70 R.C. Bahler, T. Mohyuddin, R.S. Finkelhor, I.B. Jacobs: Contribution of doppler tissue imaging and myocardial performance index to assessment of left ventricular function in patients with duchenne's muscular dystrophy, J. Am. Soc. Echocardiogr. **18**(6), 666–673 (2005)
21.71 J.K. Campbell, J.M. Clark, C.O. Jenkins, D.N. White: Ultrasonic studies of brain movements, Neurology **20**(4), 418 (1970)
21.72 S. Sikdar, K.W. Beach, S. Vaezy, Y. Kim: Ultrasonic technique for imaging tissue vibrations: preliminary results, Ultrasound Med. Biol. **31**, 221–232 (2005)
21.73 A. Evans, D.N. Walder: Detection of circulating bubbles in the intact mammal, Ultrasonics **8**(4), 216–217 (1970)
21.74 C. Shub, A.J. Tajik, J.B. Seward, D.E. Dines: Detecting intrapulmonary right-to-left shunt with contrast echocardiography. Observations in a pa-

Amazon EX1014 Page 902

tient with diffuse pulmonary arteriovenous fistulas, Mayo Clin. Proc. **51**(2), 81–84 (1976)
21.75 E. Grube, H. Simon, M. Zywietz, G. Bodem, G. Neumann, A. Schaede: Echocardiographic contrast studies for the delineation of the heart cavities using peripheral venous sodium chloride injections. A contribution to shunt diagnosis, Verh. Dtsch. Ges. Inn. Med. **83**, 366–367 (1977)
21.76 P.W. Serruys, W.B. Vletter, F. Hagemeijer, C.M. Ligtvoet: Bidimensional real-time echocardiological visualization of a ventricular right-to-left shunt following peripheral vein injection, Eur. J. Cardiol. **6**(2), 99–107 (1977)
21.77 D. Danilowicz, I. Kronzon: Use of contrast echocardiography in the diagnosis of partial anomalous pulmonary venous connection, Am. J. Cardiol. **43**(2), 248–252 (1979)
21.78 C. Tei, T. Sakamaki, P.M. Shah, S. Meerbaum, K. Shimoura, S. Kondo, E. Corday: Myocardial contrast echocardiography: a reproducible technique of myocardial opacification for identifying regional perfusion deficits, Circulation **67**(3), 585–593 (1983)
21.79 J.S. Rasor, E.G. Tickner: Microbubble precursors and methods for their production and use. US Patent 4 442 843 (1984)
21.80 J.L. Nelson, B.L. Roeder, J.C. Carinen, F. Roloff, W.G. Pitt: Ultrasonically activated chemotherapeutic drug delivery in a rat model, Cancer Res. **62**, 7280–7283 (2002)
21.81 S.A. Sapareto, W.C. Dewey: Thermal dose determination in cancer therapy, Int. J. Radiat. Oncol. Biol. Phys. **10**, 787–800 (1984)
21.82 M.R. Bailey, L.A. Crum, A.P. Evan, J.A. McAteer, J.C. Williams, O.A. Sapozhinikov, R.O. Cleveland, T. Colonius: *Cavitation in Shock Wave Lithotripsy (Cav03-0s-2-1-006)* (Fifth Int. Symp. Cavitation (CAV2003), Osaka 2003), http://cav2003.me.es.osaka-u.ac.jp/Cav2003/Papers/Cav03-OS-2-1-006.pdf
21.83 E.A. Noser, H.M. Shaltoni, C.E. Hall, A.V. Alexandrov, Z. Garami, E.D. Cacayorin, J.K. Song, J.C. Grotta, M.S. Campbell: Aggressive mechanical clot disruption. A safe adjunct to thrombolytic therapy in acute stroke?, Stroke **36**(2), 292–296 (2005)
21.84 S. Pfaffenberger, B. Devcic-Kuhar, C. Kollmann, S.P. Kastl, C. Kaun, W.S. Speidl, T.W. Weiss, S. Demyanets, R. Ullrich, H. Sochor, C. Wober, J. Zeitlhofer, K. Huber, M. Groschl, E. Benes, G. Maurer, J. Wojta, M. Gottsauner-Wolf: Can a commercial diagnostic ultrasound device accelerate thrombolysis? An in vitro skull model, Stroke **36**(1), 124–128 (2005)
21.85 S. Schafer, S. Kliner, L. Klinghammer, H. Kaarmann, I. Lucic, U. Nixdorff, U. Rosenschein, W.G. Daniel, F.A. Flachskampf: Influence of ultrasound operating parameters on ultrasound-induced thrombolysis in vitro, Ultrasound Med. Biol. **31**(6), 841–847 (2005)
21.86 D.S. Jeon, H. Luo, M.C. Fishbein, T. Miyamoto, M. Horzewski, T. Iwami, J.M. Mirocha, F. Ikeno, Y. Honda, R.J. Siegel: Noninvasive transcutaneous ultrasound augments thrombolysis in the left circumflex coronary artery – An in vivo canine study, Thromb. Res. **110**(2–3), 149–158 (2003)
21.87 A.V. Alexandrov, C.A. Molina, J.C. Grotta, Z. Garami, S.R. Ford, J. Alvarez-Sabin, J. Montaner, M. Saqqur, A.M. Demchuk, L.A. Moye, M.D. Hill, A.W. Wojner, CLOTBUST Investigators: Ultrasound-enhanced systemic thrombolysis for acute ischemic stroke, N. Engl. J. Med. **351**(21), 2170–2178 (2004)
21.88 J. Eggers, G. Seidel, B. Koch, I.R. Konig: Sonothrombolysis in acute ischemic stroke for patients ineligible for rt-PA, Neurology **64**(6), 1052–1054 (2005)
21.89 D. Harpaz: Ultrasound enhancement of thrombolytic therapy: observations and mechanisms, Int. J. Cardiovasc. Intervent. **3**(2), 81–89 (2000)
21.90 S.H. Eik-Nes, O. Okland, J.C. Aure, M. Ulstein: Ultrasound screening in pregnancy: A randomised controlled trial, Lancet **1**(8390), 1347 (1984)
21.91 FDA, U.S. Food and Drug Administration: *Information for Manufacturers Seeking Marketing Clearance of Diagnostic Ultrasound Systems and Transducers* (Center for Devices and Radiological Health U.S. Food and Drug Administration, Rockville 1997)
21.92 FDA: *510(k) Guide for Measuring and Reporting Output of Diagnostic Ultrasound Medical Devices* (Center for Devices and Radiological Health, U.S. Food and Drug Administration, Rockville 1991)
21.93 AIUM/NEMA: *Standard for Real-Time Display of Thermal and Mechanical Acoustic Output Indices on Diagnostic Ultrasound Equipment* (Am. Inst. Ultrasound Medicine, Laurel 1992)
21.94 M. Fatemi, P.L. Ogburn, J.F. Greenleaf: Fetal stimulation by pulsed diagnostic ultrasound, J. Ultrasound Med. **20**, 883–889 (2001)
21.95 M.A. Dinno, M. Dyson, S.R. Young, A.J. Mortimer, J. Hart, L.A. Crum: The significance of membrane changes in the safe and effective use of therapeutic and diagnostic ultrasound, Phys. Med. Biol. **34**(11), 1543–1552 (1989)

Amazon EX1014 Page 903

Structura

Part G

Part G Structural Acoustics and Noise

22 Structural Acoustics and Vibrations
Antoine Chaigne, Palaiseau, France

23 Noise
George C. Maling, Jr., Harpswell, USA

Amazon EX1014 Page 904

22. Structural Acoustics and Vibrations

This chapter is devoted to vibrations of structures and to their coupling with the acoustic field. Depending on the context, the radiated sound can be judged as desirable, as is mostly the case for musical instruments, or undesirable, like noise generated by machinery. In architectural acoustics, one main goal is to limit the transmission of sound through walls. In the automobile industry, the engineers have to control the noise generated inside and outside the passenger compartment. This can be achieved by means of passive or active damping. In general, there is a strong need for quieter products and better sound quality generated by the structures in our daily environment.

Structural acoustics and vibration is an interdisciplinary area, with many different potential applications. Depending on the specific problem under investigation, one has to deal with material properties, structural modifications, signal processing and measurements, active control, modal analysis, identification and localization of sources or nonlinear vibrations, among other hot topics.

In this chapter, the fundamental methods for the analysis of vibrations and sound radiation of structures are presented. It mainly focuses on general physical concepts rather than on specific applications such as those encountered in ships, planes, automobiles or buildings. The fluid–structure coupling is restricted to the case of light compressible fluids (such as air). Practical examples are given at the end of each section.

After a brief presentation of the properties of the basic linear single-degree-of-freedom oscillator, the linear vibrations of strings, beams, membranes, plates and shells are reviewed. Then, the structural–acoustic coupling of some elementary systems is presented, followed by a presentation of the main dissipation mechanisms in structures. The last section is devoted to nonlinear vibrations. In conclusion, a brief overview of some advanced topics in structural acoustics and vibrations is given.

22.1 **Dynamics of the Linear Single-Degree-of-Freedom (1-DOF) Oscillator** 903
22.1.1 General Solution 903
22.1.2 Free Vibrations 903
22.1.3 Impulse Response and Green's Function 904
22.1.4 Harmonic Excitation 904
22.1.5 Energetic Approach 905
22.1.6 Mechanical Power 905
22.1.7 Single-DOF Structural–Acoustic System 906
22.1.8 Application: Accelerometer 907

22.2 **Discrete Systems** 907
22.2.1 Lagrange Equations 907
22.2.2 Eigenmodes and Eigenfrequencies 909
22.2.3 Admittances 909
22.2.4 Example:2-DOF Plate–Cavity Coupling 911
22.2.5 Statistical Energy Analysis 912

22.3 **Strings and Membranes** 913
22.3.1 Equations of Motion 913
22.3.2 Heterogeneous String. Modal Approach 914
22.3.3 Ideal String 916
22.3.4 Circular Membrane in Vacuo 919

22.4 **Bars, Plates and Shells** 920
22.4.1 Longitudinal Vibrations of Bars ... 920
22.4.2 Flexural Vibrations of Beams 920
22.4.3 Flexural Vibrations of Thin Plates 923
22.4.4 Vibrations of Thin Shallow Spherical Shells 925
22.4.5 Combinations of Elementary Structures 926

22.5 **Structural–Acoustic Coupling** 926
22.5.1 Longitudinally Vibrating Bar Coupled to an External Fluid 927
22.5.2 Energetic Approach to Structural–Acoustic Systems 932
22.5.3 Oscillator Coupled to a Tube of Finite Length 934
22.5.4 Two-Dimensional Elasto–Acoustic Coupling 936

Amazon EX1014 Page 905

22.6 **Damping** 940
22.6.1 Modal Projection in Damped Systems 940
22.6.2 Damping Mechanisms in Plates ... 943
22.6.3 Friction 945
22.6.4 Hysteretic Damping 947
22.7 **Nonlinear Vibrations** 947
22.7.1 Example of a Nonlinear Oscillator 947
22.7.2 Duffing Equation 949
22.7.3 Coupled Nonlinear Oscillators 951
22.7.4 Nonlinear Vibrations of Strings ... 955
22.7.5 Review of Nonlinear Equations for Other Continuous Systems 956
22.8 **Conclusion. Advanced Topics** 957
References 958

In this chapter, the fundamental methods for the analysis of vibrations and sound radiation of structures are presented. It mainly focuses on general physical concepts rather than on specific applications such as those encountered in ships, planes, automobiles or buildings. The fluid–structure coupling is restricted to the case of light compressible fluid (such as air). The case of strong coupling with heavy fluid (water) is not treated.

If the magnitude of the vibratory and acoustical quantities of interest can be considered as sufficiently small, then the equations that govern the structural–acoustics phenomena can be linearized. The linear theory of vibrations applied to simple continuous elastic structures, such as bars, membranes, shells and plates, forms a reference framework for numerous studies involving more-complex geometries. In some practical situations, it is not necessary to know the exact vibratory shape at each point of a given system: to take advantage of this, a continuous structure can often be represented as a discrete system built with rigid masses connected to springs and dampers. The main results of the linear theory for the vibration of discrete and continuous systems are presented in Sects. 22.1–22.4. Section 22.1 is devoted to the linear single-degree-of-freedom (DOF) oscillator for which the fundamental results are derived with the help of the Laplace transform. In Sect. 22.2, the case of discrete systems with multiple DOFs is used to introduce the concepts of eigenmodes, eigenfrequencies, the admittance and modal analysis. As an illustration, one example of coupled oscillators is solved in detail. Also the fundamental energy equation of statistical energy analysis (SEA) that governs the mean power flow between coupled oscillators is summarized. Section 22.3 deals with the transverse vibrations of strings and membranes, which can be viewed as limiting cases of prestressed structures with negligible stiffness. In Sect. 22.4, longitudinal and transverse vibrations of bars are presented. The case of flexural vibrations is extended to two-dimensional (2-D) structures such as plates and shallow shells. In this latter case, the influence of curvature is emphasized using the example of a spherical cap for which analytical results can be obtained.

The three remaining sections focus on specific problems of great significance in structural acoustics. The case of vibroacoustic coupling is treated in Sect. 22.5 through examples of increasing complexity. Starting from the simple case of a longitudinally vibrating bar coupled to a semi-infinite tube, it is shown that modes of the structure are coupled to the radiated field, and that eigenfrequencies and modal shapes of the in vacuo structure are modified by this coupling. An energetic approach to the structural–acoustic coupling allows the introduction of radiation filters and radiation efficiencies. A state-space formulation of the phenomena is presented, which is of particular interest for the control of radiated sound. The example of a single-DOF oscillator coupled to a tube illustrates the coupling between a structure and a cavity. Finally, attention is paid to fluid–plate coupling, with the introduction of the concept of the critical frequency. Section 22.6 is devoted to the presentation of important causes of damping in structures. Also some indications are given with regard to the validity of the modal approach for damped discrete and continuous systems.

For structures subjected to motion with large amplitude, most of the concepts and methods developed for linear vibrations no longer apply. Specific methods must be used to account for the observed phenomena of distortion, amplitude-dependent resonance, jump, hysteresis, instability and chaos. Section 22.7 introduces the basic concepts of nonlinear vibrations with some examples. The Duffing equation and the example of two nonlinearly coupled oscillators are analyzed in detail. These examples illustrate the use of perturbation methods for solving nonlinear equations of motion for vibrating systems. Finally, some equations for the vibrations of nonlinear continuous systems (strings, beams, shells and plates) are briefly reviewed.

Amazon EX1014 Page 906

22.1 Dynamics of the Linear Single-Degree-of-Freedom (1-DOF) Oscillator

In the low-frequency range, the linear motion of an electrodynamical loudspeaker, for example, can be described by a single-degree-of-freedom oscillator. This is also the case for any complex structure considered as a rigid body for which the equivalent stiffness is represented by a unique spring, and where all the dissipation mechanisms are approximated by a unique dashpot or *fluid damping* constant; one can think of the rigid-body mode of vibration of an automobile. Also the 1-DOF oscillator has fundamental mathematical properties of great interest in the field of vibrations, since linear vibrations of discrete and continuous structures can be represented by a set of oscillators, as will be shown in the following sections.

The motion of a standard 1-DOF oscillator is governed by a second-order differential equation involving an excitation force $F(t)$ and the response of the structure. Using a formulation with the velocity $v(t)$, we get

$$F = M\frac{\mathrm{d}v}{\mathrm{d}t} + Rv + K\int v\,\mathrm{d}t\,. \tag{22.1}$$

This equation accounts for the motion of a mass M subjected to a restoring force due to a linear spring of stiffness K and a dashpot R which represents a linear viscous fluid damping (Fig. 22.1).

Equation (22.1) can be written alternatively, using the mass displacement $\xi(t)$ and the usual reduced parameters:

$$F = M\left(\frac{\mathrm{d}^2\xi}{\mathrm{d}t^2} + 2\zeta_0\omega_0\frac{\mathrm{d}\xi}{\mathrm{d}t} + \omega_0^2\xi\right)\,, \tag{22.2}$$

where $\omega_0 = \sqrt{M/K}$ is the eigenfrequency of the lossless system and $\zeta_0 = R/2M\omega_0$ is the nondimensional damping coefficient.

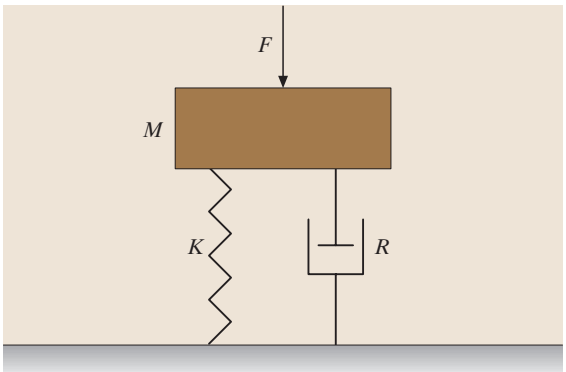


Fig. 22.1 Single-DOF oscillator

22.1.1 General Solution

One strategy for solving a linear equation such as (22.2) is to make use of the Laplace transform [22.1]. Using this transform, (22.2) becomes

$$s^2\mathcal{X}(s) - s\xi(0) - \dot{\xi}(0) + 2\zeta_0\omega_0\left[s\mathcal{X}(s) - \xi(0)\right] + \omega_0^2\mathcal{X}(s) = \frac{\mathcal{F}(s)}{M}\,, \tag{22.3}$$

where $\mathcal{X}(s)$ and $\mathcal{F}(s)$ are the Laplace transforms of $\xi(t)$ and $F(t)$, respectively. Using the tables and properties of the Laplace transforms, we obtain the general solution

$$\xi(t) = \frac{1}{M}\int_0^t F(\theta)G(t-\theta)\,\mathrm{d}\theta + \left[2\zeta_0\omega_0\xi(0) + \dot{\xi}(0)\right]G(t) + \xi(0)\dot{G}(t)\,, \tag{22.4}$$

where $G(t)$ can take different forms, depending on the value of the damping coefficient ζ_0:

- if $\zeta_0 < 1$, which corresponds to the so-called *underdamped* case, then

$$G(t) = \mathrm{e}^{-\zeta_0\omega_0 t}\frac{\sin\omega_0\sqrt{1-\zeta_0^2}\,t}{\omega_0\sqrt{1-\zeta_0^2}}\,; \tag{22.5}$$

- if $\zeta_0 = 1$, which corresponds to the *critical* case, we obtain

$$G(t) = t\,\mathrm{e}^{-\omega_0 t}\,; \tag{22.6}$$

- finally, if $\zeta_0 > 1$, which corresponds to the *overdamped* case, we get

$$G(t) = \mathrm{e}^{-\zeta_0\omega_0 t}\frac{\sinh\omega_0\sqrt{\zeta_0^2-1}\,t}{\omega_0\sqrt{\zeta_0^2-1}}\,. \tag{22.7}$$

22.1.2 Free Vibrations

Free vibrations are characterized by the absence of an external force. With $F(t) = 0$ in (22.4), we get

$$\xi(t) = \left[2\zeta_0\omega_0\xi(0) + \dot{\xi}(0)\right]G(t) + \xi(0)\dot{G}(t)\,, \tag{22.8}$$

- if $\zeta_0 < 1$, the displacement $\xi(t)$ is given by

$$\xi(t) = \mathrm{e}^{-\zeta_0\omega_0 t}\left\{\xi(0)\cos\omega_0\sqrt{1-\zeta_0^2}\,t + \left[\xi(0)\frac{\zeta_0}{\sqrt{1-\zeta_0^2}} + \dot{\xi}(0)\frac{1}{\omega_0\sqrt{1-\zeta_0^2}}\right] \times \sin\omega_0\sqrt{1-\zeta_0^2}\,t\right\} . \tag{22.9}$$

  In this case, the free regime is characterized by a damped sinusoid with oscillation frequency $\omega_0\sqrt{1-\zeta_0^2}$ and decay time $\tau = 1/\zeta_0\omega_0$. The total energy of the system decreases with time.
- if $\zeta_0 = 1$, we obtain

$$\xi(t) = \mathrm{e}^{-\omega_0 t}\left[\xi(0)(1+\omega_0 t) + \dot{\xi}(0)t\right] . \tag{22.10}$$

  The motion exhibits no oscillation. This critical case corresponds to the situation where we get the fastest non-oscillatory motion toward equilibrium;
- if $\zeta_0 > 1$ the displacement $\xi(t)$ becomes

$$\xi(t) = \mathrm{e}^{-\zeta_0\omega_0 t}\left\{\xi(0)\cosh\omega_0\sqrt{\zeta_0^2-1}t + \left[\xi(0)\frac{\zeta_0}{\sqrt{\zeta_0^2-1}} + \dot{\xi}(0)\frac{1}{\omega_0\sqrt{\zeta_0^2-1}}\right] \times \sinh\omega_0\sqrt{\zeta_0^2-1}\,t\right\} . \tag{22.11}$$

  Here again, no oscillation exists. The decay is governed by the combination of two exponentials with decay time τ such that $1/\tau = \omega_0\left(\zeta_0 \pm \sqrt{\zeta_0^2-1}\right)$.

22.1.3 Impulse Response and Green's Function

Consider now the case where $\xi(0) = \dot{\xi}(0) = 0$ and where $F(t)$ is the Dirac delta function $\delta(t)$ whose fundamental property is

$$\int_{-\infty}^{\infty} u(t)\delta(t-a)\,\mathrm{d}t = u(a) , \tag{22.12}$$

where $u(t)$ is a test function. The response $\xi(t)$ can therefore be written as

$$\xi(t) = \frac{1}{M}\int_0^t \delta(\theta)G(t-\theta)\,\mathrm{d}\theta = \frac{1}{M}\int_0^t \delta(t-\theta)G(\theta)\,\mathrm{d}\theta = \frac{G(t)}{M} . \tag{22.13}$$

The function $G(t)$ defined in Sect. 22.1.1 can therefore be defined as the impulse response of the oscillator with mass equal to unity. This function is also referred to as the *Green's function* of the oscillator. For an oscillator initially at rest and excited by an arbitrary time function $F(t)$, the response is given by the convolution integral of $F(t)$ and the Green's function $G(t)$. Equation (22.4) shows, in addition, that for $F(t) = 0$ and $\xi(0) = 0$, the displacement is given by

$$\xi(t) = \dot{\xi}(0)G(t) . \tag{22.14}$$

Therefore, we can see that the solution obtained with a Dirac delta force is proportional to the one obtained with an initial velocity $\dot{\xi}(0)$.

22.1.4 Harmonic Excitation

For harmonic excitation, $F(t) = F_\mathrm{M}\sin\Omega t$, of the oscillator in the underdamped case, (22.4) gives

$$\xi(t) = \frac{F_\mathrm{M}}{M}\frac{\left(\omega_0^2-\Omega^2\right)\sin\Omega t - 2\zeta_0\omega_0\Omega\cos\Omega t}{\left(\omega_0^2-\Omega^2\right)^2 + \left(2\zeta_0\omega_0\Omega\right)^2} + \alpha G(t) + \beta\dot{G}(t) , \tag{22.15}$$

where α and β are constants that depend on the initial conditions. The Green's function $G(t)$ and its time derivative are proportional to $\mathrm{e}^{-\zeta_0\omega_0 t}$ and become negligible for $\zeta_0\omega_0 t \gg 1$. With this assumption, the response to the forcing term at frequency Ω is given by the first term on the right-hand side of (22.15). This term can be written alternatively as

$$\xi(t) = A(\Omega)\sin\left[\Omega t - \Phi(\Omega)\right] \tag{22.16}$$

with

$$A(\Omega) = \frac{F_\mathrm{M}}{M}\frac{1}{\sqrt{\left(\omega_0^2-\Omega^2\right)^2 + (2\zeta_0\omega_0\Omega)^2}}$$

Amazon EX1014 Page 908

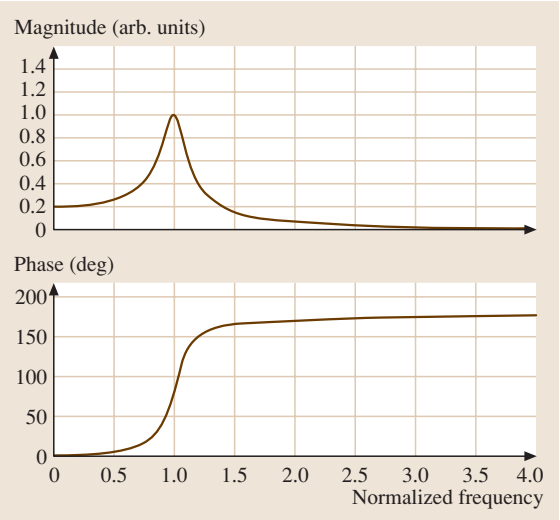


Fig. 22.2 Magnitude and phase of the mass displacement for the forced underdamped oscillator as a function of the normalized frequency Ω/ω_0

and

$$\tan \Phi(\Omega) = \frac{2\zeta_0\omega_0\Omega}{\omega_0^2 - \Omega^2} \,. \tag{22.17}$$

Figure 22.2 shows the variations of A and Φ with Ω in the underdamped case. The amplitude A reaches its maximum for frequency $\Omega = \omega_0\sqrt{1-2\zeta_0^2}$, which is very close to ω_0 for $\zeta_0 \ll 1$. The maximum is equal to $F_\mathrm{M}/2M\zeta_0\omega_0\Omega$.

22.1.5 Energetic Approach

The instantaneous mechanical power $p_\mathrm{m}(t)$ into the system is given by the scalar product of F and v, which yields

$$p_\mathrm{m} = \frac{\mathrm{d}}{\mathrm{d}t}\left(\frac{1}{2}Mv^2 + \frac{1}{2}K\xi^2\right) + Rv^2 \,. \tag{22.18}$$

The terms on the right-hand side of (22.18) represent the kinetic energy of the mass M, the elastic energy of the spring K and the energy dissipated in the mechanical resistance R, respectively. In a number of applications, we are mostly interested in the time-averaged value of $p_\mathrm{m}(t)$ rather than in details of its time evolution. In audio acoustics, for example, the human ear is sensitive to the sound level, which is correlated to the average value of the instantaneous acoustic power, after integration over a duration of nearly 50 ms. Therefore, after defining an integration duration T, whose appropriate selection is discussed later in this section, we can define the average mechanical power $\mathcal{P}_\mathrm{m}(T)$ as

$$\begin{aligned}\mathcal{P}_\mathrm{m}(T) &= \frac{1}{2T}\left[Mv^2(T) + K\xi^2(T) - Mv^2(0) - K\xi^2(0)\right] \\ &\quad + \frac{1}{T}\int_0^T Rv^2(t)\,\mathrm{d}t \,. \end{aligned} \tag{22.19}$$

In a conservative system, the sum of the kinetic and elastic energy remains constant over time, so that the term between the square brackets in (22.19) is equal to zero. As a consequence, the average input power becomes:

$$\mathcal{P}_\mathrm{m}(T) = \frac{1}{T}\int_0^T Rv^2(t)\,\mathrm{d}t = \mathcal{P}_\mathrm{s}(T) \,, \tag{22.20}$$

where $\mathcal{P}_\mathrm{s}(T)$ represents the mean *structural* power dissipated in the mechanical resistance R.

22.1.6 Mechanical Power

A particular case of importance is the steady-state harmonic motion of the mechanical oscillator with angular frequency ω. Given an excitation force $F(t) = F_\mathrm{M}\sin\omega t$, then, due to the assumed linearity of the system, the mass velocity is written $v(t) = V_\mathrm{M}\sin(\omega t + \phi)$. Therefore, $\mathcal{P}_\mathrm{m}(T)$ is given by

$$\mathcal{P}_\mathrm{m}(T) = \frac{1}{T}\int_0^T F_\mathrm{M}V_\mathrm{M}\sin\omega t\,\sin(\omega t + \phi)\,\mathrm{d}t \,. \tag{22.21}$$

Denoting the period of motion by $\tau = 2\pi/\omega$, we can write $T = n\tau + \tau_0$, where n is a positive integer. In this case, the mean power can be rewritten

$$\begin{aligned}\mathcal{P}_\mathrm{m}(T) &= \frac{1}{2}F_\mathrm{M}V_\mathrm{M}\cos\phi + \frac{F_\mathrm{M}V_\mathrm{M}}{4(2\pi n + \tau_0\omega)} \\ &\quad \times [\sin\phi - \sin(2\omega\tau_0 + \phi)] \,. \end{aligned} \tag{22.22}$$

Comment. This equation (22.22) shows that the mean (or average) power $\mathcal{P}_\mathrm{m}(T)$ is nearly equal to $1/2F_\mathrm{M}V_\mathrm{M}\cos\phi$ only if the average duration T contains a sufficiently large number n of periods. If T is equal to $n\tau$, then the previous result is strict. In what follows, it will be assumed that this condition is fulfilled, so that the dependence versus integration time T of the mean power terms will be suppressed. For a given force, the

velocity amplitude V_M and phase angle ϕ are given by

$$V_M = \frac{F_M}{M} \frac{\omega}{\sqrt{\left(\omega^2 - \omega_0^2\right)^2 + 4\zeta_0^2\omega^2\omega_0^2}} , \quad (22.23)$$

$$\cos\phi = \frac{2\zeta_0\omega_0\omega}{\sqrt{\left(\omega^2 - \omega_0^2\right)^2 + 4\zeta_0^2\omega^2\omega_0^2}} , \quad (22.24)$$

and the mean power becomes:

$$\mathcal{P}_m = \frac{F_M^2}{2R} \frac{4\zeta_0^2\omega_0^2\omega^2}{\left(\omega^2 - \omega_0^2\right)^2 + 4\zeta_0^2\omega^2\omega_0^2} . \quad (22.25)$$

Equation (22.25) shows that the maximum of the dissipated power, and thus the maximum of the input power, is obtained for $\omega = \omega_0$, i. e. when the excitation frequency is equal to the eigenfrequency of the oscillator. In this case, we obtain:

$$\mathrm{Max}\left(\mathcal{P}_m\right) = \frac{F_M^2}{2R} . \quad (22.26)$$

Since F_M is known, in general, (22.26) can be used for estimating the mechanical resistance R.

Remark. Recall that (22.25) is only valid in the dynamic equilibrium, which does not correspond to many experimental (or numerical) situations where, for obvious causality reasons, the force is applied at a given instant of time, usually taken as origin. In this more realistic case, the force signal should be written as $F(t) = F_M H(t) \sin\omega t$, where $H(t)$ is the Heaviside function. In this case, the Laplace transform of the velocity is

$$V(s) = \frac{F_M}{M} \frac{s\omega}{\left(s^2 + \omega^2\right)\left(s^2 + 2\zeta_0\omega_0 s + \omega_0^2\right)} . \quad (22.27)$$

From which the velocity is derived

$$v(t) = \frac{F_M\omega}{M\sqrt{D(\omega)}} + A(\omega)\exp(-\zeta_0\omega_0 t)\times \sin\left[\omega_0\sqrt{1-\zeta_0^2}\, t + \psi(\omega)\right] , \quad (22.28)$$

where $D(\omega) = \left(\omega^2 - \omega_0^2\right)^2 + 4\zeta_0^2\omega^2\omega_0^2$. $A(\omega)$ and $\psi(\omega)$ are also functions of the excitation frequency whose exact expressions do not add significant matter to the present discussion. The first term in the expression of $v(t)$ corresponds to the steady-state regime. The important features of the second term are the following:

- It is non-negligible as long as the time is small compared to the decay time $(\zeta_0\omega_0)^{-1}$. For lightly damped structural modes, the decay time can be of the order of 0.1 ms or more. The second term cannot then be neglected during the first 0.5–1.0 s of the sound, if one wants to estimate the mean sound power correctly.
- When multiplying $v(t)$ by $F(t)$ and integrating over time, terms with frequencies $\omega + \omega_0\sqrt{1-\zeta_0^2}$ and $\left|\omega - \omega_0\sqrt{1-\zeta_0^2}\right|$ appear in the expression of $\mathcal{P}_m$. As a consequence, the mean power fluctuates at low frequency, which is another cause of difficulty for estimating its value properly.

22.1.7 Single-DOF Structural–Acoustic System

We now investigate the simple example of a mechanical oscillator acting as a piston at one end of an air-filled semi-infinite tube presenting an additional acoustical resistance $R_a = \rho c S$. The oscillator motion is now governed by the equation

$$F = M\frac{\mathrm{d}v}{\mathrm{d}t} + Rv + \int v\,\mathrm{d}t + R_a v . \quad (22.29)$$

The instantaneous input power is given by

$$p_m(t) = \frac{\mathrm{d}}{\mathrm{d}t}\left(\frac{1}{2}Mv^2 + \frac{1}{2}K\xi^2\right) + (R + R_a)v^2 . \quad (22.30)$$

The average input power becomes

$$\mathcal{P}_m(T) = \frac{1}{T}\int_0^T Rv^2(t)\,\mathrm{d}t + \frac{1}{T}\int_0^T R_a v^2(t)\,\mathrm{d}t = \mathcal{P}_s(T) + \mathcal{P}_a(T) , \quad (22.31)$$

where $\mathcal{P}_a(T)$ is the acoustic mean power radiated in the tube. The acoustical efficiency of the system is given by .

$$\eta = \frac{\mathcal{P}_a(T)}{\mathcal{P}_m(T)} = \frac{\mathcal{P}_a(T)}{\mathcal{P}_s(T) + \mathcal{P}_a(T)} = \frac{R_a}{R + R_a} \quad (22.32)$$

Some remarks can be formulated with regards to (22.32).

- The expression for the acoustical efficiency is independent of the integration time T.
- Though (22.32) appears simple in form, the experimental (or numerical) determination of the efficiency is generally not straightforward. R can be estimated through calculation of the mechanical power in vacuo $\mathcal{P}_{mo}(T)$.
- In the simple example discussed here, the acoustical resistance, and hence the acoustic power, is known.

This does not include the case where the acoustic power is not known, and has to be estimated by measurements of the acoustic intensity in the fluid, for example.

Link Between Sound Power and Free-Vibration Decay Times

For a single-DOF system, an alternative method for estimating the sound power consists of estimating the decay times of free vibrations through experiments or numerical calculations. Let us take the example of the previously described oscillator loaded by the semi-infinite tube. We consider the case $F(t) = 0$, with the mass initially moved from equilibrium by a quantity $\xi(0) = \xi_0$ and released with zero velocity at $t = 0$. The equation of motion is written as

$$\frac{\mathrm{d}^2\xi}{\mathrm{d}t^2} + 2\zeta\omega_0\frac{\mathrm{d}\xi}{\mathrm{d}t} + \omega_0^2\xi = 0 \qquad (22.33)$$

with

$$\zeta = \frac{R + R_\mathrm{a}}{2M\omega_0} .$$

The Laplace transform of the displacement is given by

$$\xi(s) = \xi_0\frac{s + 2\zeta\omega_0}{s^2 + 2\zeta\omega_0 s + \omega_0^2} \qquad (22.34)$$

from which the time evolution of the mass displacement is obtained (assuming $\zeta < 1$)

$$\xi(t) = \exp(-\zeta\omega_0 t)\left[\cos\left(\omega_0\sqrt{1-\zeta^2}t\right) + \frac{\zeta}{\sqrt{1-\zeta^2}}\sin\left(\omega_0\sqrt{1-\zeta^2}t\right)\right] . \qquad (22.35)$$

Equation (22.35) shows that the *decay factor* α (equal to the inverse of the decay time) is equal to $\zeta\omega_0 = (R + R_\mathrm{a})/2M$. The same mathematical derivations applied to the oscillator in vacuo yields $\alpha_0 = \zeta_0\omega_0 = R/2M$. In conclusion, this shows that, for the 1-DOF system studied here, the acoustical efficiency can be estimated in the time domain by the expression

$$\eta = \frac{\alpha - \alpha_0}{\alpha} . \qquad (22.36)$$

22.1.8 Application: Accelerometer

Accelerometers are piezoelectric transducers which are widely used for vibration measurements. An accelerometer has a base, a piezoelectric crystal and a seismic mass (Fig. 22.3). It delivers an electric signal which is proportional to the compression force applied to the crystal. Such a device can be modeled by a 1-DOF oscillator equation. Let us denote by k the equivalent stiffness of the crystal, by m the seismic mass, and by $\omega_0 = \sqrt{k/m}$ the resonance frequency of the accelerometer. Internal damping is neglected here, for simplicity. For a sinusoidal excitation $A\sin\Omega t$ of the base, the compression force is [22.2]:

$$F \simeq -\frac{k\Omega^2}{\omega_0^2 - \Omega^2} A\sin\Omega t . \qquad (22.37)$$

Therefore, we can see that if $\Omega \ll \omega_0$, then the signal delivered by the accelerometer is proportional to the acceleration of the base. The frequency response curve of an accelerometer is flat below its resonance frequency, which gives the upper limit of its valid frequency range.

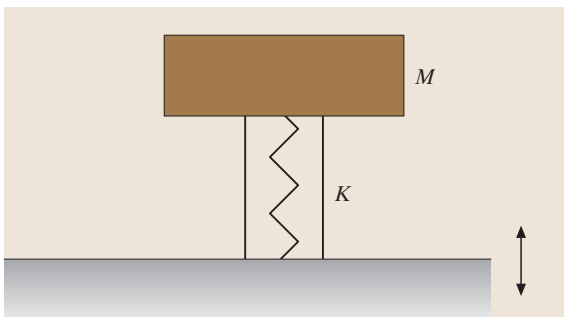


Fig. 22.3 Accelerometer

22.2 Discrete Systems

In a number of applications, real structures can be approximated by an assembly of discrete rigid substructures, which leads to enormous computational simplifications. In fact numerical modeling (finite elements, finite differences) is such an example where continuous structures are replaced by an equivalent set of discretely connected elements. In experimental techniques, such as modal analysis, measurements are taken at discrete positions on the structure under study, and thus the measurements are treated by methods applicable to discrete systems.

Amazon EX1014 Page 911

22.2.1 Lagrange Equations

For a discrete system with n degrees of freedom, the kinetic energy E_k can be formulated as a function of the generalized coordinates q_n and velocities $\dot{q}_n$

$$E_\mathrm{k} = E_\mathrm{k}(q_1, q_2, \ldots, q_n, \dot{q}_1, \dot{q}_2, \ldots \dot{q}_n) = E_\mathrm{k}(q, \dot{q}) \tag{22.38}$$

Thus, given virtual vectors of displacements δq and velocities $\delta\dot{q}$, the variation of the kinetic energy is written

$$\delta E_\mathrm{k} = \sum_{k=1}^{n} \frac{\partial E_\mathrm{k}}{\partial q_k}\delta q_k + \frac{\partial E_\mathrm{k}}{\partial \dot{q}_k}\delta\dot{q}_k \,. \tag{22.39}$$

Remark. Recall that δq has to be kinematically compatible with the system, though not necessarily equal to a real displacement, so that the partial derivatives of T versus δq and $\delta\dot{q}$ are independent.

Applying Hamilton's principle, with $\delta q = 0$ at t_1 and t_2, we can write the minimization integral as

$$\int_{t_1}^{t_2} \left(\delta E_\mathrm{k} - \delta V + \delta W_\mathrm{nc}\right) \mathrm{d}t = 0 \tag{22.40}$$

where V is the potential energy of the system and W_nc is the energy of the nonconservative applied external forces. Through integration by parts, we can write

$$\begin{aligned}
&\int_{t_1}^{t_2} \frac{\partial E_\mathrm{k}}{\partial \dot{q}_k}\delta\dot{q}_k \,\mathrm{d}t \\
&= \left[\frac{\partial E_\mathrm{k}}{\partial \dot{q}_k}\delta q_k\right]_{t_1}^{t_2} - \int_{t_1}^{t_2} \frac{\mathrm{d}}{\mathrm{d}t}\left(\frac{\partial T}{\partial \dot{q}_k}\right)\delta q_k \,\mathrm{d}t \\
&= -\int_{t_1}^{t_2} \frac{\mathrm{d}}{\mathrm{d}t}\left(\frac{\partial E_\mathrm{k}}{\partial \dot{q}_k}\right)\delta q_k \,\mathrm{d}t \,.
\end{aligned} \tag{22.41}$$

Assuming that $V = V(q)$, which corresponds to a large class of problems in dynamics and vibrations,

$$\delta V = \sum_{k=1}^{n} \frac{\partial V}{\partial q_k}\delta q_k \,. \tag{22.42}$$

Finally, the virtual work δW_nc can be written as the scalar product of the vectors F of generalized forces and virtual displacement δq in the form $\delta W_\mathrm{nc} = \sum_{k=1}^{n} F_k \delta q_k$, so that (22.40) becomes

$$\sum_{k=1}^{n} \int_{t_1}^{t_2} \left[\frac{\partial E_\mathrm{k}}{\partial q_k} - \frac{\mathrm{d}}{\mathrm{d}t}\left(\frac{\partial E_\mathrm{k}}{\partial \dot{q}_k}\right) - \frac{\partial V}{\partial q_k} + F_k\right]\delta q_k \,\mathrm{d}t = 0 \,. \tag{22.43}$$

Since the integral in (22.43) must be equal to zero for any δq this implies, for each k

$$\frac{\mathrm{d}}{\mathrm{d}t}\left(\frac{\partial E_\mathrm{k}}{\partial \dot{q}_k}\right) - \frac{\partial E_\mathrm{k}}{\partial q_k} + \frac{\partial V}{\partial q_k} = F_k \,. \tag{22.44}$$

The set of n differential equations (22.44) are the Lagrange equations of the discrete system. This set yields the equations of motion in a very elegant and practical manner.

Small Displacements. Linearization

For small perturbations from equilibrium, we can write $q_k = Q_k + \varepsilon X_k$, where $\varepsilon \ll 1$. Assuming that Q is given by the Lagrange equations and that the generalized forces F are independent of q, a first-order approximation of (22.44), for each k, gives

$$\begin{aligned}
&\frac{\partial^2 E_\mathrm{k}}{\partial \dot{q}_k \partial \dot{q}_j}\ddot{X}_k + \\
&\left[\frac{\mathrm{d}}{\mathrm{d}t}\left(\frac{\partial^2 E_\mathrm{k}}{\partial \dot{q}_k \partial \dot{q}_j}\right) + \frac{\partial^2 E_\mathrm{k}}{\partial q_k \partial \dot{q}_j} - \frac{\partial^2 E_\mathrm{k}}{\partial \dot{q}_k \partial q_j}\right]\dot{X}_k + \\
&\left[\frac{\mathrm{d}}{\mathrm{d}t}\left(\frac{\partial^2 E_\mathrm{k}}{\partial q_k \partial \dot{q}_j}\right) + \frac{\partial^2 V}{\partial q_k \partial q_j} - \frac{\partial^2 E_\mathrm{k}}{\partial q_k \partial q_j}\right] X_k = 0 \,,
\end{aligned} \tag{22.45}$$

which becomes in matrix form

$$\mathbf{M}\ddot{\boldsymbol{X}} + \mathbf{C}\dot{\boldsymbol{X}} + \mathbf{K}\boldsymbol{X} = 0 \,. \tag{22.46}$$

1. Since the kinetic energy E_k is a positive quadratic form of the velocity, the mass matrix $\mathbf{M}$ is a symmetric positive operator.
2. The matrix $\mathbf{C}$ is a generalized damping matrix made up of three terms:
   - The first, with generic element $C_{kj1} = \frac{\mathrm{d}}{\mathrm{d}t}\left(\frac{\partial^2 E_\mathrm{k}}{\partial \dot{q}_k \partial \dot{q}_j}\right)$ is associated with the temporal variation of the mass matrix;
   - The two other terms $\frac{\partial^2 E_\mathrm{k}}{\partial q_k \partial \dot{q}_j} - \frac{\partial^2 E_\mathrm{k}}{\partial \dot{q}_k \partial q_j}$ relate to gyroscopic forces. This part of the matrix $\mathbf{C}$ is antisymmetric and does not lead to dissipation.
3. The stiffness matrix $\mathbf{K}$ also is a sum of three terms:
   - The first is associated with the time variation of the first gyroscopic term in $\mathbf{C}$;
   - The second is governed by the q dependence of V;
   - The third is governed by the q dependence of E_k.

In what follows, we restrict our attention to conservative systems where E_k is independent of q and where

Amazon EX1014 Page 912

the mass matrix is taken to be constant with time. In this case, (22.46) becomes

$$\mathbf{M}\ddot{\boldsymbol{X}} + \mathbf{K}\boldsymbol{X} = 0 \tag{22.47}$$

with

$$\begin{cases} M_{kj} = M_{jk} = \dfrac{\partial^2 E_\mathrm{k}}{\partial \dot{q}_k \partial \dot{q}_j} \\ K_{kj} = K_{jk} = \dfrac{\partial^2 V}{\partial q_k \partial q_j} \end{cases} . \tag{22.48}$$

22.2.2 Eigenmodes and Eigenfrequencies

Natural modes (or eigenmodes) are the sinusoidal (or harmonic) solutions of (22.47) with frequency ω in the absence of a driving term. As a consequence, the natural modes are solutions of the equation

$$\left(-\omega^2\mathbf{M} + \mathbf{K}\right)\boldsymbol{X} = 0 \tag{22.49}$$

with roots (or eigenvalue, or eigenfrequency) ω_n solutions of the characteristic equation

$$\det\left(-\omega^2\mathbf{M} + \mathbf{K}\right) = 0\,. \tag{22.50}$$

The eigenvector $\boldsymbol{\Phi}_n$ associated to each eigenfrequency ω_n is given by

$$\left(-\omega_n^2\mathbf{M} + \mathbf{K}\right)\boldsymbol{\Phi}_n = 0\,. \tag{22.51}$$

$\boldsymbol{\Phi}_n$ is defined with an arbitrary multiplicative constant. The natural modes are defined by the set of eigenvalues ω_n and associated eigenvectors $\boldsymbol{\Phi}_n$. Spectral analysis theory shows that the $\boldsymbol{\Phi}_n$ form an $\mathbf{M}$ and $\mathbf{K}$ orthogonal basis set, so that

$${}^{\mathrm{t}}\boldsymbol{\Phi}_m\mathbf{M}\boldsymbol{\Phi}_n = 0$$

and

$${}^{\mathrm{t}}\boldsymbol{\Phi}_m\mathbf{K}\boldsymbol{\Phi}_n = 0 \quad \text{for} \quad m \neq n \tag{22.52}$$

The orthogonality properties of the eigenmodes mean that the inertial (stiffness) forces developed in a given mode do not affect the motion of the other modes. The modes are mechanically independent. As a consequence, it is possible to expand any motion onto the eigenmodes. Given a force distribution $\boldsymbol{F}$, the motion of the system is governed by the equation

$$\mathbf{M}\ddot{\boldsymbol{X}} + \mathbf{K}\boldsymbol{X} = \boldsymbol{F}\,. \tag{22.53}$$

The modal projection is written in the form:

$$\boldsymbol{X} = \sum_n \boldsymbol{\Phi}_n q_n(t)\,. \tag{22.54}$$

The functions $q_n(t)$ in (22.54) are the modal participation factors. Inserting (22.54) into (22.53) and, after taking the scalar product of both sides of the equation with an eigenfunction $\boldsymbol{\Phi}_m$, we find

$$\langle\boldsymbol{\Phi}_n, \mathbf{M}\boldsymbol{\Phi}_n\rangle\ddot{q}_n + \langle\boldsymbol{\Phi}_n, \mathbf{K}\boldsymbol{\Phi}_n\rangle q_n = \langle\boldsymbol{\Phi}_n, \boldsymbol{F}\rangle \tag{22.55}$$

where the notation $\langle\boldsymbol{A}, \boldsymbol{B}\rangle$ denotes the scalar product ${}^{\mathrm{t}}\boldsymbol{A}.\boldsymbol{B}$ between vectors the $\boldsymbol{A}$ and $\boldsymbol{B}$. Equation (22.55) shows that the generalized displacements are uncoupled. Each q_n is governed by a single-DOF oscillator differential equation. The quantity

$$m_n = \langle\boldsymbol{\Phi}_n, \mathbf{M}\boldsymbol{\Phi}_n\rangle \tag{22.56}$$

is the modal mass associated with the mode n. These coefficients are defined with an arbitrary multiplicative constant. Similarly,

$$\kappa_n = \langle\boldsymbol{\Phi}_n, \mathbf{K}\boldsymbol{\Phi}_n\rangle \tag{22.57}$$

is the modal stiffness, related to the modal mass through the relationship

$$\kappa_n = m_n\omega_n^2\,. \tag{22.58}$$

Finally, the quantity

$$f_n = \langle\boldsymbol{\Phi}_n, \boldsymbol{F}\rangle \tag{22.59}$$

is the projection of the nonconservative forces onto mode n. Each independent oscillator equation can then be rewritten as

$$\ddot{q}_n + \omega_n^2 q_n = \frac{f_n}{m_n}\,. \tag{22.60}$$

Remark. Since the eigenvectors are defined with arbitrary multiplicative constants C_n, (22.56) shows that the modal mass is proportional to C_n^2. In addition, (22.58) shows that f_n is also proportional to C_n. Therefore, through (22.60), q_n is proportional to C_n^{-1} and from (22.54), $\boldsymbol{X}$ is independent of C_n.

Normal Modes. The normal modes Ψ_n correspond to the case where the arbitrary constant is such that the modal masses become unity. In this case, we can write

$$\Psi_n = \frac{\Phi_n}{\sqrt{m_n}}\,. \tag{22.61}$$

Amazon EX1014 Page 913

Consequently, (22.57) becomes

$$\langle \boldsymbol{\Psi}_n, \mathbf{K}\boldsymbol{\Psi}_n \rangle = \omega_n^2 \,. \tag{22.62}$$

22.2.3 Admittances

In general, a given structure vibrates as a result of the action of localized and distributed forces and moments. For both numerical and experimental reasons, one often has to work on a discrete representation of the structure. In practice, the geometry of the structure is represented by a mesh consisting of a number N of areas with dimensions smaller than the wavelengths under consideration. This results in having to consider the structure as an N-DOF system. At each point of the mesh, the motion is defined by three translation components plus three rotation components. Similarly, the action of the external medium on the structure can be reduced to three force components plus three moment components, here denoted by F_l. The translational and rotational velocity components V_k at each point are thus related to the forces and moments through a 6×6 admittance matrix, such that

$$\boldsymbol{V} = \mathbf{Y}\boldsymbol{F} \tag{22.63}$$

For each force component at a given point j on the structure, denoted $F_{j|l}$, a motion at another point i, denoted by $V_{i|k}$, can be generated. As a consequence one can define the transfer admittance

$$Y_{ij|kl} = \frac{V_{i|k}}{F_{j|l}} \quad \text{with} \quad 1 \le i, j \le N \quad \text{and} \quad 1 \le k, l \le 6 \,.$$

In summary, the transfer admittance matrix is defined by $6N\times6N$ coefficients such as $Y_{ij|kl}$.

Notation. In what follows, the indices (k, l) are omitted, for the sake of simplicity. The transfer admittances are written as Y_{ij}, which reduces to Y_{ii} (or, even to Y_i) in the case of a driving-point admittance. Attention here is mostly focused on translation, though the formalism remains valid for rotation.

The previous results obtained on modal decomposition are now used to investigate the frequency dependence of the admittances. Here, $X(x_i) \equiv X_i$ is one component of displacement at point x_i and $F(x_j) \equiv F_j$ is one force component at point x_j. The structure is subjected to a forced motion at frequency ω. We have

$$\left(\mathbf{K} - \omega^2\mathbf{M}\right) X_i = F_j \,, \tag{22.64}$$

where $X_i = \sum \Phi_n(x_i) q_n(t)$ and

$$\left(\omega_n^2 - \omega^2\right) q_n = \frac{f_n}{m_n} = \frac{{}^{\mathrm{t}}\Phi_n(x_j) F_j(\omega)}{m_n} \,. \tag{22.65}$$

For a structure discretized on N points, the displacement at point x_i is given by

$$X_i(\omega) = \sum_{n=1}^{N} \frac{\Phi_n(x_i)\, {}^{\mathrm{t}}\Phi_n(x_j)}{m_n\left(\omega_n^2 - \omega^2\right)} F_j(\omega) \,. \tag{22.66}$$

The complete set of functions $X_i(\omega)$ given in (22.66) is the operating deflexion shape (ODS) at frequency ω. The transfer admittance between points x_i and x_j is written

$$Y_{ij}(\omega) = \mathrm{i}\omega \sum_{n=1}^{N} \frac{\Phi_n(x_i)\, {}^{\mathrm{t}}\Phi_n(x_j)}{m_n\left(\omega_n^2 - \omega^2\right)} \,. \tag{22.67}$$

The driving-point admittance at point x_i becomes

$$Y_i(\omega) = \mathrm{i}\omega \sum_{n=1}^{N} \frac{[\Phi_n(x_i)]^2}{m_n\left(\omega_n^2 - \omega^2\right)} \tag{22.68}$$

Remark. To include damping, (22.67) can be written

$$Y_{ij}(\omega) = \mathrm{i}\omega \sum_{n=1}^{N} \frac{\Phi_n(x_i)\, {}^{\mathrm{t}}\Phi_n(x_j)}{m_n\left(\omega_n^2 + 2\mathrm{i}\zeta_n\omega_n\omega - \omega^2\right)} \,, \tag{22.69}$$

where ζ_n is a nondimensional damping factor. The physical origin of the damping terms will be presented in more detail in Sect. 22.6.1.

Frequency Analysis and Approximations

For weak damping, and low modal density, the modulus of $Y_{ij}(\omega)$ passes through maxima at frequencies close to the eigenfrequencies $\omega = \omega_n$ (Fig. 22.4).

- For $\omega \approx \omega_n$, the main term in $Y_{ij}(\omega)$ is equal to

$$\mathrm{i}\omega \frac{\Phi_n(x_i)\, {}^{\mathrm{t}}\Phi_n(x_j)}{m_n\left(\omega_n^2 - \omega^2\right)} \,. \tag{22.70}$$

- For $\omega \gg \omega_n$, the admittance becomes

$$Y_{ij} \approx \mathrm{i}\omega \sum_{l>n} \frac{\Phi_l(x_i)\, {}^{\mathrm{t}}\Phi_l(x_j)}{-m_l\omega^2} \approx \frac{1}{\mathrm{i}M\omega}$$

with

$$\frac{1}{M} = \sum_{l>n} \frac{\Phi_l(x_i)\, {}^{\mathrm{t}}\Phi_l(x_j)}{m_l} \tag{22.71}$$

It can be seen that the modes with a rank larger than a given mode n play the role of a mass M.

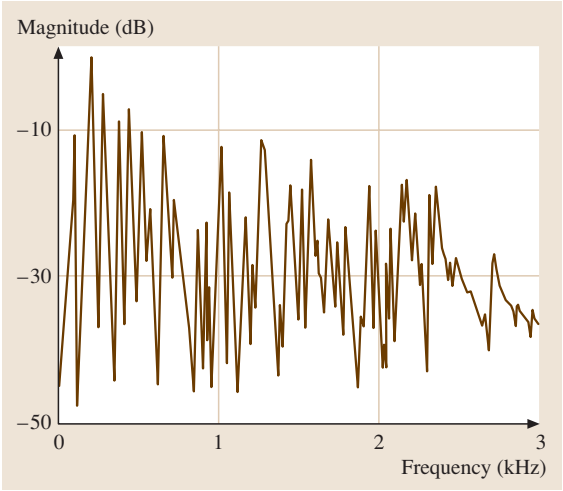


Fig. 22.4 Typical frequency dependence of an admittance modulus for a lightly damped structure. (After *Derveaux* et al. [22.3]

- Similarly, for modes with a rank smaller than n, we find

$$Y_{ij} \approx \mathrm{i}\omega \sum_{l<n} \frac{\Phi_l(x_i)\,{}^{\mathrm{t}}\Phi_l(x_j)}{m_l\omega_l^2} \approx \frac{\mathrm{i}\omega}{K}$$

with

$$\frac{1}{K} = \sum_{l<n} \frac{\Phi_l(x_i)\,{}^{\mathrm{t}}\Phi_l(x_j)}{m_l\omega_l^2} \,. \qquad (22.72)$$

Here, the contribution of the modes is equivalent to a stiffness K.

In summary, in the vicinity of a resonance of mode n, the transfer admittance can be written

$$Y_{ij}(\omega) \approx \mathrm{i}\omega \frac{\Phi_n(x_i)\,{}^{\mathrm{t}}\Phi_n(x_j)}{m_n\left(\omega_n^2-\omega^2\right)} + \frac{\mathrm{i}\omega}{K} + \frac{1}{\mathrm{i}M\omega} \,. \qquad (22.73)$$

22.2.4 Example: 2-DOF Plate–Cavity Coupling

To illustrate the previous concepts, a simple example of structural–acoustic coupling represented by a moving plate over a cavity with a hole is considered. This corresponds to a crude low-frequency model for stringed instruments or vented boxes [22.4]. V is the volume of the cavity, A_h is the section of the air piston of mass m_h and displacement x_h, and m_p is the mass of the plate with area A_p (Fig. 22.4). It is assumed that all points of the plate move in phase with the displacement x_p;

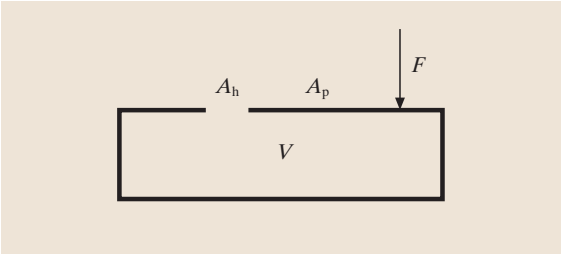


Fig. 22.5 Two-DOF plate–cavity coupling

k_p is the equivalent stiffness of the elastic plate and $\omega_{\mathrm{p},0} = \sqrt{k_\mathrm{p}/m_\mathrm{p}}$ denotes its eigenfrequency in the absence of coupling to the cavity. As the plate and piston are set in motion, the change of volume in the cavity is equal to $\Delta V = A_\mathrm{p}x_\mathrm{p} + A_\mathrm{h}x_\mathrm{h}$. Consequently, the pressure change in the cavity is $\Delta p = -\frac{\rho c^2 \Delta V}{V}$. F is the vertical external force applied to the plate, R_p and R_h are fluid damping coefficients. The equations that govern the motion of the coupled oscillators can be written

$$\begin{cases} m_\mathrm{p}\ddot{x_\mathrm{p}} = F - k_\mathrm{p}x_\mathrm{p} - R_\mathrm{p}\dot{x_\mathrm{p}} + A_\mathrm{p}\Delta p \,, \\ m_\mathrm{h}\ddot{x_\mathrm{h}} = A_\mathrm{h}\Delta p - R_\mathrm{h}\dot{x_\mathrm{h}} \end{cases} \,. \qquad (22.74)$$

Let us write $\mu = c^2\rho/V$. If the cavity is closed ($A_\mathrm{h} = 0$), then the eigenfrequency of the plate is given by $\omega_\mathrm{p} = \sqrt{\left(k_\mathrm{p} + \mu A_\mathrm{p}^2\right)/m_\mathrm{p}}$. If the stiffness k_p of the plate tends to zero, then the eigenfrequency of the plate coupled to the cavity becomes $\omega_\mathrm{a} = \sqrt{\mu A_\mathrm{p}^2/m_\mathrm{p}}$. Finally, if the plate is assumed to be completely rigid ($x_\mathrm{p} = 0$), then the eigenfrequency of the cavity–hole system (Helmholtz resonance) is $\omega_\mathrm{h} = \sqrt{\mu A_\mathrm{h}^2/m_\mathrm{h}}$. Solving (22.74) for a sinusoidal excitation $F\mathrm{e}^{\mathrm{i}\omega t}$, with $\gamma_\mathrm{p} = R_\mathrm{p}/m_\mathrm{p}$ and $\gamma_\mathrm{h} = R_\mathrm{h}/m_\mathrm{h}$, yields for the plate velocity u_p and air velocity u_h in the piston:

$$u_\mathrm{p} = \mathrm{i}\omega \frac{F}{m_\mathrm{p}} \frac{\left(\omega_\mathrm{h}^2 - \omega^2 + j\omega\gamma_\mathrm{h}\right)}{D} \qquad (22.75)$$

and

$$u_\mathrm{h} = -\mathrm{i}\omega \frac{F}{m_\mathrm{p}} \frac{A_\mathrm{p}}{A_\mathrm{h}} \frac{\omega_\mathrm{h}^2}{D} \qquad (22.76)$$

with

$$D = \left(\omega_\mathrm{p}^2 - \omega^2 + \mathrm{i}\omega\gamma_\mathrm{p}\right)\left(\omega_\mathrm{h}^2 - \omega^2 + \mathrm{i}\omega\gamma_\mathrm{h}\right) - \omega_\mathrm{ph}^4 \,, \qquad (22.77)$$

where

$$\omega_\mathrm{ph}^4 = \omega_\mathrm{h}^2\omega_\mathrm{a}^2 \,.$$

Amazon EX1014 Page 915

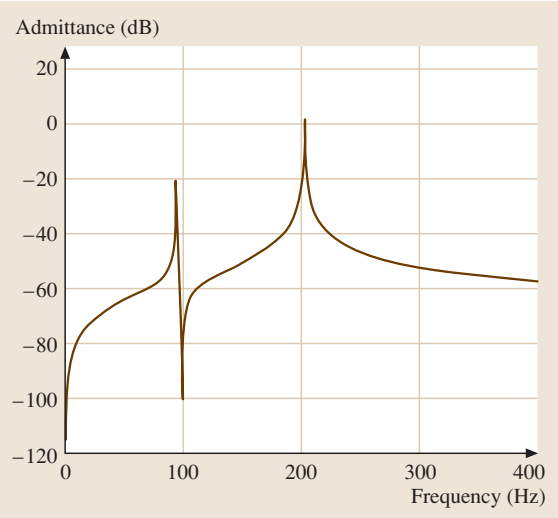


Fig. 22.6 Driving-point admittance of a plate loaded by a cavity. $A_p = 0.01\,m^2$; $V = 0.1\,m^3$; $f_h = 100\,Hz$; $f_p = 200\,Hz$; $\gamma_h = 1.0\,s^{-1}$; $\gamma_p = 2.0\,s^{-1}$; $m_p = 0.4\,kg$; Admittance Y (in dB) $= 20 \log |u_p/F|$

The eigenfrequencies of the coupled system correspond to the roots of the denominator D. Neglecting the influence of losses, these eigenfrequencies are solutions of the equation

$$\left(\omega_p^2 - \omega^2\right)\left(\omega_h^2 - \omega^2\right) - \omega_{ph}^4 = 0\,. \tag{22.78}$$

The solutions ω_+ and ω_- satisfy the relation

$$\omega_+^2 + \omega_-^2 = \omega_p^2 + \omega_h^2\,, \tag{22.79}$$

which shows that the difference between the eigenfrequencies increases due to the coupling between the plate and the Helmholtz resonator, compared to the uncoupled case. Figure 22.6 shows the modulus of the driving-point admittance $|u_p/F|$ of the plate, showing two maxima at ω_+ and ω_- and a zero at ω_h.

In stringed instruments and vented boxes, the main effect of the open cavity is to enhance the radiated sound in the low-frequency range, below the lowest resonance of the moving structure (the top plate or loudspeaker diaphragm).

22.2.5 Statistical Energy Analysis

The aim of statistical energy analysis (SEA) is to use power flows as a means for estimating the responses of complex systems. It is of particular interest for the analysis of coupled structures such as those encountered in the transportation industry. It is often used for the preliminary design of structures, or for identifying energy transmission paths [22.5].

One main advantage of SEA is that it usually leads to a substantial reduction of the number of degrees of freedom. The price to pay is that results are only given in terms of average and variance over frequency and space. It is particularly suitable when structural details are not known, or when measurements yield uncertainty in the modal parameters. SEA techniques focus on the analysis of energy levels in resonant modes of dynamical systems. Its main principle is based on the property that the average power flow between two coupled systems (or subsystems) is proportional to the difference in the average modal energies of each system. In order to illustrate this basic concept of SEA, the case of two coupled 1-DOF oscillators is summarized below. Detailed developments can be found in [22.6].

To consider a general case, it is assumed that both oscillators are coupled by means of a coupling spring with stiffness coefficient k_{12} and a gyroscopic constant B. The equations of motion of this system are given by

$$\begin{cases} m_1 \dfrac{d^2\xi_1}{dt^2} + r_1 \dfrac{d\xi_1}{dt} + s_1\xi_1 + B\dfrac{d\xi_2}{dt} + k_{12}\xi_2 = F_1\,, \\ m_2 \dfrac{d^2\xi_2}{dt^2} + r_2 \dfrac{d\xi_2}{dt} + s_2\xi_2 - B\dfrac{d\xi_1}{dt} + k_{12}\xi_1 = F_2\,, \end{cases} \tag{22.80}$$

where m_1 and m_2 are the masses of the oscillators, $r_1 = 2\delta_1 m_1$ and $r_2 = 2\delta_2 m_2$ are the mechanical resistances, $s_1 = k_1 - k_{12}$ and $s_2 = k_2 - k_{12}$ are stiffness coefficients, and F_1 and F_2 are the magnitudes of the forces applied to each mass. For a harmonic motion with frequency ω, the power flow between the oscillators is given by

$$P_{12} = \frac{1}{2}\,\mathrm{Re}\left(F_{12}v_2^*\right)\,, \tag{22.81}$$

where v_2^* is the complex conjugate of the velocity for the second oscillator and F_{12} is the force applied by oscillator 1 to oscillator 2. Using (22.80), the power flow at frequency ω is written [22.6]

$$P_{12} = \frac{\omega^2 s_{12}^2 + \omega^4 B^2}{m_1^2 m_2^2 |D(\omega)|^2}\left(m_2\delta_2|F_1|^2 - m_1\delta_1|F_2|^2\right)\,, \tag{22.82}$$

where

$$D(\omega) = \omega^4 - 2\mathrm{i}\omega^3\left(\delta_1+\delta_2\right) - \omega^2\left(\omega_1^2+\omega_2^2+4\delta_1\delta_2+\frac{B^2}{m_1m_2}\right) + 2\mathrm{i}\omega\left(\delta_1\omega_2^2+\delta_2\omega_1^2\right) - \frac{k_{12}}{m_1m_2}+\omega_1^2\omega_2^2 \,. \tag{22.83}$$

In (22.83), ω_1 and ω_2 are the natural frequencies of the undamped uncoupled oscillators. It can be shown that (22.82) can be generalized to a broadband excitation with frequency bandwidth $\Delta\omega$. One basic property of SEA follows from the fact that P_{12} is proportional to the energy difference $W_1 - W_2$ of the oscillators. For a broadband excitation, these energies are given by

$$W_i = \frac{m_i}{2\Delta\omega}\int_{-\infty}^{+\infty} |v_i(\omega)|^2\,\mathrm{d}\omega \tag{22.84}$$

and the basic SEA equation becomes

$$P_{12} = \beta\left(W_1 - W_2\right)$$

give the rate at which energy is transferred from one subsystem to the other. The SEA theory can be used, for example, for predicting the vibration level of coupled

with

$$\beta = \frac{2}{m_1m_2}\,\frac{\left(\delta_1\omega_2^2+\delta_2\omega_1^2\right)B^2+\left(\delta_1+\delta_2\right)k_{12}^2}{\left(\omega_1^2-\omega_2^2\right)^2+2\left(\delta_1+\delta_2\right)\left(\delta_1\omega_2^2+\delta_2\omega_1^2\right)} \,. \tag{22.85}$$

Equation (22.85) shows that β is positive and depends on the parameters of the oscillators and on the coupling parameters B and k_{12}. This equation can be generalized to the coupling between any mode m_1 of a given subsystem with N_1 modes and a mode m_2 of another subsystem with N_2 modes. Considering a frequency band with central frequency ω_c, the generalization leads to the following expression for the power flow from subsystem 1 to subsystem 2

$$P_{12} = \omega_c\left(\eta_{12}W_1 - \eta_{21}W_2\right) \,, \tag{22.86}$$

where η_{12} and η_{21} are the coupling loss factors obtained through averaging of the parameters $\beta_{m_1m_2}$ analogous to that defined in (22.85)

$$\eta_{12} = \frac{N_2}{\omega_c}\langle\beta_{m_1m_2}\rangle_{N_1N_2} \quad\text{and}\quad \eta_{21} = \frac{N_1}{N_2}\eta_{12} \,. \tag{22.87}$$

$W_1 = N_1W_{m_1}$ and $W_2 = N_2W_{m_2}$ are the total modal energies in both subsystems, averaged over a frequency band, with the assumption that both energies are equally divided among the modes. The coupling loss factors plates over a large frequency range, where standard numerical methods, such as the finite-element method are too costly [22.6].

22.3 Strings and Membranes

Strings and membranes belong to that category of structures where the stiffness is due to external tension. This is sometimes called *geometrical* stiffness, in contrast with the *elastic* stiffness of most vibrating solids. In practice, strings and membranes also are made of elastic materials and, consequently, show more or less elastic stiffness due to their Young's moduli. This elastic stiffness will be neglected in the present section. The relative contributions of both stiffnesses will be discussed in Sect. 22.4 in the case of prestressed beams.

22.3.1 Equations of Motion

Consider a small element at a given point of Cartesian coordinates $\boldsymbol{x}$ on a stretched membrane of density $\rho(\boldsymbol{x})$. The membrane is assumed to be in equilibrium in the plane $\boldsymbol{e}_x, \boldsymbol{e}_y$ and subjected to a tension field $\tau(\boldsymbol{x})$ so that the resulting forces per unit length are (Fig. 22.7):

$$\begin{cases} \text{on both sides oriented in the } \boldsymbol{e}_x \text{ direction:} \\ \quad \boldsymbol{\tau}_x = \tau_{11}\boldsymbol{e}_x + \tau_{21}\boldsymbol{e}_y \,, \\ \text{on both sides oriented in the } \boldsymbol{e}_y \text{ direction:} \\ \quad \boldsymbol{\tau}_y = \tau_{12}\boldsymbol{e}_x + \tau_{22}\boldsymbol{e}_y \,, \end{cases} \tag{22.88}$$

where $\tau_{12} = \tau_{21}$ to ensure the moment equilibrium (reciprocity principle). In the general case, τ_{ij} are functions of the coordinates $\boldsymbol{x}$. The membrane is subjected to a small displacement in the direction $\boldsymbol{e}_z$ and released, so that its vertical motion $u(x, y, t)$ is governed by the balance between inertial forces and elastic forces due to tension. Gravity is neglected. After balance of forces on the four sides of the membrane element and projection on the vertical axis, with the assumption of small displace-

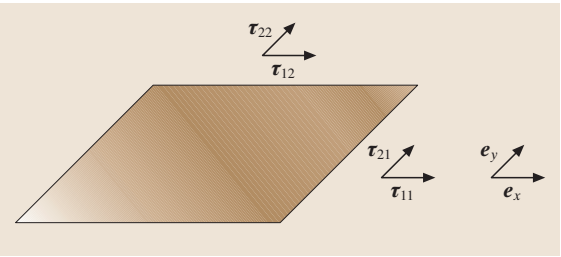


Fig. 22.7 Balance of forces on a membrane element

ments, one obtains the equation that governs the flexural motion of a nonuniformly stretched membrane:

$$\rho(\boldsymbol{x})h\ddot{u} = \frac{\partial}{\partial x}\left(\tau_{11}\frac{\partial u}{\partial x} + \tau_{12}\frac{\partial u}{\partial y}\right) + \frac{\partial}{\partial y}\left(\tau_{12}\frac{\partial u}{\partial x} + \tau_{22}\frac{\partial u}{\partial y}\right), \tag{22.89}$$

where h is the thickness. The tension field

$$\boldsymbol{\tau} = \begin{bmatrix} \tau_{11} & \tau_{12} \\ \tau_{12} & \tau_{22} \end{bmatrix} \tag{22.90}$$

is a symmetric tensor of order two, and

$$\mathbf{grad}\, u = \frac{\partial u}{\partial x}\boldsymbol{e}_x + \frac{\partial u}{\partial y}\boldsymbol{e}_y\,. \tag{22.91}$$

The previous equation can be written in the more compact form

$$\mathrm{div}\left(\boldsymbol{\tau}.\,\mathbf{grad}\, u\right) = \rho(\boldsymbol{x})h\ddot{u}\,, \tag{22.92}$$

where this last formulation has the advantage of being independent of the selected system of coordinates.

One-Dimensional (1-D) Approximation. Transverse Motion of Strings

Strings can be viewed as membranes where one dimension (the length) is much larger than the other two, so that a 1-D approximation is justified. Thus, rewriting (22.89) after integrating mass and tension along the axis $\boldsymbol{e}_y$, one obtains the equation of transverse motion for a string with nonuniform tension

$$\mu(x)\ddot{u} = \frac{\partial}{\partial x}\left[T(x)\frac{\partial u}{\partial x}\right], \tag{22.93}$$

where $\mu = \rho S$ is the linear mass density, S is the cross-sectional area and T is the tension.

Remark.

1. A similar equation can be obtained for the transverse motion $v(x, t)$ of the string in the direction $\boldsymbol{e}_y$. Therefore, two transverse motions polarized in orthogonal directions can exist on a string.
2. In the absence of coupling terms, u and v are independent. However, induced motion at the ends and/or nonlinear terms usually lead to coupling between these motions (Sect. 22.7).
3. Strings and membranes are also subjected to longitudinal motion. This motion is due to the variation of tension resulting from the variation in strain associated with the motion.

Homogeneous and Uniformly Stretched Strings and Membranes

For a uniformly stretched and homogeneous membrane, (22.92) reduces to

$$\tau\,\mathrm{div}\left(\mathbf{grad}\, u\right) = \tau\,\Delta u = \rho h\ddot{u}\,, \tag{22.94}$$

where the Laplacian is written in Cartesian coordinates as

$$\Delta u = \frac{\partial^2 u}{\partial x^2} + \frac{\partial^2 u}{\partial y^2} \tag{22.95}$$

For a string, we get the well-known wave equation

$$\mu\ddot{u} = T\frac{\partial^2 u}{\partial x^2}\,. \tag{22.96}$$

22.3.2 Heterogeneous String. Modal Approach

Extending the previous results to continuous structures shows that, in the linear regime, these structures have an infinite number of eigenmodes with similar properties of orthogonality with respect to mass and stiffness to those presented in Sect. 22.2 for discrete systems. In this case, the previously defined eigenvectors $\boldsymbol{\Phi}_n$ become continuous functions of the space coordinates $\Phi(\boldsymbol{x})$. To illustrate the modal approach for continuous systems, consider the case of an heterogeneous string (i. e., a nonuniformly stretched string with variable density), rigidly fixed at both ends and subjected to a force density $f(x, t)$:

$$\rho(x)S(x)\frac{\partial^2 y}{\partial t^2} - \frac{\partial}{\partial x}\left[T(x)\frac{\partial y}{\partial x}\right] = f(x,t)\,, \tag{22.97}$$

$\Phi_n(x)$ are the eigenfunctions of the string, which account for the boundary conditions. We seek solutions of the

form

$$y(x,t) = \sum_n \Phi_n(x) q_n(t) \,. \tag{22.98}$$

Multiplying both sides of (22.97) by the eigenfunction $\Phi_m(x)$ and integrating over the length of the string yields

$$\begin{aligned} &\sum_n \ddot{q}_n(t) \int_0^L \Phi_n(x)\Phi_m(x)\rho(x)S(x)\,\mathrm{d}x \\ &- \sum_n q_n(t) \int_0^L \Phi_m(x) \frac{\mathrm{d}}{\mathrm{d}x}\left[T(x)\frac{\mathrm{d}\Phi_n(x)}{\mathrm{d}x}\right]\mathrm{d}x \\ &= \int_0^L \Phi_m(x) f(x,t)\,\mathrm{d}x \end{aligned} \tag{22.99}$$

which can be written in symbolic form as

$$\mathcal{M}\left(\ddot{y}, \Phi_m\right) + \mathcal{K}\left(y, \Phi_m\right) = \langle f, \Phi_m \rangle \,. \tag{22.100}$$

Equation (22.100) is general and can be applied to all conservative systems. $\mathcal{M}$ denotes the mass operator and $\mathcal{K}$ the stiffness operator.

Orthogonality Properties of the Eigenmodes

Each eigenmode $\Phi_n(x)$ is a solution of the equation

$$-\omega_n^2 \rho(x) S(x) \Phi_n(x) = \frac{\mathrm{d}}{\mathrm{d}x}\left[T(x)\frac{\mathrm{d}\Phi_n(x)}{\mathrm{d}x}\right] . \tag{22.101}$$

These eigenfunctions are orthogonal with respect to the mass

$$\int_0^L \Phi_n(x)\Phi_m(x)\rho(x)S(x)\,\mathrm{d}x = 0 \tag{22.102}$$

and orthogonal with respect to the stiffness

$$\int_0^L T(x)\frac{\mathrm{d}\Phi_m(x)}{\mathrm{d}x}\frac{\mathrm{d}\Phi_n(x)}{\mathrm{d}x}\,\mathrm{d}x = 0 \,. \tag{22.103}$$

Generalized Coordinates

Taking the orthogonality properties of the eigenmodes into account, we can write

$$-\frac{\mathrm{d}}{\mathrm{d}x}\left[T(x)\frac{\mathrm{d}\Phi}{\mathrm{d}x}\right] = \omega^2 \rho(x) S(x) \Phi(x) \tag{22.104}$$

so that (22.100) becomes:

$$\ddot{q}_n(t) + \omega_n^2 q_n(t) = \frac{f_n(t)}{m_n} \,, \tag{22.105}$$

where the modal mass is given by:

$$m_n = \int_0^L \Phi_n^2(x)\rho(x)S(x)\,\mathrm{d}x \tag{22.106}$$

with

$$f_n(t) = \int_0^L f(x,t)\Phi_n(x)\,\mathrm{d}x \,. \tag{22.107}$$

The equations that govern the generalized displacements are therefore formally identical to those obtained for discrete systems. For continuous systems, truncation of the theoretically infinite number of differential equations has to be performed. The truncation criteria are often determined by the frequency domain under consideration. For a lossless string of length L with perfect boundary conditions excited by a source term $f(x,t)$, the general solution can be written in the modal domain as

$$y(x,t) = \sum_n \Phi_n(x) q_n(t) \tag{22.108}$$

where

$$\ddot{q}_n(t) + \omega_n^2 q_n(t) = \frac{f_n(t)}{m_n}$$

with

$$f_n(t) = \langle f(x,t), \Phi_n(x) \rangle = \int_0^L \Phi_n(x) f(x,t)\,\mathrm{d}x \,.$$

Let us assume an initial shape $y(0,t)$ and an initial velocity $\dot{y}(0,t)$. The initial values of the $q_n(t)$ are thus given by

$$\begin{cases} q_n(0) = \dfrac{1}{m_n}\displaystyle\int_0^L \rho(x)S(x)y(0,t)\Phi_n(x)\,\mathrm{d}x \\ \text{and} \\ \dot{q}_n(0) = \dfrac{1}{m_n}\displaystyle\int_0^L \rho(x)S(x)\dot{y}(0,t)\Phi_n(x)\,\mathrm{d}x \end{cases} . \tag{22.109}$$

Denoting the Laplace transform of $q_n(t)$ by $Q_n(s)$, we have

$$Q_n(s) = \frac{1}{s^2+\omega_n^2}\left[\frac{F_n(s)}{m_n} + sq_n(0) + \dot{q}_n(0)\right], \tag{22.110}$$

where $F_n(s)$ is the Laplace transform of $f_n(t)$. The first term of $Q_n(s)$ is a product of two transforms which, in the time domain, corresponds to a convolution. Using transform tables, we obtain

$$q_n(t) = \frac{1}{m_n\omega_n}\int_0^t f_n(\theta)\sin\omega_n(t-\theta)\,\mathrm{d}\theta + q_n(0)\cos\omega_n t + \dot{q}_n(0)\frac{\sin\omega_n t}{\omega_n}. \tag{22.111}$$

If $f_n(t)$ is a Dirac delta function of the form $f_{n0}\delta(t)$, the Laplace transform reduces to $F_n(s) = f_{n0}$ Equation (22.111) can then be written

$$q_n(t) = \frac{f_{n0}}{m_n}\frac{\sin\omega_n t}{\omega_n} + q_n(0)\cos\omega_n t + \dot{q}_n(0)\frac{\sin\omega_n t}{\omega_n}. \tag{22.112}$$

From the above impulse response for mode n of the string, we note the following:

1. There is an equivalence between $q_n(t)$ from the impulse source term and the initial velocity term. In other words, the motion of the string induced by an initial velocity profile is equivalent if the string is excited by a spatial distribution of Dirac delta function forces.
2. A source term localized at a given point x_0 can be written $f(x,t) = A\delta(x-x_0)\delta(t)$. In this case, $f_n(t) = \langle f(x,t), \Phi_n(x)\rangle = A\Phi_n(x_0)\delta(t)$. Therefore, the mode n will not be excited if the force is applied on a node of vibration.
3. The first term of the function $g_n(t) = \sin\omega_n t/m_n\omega_n$ is the Green's function of mode n.

String with a Finite Mass at One End

To present general results, the string is still assumed to be heterogeneous. The purpose of this section is to give the orthogonality properties of the modes for a heterogeneous string terminated by a finite mass M. The boundary conditions are

$$y(0,t) = 0 \quad \text{and} \quad -T(x)\frac{\partial y}{\partial x} = M\frac{\partial^2 y}{\partial t^2}, \quad \text{at} \quad x = L. \tag{22.113}$$

The eigenfunctions $\Phi(x)$ therefore have to satisfy

$$\begin{aligned} \rho(x)S(x)\omega^2\Phi(x) &= -\frac{\mathrm{d}}{\mathrm{d}x}\left[T(x)\frac{\mathrm{d}\Phi(x)}{\mathrm{d}x}\right] = 0, \\ \text{for} \quad & 0 < x < L \\ \text{with} \quad & \Phi(0) = 0 \\ \text{and} \quad & T(x)\mathrm{d}\Phi/\mathrm{d}x = \omega^2 M\Phi(x), \\ \text{at} \quad & x = L. \end{aligned}$$

For $n \neq m$, the orthogonality condition with respect to mass becomes

$$\int_0^L \rho(x)S(x)\Phi(x)\Phi_m(x)\,\mathrm{d}x + M\Phi_n(L)\Phi_m(L) = 0 \tag{22.114}$$

and the orthogonality condition with respect to stiffness remains

$$\int_0^L T(x)\frac{\mathrm{d}\Phi_n(x)}{\mathrm{d}x}\frac{\mathrm{d}\Phi_m(x)}{\mathrm{d}x}\,\mathrm{d}x = 0. \tag{22.115}$$

For a homogeneous string with uniform tension and constant diameter, these conditions reduce to

$$\int_0^L \Phi_n(x)\Phi_m(x)\,\mathrm{d}x = -\frac{M}{\rho S}\Phi_n(L)\Phi_m(L) \tag{22.116}$$

and

$$\int_0^L \frac{\mathrm{d}\Phi_n(x)}{\mathrm{d}x}\frac{\mathrm{d}\Phi_m(x)}{\mathrm{d}x}\,\mathrm{d}x = 0. \tag{22.117}$$

22.3.3 Ideal String

To solve initial-boundary problems in simple cases, we assume that the lossless string is homogeneous with density ρ, constant tension T and constant cross section S. In this case, the vertical displacement is given by the wave equation

$$\frac{1}{c^2}\frac{\partial^2 u}{\partial t^2} = \frac{\partial^2 u}{\partial x^2}, \tag{22.118}$$

where $c = \sqrt{T/\rho S}$ is the transverse wave velocity.

D'Alembert's Solution in the Time Domain

In order to show the correspondence between the wave and modal approaches, a time-domain method is used

first to solve the wave equation (22.118) with initial conditions [22.7]

$$u(x,0)=f(x) \quad \text{and} \quad \frac{\partial u}{\partial t}(x,0)=g(x)\,. \tag{22.119}$$

Using the change of variables $\xi=x-ct$ and $\eta=x+ct$, we have

$$u(x,t)=U(\xi,\eta) \tag{22.120}$$

from (22.120), we obtain:

$$\begin{cases} \dfrac{\partial^2 u}{\partial t^2}=c^2\left(\dfrac{\partial^2 U}{\partial \xi^2}-2\dfrac{\partial^2 U}{\partial \xi\,\partial \eta}+\dfrac{\partial^2 U}{\partial \eta^2}\right) \\ \dfrac{\partial^2 u}{\partial x^2}=\dfrac{\partial^2 U}{\partial \xi^2}+2\dfrac{\partial^2 U}{\partial \xi\,\partial \eta}+\dfrac{\partial^2 U}{\partial \eta^2} \end{cases}\,. \tag{22.121}$$

Inserting (22.121) into (22.118) yields $\left(\partial^2 U\right)/\left(\partial\xi\,\partial\eta\right)=0$ which implies

$$u(x,t)=F(x-ct)+G(x+ct)\,, \tag{22.122}$$

where F and G are are two twice-differentiable functions. $F(x-ct)$ represents a travelling wave moving to the right (direction of increasing values for x), while $G(x+ct)$ is a travelling wave moving to the left. Using (22.119) implies that F and G must fulfill the conditions

$$\begin{cases} F(x)+G(x)=f(x) \\ -cF'(x)+cG'(x)=g(x) \end{cases}\,. \tag{22.123}$$

Solving (22.123) yields

$$\begin{cases} F(x) &= \dfrac{1}{2}f(x)-\dfrac{1}{2}\left[-F(0)+G(0)\right] \\ &\quad -\dfrac{1}{2c}\displaystyle\int_0^x g(s)\,\mathrm{d}s \\ G(x) &= \dfrac{1}{2}f(x)+\dfrac{1}{2}\left[-F(0)+G(0)\right] \\ &\quad +\dfrac{1}{2c}\displaystyle\int_0^x g(s)\,\mathrm{d}s \end{cases}\,. \tag{22.124}$$

Finally, the solution of the wave equation is written explicitly

$$u(x,t)=\frac{1}{2}\left[f(x-ct)+f(x+ct)\right]+\frac{1}{2c}\int_{x-ct}^{x+ct} g(s)\,\mathrm{d}s\,. \tag{22.125}$$

Semi-infinite String. For a semi-infinite string rigidly fixed at $x=0$, we have the boundary condition $u(0,t)=0$. This requires:

$$F(-ct)+G(ct)=0 \tag{22.126}$$

and, finally, with the appropriate change of variables

$$\begin{aligned} u(x,t) &= -G(x-ct)+G(x+ct) \\ &= F(x-ct)-F(-x-ct)\,. \end{aligned} \tag{22.127}$$

Equation (22.127) expresses the fact that, due to the fixed end at $x=0$, the left-traveling wave is reflected with a change of sign and becomes a right-traveling wave. The validity domain for (22.127) is $0\le x<+\infty$ and $t>0$.

String of Finite Length. In the case of an ideal string fixed at both ends, the wave approach can still be used, with the additional boundary condition $u(L,t)=0$, which yields

$$\begin{aligned} u(L,t) &= -G(L-ct)+G(L+ct) \\ &= F(L-ct)-F(-L-ct)=0\,. \end{aligned} \tag{22.128}$$

Equation (22.128) can be rewritten $F(z)=F(z-2L)$, which shows that F (and G) are now periodic functions with spatial period $2L$ or, equivalently, temporal period $2L/c$. The validity domain of (22.128) is now $0\le x\le L$ and $t>0$. Equations (22.126)–(22.128) can be used for step-by-step constructions of the string shape at successive instants of time.

String Fixed at Both Ends. Eigenmodes

Injecting a harmonic wave of the form $u(x,t)=\mathrm{e}^{\mathrm{i}(\omega t-kx)}$ in (22.118), we find the dispersion equation $D(\omega,k)$ that governs the relationship between frequency ω and wavenumber k. Here, we obtain

$$D(\omega,k)=\omega^2-c^2k^2=0\,. \tag{22.129}$$

This equation shows that the ratio between the frequency and wavenumber is constant, which is a characteristic property of a nondispersive medium. If we assume further that the string is rigidly fixed at both ends, the eigenmodes must satisfy the equation

$$\frac{\mathrm{d}^2\Phi(x)}{\mathrm{d}x^2}+\frac{\omega^2}{c^2}\Phi(x)=0 \tag{22.130}$$

with the boundary conditions $\Phi(0)=\Phi(L)=0$ from which we obtain

$$\Phi_n(x)=\sin k_n x\,. \tag{22.131}$$

The only possible values for the wavenumber are given by the discrete series

$$k_n = n\pi/L \quad \text{so that} \quad \omega_n = n\pi c/L \,. \tag{22.132}$$

Using (22.106), the modal mass is $m_n = \rho SL/2 = M_s/2$, where M_s is the total mass of the string. Recall, however, that the ratio $m_n/M_s = 1/2$ is purely arbitrary since the modal masses are defined with an arbitrary multiplicative constant. The important result here is that all modal masses are equal and do not depend on the rank n of the mode.

Application: Plucked String. Modal Approach

The particular case where the string is released from an initial triangular shape at the origin of time without initial velocity is now examined. With the assumption of no stiffness, the initial profile of the string is given by

$$u(0,t) = \begin{cases} \dfrac{hx}{x_0} & \text{for } 0 \le x \le x_0 \\ \dfrac{h(L-x)}{L-x_0} & \text{for } x_0 \le x \le L \end{cases} . \tag{22.133}$$

The modal method consists of looking for solutions of the form

$$u(x,t) = \sum_n \Phi_n(x) q_n(t) \,. \tag{22.134}$$

At the origin of time, we can write

$$u(0,t) = \sum_n \Phi_n(x) q_n(0) \,. \tag{22.135}$$

The unknowns of the problem are the functions $q_n(0)$. Exploiting again the orthogonality properties of the eigenmodes, we find

$$q_n(0) = \frac{2hL^2}{n^2\pi^2 x_0(L-x_0)} \sin k_n x_0 \,. \tag{22.136}$$

The functions $q_n(t)$ are given by the oscillator equations

$$\ddot{q}_n + \omega_n^2 q_n = 0 \tag{22.137}$$

which, in the case of zero initial velocity, leads to $q_n(t) = q_n(0)\cos\omega_n t$. In summary, the transverse displacement of the string is given by

$$u(x,t) = \sum_n \frac{2hL^2}{n^2\pi^2 x_0(L-x_0)} \times \sin k_n x_0 \sin k_n x \cos\omega_n t \,. \tag{22.138}$$

Despite the simplicity of this example, a number of important issues can be derived from this result:

1. The eigenfrequencies are integer multiples of the fundamental $f_1 = c/2L$. The solution is periodic and the fundamental frequency is the inverse of the period of vibration.
2. The amplitudes of the modal components decrease as $1/n^2$ with the rank n of the modes.
3. Because the magnitude is proportional to $\sin k_n x_0$, a modal component n can be suppressed by selecting the plucking point $x_0 = pL/n$, where p is an integer $< n$.
4. The excitation point x_0 and observation point x can be interchanged in (22.138). This is an illustration of the reciprocity principle.

Moving End

To a first approximation, a vibrating string radiates as a dipole. Because of its small diameter compared to the acoustic wavelength, it is a poor radiator. If significant sound is to be radiated, one end of the string must be coupled to a component with a considerable vibrating area (plate, shell, etc.). In Sect. 22.3.2, the general properties of a heterogeneous string attached to a mass were obtained. In this section, the simple example of an ideal string coupled to a spring will be considered to illustrate the influence of such coupling on the eigenmodes, eigenfrequencies and modal masses. We consider a string fixed at point $x = 0$ to a spring of stiffness K_0. The boundary condition at this end is then

$$T\left(\frac{\partial u}{\partial x}\right)_{x=0} = K_0\, u(0,t) \,. \tag{22.139}$$

The string is rigidly fixed at the other end, so that $u(L,t) = 0$. We look for solutions of the form $u(x,t) = \Phi(x)\cos\omega t$. Following (22.118), the eigenfunctions $\Phi(x)$ must satisfy the equation

$$\frac{\mathrm{d}^2\Phi}{\mathrm{d}x^2} + k^2\Phi = 0 \tag{22.140}$$

and the boundary conditions. Thus, we derive the equation for the eigenvalues k_n

$$\tan(k_n L) = -\frac{k_n T}{K_0} \quad \text{with} \quad k_n > 0 \,. \tag{22.141}$$

The graphical representation of (22.141) shows that the k_n are no longer integer multiples of k_1 (Fig. 22.8). As a consequence, the free vibration of the string is no longer periodic. Note that the spring decreases the eigenfrequencies relative to those of a perfectly rigid end.

The eigenfunctions become

$$\Phi_n(x) = \sin k_n x + \frac{k_n T}{K_0}\cos k_n x = \frac{\sin k_n(L-x)}{\cos k_n L} \tag{22.142}$$

Amazon EX1014 Page 922

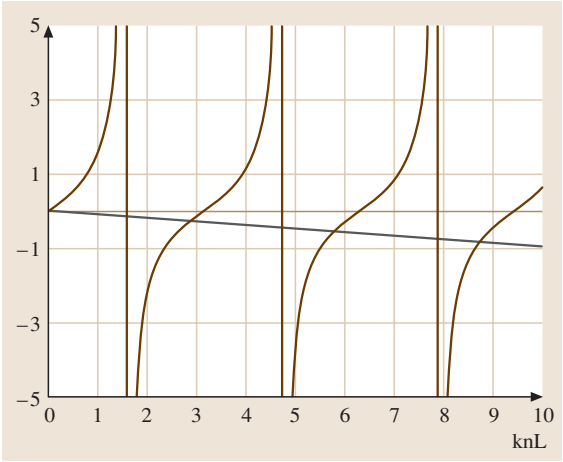


Fig. 22.8 Graphical resolution of the eigenvalue problem for a string attached to a spring (22.141)

from which the initial values $q_n(0)$ and the modal masses can be derived. We obtain:

$$m_n = \int_0^L \rho S \left(\sin k_n x + \frac{k_n T}{K_0} \cos k_n x \right)^2 \mathrm{d}x$$
$$= \frac{M_\mathrm{s}}{2} \left[1 + \left(\frac{k_n T}{K_0} \right)^2 \right] . \qquad (22.143)$$

Equation (22.143) shows here that the modal masses increase with the rank n of the mode. In the case of a mass termination, a similar procedure would lead to the eigenvalue equation

$$\tan(k_n L) = \frac{\rho S}{M_0 k_n} . \qquad (22.144)$$

Here, the inertial load at the end leads to an increase of the eigenfrequencies.

Application to Stringed Instruments. In plucked and struck strings instruments (guitar, piano, harp, etc.), the main part of the sound is due to the free regime of vibration, and the spectrum is composed of the eigenfrequencies of the vibrating system. Previous considerations show that the coupling between the strings and the radiating body (top plate, soundboard) alters the frequencies, compared to the perfect harmonic case. Though this alteration is usually relatively small, it has the consequence that the waveform is not perfectly periodic anymore. This might have in turn some perceptual effects on the produced sound. See the chapter on musical acoustics (Chap. 15) in this Handbook for more details.

22.3.4 Circular Membrane in Vacuo

Membranes are used in percussion instruments, microphones, loudspeakers and wall resonators. Because of their small thickness, the influence of air loading cannot be neglected in most applications. However, we limit ourselves here by solving the equation for transverse vibrations of a homogeneous membrane in vacuo. Fluid-loading effects on structures are discussed in later sections. From (22.94) the membrane equation, in circular geometry, is

$$\sigma \frac{\partial^2 u}{\partial t^2} = \tau \Delta u = \tau \left(\frac{\partial^2 u}{\partial r^2} + \frac{1}{r} \frac{\partial u}{\partial r} + \frac{1}{r^2} \frac{\partial^2 u}{\partial \theta^2} \right) , \qquad (22.145)$$

where $\sigma = \rho h$. Equation (22.145) can be solved by using the method of separation of variables [22.8]. For zero displacement at the edge, $z(r = a, \theta, t) = 0$, and neglecting losses, the expansion of the displacement on the eigenmodes can be expressed as

$$u(r, \theta, t) = \sum_{m=1}^{\infty} \left[\sum_{n=0}^{\infty} U_{nm}(r, \theta) \times \left(A_{nm} \cos \omega t + B_{nm} \sin \omega t \right) + \sum_{n=1}^{\infty} \tilde{U}_{nm}(r, \theta) \times \left(\tilde{A}_{nm} \cos \omega t + \tilde{B}_{nm} \sin \omega t \right) \right] . \qquad (22.146)$$

In (22.146), the eigenfunctions are

$$U_{nm}(r, \theta) = J_n(\beta_{nm} r) \cos n\theta$$

and

$$\tilde{U}_{nm}(r, \theta) = J_n(\beta_{nm} r) \sin n\theta , \qquad (22.147)$$

where J_n is the order-n Bessel function of the first kind [22.9]. The indices n and m refer to the number of nodal lines and to the number of nodal circles, respectively (Fig. 22.9).

The fixed edge corresponds to one nodal circle. The symmetrical modes are those where there are no nodal diameters. In this case, the eigenfunctions are of the form $J_n(\beta_{0m} r)$. All other modes can be viewed as *pairs of modes* with the same eigenfrequency and the same dependence versus r. They only differ by an angle of $\pi/2n$. The discrete values β_{mn} of the wavenumbers are derived from the boundary condition at the edge, such that

$$J_n(\beta a) = 0 . \qquad (22.148)$$

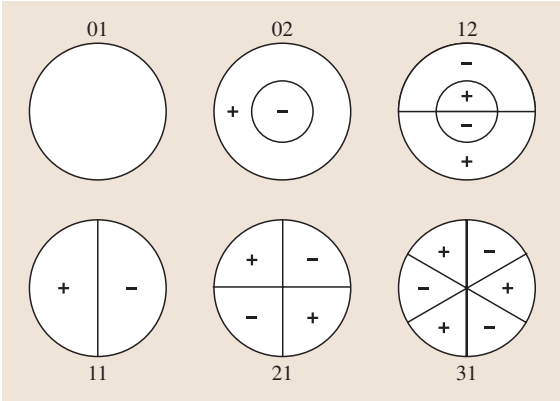


Fig. 22.9 Eigenmodes (n, m) of a circular membrane invacuo

For each value of n, we obtain an infinite series of roots β_{nm}. For $n = 0$, for example, $J_0(\beta a) = 0$ yields $\beta_{0m}a = 2.405,\ 5.520,\ 8.654,\ 11,792,\ 14,931, \ldots$. Similarly, the roots of $J_1(\beta a) = 0$ are given by $\beta_{1m}a = 3.832,\ 7.016,\ 10.173,\ 13.324,\ 16.471, \ldots$.

Finally, the eigenfrequencies ω_{nm} are obtained from the 2-D wave equation (22.145):

$$\omega_{nm} = c\beta_{nm}\,, \quad \text{where} \quad c = \sqrt{\frac{\tau}{\sigma}}\,. \tag{22.149}$$

Unlike the case of ideal strings, the eigenfrequencies of a circular membrane in vacuo are not harmonically related. It has been shown by different authors that the fluid and cavity loading both contribute to restore the harmonic character of timpani sound, although the fundamental is missing [22.10, 11].

22.4 Bars, Plates and Shells

In this section, we consider the flexural vibrations of bars, plates and shells, since these structures are of the most practical use for the radiation of sound. First, the longitudinal vibrations of bars are presented, to show the analogies with the string wave equation, and also because this example will be used in Sect. 22.5.1 to illustrate the basic concepts of fluid–structure interactions.

22.4.1 Longitudinal Vibrations of Bars

The longitudinal vibrations of a 1-D bar in vacuo, clamped at one end and free at the other, are governed by the equations

$$\begin{cases} \rho_s S\dfrac{\partial^2\xi}{\partial t^2} = ES\dfrac{\partial^2\xi}{\partial x^2}\,, \\ \xi(0,t) = 0\,; \qquad \dfrac{\partial\xi}{\partial x}(L,t) = 0\,. \end{cases} \tag{22.150}$$

The eigenfunctions are

$$\phi_n(x) = \sin(2n-1)\frac{\pi x}{2L} = \sin k_n x \tag{22.151}$$

with $k_n = \omega_n/c_L$ and thus the linear solution can be written as

$$\xi(x,t) = \sum_n \phi_n(x)q_n(t)\,, \tag{22.152}$$

where the generalized displacements obey

$$\ddot{q}_n + \omega_n^2 q_n = 0\,. \tag{22.153}$$

Equation (22.153) yields a harmonic solution with eigenfrequency ω_n.

22.4.2 Flexural Vibrations of Beams

The flexural vibrations of a slender isotropic beam are presented, within the framework of the Euler–Bernoulli assumptions [22.8]. The beam is oriented along the x-axis, and the cross section $S(x)$ is in the (y, z) plane. The flexural displacement $v(x, t)$ is in the direction of the y-axis. $E(x)$ is the Young's modulus, $\rho(x)$ is the density, and $I_z(x)$ is the moment of inertia of a cross section with respect to its neutral midplane. $f(x, t)$ represents a source term. Applying Hamilton's principle, we obtain the well-known equation

$$\rho(x)S(x)\ddot{v} + \frac{\partial^2}{\partial x^2}\left[E(x)I_z(x)\frac{\partial^2 v}{\partial x^2}\right] = f(x,t) \tag{22.154}$$

with the additional conditions to be satisfied

$$\left[E(x)I_z(x)\frac{\partial^2 v}{\partial x^2}\frac{\partial v}{\partial x}\right]_0^L = 0$$

and

$$\left[\frac{\partial}{\partial x}\left(E(x)I_z(x)\frac{\partial^2 v}{\partial x^2}\right)v\right]_0^L = 0\,. \tag{22.155}$$

Equation (22.154) is fourth order in the spatial coordinate. Therefore, four boundary conditions (two

conditions at each end) are necessary to solve the boundary-value problem. Following (22.155), four different situations are compatible at each end:

$$\begin{aligned}
&\text{Supported} && v = 0 \\
&\text{and} && \mathcal{M}(x) = E(x) I_z(x) \frac{\partial^2 v}{\partial x^2} = 0 \,; \\
&\text{Clamped} && \frac{\partial v}{\partial x} = 0 \\
&\text{and} && v = 0 \,; \\
&\text{Free} && \mathcal{T}(x) = \frac{\partial}{\partial x}\left[E(x) I_z(x) \frac{\partial^2 v}{\partial x^2} \right] = 0 \\
&\text{and} && \mathcal{M}(x) = E(x) I_z(x) \frac{\partial^2 v}{\partial x^2} = 0 \,; \\
&\text{Guided} && \mathcal{T}(x) = \frac{\partial}{\partial x}\left[E(x) I_z(x) \frac{\partial^2 v}{\partial x^2} \right] = 0 \\
&\text{and} && \frac{\partial v}{\partial x} = 0 \,,
\end{aligned}$$

where $\mathcal{M}(x)$ is the bending moment and $\mathcal{T}(x)$ is the shear force.

Free–Free Beam with a Constant Section

As a specific example of (22.154), we consider a homogeneous and isotropic beam of length L, thickness h, width b, with a constant rectangular section $S = bh$ whose moment of inertia with respect to the z-axis is $I_z = I = bh^3/12$ (Fig. 22.10).

In this case, (22.154) reduces to

$$EI \frac{\partial^4 v}{\partial x^4} + \rho S \frac{\partial^2 v}{\partial t^2} = 0 \,. \tag{22.156}$$

Looking for solutions for (22.156) of the form $v(x, t) = \Phi(x) \cos \omega t$ yields the general solution

$$\Phi(x) = A \cosh \frac{\omega x}{c} + B \sinh \frac{\omega x}{c} + C \cos \frac{\omega x}{c} + D \sin \frac{\omega x}{c} \tag{22.157}$$

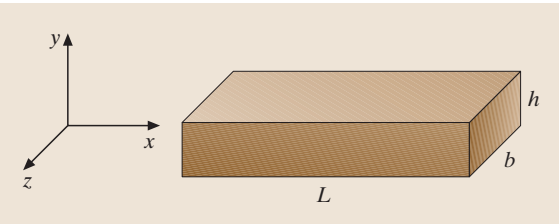


Fig. 22.10 Geometry of a beam with constant section

with

$$c = \sqrt{\omega c_L} \sqrt[4]{\frac{I}{S}} \quad \text{and} \quad c_L = \frac{E}{\rho} \,. \tag{22.158}$$

This expression shows that the phase velocity c of the flexural waves is proportional to $\sqrt{\omega}$. The dispersion relationship is given by

$$EIk^4 + \rho S \omega^2 = 0 \,. \tag{22.159}$$

From (22.159), we can see that the group velocity $c_g = \mathrm{d}\omega/\mathrm{d}k$ is also proportional to $\sqrt{\omega}$. The group velocity refers to the propagation velocity of wave energy and envelope of slowly varying amplitude. Flexural waves in the beam are thus dispersive with the higher frequencies propagating faster than the lower ones.

Remark. There is a paradox in (22.157) in the sense that the group velocity tends to infinity as the frequency tends to infinity. This results from the Euler–Bernoulli assumptions, where shear and rotation inertia of the cross sections are neglected. Introducing these two effects in the model (the Timoshenko model) leads to a bounded asymptotic value of the group velocity as frequency increases.

For a beam free at both ends, the boundary conditions are

$$\frac{\partial^2 y}{\partial x^2}(0, t) = \frac{\partial^2 y}{\partial x^2}(L, t) = 0 \tag{22.160}$$

and

$$\frac{\partial^3 y}{\partial x^3}(0, t) = \frac{\partial^3 y}{\partial x^3}(L, t) = 0 \,, \tag{22.161}$$

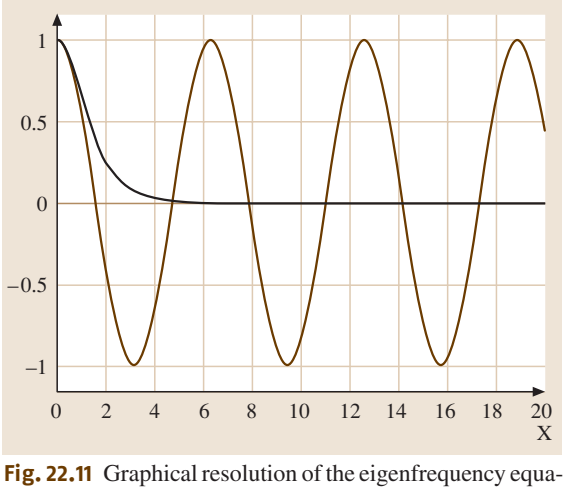


Fig. 22.11 Graphical resolution of the eigenfrequency equation for a free–free beam, with $X = \omega L/c$

which yields the equation of the eigenfrequencies (Fig. 22.11)

$$\cos\frac{\omega L}{c}\cosh\frac{\omega L}{c}=1\,. \tag{22.162}$$

The numerical resolution of (22.162) shows that the eigenfrequencies f_n (in Hz) are

$$f_n\approx\sqrt{\frac{EI}{\rho S}}\frac{\pi}{8L^2}\left[3.011^2,5^2,7^2,\ldots,(2n+1)^2\right]\,. \tag{22.163}$$

The eigenfrequencies are not harmonically related so that the impulse response of the beam is not periodic.

Beam with a Variable Cross Section

As another example, we consider the flexural vibrations for a beam with variable cross section. Here, we describe the Galerkin method [22.12]. It has the advantage that it remains valid even in the case of nonconservative systems. In this method, the eigenfunctions $\Phi(x)$ of (22.154) are approximated by a finite sum of p terms

$$\Phi^{(p)}(x)=\sum_{j=1}^{p}a_j\phi_j(x)\,, \tag{22.164}$$

where $\phi_j(x)$ are arbitrary functions that satisfy the boundary conditions at both ends of the beam. Inserting (22.164) in (22.154), and defining $\lambda^{(p)}=(\omega^2)^{(p)}$ as the approximate eigenvalues of order p, one can define the Galerkin residue

$$\mathcal{R}\left[\Phi^{(p)}(x)\right]=\frac{\mathrm{d}^2}{\mathrm{d}x^2}\left(EI(x)\frac{\mathrm{d}^2\Phi^{(p)}}{\mathrm{d}x^2}\right)-\lambda^{(p)}\rho(x)S(x)\Phi^{(p)} \tag{22.165}$$

following (22.164), this can be written as

$$\mathcal{R}\left[\Phi^{(p)}(x)\right]=\sum_{j=1}^{p}a_j\times\left\{\frac{\mathrm{d}^2}{\mathrm{d}x^2}\left[EI(x)\frac{\mathrm{d}^2\phi_j(x)}{\mathrm{d}x^2}\right]-\lambda^{(p)}\rho(x)S(x)\phi_j(x)\right\}\,. \tag{22.166}$$

The weak formulation of the problem is given by

$$\int_0^L\phi_i(x)\sum_{j=1}^{p}a_j\left\{\frac{\mathrm{d}^2}{\mathrm{d}x^2}\left[EI(x)\frac{\mathrm{d}^2\phi_j(x)}{\mathrm{d}x^2}\right]-\lambda^{(p)}\rho(x)S(x)\phi_j(x)\right\}\mathrm{d}x=0\,. \tag{22.167}$$

The goal of the method is to find the coefficients a_j for which the residue $\mathcal{R}\left[\Phi^{(p)}(x)\right]$ is equal to zero. Thus (22.167) becomes

$$\sum_{j=1}^{p}k_{ij}a_j-\lambda^{(p)}\sum_{j=1}^{p}m_{ij}a_j=0 \quad \text{for} \quad i=1,2,\ldots p\,, \tag{22.168}$$

where the mass and stiffness coefficients are

$$k_{ij}=\int_0^L\phi_i(x)\frac{\mathrm{d}^2}{\mathrm{d}x^2}\left[EI(x)\frac{\mathrm{d}^2\phi_j(x)}{\mathrm{d}x^2}\right]\mathrm{d}x \tag{22.169}$$

and

$$m_{ij}=\int_0^L\phi_i(x)\rho(x)S(x)\phi_j(x)\;\mathrm{d}x\,. \tag{22.170}$$

Equation (22.168) can be written equivalently in matrix form:

$$[\mathbf{K}-\lambda\mathbf{M}]\,\boldsymbol{a}=0\,, \tag{22.171}$$

where $\boldsymbol{a}$ is a vector with dimension p and $\mathbf{K}$ and $\mathbf{M}$ are matrices with dimension $p\times p$. The problem to be solved is therefore equivalent in form to the eigenvalue problem for a p-component discrete system (22.49).

Prestressed Beam or Stiff String

The flexural motion for a beam subjected to tension (or prestressed beam) is governed by the same equation as a string with stiffness. For a homogeneous and isotropic beam of constant section subjected to a uniform tension T, we have

$$\rho S\frac{\partial^2 v}{\partial t^2}=T\frac{\partial^2 v}{\partial x^2}-EI\frac{\partial^4 v}{\partial x^4}\,. \tag{22.172}$$

For a propagating wave of the form $y(x,t)=\mathrm{e}^{\mathrm{i}(\omega t-kx)}$, we obtain the dispersion relationship

$$\omega^2=k^2c^2\left(1+\frac{EI}{T}k^2\right)\,. \tag{22.173}$$

For a stiff string of length L, the usual order of magnitude generally implies $\varepsilon=\frac{EI}{TL^2}\ll 1$ so that (22.173) can be written:

$$\omega^2=k^2c^2\left(1+\varepsilon k^2L^2\right)\,. \tag{22.174}$$

For a stiff string with hinged ends the boundary conditions impose

$$\sin kL=0 \quad \text{so that} \quad k_nL=n\pi \tag{22.175}$$

from which we can derive through (22.174) the eigenfrequencies

$$\omega_n \approx \frac{n\pi c}{L}\left(1+\varepsilon\frac{n^2\pi^2}{2}\right) . \tag{22.176}$$

The eigenfrequencies are raised by the stiffness. The difference increases as n^2. The inharmonicity coefficient can be defined as

$$i = \varepsilon\frac{n^2\pi^2}{2} . \tag{22.177}$$

22.4.3 Flexural Vibrations of Thin Plates

The *thin plate*, or Kirchhoff–Love plate, described below is a generalization of the Euler–Bernoulli beam in 2-D [22.13]. The general case of orthotropic plates is treated here. The problem is solved in Cartesian coordinates, where $w(x, y, t)$ denotes the transverse displacement. It is assumed that the coordinates coincide with the symmetry axes of the material. The assumption of orthotropy leads to the following relations between plane stresses σ_{ij} and plane strains ε_{kl}

$$\begin{pmatrix}\sigma_{xx}\\ \sigma_{yy}\\ \sigma_{xy}\end{pmatrix} = \begin{pmatrix} \frac{E_x}{1-\nu_{xy}\nu_{yx}} & \frac{\nu_{yx}E_x}{1-\nu_{xy}\nu_{yx}} & 0 \\ \frac{\nu_{yx}E_x}{1-\nu_{xy}\nu_{yx}} & \frac{E_y}{1-\nu_{xy}\nu_{yx}} & 0 \\ 0 & 0 & 2G_{xy}\end{pmatrix} \times \begin{pmatrix}\varepsilon_{xx}\\ \varepsilon_{yy}\\ \varepsilon_{xy}\end{pmatrix} . \tag{22.178}$$

These relations involve two elastic moduli E_x and E_y, two Poisson's ratios ν_{xy} and one torsional modulus G_{xy}. In addition, we have the property $E_x\nu_{yx} = E_y\nu_{xy}$ [22.14]. The bending and twisting moments are obtained by integration of the elementary moments over the thickness h of the plate:

$$\begin{aligned}\mathcal{M}_x &= \int_{-h/2}^{h/2} z\sigma_{xx}\,\mathrm{d}z\,;\\ \mathcal{M}_y &= \int_{-h/2}^{h/2} z\sigma_{yy}\,\mathrm{d}z\,;\\ \mathcal{M}_{xy} &= \mathcal{M}_{yx} = \int_{-h/2}^{h/2} z\sigma_{xy}\,\mathrm{d}z\end{aligned} \tag{22.179}$$

which leads to the matrix relation between the moments and curvatures

$$\begin{pmatrix}\mathcal{M}_x\\ \mathcal{M}_y\\ \mathcal{M}_{xy}\end{pmatrix} = -\begin{pmatrix} D_1 & D_2/2 & 0 \\ D_2/2 & D_3 & 0 \\ 0 & 0 & D_4/2\end{pmatrix} \times \begin{pmatrix}\frac{\partial^2 w}{\partial x^2}\\ \frac{\partial^2 w}{\partial y^2}\\ \frac{\partial^2 w}{\partial x\partial y}\end{pmatrix} , \tag{22.180}$$

where

$$\begin{aligned} D_1 &= \frac{E_x h^3}{12(1-\nu_{xy}\nu_{yx})}\,;\\ D_2 &= \frac{E_x\nu_{yx}h^3}{6(1-\nu_{xy}\nu_{yx})} = \frac{E_y\nu_{xy}h^3}{6(1-\nu_{xy}\nu_{yx})} , \qquad (22.181)\\ D_3 &= \frac{E_y h^3}{12(1-\nu_{xy}\nu_{yx})}\,;\\ D_4 &= \frac{G_{xy}h^3}{3} . \qquad (22.182)\end{aligned}$$

Again, the equation of motion can be obtained using Hamilton's principle [22.12]. Finally, given an external force density term $f(x, y, t)$, we obtain the equation of motion for the plate:

$$\rho_p h\frac{\partial^2 w}{\partial t^2} = \frac{\partial^2\mathcal{M}_x}{\partial x^2} + \frac{\partial^2\mathcal{M}_y}{\partial y^2} + 2\frac{\partial^2\mathcal{M}_{xy}}{\partial x\partial y} + f(x, y, t) . \tag{22.183}$$

Boundary Conditions. As for the beam, the boundary conditions follow from integration by parts of the elastic energy. The number of possible conditions depends on the selected geometry. For rectangular plates, for example, Leissa lists 21 possible boundary conditions [22.15]. Along the principal directions, for example, the conditions of greatest practical interest are:

1. Clamped edge: displacement $w = 0$ and rotation $\frac{\partial w}{\partial x} = 0$;
2. Simply supported edge: displacement $w = 0$ and bending moment $\mathcal{M}_x = 0$;
3. Free edge: bending moment $\mathcal{M}_x = 0$ and shear force $\frac{\partial\mathcal{M}_x}{\partial x} + 2\frac{\partial\mathcal{M}_{xy}}{\partial y} = 0$.

Example: Homogeneous Rectangular Simply Supported Plate. From (22.180) and (22.183), we obtain for a homogeneous orthotropic plate

$$\rho_p h \frac{\partial^2 w}{\partial t^2} + D_1 \frac{\partial^4 w}{\partial x^4} + (D_2 + D_4) \times \frac{\partial^4 w}{\partial x^2 \partial y^2} + D_3 \frac{\partial^2 w}{\partial y^4} = 0 \,. \tag{22.184}$$

For a rectangular plate of length a and width b, simply supported at its edges, the boundary conditions are

$$\begin{cases} W(0, y, t) & = W(a, y, t) = W(x, 0, t) \\ & = W(x, b, t) = 0 \,, \\ \mathcal{M}_x(0, y, t) & = \mathcal{M}_x(a, y, t) = \mathcal{M}_y(x, 0, t) \\ & = \mathcal{M}_y(x, b, t) = 0 \,. \end{cases} \tag{22.185}$$

The eigenfunctions satisfying (22.185) are of the form

$$\Phi_{mn}(x, y) = \sin \frac{m\pi x}{a} \sin \frac{n\pi y}{b} \tag{22.186}$$

and the associated eigenfrequencies are given by:

$$\omega_{mn} = \pi^2 \sqrt{\frac{1}{\rho_p h}} \times \sqrt{D_1 \frac{m^4}{a^4} + D_3 \frac{n^4}{b^4} + (D_2 + D_4) \frac{m^2 n^2}{a^2 b^2}} \,. \tag{22.187}$$

In both expressions, m and n are positive integers. As for strings and beams, the eigenfunctions Φ_{mn} are orthogonal with respect to mass and stiffness, so that

$$\int_0^a \int_0^b \rho_p h \Phi_{mn}(x, y) \Phi_{m'n'}(x, y) \, \mathrm{d}x \, \mathrm{d}y = \begin{cases} 0 & \text{if } m \neq m' \text{ or } n \neq n' \,, \\ M_{mn} & \text{if } m = m' \text{ and } n = n' \,; \end{cases} \tag{22.188}$$

where M_{mn} is the modal mass for the mode (m, n). The eigenfrequencies for the orthotropic plate are distributed between two limiting curves in the (k, f)-plane (Fig. 22.12).

Particular Case: Isotropic Plate

In the isotropic case, the rigidity coefficients become

$$D_1 = D_3 = D = \frac{Eh^3}{12(1 - \nu^2)} \tag{22.189}$$

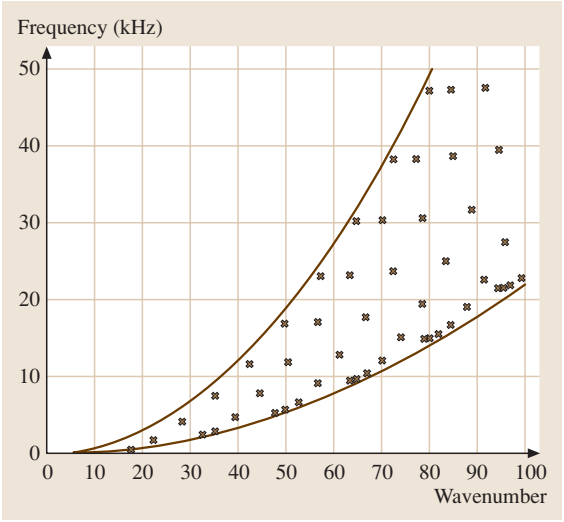


Fig. 22.12 Dispersion curves for an orthotropic plate made of carbon fibers with $D_1 = 8437\,\mathrm{MPa}$; $D_2 = 463\,\mathrm{MPa}$; $D_3 = 852\,\mathrm{MPa}$; $D_4 = 2267\,\mathrm{MPa}$; $h = 2\,\mathrm{mm}$; $\rho_p = 1540\,\mathrm{kg/m^3}$; $a = 0.4\,\mathrm{m}$; $b = 0.2\,\mathrm{m}$

and

$$D_4 = \frac{Eh^3}{6(1 + \nu)} \,,$$
$$D_2 = 2D_1 - D_4 = \frac{E\nu h^3}{6(1 - \nu^2)} \,. \tag{22.190}$$

Here, the elastic behavior of the material is fully determined by two constants: the Young's modulus E and the Poisson's ratio ν. The eigenfunctions $\Phi_{mn}(x, y)$ are the same as in (22.186). However, the eigenfrequencies now reduce to

$$\omega_{mn} = \pi^2 \sqrt{\frac{D}{\rho_p h}} \left(\frac{m^2}{a^2} + \frac{n^2}{b^2} \right) . \tag{22.191}$$

Prestressed Isotropic Plate. If a tension (or compression) T_x in the x-direction and, simultaneously, a tension (or compression) T_y in the y-direction are applied in the plate plane, then the flexural equation is modified as follows [22.1]:

$$\rho_p h \frac{\partial^2 w}{\partial t^2} + D \left(\frac{\partial^4 w}{\partial x^4} + 2 \frac{\partial^4 w}{\partial x^2 \partial y^2} + \frac{\partial^2 w}{\partial y^4} \right) - T_x \frac{\partial^2 w}{\partial x^2} - T_y \frac{\partial^2 w}{\partial y^2} = 0 \,. \tag{22.192}$$

Amazon EX1014 Page 928

In this case, the eigenfrequencies become

$$\omega_{mn} = \sqrt{\frac{1}{\rho_p h}} \times \sqrt{D\left(\frac{\pi^2 m^2}{a^2} + \frac{\pi^2 n^2}{b^2}\right)^2 + T_x \frac{m^2\pi^2}{a^2} + T_y \frac{n^2\pi^2}{b^2}} \,. \tag{22.193}$$

22.4.4 Vibrations of Thin Shallow Spherical Shells

One interest of presenting the vibrations of shallow spherical shells is to show the influence of curvature, compared to the case of flat plates. The present section focuses on the particular case of free edge, which is scarcely treated in the literature [22.16]. Linear vibrations of cymbals and gongs, for example, are conveniently described by such an idealized structure.

An isotropic spherical cap is considered, with thickness h, radius of curvature R and whose projection on a plane is a circle of radius a (Fig. 22.13). Using the Donnell–Mushtari–Vlasov assumptions for thin ($h \ll a$) and shallow ($a \ll R$) shells, the equations of motion for the free transverse displacement $w(r, \theta, t)$ of the cap is given by [22.17]

$$D\nabla^6 w + \frac{Eh}{R^2}\nabla^2 w + \rho h \nabla^2 \ddot{w} = 0 \,, \tag{22.194}$$

where E is the Young's modulus, ρ is the density, ν is the Poisson's ratio and $D = Eh^3/12(1-\nu^2)$ is the flexural rigidity of the shell. Equation (22.194) can be conveniently put into nondimensional form using the reduced variables $\overline{w} = w/w_0$, $\overline{r} = r/a$ and $\overline{t} = t/t_0$ with $t_0 = a^2\sqrt{\rho h/D}$. In this case, (22.194) becomes

$$\nabla^6 \overline{w} + \chi \nabla^2 \overline{w} + \nabla^2 \ddot{\overline{w}} = 0 \,,$$

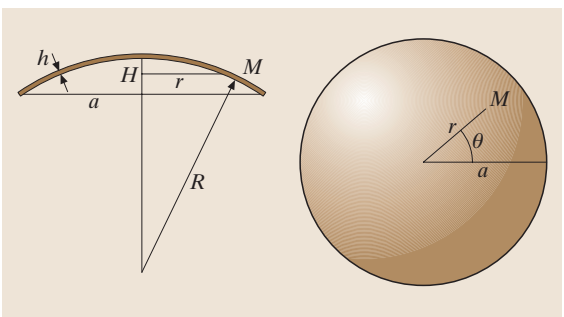


Fig. 22.13 Spherical cap

where

$$\chi = 12(1-\nu^2)\frac{a^4}{R^2h^2} \,. \tag{22.195}$$

Notice that w_0 can be selected arbitrarily in the linear case. For nonlinear vibrations, this parameter should be selected in accordance with the order of magnitude of the nonlinear perturbation terms (Sect. 22.7).

Remark. In what follows, the nondimensional equation is solved but the overlines are removed from the variables, for convenience.

Eigenmodes of the Spherical Cap with Free Edge. We look for harmonic solutions of (22.195) of the form $w(r, \theta, t) = \Phi(r, \theta)q(t)$. The solutions must fulfill one of the two following cases [22.18]:

$$\begin{cases} \text{if} & \omega^2 - \chi = \zeta^4 > 0 \\ \text{then} & \nabla^2\left(\nabla^4 - \zeta^4\right)\Phi = 0 \;\; \text{case 1} \,, \\ \text{if} & \omega^2 - \chi = -\zeta^4 < 0 \\ \text{then} & \nabla^2\left(\nabla^4 + \zeta^4\right)\Phi = 0 \;\; \text{case 2} \,. \end{cases} \tag{22.196}$$

In case 1, the eigenfunctions are given by

$$\Phi_{nm}(r, \theta) = \left[A_n r^n + B_n J_n(\zeta_{nm} r) + C_n I_n(\zeta_{nm} r)\right] \begin{vmatrix} \cos m\theta \\ \sin m\theta \end{vmatrix} \,, \tag{22.197}$$

where A_n, B_n and C_n are constants, ζ_{nm} are determined by the boundary conditions, J_n are the Bessel functions of the first kind and I_n are the modified Bessel functions of the first kind. In case 2, the eigenfunctions are given by

$$\Phi_{nm}(r, \theta) = \left[A_n r^n + B_n \mathrm{ber}_n(\zeta_{nm} r) + C_n \mathrm{bei}_n(\zeta_{nm} r)\right] \begin{vmatrix} \cos m\theta \\ \sin m\theta \end{vmatrix} \,, \tag{22.198}$$

where ber_n and bei_n are the Kelvin functions defined by [22.9]

$$\mathrm{ber}_n(x) + \mathrm{ibei}_n(x) = J_n[x \exp(3\mathrm{i}\pi/4)] \,. \tag{22.199}$$

For a free edge, the eigenvalues ζ_{mn} are determined from the equation obtained by expressing that forces and moments are equal to zero at the edge $r = a$. The four possible situations for the eigenfrequencies are

summarized below [22.19]:

$$\begin{cases} \text{for} \quad n \in 0,1, & \forall m \geq 1 \\ & \omega_{nm} = \sqrt{\chi + \omega_{nm}^{(0)2}} \,, \\ \text{for} \quad n \geq 2, & m = 0 \quad \text{and} \quad \chi < \chi_n^{\lim} \\ & \omega_{n0} = \sqrt{\chi + \zeta_{n0}^4} \,, \\ \text{for} \quad n \geq 2, & m = 0 \quad \text{and} \quad \chi > \chi_n^{\lim} \\ & \omega_{n0} = \sqrt{\chi - \zeta_{n0}^4} \,, \\ \text{for} n \quad \geq 2, & m \geq 1, \\ & \omega_{nm} = \sqrt{\chi + \zeta_{nm}^4} \,, \end{cases} \tag{22.200}$$

where $\omega_{nm}^{(0)}$ are the eigenfrequencies obtained in the case of the circular plate with free edge, corresponding to the limiting case of the spherical shell with no curvature. The limiting value $\chi_n^{\lim}$ that separates the Bessel from the Kelvin axisymmetric modes is given by [22.18]:

$$\chi_n^{\lim} = \frac{(1-\nu)(3+\nu)n^2(n^2-1)}{1+\frac{1}{4}(1-\nu)(n-2) - \frac{n^2(n-1)(1-\nu)(4n-\nu+9)}{16(n+2)^2(n+3)}} \,. \tag{22.201}$$

22.4.5 Combinations of Elementary Structures

Interesting and powerful models of complex structures can be obtained by combining together elementary components. One-dimensional models of intersecting walls, for example, can be modeled by means of connected bars, with appropriate boundary conditions at the junctions: equality of displacements, angles, forces and moments. This allows calculations of reflection and transmission coefficients in the different parts of a wall or a frame. Other examples of interest are sandwich plates. A sandwich is usually made of two plates with a thin viscoelastic (absorbing) layer between them. Again, the model contains the equation of motion for each layer plus additional boundary conditions. As a result, one can calculate, for example, the equivalent complex stiffness of the sandwich. One main advantage of such a configuration is that one can obtain a substantial increase of loss factor over a relatively wide frequency range, compared to a sytem of equal thickness composed by only one plate with a simple viscoelastic layer. However, the main drawback is that each application needs careful design of a specific sandwich in order to be effective in the frequency range of interest [22.13, 20].

Periodic structures can be found in many applications, such as ships, planes or roofs where a relatively light plate (or shell) is reinforced by stiffeners and ribs at uniform intervals. Such problems have been studied extensively in recent decades. A simple example of such a structure is the periodically supported infinite beam subjected to bending motion. By generalizing methods previously applied to atomic chains and crystals by Brillouin, different authors represent the spatial part of the wave propagation in such a beam by an equation of the form

$$w(x+L) = \exp(\lambda) w(x) \,, \tag{22.202}$$

where w is the transverse displacement, L is the spatial period of the structure and λ is the propagation constant to be determined. The problem is solved by expressing the continuity and equilibrium equations at the junctions. Two situations may occur: if λ is purely imaginary, the bending wave can propagate freely in the periodic structure. The corresponding frequency range is called the *pass band*. If λ contains a real part, then the wave becomes evanescent, and the corresponding frequency range is called the *stop band*. Recently, some authors have shown that SEA can by useful for tackling such problems [22.21].

22.5 Structural–Acoustic Coupling

If the sound is generated by a light and flexible structure, then the effect of the acoustic loading back on the structure cannot be neglected, and the system has to be considered as a whole [22.22]. In the general case, the action of a fluid on a structure has several effects: radiation damping and modification of the eigenfrequencies. Approximations can be made in the case of a light fluid and weak coupling. These points are examined in Sect. 22.5.1. The simple example of a 1-D bar coupled to a semi-infinite tube is selected in order to facilitate the presentation of the various concepts. In a number of applications, the goal is to control the amount of energy radiated by a vibrating structure. This forms the heart of Sect. 22.5.2. In particular, the state-space formulation of structural–acoustic coupling facilitates the development of active noise-reduction systems [22.23]. The concept

of radiation modes and their link with sound power and efficiency is also presented in this section [22.24, 25].

In the case of structure–cavity coupling, the effects of the cavity field are different from those of the free field. Strong structural–acoustic modes can appear, which may contribute to a substantial modification of the radiated spectrum. These features are illustrated in Sect. 22.5.3 for the example of a 1-DOF oscillator coupled to a finite tube.

The concept of coincidence (or critical) frequency is essential in the radiation of sound by structures. By comparing the dispersion equations for the structure and fluid, respectively, one can make a distinction between frequency domains where the radiation efficiency of the structure is strong and where it is weak. This is treated in Sect. 22.5.4 for an isotropic plate.

22.5.1 Longitudinally Vibrating Bar Coupled to an External Fluid

Model and Modal Projection

We consider here the simple case of a longitudinally vibrating bar of length L coupled at one end to a 1-D infinite tube filled with air, which presents a resistive loading $R_a = \rho c S$ at the end of the bar. It is assumed throughout this section that the bar has a constant cross-sectional area S and that it is clamped at one end ($x = 0$) and free at the other ($x = L$). ρ_s is the density of the bar, E its Young's modulus, $c_L = \sqrt{E/\rho_s}$ is the longitudinal wave speed and $\xi(x,t)$ the longitudinal displacement at a point M at position x along the bar ($0 \le x \le L$). Similarly, ρ denotes the air density, c the speed of sound and $p(x,t)$ the sound pressure in the tube ($L < x < \infty$) (Fig. 22.14). In the absence of an exciting force (free vibration), the equations of the problem are:

$$\begin{cases} \rho_s S \dfrac{\partial^2 \xi}{\partial t^2} = ES \dfrac{\partial^2 \xi}{\partial x^2} - Sp(L,t)\delta(x-L) \\ \qquad \text{for } 0 \le x \le L\,, \\ p(L,t) = \rho c \dot{\xi}(L,t)\,, \\ \xi(0,t) = 0\,, \\ p(x,t) = \rho c \dot{\xi}\left(L, t - \frac{x-L}{c}\right) \\ \qquad \text{for } L < x < \infty \end{cases} . \tag{22.203}$$

We look for the solution $\xi(x,t)$ expanded in terms of the in vacuo modes $\phi_n(x)$ of the bar. Both sides of the first equation in (22.203) are multiplied by any eigenfunction and integrated over the length of the bar. This gives

$$\begin{aligned} &\int_0^L \rho_s S \left[\sum_m \phi_m(x)\ddot{q}_m(t)\right]\phi_n(x)\,\mathrm{d}x \\ &- \int_0^L ES \left[\sum_m \phi_m{}''(x) q_m(t)\right]\phi_n(x)\,\mathrm{d}x \\ &= \int_0^L S\rho c \left[\sum_m \phi_m(L)\dot{q}_m(t)\right]\phi_n(x)\delta(x-L)\,\mathrm{d}x\,. \end{aligned} \tag{22.204}$$

This equation can be rewritten in a simpler form, by using the definition of the modal mass

$$m_n = \int_0^L \rho_s S \phi_n^2(x)\,\mathrm{d}x\,. \tag{22.205}$$

Because of the mass orthogonality property of the eigenfunctions, the terms of the series in the first integral on the left-hand side of (22.204) are zero for $m \neq n$, so that the integral reduces to $m_n \ddot{q}_n(t)$. The second integral can be rewritten:

$$-\int_0^L ES \frac{\omega_m^2}{c_L^2}\left[\sum_m \phi_m(x) q_m(t)\right]\phi_n(x)\,\mathrm{d}x \tag{22.206}$$

which, due to stiffness orthogonality properties of the eigenfunctions, reduces to $-\omega_n^2 m_n q_n(t)$. Finally, due to the properties of the delta function, the third integral can be rewritten:

$$-R_a \phi_n(L) \sum_m \phi_m(L)\dot{q}_m(t)\,, \tag{22.207}$$

where $R_a = \rho c S$ is the acoustic radiation resistance.

Remark. In the case of the clamped–free bar, we would get $\phi_n(L) = (-1)^{n+1}$ and, similarly, $\phi_m(L) = (-1)^{m+1}$. However, in what follows, we choose to retain the more general formulation of (22.207) so that the equations remain general.

For a 1-D bar of length L coupled to a semi-infinite tube, the displacement is given by

$$\xi(x,t) = \sum_n \phi_n(x) q_n(t)\,, \tag{22.208}$$

where the functions of times $q_n(t)$ obey the set of coupled equations

$$\begin{aligned} &m_n \ddot{q}_n(t) + m_n \omega_n^2 q_n(t) \\ &= -R_a \phi_n(L) \sum_m \phi_m(L)\dot{q}_m(t)\,. \end{aligned} \tag{22.209}$$

Once the displacement of the bar $\xi(x,t)$ is known, we can calculate the velocity $\dot{\xi}(x,t)$ at each point of the bar and, in particular, at the point $x = L$ and thus derive the radiated sound pressure inside the tube through (22.203). We now examine the consequences of the coupling on systems of small dimensions, to better understand its physical meaning.

Single-DOF System. Suppose that, for various reasons, we can reduce the previous system to one single mode. In this case, (22.209) reduces to

$$\ddot{q}_1(t) + \frac{R_a \phi_1^2(L)}{m_1}\dot{q}_1(t) + \omega_1^2 q_1(t) = 0\,. \tag{22.210}$$

This is simply the equation of a damped oscillator, where the dimensionless damping factor ζ_1 is given by

$$2\zeta_1\omega_1 = \frac{R_a\phi_1^2(L)}{m_1}\,. \tag{22.211}$$

Thus, for a single-DOF system, the acoustic coupling adds a radiation damping to the structure. This damping represents the amount of acoustic energy radiated by the vibrating bar.

Two-DOF System. Now, we truncate the system to the two lowest modes of the structure. In this case, (22.209) reduces to:

$$\begin{cases} \ddot{q}_1 + 2\zeta_1\omega_1\dot{q}_1 + \omega_1^2 q_1 &= -\dfrac{R_a\phi_1(L)\phi_2(L)}{m_1}\dot{q}_2 \\ &= C_{12}\dot{q}_2\,, \\ \ddot{q}_2 + 2\zeta_2\omega_2\dot{q}_2 + \omega_2^2 q_2 &= -\dfrac{R_a\phi_2(L)\phi_1(L)}{m_2}\dot{q}_1 \\ &= C_{21}\dot{q}_1\,. \end{cases} \tag{22.212}$$

Several conclusions can be drawn from this last result:

- The acoustic radiation introduces damping terms $2\zeta_i\omega_i\dot{q}_i$ in each equation.
- The time functions are coupled by the radiation. In general, the coupling coefficients C_{12} and C_{21} are not equal.

Taking the Laplace transform of the system in (22.212) leads to the characteristic equation

$$\begin{aligned} &\left(s^2 + 2\zeta_1\omega_1 s + \omega_1^2\right)\left(s^2 + 2\zeta_2\omega_2 s + \omega_2^2\right) \\ &- 4\zeta_1\zeta_2\omega_1\omega_2 s^2 = 0\,. \end{aligned} \tag{22.213}$$

Equation (22.213) shows that the structural–acoustic coupling modifies the eigenfrequencies and damping factors of the system, compared to the in vacuo case.

Light-Fluid Approximation. For $\zeta_1\omega_1 \ll 1$ and $\zeta_2\omega_2 \ll 1$ one can find first-order approximations for both the eigenfrequencies and decay times, due to the air–structure coupling. Denoting $s = \sigma + \mathrm{i}\omega$ and replacing it in (22.213) yields the new damping factors:

$$\begin{aligned} \sigma_1 &\approx -\left(\zeta_1\omega_1 - \frac{\omega_2}{2\omega_1}C_{12}\right)\,, \\ \sigma_2 &\approx -\left(\zeta_2\omega_2 - \frac{\omega_1}{2\omega_2}C_{21}\right)\,. \end{aligned} \tag{22.214}$$

Similarly, the new eigenfrequencies become:

$$\begin{cases} \omega_1'^2 \approx \omega_1^2 & -\left[2\zeta_1^2\omega_1^2 - (\zeta_1+\zeta_2)\omega_2 C_{12} \right. \\ & \left. + \dfrac{\omega_1}{2\omega_2}C_{21}C_{12}\right]\,, \\ \omega_2'^2 \approx \omega_2^2 & -\left[2\zeta_2^2\omega_2^2 - (\zeta_1+\zeta_2)\omega_1 C_{21} \right. \\ & \left. + \dfrac{\omega_2}{2\omega_1}C_{21}C_{12}\right]\,. \end{cases} \tag{22.215}$$

Forced Vibrations

The transfer function between the excitation force and the bar displacement is now examined. Equation (22.203) is modified through the introduction of a force term $F(x_0,t)$ at point x_0:

$$\begin{aligned} \rho_s S\frac{\partial^2\xi}{\partial t^2} &= ES\frac{\partial^2\xi}{\partial x^2} - Sp(L,t)\delta(x-L) \\ &\quad + F(x_0,t)\delta(x-x_0) \\ &\text{for} \quad 0 \le x \le L \\ &\text{and} \quad 0 \le x_0 \le L\,. \end{aligned} \tag{22.216}$$

Using the same modal projection as in the previous section, we find

$$\begin{aligned} &\ddot{q}_n + 2\zeta_n\omega_n\dot{q}_n + \omega_n^2 q_n \\ &= \sum_{m\neq n} C_{nm}\dot{q}_m + F(x_0,t)\frac{\phi_n(x_0)}{m_n} \end{aligned} \tag{22.217}$$

or, equivalently, using Laplace transforms, as

$$\tilde{q}_n(s) = H_n(s)\tilde{F}(x_0,s) + \sum_{m\neq n} K_{nm}(s)\tilde{q}_m(s) \tag{22.218}$$

with

$$H_n(s) = \frac{\phi_n(x_0)}{m_n\left(s^2 + 2\zeta_n\omega_n s + \omega_n^2\right)}$$

and

$$K_{nm}(s) = \frac{sC_{nm}}{s^2 + 2\zeta_n\omega_n s + \omega_n^2}\,. \tag{22.219}$$

Finally, the displacement is

$$\tilde{\xi}(x,s) = \sum_n \tilde{q}_n(s)\phi_n(x) = \tilde{F}(x_0,s)\sum_n \phi_n(x)H_n(s) + \sum_n \phi_n(x)\sum_{m\neq n} K_{nm}(s)\tilde{q}_m(s)\,. \quad (22.220)$$

Matrix Formulation. Equation (22.218) can then be rewritten (removing the tilde from the Laplace transforms, for convenience) as

$$\begin{pmatrix} 1 & -K_{12} & \dots & -K_{1n} \\ -K_{21} & 1 & \dots & -K_{2n} \\ \dots & \dots & \dots & \dots \\ -K_{n1} & -K_{n2} & \dots & 1 \end{pmatrix} \begin{pmatrix} q_1 \\ q_2 \\ \dots \\ q_n \end{pmatrix} = F \begin{pmatrix} H_1 \\ H_2 \\ \dots \\ H_n \end{pmatrix} \quad (22.221)$$

which can be formulated in the more compact form:

$$\mathbf{K}\boldsymbol{Q} = F\boldsymbol{H}\,. \quad (22.222)$$

The displacement of the bar is

$$\xi = \boldsymbol{Q}^{\mathrm{t}}.\boldsymbol{\phi} = \boldsymbol{Q}.\boldsymbol{\phi}^{\mathrm{t}} = (\mathbf{K}^{-1}\boldsymbol{H})^{\mathrm{t}}.\boldsymbol{\phi}F = (\mathbf{K}^{-1}\boldsymbol{H}).\boldsymbol{\phi}^{\mathrm{t}}F \quad (22.223)$$

In some applications, it is interesting to write (22.218) in a form that allows the characteristic equation to be determined immediately. In this case, (22.221) becomes:

$$\begin{pmatrix} s^2+\omega_1^2 \\ +2\zeta_1\omega_1 s \end{pmatrix} \begin{matrix} -sC_{12} & \dots & -sC_{1n} \\ s^2+\omega_2^2 \\ +2\zeta_2\omega_2 s \end{matrix} \begin{matrix} \dots & -sC_{2n} \\ \dots & \dots \\ \dots & \dots \\ -sC_{n2} & \dots & s^2+\omega_n^2 \\ & & +2\zeta_n\omega_n s \end{matrix} \begin{pmatrix} q_1 \\ q_2 \\ \dots \\ q_n \end{pmatrix} = F \begin{pmatrix} \beta_1 \\ \beta_2 \\ \dots \\ \beta_n \end{pmatrix}, \quad (22.224)$$

where $\beta_n = \dfrac{\phi_n(x_0)}{m_n}$. The equivalent matrix notation is

$$\mathbf{C}\boldsymbol{Q} = F\boldsymbol{\beta}\,. \quad (22.225)$$

The displacement of the bar is given by

$$\xi = (\mathbf{C}^{-1}\boldsymbol{\beta})^{\mathrm{t}}.\boldsymbol{\phi}F = (\mathbf{C}^{-1}\boldsymbol{\beta}).\boldsymbol{\phi}^{\mathrm{t}}F\,. \quad (22.226)$$

Inversion of the Matrix **C.** Finding explicit solutions for the generalized displacements q_i in (22.224) requires inversion of the matrix **C**. An example is given below for a subsystem of order two, where we write for convenience $D_n = s^2 + 2\zeta_n\omega_n s + \omega_n^2$. We obtain easily

$$q_1 = \frac{\beta_1 D_2 + sC_{12}\beta_2}{D_1 D_2 - s^2 C_{12}C_{21}}F$$

and

$$q_2 = \frac{\beta_2 D_1 + sC_{21}\beta_1}{D_1 D_2 - s^2 C_{12}C_{21}}F\,. \quad (22.227)$$

Or, using the ($\boldsymbol{H}$, **K**) formulation

$$q_1 = \frac{H_1 + K_{12}H_2}{1 - K_{12}K_{21}}F = L_1 F$$

and

$$q_2 = \frac{H_2 + K_{21}H_1}{1 - K_{12}K_{21}}F = L_2 F \quad (22.228)$$

from which the displacement ξ can be derived. The coupling appears in (22.224) through the fact that q_1 is not zero, even if β_1 vanishes. In other words, one can excite vibrations at ω_n even if the structure is excited at a node of the associated in vacuo mode. The new eigenfrequencies and damping factors modified by the coupling are now given by the roots of the denominator $D_1 D_2 - s^2 C_{12}C_{21}$.

Orthogonalization of the Matrix **C.** The question is now to study whether one can find an appropriate basis for decoupling the system. Approximate formulations in the case of weak coupling are derived below. We start with a 2-DOF system before generalization. The matrix **C** is

$$\begin{pmatrix} D_1 & -sC_{12} \\ -sC_{21} & D_2 \end{pmatrix}$$

with

$$D_i = s^2 + 2\zeta_i\omega_i s + \omega_i^2\,. \quad (22.229)$$

The corresponding diagonal matrix $\boldsymbol{\Lambda}$ is written

$$\begin{pmatrix} \lambda_1 & 0 \\ 0 & \lambda_2 \end{pmatrix}, \quad (22.230)$$

where the λ_i are solutions of the equation

$$\begin{vmatrix} D_1 - \lambda & -sC_{12} \\ -sC_{21} & D_2 - \lambda \end{vmatrix} = (D_2 - \lambda)(D_1 - \lambda) - s^2 C_{12}C_{21} = 0\,. \quad (22.231)$$

Denoting by $\boldsymbol{e}_i$ the corresponding eigenvectors and $\mathbf{T} = (\boldsymbol{e}_1 \ \boldsymbol{e}_2)$, then we have the following matrix equations:

$$\mathbf{T}\boldsymbol{\Lambda} = \mathbf{C}\mathbf{T} \quad \Leftrightarrow \quad \boldsymbol{\Lambda} = \mathbf{T}^{-1}\mathbf{C}\mathbf{T} \,. \tag{22.232}$$

In the general case, the λ_i are given by

$$\lambda_{1,2} = \frac{1}{2}\left[D_1 + D_2 \pm \sqrt{(D_1 - D_2)^2 + 4s^2 C_{12}C_{21}}\right] . \tag{22.233}$$

Weak-Coupling Approximation. It is convenient to define the nondimensional coupling parameter

$$\varepsilon = \frac{C_{12}C_{21}}{D_2 - D_1} = \frac{C_{12}C_{21}}{\omega_2^2 - \omega_1^2 + 2s(\zeta_2\omega_2 - \zeta_1\omega_1)} \tag{22.234}$$

so that, for $\varepsilon \ll 1$, the eigenvalues of $\mathbf{C}$ can be written to first-order approximation as

$$\lambda_1 = D_1 - \varepsilon s^2 \,; \quad \lambda_2 = D_2 + \varepsilon s^2 \,. \tag{22.235}$$

This approximation is justified if the C_{ij} are small, as in the case of a light fluid, or if the in vacuo eigenfrequencies ω_i and ω_j are not too close to each other (Sect. 22.6.1). In this case, the previously defined matrices become

$$\mathbf{T} = \begin{pmatrix} 1 & -\dfrac{\varepsilon s}{C_{21}} \\ \dfrac{\varepsilon s}{C_{12}} & 1 \end{pmatrix} \Rightarrow$$

$$\mathbf{T}^{-1} = \frac{C_{12}C_{21}}{C_{12}C_{21} + \varepsilon^2 s^2} \times \begin{pmatrix} 1 & \dfrac{\varepsilon s}{C_{21}} \\ -\dfrac{\varepsilon s}{C_{12}} & 1 \end{pmatrix} . \tag{22.236}$$

Defining further the vectors $\boldsymbol{\gamma} = \mathbf{T}^{-1}\boldsymbol{\beta}$ and $\boldsymbol{R} = \mathbf{T}^{-1}\boldsymbol{Q}$, (22.225) and (22.226) can be rewritten as

$$\boldsymbol{\Lambda}\boldsymbol{R} = F\boldsymbol{\gamma} \ \Rightarrow \quad \xi = \mathbf{T}\boldsymbol{\Lambda}^{-1}\boldsymbol{\gamma}\,\boldsymbol{\phi}^{\mathrm{t}} F \,. \tag{22.237}$$

Here, we have:

$$\boldsymbol{\Lambda}^{-1} = \frac{1}{D_1 D_2 - s^2 C_{12}C_{21}} \times \begin{bmatrix} D_2 + \varepsilon s^2 & 0 \\ 0 & D_1 - \varepsilon s^2 \end{bmatrix} , \tag{22.238}$$

$$\boldsymbol{\gamma} = \frac{C_{12}C_{21}}{C_{12}C_{21} + \varepsilon^2 s^2} \begin{pmatrix} \beta_1 + \dfrac{\varepsilon s}{C_{21}}\beta_2 \\ \beta_2 - \dfrac{\varepsilon s}{C_{12}}\beta_1 \end{pmatrix}$$

and

$$\boldsymbol{R} = \frac{C_{12}C_{21}}{C_{12}C_{21} + \varepsilon^2 s^2} \begin{pmatrix} q_1 + \dfrac{\varepsilon s}{C_{21}}q_2 \\ q_2 - \dfrac{\varepsilon s}{C_{12}}q_1 \end{pmatrix} . \tag{22.239}$$

To a first-order approximation, it can be shown that

$$\boldsymbol{\Lambda}^{-1} \approx \boldsymbol{\Lambda}_0^{-1} + \varepsilon\boldsymbol{\Lambda}_{\mathrm{c}}^{-1} \,, \tag{22.240}$$

where $\boldsymbol{\Lambda}_0^{-1}$ is the in vacuo diagonal matrix given by

$$\boldsymbol{\Lambda}_0^{-1} = \begin{pmatrix} \dfrac{1}{D_1} & 0 \\ 0 & \dfrac{1}{D_2} \end{pmatrix} \tag{22.241}$$

and $\boldsymbol{\Lambda}_{\mathrm{c}}^{-1}$ is the coupling diagonal matrix given by

$$\boldsymbol{\Lambda}_{\mathrm{c}}^{-1} = \begin{pmatrix} \left(\dfrac{s}{D_1}\right)^2 & 0 \\ 0 & -\left(\dfrac{1}{D_2}\right)^2 \end{pmatrix} . \tag{22.242}$$

This result is of particular interest for computing the perturbation due to air loading of all significant variables of the system.

Generalization. Equation (22.235) can be generalized to n coupled modes. In this case, the eigenvalues become:

$$\begin{aligned} &\lambda_i = D_i + \varepsilon_i \\ \text{with} \quad &\varepsilon_i = -s^2 \sum_j \frac{C_{ij}C_{ji}}{D_j - D_i} \\ \text{and} \quad &1 \le j \le n \\ \text{and} \quad &j \ne i \,. \end{aligned} \tag{22.243}$$

Approximate Expressions for Displacement and Mode Shapes. From the above results, we can now find a first-order approximate expression for the bar displacement ξ. As in the previous sections, we start with the simple example of a 2-DOF system. Let us write first the in vacuo displacement

$$\xi_0 = \phi_{10}q_{10} + \phi_{20}q_{20} \,. \tag{22.244}$$

N.B. The notation ϕ_{i0}, denotes the eigenmode in vacuo and should not be confused with $\phi_i(x_0)$, which de-

notes the value of this eigenmode at one particular point of the structure. For the structure vibrating in air, the displacement becomes

$$\xi = \phi_{10} q_1 + \phi_{20} q_2 \,. \tag{22.245}$$

From (22.226) one can derive a first-order approximation for the bar displacement

$$\xi = \phi_{10}\left(q_{10} + \frac{sC_{12}}{D_1} q_{20}\right) + \phi_{20}\left(q_{20} + q_{10}\frac{sC_{21}}{D_2}\right) . \tag{22.246}$$

Operating Deflexion Shapes. Equation (22.246) can be rewritten

$$\xi = q_{10}\left(\phi_{10} + \frac{sC_{21}}{D_2}\phi_{20}\right) + q_{20}\left(\phi_{20} + \phi_{10}\frac{sC_{12}}{D_1}\right)$$

$$\text{with} \quad q_{i0} = \frac{\phi_{i0}}{m_i D_i} F \,. \tag{22.247}$$

In experiments on structures, sinusoidal excitation is often used. Imagine that we apply a sudden harmonic force $F(t) = H(t)\sin\omega t$ at time $t = 0$ to the structure, with excitation location and frequency such that q_{20} is negligible compared to q_{10}. $H(t)$ is the Heaviside function. In this case, the spatial pattern of the structure is given by

$$\phi_1 = \phi_{10} + \phi_{20}\frac{sC_{21}}{D_2} \,. \tag{22.248}$$

Because of the time dependence of the second term (through the Laplace variable s), the spatial shape evolves with time. Here, we can use the Laplace limit theorem, which states that the value of $\phi(t)$ as time tends to infinity is given by the product of $s\phi(s)$ as s tends to zero. Since $s^2 C_{12}/D_2$ tends to zero as s tends to zero, the second term on the right-hand side of (22.248) vanishes after some time. Calculating the inverse Laplace transform shows that this decay time is of the order of the magnitude of the decay time of the second structural mode. After this transient regime, the spatial shape is nearly equal to the spatial shape in vacuo ϕ_{10}. In the more general case, (22.247) shows that F excites both q_{10} and q_{20}. After a transient regime, the bar displacement then finally converges to:

$$\xi(\omega, x) = \left[\frac{\phi_{10}\beta_1}{D_1(\mathrm{i}\omega)} + \frac{\phi_{20}\beta_2}{D_2(\mathrm{i}\omega)}\right] . \tag{22.249}$$

The quantity between in square brackets is called the operating deflexion shape (ODS) of the structure at frequency ω. Since it is very difficult in practice to excite a single q_{i0}, the ODS describes the multi-mode shapes that are observed for sinusoidal excitation of structures.

State-Space Formulation

The transfer function formulation is convenient if the system is initially at rest, and for time-invariant systems. For other applications, such as sound control, it is useful to express the results in terms of state-space variables [22.26–29]. In most cases, the mechanical state of the system is given by the position and the velocity of the DOFs. Since the unloaded structure is described by its eigenmodes ϕ_n, all useful information about the state of the system is contained in the modal participation factors q_n and in their first derivatives with time $\dot{q}_n$. This allows us to rewrite the equations for a 2-DOF coupled system as follows

$$\frac{\mathrm{d}}{\mathrm{d}t}\begin{pmatrix} X_1 \\ X_2 \\ X_3 \\ X_4 \end{pmatrix} = \begin{pmatrix} 0 & 0 & 1 & 0 \\ 0 & 0 & 0 & 1 \\ -\omega_1^2 & 0 & -2\zeta_1\omega_1 & C_{12} \\ 0 & -\omega_2^2 & C_{21} & -2\zeta_2\omega_2 \end{pmatrix} \times \begin{pmatrix} X_1 \\ X_2 \\ X_3 \\ X_4 \end{pmatrix} + \begin{pmatrix} 0 \\ 0 \\ \beta_1 \\ \beta_2 \end{pmatrix} F \,, \tag{22.250}$$

where

$$X_1 = q_1 \,;\; X_2 = q_2 \,;\; X_3 = \dot{q}_1 \,;\; X_4 = \dot{q}_2 \,. \tag{22.251}$$

Equation (22.250) can then be formulated equivalently as

$$\dot{\boldsymbol{X}} = \mathbf{A}\boldsymbol{X} + \boldsymbol{B}F \,, \tag{22.252}$$

where F is the *input* and $\boldsymbol{X}$ is the *state vector*. The output Y depends on the investigated mechanical problem. If we decide, for example, to investigate the displacement, then we can write for the *output*

$$Y = \begin{pmatrix} \phi_1 & \phi_2 & 0 & 0 \end{pmatrix}^{\mathrm{t}} \boldsymbol{X} = \boldsymbol{\Gamma}\,\boldsymbol{X} \,. \tag{22.253}$$

Equations (22.252) and (22.253) are general expressions for a linear system expressed in terms of state-space variables.

Remark 1. The representation presented in (22.250) is not unique. Selecting, for example

$$X_1 = q_1; \quad X_2 = \dot{q}_1; \quad X_3 = q_2; \quad X_4 = \dot{q}_2 \tag{22.254}$$

leads to different values for $\mathbf{A}$ and $\boldsymbol{B}$.

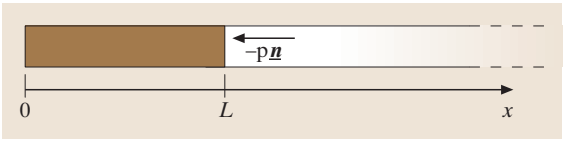


Fig. 22.14 Longitudinally vibrating bar coupled to a semi-infinite tube

Remark 2. Denoting by **M**, **R**, and **K**, the mass, resistance and stiffness matrices, respectively, of the 2-DOF system, the matrix **A** can be rewritten more generally using submatrices as

$$\mathbf{A} = \begin{pmatrix} \mathbf{0} & \mathbf{I} \\ -\mathbf{M}^{-1}\mathbf{K} & -\mathbf{M}^{-1}\mathbf{R} \end{pmatrix} , \tag{22.255}$$

where **I** is the identity matrix.

22.5.2 Energetic Approach to Structural–Acoustic Systems

Two-DOF System

We now consider a 2-DOF structure coupled to a radiating wave, but now include damping terms in the structure r_1 and r_2, to compare the power dissipated in vacuo and air, respectively. The damping terms r_{a1} and r_{a2} are due to radiation. Modal masses and stiffnesses are written explicitly, so that comparison with the case of a single oscillator becomes easier. We can then write

$$\begin{cases} m_1\ddot{q}_1 + (r_1 + r_{a1})\dot{q}_1 + k_1 q_1 + \gamma\dot{q}_2 = \phi_1(x_0)F , \\ m_2\ddot{q}_2 + (r_2 + r_{a2})\dot{q}_2 + k_1 q_2 + \gamma\dot{q}_1 = \phi_2(x_0)F , \end{cases} \tag{22.256}$$

where $\gamma = -C_{12}m_1 = -C_{21}m_2$. In what follows, we use the notations:

$$\begin{cases} 2\zeta_1\omega_1 &= \frac{r_1 + r_{a1}}{m_1} ; \\ 2\zeta_{10}\omega_1 &= \frac{r_1}{m_1} ; \\ \omega_1^2 &= \frac{k_1}{m_1} \\ 2\zeta_2\omega_2 &= \frac{r_2 + r_{a2}}{m_1} ; \\ 2\zeta_{20}\omega_2 &= \frac{r_2}{m_2} ; \\ \omega_2^2 &= \frac{k_2}{m_2} \end{cases} \tag{22.257}$$

to make a distinction between the damping factors in air and in vacuo. The force F is applied at point $x = x_0$ so that the mechanical input power is given by

$$p_{\mathrm{m}}(t) = F\frac{\mathrm{d}\xi}{\mathrm{d}t}(x_0, t) = F\left[\phi_1(x_0)\dot{q}_1 + \phi_2(x_0)\dot{q}_2\right] . \tag{22.258}$$

Using (22.256) allows $p_{\mathrm{m}}(t)$ to be written as

$$\begin{aligned} p_{\mathrm{m}}(t) = {} & m_1\ddot{q}_1\dot{q}_1 + (r_1 + r_{a1})\dot{q}_1^2 + k_1 q_1\dot{q}_1 \\ & + 2\gamma\dot{q}_1\dot{q}_2 \\ & + m_2\ddot{q}_2\dot{q}_2 + (r_2 + r_{a2})\dot{q}_2^2 + k_2 q_2\dot{q}_2 . \end{aligned} \tag{22.259}$$

Integrating $p_{\mathrm{m}}(t)$ over a duration T and removing the conservative energy terms yields the mean input power

$$\begin{aligned} \mathcal{P}_{\mathrm{m}}(T) = {} & \frac{1}{T}\int_0^T (r_1 + r_{a1})\dot{q}_1^2 + (r_2 + r_{a2})\dot{q}_2^2 \\ & + 2\gamma\dot{q}_2\dot{q}_1\,\mathrm{d}t . \end{aligned} \tag{22.260}$$

The input power is now seen as the sum of three terms:

- The mean power

$$\mathcal{P}_{\mathrm{s}}(T) = \frac{1}{T}\int_0^T r_1\dot{q}_1^2 + r_2\dot{q}_2^2\,\mathrm{d}t$$

  dissipated in the structure;
- The mean acoustic power

$$\mathcal{P}_{\mathrm{a}}(T) = \frac{1}{T}\int_0^T r_{a1}\dot{q}_1^2 + r_{a2}\dot{q}_2^2\,\mathrm{d}t$$

  radiated in the air;
- The mean coupling power

$$\mathcal{P}_{\mathrm{c}}(T) = \frac{2}{T}\int_0^T \gamma\dot{q}_2\dot{q}_1\,\mathrm{d}t$$

  due to the exchange of energy between the two oscillators via the fluid.

Let us denote the steady-state excitation frequency by ω. The transient regime is neglected, and the integration time T is supposed to be taken equal to an integer multiple of the period $T = n\tau = n2\pi/\omega$. The mean input power can then be written as

$$\begin{aligned} \mathcal{P}_{\mathrm{m}} = \frac{1}{2}\Big[& (r_1 + r_{a1})|\dot{q}_1|^2 \\ & + (r_2 + r_{a2})|\dot{q}_2|^2 + 2\gamma|\dot{q}_2||\dot{q}_1|\Big] . \end{aligned} \tag{22.261}$$

$\mathcal{P}_{\mathrm{m}}$ can be written in matrix form. Writing $\dot{\boldsymbol{Q}} = \begin{pmatrix} \dot{q}_1 \\ \dot{q}_2 \end{pmatrix}$, $\mathbf{R}_{\mathrm{s}} = \begin{pmatrix} r_1 & 0 \\ 0 & r_2 \end{pmatrix}$ and $\mathbf{R}_{\mathrm{a}} = \begin{pmatrix} r_{a1} & \gamma \\ \gamma & r_{a2} \end{pmatrix}$, we have

$$\mathcal{P}_\mathrm{m} = \dot{\boldsymbol{Q}}^\mathrm{H}\left[\mathbf{R}_\mathrm{s} + \mathbf{R}_\mathrm{a}\right]\dot{\boldsymbol{Q}}\,, \tag{22.262}$$

where $\dot{\boldsymbol{Q}}^\mathrm{H}$ is the Hermitian conjugate (conjugate transpose) of $\dot{\boldsymbol{Q}}$.

Generalization

The mean power for a multiple-DOF system is written:

$$\mathcal{P}_\mathrm{m}(T) = \frac{1}{T}\int_0^T \left[\sum_{i=1}^{n}(r_i + r_{ai})\dot{q}_i^2 + \sum_{i=1}^{n}\sum_{\substack{j=1\\ j\neq i}}^{n}\gamma_{ij}\dot{q}_i\dot{q}_j\right]\mathrm{d}t \tag{22.263}$$

with $\gamma_{ij} = -m_i C_{ij}$.

This mean power can be written in the same form as (22.262), where the resistance matrix is defined as

$$\begin{pmatrix} r_1 + r_{a1} & \dots & \gamma_{1i} & \dots & \gamma_{1j} & \dots & \gamma_{1n} \\ \dots & \dots & \dots & \dots & \dots & \dots & \dots \\ \gamma_{i1} & \dots & r_i + r_{ai} & \dots & \gamma_{ij} & \dots & \gamma_{in} \\ \dots & \dots & \dots & \dots & \dots & \dots & \dots \\ \gamma_{j1} & \dots & \gamma_{ji} & \dots & r_j + r_{aj} & \dots & \gamma_{jn} \\ \dots & \dots & \dots & \dots & \dots & \dots & \dots \\ \gamma_{n1} & \dots & \gamma_{ni} & \dots & \gamma_{nj} & \dots & r_n + r_{an} \end{pmatrix}. \tag{22.264}$$

Remark. The resistance matrix can again be viewed as the sum of a structural resistance matrix $\mathbf{R}_\mathrm{s}$ and an acoustical resistance matrix $\mathbf{R}_\mathrm{a}$. This leads to the expression for the mean acoustic power

$$\mathcal{P}_\mathrm{a} = \dot{\boldsymbol{Q}}^\mathrm{H}\mathbf{R}_\mathrm{a}\dot{\boldsymbol{Q}} \tag{22.265}$$

and acoustical efficiency

$$\eta_\mathrm{m} = \frac{\dot{\boldsymbol{Q}}^\mathrm{H}\left[\mathbf{R}_\mathrm{a}\right]\dot{\boldsymbol{Q}}}{\dot{\boldsymbol{Q}}^\mathrm{H}\left[\mathbf{R}_\mathrm{s} + \mathbf{R}_\mathrm{a}\right]\dot{\boldsymbol{Q}}} \tag{22.266}$$

which generalizes (22.32). Note that we have assumed that the structural resistance matrix $\mathbf{R}_\mathrm{s}$ is diagonal, which is usually a reasonable assumption for lightly damped structures. However, strong structural damping can also be the source of intermodal coupling. In this case, $\mathbf{R}_\mathrm{s}$ is no longer diagonal, but the general results expressed in (22.262) and (22.266) remain valid. A comparison of efficiencies between the cases of light and heavy fluids, respectively has been conducted by *Rumerman* [22.30].

Radiation Filter

Because $\mathbf{R}_\mathrm{a}$ is real, symmetric and positive definite, we can write this matrix in the form

$$\mathbf{R}_\mathrm{a} = \mathbf{P}^\mathrm{t}\boldsymbol{\Omega}\mathbf{P}\,, \tag{22.267}$$

where $\boldsymbol{\Omega}$ is a diagonal matrix [22.25]. As a consequence, the acoustic power becomes, removing for simplicity the integration time T,

$$P_\mathrm{a} = \boldsymbol{b}^\mathrm{H}\boldsymbol{\Omega}\boldsymbol{b}$$

where

$$\boldsymbol{b} = \mathbf{P}\dot{\boldsymbol{Q}}\,. \tag{22.268}$$

This can be written explicitly as

$$P_\mathrm{a} = \sum_n \Omega_n |b_n|^2\,. \tag{22.269}$$

Equation (22.269) shows that, defining the appropriate basis, the acoustic power can be expressed as a sum of quadratic terms, thus removing the cross products between the q_i in the previous subsections. Another interesting consequence of the properties of $\mathbf{R}_\mathrm{a}$ is that the acoustic power can be decomposed using the Cholesky method. This leads to the expression:

$$\begin{aligned} P_\mathrm{a} &= \dot{\boldsymbol{Q}}^\mathrm{H}\mathbf{R}_\mathrm{a}\dot{\boldsymbol{Q}} \\ &= \dot{\boldsymbol{Q}}^\mathrm{H}\mathbf{G}^\mathrm{H}\mathbf{G}\dot{\boldsymbol{Q}} = z^\mathrm{H}z = \sum_n |z_n|^2\,, \end{aligned} \tag{22.270}$$

where, by comparison with (22.269), the vector $z(\omega)$ can be viewed as the output of a set of radiation filters whose transfer functions $\mathbf{G}(\omega)$ are given by

$$\mathbf{G}(\omega) = \sqrt{\boldsymbol{\Omega}(\omega)}\mathbf{P}(\omega) \tag{22.271}$$

with input vector $\dot{\boldsymbol{Q}}$, so that

$$z = \mathbf{G}\dot{\boldsymbol{Q}}\,. \tag{22.272}$$

Impulsively Excited Structure: Total Radiated Energy

For an impulsively excited structure, the total radiated energy is given by:

$$E_\mathrm{T} = \int_0^\infty \dot{\boldsymbol{Q}}^\mathrm{H}\mathbf{R}_\mathrm{a}\dot{\boldsymbol{Q}}\,\mathrm{d}\omega = \int_0^\infty z^\mathrm{H}(\omega)z(\omega)\,\mathrm{d}\omega \tag{22.273}$$

which, by Parseval's theorem, is equivalent to [22.31]

$$E_\mathrm{T} = \int_0^\infty z^\mathrm{t}(t)z(t)\,\mathrm{d}t\,. \tag{22.274}$$

State-Space Analysis

The interest of formulating structural acoustic coupling in terms of state-space variables is now emphasized using an example. Denoting by $\boldsymbol{r}$ the internal state of filter $\mathbf{G}$ with input $\mathbf{X}$ (or $\dot{\boldsymbol{Q}}$) and output z, we can use a state-space realization of the form:

$$\begin{cases} \dot{\boldsymbol{r}} = \mathbf{A}_\mathrm{G}\boldsymbol{r} + \mathbf{B}_\mathrm{G}\boldsymbol{X}\,, \\ z = \mathbf{C}_\mathrm{G}\boldsymbol{r} + \mathbf{D}_\mathrm{G}\boldsymbol{X}\,. \end{cases} \tag{22.275}$$

Combining these equations with the equations of motion of the structure gives

$$\begin{pmatrix} \dot{\boldsymbol{X}} \\ \dot{\boldsymbol{r}} \end{pmatrix} = \begin{pmatrix} \mathbf{A} & \mathbf{0} \\ \mathbf{B}_\mathrm{G} & \mathbf{A}_\mathrm{G} \end{pmatrix} \begin{pmatrix} \boldsymbol{X} \\ \boldsymbol{r} \end{pmatrix} + \begin{pmatrix} \boldsymbol{B} \\ 0 \end{pmatrix} F \tag{22.276}$$

with the output

$$z = \begin{pmatrix} \mathbf{D}_\mathrm{G} & \mathbf{C}_\mathrm{G} \end{pmatrix} \begin{pmatrix} \boldsymbol{X} \\ \boldsymbol{r} \end{pmatrix}\,. \tag{22.277}$$

If, for example, the purpose is to minimize the total energy radiated by a source, then the cost function can be defined as

$$\mathcal{C}_f = \frac{\int_0^\infty z^\mathrm{t}(t) z(t)\,\mathrm{d}t}{\max\{E_\mathrm{T}\}}\,. \tag{22.278}$$

22.5.3 Oscillator Coupled to a Tube of Finite Length

Presentation of the Model

The purpose of this section is to present the fundamental concepts for a vibrating structure coupled to an acoustic cavity. As a simple example, we consider a single-DOF oscillator coupled to a 1-D tube of cross-sectional area S and finite length L loaded at its end $x = L$ by an impedance Z_L, defined here as the ratio between the pressure and acoustic velocity. The selected structure is a mechanical oscillator of mass M, stiffness $K = M\omega_0^2$ and dashpot $R = 2M\zeta_0\omega_0$ driven by a force $T(0, t)$ at position $x = 0$ (Fig. 22.15). The amplitude of the motion of the mass is assumed to be small, so that the acoustic velocity $v(0, t)$ is equal to the mechanical velocity $\dot{\xi}(t)$. We assume lossless wave propagation in the tube itself. The set of equations for the model is written:

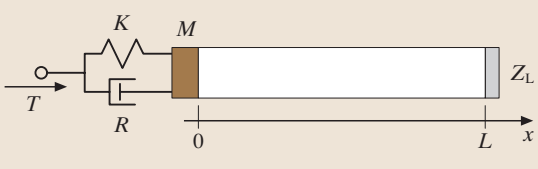


Fig. 22.15 Single-DOF mechanical oscillator coupled to a finite loaded tube

$$\begin{cases} \dfrac{1}{c^2}\dfrac{\partial^2 p}{\partial t^2} = \dfrac{\partial^2 p}{\partial x^2} \quad \text{for } 0 < x < L\,; \\ \rho\dfrac{\partial v}{\partial t} = -\dfrac{\partial p}{\partial x} \\ p(L, s) = Z_\mathrm{L} v(L, s)\,; \quad v(0, t) = \dot{\xi}(t) \\ M\left(\ddot{\xi} + 2\zeta_0\omega_0\dot{\xi} + \omega_0^2\xi\right) = -Sp(0, t) + T(t) \end{cases} \tag{22.279}$$

Mass Displacement

Using the Laplace transforms, we obtain

$$\begin{cases} p(x, s) &= \exp\left(-\frac{sx}{c}\right)F(s) + \exp\left(\frac{sx}{c}\right)G(s)\,, \\ v(x, s) &= \frac{1}{\rho c}\left[\exp\left(-\frac{sx}{c}\right)F(s) - \right. \\ & \qquad \left. \exp\left(\frac{sx}{c}\right)G(s)\right]\,, \end{cases} \tag{22.280}$$

where $F(s)$ and $G(s)$ are two functions to be determined. The boundary condition at $x = L$ gives

$$G(s) = F(s)\frac{Z_\mathrm{L} - \rho c}{Z_\mathrm{L} + \rho c}\exp\left(-\frac{2Ls}{c}\right)\,. \tag{22.281}$$

The continuity of the displacement at position $x = 0$ yields:

$$\begin{aligned} v(0, s) &= \frac{1}{\rho c}F(s)\left[1 - \frac{Z_\mathrm{L} - \rho c}{Z_\mathrm{L} + \rho c}\exp\left(-\frac{2Ls}{c}\right)\right] \\ &= s\xi(s)\,. \end{aligned} \tag{22.282}$$

Finally, the equation governing the oscillator motion becomes

$$\begin{aligned} &\left(s^2 + 2\zeta_0\omega_0 s + \omega_0^2\right)\xi(s) \\ &= \frac{T(s)}{M} - s\frac{R_\mathrm{a}}{M}\frac{z_\mathrm{L} + \tanh\left(\frac{sL}{c}\right)}{1 + z_\mathrm{L}\tanh\left(\frac{sL}{c}\right)}\xi(s) \end{aligned} \tag{22.283}$$

with

$$z_\mathrm{L} = \frac{Z_\mathrm{L}}{\rho c} \quad \text{and} \quad R_\mathrm{a} = \rho c S\,. \tag{22.284}$$

Equation (22.283) shows that, due to the loading of the oscillator by the finite tube, the damping term $2\zeta_0\omega_0$ becomes:

$$2\zeta_0\omega_0 + 2\zeta_\mathrm{a}\omega_0 Z(s)\,, \tag{22.285}$$

where

$$\frac{R_a}{M} = 2\zeta_a\omega_0$$

and

$$Z(s) = \frac{z_L + \tanh\left(\frac{sL}{c}\right)}{1 + z_L \tanh\left(\frac{sL}{c}\right)} \tag{22.286}$$

so that we can write:

$$\xi(s) = \frac{T(s)}{M} \frac{1}{s^2 + 2\omega_0\left[\zeta_0 + \zeta_a\, Z(s)\right] s + \omega_0^2} . \tag{22.287}$$

$F(s)$ is derived from (22.282):

$$\begin{aligned} F(s) &= \frac{\rho c s \xi(s)}{\left[1 - \frac{z_L - 1}{z_L + 1} \exp\left(-\frac{2sL}{c}\right)\right]} \\ &= \frac{\rho c s \xi(s) \exp\left(\frac{sL}{c}\right)(z_L + 1)}{2\left[z_L \sinh\left(\frac{sL}{c}\right) + \cosh\left(\frac{sL}{c}\right)\right]} . \end{aligned} \tag{22.288}$$

Equations (22.280) and (22.281) yield the pressure in the tube

$$p(x, s) = \rho c s \xi(s) \times \frac{z_L \cosh\left(\frac{s(x-L)}{c}\right) - \sinh\left(\frac{s(x-L)}{c}\right)}{\cosh\left(\frac{sL}{c}\right) + z_L \sinh\left(\frac{sL}{c}\right)} . \tag{22.289}$$

The pressure $p(0, s)$ acting on the oscillator is

$$\begin{aligned} p(0, s) &= \rho c s \xi(s) \frac{z_L \cosh\left(\frac{sL}{c}\right) + \sinh\left(\frac{sL}{c}\right)}{\cosh\left(\frac{sL}{c}\right) + z_L \sinh\left(\frac{sL}{c}\right)} \\ &= \rho c s \xi(s) Z(s) . \end{aligned} \tag{22.290}$$

Taking the inverse Laplace transform of (22.289) and (22.287) yields the pressure in the tube and the mass displacement in the time domain.

Discussion of $Z(s)$. Several interesting limiting cases can be examined:

- If the load at the end of the tube at $x = L$ is such that $Z_L = \rho c$, then $G(s) = 0$ and $F(s) = \rho c s \xi(s)$. This means that when the tube is loaded by its characteristic impedance there is no returning wave. In this case $Z(s) = 1$, and the only effect of the tube is to increase the damping of the oscillator, which becomes equal to $\xi_0 + \xi_a$. The increase of damping is entirely due to radiation and is, of course, identical to that obtained for the 1-DOF approximation of the vibrating bar loaded by the semi-infinite tube presented in Sect. 22.5.1.
- If the tube is closed at $x = L$, then z_L tends to ∞ so that $Z(s) = 1/\tanh(sL/c)$. If, in addition, the length L of the tube is sufficiently small so that we can make the approximation $\tanh(sL/c) \approx sL/c$, then the displacement can be written

$$\xi(s) = \frac{T(s)}{M} \frac{1}{s^2 + 2\omega_0\zeta_0 s + \omega_0^2 + \frac{2\omega_0\zeta_a c}{L}} . \tag{22.291}$$

  This is equivalent to the tube acting as an added stiffness $K_a = 2\omega_0 M \zeta_a c/L$, which increases the eigenfrequency of the mechanical oscillator.
- If the tube is open at $x = L$ and if we neglect radiation, then $z_L = 0$ and $Z(s) = \tanh(sL/c)$. For a small tube, or more generally for $sL/c \ll 1$, we obtain

$$\xi(s) = \frac{T(s)}{M} \frac{1}{s^2 + 2\omega_0\zeta_0 s + \omega_0^2 + \frac{2\omega_0\zeta_a s^2 L}{c}} . \tag{22.292}$$

  so that the tube acts as an added mass $M_a = 2M\omega_0\zeta_a L/c$, which decreases the eigenfrequency of the oscillator.

In the most general case, the coupling between a structure and a cavity yields new vibroacoustic (or structural–acoustic) modes that differ from the in vacuo modes of the structure and from the cavity modes with rigid walls [22.32]. For the present example, assuming light damping, these modes are the poles of $\xi(\omega)$, which are obtained from the equation

$$-\omega^2 + \omega_0^2 - 2\zeta_a\omega_0\omega\,\mathrm{Im}[Z(\omega)] = 0 . \tag{22.293}$$

For a lossless tube closed at $x = L$, the eigenmodes are the solutions of

$$\left(\omega_0^2 - \omega^2\right) \tan\frac{\omega L}{c} + 2\zeta_a\omega_0\omega = 0 . \tag{22.294}$$

For high frequencies, i. e., for $\omega \gg \omega_0$, the displacement of the oscillator tends to zero and (22.294) reduces to

$$\tan\frac{\omega L}{c} \approx 0 . \tag{22.295}$$

In this regime, the eigenfrequencies tend to those of the tube closed at both ends.

Amazon EX1014 Page 939

22.5.4 Two-Dimensional Elasto–Acoustic Coupling

We now turn to the case of 2-D systems. First, the case of an infinite isotropic plate is examined to introduce the concept of critical frequency. The presentation used the wave formalism and is inspired from *Filippi* et al., [22.33] and *Lesueur* [22.34]. We then consider the case of a finite plate using the wavenumber Fourier-transform method [22.35, 36].

Infinite Isotropic Plate. Critical Frequency

The case of thin plates submerged in compressible fluids and subjected to a transverse flexural displacement $\xi(x, y, t)$ is considered. Kirchhoff–Love approximations are assumed, so that shear stresses and rotary inertia are neglected. The infinite plate is located in the plane $z = 0$. In what follows, h is the plate thickness, E the Young's modulus, ν the Poisson's ratio and ρ_s the density of the plate. In the half-space $z < 0$, the pressure field is $p_1(x, y, z, t)$ in fluid 1 of density ρ_1 where the speed of sound is c_1. For $z > 0$, the pressure field is $p_2(x, y, z, t)$ in fluid 2 of density ρ_2 with speed of sound is c_2. The motion of the plate is harmonic with frequency ω. The equations of the problem are written in Cartesian coordinates:

- For $z < 0$

$$\nabla^2 p_1 + \frac{\omega^2}{c_1^2} p_1 = 0 \tag{22.296}$$

with the continuity condition

$$\frac{\partial p_1}{\partial z}(x, y, 0-) = \omega^2 \rho_1 \xi(x, y) . \tag{22.297}$$

- For $z > 0$

$$\nabla^2 p_2 + \frac{\omega^2}{c_2^2} p_2 = 0 \tag{22.298}$$

with the continuity condition

$$\frac{\partial p_2}{\partial z}(x, y, 0+) = \omega^2 \rho_2 \xi(x, y) . \tag{22.299}$$

- For $z = 0$, we have the loaded-plate equation:

$$p_1(x, y, 0-) - p_2(x, y, 0+) = -\omega^2 \rho_s h \xi(x, y) + D \nabla^4 \xi(x, y) , \tag{22.300}$$

where $D = \dfrac{Eh^3}{12(1-\nu^2)}$.

General Solution. The continuity conditions yields the following equalities for the wavenumber components

$$k_x^1 = k_x^2 = k_x \quad \text{and} \quad k_y^1 = k_y^2 = k_y . \tag{22.301}$$

Therefore the general solution of the problem can be written in the form:

$$\begin{cases} p_1(x, y, z) & = \left(A_x^1 \mathrm{e}^{-\mathrm{i}k_x x} + B_x^1 \mathrm{e}^{\mathrm{i}k_x x}\right) \\ & \quad \left(A_y^1 \mathrm{e}^{-\mathrm{i}k_y y} + B_y^1 \mathrm{e}^{\mathrm{i}k_y y}\right) B_z^1 \mathrm{e}^{\mathrm{i}k_z^1 z} , \\ p_2(x, y, z) & = \left(A_x^2 \mathrm{e}^{-\mathrm{i}k_x x} + B_x^2 \mathrm{e}^{\mathrm{i}k_x x}\right) \\ & \quad \left(A_y^2 \mathrm{e}^{-\mathrm{i}k_y y} + B_y^2 \mathrm{e}^{\mathrm{i}k_y y}\right) A_z^2 \mathrm{e}^{-\mathrm{i}k_z^2 z} , \\ \xi(x, y) & = \left(C_x \mathrm{e}^{-\mathrm{i}k_x x} + D_x \mathrm{e}^{\mathrm{i}k_x x}\right) \\ & \quad \left(C_y \mathrm{e}^{-\mathrm{i}k_y y} + D_y \mathrm{e}^{\mathrm{i}k_y y}\right) , \end{cases} \tag{22.302}$$

where the constants A, B, C, and D depend on the initial conditions. The wavenumbers in both fluids are written

$$k_1^2 = \frac{\omega^2}{c_1^2} = k_x^2 + k_y^2 + k_z^{1\,2}$$

and

$$k_2^2 = \frac{\omega^2}{c_2^2} = k_x^2 + k_y^2 + k_z^{2\,2} . \tag{22.303}$$

From (22.296–22.303) we derive the dispersion equation for the fluid-loaded plate

$$\mathrm{i}\omega^2 \left(\frac{\rho_1}{\sqrt{\frac{\omega^2}{c_1^2} - k_x^2 - k_y^2}} + \frac{\rho_2}{\sqrt{\frac{\omega^2}{c_2^2} - k_x^2 - k_y^2}} \right) + D\left(k_x^2 + k_y^2\right)^2 - \omega^2 \rho_s h = 0 \tag{22.304}$$

and the expressions for the pressure fields

$$\begin{cases} p_1 & = -\dfrac{\mathrm{i}\omega\rho_1 c_1 k_1}{\sqrt{k_1^2 - k_x^2 - k_y^2}} \xi(x, y) \mathrm{e}^{+\mathrm{i}\sqrt{k_1^2 - k_x^2 - k_y^2} z} \\ & \quad \text{with} \quad k_1 = \dfrac{\omega}{c_1} , \\ p_2 & = +\dfrac{\mathrm{i}\omega\rho_2 c_2 k_2}{\sqrt{k_2^2 - k_x^2 - k_y^2}} \xi(x, y) \mathrm{e}^{-\mathrm{i}\sqrt{k_2^2 - k_x^2 - k_y^2} z} \\ & \quad \text{with} \quad k_2 = \dfrac{\omega}{c_2} . \end{cases} \tag{22.305}$$

Equation (22.305) shows that the acoustic waves can be either progressive or evanescent, depending on the values of the wavenumber components k_x and k_y.

Radiated Power. The mean acoustic power in the fluids are given by

$$\begin{cases} \langle \mathcal{P}_1 \rangle &= \int_{(S)} \frac{1}{2} \operatorname{Re}\left(p_1 \left[\mathrm{i}\omega\xi\right]^*\right) \mathrm{d}S \\ &= -\frac{1}{2}\omega^2 \rho_1 c_1 \int_{(S)} \operatorname{Re}\left(\frac{k_1}{\sqrt{k_1^2 - k_x^2 - k_y^2}}\right) \\ &\quad \times \left|\xi(x,y)\right|^2 \mathrm{d}S \,, \\ \langle \mathcal{P}_2 \rangle &= \int_{(S)} \frac{1}{2} \operatorname{Re}\left(p_2 \left[\mathrm{i}\omega\xi\right]^*\right) \mathrm{d}S \\ &= +\frac{1}{2}\omega^2 \rho_2 c_2 \int_{(S)} \operatorname{Re}\left(\frac{k_1}{\sqrt{k_2^2 - k_x^2 - k_y^2}}\right) \\ &\quad \times \left|\xi(x,y)\right|^2 \mathrm{d}S \,. \end{cases} \tag{22.306}$$

The minus sign in $\langle \mathcal{P}_1 \rangle$ follows from the fact that the acoustic intensity vector in fluid 1 is oriented towards the negative direction of the z-axis. The radiation efficiencies σ_i of the plate in both fluids (with $i \in [1, 2]$) are defined as

$$\sigma_i = \left| \frac{\langle \mathcal{P}_i \rangle}{\rho_i c_i \langle V^2 \rangle} \right|$$

with

$$\langle V^2 \rangle = \frac{1}{2} \int_{(S)} \omega^2 \left|\xi(x,y)\right|^2 \mathrm{d}S \tag{22.307}$$

which gives

$$\sigma_i = \operatorname{Re}\left(\frac{k_i}{k_z^i}\right) . \tag{22.308}$$

These quantities represent the ratio between the amount of acoustic energy radiated in fluid and the total kinetic energy of the plate. Equation (22.308) shows that, if k_i^z is real, we have a propagating acoustic wave and the mean radiated power is different from zero. In the opposite case, the acoustic wave is evanescent and the mean radiated power is equal to zero.

Particular Case of Two Identical Fluids. One particular case of interest corresponds to the practical situation where the plate is coupled to the same fluid on both sides. In this case, the dispersion equation becomes:

$$2\mathrm{i}\omega^2 \frac{\rho}{\sqrt{k^2 - k_\mathrm{F}^2}} - \omega^2 \rho_\mathrm{s} h + D k_\mathrm{F}^4 = 0 \,, \tag{22.309}$$

where $k_x = k_\mathrm{F} \cos\theta$ and $k_y = k_\mathrm{F} \sin\theta$. k_F is the flexural wavenumber coupled to the fluid, θ is the angle of propagation and $k = \omega/c$ is the acoustic wavenumber.

For a plate vibrating in vacuo, the flexural wavenumber is written

$$k_{\mathrm{F}0} = \left(\frac{\omega^2 \rho_\mathrm{s} h}{D}\right)^{1/4} \tag{22.310}$$

so that the dispersion equation can be rewritten

$$\frac{k_\mathrm{F}^4}{k_{\mathrm{F}0}^4} = 1 - \frac{2\mathrm{i}\rho}{\rho_\mathrm{s} h k_z} \tag{22.311}$$

Light-Fluid Approximation. The light-fluid approximation corresponds to

$$\left| \frac{2\mathrm{i}\rho}{\rho_\mathrm{s} h k_z} \right| \ll 1 \,. \tag{22.312}$$

In this case, the wavenumbers are given by:

$$k_\mathrm{F} = k_{\mathrm{F}0} \quad \text{or} \quad k_\mathrm{F} = \mathrm{i} k_{\mathrm{F}0} \,. \tag{22.313}$$

The case $k_\mathrm{F} = k_{\mathrm{F}0}$ corresponds to propagating waves. In this case, the radiation efficiency becomes

$$\begin{cases} \sigma &= \operatorname{Re}\left(\frac{k}{k_z}\right) = \frac{1}{\sqrt{1 - \frac{k_{\mathrm{F}0}^2}{k^2}}} \\ &= \frac{1}{\sqrt{1 - \frac{\omega_\mathrm{c}}{\omega}}} \quad \text{if} \quad \omega > \omega_\mathrm{c} \\ &\text{with} \quad \omega_\mathrm{c} = \frac{c^2}{h} \sqrt{\frac{12(1-\nu^2)\mu}{E}} \\ &= 0 \quad \text{if} \quad \omega < \omega_\mathrm{c} \,; \end{cases} \tag{22.314}$$

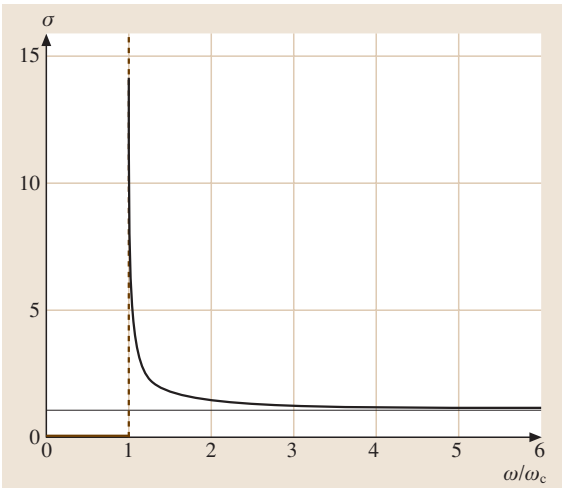


Fig. 22.16 Radiation efficiency σ for progressive flexural waves in an infinite isotropic plate submerged in a light fluid, ω_c is the critical frequency

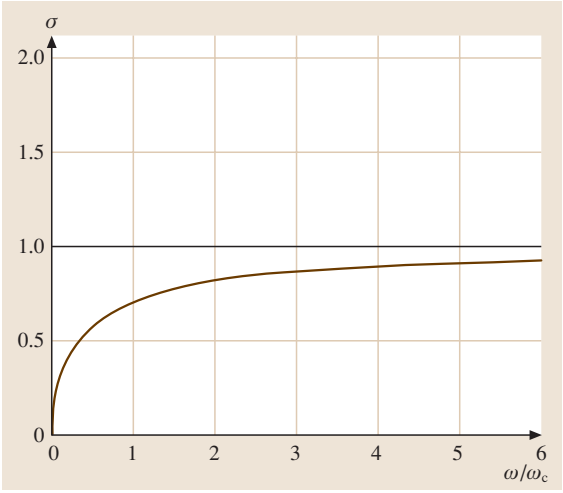


Fig. 22.17 Radiation efficiency for evanescent flexural waves in an infinite isotropic plate submerged in a light fluid

ω_c is the critical (or coincidence) frequency of the plate coupled to the light fluid. For this frequency, the wavelength in the plate is equal to the wavelength in the fluid. For $\omega > \omega_c$ ($k_{F0} < k$), the flexural waves are *supersonic*. The radiation efficiency tends to infinity as ω tends to ω_c and tends to unity as ω tends to infinity (Fig. 22.16). σ tends to infinity for $\omega = \omega_c$ because we are dealing with an infinite plate.

For $\omega < \omega_c$, the flexural waves are *subsonic*. The radiation efficiency is equal to zero which means that the plate does not radiate sound. This result follows from the fact that acoustic pressure and velocity are in quadrature.

The solution $k_F = ik_{F0}$ corresponds to evanescent waves in the plate. In this case, the radiation efficiency becomes

$$\sigma = \mathrm{Re}\left(\frac{k}{k_z}\right) = \frac{1}{\sqrt{1+\frac{k_{F0}^2}{k^2}}} = \frac{1}{\sqrt{1+\frac{\omega_c}{\omega}}} \,. \qquad (22.315)$$

Equation (22.315) shows that the radiation efficiency of a flexural evanescent wave increases with frequency and tends to unity as the frequency tends to infinity (Fig. 22.17).

Simply Supported Radiating Isotropic Plate

Equations of Motion. We address the problem of structural–acoustic interaction for a 2-D, rectangular, baffled, simply supported isotropic thin plate radiating in air.

The system is described by the equations

$$\begin{cases} D\nabla^4\xi(x,y,t) + \rho_s h\dfrac{\partial^2\xi}{\partial t^2}(x,y,t) \\ = p(x,y,0-,t) - p(x,y,0+) \\ \quad \text{for} \quad 0 < x < L_x \quad \text{and} \quad 0 < y < L_y \,, \\ \xi(0,y,t) = \xi(L_x,y,t) = \xi(x,0,t) \\ = \xi(x,L_y,t) = 0 \,, \\ \xi''(0,y,t) = \xi''(L_x,y,t) = \xi''(x,0,t) \\ = \xi''(x,L_y,t) = 0 \,, \\ v_z(x,y,0+,t) = -v_z(x,y,0-,t) = \dot{\xi}(x,y,t) \\ \quad \text{for} \quad 0 < x < L_x \quad \text{and} \quad 0 < y < L_y \,, \\ v(x,y,0) = 0 \\ \quad \text{for} \quad x \notin]0, L_x[\ \text{or} \ y \notin]0, L_y[\,, \\ \rho\dfrac{\partial \boldsymbol{v}}{\partial t} + \nabla p = 0 \,, \\ \nabla^2 p - \dfrac{1}{c^2}\dfrac{\partial^2 p}{\partial t^2} = 0 \,, \end{cases} \qquad (22.316)$$

where h is the thickness of the plate, $D = EI = \frac{Eh^3}{12(1-\nu^2)}$ is the flexural rigidity factor, E is the Young's modulus, ν is the Poisson's ratio and ρ_s is the plate's density. The transverse displacement of the plate is denoted by $\xi(x,y,t)$. The acoustic variables are the pressure $p(x,y,z,t)$ and the velocity $\boldsymbol{v}(x,y,z,t)$. ρ is the air density and c is the speed of sound in air.

Eigenmodes in Vacuo. Solving the plate equations in vacuo with simply supported boundary conditions yields the eigenmodes

$$\phi_{mn}(x,y) = \phi_m(x)\phi_n(y) = \sin\frac{\pi m x}{L_x}\sin\frac{\pi n y}{L_y} \qquad (22.317)$$

allowing the displacement to be expanded as follows

$$\begin{aligned} \xi(x,y,t) &= \sum_{m,n}\phi_{mn}(x,y)q_{mn}(t) \\ &= \phi_m(x)\phi_n(y)q_{mn}(t) \,. \end{aligned} \qquad (22.318)$$

Defining the vectors

$$\begin{cases} \boldsymbol{Q}^t = (q_{01}\ q_{10}\ q_{11}\ \ldots\ q_{MN}) \,, \\ \text{and} \\ \boldsymbol{\Phi}^t = (\phi_{01}\ \phi_{10}\ \phi_{11}\ \ldots\ \phi_{MN}) \,, \end{cases} \qquad (22.319)$$

Amazon EX1014 Page 942

(22.318) can be written

$$\xi(x, y, t) = \boldsymbol{Q}^{\mathrm{t}}\boldsymbol{\Phi} \tag{22.320}$$

which is similar in form to the 1-D systems studied in Sect. 22.5.1. In (22.318), the number of considered modes (with indices M and N in both directions, respectively) depends on the nature and frequency content of the practical problem to be solved.

Calculation of the Radiated Sound Field Using Wavenumber Fourier Transform. Using the spatial Fourier transform enables the pressure on the plate surface to be easily determined [22.36]. For any 2-D spatial function $f(x, y)$, the transform is defined by:

$$\begin{cases} F(k_x, k_y) & = \displaystyle\int_{-\infty}^{+\infty}\int_{-\infty}^{+\infty} f(x, y)\,\mathrm{e}^{\mathrm{i}(k_x x + k_y y)}\,\mathrm{d}x\,\mathrm{d}y\,, \\ f(x, y) & = \dfrac{1}{(2\pi)^2}\times \\ & \displaystyle\int_{-\infty}^{+\infty}\int_{-\infty}^{+\infty} F(k_x, k_y)\,\mathrm{e}^{-\mathrm{i}(k_x x + k_y y)}\,\mathrm{d}k_x\,\mathrm{d}k_y\,. \end{cases} \tag{22.321}$$

This allows us to transform the wave equation for a harmonic sound pressure in space as follows

$$\int_{-\infty}^{+\infty}\int_{-\infty}^{+\infty} (\nabla^2 + k^2) p(x, y, z)\,\mathrm{e}^{\mathrm{i}(k_x x + k_y y)}\,\mathrm{d}x\,\mathrm{d}y = 0\,. \tag{22.322}$$

This leads to:

$$\left(k^2 - k_x^2 - k_y^2 + \frac{\partial^2}{\partial z^2}\right) P(k_x, k_y, z) = 0 \tag{22.323}$$

with a solution given by

$$P(k_x, k_y, z) = \frac{\omega\rho\dot{\Xi}(k_x, k_y)}{k_z}\,\mathrm{e}^{-\mathrm{i}k_z z}$$

with

$$k_z = \sqrt{k^2 - k_x^2 - k_y^2}\,, \tag{22.324}$$

where $\dot{\Xi}(k_x, k_y)$ is the wavenumber transform of the transverse plate velocity $\dot{\xi}(x, y)$. The complex sound pressure in space is obtained by using the inverse transform, so that

$$p(x, y, z) = \frac{\omega\rho}{(2\pi)^2}\int_{-\infty}^{+\infty}\int_{-\infty}^{+\infty} \frac{\dot{\Xi}(k_x, k_y)}{k_z} \times \mathrm{e}^{-\mathrm{i}(k_x x + k_y y + k_z z)}\,\mathrm{d}k_x\,\mathrm{d}k_y\,. \tag{22.325}$$

This equation can be solved by using the method of stationary phase or the fast Fourier transform algorithm [22.37].

Radiated Sound Power and the Radiation Impedance Matrix. In the harmonic case, the total sound power radiated by the plate is given by

$$\mathcal{P}_{\mathrm{a}} = \frac{1}{2}\,\mathrm{Re}\left[\int_{-\infty}^{+\infty}\int_{-\infty}^{+\infty} p(x, y, 0)\,\dot{\xi}^*(x, y)\,\mathrm{d}x\,\mathrm{d}y\right], \tag{22.326}$$

where (*) denotes the complex conjugates. Using Parseval's theorem and (22.324) yields

$$\mathcal{P}_{\mathrm{a}} = \frac{\omega\rho}{8\pi^2}\,\mathrm{Re}\left[\int_{-\infty}^{+\infty}\int_{-\infty}^{+\infty} \frac{|\dot{\Xi}(k_x, k_y)|^2}{k_z}\,\mathrm{d}k_x\,\mathrm{d}k_y\right]. \tag{22.327}$$

Notice that this last result is only valid for wavenumbers such that $\sqrt{k_x^2 + k_y^2} \le k$. Alternatively, the sound power can be written in terms of the wavenumber transform of the acoustic pressure, such that

$$\mathcal{P}_{\mathrm{a}} = \frac{1}{8\omega\rho\pi^2}\iint_{k_x^2 + k_y^2 \le k^2} |P(k_x, k_y)|^2\,k_z\,\mathrm{d}k_x\,\mathrm{d}k_y\,. \tag{22.328}$$

Using (22.320) for the plate velocity and $\boldsymbol{\Phi}(k_x, k_y)$ as the wavenumber transform of $\boldsymbol{\Phi}(x, y)$ yields the squared modulus of the velocity field

$$\begin{aligned} |\dot{\Xi}(k_x, k_y)|^2 &= |\dot{\boldsymbol{Q}}^{\mathrm{t}}\boldsymbol{\Phi}(k_x, k_y)|^2 \\ &= \dot{\boldsymbol{Q}}^{\mathrm{H}}\boldsymbol{\Phi}^*(k_x, k_y)\boldsymbol{\Phi}^{\mathrm{t}}(k_x, k_y)\dot{\boldsymbol{Q}}\,. \end{aligned} \tag{22.329}$$

Finally, substituting this result into (22.327), the acoustic power can be written as

$$\mathcal{P}_{\mathrm{a}} = \dot{\boldsymbol{Q}}^{\mathrm{H}}\mathbf{R}_{\mathrm{a}}\dot{\boldsymbol{Q}}\,. \tag{22.330}$$

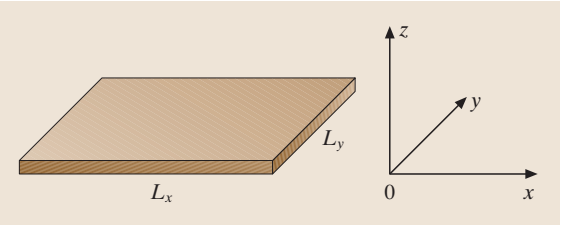


Fig. 22.18 Geometry of the thin isotropic baffled radiating plate

The radiation impedance matrix $\mathbf{R}_a$ is defined as

$$\mathbf{R}_a = \frac{\omega\rho}{8\pi^2}\,\mathrm{Re}\left(\iint \frac{\boldsymbol{\Phi}^*(k_x,k_y)\boldsymbol{\Phi}^t(k_x,k_y)}{\sqrt{k^2-k_x^2-k_y^2}}\,\mathrm{d}k_x\,\mathrm{d}k_y\right) \tag{22.331}$$

which generalizes the results obtained in (22.265) to 2-D systems. Each element $(\mathbf{R}_a)_{ij}$ of the matrix $\mathbf{R}_a$ quantifies the mutual radiation resistance resulting from the interference between the fields of modes (m,n) and (m',n'), respectively. If $(m,n)=(m',n')$, we obtain the self-radiation resistances, which are the diagonal terms of the matrix $\mathbf{R}_a$. These terms can be written explicitly as

$$(\mathbf{R}_a)_{ij} = (\mathbf{R}_a)_{mn,m'n'} = \frac{\omega\rho}{8\pi^2}\,\mathrm{Re}\iint \frac{\Phi_m^*(k_x)\,\Phi_n^*(k_y)\Phi_{m'}(k_x)\,\Phi_{n'}(k_y)}{\sqrt{k^2-k_x^2-k_y^2}}\,\mathrm{d}k_x\,\mathrm{d}k_y\,. \tag{22.332}$$

For a baffled simply supported plate, the radiation resistances become

$$(\mathbf{R}_a)_{mn,m'n'} = \frac{mm'nn'\omega\rho\pi^2}{8L_x^2L_y^2} \times \mathrm{Re}\left(\iint (f_{mm'}(k_xL_x)\;f_{nn'}(k_yL_y)\,\mathrm{d}k_x\,\mathrm{d}k_y) \Big/ \Big(\big[k_x^2-(m\pi/L_x)^2\big]\big[k_x^2-(m'\pi/L_x)^2\big] \big[k_y^2-(n\pi/L_y)^2\big]\big[k_y^2-(n'\pi/L_y)^2\big]\Big)\right), \tag{22.333}$$

where the functions of the form $f_{mm'}(k_xL_x)$ are given by

$$f_{mm'}(k_xL_x) = \begin{cases} 2(1-\cos k_xL_x) & \text{for } m \text{ even}, \quad m' \text{ even} \\ 2(1+\cos k_xL_x) & \text{for } m \text{ odd}, \quad m' \text{ odd} \\ 2\mathrm{i}\sin k_xL_x & \text{for } m \text{ odd}, \quad m' \text{ even} \\ -2\mathrm{i}\sin k_xL_x & \text{for } m \text{ even}, \quad m' \text{ odd} \end{cases}. \tag{22.334}$$

For the application of the radiation modal expansion to active structural control of sound, see, for example, the work by *Gibbs* et al.[22.38]. In a recent work, *Kim* investigated structural–acoustic coupling for active control purpose, using an impedance/mobility approach [22.39]. Alternative techniques make use of multipole expansion of the radiated sound pressure [22.40].

22.6 Damping

In this section, we start by summarizing briefly the conditions for modal decoupling in discrete damped systems, and the concept of proportional damping is introduced. The modal approach is convenient for treating the case of localized damping (Sect. 22.6.1). The following example of a string with a dissipative end illustrates the limit of the modal approach, and shows that such a system cannot exhibit stationary solutions. A physical interpretation is presented in terms of damped propagating waves. Other authors use a state-space modal approach to address the analysis of damped structures [22.41, 42].

The section continues with the presentation of three damping mechanisms in plates: thermoelasticity, viscoelasticity and radiation, with emphasis on the time-domain formulation. The section ends with a brief presentation of friction, stick–slip vibrations and hysteretic damping, which are often encountered in structural damping models.

22.6.1 Modal Projection in Damped Systems

Discrete Systems

For a linear system with multiple degrees of freedom, with a dissipation energy of the form

$$\mathcal{E}_D = \frac{1}{2}\,{}^t\dot{\boldsymbol{X}}\mathbf{C}\dot{\boldsymbol{X}}\,, \tag{22.335}$$

where $\mathbf{C}$ is a symmetric damping matrix with positive elements, the equations of motion can be written as

$$\mathbf{M}\ddot{\boldsymbol{X}} + \mathbf{C}\dot{\boldsymbol{X}} + \mathbf{K}\boldsymbol{X} = \boldsymbol{F}\,. \tag{22.336}$$

Denoting the eigenfrequencies and eigenfunctions of the associated conservative system by ω_n and $\boldsymbol{\Phi}_n$, respectively, we use the expansion $\boldsymbol{X} = \sum_m \boldsymbol{\Phi}_m q_m(t)$. Denoting by ζ_{nm} the intermodal coefficients, the generalized coordinates are governed by the system of coupled differential equations

$$\ddot{q}_n + 2\omega_n \zeta_n \dot{q}_n + \omega_n^2 q_n = \frac{f_n}{m_n} - 2\omega_n \sum_{m \neq n} \zeta_{nm} \dot{q}_m \,. \tag{22.337}$$

Weakly Damped Systems. In the case of weak damping, a first-order development of both the eigenfrequencies and eigenvectors of the form

$$\omega'_n = \omega_n + \Delta\omega_n \;\; ; \;\; \boldsymbol{\Phi}'_n = \boldsymbol{\Phi}_n + \Delta\boldsymbol{\Phi}_n \tag{22.338}$$

in (22.336), with $\boldsymbol{F} = 0$, leads to the matrix equation

$$\left(\mathbf{K} - \omega_n^2 \mathbf{M}\right) \Delta\boldsymbol{\Phi}_n + \omega_n \left(-2\Delta\omega_n \mathbf{M} + \mathbf{C}\right) \boldsymbol{\Phi}_n \simeq 0 \tag{22.339}$$

from which we get:

$$\Delta\omega_n \simeq \mathrm{i}\zeta_n \omega_n \,. \tag{22.340}$$

Equation (22.340) yields two significant results:

1. The correction frequency is purely imaginary. As a consequence, the eigenmode is transformed into a damped sinusoid of the form $\mathrm{e}^{\mathrm{i}\omega_n t}\,\mathrm{e}^{-\zeta_n \omega_n t}$.
2. To first order, the correction frequency is independent of the intermodal coefficients, thus the damping matrix is diagonal.

The perturbation of the eigenvectors due to damping is given by

$$\Delta\boldsymbol{\Phi}_n = \sum_{m \neq n} \alpha_m \boldsymbol{\Phi}_m$$

with

$$\alpha_m = 2\mathrm{i}\zeta_{mn} \frac{m_n \omega_n^2}{m_m \left(\omega_n^2 - \omega_m^2\right)} \,. \tag{22.341}$$

Consequently, in the presence of damping, the eigenvectors become

$$\boldsymbol{\Phi}'_n = \boldsymbol{\Phi}_n + 2\mathrm{i} m_n \omega_n^2 \sum_{m \neq n} \boldsymbol{\Phi}_m \frac{\zeta_{mn}}{m_m \left(\omega_n^2 - \omega_m^2\right)} \,. \tag{22.342}$$

Equation (22.342) shows that

1. If the eigenfrequencies of the associated conservative system are sufficiently different from each other then, to first order, the perturbation of the eigenvectors are of the same order of magnitude as the intermodal damping ζ_{mn}. If $\omega_n \approx \omega_m$, terms of the form $\omega_n^2 - \omega_m^2$ in the denominator can lead to significant corrections.
2. The correction terms for the eigenvectors are also purely imaginary. Thus, the eigenmodes are no longer in phase (or in antiphase) as for the conservative case.

Proportional Damping. The system can be decoupled without any approximations if the damping matrix can be written in the form of a linear combination of mass and stiffness matrices $\mathbf{C} = \alpha\mathbf{M} + \beta\mathbf{K}$ where α and β are real constants. This corresponds to the so-called proportional damping case. In this case, we obtain

$$\ddot{q}_n + 2\omega_n \zeta_n \dot{q}_n + \omega_n^2 q_n = \frac{f_n}{m_n}$$

with

$$\zeta_n = \frac{\alpha}{2\omega_n} + \frac{\beta\omega_n}{2} \,. \tag{22.343}$$

We therefore obtain a frequency-dependent modal damping that decreases with frequency below $\omega = \sqrt{\alpha/\beta}$, and increases with frequency above this value. This damping law does not correspond to particular physical phenomena, but is rather used for practical mathematical considerations. It can be useful in some cases for fitting experimental curves over a restricted frequency range.

Localized Damping in Continuous Systems

In some applications, the damping of the vibrations of continuous systems is localized at discrete points of the structure. In this section, this problem is illustrated by the case of a string of finite length L with eigenfrequencies ω_n and eigenfunctions $\Phi_n(x)$. A *fluid damping* term is introduced at position $x = x_0$, with $0 < x_0 < L$, so that this term is of the form $-R\dot{y}(x,t)\delta(x - x_0)$. The equation of motion can therefore be written

$$\rho(x)S(x)\frac{\partial^2 y}{\partial t^2} + R\frac{\partial y}{\partial t}\delta(x - x_0) - \frac{\partial}{\partial x}\left[T(x)\frac{\partial y}{\partial x}\right] = f(x,t) \,. \tag{22.344}$$

Applying the usual scalar products, we can write

$$\sum_m \ddot{q}_m(t)\int_0^L \Phi_m(x)\Phi_n(x)\rho(x)S(x)\,\mathrm{d}x + \sum_m \dot{q}_m(t)\int_0^L R\delta(x-x_0)\Phi_m(x)\Phi_n(x)\,\mathrm{d}x - \sum_m q_m(t)\int_0^L \Phi_n(x)\frac{\mathrm{d}}{\mathrm{d}x}\left(T(x)\frac{\mathrm{d}\Phi_m(x)}{\mathrm{d}x}\right)\mathrm{d}x = \int_0^L \Phi_n(x)f(x,t)\,\mathrm{d}x\,. \tag{22.345}$$

The generalized displacements are governed by the equations

$$\ddot{q}_n + 2\omega_n\sum_m \zeta_{nm}\dot{q}_m + \omega_n^2 q_n = \frac{f_n}{m_n}\,, \tag{22.346}$$

where the intermodal coefficients are written here

$$\zeta_{nm} = \frac{R\Phi_n(x_0)\Phi_m(x_0)}{2m_n\omega_n}\,. \tag{22.347}$$

For weak damping, we have

$$\ddot{q}_n + 2\omega_n\zeta_n\dot{q}_n + \omega_n^2 q_n \simeq \frac{f_n}{m_n}\,, \tag{22.348}$$

where the modal damping coefficient are given by

$$\zeta_n = \frac{R\Phi_n^2(x_0)}{2m_n\omega_n}\,. \tag{22.349}$$

Example. For a homogeneous string rigidly fixed at both ends, we have: $\Phi_n(x) = \sin k_n x$ and $\omega_n = ck_n = n\pi c/L$. With a damper fixed at position $x_0 = L/2$, we get $\zeta_n = \frac{R\sin^2(n\pi/2)}{2m_n\omega_n}$. Two cases can be differentiated:

1. If n is odd, $\sin^2(n\pi/2) = 1$ and $\zeta_n = \frac{R}{2m_n\omega_n}$;
2. If n is even, $\zeta_n = 0$.

In this case, only the odd modes are damped.

String With a Dissipative End. The case of a dissipative end is slightly more delicate to handle since the dissipation is localized at a boundary, and thus is directly involved in the definition of the eigenmodes. The equations of the problem are

$$\rho S\frac{\partial^2 y}{\partial t^2} - T\frac{\partial^2 y}{\partial x^2} = 0 \tag{22.350}$$

with the boundary conditions

$$y(0,t) = 0 \quad \text{and} \quad T\frac{\partial y}{\partial x}(L,t) = -R\frac{\partial y}{\partial t}(L,t)\,. \tag{22.351}$$

One strategy consists of looking for complex solutions of the separate variables $y(x,t) = f(x)g(t)$. The time dependence is assumed to be of the form

$$g(t) = A\,\mathrm{e}^{-st} + B\,\mathrm{e}^{st} \tag{22.352}$$

with A, B and $s \in \mathbb{C}$. Inserting (22.352) into (22.350), we find that $f(x)$ is of the form

$$f(x) = C\,\mathrm{e}^{-sx/c} + D\,\mathrm{e}^{sx/c} \quad \text{with} \quad c = \sqrt{\frac{T}{\rho S}}\,, \tag{22.353}$$

where C and $D \in \mathbb{C}$. The boundary solution at $x = 0$ yields $C = -D$. The boundary condition at $x = L$ yields two possible cases:

$$\begin{cases} \cosh\dfrac{sL}{c} = r\sinh\dfrac{sL}{c} \text{ and } B = 0\,, \\ \cosh\dfrac{sL}{c} = -r\sinh\dfrac{sL}{c} \text{ and } A = 0\,, \end{cases} \tag{22.354}$$

where $r = R/Z_c$ and $Z_c = T/c$ is the characteristic impedance of the string. Defining $s = \mathrm{i}\omega + \alpha$, we find two sets of solutions depending on whether R is larger or smaller than Z_c.

1. For $r < 1$,

$$\begin{cases} \cos\dfrac{\omega L}{c} = 0\,, \quad \tanh\dfrac{\alpha L}{c} = r \text{ and } B = 0\,, \\ \cos\dfrac{\omega L}{c} = 0\,, \quad \tanh\dfrac{\alpha L}{c} = -r \text{ and } A = 0\,. \end{cases} \tag{22.355}$$

2. For $r > 1$,

$$\begin{cases} \sin\dfrac{\omega L}{c} = 0\,, \quad \tanh\dfrac{\alpha L}{c} = \dfrac{1}{r} \text{ and } B = 0\,, \\ \sin\frac{\omega L}{c} = 0\,, \quad \tanh\dfrac{\alpha L}{c} = -\dfrac{1}{r} \text{ and } A = 0\,. \end{cases} \tag{22.356}$$

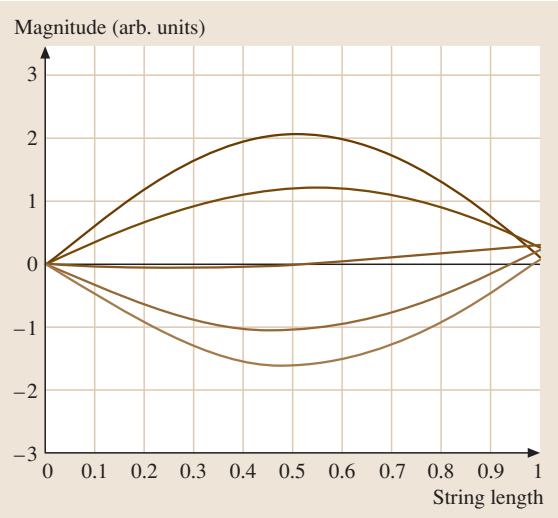


Fig. 22.19 Temporal evolution of a string with one dissipative end

We focus on the case $r > 1$. Defining $a = AC$ and $b = BC$, and taking (22.355) into account, we obtain

$$\begin{aligned} y(x,t) = {} & \mathrm{e}^{-\alpha t} \sum_n a_n \mathrm{e}^{-\mathrm{i}\omega_n t} \\ & \times \left(\mathrm{e}^{-(\mathrm{i}\omega_n + \alpha)x/c} - \mathrm{e}^{(\mathrm{i}\omega_n + \alpha)x/c} \right) \\ & + \mathrm{e}^{-\alpha t} \sum_n b_n \mathrm{e}^{\mathrm{i}\omega_n t} \\ & \times \left(\mathrm{e}^{-(\mathrm{i}\omega_n - \alpha)x/c} - \mathrm{e}^{(\mathrm{i}\omega_n - \alpha)x/c} \right) \end{aligned} \tag{22.357}$$

which can be rearranged, in condensed form, as:

$$y(x,t) = \mathrm{e}^{-\alpha t} \left[\mathrm{e}^{-\alpha x/c} F\left(t + \frac{x}{c}\right) - \mathrm{e}^{\alpha x/c} F\left(t - \frac{x}{c}\right) \right] \tag{22.358}$$

with

$$F(t) = \sum_n \left(a_n \mathrm{e}^{-\mathrm{i}\omega_n t} - b_n \mathrm{e}^{\mathrm{i}\omega_n t} \right) . \tag{22.359}$$

The complex constants a_n and b_n are determined by the initial conditions of the problem. It can be shown that (22.359) yields a real function $F(t)$. Several conclusions can be drawn from this example:

1. The mechanical resistance R yields a decay time $1/\alpha$ which is independent of frequency.
2. The term in square brackets in (22.358) corresponds to two traveling waves in opposite directions with different amplitudes, except at $x = 0$ where the rigidly fixed boundary condition must be fulfilled. As a consequence, we cannot get a steady-state solution.

In conclusion, as shown in Fig. 22.19, the string with a dissipative end cannot exhibit stationary wave solutions. We cannot make reference to nodes and antinodes, since the points of maximum (and minimum) amplitude are moving with time, though first-order approximations can be made for weak dissipation.

22.6.2 Damping Mechanisms in Plates

In vibrating structures, the dissipation of energy is partly due to radiation, and partly due to other internal damping mechanisms such as thermoelasticity and viscoelasticity. The relative prominence of these mechanisms is dependent on the material. In this section, models for these three mechanisms are briefly reviewed in the particular case of free rectangular plates, for which the losses at the boundaries are neglected.

Thermoelasticity

Thermoelastic damping affects the vibrations of plates with significant thermal conductivity, such as metallic plates. A model for such damping can be derived from the equations that govern the coupling between plate vibrations and the diffusion of heat [22.43, 44]. Here, the method previously used by *Cremer* for isotropic bars is extended to orthotropic plates to derive the expressions for the complex rigidity constants [22.20]. The temperature change θ is assumed to be sufficiently small, so that the stress–strain relationships can be linearized. The plate is located in the (x, y) plane and is subjected to transverse flexural vibrations. $w(x, y, t)$ is the transverse displacement. The stress components are given by:

$$\begin{aligned} \sigma_{xx} &= -12z\left(D_1 w_{,xx} + \frac{D_2}{2} w_{,yy} \right) - \phi_x \theta \, , \\ \sigma_{yy} &= -12z\left(D_3 w_{,yy} + \frac{D_2}{2} w_{,xx} \right) - \phi_y \theta \, , \\ \sigma_{xy} &= -6z D_4 w_{,xy} \, , \end{aligned} \tag{22.360}$$

where ϕ_x and ϕ_y are the thermal coefficients of the material. In the particular case of an isotropic material, we have $\phi_x = \phi_y = \phi$. Equation (22.360) has to be complemented by the heat diffusion equation. Assuming that θ only depends on z, we have

$$\kappa \theta_{,zz} - \rho C s \theta = -z T_0 s \left(\phi_x w_{,xx} + \phi_y w_{,yy} \right) , \tag{22.361}$$

where T_0 is the absolute temperature, C is the specific heat at constant strain, and κ is the thermal conductivity.

Amazon EX1014 Page 947

It is assumed that $\theta(z)$ is given by an equation of the form [22.20]

$$\theta(z) = \theta_0 \sin\frac{\pi z}{h} \text{ for } z \in \left[-\frac{h}{2}, \frac{h}{2}\right] , \qquad (22.362)$$

which takes into account the fact that there is no heat transmission between plate and air. Through integration of $z\sigma_{ij}$ over the thickness h of the plate, one obtains, in the Laplace domain, the relationship between the bending and twisting moments M_{ij} and the partial derivatives of the transverse displacement w of the plate. The rigidity factors are now complex functions of the form [22.45]:

$$\begin{aligned}
\tilde{D}_1(s) &= D_1 + \phi_x^2 \frac{s\zeta}{1+\tau s} , \\
\tilde{D}_2(s) &= D_2 + 2\phi_x\phi_y \frac{s\zeta}{1+\tau s} , \\
\tilde{D}_3(s) &= D_3 + \phi_y^2 \frac{s\zeta}{1+\tau s} , \\
\tilde{D}_4(s) &= D_4 , \qquad (22.363)
\end{aligned}$$

where the thermoelastic relaxation time τ and the thermal constant ζ are given by

$$\tau = \frac{\rho C h^2}{\kappa\pi^2} \quad \text{and} \quad \zeta = \frac{8T_0 h^2}{\kappa\pi^6} . \qquad (22.364)$$

As a consequence of (22.364), the thermoelastic losses decrease as the thickness h of the plate increases. Notice also that D_4 is real. As a consequence, the particular flexural modes of the plate, such as the torsional modes, which involve this rigidity factor will be relatively less affected by thermoelastic damping than the other modes. In other words, the thermoelastic damping factors depend on the modal shapes [22.46]. The complex rigidities can be rewritten in the form

$$\begin{aligned}
\tilde{D}_i(s) &= D_i\left[1+\tilde{d}_{it}(s)\right] \\
&= D_i\left[1+\frac{sR_i}{s+c_1/h^2}\right], \; i=[1,2,3] , \\
\tilde{D}_4(s) &= D_4 . \qquad (22.365)
\end{aligned}$$

Because the thermoelastic damping is small for most materials, the $\tilde{d}_{it}(s)$ can often be considered as perturbation terms of the complex rigidities. For convenience, these terms are written in (22.365) using the following nondimensional numbers

$$\begin{aligned}
R_1 &= \frac{8T_0\phi_x^2}{\pi^4 D_1 \rho C} ; \\
R_2 &= \frac{16T_0\phi_x\phi_y}{\pi^4 D_3 \rho C} ; \\
R_3 &= \frac{8T_0\phi_y^2}{\pi^4 D_3 \rho C} . \qquad (22.366)
\end{aligned}$$

The decay factor $1/\tau$ is written here in the form c_1/h^2 in order to highlight the fact that this factor is proportional to the inverse squared thickness of the plate.

Viscoelasticity

A large class of materials is subject to viscoelastic damping [22.47]. A convenient method for representing viscoelastic phenomena is to use a differential formulation between the stress σ and strain ε tensors of the form

$$\sigma + \sum_{w=1}^{N} q_w \frac{\partial^w \sigma}{\partial t^w} = E\left(\varepsilon + \sum_{v=1}^{N} q_v \frac{\partial^v \varepsilon}{\partial t^v}\right) . \qquad (22.367)$$

As a consequence, the differential equations involving the flexural displacements and moments in thin plates contain time derivatives up to order N. By taking the Laplace transform of both sides in (22.367) and inserting it into the plate equation, one obtains the complex rigidities due to viscoelasticity:

$$\tilde{D}_i(s) = D_i\left[1+\tilde{d}_{iv}(s)\right] = D_i \frac{1+\sum_{v=1}^{N} s^v p_{iv}}{1+\sum_{w=1}^{N} s^w q_w} . \qquad (22.368)$$

Equation (22.368) is a particular class of representation for the complex rigidities. The operator is bounded by the condition [22.48]

$$q_N \neq 0 . \qquad (22.369)$$

Another restrictive condition on the coefficients in (22.368) follows from the fact that the energy for deforming the material from its initial undisturbed state must be positive. For a generalized viscoelastic strain–stress relationship, the Laplace transform is given by

$$\tilde{\sigma}_{ij} = \sum_{k,l} \tilde{a}_{ijkl}(s)\tilde{\epsilon}_{kl} . \qquad (22.370)$$

Gurtin and *Sternberg* [22.48] have proven that one necessary condition for the model to be dissipative is

$$\mathrm{Im}[X_{ij}\tilde{a}_{ijkl}(\mathrm{i}\omega)X_{kl}] \geq 0 \quad \text{for} \quad \omega \geq 0 \qquad (22.371)$$

for any real symmetric tensor X_{ij}. For the viscoelastic orthotropic plate model, (22.371) together with (22.368) yield the following conditions

$$\begin{cases} p_{1N} > 0\,, \quad p_{3N} > 0?;\,, \quad p_{4N} > 0\,, \\ p_{1N}\,p_{3N} - \dfrac{D_2\ {p_{2N}}^2}{4D_1 D_3} > 0\,. \end{cases} \tag{22.372}$$

As for thermoelastic damping, if the viscoelastic losses in the materials are sufficiently small, the corresponding terms can be viewed as first-order corrections to the rigidity.

Time-Domain Model of Radiation Damping in Isotropic Plates

In this section, an approximate time-domain model for isotropic plates is presented that takes the effect of radiation into account. The leading idea is to use a differential operator for the radiation losses (i. e., a polynomial formulation in the Laplace domain), similar to that presented in the previous paragraphs for thermoelastic and viscoelastic damping. Experiments performed on freely suspended plates show that in the *low-frequency* domain (i. e., below the critical frequency), viscoelastic and/or thermoelastic losses are the main causes of damping [22.45]. Above the critical frequency, damping is mainly governed by radiation.

The equations that govern the flexural motion of an isotropic plate surrounded by air are given in (22.316). For a travelling wave of the form $w(x, y, t) = W(x, y)\exp[\mathrm{i}(\tilde{\omega}t - \boldsymbol{k}.\boldsymbol{x})]$, where k is the wavenumber and $\tilde{\omega} = \omega + \mathrm{i}\alpha_\mathrm{r}$ is the complex frequency, one obtains the dispersion equation

$$-\tilde{\omega}^2\left(1 + \frac{2\rho_\mathrm{a}}{\rho h}\frac{1}{\sqrt{k^2 - \frac{\tilde{\omega}^2}{c^2}}}\right) + \frac{Dh^2}{\rho}k^4 = 0\,. \tag{22.373}$$

With the assumption of a light fluid, one can derive the radiation decay factor α_r from (22.373) by reformulating this equation through the introduction of a rigidity modulus $\tilde{D}$ of the form

$$\tilde{D} \simeq D\left(1 - \frac{2\rho_\mathrm{a}c}{\omega_\mathrm{c}\rho h}\frac{1}{\sqrt{\Omega - \Omega^2}}\right)$$

with

$$\omega_\mathrm{c} = c^2\sqrt{\frac{\rho}{h^2 D}}$$

and

$$\Omega = \frac{\omega}{\omega_\mathrm{c}}\,. \tag{22.374}$$

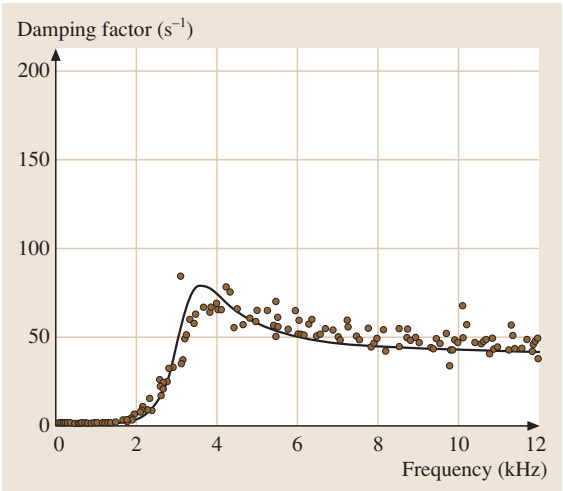


Fig. 22.20 Comparison between damping model (*solid line*) and measurements (○) for a free rectangular aluminum plate. Damping factors (in s^{-1}) as a function of frequency (in kHz). (After *Chaigne* et al. [22.45])

The complex rigidity $\tilde{D}$ can be rewritten in the form of a third-order Padé development:

$$\begin{aligned}\tilde{D}(s) &\triangleq D\left(1 + \frac{2\rho_\mathrm{a}c}{\omega_\mathrm{c}\rho h}\frac{\sum_{m=1}^{3} b_m\left(\frac{s}{\omega_\mathrm{c}}\right)^m}{\sum_{n=0}^{3} a_n\left(\frac{s}{\omega_\mathrm{c}}\right)^n}\right) \\ &= D\left[1 + \tilde{d}_\mathrm{r}(s)\right]\end{aligned} \tag{22.375}$$

with

$$\begin{aligned} &a_0 = 1.1669\,,\ a_1 = 1.6574\,, \\ &a_2 = 1.5528\,,\ a_3 = 1\,, \\ &b_1 = 0.0620\,,\ b_2 = 0.5950\,, \\ &b_3 = 1.0272\,. \end{aligned}$$

Figure 22.20 shows a comparison between this asymptotic model and experimental data in the case of an aluminum plate. The present formulation of radiation damping cannot be easily generalized to anisotropic plates where the dispersion equation depends on the direction of wave propagation [22.14].

22.6.3 Friction

Elementary 1-DOF Oscillator with Coulomb Damping

The Coulomb damping corresponds to the simple modeling of a friction force applied to a solid sticking and/or sliding on dry surfaces. Figure 22.21 shows a 1-DOF oscillator subjected to Coulomb damping. For an initial

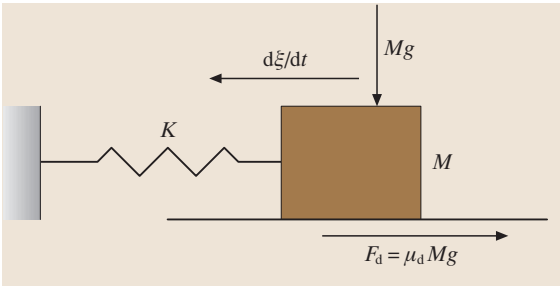


Fig. 22.21 One-DOF oscillator subjected to Coulomb damping

displacement $\xi(0) = \xi_0$, the motion of the mass M can occur under the condition that the restoring force $K\xi_0$ due to the spring is larger than the static friction force $F_s = \mu_s Mg$, where μ_s is the static friction coefficient with $0 < \mu_s < 1$. After the motion has started, the mass is subjected to a dynamic frictional force $F_d = \mu_d Mg$ where $\mu_d < \mu_s$. This force is in the opposite direction to the velocity, so that the equation of motion can be written [22.12]

$$M\frac{d^2\xi}{dt^2} + F_d \operatorname{sgn}\left(\frac{d\xi}{dt}\right) + K\xi = 0$$
$$\text{where} \quad \operatorname{sgn}\left(\frac{d\xi}{dt}\right) = \frac{\frac{d\xi}{dt}}{\left|\frac{d\xi}{dt}\right|} . \qquad (22.376)$$

During the initial part of the motion, we have

$$\frac{d^2\xi}{dt^2} + \omega_0^2\xi = \omega_0^2\frac{F_d}{K} \qquad (22.377)$$

whose solution is

$$\xi(t) = \left(\xi_0 - \frac{F_d}{K}\right)\cos\omega_0 t + \frac{F_d}{K}$$
$$\text{for} \quad 0 \le t \le t_1 = \frac{\pi}{\omega_0} . \qquad (22.378)$$

The solution (22.378) remains valid until the time $t_1 = \pi/\omega_0$ where the velocity reduces to zero. At that time, the displacement is $\xi(t_1) = \xi_1 = 2F_d/K - \xi_0$. If $K\xi_1 > \mu_s Mg$, then the motion is governed by

$$\frac{d^2\xi}{dt^2} + \omega_0^2\xi = -\omega_0^2\frac{F_d}{K} \qquad (22.379)$$

whose solution is

$$\xi(t) = \left(\xi_0 - 3\frac{F_d}{K}\right)\cos\omega_0 t - \frac{F_d}{K}$$
$$\text{for} \quad t_1 \le t \le t_2 = \frac{2\pi}{\omega_0} . \qquad (22.380)$$

At the time $t_2 = 2\pi/\omega_0$, the displacement is $\xi(t_2) = \xi_2 = \xi_0 - 4F_d/K$. The motion decreases linearly with time and the equation of the envelope is $\xi_0 - (2F_d)/(\pi\sqrt{KM})t$. The motion stops abruptly at time t_n where $\xi(t_n) < \mu_s F_d/\mu_d K$.

Stick–Slip Vibrations

A number of acoustic sources are due to frictional effects [22.49]. The sounds produced can be perceived as noise (such as squeal) or music (like for violin bowed strings). In all cases, the vibrations are the result of self-sustained oscillations. The simplest example of such systems is a 1-DOF oscillator whose mass is resting on a belt moving at constant velocity V_0 (Fig. 22.22).

The equation of motion of such an oscillator can be written in a general form

$$M\ddot{\xi} + R\dot{\xi} + K\xi = F(v_r, \xi)$$
$$\text{with} \quad v_r = V_0 - \dot{\xi} . \qquad (22.381)$$

The previous Coulomb model presented in Sect. 22.6.3 does not account for the energy exchange between oscillator and belt. One widely used semi-empirical model assumes a friction force $F(t) \le F_s = \mu_s Mg$ during the sticking phase, while the sliding frictional force decreases with relative mass-belt velocity (Fig. 22.23). Various mathematical formulations have been proposed for such frictional forces. *Leine* et al. [22.50], for example, make use of the following model

$$F(v_r, \xi) = \begin{cases} F(\xi) & = \min(|K\xi|, F_s)\operatorname{sgn}(K\xi) , \\ v_r & = 0 \quad \text{stick} , \\ F(v_r) & = \frac{F_s \operatorname{sgn} v_r}{1+\delta|v_r|} \\ v_r & \neq 0 \quad \text{slip} , \end{cases} \qquad (22.382)$$

where δ is an arbitrary constant. In fact, the energy exchange depends on many factors: material properties,

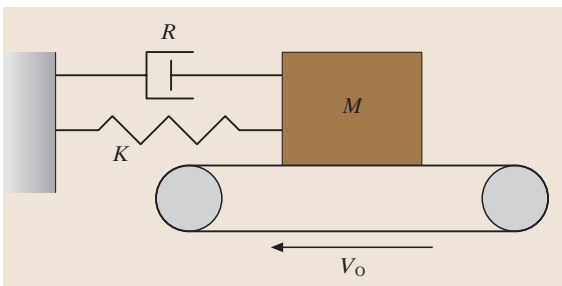


Fig. 22.22 One-DOF oscillator in stick–slip vibrations

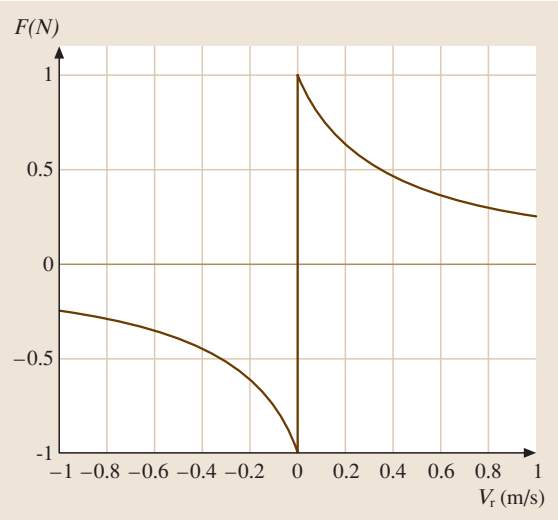


Fig. 22.23 Typical frictional force versus relative mass/belt velocity

surface roughness, thermal properties of the materials in contact [22.51], etc. See, for example, [22.52] and [22.49] for a review of friction models.

A periodic oscillation can be obtained for specific ranges of belt velocity and friction parameters. In many cases, such a complex system leads to bifurcations and chaos [22.53].

22.6.4 Hysteretic Damping

Hysteretic damping is a widely used model of structural damping. In the frequency domain, it corresponds to the case of a frequency-dependent dashpot that leads to a loss factor independent of frequency. Recall that the loss factor η is defined as the ratio between the energy lost in the system during a period and the maximum of the potential energy [22.54]. For a 1-DOF system, the equation of motion is written in the frequency domain as

$$[-M\omega^2 + \mathrm{i}\omega R(\omega) + K]\Xi(\omega) = F(\omega) \qquad (22.383)$$

or, equivalently,

$$\left\{-M\omega^2 + K\left[1 + \mathrm{i}\eta\ \mathrm{sgn}(\omega)\right]\right\}\Xi(\omega) = F(\omega)\,. \qquad (22.384)$$

This formulation accounts for steady-state oscillations of the system. However, its major drawback follows from the fact that the corresponding time-domain description is not causal. In the frequency domain, the dashpot force is $F_\mathrm{d}(\omega) = \mathrm{i}\omega R(\omega)\Xi(\omega) = \mathrm{i}K\eta\ \mathrm{sgn}(\omega)\Xi(\omega)$. Taking the inverse Fourier transform of $F_\mathrm{d}(\omega)$ yields [22.54]

$$f_\mathrm{d}(t) = \frac{\mathrm{i}K\eta}{2\pi}\int_{-\infty}^{+\infty}\mathrm{sgn}(\omega)\,\mathrm{e}^{\mathrm{i}\omega t}\,\mathrm{d}\omega\int_{-\infty}^{+\infty}\xi(\tau)\mathrm{e}^{-\mathrm{i}\omega\tau}\,\mathrm{d}\tau\,. \qquad (22.385)$$

Inverting (22.385) yields the displacement of the mass

$$\xi(t) = \frac{1}{2\pi K\eta}\int_{-\infty}^{+\infty}\frac{\mathrm{e}^{\mathrm{i}\omega t}}{\mathrm{isgn}(\omega)}\,\mathrm{d}\omega\int_{-\infty}^{+\infty}f_\mathrm{d}(\tau)\mathrm{e}^{-\mathrm{i}\omega\tau}\,\mathrm{d}\tau\,. \qquad (22.386)$$

Selecting, for example, $f_\mathrm{d}(t) = \delta(t)$ where $\delta(t)$ is the Dirac delta function leads to

$$\xi(t) = \frac{1}{\pi K\eta}\frac{1}{t} \qquad -\infty < t < +\infty \qquad (22.387)$$

which is clearly not causal, since the response anticipates the excitation [22.54]. Thus, hysteretic damping is generally not appropriate in the time domain, and one has to find other strategies for modeling frequency-dependent damping while preserving the causality.

22.7 Nonlinear Vibrations

Nonlinearities in structures can be either due to nonlinear properties of the material or to large amplitude of vibration affecting the equations of motion. We limit our attention to this latter case, which is called *geometrical nonlinearity*. The most frequently encountered nonlinear terms are cubic and quadratic. These nonlinearities are responsible for many important phenomena: existence of harmonics of the excitation frequency in the response, combination of modes, jumps and hysteresis in response curves, instability and chaos. The purpose of this section is to introduce most of these properties for simple systems: single and coupled nonlinear oscillators. Finally, a number of nonlinear equations for continuous structures are briefly reviewed.

22.7.1 Example of a Nonlinear Oscillator

Equation of Motion

To introduce the fundamental concepts of nonlinear vibrations, we start with a simple example of a nonsymmetrical oscillator: the interrupted pendulum (Fig. 22.24). The oscillator consists of a point mass m suspended by a massless thread of length L and subjected to gravity g. The length of the thread varies with time, as it moves around the pulley of radius R [22.55].

The equation of motion can be derived from the Lagrange equations (Sect. 22.2). Selecting the angle θ between the vertical axis and the actual direction of the thread as the parameter of the system, the kinetic energy is written $E_k = 1/2m(L - R\theta)^2\dot{\theta}^2$ and the equation of motion becomes

$$\ddot{\theta} + \omega_0^2 \sin\theta = \rho \frac{d}{dt}(\theta\dot{\theta}) , \qquad (22.388)$$

where $\omega_0^2 = g/L$ and $\rho = R/L$. As R tends to zero in (22.388), we find the well-known equation for a pendulum where the only nonlinear term is due to $\sin\theta$. The nonlinear right-hand side member of the equation is due to the rigid support. The validity domain of this equation is $\theta \in [0, \theta_{max}]$ where $\theta_{max} = \min\left(1/\rho, \pi/2\right)$. We assume that the pendulum is released at time $t = 0$ from its initial position θ_0 with zero initial velocity.

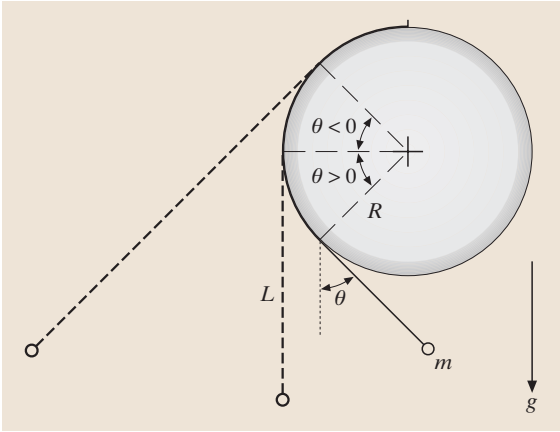


Fig. 22.24 Interrupted pendulum (After *Denardo* [22.55])

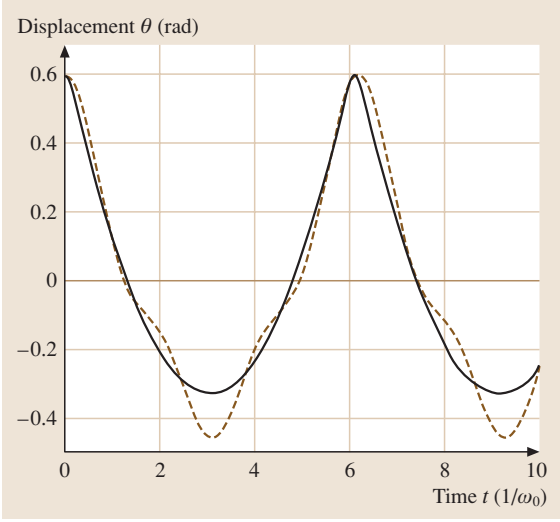


Fig. 22.25 Interrupted pendulum (after *Denardo*). Waveform: exact solution (*solid line*). Perturbative solution to the third order (*dashed line*)

Resolution with the Harmonic Balance Method

It is observed experimentally that the solution is periodic for small amplitudes with $\rho < 1$, with a period of oscillation that depends on amplitude (Fig. 22.25). With increasing amplitude, the solution departs more and more from the linear harmonic reference motion. This encourages us to look for solutions of the form

$$\begin{cases} \theta & = \varepsilon A\cos\omega t + \varepsilon^2 B\cos 2\omega t \\ & \quad + \varepsilon^3 C\cos 3\omega t + \ldots \\ & = \varepsilon\theta_1 + \varepsilon^2\theta_2 + \varepsilon^3\theta_3 + \ldots \\ \omega^2 & = \omega_0^2 + \varepsilon\omega_1^2 + \varepsilon^2\omega_2^2 + \varepsilon^3\omega_3^2 + \ldots \end{cases} . \qquad (22.389)$$

In (22.389), the solution is expanded in the form of a Fourier series, where the amplitudes of the expansion terms are proportional to increasing powers of a nondimensional parameter $\varepsilon \ll 1$. Similarly, the frequency ω is expanded in terms of increasing power of ε. The basic principle of the harmonic balance method used here for solving this nonlinear equation consists of inserting (22.389) in (22.388) and matching sinusoidal terms to calculate the unknowns $(A, B, C, \omega_1, \omega_2, \omega_3)$ from the equations, obtained separately for each power of ε [22.55]. An example up to the third order in ε is given below. We start by defining a nondimensional time variable $\tau = \omega t$. Limiting the development of $\sin\theta$ to the third order, we obtain

$$\omega^2 \frac{d^2\theta}{d\tau^2} + \omega_0^2\left(\theta - \theta^3/6\right) = \rho\omega^2 \frac{d}{d\tau}\left(\theta\frac{d\theta}{d\tau}\right) . \qquad (22.390)$$

Inserting (22.389) in (22.390) and equating terms of equal power in ε, we find

$$\frac{d^2\theta_1}{d\tau^2} + \theta_1 = 0 \qquad (22.391)$$

Amazon EX1014 Page 952

whose solution is $\theta_1 = A\cos\omega\tau$. With the same procedure applied to the term in ε^2, one obtains

$$\frac{d^2\theta_2}{d\tau^2} + \theta_2 = \frac{\omega_1^2}{\omega_0^2}\theta_1 + \rho\frac{d}{d\tau}\left(\theta_1\frac{d\theta_1}{d\tau}\right). \qquad (22.392)$$

Equation (22.392) yields the following relation

$$-3B\cos 2\tau = \frac{\omega_1^2}{\omega_0^2}A\cos\tau - \rho A^2\cos 2\tau\,. \qquad (22.393)$$

Using the harmonic balance method for each component $n\tau$ leads to

$$\omega_1 = 0 \quad \text{and} \quad B = \frac{\rho A^2}{3}\,. \qquad (22.394)$$

At this stage, (22.394) shows that the pulley is responsible for a nonlinear quadratic perturbation. To first order, the quadratic nonlinearity has no effect on the frequency. However, extending the calculations to the third order in ε, we get

$$\frac{d^2\theta_3}{d\tau^2} + \theta_3 = \frac{\omega_2^2}{\omega_0^2}\theta_1 + \frac{\theta_1^3}{6} + \rho\frac{d^2}{d\tau^2}(\theta_1\theta_2)\,. \qquad (22.395)$$

Using the harmonic balance method in (22.395) now yields

$$C = \frac{A^3}{192}(36\rho^2 - 1)$$

and

$$\frac{\omega_2^2}{\omega_0^2} = \frac{A^2}{24}(4\rho^2 - 3)\,. \qquad (22.396)$$

In summary, by defining $\theta_{10} = \varepsilon A$ as the amplitude of the fundamental, we find the third-order perturbation solution

$$\begin{cases} \theta & = \theta_{10}\cos\omega t + \dfrac{\rho\theta_{10}^2}{3}\cos 2\omega t \\ & \quad + (36\rho^2 - 1)\dfrac{\theta_{10}^3}{192}\cos 3\omega t \\ \text{and} & \\ \omega^2 & = \omega_0^2\left[1 + \dfrac{\theta_{10}^2}{24}(4\rho^2 - 3)\right] \end{cases}. \qquad (22.397)$$

The following comments can be made:

- To third order, θ_{10} is linked to the initial angle θ_0 by the relation:

$$\theta_0 \simeq \theta_{10} + \frac{\rho\theta_{10}^2}{3} + (36\rho^2 - 1)\frac{\theta_{10}^3}{192}\,. \qquad (22.398)$$

- Figure 22.25 shows that the third-order approximation yields a good estimation of the period. In addition, the waveform is also correctly predicted for $\theta > 0$. However, the estimation is less good for $\theta < 0$.
- For $\rho = 0$, we have $\omega \simeq \omega_0(1 - \theta_{10}^2/16)$, and the term $\cos 2\omega t$ is equal to zero. The system exhibits a cubic nonlinearity due to gravity.
- For $0 < \rho < \sqrt{3}/2$, the oscillation frequency decreases as the amplitude increases. A softening effect is obtained.
- For $\rho > \sqrt{3}/2$, the oscillation frequency increases with amplitude we have an hardening effect.
- For $\rho = \sqrt{3}/2$, it is observed that the frequency is independent of the magnitude. The softening effect due to gravity is compensated by the hardening effect due to the rigid pulley. This result remains valid up to fourth order.

Many of the nonlinear effects derived for this simple oscillator, such as amplitude-dependent frequency and softening/hardening effects, are found in more-complex systems.

22.7.2 Duffing Equation

A number of nonlinear vibrations are governed by the Duffing equation. This presentation starts with the example of an elastic pendulum. General results for this cubic nonlinearity are then discussed.

Elastic Pendulum

To illustrate the Duffing equation, the elastic pendulum shown in Fig. 22.26 is considered [22.56]. The mass M moves horizontally due to the harmonic force $F\cos\Omega t$. Two springs with stiffness k, and length L_0 at rest, are

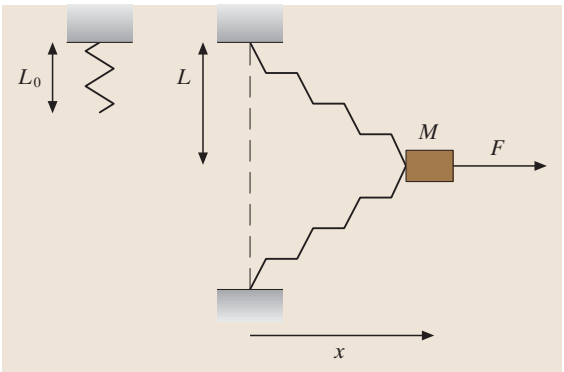


Fig. 22.26 Elastic pendulum

stretched to the length L when attached to the mass. The displacement of the mass from its equilibrium position is x. We introduce the dimensionless parameters $\lambda = L_0/L < 1$ and $y = x/L$. During the motion, the actual length of the spring is $l(y) = L\sqrt{1+y^2}$ and the elastic potential energy is $V = 1/2k(l-L_0)^2$. By differentiating this expression with respect to y, the elastic force is obtained from which the equation of motion for the mass is derived

$$M\frac{\mathrm{d}^2y}{\mathrm{d}t^2} + 2ky\left(1 - \frac{\lambda}{\sqrt{1+y^2}}\right) = \frac{F}{L}\cos\Omega t\ . \tag{22.399}$$

With the additional assumption of small amplitude ($y_{\max} \ll 1$), and defining further $\omega_0^2 = 2k/M$ we obtain the first-order approximation

$$\frac{\mathrm{d}^2y}{\mathrm{d}t^2} + \omega_0^2(1-\lambda)y + \frac{\omega_0^2\lambda}{2}y^3 = \frac{F}{ML}\cos\Omega t \tag{22.400}$$

which can be written in nondimensional form, after defining $\tau = \omega t$ with $\omega^2 = \omega_0^2(1-\lambda)$ and $\gamma = \Omega/\omega$, as

$$\frac{\mathrm{d}^2y}{\mathrm{d}\tau^2} + y + \eta y^3 = \alpha\cos\gamma\tau\ , \tag{22.401}$$

where $\eta = \lambda/(2(1-\lambda))$ and $\alpha = F/ML\omega^2$. Equation (22.401) is a forced Duffing equation with a hardening cubic coefficient ($\eta > 0$).

Forced Vibrations

We consider the case where $\eta > 0$ and α defined in (22.401) are small compared to unity. By analogy with the linear case, a first approximation of the solution is $y_1(t) = A\cos\gamma\tau$, where A is the unknown. Inserting y_1 into (22.401), we get the differential equation that governs the second-order approximation $y_2(t)$

$$\frac{\mathrm{d}^2y_2}{\mathrm{d}\tau^2} = -A\cos\gamma\tau - \eta A^3\cos^3\gamma\tau + \alpha\cos\gamma\tau\ . \tag{22.402}$$

Using the equality $4\cos^3\gamma\tau = 3\cos\gamma\tau + \cos 3\gamma\tau$ and selecting the appropriate origin of time to avoid constant terms, we get

$$y_2(t) = \frac{A + 3\eta A^3/4 - \alpha}{\gamma^2}\cos\gamma\tau + \frac{\eta A^3}{36\gamma^2}\cos 3\gamma\tau\ . \tag{22.403}$$

Using the method originally used by Duffing, we look for the value of A that is equal to the lowest terms of the series in (22.403), which yields:

$$(1-\gamma^2)A + \frac{3\eta A^3}{4} = \alpha\ . \tag{22.404}$$

In order to plot the resonance curve, this can be written as

$$(\gamma^2 - 1) = \frac{3\eta A^2}{4} \pm \frac{\alpha}{|A|}\ . \tag{22.405}$$

With $\alpha = 0$, the free regime is obtained. For $\alpha \neq 0$, two branches of solution are obtained, depending on whether A is positive or negative. A nonlinear oscillator of the hardening type is obtained here, since the resonance frequency increases with the amplitude (Fig. 22.27).

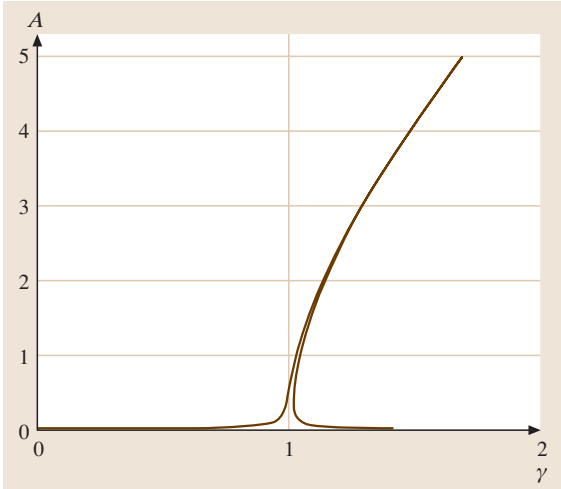


Fig. 22.27 Frequency response curve of the undamped Duffing equation with $\eta > 0$. $\gamma = \Omega/\omega$ is the reduced frequency

Duffing Equation with a Viscous Damping Term. With the introduction of a viscous damping term, we obtain the nondimensional equation

$$\frac{\mathrm{d}^2y}{\mathrm{d}\tau^2} + \beta\frac{\mathrm{d}y}{\mathrm{d}\tau} + y + \eta y^3 = \alpha\cos\gamma\tau\ . \tag{22.406}$$

In this case, the response curves are governed by the equation

$$\left[(1-\gamma^2)A + \frac{3\eta A^3}{4}\right]^2 + \beta^2A^2 = \alpha^2 \tag{22.407}$$

which corresponds to the curves shown in Fig. 22.28.

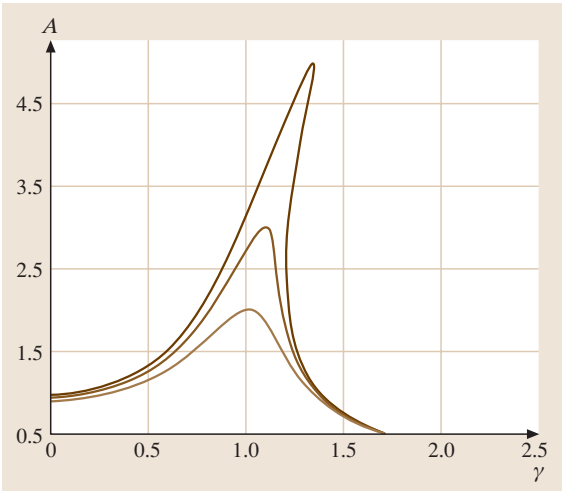


Fig. 22.28 Response curves of the damped Duffing equation

Jump and Hysteresis. It can be seen from Fig. 22.28 that a frequency range exists where three different values for $|A|$ correspond to one single value of the reduced frequency γ. Only the two extreme solutions are stable, while the intermediate value is unstable. As a consequence, on decreasing or increasing the frequency, a jump phenomenon is observed at points corresponding to the vertical tangents. The hysteresis cycle include these two jumps in addition to the stable portions of the upper and lower resonance curves.

Generation of Subharmonics. An important property of nonlinear oscillators is that they exhibit spectral components that are not present in the forcing terms, and which are also distinct from their eigenfrequencies. The generation of subharmonics is examined here. The Duffing equation with a forcing term at reduced frequency 3γ is considered

$$\frac{\mathrm{d}^2 y}{\mathrm{d}\tau^2} + y + \eta y^3 = \alpha \cos 3\gamma\tau \qquad (22.408)$$

with $\eta \ll 1$. We look for solutions of the form

$$y(\tau) = y_0(\tau) + \eta y_1(\tau) \quad \text{with} \quad \gamma^2 = 1 + \eta\gamma_1^2 \,. \qquad (22.409)$$

By inserting (22.409) in (22.408) and eliminating the higher-order terms in η, we get

$$\frac{\mathrm{d}^2 y_0}{\mathrm{d}\tau^2} + \gamma^2 y_0 - \eta\gamma_1^2 y_0 + \eta\frac{\mathrm{d}^2 y_1}{\mathrm{d}\tau^2} + \eta\gamma^2 y_1 + \eta y_0^3 = \alpha \cos 3\gamma\tau \,. \qquad (22.410)$$

The linear solution (zero-order term) is obtained by imposing $\eta = 0$ in (22.410), which yields:

$$\frac{\mathrm{d}^2 y_0}{\mathrm{d}\tau^2} + \gamma^2 y_0 = \alpha \cos 3\gamma\tau \,. \qquad (22.411)$$

With the appropriate initial conditions, we obtain the zero-order solution $y_0(\tau) = A\cos\gamma\tau + C\cos 3\gamma\tau$ with $C = -\alpha/8\gamma^2$. By pursuing the mathematical derivations iteratively, we obtain the first-order approximation y_1

$$\frac{\mathrm{d}^2 y_1}{\mathrm{d}\tau^2} + \gamma^2 y_1 = \gamma_1^2 y_0 - y_0^3 \,. \qquad (22.412)$$

Inserting the expression for $y_0(\tau)$ in (22.412) it is found that $y_1(\tau)$ must be a solution of the equation

$$\frac{\mathrm{d}^2 y_1}{\mathrm{d}\tau^2} + \gamma^2 y_1 = A\left[\gamma_1^2 - \frac{3}{4}\left(A^2 + \frac{3\alpha^2}{64\gamma^4} - \frac{A\alpha}{8\gamma^2}\right)\right]\cos\gamma\tau + \text{terms in } 3\gamma,\ 5\gamma,\ 7\gamma,\ 9\gamma \,. \qquad (22.413)$$

The first term on the right-hand side of (22.413) is a resonant excitation term or *secular term*, which leads to an infinitely growing solution. As such a solution is not physically possible, this secular terms must be eliminated, which leads to the condition:

$$\gamma_1^2 = \frac{3}{4}\left(A^2 + \frac{3\alpha^2}{64\gamma^4} - \frac{A\alpha}{8\gamma^2}\right) . \qquad (22.414)$$

Equation (22.414) yields the condition of existence, in terms of amplitude A and nonlinear strength η, for subharmonics of order three

$$\gamma^6 - \gamma^4 - \frac{3\eta}{256}\left(64A^2\gamma^4 - 8A\alpha\gamma^2 + 2\alpha^2\right) = 0 \,. \qquad (22.415)$$

Similarly, one can show that the Duffing oscillator can yield superharmonics of order three. The method consists of imposing a forcing term with reduced frequency γ and looking for the condition of existence of solutions with frequency 3γ.

22.7.3 Coupled Nonlinear Oscillators

Continuous systems and discrete systems with several degrees of freedom subjected to large amplitude of motion show multiple nonlinear coupling effects. In this section, we limit ourselves to nonlinear coupling between two oscillators, which represents a significant step forward in terms of complexity compared to the single-DOF nonlinear oscillator.

Example of a Quadratic Nonlinear Coupling

Here, the case of a quadratic nonlinear coupling between two oscillators is investigated using the multiple-scales method [22.57]. The equations are:

$$\begin{cases} \ddot{x}_1 + \omega_1^2 x_1 &= \varepsilon\left(-\beta_{12} x_1 x_2 - 2\mu_1 \dot{x}_1\right), \\ \ddot{x}_2 + \omega_2^2 x_2 &= \varepsilon\left(-\beta_{21} x_1^2 - 2\mu_2 \dot{x}_2 + P\cos\Omega t\right), \end{cases} \tag{22.416}$$

where x_1 and x_2 are the displacements, ω_1 and ω_2 are the eigenfrequencies of the oscillators in the linear range. The perturbation terms are grouped on the right-hand side of (22.416). The nondimensional parameter $\varepsilon \ll 1$ indicates that these terms are small. The quadratic nonlinear coupling is due to the presence of the terms $\beta_{12} x_1 x_2$ and $\beta_{21} x_1^2$. It is assumed that the system has a so-called *internal resonance* in the sense that $\omega_2 = 2\omega_1 + \varepsilon\sigma_1$, where σ_1 is the internal detuning parameter. The forcing frequency Ω is close to ω_2 so that we can write $\Omega = \omega_2 + \varepsilon\sigma_2$ where σ_2 is the external detuning parameter, and μ_1 and μ_2 are viscous damping parameters.

Resolution with the Method of Multiple Scales

Solving the above equations involves calculating the amplitudes a_1 and a_2 of both oscillators as a function of the external detuning parameter σ_2. Another goal is to determine the values of the threshold in terms of amplitude and frequency, at which the nonlinear set of oscillators exhibit bifurcations and unstable behavior. The present example contains most of the concepts and methods used in the theory of multiple scales applied to nonlinear oscillators. The main steps of the calculations are the following:

1. Definition of time scales and general form of the solution
2. Solvability conditions. Elimination of secular terms
3. Autonomous system and fixed points
4. Stability of the system
5. Amplitudes and phases of the solution

Definition of Time Scales and General Form of the Solution. The time scales are defined as

$$T_j = \varepsilon^j t \quad \text{with} \quad j \geq 0 \tag{22.417}$$

and the solutions are expanded into

$$\begin{cases} x_1(t) = x_{10}(T_0, T_1) + \varepsilon x_{11}(T_0, T_1) + O(\varepsilon^2) \\ x_2(t) = x_{20}(T_0, T_1) + \varepsilon x_{21}(T_0, T_1) + O(\varepsilon^2) \end{cases}, \tag{22.418}$$

where the expansion is limited here to the first order in ε. The differentiation operators can be written

$$\begin{cases} \dfrac{\partial}{\partial t} &= \dfrac{\partial}{\partial T_0} + \varepsilon \dfrac{\partial}{\partial T_1}, \\ \dfrac{\partial^2}{\partial t^2} &= \dfrac{\partial^2}{\partial T_0^2} + 2\varepsilon \dfrac{\partial}{\partial T_0}\dfrac{\partial}{\partial T_1}. \end{cases} \tag{22.419}$$

In what follows, we write $D_j = \partial/\partial T_j$. Inserting (22.419) into (22.416) and matching the coefficients of terms with the same power in ε yields:

- for the zero-order term $\varepsilon^0 = 1$

$$D_0^2 x_{10} + \omega_1^2 x_{10} = 0\,; \quad D_0^2 x_{20} + \omega_2^2 x_{20} = 0\,; \tag{22.420}$$

- for the first-order term ε:

$$\begin{cases} D_0^2 x_{11} + \omega_1^2 x_{11} \\ = -2D_0 D_1 x_{10} - \beta_{12} x_{10} x_{20} - 2\mu_1 D_0 x_{10}, \\ D_0^2 x_{21} + \omega_2^2 x_{21} \\ = -2D_0 D_1 x_{20} - \beta_{21} x_{10}^2 \\ \quad -2\mu_2 D_0 x_{20} + P\cos\Omega t. \end{cases} \tag{22.421}$$

The solutions of (22.420) can be written

$$\begin{aligned} x_{10}(t) &= A_1(T_1)\mathrm{e}^{\mathrm{i}\omega_1 t} + A_1^*(T_1)\mathrm{e}^{-\mathrm{i}\omega_1 t}\,; \\ x_{20}(t) &= A_2(T_1)\mathrm{e}^{\mathrm{i}\omega_2 t} + A_2^*(T_1)\mathrm{e}^{-\mathrm{i}\omega_2 t}, \end{aligned} \tag{22.422}$$

where the (*) indicates the complex conjugate.

Solvability Conditions. In order to calculate the complex terms $A_1(T_1)$ and $A_2(T_1)$, the expressions (22.422) are inserted into (22.421). Then, conditions are determined so that no secular terms, such as $t\cos\omega t$, exist in the solution. This leads to the so-called solvability conditions:

$$\begin{cases} -2\mathrm{i}\omega_1\left(\dfrac{\partial A_1}{\partial T_1} + \mu_1 A_1\right) - \beta_{12} A_1^* A_2 \mathrm{e}^{\mathrm{i}\sigma_1 T_1} &= 0, \\ -2\mathrm{i}\omega_2\left(\dfrac{\partial A_2}{\partial T_1} + \mu_2 A_2\right) - \beta_{21} A_1^2 \mathrm{e}^{-\mathrm{i}\sigma_1 T_1} \\ + \dfrac{P}{2}\mathrm{e}^{\mathrm{i}\sigma_2 T_1} &= 0. \end{cases} \tag{22.423}$$

Equations (22.423) are usually written in polar form

$$A_1(T_1) = \frac{a_1}{2} e^{i\theta_1} ;$$
$$A_2(T_1) = \frac{a_2}{2} e^{i\theta_2} , \qquad (22.424)$$

where the amplitudes a_i and phases θ_i are functions of T_1. Substituting (22.424) in (22.423) yields the system that governs the slow temporal evolution of the response, with scale $T_1 = \varepsilon t$:

$$\begin{cases} \dfrac{\partial a_1}{\partial T_1} = -\mu_1 a_1 - \dfrac{\beta_{12} a_1 a_2}{4\omega_1} \sin(\sigma_1 T_1 + \theta_2 - 2\theta_1) , \\ a_1 \dfrac{\partial \theta_1}{\partial T_1} = \dfrac{\beta_{12} a_1 a_2}{4\omega_1} \cos(\sigma_1 T_1 + \theta_2 - 2\theta_1) , \\ \dfrac{\partial a_2}{\partial T_2} = -\mu_2 a_2 + \dfrac{\beta_{21} a_1^2}{4\omega_2} \sin(\sigma_1 T_1 + \theta_2 - 2\theta_1) + \dfrac{P}{2\omega_2} \sin(\sigma_2 T_1 - \theta_2) , \\ a_2 \dfrac{\partial \theta_2}{\partial T_2} = \dfrac{\beta_{21} a_1^2}{4\omega_2} \cos(\sigma_1 T_1 + \theta_2 - 2\theta_1) - \dfrac{P}{2\omega_2} \cos(\sigma_2 T_1 - \theta_2) . \end{cases} \qquad (22.425)$$

Autonomous System and Fixed Points. Now, the system is written in autonomous form, i. e. in the form $\dot{X} = F(X)$. In practice, this is achieved with the changes of variables $\gamma_1 = \sigma_2 T_1 - \theta_2$ and $\gamma_2 = \sigma_1 T_1 + \theta_2 - 2\theta_1$. As a consequence (22.425) becomes:

$$\begin{cases} \dfrac{\partial a_1}{\partial T_1} = -\mu_1 a_1 - \dfrac{\beta_{12} a_1 a_2}{4\omega_1} \sin\gamma_2 , \\ \dfrac{\partial \gamma_1}{\partial T_1} = \sigma_2 - \dfrac{\beta_{21} a_1^2}{4\omega_2 a_2} \cos\gamma_2 + \dfrac{P}{2\omega_2 a_2} \cos\gamma_1 , \\ \dfrac{\partial a_2}{\partial T_2} = -\mu_2 a_2 + \dfrac{\beta_{21} a_1^2}{4\omega_2} \sin\gamma_2 + \dfrac{P}{2\omega_2} \sin\gamma_1 , \\ \dfrac{\partial \gamma_2}{\partial T_2} = \sigma_1 - \dfrac{\beta_{12} a_2}{2\omega_1} \cos\gamma_2 + \dfrac{\beta_{21} a_1^2}{4\omega_2 a_2} \cos\gamma_2 - \dfrac{P}{2\omega_2 a_2} \cos\gamma_1 . \end{cases} \qquad (22.426)$$

The fixed points correspond to the steady-state solutions, which are those of interest in the case of forced vibrations. These solutions are obtained through cancelation of the time derivatives in (22.426), which gives:

$$\begin{cases} a_1 \left(\mu_1 + \dfrac{\beta_{12} a_2}{4\omega_1} \sin\gamma_2 \right) = 0 , \\ \sigma_2 - \dfrac{\beta_{21} a_1^2}{4\omega_2 a_2} \cos\gamma_2 + \dfrac{P}{2\omega_2 a_2} \cos\gamma_1 = 0 , \\ -\mu_2 a_2 + \dfrac{\beta_{21} a_1^2}{4\omega_2} \sin\gamma_2 + \dfrac{P}{2\omega_2} \sin\gamma_1 = 0 , \\ \sigma_1 + \dfrac{\beta_{21} a_1^2}{4\omega_2 a_2} \cos\gamma_2 - \dfrac{P}{2\omega_2 a_2} \cos\gamma_1 - \dfrac{\beta_{12} a_2}{2\omega_1} \cos\gamma_2 = 0 . \end{cases} \qquad (22.427)$$

Imposing $a_1 = 0$ in (22.427) yields the response curve a_2 of the second oscillator in the linear case (Fig. 22.29)

$$a_2 = \frac{P}{2\omega_2 \sqrt{\sigma_2^2 + \mu_2^2}} . \qquad (22.428)$$

Stability of the Nonlinear Coupled System. Intuitively, a physically unstable system behaves in such a way that, subjected to a small departure from equilibrium, its motion will never bring it back to its initial position but will rather continue its deviation. From a mathematical point of view, the deviations from an equilibrium position for a system with multiple variables such as (22.427) are calculated from the partial derivatives of each equation with regard to all variables of the system. This leads to

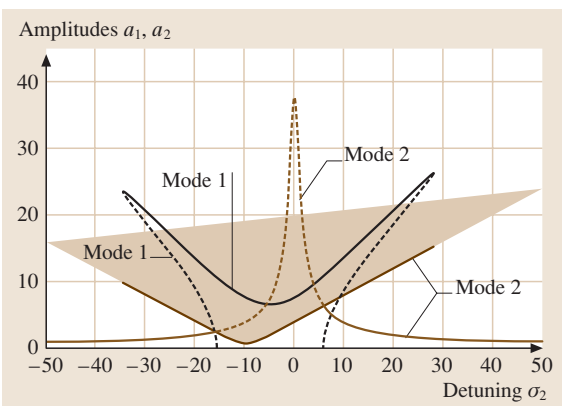


Fig. 22.29 Frequency response curves of the nonlinearly coupled oscillators as a function of the external detuning parameter

the definition of the Jacobian matrix $\mathcal{J}$ of the system:

$$\mathcal{J} = \begin{vmatrix} \frac{\partial f_1}{\partial a_1} & \frac{\partial f_1}{\partial \gamma_1} & \frac{\partial f_1}{\partial a_2} & \frac{\partial f_1}{\partial \gamma_2} \\ \frac{\partial f_2}{\partial a_1} & \frac{\partial f_2}{\partial \gamma_1} & \frac{\partial f_2}{\partial a_2} & \frac{\partial f_2}{\partial \gamma_2} \\ \frac{\partial f_3}{\partial a_1} & \frac{\partial f_3}{\partial \gamma_1} & \frac{\partial f_3}{\partial a_2} & \frac{\partial f_3}{\partial \gamma_2} \\ \frac{\partial f_4}{\partial a_1} & \frac{\partial f_4}{\partial \gamma_1} & \frac{\partial f_4}{\partial a_2} & \frac{\partial f_4}{\partial \gamma_2} \end{vmatrix} . \tag{22.429}$$

In our case, the eigenvalues of this Jacobian are

$$\begin{cases} \lambda_1 = -\mu_2 + \mathrm{i}\sigma_2 \, ; \\ \lambda_2 = -\mu_2 - \mathrm{i}\sigma_2 \, ; \\ \lambda_3 = -\dfrac{\beta_{12} a_2}{4\omega_1} \sin\gamma_2 - \mu_1 \, ; \\ \lambda_4 = \dfrac{\beta_{12} a_2}{2\omega_1} \sin\gamma_2 \, . \end{cases} \tag{22.430}$$

The system is unstable if the real part of any one of these eigenvalues is positive. In (22.430), the real parts of λ_1 and λ_2 are negative, because of the damping term μ_2. However, calculating the product of the two other eigenvalues yields

$$\lambda_3 \lambda_4 = -\frac{\mu_1 \beta_{12} a_2}{2\omega_1} \sin\gamma_2 - \frac{\beta_{12}^2 a_2^2}{8\omega_1^2} \sin^2\gamma_2 \, . \tag{22.431}$$

This product can be negative, leading to an instability, if

$$a_2 > \frac{2\omega_1}{|\beta_{12}|} \sqrt{4\mu_1^2 + (\sigma_1 + \sigma_2)^2} \, . \tag{22.432}$$

The instability domain corresponding to (22.432) is the shaded area in Fig. 22.29.

Amplitudes and Phases of the Solution. Solutions for the nonlinear coupled system are obtained by combining (22.422) with (22.424), taking the definitions of T_1, σ_1, σ_2 γ_1 and γ_2 into account. We then obtain

$$\begin{cases} x_{10} &= a_1 \cos(\omega_1 t + \theta_1) \\ &= a_1 \cos\left(\frac{\Omega}{2} t - \frac{\gamma_1 + \gamma_2}{2}\right) , \\ x_{20} &= a_2 \cos(\omega_2 t + \theta_2) = a_2 \cos\left(\Omega t - \gamma_1\right) , \end{cases} \tag{22.433}$$

where, by solving the system (22.427), the amplitudes of the oscillators are given by

$$\begin{cases} a_2 = \dfrac{2\omega_1}{|\beta_{12}|} \sqrt{(\sigma_1 + \sigma_2)^2 + 4\mu_1^2} \, , \\ a_1 = 2\left[-\Gamma_1 \pm \sqrt{P^2/\left(4\beta_{21}^2\right) - \Gamma_2^2} \right]^{1/2} , \\ \text{with} \quad \Gamma_1 = \dfrac{2\omega_1\omega_2}{\beta_{12}\beta_{21}} \left[2\mu_1\mu_2 - \sigma_2(\sigma_1 + \sigma_2) \right] \, , \\ \text{and} \quad \Gamma_2 = \dfrac{2\omega_1\omega_2}{\beta_{12}\beta_{21}} \left[2\mu_1\sigma_2 - \mu_2(\sigma_1 + \sigma_2) \right] \, . \end{cases} \tag{22.434}$$

Equation (22.433) shows that, for steady-state oscillations, the forcing frequency Ω is the same as the oscillation frequency of the second oscillator whereas, for appropriate conditions of instability, the first one oscillates with frequency $\Omega/2$, as a result of the nonlinear coupling. Figure 22.29 shows the resonance curves of the coupled nonlinear oscillators as a function of σ_2. By increasing this parameter progressively, successive phenomena occur:

1. First the resonance curve is that of the second oscillator. No subharmonics are observed as long as the amplitude remains below the instability region.
2. As the amplitude of the second oscillator reaches the instability limit given in (22.432), the first oscillator starts to oscillate. In our example, its magnitude a_1 is larger than a_2.

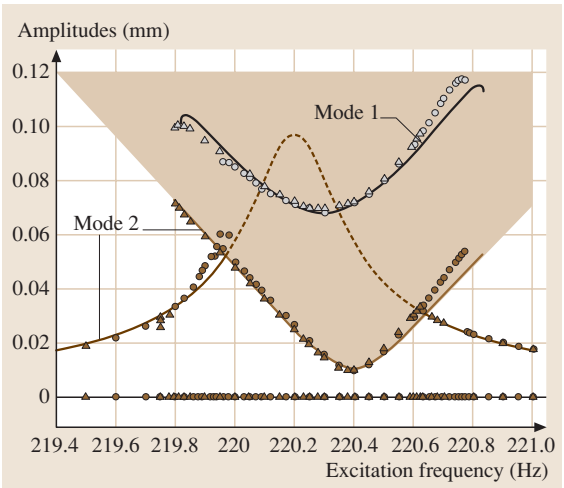


Fig. 22.30 Experimental response curves for two nonlinearly coupled degrees of freedom of a harmonically forced spherical shell (after *Thomas* et al. [22.19])

3. As the amplitude reaches the top of the resonance curve 1, it suddenly jumps back to the resonance curve 2, and oscillation at $\Omega/2$ disappears.
4. Following the frequency axis in the reverse direction, similar phenomena are observed, although the jumps do not occur at the same frequencies. Also the values of the instability thresholds are different.

To illustrate this theoretical part, Fig. 22.30 shows an example of experimental results for nonlinear coupling between two particular degrees of freedom of a spherical shell with free edge subjected to large-amplitude motion [22.19].

22.7.4 Nonlinear Vibrations of Strings

As an example of nonlinear coupling in a continuous system, the forced vibrations of a homogeneous elastic string is examined. Following the presentation by *Murthy* and *Ramakrishna*, only the coupling between the two polarizations $y(x,t)$ and $z(x,t)$ is presented [22.58, 59]. Other complicating effects such as torsional and longitudinal motions are neglected. See, for example, [22.60] for a more complete description of the nonlinear vibrating string.

Equations of Motion

As a result of the initial tension T_0 applied to the string, the length of a small element $\mathrm{d}x$ increases by a relative quantity λ, so that the actual length $\mathrm{d}s$ is given by:

$$\mathrm{d}s - \mathrm{d}x = \lambda\,\mathrm{d}x\,. \tag{22.435}$$

As a result, for a string with a Young's modulus of E and cross-sectional area of A, the actual tension becomes

$$T = T_0 + EA\lambda\,. \tag{22.436}$$

In the general case, we have $\mathrm{d}s = [\mathrm{d}x^2 + \mathrm{d}y^2 + \mathrm{d}z^2]^{1/2}$, which, by means of a second-order development is written

$$\mathrm{d}s = \mathrm{d}x\left\{1 + \frac{1}{2}\left[\left(\frac{\partial y}{\partial x}\right)^2 + \left(\frac{\partial z}{\partial x}\right)^2\right] - \frac{1}{8}\left[\left(\frac{\partial y}{\partial x}\right)^2 + \left(\frac{\partial z}{\partial x}\right)^2\right]^2 + \ldots\right\}. \tag{22.437}$$

With the additional assumption that $EA \gg T_0$, the potential energy of the string of length L rigidly fixed at both ends is written [22.58]

$$V = \int_0^L \left\{\frac{T_0}{2}\left[\left(\frac{\partial y}{\partial x}\right)^2 + \left(\frac{\partial z}{\partial x}\right)^2\right] + \frac{EA}{8}\left[\left(\frac{\partial y}{\partial x}\right)^2 + \left(\frac{\partial z}{\partial x}\right)^2\right]^2\right\}\mathrm{d}x\,. \tag{22.438}$$

The kinetic energy of the string is given by

$$E_\mathrm{k} = \frac{\mu}{2}\int_0^L \left[\left(\frac{\partial y}{\partial t}\right)^2 + \left(\frac{\partial z}{\partial t}\right)^2\right]\mathrm{d}x\,. \tag{22.439}$$

Using Hamilton's principle, and considering further that a sinusoidal force $f(x)\cos\omega t$ is applied to the string in the y-direction, we get the coupled equations of motion, where the derivatives are written with subscripts for convenience

$$\begin{cases} y_{tt} - c_0^2 y_{xx} = \dfrac{c_1^2}{2}\left[3y_{xx}y_x^2 + \dfrac{\partial}{\partial x}\left(y_x z_x^2\right)\right] + \dfrac{f(x)}{\mu}\cos\omega t\,, \\ z_{tt} - c_0^2 z_{xx} = \dfrac{c_1^2}{2}\left[3z_{xx}z_x^2 + \dfrac{\partial}{\partial x}\left(z_x y_x^2\right)\right], \end{cases} \tag{22.440}$$

where $c_0 = \sqrt{T_0/mu}$ and $c_1 = \sqrt{EA/\mu}$ are the transverse and longitudinal velocities in the linear case. It can be seen that the nonlinear terms on the right-hand side of (22.440) are negligible, as long as the slopes y_x and z_x are small. The terms on the left-hand side of (22.440) correspond to the linear case. The coupling between the two polarizations is due to the presence of the nonlinear terms. As a consequence, a force applied in the y-direction can give rise to a motion in the z-direction.

Forced Vibrations

Neglecting the nonlinear terms in (22.440) is generally not justified near resonance. We assume that the excitation frequency ω is close to one particular (linear) eigenfrequency $\omega_n = n\pi c_0/L$ of the string. If the coupling between the modes is neglected (which might not always be justified, see [22.59]) then the motion of the string can be described, to a first approximation by

$$y(x,t) = a_{ny}\sin\frac{n\pi x}{L}\cos\omega t$$

and

$$z(x,t) = a_{nz}\sin\frac{n\pi x}{L}\sin\omega t\,. \tag{22.441}$$

This leads to the following relations between the amplitudes a_{ny} and a_{nz}

$$\begin{cases} (\omega_n^2-\omega^2)a_{ny}+\dfrac{9c_1^2}{32}\left(\dfrac{n\pi}{L}\right)^4 a_{ny}^3 \\ +\dfrac{3c_1^2}{32}\left(\dfrac{n\pi}{L}\right)^4 a_{ny}a_{nz}^2=\dfrac{\alpha_n}{\mu}\,, \\ (\omega_n^2-\omega^2)a_{nz}+\dfrac{9c_1^2}{32}\left(\dfrac{n\pi}{L}\right)^4 a_{nz}^3 \\ +\dfrac{3c_1^2}{32}\left(\dfrac{n\pi}{L}\right)^4 a_{nz}a_{ny}^2=0\,, \end{cases} \tag{22.442}$$

where α_n is the projection of the excitation force onto the nth mode of the string.

Planar Motion. The case of planar motion for the string is obtained by setting $a_{nz}=0$ in (22.442). In this case, the amplitude in the y-direction is governed by the nonlinear equation

$$(\omega_n^2-\omega^2)a_{ny}+\frac{9c_1^2}{32}\left(\frac{n\pi}{L}\right)^4 a_{ny}^3=\frac{\alpha_n}{\mu} \tag{22.443}$$

which is similar in form to (22.404), obtained in the case of a discrete Duffing oscillator. Therefore, all properties of Duffing oscillators of the hardening type presented in Sect. 22.7.2 can be transposed here.

Nonplanar Motion. Eliminating a_{nz} between the two equations in (22.442) yields first for a_{ny}

$$(\omega_n^2-\omega^2)a_{ny}+\frac{3c_1^2}{8}\left(\frac{n\pi}{L}\right)^4 a_{ny}^3=\frac{\alpha_n}{\mu}\,, \tag{22.444}$$

which is similar in form to (22.443) except that the nonlinear term has increased by a factor of $4/3$ compared to the planar case. The second equation can be written in the form:

$$a_{nz}^2=a_{ny}^2-\frac{16}{3}\frac{\alpha_n}{\mu c_1^2\left(\frac{n\pi}{L}\right)^4 a_{ny}}\,. \tag{22.445}$$

Equation (22.445) shows that the string can exhibit nonplanar motion under the condition

$$a_{ny}>a_{ny}^{\text{crit}}=\left(\frac{16\alpha_n}{3\mu c_1^2\left(\frac{n\pi}{L}\right)^4}\right)^{1/3}\,. \tag{22.446}$$

This condition can be obtained either by increasing the excitation force or by varying the frequency to come closer to resonance.

22.7.5 Review of Nonlinear Equations for Other Continuous Systems

Beams

In this paragraph, the influence of amplitude on the flexural equations of beams is summarized. For more-extensive developments, one can refer to the review by *Nayfeh* [22.57]. The same notations as in Sect. 22.4.2 are used. The case of a homogeneous beam with constant cross section is considered. The plane cross sections remain plane during the motion. The radius of gyration $r=\sqrt{I_z/S}$ is assumed to be small compared to the wavelength so that transverse shear and rotary inertia are neglected. We assume planar motion, and the losses are simply modeled by a linear viscous term. Given an arbitrary characteristic length w_0, we can define the set of dimensionless variables [22.57]

$$x^*=\frac{x}{w_0}\,,\ w^*=\frac{w}{w_0}\,,\ L^*=\frac{L}{w_0}\,,$$
$$r^*=\frac{r}{w_0}\,,\ t^*=t\frac{r}{w_0^2}\sqrt{\frac{E}{\rho}}\,. \tag{22.447}$$

In this case, the nonlinear flexural equation of a beam hinged at both ends is written in nondimensional form (removing the asterisk for convenience):

$$r^2\left(w_{tt}+\mu w_t+w_{xxxx}\right) =\left(\frac{1}{2L}\int_0^L w_x^2\,\mathrm{d}x\right)w_{xx}+f(x,t)\,, \tag{22.448}$$

where μ is the dimensionless viscous damping parameter, and where the indices refer to the derivatives. Equation (22.448) shows that the nonlinear term is due to the increase in axial tension consecutive to large-amplitude motion. Expanding the solution on the linear eigenmodes $w(x,t)=\sum_n \Phi_n(x)q_n(t)$, we obtain, for the special case of the hinged–hinged beam, the following set of nonlinearly coupled differential equations:

$$\ddot{q}_n+\omega_n^2 q_n=-\varepsilon\left(\mu\dot{q}_n+\frac{\omega_n^2}{2n^2}q_n\sum_{m=1}^{\infty}m^2q_{\mathrm{m}}^2\right)+f_n(t)\,, \tag{22.449}$$

where ε is a small dimensionless parameter indicating that the slenderness ratio of the beam is small. Equation (22.449) generalizes (22.416) obtained for two nonlinearly coupled oscillators, though an important difference is that we have to deal here with cubic nonlinear terms, instead of the quadratic terms in the previously mentioned 2-DOF nonlinear system.

Amazon EX1014 Page 960

Shallow Spherical Shells and Plates

Similarly, the case of large deflections for transverse vibrations of shallow spherical shells is now examined. The same notations and assumptions as in Sect. 22.4.4 are used. The only difference is that we assume here large displacements and moderate rotations. Moderate rotations mean that it is justified to linearize the angular functions $\sin\theta$ and $\cos\theta$ in the equations. The definition of large displacement depends on the order of magnitude of the characteristic length used for obtaining the dimensionless equations of motions (see below). These standard assumptions lead to the well-known von Kármán equations, also called Marguerre's or Koiter's equations in the literature [22.19, 61]. *Hamdouni* and *Millet* have shown recently that these equations can also be obtained through an asymptotic method applied to the general equations of elasticity [22.62]. Like in the linear case (Sect. 22.4.4), the assumption of thin shallow shell allows one to write the equations of motion as a function of the circular coordinates (r, θ) that refer to the projection of a current point of the shell on the horizontal plane. Finally, we obtain [22.19]

$$\begin{cases} \nabla^4 w + \dfrac{\nabla^2 F}{R} + \rho h \ddot{w} = L(w, F) - \mu \dot{w} + p \,, \\ \nabla^4 F - \dfrac{Eh}{R}\nabla^2 w = -\dfrac{Eh}{2} L(w, w) \,, \end{cases} \tag{22.450}$$

where F is the Airy stress function, and where L is a bilinear quadratic operator which is written in circular coordinates as

$$L(w, F) = w_{rr}\left(\frac{F_r}{r} + \frac{F_{\theta\theta}}{r^2}\right) + F_{rr}\left(\frac{w_r}{r} + \frac{w_{\theta\theta}}{r^2}\right) - 2\left(\frac{w_{r\theta}}{r} - \frac{w_\theta}{r^2}\right)\left(\frac{F_{r\theta}}{r} - \frac{F_\theta}{r^2}\right) . \tag{22.451}$$

In (22.450), F contains linear and quadratic terms in w. Therefore, $L(w, F)$ contains quadratic and cubic terms in w. In total, the nonlinear equations of the shell contain linear, quadratic and cubic terms. With $R \to \infty$, (22.450) reduces to the nonlinear plate equations. In this case, only cubic terms are present.

Equation (22.450) can be put into nondimensional form with the change of variables [22.19]

$$\begin{aligned} r &= a\overline{r} \,, \\ t &= a^2\sqrt{\rho h/D}\,\overline{t} \,, \\ w &= h^3/a^2\,\overline{w} \,, \\ F &= Eh^7/a^4\overline{F} \,, \\ \mu &= \left(2Eh^4/Ra^2\right)\sqrt{\rho h/D}\,\overline{\mu} \,, \\ p &= Eh^7/Ra^6\overline{p} \,. \end{aligned} \tag{22.452}$$

Equation (22.450) becomes, with the overbars dropped for convenience,

$$\begin{cases} \nabla^4 w + \varepsilon_q \nabla^2 F + \ddot{w} \\ = \varepsilon_c L(w, F) + \varepsilon_q\left(-\mu\dot{w} + p\right) \,, \\ \nabla^4 F - \dfrac{a^4}{Rh^3}\nabla^2 w = -\dfrac{1}{2} L(w, w) \,. \end{cases} \tag{22.453}$$

Equation (22.453) has the advantage of highlighting a quadratic perturbation coefficient $\varepsilon_q = 12(1-\nu^2)h/R$ and a cubic perturbation coefficient $\varepsilon_c = 12(1-\nu^2)h^4/a^4$. In view of the assumptions of a thin shallow shell, the cubic nonlinear terms are much smaller than the quadratic ones. The quadratic terms are due to the curvature of the shell.

Expanding the solution on the linear eigenmodes

$$w(r, \theta, t) = \sum_n \Phi_n(r, \theta) q_n(t) \tag{22.454}$$

yields the set of coupled differential equations

$$\ddot{q}_n + \omega_n^2 q_n = \varepsilon_q\left(-\sum_p \sum_q \alpha_{npq} q_p q_q - \mu\dot{q} + p_n\right) + \varepsilon_c \sum_q \sum_q \sum_r \beta_{npqr} q_p q_q q_r \,, \tag{22.455}$$

which shows multiple cubic and quadratic coupling. For a plate, the coefficients α_{npq} are equal to zero. For shells, one can see an analogy with the interrupted pendulum presented in Sect. 22.7.1 in the sense that the quadratic nonlinearity is due to the asymmetry arising from the curvature.

22.8 Conclusion. Advanced Topics

A number of applications of interest in the field of structural acoustics and vibrations were not described in this chapter, since they are exhaustively presented in other chapters; this is, for example, the case of near-field acoustical holography and modal analysis. Also the area of active control of sound was only briefly men-

tioned, since the presentation of this technique would need a significant part devoted to signal processing.

In recent years, new theories have been developed in order to allow better prediction and modeling of structures and the related acoustic field in the medium frequency range, i. e., when modes overlap due to both damping and increasing modal density. In this context, a new model and the associated numerical method based on the theory of structural fuzzy has been given by *Soize* [22.63]. Fuzzy structures are systems composed by a well-defined *master* structure with other smaller subsystems attached on it, whose location, geometry and material properties are not known with certainty. One can think of the main body of a ship (or of a plane), with some attached equipment and/or ribs. The general idea is to describe the behavior of the subsystems with a probabilistic law; the input data are given in terms of mean value and dispersion. The advantage of such a technique is to greatly reduce the number of degrees of freedom. A recent paper by *Lyon* shows the analogy between SEA and structural fuzzy framework [22.64].

Several analytical models of structural acoustics and vibrations have been presented in this chapter. However, one should be aware of the fact that analytical solutions are generally hard to obtain in engineering applications. Therefore, numerical methods are required, and considerable work has been done in the field of computational structural dynamics over the last decades. Notice that analytical results are nonetheless very useful for testing the validity of numerical models. One can refer, for example, to the review by *Wachulec* et al. in order to get a comprehensive overview of the advantages and drawbacks of the main numerical methods applied to structure-borne sound, depending on the frequency range and structural complexity [22.65].

Finally, the design of smart materials for the active control of vibrations and sound is an active field and a good example of interdisciplinary work in structural acoustics. The goal in this area is often to use appropriate actuators and sensors in order to reduce the noise generated by structures. However, other applications such as enhancing or modifying intentionally some modal parameters, for example in musical instruments, are also potential applications. One difficulty is finding the appropriate locations for the actuators. Another problem is to find transducers that are insensitive to external electromagnetic fields. The interested reader can refer to a recent work by *Shih* et al. for more information [22.66].

References

22.1 F. Axisa: *Modelling of Mechanical Systems* (Kogan Page Science, London 2003)

22.2 K.G. McConnell: *Vibration Testing, Theory and Practice* (Wiley, New York 1995)

22.3 G. Derveaux, A. Chaigne, E. Becache, P. Joly: Time-domain simulation of a guitar: Model and method, J. Acoust. Soc. Am. **114**(6), 3368–3383 (2003)

22.4 O. Christensen, B.B. Vistisen: Simple model for low-frequency guitar function, J. Acoust. Soc. Am. **68**(3), 758–766 (1980)

22.5 R.H. Lyon, R.G. Dejong: *Theory and Applications of Statistical Energy Analysis* (Butterworth Heinemann, Newton 1995)

22.6 C.B. Burroughs, R.W. Fisher, F.R. Kern: An introduction to statistical energy analysis, J. Acoust. Soc. Am. **101**(4), 1779–1789 (1997)

22.7 R. Knobel: *An Introduction to the Mathematical Theory of Waves* (Am. Math. Soc., Providence 2000)

22.8 K.F. Graff: *Wave Motion in Elastics Solids* (Dover, Mineola 1991)

22.9 M. Abramowitz, I.A. Stegun: *Handbook of Mathematical Functions, with Formulas, Graphs, and Mathematical Tables* (Dover, Mineola 1972)

22.10 L. Rhaouti, A. Chaigne, P. Joly: Time-domain simulation and numerical modeling of the kettledrum, J. Acoust. Soc. Am. **105**(6), 3545–3562 (1999)

22.11 R.S. Christian, R.E. Davis, A. Tubis, C.A. Anderson, R.I. Mills, T.D. Rossing: Effect of air loading on timpani membrane vibrations, J. Acoust. Soc. Am. **76**(5), 1336–1345 (1984)

22.12 L. Meirovitch: *Fundamentals of Vibrations* (McGrawHill, New York 2001)

22.13 Y.Y. Yu: *Vibrations of Elastic Plates* (Springer, Berlin, Heidelberg 1996)

22.14 R.F.S. Hearmon: *An Introduction to Applied Anisotropic Elasticity* (Oxford Univ. Press, Oxford 1961)

22.15 A. Leissa: *Vibrations of Plates* (Acoust. Soc. Am., Melville 1993)

22.16 K.M. Liew, C.W. Lim, S. Kitipornchai: Vibrations of shallow shells: A review with bibliography, Trans. ASME Appl. Mech. Rev. **8**, 431–444 (1997)

22.17 W. Soedel: *Vibrations of Shells and Plates* (Marcel Dekker, New York 1981)

22.18 M.W. Johnson, E. Reissner: On transverse vibrations of spherical shells, Quart. Appl. Math. **15**(4), 367–380 (1956)

22.19 O. Thomas, C. Touzé, A. Chaigne: Non-linear vibrations of free-edge thin spherical shells: modal interaction rules and 1:1:2 internal resonance, Int. J. Solid Struct. **42**(1), 3339–3373 (2005),

Amazon EX1014 Page 962

22.20 L. Cremer, M. Heckl: *Structure-Borne Sound. Structural Vibration and Sound Radiation at Audio Frequencies* (Springer, Berlin, Heidelberg 1988)

22.21 Y.K. Tso, C.H. Hansen: The transmission of vibration through a complex periodic structure, J. Sound Vib. **215**(1), 63–79 (1998)

22.22 M.C. Junger, D. Feit: *Sound, Structures and Their Interaction* (Acoust. Soc. Am., Melville 1993)

22.23 S.D. Snyder, N. Tanaka: Calculating total acoustic power output using modal radiation efficiencies, J. Acoust. Soc. Am. **97**(3), 1702–1709 (1995)

22.24 P.T. Chen, J.H. Ginsberg: Complex power, reciprocity and radiation modes for submerged bodies, J. Acoust. Soc. Am. **98**(6), 3343–3351 (1995)

22.25 S.J. Elliott, M.E. Johnson: Radiation modes and the active control of sound power, J. Acoust. Soc. Am. **94**(4), 2194–2204 (1993)

22.26 L. Meirovitch: *Dynamics and Control of Structures* (Wiley, New York 1990)

22.27 J.N. Juang, M.Q. Phan: *Identification and control of mechanical systems* (Cambridge Univ. Press, New York 2001)

22.28 C.R. Fuller, S.J. Elliott, P.A. Nelson: *Active Control of Vibration* (Academic, London 1996)

22.29 A. Preumont: *Vibration Control of Active Structures* (Kluwer Academic, Dordrecht 2002)

22.30 M.L. Rumerman: The effect of fluid loading on radiation efficiency, J. Acoust. Soc. Am **111**(1), 75–79 (2002)

22.31 W.T. Baumann: Active suppression of acoustic radiation from impulsively excited structures, J. Acoust. Soc. Am. **90**(6), 3202–3208 (1991)

22.32 R. Ohayon, C. Soize: *Structural Acoustics and Vibration. Mechanical models, Variational Formulations and Discretization* (Academic, London 1998)

22.33 P. Filippi, D. Habault, J.P. Lefebvre, A. Bergassoli: *Acoustics: Basic physics, Theory and Methods* (Academic, London 1999)

22.34 C. Lesueur: *Rayonnement Acoustique des Structures, Collection de la Direction des Etudes et Recherches d'EDF* (Eyrolles, Paris 1988)

22.35 F. Fahy: *Foundations of Engineering Acoustics* (Academic, London 2001)

22.36 E.G. Williams: *Fourier Acoustics: Sound Radiation and NearField Acoustical Holography* (Academic, New York 1999)

22.37 A. Le Pichon, S. Berge, A. Chaigne: Comparison between experimental and predicted radiation of a guitar, Acustica united with Acta Acustica **84**, 136–145 (1998)

22.38 G.P. Gibbs, R.L. Clark, D.E. Cox, J.S. Vipperman: Radiation modal expansion: Application to active structural acoustic control, J. Acoust. Soc. Am. **107**(1), 332–339 (2000)

22.39 S.M. Kim, M.J. Brennan: Active control of harmonic sound transmission into an acoustic enclosure using both structural and acoustic actuators, J. Acoust. Soc. Am. **107**(5), 2523–2534 (2000)

22.40 S.D. Snyder, N.C. Burgan, N. Tanaka: An acoustic-based modal filtering approach to sensing system design for active control of structural acoustic radiation: theoretical development, Mech. Syst. Sig. Process. **16**(1), 123–139 (2002)

22.41 J.H. Ginsberg: *Mechanical and Structural Vibrations. Theory and Applications* (Wiley, New York 2001)

22.42 J. Woodhouse: Linear damping models for structural vibrations, J. Sound Vib. **215**(3), 547–569 (1998)

22.43 M.A. Biot: Thermoelasticity and irreversible thermodynamics, J. Appl. Phys. **27**(3), 240–253 (1956)

22.44 C. Zener: Internal friction in solids – I theory of internal friction in reeds, Phys. Rev. **215**, 230–235 (1937)

22.45 A. Chaigne, C. Lambourg: Time-domain simulation of damped impacted plates. Part I. Theory and experiments, J. Acoust. Soc. Am. **109**(4), 1422–1432 (2001)

22.46 M.E. McIntyre, J. Woodhouse: The influence of geometry on linear damping, Acustica **39**(4), 209–224 (1978)

22.47 R.M. Christensen: *Theory of Viscoelasticity. An Introduction* (Academic, New York 1982)

22.48 M.E. Gurtin, E. Sternberg: On the linear theory of viscoelasticity, Arch. Ration. Mech. Anal. **11**, 291–356 (1962)

22.49 A. Akay: Acoustics of friction, J. Acoust. Soc. Am **111**(4), 1525–1548 (2002)

22.50 R.I. Leine, D.H. Van Campen, A. De Kraker, I. Van den Steen: Stick-Slip Vibrations Induced by Alternate Friction Models, Nonlin. Dyn. **16**, 41–54 (1998)

22.51 J.H. Smith, J. Woodhouse: The tribology of rosin, J. Mech. Phys. Solids **48**, 1633–1681 (2000)

22.52 A.J. McMillan: A non-linear friction model for self-excited vibrations, J. Sound Vib. **205**(3), 323–335 (1997)

22.53 Y. Yoshitake, A. Sueoka: Forced self-excited vibration with dry friction. In: *Applied Nonlinear Dynamics and Chaos of Mechanical Systems with Discontinuities, number 28 in World Scientific Series on Nonlinear Science*, ed. by M. Wiercigroch, B. de Kraker (World Scientific, Singapore 2000) pp. 237–257

22.54 S.H. Crandall: The role of damping in vibration theory, J. Sound Vib. **11**(1), 3–18 (1970)

22.55 B. Denardo: Nonanalytic nonlinear oscillations: Christiaan Huygens, quadratic Schroedinger equations, and solitary waves, J. Acoust. Soc. Am. **104**(3), 1289–1300 (1998)

22.56 L.N. Virgin: *Introduction to Experimental Nonlinear Dynamics. A Case Study in Mechanical Vibrations* (Cambridge Univ. Press, New York 2000)

22.57 A.H. Nayfeh, D.T. Mook: *Nonlinear Oscillations* (Wiley, New York 1979)

Amazon EX1014 Page 963

22.58 G.S.S. Murthy, B.S. Ramakrishna: Nonlinear Character of Resonance in Stretched Strings, J. Acoust. Soc. Am. **38**, 461–471 (1965)
22.59 C. Valette: The mechanics of vibrating strings. In: *Mechanics of Musical Instruments*, *CISM Courses Lect.*, Vol. 355, ed. by A. Hirschberg, J. Kergomard, G. Weinreich (Springer, Wien 1995) pp. 115–183,
22.60 A. Watzky: Non-linear three-dimensional large-amplitude damped free vibration of a stiff elastic string, J. Sound Vib. **153**(1), 125–142 (1992)
22.61 M. Amabili, M.P. Paidoussis: Review of studies on geometrically nonlinear vibrations and dynamics of circular cylindrical shells and panels, with and without fluid-structure interaction, ASME Appl. Mech. Rev. **56**(4), 349–381 (2003)
22.62 A. Hamdouni, O. Millet: Classification of thin shell models deduced from the nonlinear three-dimensional elasticity. Part I: The shallow shells, Arch. Mech. **55**(2), 135–175 (2003)
22.63 C. Soize: A model and numerical method in the medium frequency range for vibroacoustic predictions using the theory of structural fuzzy, J. Acoust. Soc. Am. **94**(2), 849–865 (1993)
22.64 R.H. Lyon: Statistical energy analysis and structural fuzzy, J. Acoust. Soc. Am. **97**(5), 2878–2881 (1995)
22.65 M. Wachulec, P.H. Kirkegaard, S.R.K. Nielsen: *Methods of estimation of structure borne noise in structures – Review*, *Techn. Rep.*, Vol. 20 (Aalborg Univ., Aalborg 2000)
22.66 H.R. Shih, H.S. Tzou, M. Saypuri: Structural vibration control using spatially configured opto-electromechanical actuators, J. Sound Vib. **284**, 361–378 (2005)

Amazon EX1014 Page 964

Noise

23. Noise

Noise is discussed in terms of a source–path–receiver model. After an introduction to sound propagation and radiation efficiency, the quantities measured for noise control are defined, and the instruments used for noise measurement and control are described.

The noise emission of sources is discussed with emphasis on the determination of the sound power level of a variety of sources. The properties of two very significant sources of environmental noise, aircraft and motor vehicles, are presented. Tire noise is identified as a major noise source for motor vehicles. Criteria for the noise emission of sources are given, and the basic principles of noise control are presented. A section on active control of noise is included.

The path from the source to the receiver includes propagation in the atmosphere, noise barriers, the use of sound-absorptive materials, and silencers. Guidance is given on the determination of sound pressure level in a room when the sound power output of the source is known.

At the receiver, the effects of noise are presented, including both hearing damage and annoyance. A brief section is devoted to sound quality.

Finally, noise regulations and policies are discussed. Many activities of the US government are discussed, and information on both state and local noise policies and regulations are presented. The activities of the European Union are included, as are the noise policies in many countries.

23.0.1 The Source–Path–Receiver Model 961
23.0.2 Properties of Sound Waves 962
23.0.3 Radiation Efficiency 963
23.0.4 Sound Pressure Level of Common Sounds 965
23.1 **Instruments for Noise Measurements** 965
23.1.1 Introduction 965
23.1.2 Sound Level 966
23.1.3 Sound Exposure and Sound Exposure Level 967
23.1.4 Frequency Weightings 967
23.1.5 Octave and One-Third-Octave Bands 967
23.1.6 Sound Level Meters 968
23.1.7 Multichannel Instruments 969
23.1.8 Sound Intensity Analyzers 969
23.1.9 FFT Analyzers 969
23.2 **Noise Sources** 970
23.2.1 Measures of Noise Emission 970
23.2.2 International Standards for the Determination of Sound Power ... 973
23.2.3 Emission Sound Pressure Level 977
23.2.4 Other Noise Emission Standards .. 978
23.2.5 Criteria for Noise Emissions 979
23.2.6 Principles of Noise Control 981
23.2.7 Noise From Stationary Sources 984
23.2.8 Noise from Moving Sources 987
23.3 **Propagation Paths** 991
23.3.1 Sound Propagation Outdoors 991
23.3.2 Sound Propagation Indoors 993
23.3.3 Sound-Absorptive Materials 995
23.3.4 Ducts and Silencers 998
23.4 **Noise and the Receiver** 999
23.4.1 Soundscapes 999
23.4.2 Noise Metrics 1000
23.4.3 Measurement of Immission Sound Pressure Level 1000
23.4.4 Criteria for Noise Immission 1000
23.4.5 Sound Quality 1004
23.5 **Regulations and Policy for Noise Control** 1006
23.5.1 United States Noise Policies and Regulations 1006
23.5.2 European Noise Policy and Regulations 1009
23.6 **Other Information Resources** 1010
References 1010

Amazon EX1014 Page 965

23.0.1 The Source–Path–Receiver Model

The standard definition of noise is *unwanted sound*. This definition implies that there is an observer who hears the noise and makes a judgment based on a number of factors that what is heard is not wanted. This judgment may be made because the sound is too loud, is annoying, or has an unpleasant quality. In all cases, the receiver applies some metric to what is heard in order to characterize sound as noise. In other cases, the level of the sound is high enough to cause hearing damage, and the listener may accept the noise levels, as in an industrial situation, or may actually want the sound, as at a loud concert or in an automobile with a very loud audio system. The concept of *unwanted sound* also implies that there is a person who wants the sound level reduced; hence, the field of noise control has been developed to satisfy these needs. In some cases, control of noise is an administrative matter such as setting hours of operation for noisy outdoor activities or otherwise managing noise sources to make the levels acceptable. In most cases, however, a technical analysis of the source, an understanding of the propagation of sound from the source to the receiver, and application of one or more psychoacoustic metrics is required to find a solution to a noise problem. This process may be called *noise control engineering*. This source–path–receiver model was first proposed by *Bolt* and *Ingard* in 1956 [23.1], and has proved to be very useful as a systematic way to approach noise control problems. There are many situations where the distinction between a source and a path is not clear; for example when sound travels from a source through a structure and is radiated by the structure Chap. 22. Nevertheless, the above model has proved to be useful in many practical situations.

Another concept that has proved to be useful is the distinction between *emission* and *immission*. The verb emit is common in the English language, and means to send out. The verb *immit* is currently much less common, but has a long history, and means to receive [23.2]. Noise control then deals with noise emission from sources – using a variety of metrics – and noise immission is the reception of sound by an observer – expressed as some metric based on sound pressure level.

23.0.2 Properties of Sound Waves

Noise propagation, for the purposes of this chapter, can be described in terms of linear acoustics Chap. 3. Exceptions include propagation of sonic booms and very-high-amplitude sound waves such as in gas turbines and other devices. For such problems, nonlinear acoustical theory is needed Chap. 8, which will not be covered here. The physical quantities most often used in noise control are sound pressure, particle velocity, sound intensity and sound power. A one-dimensional treatment serves to illustrate the principles involved. The linear one-dimensional wave equation may be expressed in terms of sound pressure as

$$\frac{\partial^2 p}{\partial x^2} - \frac{1}{c^2}\frac{\partial^2 p}{\partial t^2} = Q\,, \tag{23.1}$$

where p is the sound pressure, x is distance, and t is time. The speed of sound c is given by

$$c = 20.05\sqrt{T}\,, \tag{23.2}$$

where T is the temperature in Kelvin. At 20 °C, $c = 343.3$ m/s, rounded to 344 m/s for most noise control problems.

The *source term* Q in (23.2) represents the various sources of sound, and may be in the form of fluctuations in mass, force, or heat introduced into the medium. Or, it may be nonlinear terms placed on the right-hand side of the equation as in the *acoustic analogy* proposed by *Lighthill* [23.3] which explains the generation of sound by turbulence Chap. 3.

For $Q = 0$ in an unbounded medium at rest, any function, $f(x - ct)$, a propagating wave, satisfies the wave equation. The exact solution is determined by the nature of the sources and the boundary conditions. The particle velocity (for one-dimensional propagation) is found from

$$\rho\frac{\partial u}{\partial t} = -\frac{\partial p}{\partial x}\,. \tag{23.3}$$

Where u is the particle velocity. As will be shown below, the sound pressure and particle velocity in almost all cases are small compared with atmospheric pressure and the speed of sound, respectively. Therefore, air can be considered a linear medium for the propagation of sound waves, and the sound pressures as a function of time from two (or more) sources can be added to find the total pressure p

$$p(t) = p_1(t) + p_2(t)\,. \tag{23.4}$$

However, the quantity measured by sound level meters and other analyzers is the root-mean-square (RMS) pressure over some time interval, which may be very short. In this case, the way two sound pressures are combined depends on the correlation coefficient between them. The total mean-square pressure is

$$\overline{p^2} = \overline{p_1^2} + \overline{p_2^2} + \overline{2p_1 p_2}\,, \tag{23.5}$$

where the overbars represent time averages. When p_1 and p_2 are uncorrelated, the cross-term in (23.5) is zero, and it is the mean square pressures that add. This is the case in most noise control situations where the noise comes from one or more different sources. When $p_1 = p_2$, it is the pressures that add. When $p_1 = -p_2$, generally the objective in active noise control, the resulting mean-square pressure is zero. For sinusoidal signals, the mean-square pressure depends on the amplitudes of the waves and the phase difference between them.

Other quantities of importance are the intensity $\boldsymbol{I}$ of the sound wave, a vector in the direction of propagation that is the sound energy per unit of area perpendicular to an element of surface area $\mathrm{d}\boldsymbol{S}$, Chap. 6. For a source of sound, the total sound power W radiated by the source is given by

$$W = \int_S \boldsymbol{I} \cdot \mathrm{d}\boldsymbol{S} \,, \tag{23.6}$$

where the integral is over a surface that surrounds the source. Sound power is a widely used measure of the noise emission of the source. Its determination using sound intensity is advantageous in the presence of background noise because, in the absence of sound-absorptive materials inside the surface, any sound energy that enters the surface from the outside also leaves the surface from the inside, and thus does not affect the radiated power. In practice, the sound intensity on the surface is determined by scanning or by measurements at a finite number of measurement positions, and only an approximation to the ideal situation is obtained Chap. 6. Other techniques for the determination of the sound power of sources depend on an approximation of the intensity in terms of mean-square pressure, and are discussed later in this chapter.

The Decibel as a Unit of Level

As will be shown below, the magnitude of the quantities associated with a sound wave described above vary over a very wide range, and it is convenient to use logarithms to compress the scale. Logarithms are also useful in many noise transmission problems because quantities that are multiplicative in terms of the quantities themselves are additive using logarithms. The decibel is a unit of level, and is defined as

$$L_x = 10 \log \frac{X}{X_0} \,, \tag{23.7}$$

where X is a quantity related to energy, X_0 is a reference quantity, and log is the logarithm to the base 10. In the case of sound pressure, $X = p^2$, the mean square pressure and $X_0 = p_0^2$. The reference pressure p_0 is standardized at 20 μPa (2×10^{-5} N/m^2). The sound pressure level can then be written as

$$L_\mathrm{p} = 10 \log \frac{p^2}{(2 \times 10^{-5})^2} \mathrm{dB} \,. \tag{23.8}$$

For sound power and sound intensity, the reference levels are 10^{-12} W and 10^{-12} W/m^2, respectively, and the corresponding sound power and sound intensity levels are

$$L_\mathrm{W} = 10 \log \frac{W}{10^{-12}} \ \mathrm{dB} \,, \tag{23.9}$$

$$L_\mathrm{I} = 10 \log \frac{I}{10^{-12}} \ \mathrm{dB} \,. \tag{23.10}$$

Note that all three quantities above are expressed in decibels; the decibel is a *unit of level*, and may be used to express a variety of quantities related to energy relative to a reference level. This fact often causes confusion because the quantity being expressed in decibels is often not stated ("The level is 75 dB."), and the meaning of the statement is not clear. The wide use of sound power level as a measure of noise emission can easily cause confusion between sound power level and sound pressure level. In this situation, it is convenient, and common in the information technology industry, to omit the 10 before the logarithm in (23.9), and express the sound power level in bels, where one bel = 10 dB.

Relative Magnitudes

As mentioned above, the quantities associated with a sound wave are small. For example, a sound pressure level of 90 dB is relatively high and corresponds to an RMS sound pressure of

$$p_A = \sqrt{\left[\left(4 \times 10^{-10}\right) \mathrm{x} 10^{90/10}\right]} = 0.63 \,\mathrm{Pa} \,. \tag{23.11}$$

Since atmospheric pressure p_at is nominally 1.01×10^5 Pa, the ratio p_0/p_at is very small: 0.62×10^{-5}.

The particle velocity can be determined from (23.3) assuming plane wave propagation of a sinusoidal wave having a radian frequency ω ($\omega = 2\pi f$). In this case, (23.3) reduces to $p = \rho c u$ where ρ is the density of air, nominally 1.18 kg/m^2. The particle velocity is then

$$u = 0.63/(1.18\mathrm{x}344) = 1.6 \times 10^{-3} \,\mathrm{m/s} \tag{23.12}$$

and the ratio u/c is 4.7×10^{-6}. The particle velocity is very small compared with the speed of sound, and the model of a wave traveling with speed c and having a particle velocity u is justified. When this is not the case, the compressional portion of the wave travels with

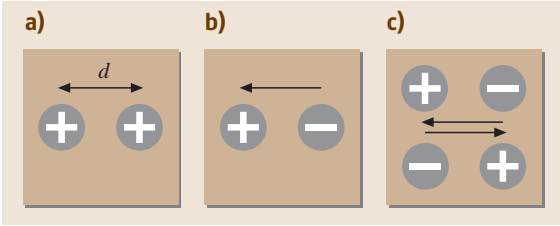


Fig. 23.1a–c Schematic of loudspeakers in an enclosure. **(a)** Two loudspeakers operating in phase to form a monopole. **(b)** Two loudspeakers operating out of phase to form a dipole. **(c)** Four speakers that form a quadrupole

speed $c+u$ and the rarefaction travels with speed $c-u$. This phenomenon is important when considering the propagation of sonic booms and other finite-amplitude waves.

23.0.3 Radiation Efficiency

The radiation efficiency of ideal sources is best described in terms of the sound power radiated by higher-order sources relative to monopole radiation, as discussed below. For actual sources, the radiation efficiency can be expressed in terms of the sound power output of the source relative to the mechanical power input. As shown below, the acoustic power radiated by an actual source is a very small fraction of the mechanical power of the source.

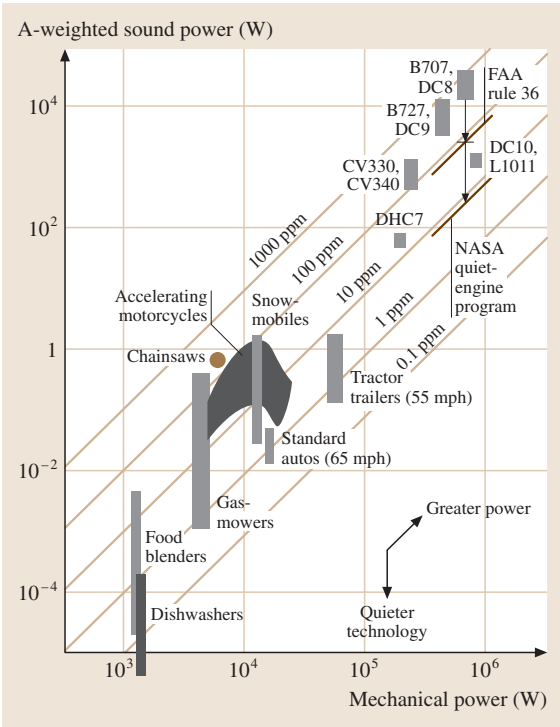


Fig. 23.2 A-weighted sound power versus mechanical power. (After Shaw [23.4] with permission, Phys. Today 28(1), 46 (1975) ©1975, AIP)

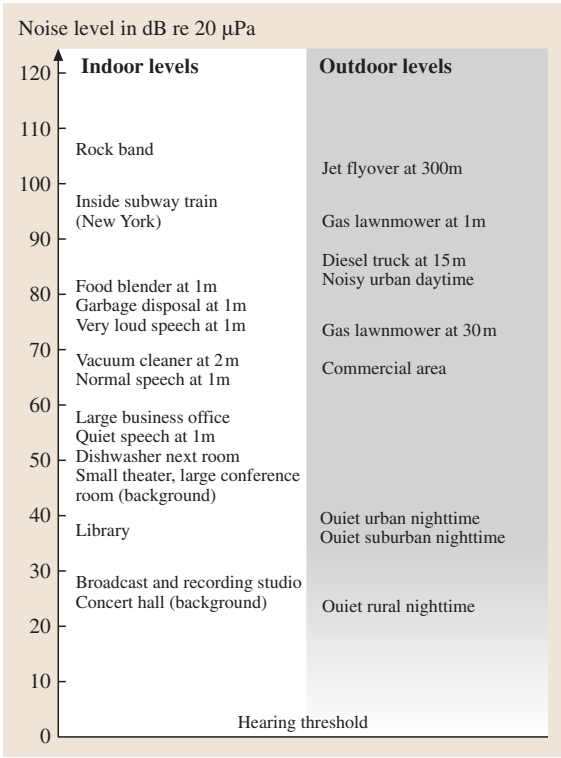


Fig. 23.3 Typical levels for indoor and outdoor environments. (After Burgé [23.5], with permission)

Radiation Efficiency of Ideal Sources

One way of classifying sources and determining the efficiency of the radiation of sound is in terms of a monopole and higher-order sources. If a sinusoidal source, such as two small baffled loudspeakers operating in phase having a radian frequency $\omega = 2\pi f$ injects mass per second with amplitude Q_o into the air, the power W_m radiated by the combination of the two sources can be shown to be [23.6]

$$W_{\mathrm{m}} = \frac{(\omega^2 Q_o^2)}{8\pi\rho c} \,. \tag{23.13}$$

The situation is illustrated in Fig. 23.1.

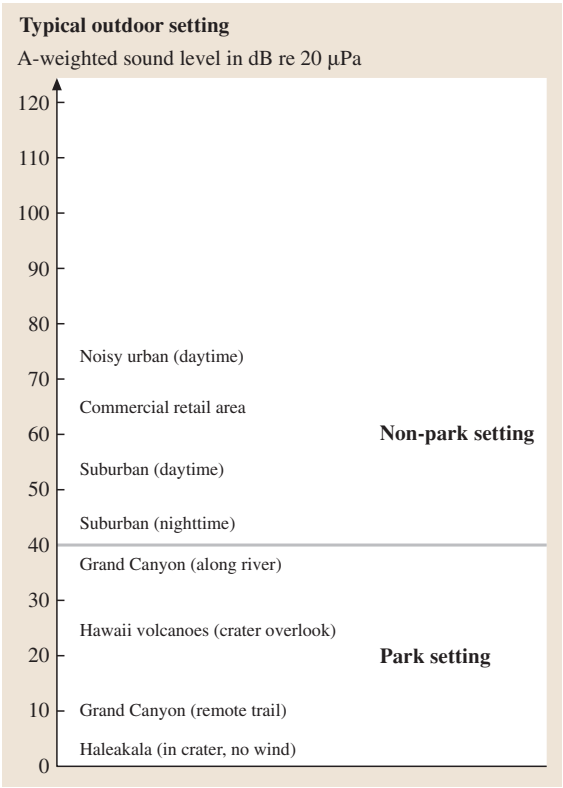


Fig. 23.4 Comparison of outdoor A-weighted levels in different environments. (After Miller [23.7], with permission)

The plus signs indicate that the two loudspeakers are operating in phase. The distance between all loudspeakers is d. In the second case (b) the two loudspeakers are operated out of phase and form a dipole with a dipole moment in the direction shown. In this case, the total power radiated relative to monopole radiation can be shown [23.6] to be

$$W_\mathrm{d} = \frac{1}{24}\,(kd)^2\,W_\mathrm{m}\,, \qquad (23.14)$$

where k is the wave number (ω/c) and d is the distance between the two sources. If two dipoles with opposite dipole moments are combined, the result is a quadrupole – as illustrated in (c). In this case, the total power radiated relative to monopole radiation can be shown [23.6] to be:

$$W_\mathrm{q} = \frac{1}{120}\,(kd)^4\,W_\mathrm{m}\,. \qquad (23.15)$$

It can be seen that at small values of kd (low frequencies), dipole and quadrupole sources of sound are much less efficient in radiating sound than monopoles. The dipole case is especially important because one way to reduce the source noise level is to create a secondary source of opposite phase near the primary sources. The sound radiated by the secondary source partially cancels the sound radiated by the primary source, and the radiation efficiency is reduced.

Radiation Efficiency of Machines

The sound power radiated by a source is also a very small fraction of the mechanical power driving the source. *Shaw* [23.4] studied the radiation efficiency of a number of practical sources, and found that only a small fraction of the mechanical power was converted to sound. Fig. 23.2 shows the relationship between A-weighted sound power and mechanical power for a wide variety of sources.

23.0.4 Sound Pressure Level of Common Sounds

Many authors have shown the relationship between sound pressure level and many common sounds. Data adapted from *Burgé* [23.5] are shown in Fig. 23.3. A-weighted sound pressure levels range from about 25 to 110 dB, which is a range in sound pressure of approximately 1:18 000. Similar data, but at lower sound pressure levels, have been adapted from Miller and are shown in Fig. 23.4. The vertical scales are labeled differently to conform to the practice of each author. As can be seen, there is a considerable difference for certain common terms; environmental levels may vary greatly in urban and suburban areas.

23.1 Instruments for Noise Measurements

23.1.1 Introduction

The most common quantity for control and assessment of noise is the frequency-weighted sound level, as measured by a sound level meter. Exponential time weighting may also be employed for measurements of frequency-weighted sound level. Sound pressure levels are usually measured through constant-percentage-bandwidth filters. Sound intensity is commonly used for localization of noise sources and for direct determination of sound

power level. As discussed in Sect. 23.2.1, measurements of time-average sound pressure levels are also widely used for the determination of sound power levels. The time-average sound level is also known as the equivalent-continuous sound level.

23.1.2 Sound Level

Sound pressure almost always varies with the position of the receiver in space and with time. When measured by a sound level meter, the instantaneous sound pressure signal is frequency weighted, squared, time integrated, and time averaged before the logarithm is taken to display the result in decibels relative to the standard reference pressure. The process is illustrated by the following expression for a time-averaged frequency-weighted sound level L_{wT} in decibels:

$$L_{\mathrm{wT}} = 10\log\left(\frac{\left[(1/T)\int_{-T}^{t} p_{\mathrm{w}}^2(\xi)\,\mathrm{d}\xi\right]^{1/2}}{p_0}\right)^2, \tag{23.16}$$

where T is the duration of the averaging time interval, ξ is a dummy variable for time integration over the averaging time interval ending at the time of observation t, $p_{\mathrm{w}}(\xi)$ is the instantaneous frequency-weighted sound pressure signal in Pascals, and p_0 is the standard reference pressure of 20 μPa.

The numerator of the argument of the logarithm in (23.16) represents the root-mean-square frequency-weighted sound pressure over the duration of the averaging time interval. In principle, there is no time weighting involved in a determination of a root-mean-square sound pressure.

The frequency weighting applied to the instantaneous sound-pressure signal could be either the standard A or C weighting described below, or the weighting of a bandpass filter, in which case the result is a band sound pressure level. When reporting the result of a measurement of sound level, the frequency weighting should always be stated.

In general, for measurements of time-average sound level, it is important to record both the duration of the averaging time interval and the time of observation at the end of the averaging time. Sound level meters that display time-average sound levels are integrating–averaging sound level meters.

For applications such as determining estimates of the sound level that would have been indicated if the contaminating influence of background noise had not been present, for combining narrow-band sound pressure levels into wider-bandwidth sound pressure level, or for calculating sound power levels from measurements of corresponding sound pressure levels, it is necessary to work with mean-square sound pressures, not with root-mean-square sound pressures.

Before the development of digital technology, sound level meters utilized a dial-and-pointer system to display the level of the sound pressure signal. These instruments employ exponential time weighting as illustrated by the following expression for exponential-time-weighted frequency-weighted sound level $L_{w\tau}(t)$ in decibels:

$$L_w\tau(t) = 10\log\left(\frac{\left[(1/\tau)\int_{-\infty}^{t} p_{\mathrm{w}}^2(\xi)\mathrm{e}^{-(t-\xi)/\tau}\,\mathrm{d}\xi\right]^{1/2}}{p_0}\right)^2, \tag{23.17}$$

where τ is one of the standardized time constants, ξ is a dummy variable of time integration from some time in the past, as indicated by the $-\infty$ for the lower limit of the integral, to the time t when the level is observed, and the other terms are as described above for the time-average sound level. The numerator in the argument of the logarithm in (23.17) represents an exponentially-time-weighted quasi-RMS sound pressure. The exponential time weighting de-emphasizes the contributions to the integral from sound-pressure signals at earlier times, with the degree of de-emphasis increasing as the time constant increases.

By international agreement, the two standardized exponential time constants are 125 ms for *fast* or F time weighting and 1000 ms for *slow* or S time weighting. The time weighting is applied to the square of the instantaneous frequency-weighted sound-pressure signal. Instruments that measure time-weighted sound levels are conventional sound level meters.

Note that in contrast to a time-average sound level, indications of exponential-time-weighted sound level vary continuously on the display device of the sound level meter.

A maximum sound level is the highest time-weighted sound level occurring within a stated time interval. A *hold* capability is needed to display an indication of a maximum sound level on a conventional sound level meter. Maximum sound levels are not the same as peak sound levels.

Although a proper description of a measurement of a sound level is, for example, "the A-weighted sound level was 90 dB", the statement "the sound level was

90 dB(A)" is widely used, and implies that the decibel is A-weighted. The instantaneous sound pressure signal is frequency weighted, not the decibel.

23.1.3 Sound Exposure and Sound Exposure Level

For transient sounds (including the sounds produced by many different kinds of machines, the sound of the pass by of an automobile or motorcycle or the overflight of an aircraft, the sound from blasting or explosions, and sonic booms), the most appropriate quantity to measure is sound exposure or sound exposure level. Instruments that measure sound exposure level are integrating sound level meters. Sound exposure may be measured with one of the standardized frequency weightings.

Sound exposure encompasses the magnitude or level of the sound pressure and its duration in a single quantity. The expression for a frequency-weighted sound exposure E_w, in Pascal-squared seconds, is as follows

$$E_w = \int_{t_1}^{t_2} p_w^2(t)\,dt \qquad (23.18)$$

with running time in seconds. In principle, no time weighting is involved in a determination of sound exposure according to (23.18).

The frequency-weighted sound exposure level L_{wE} in decibels, is given by

$$L_{wE} = 10 \log E_w/E_0)\,, \qquad (23.19)$$

where E_0 is the reference sound exposure equal to $(p_0^2 T_0) = (20\mu Pa)^2$ x$(1s)$ or the product of the square of the reference pressure and the reference time for sound exposure of $T_0 = 1s$.

It is often necessary to make use of the link between a measurement of the sound exposure level for a transient sound occurring in a given time interval and the corresponding time-average sound level. For a given frequency weighting, the relation is given by the following

$$L_{wT} = L_{wE} - 10 \log (T/T_0)\,, \qquad (23.20)$$

where T is the averaging time for the determination of time-average sound level, in seconds, and T_0 is the reference time of 1 s. The relationship of (23.20) may be extended to the determination of the time-average sound level corresponding to the total sound exposure of a series of transient sounds occurring within a given time interval such as 8 h or 24 h.

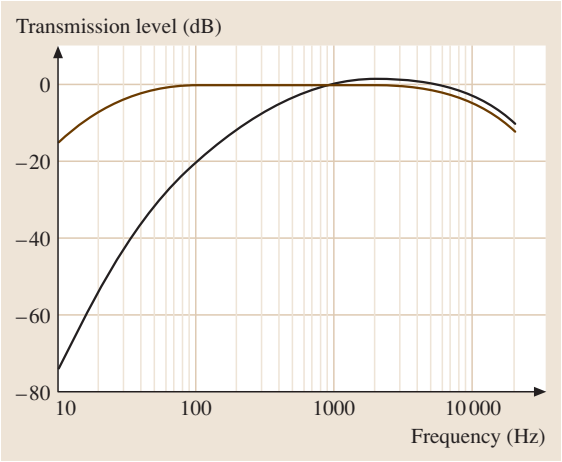


Fig. 23.5 Design goals for A- and C-frequency weightings

23.1.4 Frequency Weightings

Specifications for A- and C-weighting as well as a new Z-weighting are given in IEC 61672-1:2002 [23.8]. Design goals for the A- and C-weightings are shown in Fig. 23.5. The design goal for the Z-weighting is flat (transmission level = 0 dB) over the frequency range 10–20 kHz.

23.1.5 Octave and One-Third-Octave Bands

In general, frequency-weighted sound levels are not adequate for the diagnosis of noise problems and the design and implementation of engineering controls. Sound levels do not contain enough information to calculate measures of human response such as loudness level

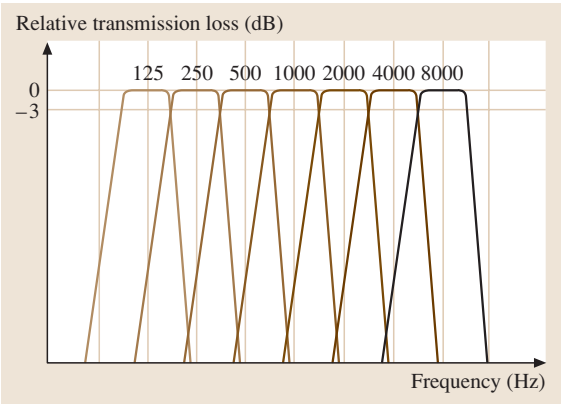


Fig. 23.6 Idealized octave-band filters for nominal mid-band frequencies from 125 Hz to 8 kHz

Table 23.1 Nominal octave and one-third-octave midband frequencies in Hz

ob	(1/3)ob	ob	(1/3)ob	ob	(1/3)ob
31.5	16	250	200	2000	1600
	31.5		250		2000
	40		315		2500
63	50	500	400	4000	3150
	63		500		4000
	80		630		5000
125	100	1000	800	8000	6300
	125		1000		8000
	160		1250		10000

ob = octave band

or ratings of room noise such as those obtained from noise criterion (NC) and other criteria by means of a curve-tangent method (Chap. 11). In these cases, a set of bandpass filters covering octave- or one-third-octave frequency bands should be used. The filters may be implemented by analog or digital techniques. Idealized octave-band filter shapes are shown in Fig. 23.6 for the 125 Hz to 8 kHz range of nominal midband frequencies. This range is adequate for many noise problems. Sound pressure levels in the octave bands with nominal midband frequencies of 31.5 Hz and 63 Hz are important for many applications, e.g., noise from heating, ventilating, and air-conditioning equipment in rooms.

There are three one-third-octave bands in each octave band. Nominal midband frequencies are shown in Table 23.1. The standardized midband frequencies increase by a factor of ten in each decade. Specifications for octave-band and fractional-octave-band filters are given in IEC 61260:1995.

23.1.6 Sound Level Meters

A sound level meter consists of a microphone, an amplifier and means to process the waveform of the sound-pressure signal from the microphone according to the equations above. There may be an analog or a digital readout or other device to indicate the measured sound levels. Extensive analog, or digital, or a combination of analog and digital signal processing may be utilized. Storage devices may include digital memory, computers, and printers.

A sound level meter should conform to the requirements of IEC 61672-1:2002 [23.8]. This standard provides design goals for various electroacoustical requirements along with appropriate tolerance limits around the design goals for class 1 and class 2 performance categories. The two performance classes differ mainly in the tolerance limits and the ranges of environmental conditions over which an instrument conforms to the requirements within the tolerance limits.

Sound level meters are intended for measurement of sounds that are audible to humans, generally assumed to be in the frequency range from 20 Hz to 20 kHz.

Microphones are covered in detail in Chap. 24. Sound level meters generally use a condenser microphone, either with a direct-current (DC) polarizing voltage or pre-polarization to provide the electrostatic field between the diaphragm and back plate.

The acoustical sensitivity of a measuring system should be checked using a class 1 or class 2 sound calibrator that produces a known sound pressure level at a specified frequency in the cavity of a coupler into which the microphone is inserted [23.9]. More details on means to establish the sensitivity of acoustical instruments may be found in Chap. 15.

In the presence of turbulent airflow, pressure fluctuations at the microphone diaphragm will occur that are not related to the sound pressure in the sound field. In this case, a windscreen – which may be made from an open-cell material, a metal, or a nonmetallic fabric – may be used. The insertion loss of a windscreen is the difference between the sound pressure level measured without and with the windscreen (in the absence of airflow), and may be determined in a free or a diffuse sound field. A standard for measurement of windscreen performance is available [23.10]. The insertion loss of windscreens that do not have spherical shapes may vary with sound incidence angle.

Microphones are generally designed to have their best frequency response from a specified reference direction of sound incidence in a free sound field or in response to sounds incident on the microphone from random directions, i. e., so-called free-field or random-incidence microphones. The specifications in IEC 61672-1:2002 apply equally to either microphone type when installed on a sound level meter.

A free-field microphone should be used when there is a principal direction from which the sound is incident on the microphone. A random-incidence microphone is preferred for applications where the direction of sound incidence is unknown, unpredictable, or varies with time, a situation commonly encountered when measuring noise levels in a factory or community.

In addition to the time-average, time-weighted, and peak sound levels described above, many sound level meters can record maximum and minimum levels in a given time interval, as well as statistical measures

Amazon EX1014 Page 972

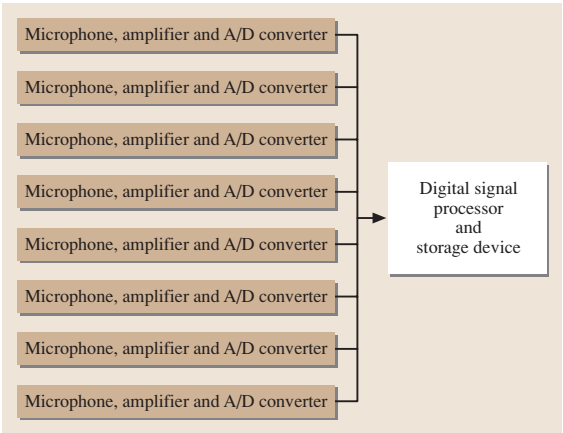


Fig. 23.7 Block diagram of a multichannel instrument using digital signal processing

such as the sound level exceeded at various percentages of a time interval, e.g., 10% of the time in an hour of observations. Performance specifications for the measurement of percentile sound level are not standardized, and the results may vary depending on the manufacturer of the instrument and the percentile of interest, with the greatest variations at the extremes of the percentiles.

23.1.7 Multichannel Instruments

Many applications for noise control are best satisfied by use of a microphone array. These include measurement of sound pressure level at multiple positions on a measurement surface for determination of sound power, and measurements at several locations around a time-varying sound source. In the first case, several microphones may be connected to a multiplexer, and the outputs sampled sequentially. In the second case, the microphones may each be connected to an amplifier and analog-to-digital (A/D) converter. High sampling rates (e.g., greater than 40 kHz) are required. The data are sent to a digital signal processor and storage device, for example, a digital computer. A block diagram of such a system is shown in Fig. 23.7.

The number of samples of sound pressure level data that can be stored in a multichannel measurement system depends on the available storage capacity, which can be quite large in the case of systems used for monitoring noise in the community and around airports.

23.1.8 Sound Intensity Analyzers

Sound intensity is covered in detail in Chap. 25. Sound intensity analyzers often use two closely spaced microphones to approximate the pressure gradient in a sound field. Particle velocity is found by integration of the time derivative of the sound-pressure gradient (23.3). Sound pressure is the average of the pressures at the two microphones. A block diagram of a sound intensity meter is shown in Fig. 23.8. Processing of the sampled signals may be accomplished either with analog circuits or digitally. Standards for sound intensity analyzers are available [23.11, 12].

23.1.9 FFT Analyzers

Unlike octave-band and one-third-octave band filters, which are proportional (or constant-percentage) bandwidth filters, a fast Fourier transform (FFT) analyzer is essentially a set of fixed-bandwidth filters. The FFT is a computational implementation of the discrete Fourier transform that produces a set of discrete-frequency spectral lines. The number of spectral lines in a given frequency interval depends on the number of samples of the time series obtained from digital sampling of the sound-pressure signal. If a periodic wave is sampled

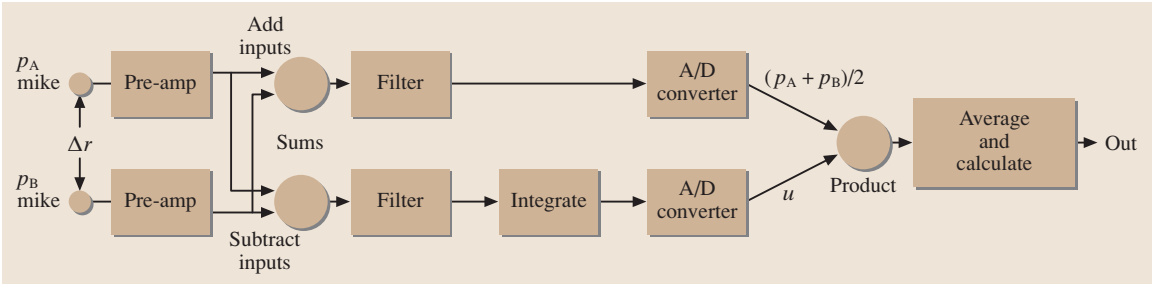


Fig. 23.8 Block diagram of an analog-to-digital sound intensity analyzer with octave-band filters. Alternatively, the preamplifier outputs of the microphones could be suitably amplified and converted to digital format; all further processing would then be done digitally

Amazon EX1014 Page 973

with a sampling period that is not an integral number of wavelengths of the wave, spectral *leakage* occurs. FFT analyzers contain *windows* to improve spectral estimates – the Hanning window is the most common. There are no national or international standards for the performance of FFT analyzers. The results of measurements by FFT analyzers may vary depending on the design implementation by the manufacturer or computer programmer.

23.2 Noise Sources

In this section, methods for the specification of noise emissions are given, noise emission criteria are described, and some basic principles of noise control are presented. A general description of noise control for stationary sources is presented, and some information on vehicle noise and aircraft noise is given. A short section on the principles of active noise control is included.

23.2.1 Measures of Noise Emission

This section is an edited version of a textbook chapter of [23.13].

Two quantities are needed to describe the strength of a noise source, its *sound power level* and its *directivity*.

The sound power level is a measure of the total sound power radiated by the source in all directions and is usually stated as a function of frequency, for example, in one-third octave bands. The sound power level is then the preferred descriptor for the emission of sound energy by noise sources.

The directivity of a source is a measure of the variation in its sound radiation with direction. Directivity is usually stated as a function of angular position around the acoustical center of the source and also as a function of frequency.

From the sound power level and directivity, it is possible to calculate the sound pressure levels produced by the source in the acoustical environment in which it operates. In Sect. 23.3.2, a classical method for this calculation is presented – as is an alternative method for long and flat rooms.

A source may set a nearby surface into vibration if it is rigidly attached to that surface, causing more sound power to be radiated than if the source were vibration isolated. Both the operating and mounting conditions of the source therefore influence the amount of sound power radiated as well as the directivity of the source. Nonetheless, the sound power level alone is useful for: comparing the noise radiated by machines of the same type and size as well as by machines of different types and sizes; determining whether a machine complies with a specified upper limit of noise emission; planning in order to determine the amount of transmission loss or noise control required; and engineering work to assist in developing quiet machinery and equipment.

Expanding the dot product in (23.6) allows the surface integral to be written in terms of scalar quantities

$$W = \int_S I_n \, \mathrm{d}S \,, \tag{23.21}$$

where $I_n = I\cos(\theta)$ is the component of sound intensity *normal* to the surface at the location of $\mathrm{d}\boldsymbol{S}$; $\mathrm{d}\boldsymbol{S}$ is the magnitude of the elemental surface area vector.

The integral may be carried out over a spherical or hemispherical surface that surrounds the source. Other regular surfaces, such as a parallelepiped or a cylinder, are also used in practice, and, in principle, any closed surface can be used. If the source is nondirectional and the integration is carried out over a spherical surface having a radius r and centered on the source, sound intensity and sound power are related by

$$I(\text{at } r) = I_n(\text{at } r) = \frac{W}{S} = \frac{W}{4\pi r^2} \,, \tag{23.22}$$

where I is the magnitude of intensity on the surface (at radius r), I_n is the normal component of intensity on the surface (at radius r), W is the sound power, S is the area of spherical surface ($4\pi r^2$), and r is the radius of the sphere.

In general, a source is directional, and the sound intensity is not the same at all points on the surface. Consequently, an approximation must be made to evaluate the integral of (23.21). It is customary to divide the measurement surface into a number of subsegments, each having an area S_i, and to approximate the normal component of the sound intensity on each surface subsegment. The sound power of the source may then be calculated by a summation over all of the surface subsegments:

$$W = \sum_i I_{ni} S_i \,, \tag{23.23}$$

here I_{ni} is the normal component of sound intensity averaged over the i-th area segment, S_i is the i-th area segment, and i is the number of segments.

Amazon EX1014 Page 974

When each segment of the measurement surface has the same area,

$$W = S \times \sum_i I_{ni} = S \times \langle I_n \rangle \,, \tag{23.24}$$

where $\langle I_n \rangle$ is the average value of the normal sound intensity over the measurement surface, and S is the total area of the measurement surface.

The sound power level is then

$$L_W = 10 \log \frac{W}{W_0} \,, \tag{23.25}$$

where W_0 is the standard reference power, 10^{-12} W.

Equation (23.24) is usually used to determine the sound power of a source from the sound intensity level except when the source is highly directional. For directional sources, the subareas of the measurement surface may be selected to be unequal and (23.23) should be used.

Table 23.2 A-frequency weightings for octave- and one-third-octave bands

Mid band center frequency (Hz)	One-third octave band weightings (dB)	Octave-band weightings (dB)
50	-30.2	-26.2
63	-26.2	
80	-22.5	
100	-19.1	-16.1
125	-16.1	
160	-13.4	
200	-10.9	-8.6
250	-8.6	
315	-6.6	
400	-4.8	-3.2
500	-3.2	
630	-1.9	
800	-0.8	0
1000	0	
1250	0.6	
1600	1.0	1.2
2000	1.2	
2500	1.3	
3150	1.2	1.0
4000	1.0	
5000	0.5	
6300	-0.1	-1.1
8000	-1.1	
10000	-2.5	

A-Weighted Sound Power

All procedures described in this section apply to the determination of sound power levels in octave or one-third-octave bands. The techniques are independent of bandwidth. The A-weighted sound power level is obtained by summing (on a mean-square basis) the octave-band or one-third octave-band data after applying the appropriate A-weighting corrections. A-weighting values are listed Table 23.2.

Measurement Environments

Three different types of laboratory environments in which noise sources are measured are found in modern acoustics laboratories: anechoic rooms (free field), hemi-anechoic rooms (free field over a reflecting plane), and reverberation rooms (diffuse field). In an anechoic room, all of the boundaries are highly absorbent, and the free-field region extends very nearly to the boundaries of the room. Because the floor itself is absorptive, anechoic rooms usually require a suspended wire grid or other mechanism to support the sound source, test personnel, and measurement instruments. A hemi-anechoic room has a hard, reflective floor, but all other boundaries are highly absorbent. Both anechoic and hemi-anechoic environments are used to determine the sound power level of a source, but the hemi-anechoic room is clearly more practical for testing large, heavy sources.

In a reverberation room, where all boundaries are acoustically hard and reflective, the reverberant field extends throughout the volume of the room except for a small region in the vicinity of the source. The sound power level of a source may be determined from an estimate of the average sound pressure level in the diffuse field region of the room coupled with a knowledge of the absorptive properties of the boundaries, or by comparison with a reference sound source of known sound power output. A standard for the calibration of reference sound sources is available [23.14].

Free-Field Approximation for the Determination of Sound Power

For the far field of a source radiating into free space, the magnitude of the intensity at a point a distance r from the source is:

$$I(\text{at } r) = \frac{p^2_{\text{RMS}}(\text{at } r)}{\rho c} \,, \tag{23.26}$$

where ρc is the characteristic resistance of air equal to about 406 MKS Rayl at normal room conditions, and p_{RMS} is the root-mean-square sound pressure, at r.

Strictly speaking, this relationship is only correct in the far field of a source radiating into free space. Good approximations to free-space, or free-field, conditions can be achieved in properly designed anechoic or hemi-anechoic rooms, or outdoors. Hence, (23.26) is approximately correct in the far field of a source over a reflecting plane, provided that the space above the reflecting plane remains essentially a free field at distance r. Even if the free field is not perfect, and a small fraction of the sound is reflected from the walls and ceiling of the room, an environmental correction may be introduced to allow valid measurements to be taken in the room. The relations below are widely used in standards that determine the sound power of a source from a measurement of sound pressure level.

If a closed measurement surface is placed around a source so that all points on the surface are in the far field, and if the intensity vector is assumed to be essentially normal to the surface so that $I = I_n$ at all points on the surface, then (23.23) and (23.26) can be combined to yield

$$W = \frac{1}{\rho c} \sum_i p_i^2 S_i \,, \tag{23.27}$$

here p_i is the average RMS sound pressure over area segment S_i.

The sound power level is as expressed in (23.25). If all segments are of equal area,

$$W = \frac{S}{\rho c} \frac{1}{N} \sum_i p_i^2 = \frac{S}{\rho c} \langle p^2 \rangle \,, \tag{23.28}$$

where S is the total area of the measurement surface, N is the number of area segments, and $\langle p^2 \rangle$ is the average mean square pressure over the measurement surface.

In logarithmic form with reference power 10^{-12} W and reference pressure 20 μPa, the sound power level is

$$L_W = L_p + 10 \log \frac{S}{S_0} + 10 \log \frac{400}{\rho c} \,, \tag{23.29}$$

where $S_0 = 1\,\mathrm{m}^2$.

For $\rho c = 406$ MKS Rayl, the last term in (23.29) is -0.064, and can usually be neglected.

Hence, the sound power level of a source can be computed from sound pressure level measurements made in a free field. Equation (23.29) is widely used in standardized methods for the determination of sound power levels in a free field or in a free field over a reflecting plane.

Sound Power Determination in a Diffuse Field

The sound power level of a source can also be computed from sound pressure level measurements made in an enclosure with a diffuse sound field because in such a field the sound energy density is constant; it is directly related to the mean-square sound pressure and, therefore, to the sound power radiated by the source. The sound pressure level in the reverberant room builds up until the total sound power absorbed by the walls of the room is equal to the sound power generated by the source. The sound power is determined by measuring the mean-square sound pressure in the reverberant field. This value is either compared with the mean-square pressure of a source of known sound power output (*comparison method*) or calculated directly from the mean-square pressure produced by the source and a knowledge of the sound-absorptive properties of the reverberant room (*direct method*).

The procedure for determining the sound power level of a noise source by the comparison method requires the use of a reference sound source of known sound power output. The procedure is essentially as follows.

With the equipment being evaluated at a suitable location in the room, determine, in each frequency band, the average sound pressure level (on a mean-square basis) in the reverberant field using the microphone array or traverse described above.

Replace the source under test with the reference sound source and repeat the measurement to obtain the average level for the reference sound source.

The sound power level of the source under test L_W for a given frequency band is calculated from

$$L_W = L_{Wr} + \left(\langle L_p \rangle - \langle L_p \rangle_r \right) \tag{23.30}$$

where L_W is the one-third-octave band sound power level for the source being evaluated, $\langle L_p \rangle$ is the space-averaged one-third octave band sound pressure level of source being evaluated, L_{Wr} is the calibrated one-third-octave band sound power level of the reference source, and $\langle L_p \rangle_r$ is the space-averaged one-third-octave band sound pressure level of the reference sound source.

The direct method does not use a reference sound source. Instead, this method requires that the sound-absorptive properties of the room be determined by measuring the reverberation time in the room for each frequency band. Measurement of T_{60} is described in Chap. 11.

With this method, the space-averaged sound pressure level for each frequency band of the source being evaluated is determined as described above for the comparison method. The sound power level of the source is

found from

$$L_W = \overline{L_p} + \left[10 \log \frac{A}{A_0} + 4.34 \frac{A}{S} + 10 \log \left(1 + \frac{S\,c}{8Vf} \right) - 25 \log \left(\frac{427}{400} \sqrt{\frac{273}{273+\theta}} \frac{B}{B_0} \right) - 6 \right] \text{dB re } 10^{-12}\,\text{W}\,, \quad (23.31)$$

where L_W is the band sound power level of the sound source under test, $\overline{L_p}$ is the band space-averaged sound pressure level of the sound source under test, A is the equivalent absorption area of the room, given by:

$$A = \frac{55.26}{c} \left(\frac{V}{T_{rev}} \right)\,,$$

V is the room volume, T_{rev} is the reverberation time for the particular band, A_0 is the reference absorption area, S is the total surface area of the room, f is the midband frequency of the measurement, c is the speed of sound at temperature θ in $^\circ C$, B is the atmospheric pressure, with $B_0 = 1.013 \times 10^5$ Pa, $V_0 = 1\,\text{m}^3$, $T_0 = 1$ s.

Diffuse sound fields can be obtained in laboratory reverberation rooms. Sufficiently close engineering approximations to diffuse-field conditions can be obtained in rooms that are fairly reverberant and irregularly shaped. When these environments are not available or when it is not possible to move the noise source under test, other techniques valid for the in situ determination of sound power level may be used and are described later in this section.

Non-steady and impulsive noises are difficult to measure under reverberant-field conditions. Measurements on such noise sources should be made under free-field conditions.

Sound Power Determination in an Ordinary Room

The sound pressure field in an ordinary room such as an office or laboratory space that has not been designed for acoustical measurements is neither a free-field nor a diffuse field. Here the relationship between the sound intensity and the mean-square pressure is more complicated. Instead of measuring the mean-square pressure, it is usually more advantageous to use a sound intensity analyzer that measures the sound intensity directly (Sect. 23.1.8). By sampling the sound intensity at defined locations in the vicinity of the source, the sound power level of the source can be determined. A standard for the in situ determination of sound power is also available, and is described below.

Source Directivity

Most sources of sound [23.15, 16] of practical interest are directional to some degree. If one measures the sound pressure level in a given frequency band a fixed distance away from the source, different levels will generally be found for different directions. A plot of these levels in polar fashion at the angles for which they were obtained is called the *directivity pattern* of the source.

The directivity factor Q_θ is defined as the ratio of the mean-square sound pressure, p_θ^2, at angle θ and distance r from an actual source radiating W and the mean-square sound pressure p_S^2 at the same distance from a nondirectional source radiating the same acoustic power W. Alternatively, Q_θ is defined as the ratio of the intensity in the direction of propagation W/m^2 at angle θ and distance r from an actual source to the intensity at the same distance from a nondirectional source, both sources radiating the same sound power W. It must be assumed that the directivity factor is independent of distance from the source.

The directivity index DI_θ of a sound source on a rigid plane (radiating into hemispherical space) at angle θ and for a given frequency band is computed from

$$DI_\theta = L_{p\theta} - \langle L_p \rangle_H + 3\,\text{dB}\,, \quad (23.32)$$

where $L_{p\theta}$ is the sound pressure level measured a distance r and angle θ from the source, and $\langle L_p \rangle_H$ is the sound pressure level of the space-averaged mean-square pressure averaged over a test hemisphere of radius r (and area $2\pi r^2$) centered on and surrounding the source.

The 3 dB in this equation is added to $\langle L_p \rangle_H$ because the measurement was made over a hemisphere instead of a full sphere. The reason for this is that the intensity at radius r is twice as large if a source radiates into a hemisphere as compared to a sphere. That is, if a nondirectional source were to radiate uniformly into hemispherical space, $DI_\theta = DI = 3$ dB. Equations are available for sound radiation into a sphere and into a quarter sphere [23.15, 16].

23.2.2 International Standards for the Determination of Sound Power

The International Organization for Standardization (ISO) has published a series of international standards, the ISO 3740 series [23.17], which describes several methods for determining the sound power levels of noise sources. Table 23.3 summarizes the applicability of each of the basic standards of the ISO 3740 series. The most important factor in selecting an appropriate noise mea-

Table 23.3 Description of the ISO 3740 series of standards for determination of sound power

ISO standard	Test environment	Criteria for suitability of test environment	Volume of source	Character of noise	Limitation on background noise	Sound power levels obtainable	Optional information available
ISO 3741 precision (grade 1)	Reverberation room meeting specified requirements	Room volume and reverberation time to be qualified	Preferably less than 2% of room volume	Steady, broadband, narrow-band, or discrete-frequency	$\Delta L \geq 10$ dB $K_1 \leq 0.5$ dB	A-weighted and in one-third-octave or octave bands	Other frequency-weighted sound power levels
ISO 3743-1 Engineering (grade 2)	Hard-walled room	Volume $\geq 40\ m^3$ $\alpha \leq 0.20$	Preferably less than 1% of room volume	Any, but no isolated bursts	$\Delta L \geq 6$ dB $K_1 \leq 1.3$ dB	A-weighted and in octave bands	Other frequency-weighted sound power levels
ISO 3743-2 Engineering (grade 2)	Special reverberation room	$70\ m^3 \leq V \leq 300\ m^3$ $0.5\ s \leq T_{nom} \leq 1.0\ s$	Preferably less than 1% of room volume	Any, but no isolated bursts	$\Delta L \geq 4$ dB $K_1 \leq 2.0$ dB	A-weighted and in octave bands	Other frequency-weighted sound power levels
ISO 3744 Engineering (Grade 2)	Essentially free field over a reflecting plane	$K_2 \leq 2$ dB	No restrictions; limited only by available test environment	Any	$\Delta L \geq 6$ dB $K_1 \leq 1.3$ dB	A-weighted and in one-third-octave or octave bands	Source directivity; SPL as a function of time; single-event SPL; Other frequency-weighted sound power levels
ISO 3745 Precision (Grade 1)	Anechoic or hemi-anechoic room	Specified requirements; measurement surface must lie wholly inside qualified region	Characteristic dimension not greater than 1/2 measurement surface radius	Any	$\Delta L \geq 10$ dB $K_1 \leq 0.5$ dB	A-weighted and in one-third-octave or octave bands	Same as above plus sound energy level
ISO 3746 Survey (Grade 3)	No special test environment	$K_2 \leq 7$ dB	No restrictions; limited only by available test environment	Any	$\Delta L \geq 3$ dB $K_1 \leq 3$ dB	A-weighted	Sound pressure levels as a function of time
ISO 3747 Engineering or Survey (Grade 2 or 3)	Essentially reverberant field in situ, subject to stated qualification requirements	Specified requirements	No restrictions; limited only by available test environment	Steady, broadband, narrow-band, or discrete-frequency	$\Delta L \geq 6$ dB $K_1 \leq 1.3$ dB	A-weighted from octave bands	Sound pressure levels as a function of time

Notes:
1. ΔL is the difference between the sound pressure levels of the source-plus-background noise and the background noise alone
2. K_1 is the correction for background noise, defined in the associated standard
3. V is the test room volume
4. α is the sound absorption coefficient
5. T_{nom} is the nominal reverberation time for the test room, defined in the associated standard
6. K_2 is the enviromental correction, defined in the associated standard
7. SPL is an abbreviation for *sound pressure level*

Amazon EX1014 Page 978

surement method is the ultimate use of the sound power level data that are to be obtained.

In making a decision on the appropriate measurement method to be used, several factors should be considered: (a) the size of the noise source, (b) the moveability of the noise source, (c) the test environments available for the measurements, (d) the character of the noise emitted by the noise source, and (e) the grade (classification) of accuracy required for the measurements. The methods described in this chapter are consistent with those of the ISO 3740 series. A set of standards with the same objectives is available from the American National Standards Institute (ANSI) or the Acoustical Society of America (ASA).

Determination of Sound Power in a Free Field

The basis for sound power level in a free field using sound pressure is the approximate relationships in (23.28) and (23.29) above. Essentially, a measurement surface is chosen and microphone positions are defined over this surface. Sound pressure level measurements are taken at each microphone position for each frequency band, and from these, the sound power levels are computed. The relevant ISO standards are ISO 3744, ISO 3745, and ISO 3746.

Selection of a Measurement Surface. The international standards allow a variety of measurement surfaces to be used; some are discussed here. In selecting the shape of the measurement surface to be used for a particular source, an attempt should be made to choose one where the direction of sound propagation is approximately normal to the surface at the various measurement points. For example, for small sources that approximate a point source, the selection of a spherical or hemispherical surface may be the most appropriate; the direction of sound propagation will be essentially normal to this surface. For machines in a hemi-anechoic environment that are large and in the shape of a box, the parallelepiped measurement surface may be preferable. For tall machines in a hemi-anechoic environment having a height much greater than the length and depth, a cylindrical measurement surface [23.18, 19] may be the most appropriate.

Measurement in Hemi-anechoic Space. The sound power determination in a hemi-anechoic space may be performed according to ISO 3744 for engineering-grade accuracy or according to ISO 3745 for precision-grade accuracy. ISO 3744 is strictly for hemi-anechoic environments, while ISO 3745 includes requirements for both hemi-anechoic and fully anechoic environments. These standards specify requirements for the measurement surfaces and locations of microphones, procedures for measuring the sound pressure levels and applying certain corrections, and the method for computing the sound power levels from the surface-average sound pressure levels. In addition, they provide detailed information and requirements on criteria for the adequacy of the test environment and background noise, calibration of instrumentation, installation and operation of the source, and information to be reported. Several annexes in each standard include information on measurement uncertainty and the qual-

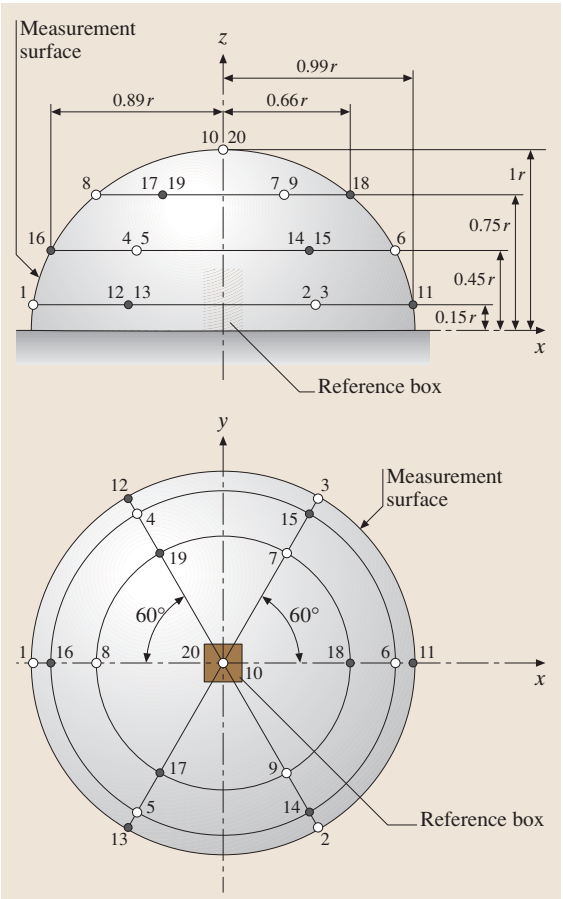


Fig. 23.9 Microphone positions for a hemispherical measurement surface according to ISO 3744. [ISO CD 3744 (N1497)]. (Courtesy of the International Organization for Standardization, Geneva, Switzerland. ©ISO, www.iso.org)

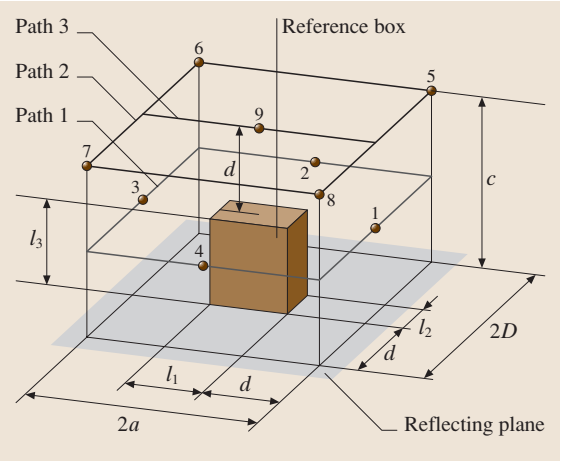


Fig. 23.10 Microphone positions for a rectangular measurement surface according to ISO 3744. [ISO CD 3744 (N1497)]. (Courtesy of the International Organization for Standardization, Geneva, Switzerland. ©ISO, www.iso.org)

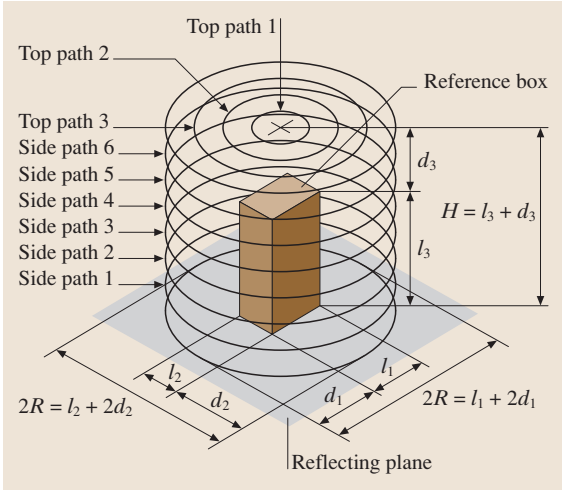


Fig. 23.11 Microphone positions for a cylindrical measurement surface

ification of the test rooms. ISO 3746 is a survey method.

As examples, microphone positions for a hemispherical measurement surface, a rectangular measurement surface, and a cylindrical measurement surface are shown in Figs. 23.9–23.11, respectively.

Determination of Sound Power in a Diffuse Field

ISO 3741 is a precision method for the determination of sound power level in a reverberant test environment. The standard includes both the direct method and the comparison method described above. Requirements on the volume of the reverberation room are specified. Qualification procedures for both broadband and discrete frequency sound, are included, the minimum distance between the source and the microphone(s) are specified, and other measurement details are given.

Determination of Sound Power in Situ

In ISO 3747, engineering or survey methods are given for determination of the sound power of a source in situ, when the source cannot be moved.

Determination of Sound Power Using Sound Intensity

Sound intensity is discussed in detail in Chap. 25. The fundamental procedures for the determination of sound power from sound intensity are discussed above.

The sound intensity is measured over a selected surface enclosing the source. In principle, the integral over any surface totally enclosing the source of the scalar product (dot product) of the sound intensity vector and the associated elemental area vector provides a measure of the sound power radiated directly into the air by all sources located within the enclosing surface.

The use of sound intensity to determine sound power has several advantages over the free-field methods described above using sound pressure.

1. It is not necessary to make the approximation $I = p^2/\rho c$. Therefore, it is not necessary to make any assumption about the direction of sound intensity relative to the measurement surface. What is required is proper orientation of the intensity probe.
2. If there is no sound absorption within the measurement surface, the sound energy that enters the measurement surface from the outside also exits. Therefore, the sound power measurement is less sensitive to background noise levels and reflections from room surfaces than the pressure methods described above. The pressure methods require corrections for background noise and, in some cases, environmental corrections for reflections from room surfaces.
3. Measurements can often be made in an ordinary room.

There are, however, disadvantages to the intensity method.

Amazon EX1014 Page 980

An intensity analyzer is more complex than a sound level meter in the sense that the two channels required for the measurements (Sect. 23.1.8) must be carefully matched in phase. When using discrete microphone positions, a very large number of microphone positions may be required to obtain a specified accuracy in the measurements. Mean square sound pressures on a measurement surface are always positive, whereas sound intensity may be outward from the measurement surface (positive) or inward (negative). Thus, the summation of sound intensities over the measurement surface may produce a small number, and the accuracy of the measurement may be difficult to determine.

Standards have been developed to overcome these disadvantages. Instrument standards have been developed [23.11, 12] and there are standards available for the determination of sound power via sound intensity both for fixed intensity-probe positions [23.20] and for scanning [23.21–23] with an intensity probe over the measurement surface. The standards also describe *field indicators* that can be used to estimate the accuracy of the sound power determination, and technical information on the use of field indicators is available [23.24, 25].

After substantial experience with the determination of sound power via sound intensity has been achieved, it is expected that these standards will be revised.

Determination of Sound Power in a Duct

The most common application of in-duct measurements is to determine the sound power radiated by air-moving devices. The sound power level of a source in a duct can be determined according to ISO 5136 [23.26] from sound pressure level measurements, provided that the sound field in the duct is essentially a plane progressive wave, using the equation

$$L_W = L_p + 10 \log \frac{S}{S_0} , \qquad (23.33)$$

where L_W is the level of total sound power traveling down duct, L_p is the sound pressure level measured just off centerline of duct, S is the cross-sectional area of duct, and $S_0 = 1\,m^2$.

The above relation assumes not only a nonreflecting termination for the end of the duct opposite the source but also a uniform sound intensity across the duct. At frequencies near and above the first cross resonance of the duct the latter assumption is no longer satisfied. Also, when following the measurement procedures of ISO 5136, several correction factors are incorporated into (23.33) to account for microphone response and atmospheric conditions.

Equation (23.33) can still be used provided L_p, is replaced by a suitable space average $\langle L_p \rangle$ obtained by averaging the mean square sound pressures obtained at selected radial and circumferential positions in the duct, or by using a traversing circumferential microphone. The number of measurement positions across the cross section used to determine $\langle L_p \rangle$ will depend on the accuracy desired and the frequency [23.27].

In practical situations, reflections occur at the open end of the duct, especially at low frequencies. The effect of branches and bends must be considered [23.28]. When there is flow in the duct, it is also necessary to surround the microphone by a suitable windscreen. This is necessary to reduce turbulent pressure fluctuations at the microphone, which can cause an error in the measured sound pressure level.

23.2.3 Emission Sound Pressure Level

Another measure of the noise emission of a source is the *emission sound pressure level*. The sound pressure level measured in the vicinity of a noise source is dependent not only on its operating condition, but also the distance from the source and the acoustical environment – primarily reflections from the room surfaces – but also on the presence of other nearby sources. There are, however, cases where the noise emissions of a source can be described using sound pressure levels. These levels may be specified at an operator's position and at selected bystander positions, and in a controlled acoustical environment. Peak C-weighted sound levels (Sect. 23.1.4) may also be important when the levels are high enough to cause hearing damage, and these levels are not determined when using sound power level as a measure of noise emissions.

A series of international standards has been developed to ensure consistency in the measurement process and to estimate emission sound pressure levels when only sound power level information is available. ISO 11200 [23.29] provides an introduction and overview of the series. ISO 11201 [23.30] provides guidance for measurements at the operating position and bystander position when the acoustical environment is a free field over a reflecting plane. If the measurements cannot be made in a free field over a reflecting plane, it may be necessary to use a semi-reverberant environment. Using this method, A-weighted or C-weighted peak sound levels may be measured using ISO 11202 [23.31]. When only the sound power level of the source is available, it may be necessary to make estimates of the emission sound pressure level, and

Amazon EX1014 Page 981

this procedure is covered in ISO 11203 [23.32]. As in the case of engineering and survey methods for determination of sound power level, environmental corrections may be needed in the measurement of emission sound pressure level, and this subject is covered in ISO 11204 [23.33]. Sound intensity level may be used to determine sound power level of a source, as described in the previous section. Sound intensity measurement may also be used in the determination of emission sound pressure level. The procedures are standardized in ISO 11205 [23.34].

23.2.4 Other Noise Emission Standards

Many standards organizations, trade associations, and other organizations have developed standards to determine the noise emissions of specific sources. This section is devoted to a brief description of such standards.

ISO Standards

The ISO has many standards for specific noise sources.

- Noise emitted by road vehicles [23.35–41]
- Information technology equipment [23.42–44]
- Noise emitted by rotating electrical machinery [23.45]
- Shipboard noise [23.46, 47]
- Aircraft noise [23.48, 49]
- Industrial plants [23.50, 51]
- Construction machinery [23.52]
- Agricultural machinery [23.53, 54]
- Earth-moving machinery [23.55–58]
- Lawn care equipment [23.59]
- Air terminal devices [23.60]
- Pipes and valves [23.61]
- Brush saws [23.62].

For other equipment, the ISO has published standards related to the writing of noise test codes [23.63].

American National Standards

The determination of noise emissions from a wide variety of mechanical equipment is the subject of two American national standards. ANSI S12.15-1992 [23.64] defines microphone positions and other information for determining noise emissions from a wide variety of tools. It defines measurement surfaces for portable tools and gives information on determination of sound power level for stationary tools. The tools covered include the following.

Portable electric tools:

- Circular hand saws
- Drills
- Grinders
- Polishers
- Reciprocating saws
- Nibblers
- Screwdrivers
- Nut settlers and tappers
- Hedge trimmers
- Shears
- Grass shears
- Routers
- Planers
- Edge trimmers
- Rotary cultivators

Stationary and fixed electric tools:

- Drill presses
- Scroll saws
- Scroll saws
- Disk sanders
- Joiner/planers
- Bench grinders
- Belt sanders
- Radial saws
- Hacksaws
- Band saws

A second American national standard, ANSI S12.16-1992(R2002) [23.65], gives guidance to users on how to request noise emission data for machinery, and refers to industry standards for a wide variety of equipment. The applicable standard is given and the data to be reported. Examples of equipment included in the standard are:

- Fans
- Hydraulic fluid power pumps
- Hydraulic fluid power motors
- Pneumatic tools
- Gear drives and gear motors
- Mechanical equipment (general)
- Liquid immersed transformers
- Dry type ventilated and non ventilated and sealed transformers
- Control valves and associated piping
- Air-conditioning equipment; refrigeration equipment, chillers, etc.
- Stationary heavy duty internal combustion engines
- Electric motors, turbines, and generators
- Machine tools

Amazon EX1014 Page 982

23.2.5 Criteria for Noise Emissions

Criteria for noise emissions can be divided into standards for making a noise declaration, specific criteria for both indoor and outdoor sources, and criteria for obtaining an environmental label for a product.

General Noise Declaration Standards

After the sound power level of a product has been determined, the results are usually communicated to users either in the form of a product noise declaration published in product literature, on the manufacturer's web site, or a physical label attached to the product. The emission sound pressure level may also be declared (Sect. 23.2.3). Noise declarations are generally in terms of a statistical upper limit determined according to national or international standards. The basic statistical procedures are contained in ISO 7574, a four-part series of standards [23.66].

The preferred descriptor of product noise emissions is the *declared A-weighted sound power level*, L_{WAd}. A widely used international standard is ISO 4871:1996 [23.67] for machinery in general. This standard is an implementation of ISO 7574 and must be followed by noise test codes. ISO 9296:1998 [23.68] is an example of such a code specifically for computer and business equipment (information technology equipment).

Noise Emission Limits

Below, two examples of upper limits for noise emissions are given, one for office equipment widely used for specification of noise emissions of information technology equipment, and the other for specification of outdoor equipment.

Indoor Equipment. Since the middle of the 1980s, recommended limits for equipment in the information technology industry have been published by the Swedish Agency for Public Management, Statskontoret [23.69]. The limits are in terms of the statistical upper-limit A-weighted sound power level of the equipment in bels. Since a wide variety of products are produced in this industry, it is necessary, in addition to upper limits, to specify the environment in which the equipment will be operated. A category 1 product is intended for use in a large data-processing installation, either generally attended or generally unattended, where the installation noise level is determined by a large number of machines. Category 2 products are intended for use in a business office where many persons operate workstations. A category 3 product is intended for use in a private office where, for example, personal computers or low-noise copiers are operated. Users are encouraged to obtain the latest version of the standard; it contains a great deal of information in addition to the recommended upper limits in the table below. Information on the presence of impulsive noise and prominent discrete tones is also required in the version below, and there is information on determination of the emission sound pressure level determined according to the ISO 11200 series of international standards [23.29–34]. While the limits in the table below are recommended, they can become a requirement when written into a purchase contract or other document.

Note that in the table below, the sound power level is expressed in bels (1 bel = 10 decibels).

Outdoor Equipment. A source of noise emission requirements for outdoor equipment may be found in European Union directive 2000/14/EC [23.70]. The directive specifies demanding noise limits and noise markings for about 55 different types of equipment. The intent is that the state of the art in noise reduction permits manufacturers to meet these limits without excessive additional costs. The limits are stated in terms of the A-weighted sound power level L_{WA} and the measurements are to be made according to European standards (EN) that correspond to ISO standards 3744 and 3746 [23.17].

The permissible sound power level shall be rounded to the nearest whole number (less than 0.5 use the lower number, greater than or equal to 0.5 use the higher number).

Environmental Labels

An alternative to the declaration of a specific noise level is the submission of product noise emission data to an independent body, which makes a judgment of the data



Fig. 23.12 German *Blue Angel* logo

relative to other similar products and allows an environmental label to be used. Such labels are not limited to noise levels, but are issued to products that display a variety of favorable environmental characteristics. The general objective of environmental labels (eco-labels) is to provide a voluntary system to both allow manufacturers to identify environmentally friendly products and to provide the public with a recognizable label that designates environmental quality.

The first eco-label was the German *Blue Angel* label [23.71]. Noise as a requirement to obtain the *Blue Angel* label, illustrated in Fig. 23.12, is covered in specific documents for a number of products. The verification criteria are prepared by the German Institute for Quality Assurance and Certification (RAL).



Fig. 23.13 European Union (EU) *Flower* logo

Table 23.6 shows product categories and document numbers for products with noise emission requirements.

Table 23.4 Recommended upper limits of declared A-weighted sound power level (From Statskontoret standard 26.5, 2002-10-01, Table 1)

Product description	**Recommended upper limit A-weighted sound power level in** bels	
	L_{WAd} **Operating**	L_{WAd} **Idle**
Category I: Equipment for use in data processing (DP) areas		
A. Products in unattended DP areas	$8.0 + L$	$8.0 + L$
B. Products in generally attended DP areas	$7.5 + L$	$7.5 + L$
Category II: Equipment for use in general business areas		
A. Fully-formed character typewriters and printers	7.2	5.5
B. Printers and copiers more than 4 m distance from workstations	7.2	6.5
C. Tabletop printers and tabletop copiers	7.0	5.5
D. Processors, controllers, disk and tape drives, etc. (more than 4 m distant from workstations)	$7.0 + L$	$7.0 + L$
E. Processors, controllers, disk and tape drives, etc. (less than 4 m distant from workstations)	6.8	6.6
Category III: Floor-standing use in quiet office areas		
A. Printers, typewriters, plotters	6.5	5.0
B. Keyboards	6.2	N/A
C. Processors	6.0	5.5
D. Tabletop processors, controllers, system units including built-in disk drives and/or tapes, display units with fans [4]	5.8	5.0
E. Display units (no moving parts)	4.5	4.5

Notes:
1. $L = \log(S/S_0)$. S is the footprint area of the product, in square meters. S_0 is the reference footprint area, equal to 1 m^2. If $S < 1\ m^2$, S shall be set equal to 1.0. (Thus the specification will not get lower than 8.0 and 7.5 and 7.0 bels for Category IA and IB and IID, respectively)
2. For products comprised of multiple racks or frames of equal footprint areas linked together, the reference footprint area S_0 shall be set equal to the footprint area of the individual racks or frames, or to 1.0 m^2, whichever is smaller
3. The calculated value of the recommended upper limit (for Category IA, IB, and IID) may be rounded to the nearest upper 0.1 bel
4. For Category IIID products, especially for personal computers to be used in the home, lower values are often recommended (e.g., $L_{WAd} = 5.5$ B operating and $L_{WAd} = 4.8$ B idle; see, for instance, European Commission decision 2001/686/EC and Swedish TCO 99)

Table 23.5 Table of limit values from EU directive 2000/14/EC

Type of equipment	Net installed power P (in kW); Electric Electric power P_{el} in kW; Mass of appliance m in kg; cutting width L in cm	Permissible sound power level (dB/1pW) Stage I as from 3 January 2002	Stage II as from 3 January 2006
Compaction machines (vibrating rollers, vibrating plates, vibratory hammers	$P \leq 8$ $8 < P \leq 70$ $P > 70$	108 109 $89 + 11 \log P$	105 106 $86 + 11 \log P$
Tracked dozers, tracked loaders, tracked excavators–loaders	$P \leq 55$ $P > 55$	106 $87 + 11 \log P$	103 $84 + 11 \log P$
Wheeled dozers, wheeled loaders, dumpers, graders, loader-type landfill compactors, combustion-engine driven counterbalanced lift trucks, mobile cranes, compaction machines (non-vibrating rollers) paver finishers, hydraulic power packs	$P \leq 55$ $P > 55$	104 $85 + 11 \log P$	101 $82 + 11 \log P$
Excavators, builder's hoists for the transport of goods, construction winches motor hoes	$P \leq 15$ $P > 15$	96 $83 + 11 \log P$	93 $80 + 11 \log P$
Hand-held concrete breakers and picks	$m \leq 15$ $15 < m < 30$ $m \geq 30$	107 $94 + 11 \log P$ $96 + 11 \log P$	105 $92 + 11 \log m$ $94 + 11 \log m$
Tower cranes		$98 + \log P$	$96 + \log P$
Welding and power generators	$P_{el} \leq 2$ $2 < P_{el} \leq 10$ $P_{el} > 10$	$97 + \log P_{el}$ $98 + \log P_{el}$ $97 + \log P_{el}$	$95 + \log P_{el}$ $96 + \log P_{el}$ $95 + \log P_{el}$
Compressors	$P \leq 15$ $P > 15$	99 $97 + 2 \log P$	97 $95 + 2 \log P$
Lawnmowers, lawn trimmers/ lawn edge trimmers	$L \leq 50$ $50 < L \leq 70$ $70 < L \leq 120$ $L > 120$	96 100 100 105	94(2) 98 98(2) 103(2)

Notes:
1. P_{el} for welding generators: conventional welding current multiplied by the conventional load voltage for the lowest value of the duty factor given by the manufacturer
2. P_{el} for power generators: prime power according to ISO 8528-1:1993, point 13.3.2
3. Indicative figures only. Definitive figures will depend on amendment of the directive following the report required in article 20(3). In the absence of any such amendment, the figures for stage I will continue to apply for stage II

A review of *Blue Angel* requirements specifically for noise emissions of construction equipment is available [23.72].

A more recent eco-label is the European Union *EU Flower* designation [23.73]. Currently, only personal computers [23.74] and portable computers [23.75] have noise emissions included with other environmental requirements. The *EU Flower* label is illustrated in Fig. 23.13.

Other European countries with eco-label programs include Austria, France, and the Nordic countries.

23.2.6 Principles of Noise Control

As illustrated in the previous section, the noise emissions of a wide variety of equipment are of importance, and it is not possible to present noise reduction on each type here. It is however, possible to present general principles

Table 23.6 German *Blue Angel* product categories with noise criteria

Product category	Relevant document
Automobile tires, low noise	RAL-UZ 89
Commercial vehicles and buses	RAL-UZ 59a and RAL-UZ 59b
Workstation computers	RAL-UZ 78
Construction machinery	RAL-UZ 53
Garden shredders	RAL-UZ 54
Portable computers	RAL-UZ 93
Printers	RAL-UZ 85
Copiers	RAL-UZ 62
Low-noise and low-pollutant chain saws	RAL-UZ 83
Low-noise waste-glass containers	RAL-UZ 21

of noise reduction. A widely distributed set of principles was prepared by *Ingemansson* [23.76]. One principle and its application is shown in Fig. 23.14.

The text below is partly organized according to those principles. In the following section, examples of the control of stationary noise sources are given.

As discussed in Sect. 23.0.2, sources of sound in the wave equation include mass introduced into a region, the application of a fluctuating force, transfer of heat, or stresses induced by turbulence. A fluctuating force or excess force produced by the speed of moving mechanical parts produce noise, and reduction of this force will reduce noise levels. In particular, high-frequency noise is generated by abrupt changes in force. Lower-frequency noise is produced by more gradual changes in force. Heavy objects impacting at high speeds generally produce less noise than lighter objects at low speeds.

Forces transmitted to large radiating surfaces also cause sound to be radiated, and these forces can be reduced by vibration isolation. Practical vibration isolators include rubber–plastic materials, cork, and various types of springs.

A reduction in the area of vibrating surfaces also reduces noise levels. When a plate, such as a cover over a portion of a rotating machine is not used to provide transmission loss, a perforated plate will reduce the vibrating area and reduce the radiation from the plate. Sound cancelation takes place between the front and back of a vibrating device such as a loudspeaker or a plate. Cancelation is more effective for a long narrow plate than for a square plate having the same area. This may have applications, for example, in the design of belt drives. Cancelation is also more effective for plates with free edges rather than edges which are clamped. Plates may also be covered with materials with a high degree of internal damping, thus producing absorption of sound that might otherwise be radiated as sound. This may apply, for example to objects that resonate such as saw blades. In general, damping is most effective at high frequencies.

In solid structures, structure-borne sound may travel over long distances, and its effect on radiated sound can be reduced by vibration isolation. Flexible connections are useful for prevention of noise transmission from a machine into a pipeline. Separate isolation pads may be used for mounting machinery, and heavy rigid foundations are generally most effective.

When the wavelength of sound is small (high-frequency sound), sound-absorptive materials are most effective, and enclosures may be an effective means of noise control. The sound attenuation in air is also greater for high-frequency sound than low-frequency sound, which means that there can be additional attenuation due to the distance between a source and an observer (Sect. 23.3.1 and Chap. 4). However, a high-frequency sound pressure level is perceived to be louder than a low-frequency sound of the same level. This difference is expressed in the A-weighting curves in Sect. 23.1.4. Thus, conversion of a high-frequency sound to a low-frequency sound may result in a reduction in perceived noise level, and a reduction measured using A-weighting on a sound level meter.

Tones can be produced when air flows past an object. An example is wind passing over high tension wires. Vortices are shed from the wire (Karman vortex street), and this produces a fluctuating force on the wire, which results in radiation of sound. Adding an irregular structure to the object may reduce the strength of such forces and reduce the noise level. Tones can also be generated by wind passing over resonators, and noise levels may be reduced by altering the geometry of the resonator.

In pipes carrying fluid, constrictions, as may be produced by a valve, bends, and other obstructions generate forces in the system which lead to sound radiation. Noise can be reduced by gradual changes in bends, cross sections, and pipe lengths that are long enough to allow the levels of turbulence to be reduced. Lower exhaust air flows also result in reduced noise levels, especially in high-Mach-number regions where the noise is generated aerodynamically, and the radiated noise is proportional to the eighth power of the Mach number. Another way to reduce noise from exhaust air flows is to add secondary flow of a lower speed around a high-speed exhaust jet.

Amazon EX1014 Page 986

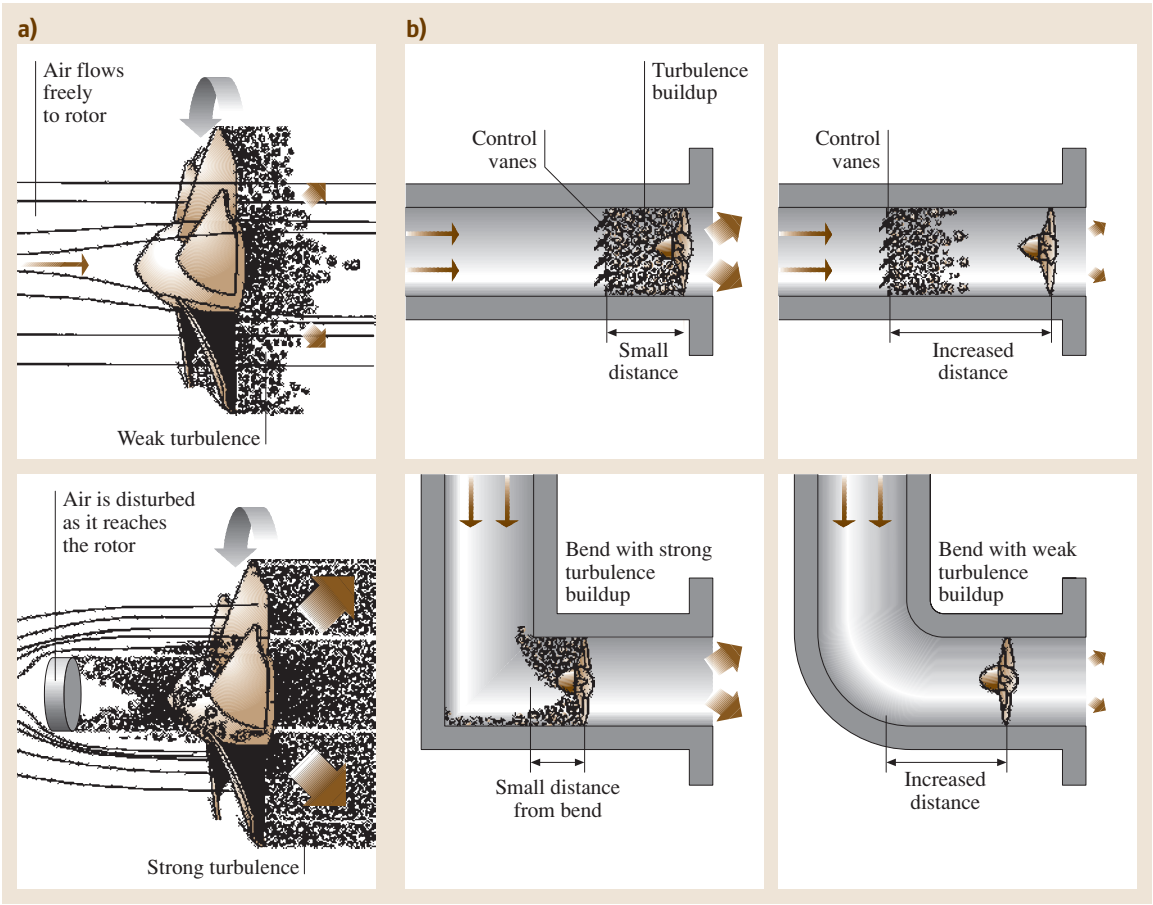


Fig. 23.14a,b An example of how fans make less noise when placed in smooth undisturbed air streams. Illustrations courtesy of Ingemansson Technology, Gothenburg, Sweden. **(a)** principle, **(b)** application with ventilation

This is the principle of the high-bypass-ratio jet engine, and may also apply to compressed-air nozzles when used as part of a cleaning system in industrial applications. In air-moving devices, particularly axial flow fans, turbulence in the inlet air stream causes the angle of attack of the flow incident on the fan blades (airfoils) to vary, and generates fluctuating lift forces on the blades. Thus, obstructions in inlet air streams should be avoided.

The presence of solid surfaces affects the radiation of sound. For idealized sources such as monopoles, dipoles, and quadrupoles (Sect. 23.0.3), the reflected pressure from one or more surfaces may be in phase with the particle velocity of the source on a small surface surrounding the source and thus produce a radiated sound power that is greater than the sound power that would be radiated by the source in a free field [23.77]. For actual machines, placement in, for example, a corner results in reflected sound waves that increase the measured sound pressure level. Thus, machines should be spaced a distance from walls and corners to reduce noise level. This effect is included in the prediction algorithm described in Sect. 23.3.3.

Acoustical materials for noise reduction are described in Sect. 23.3.3. Because good sound absorption requires a particle velocity in the material, and the particle velocity in a sound wave is small near a rigid surface, thick materials tend to be better sound absorbers than thin materials when placed on a rigid surface. Also, an air gap between a rigid wall and sound-absorptive material tends to increase sound absorption (Sect. 23.3.3). A layer of perforated metal with relatively large perforations is effective in protecting the surface of the material from abrasion, and has relatively little effect on the sound-absorptive performance of the material. The

shape of the perforations may take many different forms. Sound-absorptive material is also effective when used on ceilings in conjunction with screens in an office environment, since sound transmitted over the screen may be reflected before reaching an observer on the other side of the screen.

When sound travels in a tube, an expansion chamber as part of the tube may reduce noise levels. This principle may be used in reactive silencers. An example of a generic reactive silencer is given in Sect. 23.3.4. Such silencers with added sound-absorptive material may provide additional sound absorption. Dissipative silencers contain sound-absorptive materials, as discussed in the same section. Sound cancelation at selected frequencies may be achieved by using a tube with a side path which is long enough to produce sound cancelation between the wave that travels down the duct and the wave that travels over the side path.

The effect of wall constructions on noise reduction is covered in Chap. 11.

23.2.7 Noise From Stationary Sources

One of the most pervasive sources of noise is noise generated by air-moving devices. The general principles of control of noise from these devices is described below. Noise from other stationary sources is the subject of current research.

Air-Moving Device Noise

Air moving devices (AMDs) (e.g., fans and blowers) are widely used in a variety of equipment, and are a pervasive source of noise. These devices (AMDs) may have a very large diameter, and used in ventilating systems for buildings as well as in industrial processes. Large fans are usually axial devices and large blowers are centrifugal devices that may have either forward-curved or backward-curved blades. Smaller units may be used for home heating and ventilating as well as in industrial equipment such as that produced for the information technology industry. Axial fans are most common, but centrifugal blowers are also used when the system resistance (see below) is relatively high. Other air-moving devices, such as cross-flow fans, motorized impellers, or mixed-flow devices may also be used.

The primary source of noise is fluctuating lift forces on the blades as turbulent air passes through the unit. For high values of inlet turbulence, there is a fluctuating angle of attack on the blades, and this leads to fluctuating lift forces. Forces are also produced by flow separation from the blade, and by vortices being shed from the blades. The radiated noise is broadband in character with discrete frequency components at the blade passage frequency and its harmonics. The blade passage frequency is

$$f = B \times \frac{N}{60} , \tag{23.34}$$

where f is the frequency in Hz, B is the number of blades and N is the device speed in revolutions per minute (rpm).

A performance curve is common to all types of air-moving devices, illustrated in Fig. 23.15 for a small centrifugal device. All systems have a resistance to air flow, and the system resistance can generally be defined as a quadratic function of air flow, as illustrated in the figure. The intersection of these two curves is the operating point for the device. If the flow rate is zero, the condition is known as *shutoff*, and when the static pressure is zero, the condition is known as *free delivery*. The air flow through the blades under either condition is poor, the noise level tends to rise as discussed below.

The static efficiency of an air-moving device is generally defined as

$$\eta_s = \frac{PQ}{W_{in}} , \tag{23.35}$$

where P is the static pressure rise in Pa (N/m^2), Q is the volume flow rate in m^3/s, and W_{in} is the input power to the device in W. The static efficiency is a maximum at some point on the performance curve, as illustrated in Fig. 23.16 for a constant input power. An operating point near the point of maximum static efficiency is desirable for low noise radiation, and is usually a design goal for

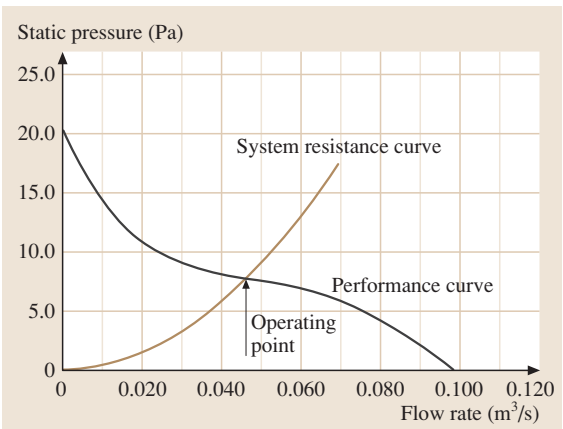


Fig. 23.15 Performance curve for a small centrifugal blower

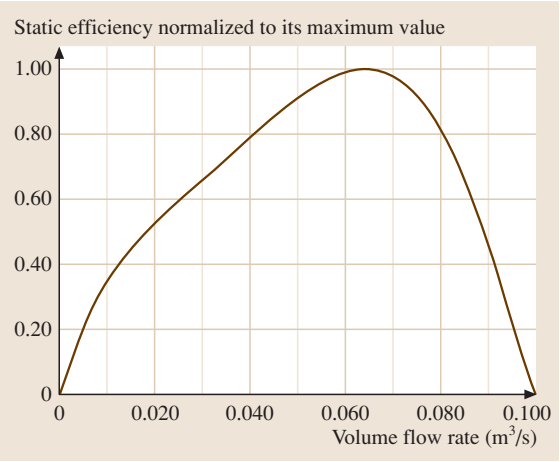


Fig. 23.16 Illustration of air-moving device static efficiency for a constant input power

large devices. In the design of small ventilating systems, the system resistance is often not known accurately, and optimal design may be difficult to achieve. However, an operating point to the left of the point of maximum static efficiency is usually undesirable, both from the viewpoint of flow instability and increased noise.

The choice of a type of air-moving device is usually dictated by the desired *specific speed* N_s defined as

$$N_s = \frac{NQ^{1/2}}{P^{3/4}} , \tag{23.36}$$

where N is the rotational speed of the air moving device, and P and Q are defined above. Axial flow devices are generally used at low pressures and high-volume flow rates (high specific speed), and centrifugal devices are usually used at relatively high pressures and low-volume flow rates (low specific speed).

For noise radiation from large air-moving devices, it is often useful to use a sound law first proposed by *Madison* [23.78]. Its validity depends on the point of rating for a homologous series of air-moving devices. For such a series, it is useful to define dimensionless parameters, the *pressure coefficient* ψ and the *flow coefficient* ϕ as:

$$\psi = \frac{2P}{\rho\,(\pi DN)^2} , \tag{23.37}$$

$$\phi = \frac{Q}{\pi D^3 N} , \tag{23.38}$$

where D is a characteristic dimension (diameter), and N is the rotational speed of the device. Then, the performance curve for any device in the series can be expressed as a single curve of ψ versus ϕ and the operating point discussed above becomes the point of rating for the series.

The sound law is then

$$W = W_s \times \frac{P^2 Q}{P_0^2 Q_0} , \tag{23.39}$$

where W_s is the specific sound power, and W is the radiated sound power of the device P_0 and Q_0 are 1 Pa and 1 m^3/s, respectively.

No frequency dependence was given in (23.39), but values of W_s are often published in octave bands. It must be emphasized that (23.39) is valid only at a given point of rating. If the operating point goes from shutoff ($P = 0$) to free discharge ($Q = 0$), the point of rating is changing, and the radiated sound power does not go to zero at these extremes; in fact, it generally increases, as illustrated in Fig. 23.17. The above sound law is most useful in the design of large systems when the system resistance is known and the air-moving device operates near its point of maximum static efficiency. Using (23.37), (23.38), and (23.39), it can be shown that at a given point-of-rating, the sound power is proportional to the fifth power of the speed of the device.

For small air-moving devices, it is most meaningful to obtain sound power level data on the device itself, usually as a function of speed, operating point, or both. An apparatus for determination of sound power of small devices has been standardized both nationally and internationally [23.79,80] and is shown in Fig. 23.18 [23.81]. The AMD is mounted on a flexible membrane for airborne noise tests. Small fans mounted on lightweight structures are known to transmit energy into the structure, which can then be radiated as sound. The same test apparatus can also be used for evaluation of the structure-borne vibration of small AMDs if the membrane is replaced by a specially designed plate [23.82].

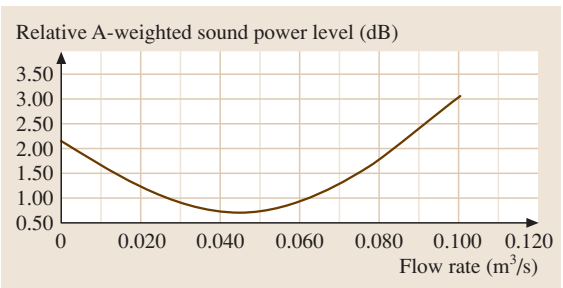


Fig. 23.17 An illustration of relative sound power level as a function of flow for a small air-moving device

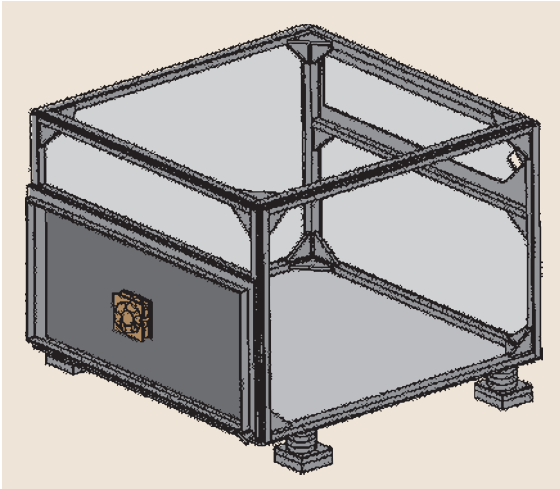


Fig. 23.18 Test plenum for determination of the sound power level of small air-moving devices (In 1962, an early version of this apparatus was first used to determine the sound power output of centrifugal blowers [23.81])

A history of noise control in small air-moving devices is available [23.83]. The following guidelines have proved to be useful for the design of cooling systems for electronic equipment [23.84].

1. Design the system to be cooled to have the lowest possible static pressure rise for the required air flow. A low static pressure rise indicates that the AMD can operate at a low tip speed, resulting in a low noise level. The static pressure rise across a system is caused by several sources of resistance such as the devices being ventilated and finger guards which may be required for safety. If unnecessary sources of resistance can be eliminated, the air flow will increase. It should then be possible to reduce the tip speed of the device (speed of the outer edge of the AMD blade) to obtain the desired air flow at a lower noise level.
2. Select an AMD so that it operates near its point of maximum static efficiency, considering the required air flow rate and the pressure drop through the system. Operation away from the point of maximum static efficiency should be in the direction of lower static pressure rise and higher air flow (see point 3).
3. Select a point of operation of a fan that is away from the best efficiency point in the direction of higher air flow and lower static pressure rise. Small fans are often unstable when operated at air flow rates less than the air flow rate at the best efficiency point. They are often very noisy under conditions of high static pressure rise and low air flow rate.
4. Select a fan or blower with a low sound power level and avoid devices that have high level peaks in their one-third-octave-band sound power spectrum. Such peaks usually indicate the presence of discrete frequency tones in the spectrum. Such tones can be difficult to eliminate and are generally a source of annoyance.
5. Select a fan or blower having the lowest speed and largest diameter consistent with the other requirements.
6. Minimize system noise levels by designing the system so that obstructions are not present within one fan diameter of the inlet to axial-flow fans so that the airflow into the inlet of axial-flow fans [23.85] is as spatially uniform as possible. Avoid the direct attachment of the AMD to lightweight sheet-metal parts.
7. Axial-flow fans should generally be mounted so that the air-flow direction is *toward* the equipment being cooled. *Pulling* air over equipment being cooled usually causes undesirable turbulence at the fan inlet, and produces an increase in noise level. See also item 6 above.
8. When possible, consider operating the AMD at a lower rotational speed. Then noise generally varies as the fifth power of the rotational speed, speed reductions produce significant reductions in noise level.

Active Noise Control

As shown in Sect. 23.0.2, in a linear medium sound pressures at a given point in space add. Therefore, in theory, if one sound pressure is created by a source and another pressure equal in amplitude and of opposite sign is created by a second source, the resulting sound pressure is zero. This is the principle of active control of noise. In practice, active control is difficult to achieve, and there are many technical issues involved.

The electronic sound absorber of *Olson* and *May* [23.86] was a very early attempt to produce active noise control. At the time, only analog circuits were available, it was necessary to control the low-frequency phase shift of both the loudspeaker and microphone used in the experiments – a subject of interest to both of the authors. With the introduction of signal processing techniques in the late 1960s and 1970s, and its rapid development in the 1980s and 1990s, active control became more practical, in spite of many limitations which still exist. Nevertheless, there have been success-

Amazon EX1014 Page 990

ful applications. Good results are obtained only at low frequencies (long wavelengths) and for sources that are small compared with the wavelength of sound. In general, discrete-frequency noise is easier to cancel than broadband noise.

There are several configurations of a source and one or more loudspeakers that can produce active noise reduction:

1. Noise control in a duct. This generally requires a microphone to determine the sound coming along the duct, a loudspeaker mounted at the side of the duct, an error microphone, and signal processing to determine the signal to the loudspeaker which will reduce the sound pressure level at the error microphone (ideally) to zero. This configuration is most successful for low-frequency sound and for plane-wave propagation in the duct.
2. Reduction of radiation efficiency. Placement of one or more canceling sources very close to the noise source. In the case of a single canceling source, the effect of the canceling source is to create a dipole source and to reduce the radiation efficiency of the combined noise source – canceling source. In principle, one could use three canceling sources which, with proper phasing, reduces the radiation efficiency even further by creating a quadrupole source.
3. Creation of an outgoing wave field. Using several loudspeakers around a source, and processing the driving signals to the loudspeakers in such a way as to produce an outgoing wave equal in amplitude and opposite in phase to the wave field of the source.
4. Creation of a *zone of silence*. Using one or more loudspeakers to cancel the noise generated by a source at a point in space, creating a *zone of silence* in the vicinity of the point. Such zones are small compared with the wavelength of sound, and in any practical application, many loudspeakers are needed.
5. Global reduction inside an enclosed space. Investigation of the modal structure of an enclosed space and placement of a large number of microphones and cancelation sources within the space. A complex signal-processing system is then used to create a net noise reduction in the space. This technique has been used in the cabins of small turboprop aircraft.
6. Active headsets. A cancellation field is created in the ear canal when a headphone is worn, thereby creating a noise-canceling headset. Such headsets are commercially available.

The literature on active noise control includes books [23.87, 88], articles [23.89, 90], conference papers [23.91–95], and collected works [23.96].

Other Stationary Sources

Noise from other stationary sources covers a very wide variety of machinery and equipment. Many examples of noise control may be found in the *Noise Control Engineering Journal* and in the INTER-NOISE and NOISE-CON series of international congresses and conferences on noise control engineering(Sect. 23.6).

23.2.8 Noise from Moving Sources

Vehicle Noise

Noise emissions from motor vehicles are an important source of environmental noise in almost every industrialized country in the world, and many steps have been taken to reduce these levels. Unlike aircraft noise, vehicle noise affects populations in a very wide geographical area, and is pervasive in any area with a well-defined roadway network. In recreational areas, noise from snowmobiles and other recreational vehicles is a major source of annoyance. However, in this section, emphasis is on road vehicles – passenger cars, buses, and trucks. Aside from reduction of the noise emissions of the vehicles themselves, noise barriers and buffer zones are the primary methods of shielding persons from motor vehicle noise. The properties of noise barriers are discussed briefly in Sect. 23.3.1, and in more detail in Chap. 4.

The major sources of vehicle noise can be divided into power-train noise (cooling fan, engine, drive train, exhaust), tire–road interaction noise, and wind noise. The latter is not a major source of noise. Fan noise has been described in Sect. 23.2.7. Engine noise is produced by pressure fluctuations within the engine due to combustion, their interactions with mechanical components, transmission into the engine block and subsequent radiation. Gear noise is produced by the drive train, and exhaust noise is attenuated by the muffler. The relative importance of these sources is highly dependent on the type of vehicle and its design. Considerable progress has been made in the reduction of all of these sources, partly because of the development of regulatory limits on pass-by noise in nearly every industrialized country in the world, but also because of the desire of manufacturers to reduce the interior noise in vehicles. As a result, tire–road interaction noise has become a major source of exterior vehicle noise, especially at high speeds.

Amazon EX1014 Page 991

As part of a study on the effect of noise regulations on traffic noise [23.97], the International Institute of Noise Control Engineering summarized some of the noise reduction measures that have been taken to reduce the noise emissions of motor vehicles. Examples are given in Table 23.7 below.

The international standard for the determination of pass-by noise, a common descriptor of vehicle noise emissions, is ISO 362 [23.98], which specifies measurement methods, including microphone position, the characteristics of the test area in the immediate vicinity of the vehicle, driving mode, and the area of the site that must be free from obstructions. In summary, this document specifies that the test vehicle is driven over a designated test area with a standardized road surface. Fixed microphones are located 7.5 m from the vehicle path center line (In the United States, the microphone distance is 15 m and the relevant standards are SAE J986 and SAE J366.). Vehicles approach the test area at a constant speed, usually 20–50 km/h, but the throttle is fully open when the vehicle is within ±10 m of the microphone positions. The maximum A-weighted fast sound level during the acceleration is measured.

The relative importance of power train and tire/road interaction noise has been studied by *Sandberg* and *Ejsmont* [23.99]. The relative importance of these sources depends on the year of vehicle manufacture, the type of vehicle (cars, heavy trucks), and engine speed. The characteristics of the tire itself (tread, sidewall stiffness, etc.) are also important – as is the character of the road surface. The relative importance of these sources may be described in terms of a crossover speed – the speed at which tire–road noise becomes more important than power train (power unit) noise.

It can be seen from Table 23.8 that at normal speeds on major highways, tire–road interaction noise is the dominant source of vehicle noise emissions. In the table caption, "SMA" refers to a stone mastic asphalt surface and "chippings" refers to stones in an asphalt concrete surface that also consists of sand, filler, and an asphalt binder.

A qualitative description of the sources of noise radiation from tires includes radial and tangential vibration

Table 23.7 Examples of noise reduction measures in motor vehicles. (Table 1 from [23.97])

Engine in general	Other vehicle components
• Switchover to turbo-charged engines • Optimization of the engine combustion process, e.g., by using electronics or by improving the shape of the combustion chamber • Encapsulation or shielding of entire engines or especially noisy parts of them • Use of hood blankets or laminated covers • Sound-absorptive material in the engine compartment • Optimization of the stiffness of the cylinder block • Use of structure-borne noise-reducing material	• Improvement of gearboxes, damped propeller shafts • Improved rear-axle transmission • Shielding of transmission components • Regulation of the fan by thermostat • Decreased speed of fan by using a larger fan or optimization of fan shape • Silencers for air compression outlet noise • Improvements of brakes for reduction of brake squeal • Improved aerodynamics • Selection of suitable tires (low noise at acceleration)
Exhaust system	**Induction system**
• Minimization of outlet and mantle emission of exhaust silencers, e.g., by increased volume • Introduction of more than one silencer • Optimization of pipes to/from the silencer, e.g., by equal length pipes or air gap pipes • Dual-mode mufflers • Use of absorptive materials • Active noise control	• 1/4-wave tuners or other resonators • Thicker duct walls, and/or lined ducts • Increased volume of air cleaner • Intake covers or shields • Active noise control

Table 23.8 Crossover speeds for various cases. According to Sandberg [23.99] "The table assumes that 'normal' tires are used, and that the road surface is a dense asphalt concrete or an SMA with max 10-14 mm chippings. 'Cruising' is constant speed, and 'Accelerating' means an 'average' way of accelerating after a stop, but not as much as in the ISO 362 driving mode." (After [23.99] Table 5.1)

Vehicle type	Cruising	Accelerating
Cars made 1985-95	30–35 km/h	45–50 km/h
Cars made 1996-	15–25 km/h	30–45 km/h
Heavy trucks made 1985-1995	40–50 km/h	50–55 km/h
Heavy trucks made 1996-	30–35 km/h	45–50 km/h

of the tire treads, axial vibrations of the sidewalls, *air pumping* due to the deformation of the tread by irregularities in the road surface, and possibly vibration of the rim of the tire. At low frequencies, there is evidence that the tire treadband can be considered to be a cylindrical beam elastically supported by the sidewall [23.100].

A quantative description of tire–road noise is best obtained by development of a model of the sound radiation. A history of past modeling attempts has been given by *Kuijpers* and *van Blokland* [23.101], and more generalized models are also available [23.102, 103].

The road surface itself has a significant effect on the generation of tire noise. The roughness of the surface affects the excitation of the tire and subsequent generation of noise; the porosity of the surface effectively changes the compressibility of trapped air, and if the acoustic impedance is in the range to absorb sound, energy can be absorbed by the surface. Information on the characteristics of porous surfaces is given in [23.99].

Tire–road interaction noise is currently the subject of intensive research. *Bernhard* et al. have given a summary of research [23.104], *Sandberg* et al. [23.105] have discussed poroelastic road surfaces, and *Thornton* et al. [23.106] have studied the variability of existing pavements. Although porous surfaces have been shown to provide noticeable reductions in traffic noise levels, questions remain about the durability of these surfaces, especially in cold climates. The durability of such surfaces in a warm climate has been studied by *Donavan* et al. [23.107].

Traffic Noise Prediction Models. The US Federal Highway Administration has released version 2.5 of the *traffic noise model*, which may be used for a wide variety of calculations related to traffic noise. The characteristics of the model are described in Sect. 23.3.1 on *outdoor noise barriers*.

Aircraft Noise

Exterior noise emissions of aircraft are of major importance to persons on the ground, and interior noise emissions are a concern of both airline passengers and crews.

Aircraft Noise Emissions. Noise emissions from civil aircraft have been regulated for more than 35 years, first by the Federal Aviation Administration in the United States, and later, internationally, by the International Civil Aviation Organization (ICAO). Nevertheless, although the noise from individual airplanes has been significantly reduced, the total exposure to aircraft noise for residents in communities near many airports has increased because of the growth in the number of aircraft operations at airports throughout the world. Consequently, operators of the airplanes and the airports continue to face limitations because of aircraft noise. This section discusses the noise emissions of aircraft; noise at the receiver is discussed in Sect. 23.4.4. Requirements for the noise levels that may be produced by aircraft are given in title 14 of the US Code of Federal Regulations, 14CFR part 36 [23.108] and in annex 16 to the Convention on International Civil Aviation (ICAO annex 16) [23.109].

The methodology of determining the noise emission of aircraft for certification purposes is well developed. Certification noise levels are not intended to, and do not, represent noise levels that may be measured in communities around airports.

Certification noise limits, in terms of effective perceived noise level (EPNL), are specified at three points – known as *lateral*, *flyover*, and *landing approach*. The limits are a function of the maximum design takeoff gross mass, and apply to both jet-powered and propeller-driven transport-category airplanes, business/executive airplanes, and helicopters. The limits apply to new-design airplanes and to retrofit modifications of old-design aircraft.

Perceived noise levels are determined from 500 ms-average one-third-octave-band sound pressure levels, at 500 ms intervals, and are adjusted for the additional noisiness caused by prominent tones, if present, or other spectral irregularities. For each of the three noise-measurement points, effective perceived noise levels are determined from the time integral of tone-corrected perceived noisiness and adjusted to reference atmospheric conditions, reference flight paths, reference airspeeds, and reference engine power settings.

Amazon EX1014 Page 993

The first issue of 14CFR part 36 became effective in 1969; ICAO annex 16 was first issued in 1971. The main objective of those regulations was to ensure that noise produced by new aircraft designs would be less than the noise produced by earlier designs. In the years since the initial issue, the certification noise level limits have been gradually reduced in stages.

Stage 1 airplanes are the noisiest, and include the as-manufactured versions of the Boeing 707 and McDonnell Douglas DC8 and various business/executive jets. Stage-2-compliant airplanes have lower noise levels than stage 1 airplanes. Noise levels from airplanes that comply with stage 3 requirements are even lower. An airplane that complies with the Stage 1, 2, or 3 requirements of 14CFR Part 36 also complies with the corresponding Chap. 1, 2 or 3 requirements of ICAO Annex 16.

ICAO Annex 16 recently introduced the Chapter 4 requirements for jet-propelled airplanes and for propeller-driven airplanes having a takeoff gross mass of more than 8618 kg. The FAA is considering adoption of similar stage 4 requirements. Noise-level limits for chapter 4 compliance are the same as for chapter 3 compliance but compliance was made more stringent by eliminating the *tradeoff provisions* that had been part of the chapter 2 and 3 (or stage 2 and 3) requirements.

As an example of the changes to the certification noise-level limits, the effective perceived noise level limit at the lateral position for a takeoff gross mass of 200 000 kg (441 000 lbf) is 107.1 dB for a chapter 2/stage 2 airplane at 650 m to the side of the takeoff flight path, and 100.4 dB for a chapter 3/stage 3 airplane (or a chapter 4 airplane) at 450 m to the side of the takeoff flight path. Changes in lateral noise levels are representative of improvements in the technology of aircraft noise reduction.

Figure 23.19 illustrates trends in the progress in reducing the noise emission from commercial jet aircraft. There are no chapter 1/stage 1 airplanes operating in most of the industrialized countries of the world and only a few chapter 2/stage 2 airplanes.

For jet-powered and propeller-driven airplanes, the engines are the principal sources of noise during ground roll, climb-out, and landing. Sound produced by vortices shed by the extended landing gear and by wing leading-and trailing-edge devices (flaps) contributes to the noise level under landing-approach flight paths, and is an important consideration as engine noise is reduced.

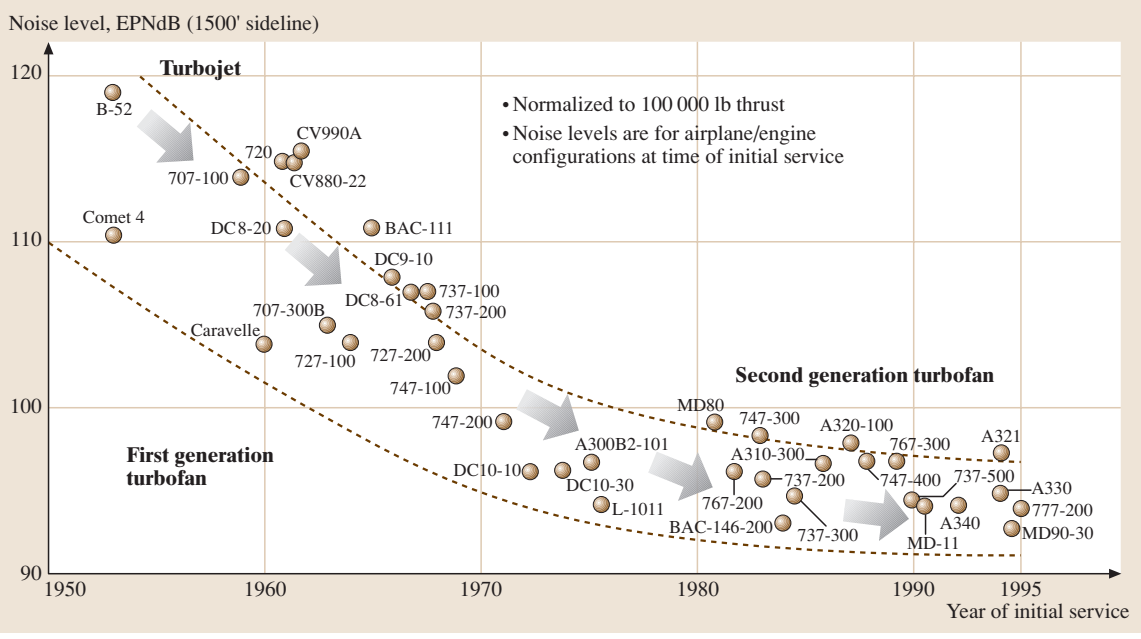


Fig. 23.19 Progress in aircraft noise reduction. Effective perceived noise level at the 450 m lateral noise-measurement point normalized to a total static thrust of 444 800 N for the noted airplane/engine configurations at the time of initial service. (After *Willshire* [23.110]; adopted from Condit [23.111])

Reduction of airplane engine noise during departure operations (as illustrated in Fig. 23.19) was achieved primarily by increasing the bypass ratio, and hence the diameter of the fan stage at the front of the turbofan engines. Bypass ratio is the ratio of the mass flow rate of the air that passes through the fan-discharge ducts to the mass flow rate through the turbine stages in the core of the engine. Design thrust is provided by moving a large amount of air at a lower exhaust-gas velocity and hence with lower levels of jet-mixing noise at high engine-power settings. Higher bypass ratios also result in better fuel efficiency for the same thrust, although at an increase in engine weight and diameter.

Discrete-frequency noise from the fan, compressor, and turbine stages is reduced by means of sound-absorbing linings in the engine inlet and discharge ducts. Tonal components in the sound from the fan stages are minimized or eliminated by careful selection of the number of blades and vanes and by increasing the spacing between the fan stage and the fan-outlet guide vanes. Inlet guide vanes ahead of the fan blades are no longer used in modern turbofan engines.

A summary of technology for engine noise-control designs is available [23.112]. A summary of retrofit applications intended to allow chapter 2/stage 2 airplanes to meet a phase-out deadline of the year 2000 for stage 3 (ICAO chapter 3) compliance has been published [23.113].

Interior Aircraft Noise. The engines and pressure fluctuations in the turbulent boundary layer outside the fuselage of an aircraft during flight are sources of noise in the interior of an airplane. Vibration from jet engines or propellers can cause the fuselage to vibrate and be radiated as sound into the cabin of an aircraft or helicopter. The air-conditioning system is often a source of noise in the interior of an aircraft.

Noise from external sound sources can be partially controlled by the design and construction of the fuselage. Sound-absorbing material is installed between the skin of the fuselage and the interior trim panels; this material also acts as a thermal insulation barrier to the cold outside air. Some propeller-driven airplanes have successfully used active noise and vibration control systems.

Control of noise in the interior of an aircraft requires a balance between the desire to achieve low cabin interior noise levels for the comfort of the passengers and the flight and cabin crews, while maintaining a degree of privacy, and an increase in airplane empty weight and maintenance costs.

Cabin noise levels vary greatly with seat location and operation of the aircraft (takeoff, cruise, and landing). Standardized test methods are now available for the specification of procedures to measure aircraft interior noise under specified cruise conditions [23.114, 115].

23.3 Propagation Paths

23.3.1 Sound Propagation Outdoors

Sound propagation in the atmosphere is discussed in Chap. 4, and only general information will be presented here. Geometrical spreading is the most important effect that reduces the sound pressure level as distance from a source is increased. There are, however, several other factors which influence outdoor sound propagation.

1. Atmospheric absorption. At long distances and at high frequencies, the effects of atmospheric absorption are significant. These effects are usually described by an attenuation coefficient in decibels per meter Chap. 4.
2. Ground effects. When the sound source is located above a ground surface, sound waves that reflect from the ground will constructively and destructively interfere with those propagating directly from the source. In general, the ground is partially reflecting; the reflected wave is modified in amplitude and phase by its interaction with the ground surface. The amount of attenuation attributable to this ground interaction, and its variation with frequency, depend on the surface characteristics, the source and receiver heights, and their separation. The effects of the ground are largest for intermediate frequencies ($\approx$ 500 Hz) when the source is above the ground (1 m or more). If the source is very close to the ground, all frequencies above about 500 Hz are highly attenuated.
3. Temperature gradients and wind speed gradients. The speed of sound is proportional to the square root of the absolute temperature of the medium. The normal temperature lapse with height above the ground means that a sound wavefront moves more rapidly near the ground surface. This causes the wavefront

to bend upwards, creating a *shadow zone* of low sound pressure level near the surface. The opposite effect occurs when the temperature lapse is abnormal. Wind velocity gradients have a similar effect since the speed of the wave is the wind speed plus the speed of sound. Since the wind speed is usually lower close to the ground, propagation upwind tends to bend the wavefront upwards, creating a shadow zone similar to that produced by a normal temperature lapse. For sound propagation downwind, the opposite effect occurs, and the wavefront is bent toward the ground; there is no significant attenuation of the sound wave relative to the attenuation in the absence of wind.

4. Turbulence. Since turbulence always accompanies wind outdoors, the effects of atmospheric turbulence must be included in any analysis of sound propagation outdoors. There are three major effects of turbulence. First, at single frequencies, atmospheric turbulence affects the coherence between waves that propagate directly from the source and waves that are reflected from the ground surface. This results in sound pressure levels that are higher than would be expected in the absence of turbulence at those points where destructive interference between the waves occurs. Second, atmospheric turbulence produces scattering into the shadow zones caused by air-temperature and wind-speed gradients that tends to raise the sound pressure level in these areas. Third, in a highly directive sound beam, the presence of turbulence results in an excess attenuation produced by sound scattering out of the beam.

A review of sound propagation outdoors has been given by *Embleton* [23.116].

Outdoor Noise Barriers

Information on the design of noise barriers may be found in Chap. 4. In this section, the current use of outdoor noise barriers is described, and a summary of the effectiveness of these barriers is given. Barriers are widely used for the control of highway traffic noise, and are also used to control noise from rail vehicles and airport ground operations. Two common alternatives to barriers exist: sound insulation of buildings when noise indoors is the problem, and the use of quiet (porous) road surfaces. Information on tire–road interaction noise is presented in Sect. 23.2.8. However, noise barriers are currently the preferred solution for the reduction of traffic noise, and they have been constructed along many highways, as described below.

Barrier Characteristics. A typical noise barrier is shown in Fig. 23.20.

The most important parameter to describe the effectiveness of the noise barrier is the Fresnel number N

$$N = \frac{(d_1 + d_2 - d_3)}{\lambda/2} \,. \tag{23.40}$$

The distances d_1, d_2, and d_3 are defined in Fig. 23.20; λ is the wavelength of sound. The noise reduction performance of the barrier for single source and receiver points may be described in terms of its insertion loss L_i; $L_i = L_{\mathrm{pb}} - L_{\mathrm{pa}}$.

L_{pb} is the sound pressure level before installation of the barrier, and L_{pa} is the sound pressure level after installation. These levels may be described in octave- or one-third-octave bands, or for an overall sound level with frequency weightings such as A or C. Since the insertion loss depends on the location of both the sound source and the receiver, standardization of the measurement procedures must be available to allow specification of barrier performance (see below). Large Fresnel numbers lead to high insertion loss, and therefore performance is best at high frequencies. A technical assessment of the performance of many noise barriers [23.117] found insertion losses (A-weighted sound levels) to be in the range 5–25 dB. Barrier heights are typically 3–8 m. The performance of a barrier depends on its height, thickness, shape, edge conditions at the top of the barrier, and ground impedance on both sides of the barrier (because ground reflections contribute to the insertion loss). The transmission loss of the barrier material itself should exceed about 25 dB, but it is often of secondary importance because structural considerations usually require massive walls.

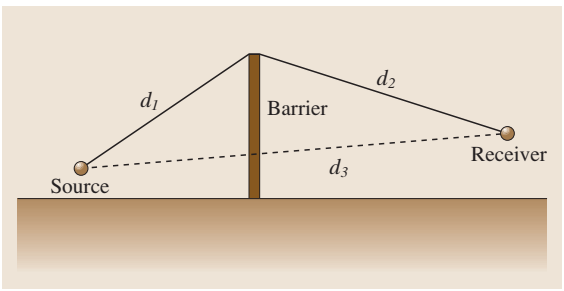


Fig. 23.20 A basic schematic showing the source of noise, barrier, and receiver

Amazon EX1014 Page 996

A variety of materials are used to construct barriers – precast concrete, block, earth berms, wood, metal, and plastics (including transparent plastics). Barriers with sound-absorptive surfaces have two advantages: the sound at the receiver point may be lowered, and reflections from the barrier are reduced. The latter may be of importance where barriers are installed on both sides of a highway and multiple reflections between the barriers can compromise insertion loss. Also, absorptive surfaces are useful where a barrier is installed on only one side of a highway, and neighbors on the opposite side may perceive increased noise due to reflections.

Determination of Barrier Insertion Loss. One method to determine the insertion loss of barriers is described in ANSI S12.8 [23.118]. The most reliable method is the direct method that uses data measured at the same site before and after construction of the barrier. Two "indirect" methods are described – one using *before* data at an equivalent site, and a second using a prediction method to obtain *before* data.

Steps must be taken to ensure that the source level is the same for the *before* and *after* measurements by using a reference microphone position not influenced by the barrier. The atmospheric conditions must be constant, the microphones must be calibrated, and corrections must be applied for calibration differences before and after a series of measurements. The standard specifies microphone heights and distances at which measurement must be made to determine the insertion loss.

Noise Barrier Construction. Data on noise barrier performance in many countries is available [23.117]. In the United States, construction of noise barriers is the responsibility of State Departments of Transportation guided by criteria specified by the US Federal Highway Administration (FHWA). According to the FHWA [23.119], by the end of 2001, the 10 states with the most noise barriers had constructed 8.53×10^6 m^2 of noise barriers (1993 linear km) at a cost of 1.89 billion US dollars (2001 dollars). Many of the barriers have been constructed using a combination of materials. However, the materials most used in single-material barriers are:

- Concrete/precast,
- block,
- wood/post and plank,
- concrete,
- berm,
- wood/glue laminated
- metal, and
- other wood construction.

A more detailed analysis of barrier construction by state, including area, length, and cost has been made by *Polcak* [23.120]. He concluded that cost figures are reliable only in general terms, and that many costs are variable from project to project. These include drainage, excavation, guard rails, utility relocation, landscaping, and the cost of the barrier system itself.

Noise Barrier Prediction Methods. Prediction of the performance of noise barriers is included in a more general noise model used to predict traffic noise, the *Traffic Noise Model* (TNM). According to the sponsor of the model, the US FHWA [23.121], the model contains the following components:

- Modeling of five standard vehicle types, including automobiles, medium trucks, heavy trucks, buses, and motorcycles, as well as user-defined vehicles,
- Modeling of both constant-flow and interrupted-flow traffic using a 1994/1995 field-measured database,
- Modeling of the effects of different pavement types, as well as the effects of graded roadways,
- Sound level computations based on a one-third-octave-band database and algorithms,
- Graphically interactive noise barrier design and optimization,
- Attenuation over/through rows of buildings and dense vegetation,
- Variable ground impedance,
- Multiple diffraction analysis,
- Parallel barrier analysis,
- Contour analysis, including sound level contours, barrier insertion loss contours, and sound level difference contours.

The TNM replaced the STAMINA/OPTIMA program, and several early versions were produced. Experience with the TNM and elements of its design have been described by *Menge* et al. [23.122], and comparisons of model predictions with experimental data have been made by *Rochat* [23.123].

23.3.2 Sound Propagation Indoors

In this section, the primary objective is to relate the sound pressure level measured in a room having specified acoustical characteristics to the sound power radiated by one or more sources in the room. Sound transmis-

sion through walls, window and other building elements is discussed in Chap. 11.

Classical Theory of Sound Propagation in Rooms

It is important to relate the sound pressure level in rooms to the sound power output of a source, and therefore the path indoors between the source and receiver should be discussed. In the classical theory of room acoustics, reflections from all of the surfaces in the room are equally important, and the difference between the sound pressure level L_p, and sound power level L_W at a distance r from a source emitting sound power L_W may be expressed as

$$L_p - L_W = 10 \log \left(\frac{Q}{4\pi r^2} + \frac{4}{R} \right), \qquad (23.41)$$

where Q is the directivity of the source in the direction of the receiver point (Sect. 23.2.1), and R is the room constant (Chap. 9). The first term on the right of the equation is the direct sound, and the second term is the reverberant sound – the sound reflected from all of the room surfaces. For an omnidirectional source ($Q = 1$), the difference between sound pressure level and sound power level is as shown in Fig. 23.21.

In many rooms of practical interest, reflections from the room surfaces are not of equal importance, and the noise emission of one or more sources in the room has been determined according to the methods described earlier in this chapter. Rooms almost always contain objects that scatter the sound waves, and this scattering is not taken into account in (23.41). Therefore, a more detailed theory must be used to characterize the path between the source and the receiver.

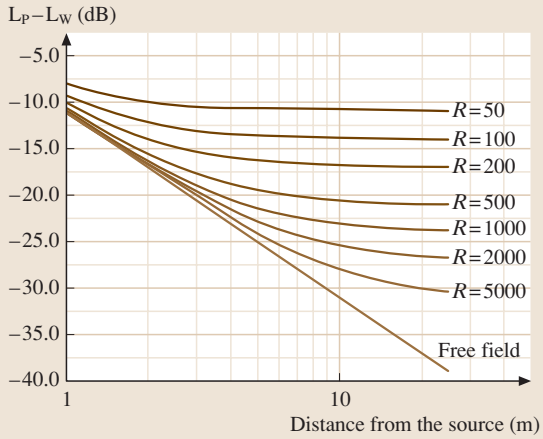


Fig. 23.21 Difference between sound pressure level and sound power level as a function of distance from an omnidirectional source

Prediction of Installation Noise Levels

One procedure for determining the path attenuation in real rooms has been published by the ECMA [23.124]. This method allows for the prediction of sound levels in rooms, and, while it was developed for use with information technology equipment, it is applicable to other noise sources when the A-weighted sound power level of the source is known. The method predicts A-weighted sound pressure levels, and the sound-absorptive properties are described in terms of a sound absorption coefficient α, which is the average of the absorption coefficients in the 250, 500, 1000, and 2000 Hz octave bands.

Three different shapes of rooms are defined in the procedure :

An *ordinary room* has a length L and a width W, smaller than $3H$, where H is the height of the room. For this room, classical theory is used with the modifications described below.

A *flat room* has $L > 3H$ and $W > 3H$. For such a room, it is assumed that the sound absorption of only the floor and ceiling is important.

A *long room* has $L > 3H$ and $W < L/2$. For such rooms, reflections from the sidewalls are assumed to be important.

For an ordinary room, the classical theory is used with the following modifications.

In a free field, the radiation from the source is through a hemispherical surface, since widely used methods for the determination of sound power level depend on sound pressure level measurements on the surface of a hemisphere.

The measured directivity of the source itself is assumed to be unity because the source directivity is not normally reported with the sound power level. However, a directivity Q is included in the calculations if the source is near a wall ($Q = 2$) or in a corner ($Q = 4$).

With these modifications, the difference $L_{pA} - L_{WA}$ as a function of distance, r, from the source in an ordinary room is

$$L_{pA} - L_{WA} = 10 \log \left(\frac{Q}{2\pi r^2} + \frac{4}{S\alpha} \right), \qquad (23.42)$$

where $S\alpha$ is the total absorption in the room weighted according to the area and absorption of each room surface and piece of furniture. Curves similar to those shown in Fig. 23.21 above may be plotted for this case.

Amazon EX1014 Page 998

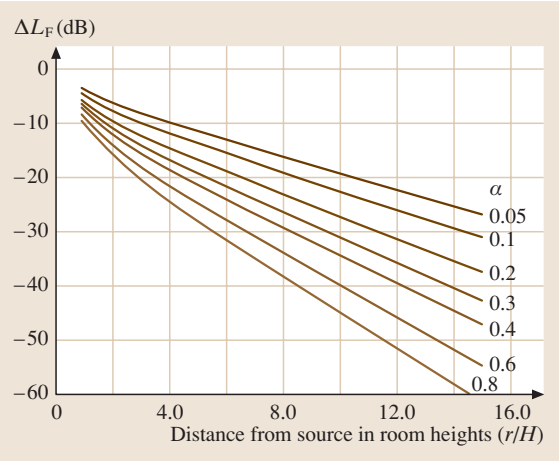


Fig. 23.22 Correction term for a furnished flat room having a density factor $q = 2$ as a function of distance from the source for several values of α

Similar, but more complex equations are given in [23.124] for flat rooms and long rooms. As an example, in a flat room with scattering objects, the absorption of the scatterers is assumed to be $\alpha_s = 0.1$ and the density factor of scattering objects q is given by

$$q = \frac{S_E}{4S_F} ,$$

where S_E is the total area of scatterers as viewed from the source in m^2, and S_F is the surface area of the room floor in m^2.

The difference $L_{pA} - L_{WA}$ in a flat furnished room is then given by

$$L_{pA} - L_{WA} = -20 \log H + \Delta L_F , \qquad (23.43)$$

where ΔL_F is a complicated function of distance from the source, density factor, and average absorption of the ceiling and floor. As an example, ΔL_F is given in Fig. 23.22 as a function of absorption coefficient for a density factor $q = 2$.

Other equations are given in [23.124], and correction terms are defined, both as equations and in graphical form.

Calculations for Multiple Sources

In general, there are several sources in a room at different distances from the receiver. In this case, the A-weighted sound pressure level is calculated for each source and distance, and converted to mean-square pressure. These mean-square pressures are added and converted to a total A-weighted sound pressure level at a given receiver position.

23.3.3 Sound-Absorptive Materials

Sound-absorptive materials are widely used for the control of noise in a variety of different situations. These include addition of absorptive materials to room surfaces to control reverberant sound generated by machinery and other equipment, installation of duct liners to increase the sound attenuation in air-conditioning ducts, liners for machine enclosures to reduce the sound radiated from the machine, hanging baffles for reduction of reverberant sound, and other applications.

Sound-absorptive materials exist in many different forms. These include:

- Glass-fiber materials,
- open-cell acoustical foams (urethane and similar materials, reticulated and partially reticulated),
- fiber board as frequently used for acoustical ceilings,
- hanging baffles used to reduce reverberation in factories, and other enclosed spaces
- felt materials,
- curtains and drapes,
- thin porous sheets, often mounted on a honeycomb structure,
- hollow concrete blocks with a small opening to the outside – to create a Helmholtz resonator,
- head liners for automobiles – of various materials, and
- carpets.

One characteristic common to nearly all sound-absorptive materials is that they are porous. That is, there is air flow through the material as a result of a pressure difference between the two sides of the material. Porous materials are frequently fragile, and, as a result, it is necessary to protect the exposed surface of the material. Typical protective surfaces include:

- Thin impervious membranes of plastic or other material,
- perforated facings of metal, plastic, or other material,
- fine wire-mesh screens,
- sprayed-on materials such as neoprene, and
- thin porous surfaces.

A full description of propagation in porous materials, the relationship between the propagation parameters and the physical properties of materials, and the matching of boundary conditions when composite structures are created is beyond the scope of this chapter. However, some of the properties of sound-absorptive materials

Amazon EX1014 Page 999

will be discussed, methods of measurement of normal impedance will be presented, and some results of calculations on composite structures will be shown.

A key parameter is the flow resistance r which can be defined as the ratio of the pressure drop across a sample of a material and the velocity through it

$$r = \frac{\Delta p}{u} \,. \tag{23.44}$$

The flow resistance is usually measured for steady flow through the material, the assumption being made that this value is equivalent, at least at low frequencies, for the particle velocity in a sound wave.

The unit of of flow resistance is $\mathrm{N\,s/m^3}$, the MKS Rayl. Actual values are often specified as a dimensionless quantity, the specific flow resistance r_s, where $r_s = r/\rho c = r/406$ for a density of air ρ of $1.18\,\mathrm{kg/m^3}$ and a speed of sound c of 344 m/s. It is also common to specify the flow resistance per unit thickness.

Another property of sound-absorptive materials is that they can often considered to be *locally reacting*. When a sound wave is incident on a locally reacting material, the local pressure at the surface produces a particle velocity normal to the surface. When the two are sinusoidal and expressed as complex numbers the ratio is the normal impedance of the surface

$$z_\mathrm{N} = \frac{p}{u} \,. \tag{23.45}$$

The normal impedance is independent of the angle of incidence of the sound wave.

Two mechanisms are mainly responsible for the absorption of sound. First, friction in the boundary layer between the air and the internal structure of the material absorbs energy, and a large particle velocity is needed for effective absorption. Second, the temperature rise during the compression phase of the sound wave results in conduction of heat into the material, further absorbing energy from the sound wave. The former is generally most important.

The sound absorption coefficient α is the ratio of the sound energy absorbed by the surface and the incident sound energy. In general, it is a function of the angle of incidence of the sound wave on the material. It varies from 0 to 1.0, although some measurement methods – described later in the section – result in values of $\alpha > 1$. The unit of sound absorption is the metric Sabine, S. Material with an area of $1\,\mathrm{m^2}$ and $\alpha = 1$ has 1 Sabine of sound absorption (10.8 Sabins in English units). The sound-absorptive properties of, for example, hanging baffles are frequently expressed in Sabins.

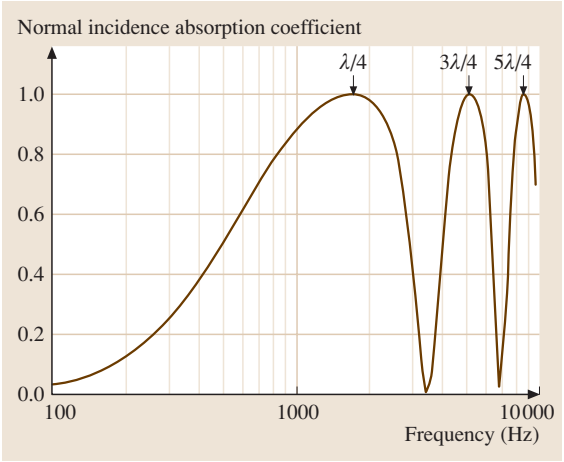


Fig. 23.23 Normal incidence sound absorption coefficient for a thin, rigid sound absorber having a flow resistance ρc placed 50 mm from a rigid termination. Calculated using a program by *Ingard* [23.125]

Sound absorption coefficients are frequently measured in octave bands, and the noise reduction coefficient (NRC) is the average absorption in the 250, 500, 1000, and 2000 Hz octave bands.

The importance of particle velocity can be illustrated for the case where a thin sound absorber having a flow resistance ρc is placed in a tube at a distance 50 mm from a rigid termination. The normal incidence absorption coefficient calculated as a function of frequency is shown in Fig. 23.23. It can be seen that the absorption coefficient is highest when the distance from the rigid termination is an odd multiple of one-quarter wavelength of the sound. It is at these distances that the particle velocity in the absorber is highest.

Galaitsis [23.126] showed that multiple resistive sheets can be used to improve the sound absorption at normal incidence, and *Ingard* [23.125] extended the analysis to diffuse fields for both locally and non-locally reacting materials. As an example, Fig. 23.24 shows the absorption coefficients for two resistive sheets having a flow resistance 1.5 ρc and a total absorber thickness of 50 mm. The first sheet is 33 mm from a rigid surface, and the spacing between the two sheets is 17 mm. The structure can be made approximately locally reacting by, for example, using a honeycomb material between the resistive layers.

Most sound-absorptive materials are relatively thick (e.g., 25 mm), and in this case, it is beneficial to have an air gap behind the material when it is mounted near a rigid surface. In the figure below, the sound-

Amazon EX1014 Page 1000

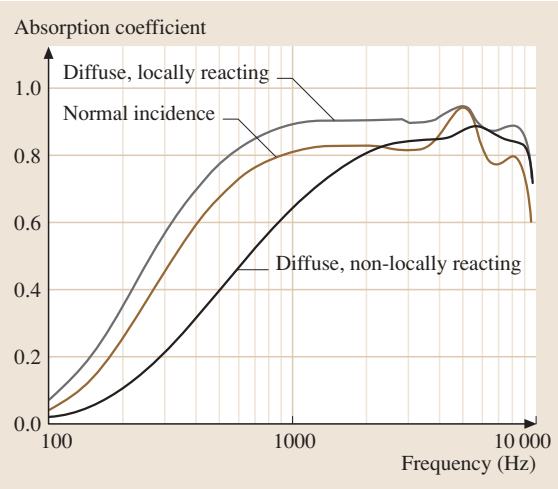


Fig. 23.24 Sound absorption coefficient for a two-screen sound absorber for normal incidence, a locally reacting structure, and a nonlocally reacting structure (After [23.127])

absorptive material is 25 mm thick, and has a total flow resistance of ρc. It is assumed that the material itself does not move. The normal incidence sound absorption coefficient as a function of spacing is shown in Fig. 23.25.

The sound-absorptive properties of flexible materials can be calculated [23.128], but this requires a knowledge of properties of the material other than flow resistance, and is beyond the scope of this chapter.

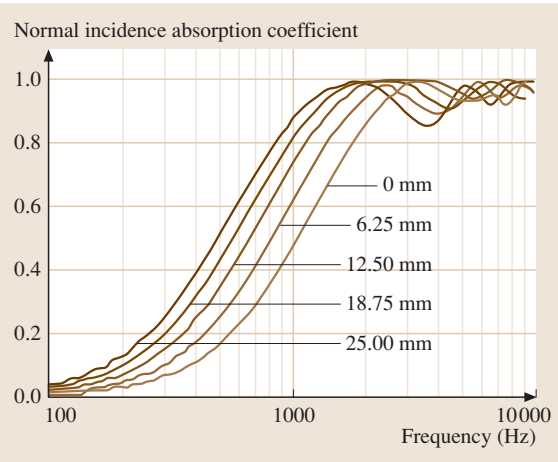


Fig. 23.25 Normal incidence sound absorption coefficient calculated for a porous material 25 mm-thick with a total flow resistance of ρc. The spacing between the material and the rigid backing is shown in the figure. Calculated using a program by *Ingard* [23.127]

Measurement of Sound Absorption Coefficients

Two methods are commonly used to measure the performance of sound-absorptive materials, the impedance tube method and the reverberation room method.

The classic impedance tube method involves two tubes to cover two frequency ranges, a 100 mm-diameter tube and a 30 mm-diameter tube. A sample of the material is mounted at one end of the tube, and a loudspeaker at the other end is used to create a plane-wave sound field in the tube. A moving probe is used to detect the sound pressure an any point. The absorption coefficient is determined from

$$\alpha = 1 - \left|R^2\right| , \qquad (23.46)$$

where $|R|$ is the magnitude of the pressure reflection coefficient in the tube, the ratio of the incident and reflected pressure. R is determined from the maximum and minimum pressures detected in the tube. The distance to the first minimum of sound pressure can also be measured, and together with R, can be used to determine the normal impedance of the material at its surface [23.129].

This method is useful to demonstrate plane-wave propagation and the interference of sound waves upon reflection, but it has several disadvantages:

1. The absorption coefficient is determined at single frequencies; it is therefore time consuming to determine its value as a function of frequency.
2. The sample size is small; 100 mm in diameter or 30 mm in diameter depending on the frequency of interest. The properties of a small sample may not be representative of a large sample of the same material.
3. The sample must be cut very accurately and very carefully mounted to achieve consistent results.

The first disadvantage may be eliminated by using the two-microphone method [23.130, 131] for probing the sound field. This method uses broadband excitation of the tube and two closely spaced phase-matched microphones; a digital signal processor is used to determine the transfer function between them. The absorption coefficient can then be calculated.

The reverberation room method [23.132] uses a large sample of material in a reverberation room, usually with rotating diffusers. The sound absorption coefficient is determined from the difference in reverberation time in the room with and without the sample present. The results approximate the diffuse-field absorption coefficient.

Amazon EX1014 Page 1001

One additional method for measuring the spherical-wave absorption coefficient in a free field over a reflecting plane has been proposed by *Nobile* [23.133]. The method uses the two-microphone technique referenced above, and makes it possible to measure the absorption coefficient as a function of the angle of incidence of the sound wave for samples of absorptive materials, which can be very large. The method therefore overcomes the disadvantages of the impedance tube method and provides more information than the reverberation room method.

23.3.4 Ducts and Silencers

Attenuation of sound in heating, ventilating, and air-conditioning ducts is covered in Chap. 11. There are, however, many other applications for devices to reduce noise between the source and the receiver. These include:

- Pumps,
- compressors,
- fans,
- cooling towers,
- engines (diesel and gas),
- power plants, and
- gas turbines.

A general schematic of a *silencer* is shown in Fig. 23.26.

It is not always appropriate to describe input and output parameters in terms of impedances, but is is convenient for the purposes of illustration. Sources of sound have an internal impedance which is Z_{int} in the figure. This can be used to quantify the effect that an acoustic load has on the power output of a source [23.6]. For example, if a monopole source is characterized by a volume velocity that is independent of load, then a reflected pressure at the source which is in phase with the particle velocity will increase the power output of a source. In the figure below, the conditions at the inlet to the silencer are represented by Z_{in}. The conditions at the output of the silencer looking down the duct are characterized by Z_d. The radiation of sound into a reverberation room, hemi-anechoic environment, or an environment in which reflections are present is characterized by Z_{rad}.

When the silencer does not contain any sound-absorptive materials (a *packless* silencer), the only mechanism that can produce an insertion loss (the ratio of the sound power radiated with the silencer in place and the sound power radiated with the silencer removed) is to create a Z_{in} which, in combination with Z_{int}, reduces the sound power input to the silencer. Such a reactive silencer works best at low frequencies, and clearly depends on the internal impedance of the source, a topic that has been studied for internal combustion engines. At low frequencies, the silencer itself can often be represented by transmission matrices [23.126]. Transmission matrices for a variety of duct elements have been defined by *Ingard* [23.134]. Characterization of the silencer in terms of lumped parameters (mass, compliance, resistance) is not generally effective. A tube, for example, is a mass element only if its end is open (low-impedance termination) whereas it is a compliance when the end is closed (high-impedance termination). Thus, a description using transmission lines in the form of T networks is an alternative. Characterization of the silencer for complex geometries and high frequencies requires a computer program.

In most practical applications, the silencer contains sound-absorptive materials and usually protective facings. The input impedance of the muffler is usually such that reflections back to the source are not important. At high frequencies, the radiation impedance is

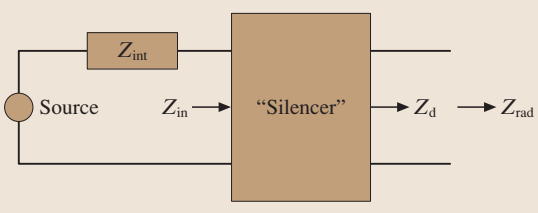


Fig. 23.26 Schematic diagram of a *silencer*

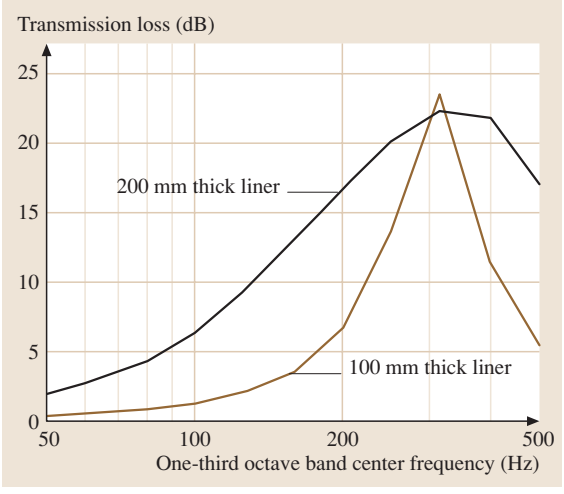


Fig. 23.27 Transmission loss in a duct as a function of frequency for two thicknesses of duct liner. Calculated using the program DuctMltl by *Ingard* [23.134]

high enough that there is little sound power reflected back down the outlet duct, and the transmission loss of the silencer (the ratio of the sound power at the outlet and the sound power at the inlet) is a good measure of silencer performance. This may not be true at low frequencies.

Duct silencers are manufactured in a wide variety of sizes, with linings, with splitters, and with aerodynamic shapes on the inlet and outlet. Standards are available for the measurement of silencer performance and guidance on their use [23.135–139]. The insertion loss of the silencer is usually measured, and its value may depend on the direction of air flow relative to the direction of propagation of sound. When the two are in the same direction (outlet duct), a sound wave is bent toward the lining whereas when the two are in opposite directions (inlet duct), sound is bent toward the center of the duct [23.140].

Calculation of Duct Transmission Loss

Computer programs for the determination of the transmission loss of ducts are available [23.134]. The duct lining may consist of air gaps, one or more layers of porous material, resistive sheets and perforated facings. As one example, Fig. 23.27 shows the transmission loss for a duct 2.5 m long having a cross section of 0.6 m × 0.6 m. The sound-absorptive material has a steel perforated facing 1.6 mm thick with perforations 3 mm in diameter and a 30% open area. The duct liner is 200 mm thick in one case, and 100 mm thick in the second. The transmission loss shown in the figure is from 50 Hz to 500 Hz because the calculation is for plane-wave transmission only. It can be seen that the peak attenuation is about the same for both cases, but the thicker liner provides a much higher transmission loss at low frequencies.

23.4 Noise and the Receiver

Section 23.2 was devoted to the characterization of sources in terms of their noise emission. The third part of the source–path–receiver model involves immission of sound at the receiver. The sound may not be *unwanted*, and is therefore not technically noise, but this section is generally devoted to the effects of noise on people. Section 23.4.5 is devoted to *sound quality*, a subject of increasing importance in the design of products.

23.4.1 Soundscapes

As discussed in Sect. 23.0.2, a sound field may be described in terms of a sound pressure, $p(r, t)$, that varies both in space and time. In practice, it is the RMS pressure that is measured since the time average of the pressure itself is zero, and several quantities measured by modern sound level meters are discussed in Sect. 23.1. The sound field can be described in the time domain or the frequency domain, or as a short-time spectrum that varies with time. Other descriptions are also possible.

The sound field $p(r, t)$ may, for the purposes of this section, be called a *soundscape*, an overall acoustical environment – both indoors and outdoors – that includes all sound, both wanted and unwanted. The interaction between an observer and this *physical* soundscape can then be described in terms of *immission* of sound. In some cases, it has been found that this interaction depends not only on the properties of the soundscape itself, but on the visual environment of the observer (the landscape). A discussion of this effect is beyond the scope of this chapter.

The soundscape includes indoor environments such as living space and industrial plants, urban and suburban areas, parks, and wilderness areas. The effects of the sound field on observers in different portions of the soundscape are varied, and in many cases difficult to quantify. These effects include hearing damage, annoyance in various forms – which can range from mild dissatisfaction to frustration and anger – as well as interference with speech communication in many settings, including meeting rooms and classrooms. Other effects include interference with sleep, and loss of productivity. Since the soundscape includes both wanted and unwanted sound, the soundscape, when properly managed can induce a sense of well-being in the observer which can have a positive effect on the quality of life. Examples include listing to natural sounds in remote areas where unwanted sound is either nonexistent, or has been reduced to an acceptable level. It is a fact that "acceptable" means different things to different persons.

A further complication is that using conventional measures of noise immission, the acceptability of a sound may depend on the source. For example, it has been found that the same level of noise from aircraft, road traffic, and rail traffic produces different human reactions. In recent years, the quality of the

sound has become an important factor in the design of machinery, particularly in automobiles and other motor vehicles. The soundscape created by a snowmobile may, for example, be quite acceptable to the operator, but unacceptable to an observer some distance from the machine.

In this section, various measures of noise level will be discussed, and generally accepted criteria for the magnitude of the level will be discussed. The management of the soundscape can be thought of as a policy issue that is partly the responsibility of individuals and partly the responsibility of federal, state, and local governments.

23.4.2 Noise Metrics

The effects of noise on people is a complicated subject, and extensive research is still in progress. Several metrics are commonly used to describe noise immission at the receiver, and most of these are in terms of the A-weighted sound pressure level. These metrics work well, both indoors and outdoors provided that the spectrum of the noise, measured in octave or one-third-octave bands is somewhat neutral in character; that is, it is not perceived as *rumbly* or *hissy*, does not contain discrete frequency components (tones), is broadband, and steady without impulsive or time-varying characteristics. Other, more complex, metrics are required when any of the above characteristics are present.

The A-weighted sound level as a function of time can be expressed as L_{Af} or L_{As}, where the subscripts f and s refer to the dynamic characteristics of a sound level meter: *fast* or *slow*. These dynamic characteristics are defined in Sect. 23.1.2.

In the early 1970s, the day–night sound level (DNL, L_{dn}) was selected as a long-term measure of noise exposure. The day–night level is the time-weighted average level over a 24 hour period, but with 10 dB added to the level during the nighttime hours from 10:00 to 07:00.

Another time-weighted average level used in Europe is the day–evening–night level (LDEN, L_{den}) where the evening hours are normally between 19:00 and 23:00, the nighttime hours are from 23:00 to 07:00, and the daytime hours are from 07:00 to 19:00. In this case, 5 dB is added to the level in the evening hours, and 10 dB is added to the level in the nighttime hours. According to the European environmental noise directive, 2002/49/EC, the evening interval may be shortened by one or two hours, with corresponding lengthening of the day and/or night periods.

Other metrics for the sound level include, L_{10}, L_{50}, and L_{90}, the levels exceed 10%, 50%, and 90% of the time, respectively. Single events may be described in terms of the sound exposure level (Sect. 23.1.3).

Indoors, other metrics are commonly used to describe noise immission. In most of the world, the equivalent sound level over an eight hour period is the metric used to relate noise level to hearing loss. This level is usually described as having a 3 dB exchange rate because an equivalent level over a time interval T_1 is the same as for a level 3 dB higher over a time interval of $T_1/2$. In the United States, the Occupational Safety and Health Administration (OSHA) has adopted a 5 dB exchange rate. In this case, the time-weighted average level over a time interval T_1 is equivalent in noise dose to a level 5 dB higher measured over a time interval of $T_1/2$.

23.4.3 Measurement of Immission Sound Pressure Level

Before presenting criteria for noise immission, it is necessary to have procedures for the measurement of sound pressure level, both indoors and outdoors. For occupational noise exposure, ANSI S12.19 [23.141] defines terms used in occupational noise exposure, including noise dose, exchange rates, and the criterion sound level used in some cases. The use of sound level meters and dosimeters are also described.

ANSI S1.13 [23.142] is a very general standard for description of noise levels. The quantities discussed in Sect. 23.1 are defined as are various temporal characteristics of noise – continuous and steady, continuous sound, fluctuating sound, impulsive and intermittent sound, and other characteristics. Characteristics in the frequency domain are also described – broadband and narrow-band noise, and noise containing discrete-frequency sound. The relationship between discrete-frequency components in a spectrum and the critical bands (Chap. 14) is discussed, and the *prominence ratio* and *tone-to-noise ratio*, measures of the prominence of discrete tones in noise, are defined.

For the measurement and description of environmental noise, there is a complete series of standards [23.143–148] available. This series covers such topics as basic quantities to be measured, measurement positions, definition of noise zones, categories of land use, land-use criteria, treatment of prominent discrete tones, and measuring positions for determination of the effect of aircraft noise exposure on sleep.

Amazon EX1014 Page 1004

23.4.4 Criteria for Noise Immission

In this section, criteria are divided into criteria for hearing damage, criteria for annoyance, and other currently used criteria.

Hearing Damage Criteria

In the United States, permissible levels for industrial noise exposure are set by the US Department of Labor, and are described in 29 CFR 1910.95. In summary, an employer shall administer a hearing conservation program when the eight hour time-weighted average level exceeds 85 dB. The requirements of such a program are described in detail in the above document – as is the requirements on audiometers for the determination of hearing loss, personnel conducting the tests, and hearing protectors when used to satisfy the requirements below. More details may be found in the *Hearing Conservation Manual* [23.149].

Permissible noise exposures are given in the regulation in Table G-16, reproduced below (Table 23.9) with an explanation of how the permissible levels are to be determined.

Currently, engineering controls are required only if the eight hour noise exposure exceeds 100 dB. For lower levels, hearing protection is an alternative.

The problem of specifying upper limits for noise in the workplace has been studied by a technical study group of the International Institute of Noise Control Engineering, and a report has been prepared and approved by the member societies of that organization [23.150]. Most countries in the world allow a time-weighted average sound level over eight hours of 85–90 dB as the upper limit, and an exchange rate of 3 dB. Selection of this exchange rate is widely believed to be the best alternative, and it greatly simplifies the measurement of levels that fluctuate during the working day. Table 23.10, from [23.150], shows hearing damage criteria in a number of countries as of 1997.

I-INCE publication 97-1 [23.150] makes specific recommendations with respect to allowable levels, exchange rate, and hearing conservation programs:

1. It is desirable for jurisdictions without regulations, or with currently higher limits, to set a limit on the level of exposure over a workshift, A-weighted and normalized to eight hours, of 85 dB as soon as may be possible given the particular economic and sociological factors that are pertinent.
2. This exposure level should include the contribution from all sounds that are present including short-term, high-intensity sounds. If such sounds are further limited in regulations to a maximum sound pressure level, then regulations should set a limit of 140 dB for C-weighted peak sound pressure level.
3. An exchange rate of 3 dB per doubling or halving of exposure time should be used. This exchange rate is implicit when the exposure level is stated in terms of eight-hour-average sound pressure level;
4. Efforts should be made to reduce levels of noise in the workplace to the lowest economically and technologically reasonable values, even when there may be no risk of long-term damage to hearing. Such action can reduce other negative effects of noise such as reduced productivity, stress and disturbed speech communication.
5. At the design stage of any new installation, consideration should be given to sound and vibration isolation between noisier and quieter areas of activity. Rooms normally occupied by people should have a significant amount of acoustical absorption in order to reduce the increase of sound due to excessive reverberation.
6. The purchase specifications for all new and replacement machinery should contain clauses specifying the maximum emission sound power level and emission sound pressure level at the operator's position when the machinery is operating.

Table 23.9 Criteria from Table G-16 of 29 CFR 1910.95. Permissible noise exposures[(1)]

Duration in hours per day	Sound level (dBA) slow response
8	90
6	92
4	95
3	97
2	100
1 1/2	102
1	105
1/2	110
1/4 or less	115

Notes:
1. When the daily noise exposure is composed of two or more periods of noise exposure of different levels, their combined effect should be considered, rather than the individual effect of each. If the sum of the following fractions: $C_1/T_1 + C_2/T_2 + \ldots C_n/T_n$ exceeds unity, then, the mixed exposure should be considered to exceed the limit value. C_n indicates the total time of exposure at a specified noise level, and T_n indicates the total time of exposure permitted at each level. Exposure to impulsive noise should not exceed 140 dB peak sound pressure level

7. A long-term noise control program should be established and implemented at each workplace where the level of the daily exposure, normalized to eight hours, exceeds 85 dB. This program should be reassessed periodically in order to exploit advances in noise control technology.
8. The use of personal hearing protection, either earplugs or other hearing protection devices, should

Table 23.10 Some features of legislation in other countries in 1997. After *Embleton* [23.150]. See the notes following the table

Some features of legislation in various countries					
Country (Jurisdiction)	**Eight hour average A-weighted sound pressure level (dB)**	**Exchange rate(dB)**	**8h average A-wtd limit for engineering or administrative controls (dB)**	**Eight hour average A- wtd limit for monitoring hearing (dB)**	**Upper limit for peak sound pressure level (dB)**
Argentina	90	3			110 A slow
Australia (varies by State)	85	3	85	85	140 unwgtd peak
Austria[a,c]	85		90		
Brazil	85	5	90, no exposure> 115 if no protection, no time limit	85	130 unwgtd peak or 115 A slow
Canada (Federal) (ON, PQ, NB) (Alta, NS, NF) (BC)	87 90 85 90	3 5 5 3	87 90 85 90	84 85[b]	140 C peak
Chile	85	5			140 unwgtd peak or 115 A slow
China	70–90	3			115 A slow
Finland[c]	85	3	90		
France[c]	85	3	90	85	135 C peak
Germany[c,d]	85	3	90	85	140 C peak
Hungary	85	3	90		140 C peak or 125 A slow
India	90				140 A peak
Israel	85	5			140 C peak or 115 A slow
Italy[c]	85	3	90	85	140 C peak
Japan	90		85 hearing protection mandatory at 90	85	
Netherlands[c]	85	3	90	80	140 C peak
New Zealand	85	3	85	85	140 unwgtd peak
Norway	85	3		80	110 A slow
Poland	85	3			135 C peak or 115 A slow
Spain[c]	85	3	90	80	140 C peak
Sweden[c]	85	3	90	80	140 C peak or 115 A fast
Switzerland	85 or 87	3	85	85	140 C peak or 125 ASEL

Amazon EX1014 Page 1006

Table 23.10 (cont.)

Some features of legislation in various countries					
Country (Jurisdiction)	**Eight hour average A-weighted sound pressure level (dB)**	**Exchange rate(dB)**	**8h average A-wtd limit for engineering or administrative controls (dB)**	**Eight hour average A- wtd limit for monitoring hearing (dB)**	**Upper limit for peak sound pressure level (dB)**
United Kingdom	85	3	90	85	140 C peak
USA[e] USA (army and air force)	90 (TWA) 85	5 3	90	85 85	140 C peak or 115 A slow 140 C peak
Uruguay	90	3			110 A slow
This Report Recommends	85 for 8 hour normalized exposure level limit	3	85, see also text under recommended engineering controls	on hiring, and at intervals thereafter, see text under audiometric programs	140 C peak

Notes:
* Information for Austria, Japan, Poland and Switzerland was provided directly by these member societies of I-INCE. For other countries not represented by member societies participating in the working party the information is taken with permission from [23.14]
[a] Austria also proposes 85 dB AU-weighted according to IEC 1012) as a limit for high-frequency noise, and a separate limit for low-frequency noise varying inversely as the logarithm of frequency
[b] A more complex situation is simplified to fit this tabulation
[c] All countries of the European Union require the declaration of emission sound power levels of machinery, the use of the quietest machinery where reasonably possible, and reduced reflection of noise in the building, regardless of sound pressure or exposure levels. In column 4, the limit for other engineering or administrative controls is 90 dB or 140 dB C-weighted peak (or lower) or 130 dB A-weighted impulse
[d] The rating level consists of time-average, A-weighted sound pressure level plus adjustments for tonal character and impulsiveness.
[e] TWA is the time-weighted average. The regulations in the USA are unusually complicated. Only A-weighted sound pressure levels of 80 dB or greater are included in the computation of TWA to determine whether or not audiometric testing and noise exposure monitoring are required. A-weighted sound pressure levels less than 90 dB are not included in the computation of TWA when determining the need for engineering controls

be encouraged when engineering and other noise control measures are unable to reduce the daily A-weighted exposure level of workers normalized to eight hours to 85 dB. The use of hearing protection devices should be mandatory when the exposure level is over 90 dB.

9. All employers should conduct audiometric testing of workers exposed to more than 85 dB at least every three years, or at shorter intervals depending on current exposure levels and past history of the individual worker. Records of the results of the audiometric tests should be preserved in the employee's permanent file.

Effect of High Noise Levels on Hearing

The result of exposure to high levels of noise is first a temporary shift in the hearing threshold (TTS), and eventually permanent hearing damage called noise-induced permanent threshold shift (NIPTS). Quantitative data have been published in ISO 1999 [23.151], and in ANSI S3.44-1996 [23.152]. The two standards contain the same information except that the ANSI standard allows exchange rates other than 3 dB through the calculation of an equivalent level. As one example (informative), exposure to an A-weighted sound level of 95 dB for 20 years is said to result in a NIPTS greater than 23 dB at 4 kHz in 50% of the population.

Noise Levels and Annoyance

It is difficult to specify criteria for annoyance, even when the descriptor for the noise is selected – usually the day–night sound level L_{dn}. There is a high variability in the response of individuals to noise, and it is difficult to describe a physical soundscape in terms of a single number. Reporting guidelines for community noise were published in 1998 [23.153] – after many surveys were performed. However, the classic work of

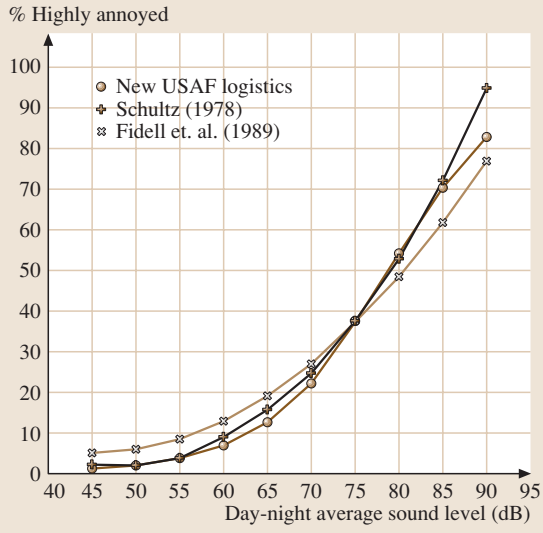


Fig. 23.28 New USAF logistic curve – together with data from *Schultz* [23.154], *Fidell* et. al. [23.156]. (After *Finegold* et al. [23.155], reprinted with permission)

Schultz [23.154] resulted in the *Schultz curve* that related the percent of persons highly annoyed and the day–night sound level. More recent data are also available, and a new logistic curve has been developed by the US Air Force [23.155]. Figure 23.28 shows this curve together with data from *Schultz* [23.154] and *Fidell* et al. [23.156].

Fidell et al. [23.156] showed that annoyance also depends on the source of sound (e.g., road traffic noise, railway noise, aircraft noise), and more recently studies by *Miedma* [23.157] and *Midema* and *Oudshoorn* [23.158] have quantified this effect with 95% confidence limits on the data. Their results are shown in Fig. 23.29.

In spite of the progress that has been made, there are doubts about the current approach to developing relationships between noise exposure and annoyance [23.159], and there may be improved methods for prediction of community response [23.160].

Criteria for Annoyance from Noise

While the figures above relate day–night sound level and the percentage of a population annoyed, there is still the question of criteria that can be used for land-use planning and other activities for which noise control is needed.

ANSI standard S12.9 [23.143–148] contains information on noise levels appropriate for various categories of land use. The data are a combination of recommendations from various sources. Table 2 from the standard is reproduced inTable 23.11.

Schomer [23.161] has studied the recommendations of several federal agencies in the United States, the World Health Organization, and the National Research Council. His recommendation is:

"For residential areas and other similarly noise sensitive land uses, noise impact becomes significant in urban areas when the DNL exceeds 55 dB. In suburban areas where the population density is between 1250 and 5000 inhabitants per square mile, noise impact becomes significant when the DNL exceeds 50 dB. And in rural areas where the population density is less than 1250 inhabitants per square mile, noise impact becomes significant when the DNL exceeds 45 dB."

Noise in Recreational Areas

Noise immission in recreational areas presents special problems. Many individuals expect a very quiet environment in parks and other recreational areas whereas others – particularly those who enjoy the use of motorized vehicles such as snowmobiles and off-road vehicles – enjoy sound levels, particularly if they are of good quality. Others enjoy recreational areas from a distance – such as in helicopters and airplanes, and the noise of these sources of concern to those on the ground. Other problems include the measurement of sounds which are often of very low level (Fig. 23.4), and may be intermittent. Measurement location is also a problem because the areas of interest are frequently very large.

A collection of 16 papers covering a variety of topics related to recreational noise is available. The papers were presented at a symposium on recreational noise held in New Zealand in 1998. *Miller* [23.7] has given a summary of the state of the art in recreational noise as of 2003.

Other Noise Criteria

A wide variety of noise criteria are discussed in a document on community noise prepared for the World Health Organization.

23.4.5 Sound Quality

In Sect. 23.0.1, noise was defined as *unwanted sound*. The field of sound quality or sound quality engineering has become important for two reasons. Noise often has characteristics that may make the sound more annoying than sounds of equivalent level using conventional measures. These include the presence of discrete-frequency

Table 23.11 A-weighted day, night, and day–night average sound levels in decibels and corresponding approximate population densities in people per square kilometer or square mile. Reprinted by permission of the Acoustical Society of America from ANSI S12.9/part 3, annex D [23.145]. This annex is for information, and is not part of the standard

	Land-use category	DNL range dB	Typical DNL dB	Day level dB	Night level dB	Approximate population density per km^2	per sq.mi.
1	Very noisy urban	> 67	70	69	61	24650	63840
2	Noisy urban residential	62–67	65	64	57	7722	20000
3	Urban and noisy suburban residential	57–62	60	58	52	2465	6384
4	Quiet urban and normal suburban residential	52–57	55	53	47	772	2000
5	Quiet suburban residential	47–52	50	48	42	247	638
6	Very quiet suburban and rural residential	< 47	45	43	37	77	200

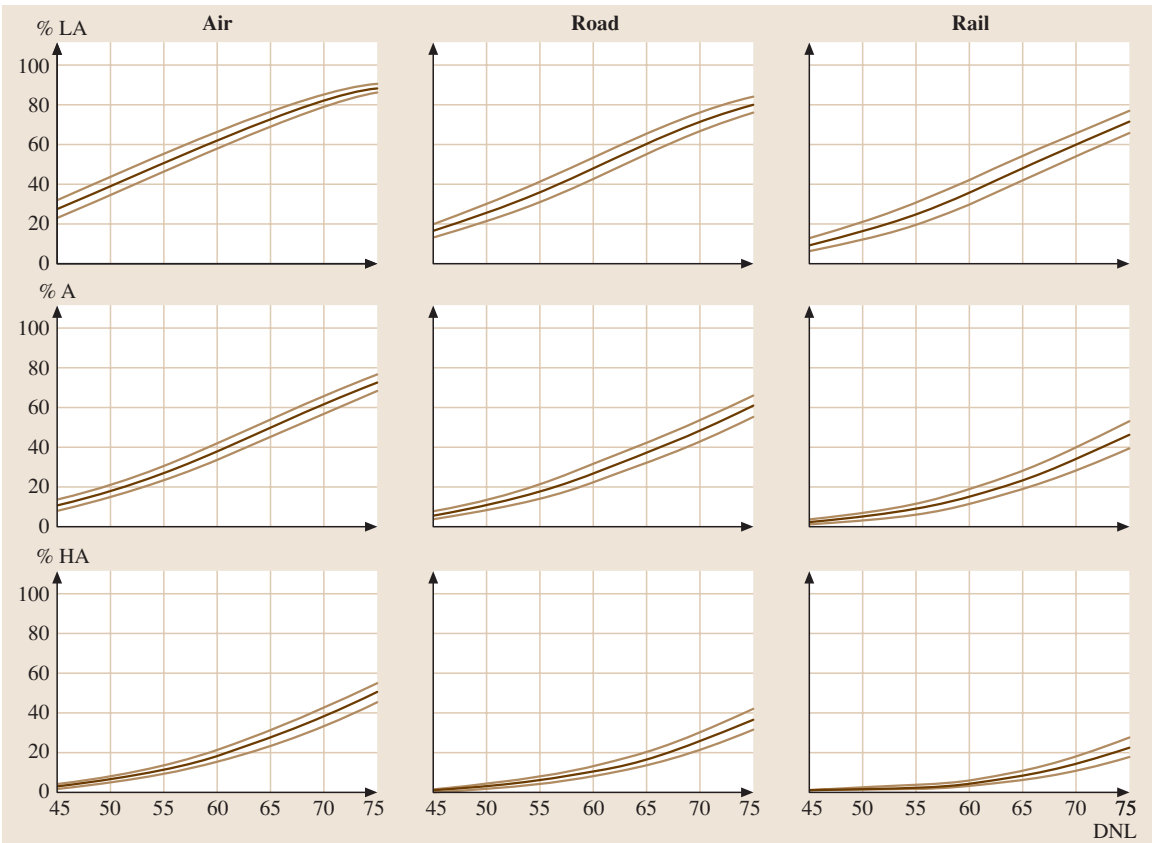


Fig. 23.29 Percentages of highly annoyed (HA), annoyed (A), and lightly annoyed (LA), with 95% confidence limits, for aircraft noise, road noise, and railway noise. (After *Miedema* [23.157] and *Miedema* and *Oudshoorn* [23.158]. Reprinted with permission)

sound, sound which is impulsive in character, and sounds that create a negative image – such as a noisy bearing which may indicate that a machine is failing. Reduction or elimination of such sounds improves the quality of the noise.

More recent work, particularly in the automobile industry has focused on the sound of engines and other automotive components to create a desirable sound for the consumer. Similarly, consumer products such as sewing machines and vacuum cleaners have been studied in an effort to eliminate sounds that the consumer finds objectionable and emphasize sounds that give a good impression of the quality of the product. There have been two sound-quality symposia that cover a wide range of topics in this field. In addition, Lyon has described the sound-quality design process [23.162], and has described a methodology by which various attributes of sound can be used to define the quality of that sound [23.163].

23.5 Regulations and Policy for Noise Control

In this section, an overview of noise policies and regulations is given. First, an overview of noise policy in the United States is given, and then information on noise policies in other countries and in the European Union is presented.

23.5.1 United States Noise Policies and Regulations

This material has been adapted from paper 302 titled "A Review of Untied States Noise Policy" by G. C. Maling, Jr. and L. S. Finegold. The paper was presented an INTER-NOISE 04, Czech Republic (2004).

The policies of the United States with respect to noise emission and noise immission have a long history. Many of the historical environmental noise documents produced in the US in the past are well known throughout the world, and have been reviewed elsewhere [23.164–170].

Funding for the US Office of Noise Abatement and Control of the US Environmental Protection Agency was discontinued in 1982, and since then there has been a lack of focus in the implementation of US noise policy. Since then, noise policies and regulations have been promulgated by a number of different federal agencies. There is a variety of state and local noise regulations; information on selected policies is given below.

Federal Government Noise Policies

The noise policies of the US federal government have been reviewed in detail elsewhere [23.169, 170]. A database of US noise policy documents has been published on CD-ROM [23.171].

Federal Aviation Administration. A number of policies related to aviation noise were in existence before 1969, but the first FAR 36 regulation [23.172] issued in 1969 by the Federal Aviation Administration, an agency of the US Department of Transportation. This regulation implemented a certification procedure for the noise emissions of aircraft, and has been amended many times to reduce noise emissions as the technology of aircraft engine design improved. More information may be found in Sect. 23.2.8.

US Environmental Protection Agency. The National Environmental Policy Act of 1969 established the Office of Noise Abatement and Control (ONAC) of the US Environmental Protection Agency (EPA), and in the early 1970s, ONAC held a series of public hearings to discuss the noise problem. These hearings led to the passage of the Noise Control Act of 1972 (NCA 72), which was landmark legislation in which the US Congress declared that it is "*the policy of the United States to promote an environment for all Americans free from noise that jeopardizes their health and welfare.*" The program included:

- development of standards and criteria,
- identification of major sources of noise,
- regulation of the noise emissions of certain vehicles, machinery, and equipment,
- product noise labeling,
- interactions with other federal agencies,
- the establishment of regional noise technical centers,
- support of research in noise control, and
- assistance to state and local governments.

Funding for ONAC was discontinued in 1982. *Finegold*, *Finegold* and *Maling* [23.169, 170] discussed the successes and failures of the program, and a history of the program has been prepared by *Maling* [23.173]. A re-

view of administrative procedures related to NCA 72 and ONAC, and recommendations for future noise abatement were prepared by the Administrative Conference of the United States in 1991 [23.174].

US Department of Housing and Urban Development. It is the policy of the US Department of Housing and Urban Development (HUD) (24 CFR part 51) to provide minimum national standards applicable to HUD programs to protect citizens against excessive noise in their communities and places of residence. HUD has defined noise exposure standards for new construction, interior noise goals, and acoustical privacy in multifamily buildings. These standards must be met if federal financing assistance is to be provided for new construction or residential rehabilitation. It is also HUD's policy to apply standards to prevent incompatible development around civil airports and military airfields. HUD requires that grantees give adequate consideration to noise exposures and sources of noise as an integral part of the urban environment when HUD assistance is provided for planning purposes. Particular emphasis is placed on the importance of compatible land-use planning in relation to airports, highways and other sources of high levels of noise exposure. HUD assistance for the construction of new noise sensitive uses is prohibited generally for projects with unacceptable noise exposures and is discouraged for projects with normally unacceptable noise exposure. Noise exposure by itself will not result in the denial of HUD support for the resale and purchase of otherwise acceptable existing buildings. However, environmental noise is a marketability factor, which HUD will consider in determining the amount of insurance or other assistance that may be given.

The Federal Energy Regulatory Commission. The Federal Energy Regulatory Commission (FERC) is an agency of the US Department of Energy, and has issued a regulation that controls noise emitted by compressors and other sources of noise related to the power industry. The regulation 18 CFR 157.206(d)(5) states that:

5. The noise attributable to any compressor facility installed pursuant to the blanket certificate shall not exceed a day–night sound level (L_{dn}) of 55 dB(A) at any noise-sensitive area unless the noise-sensitive areas (such as schools, hospitals, or residences) are established after facility construction.

US Department of Labor, Occupational Safety and Health Administration. Within the US Department of Labor, OSHA has regulations on occupational noise exposure which are detailed in the US code of federal regulations, 29 CFR 1910.95. Additional information may be found in the hearing conservation manual [23.175]. Noise policy for exposure to industrial noise is generally covered by the text in Sect. 23.4.4.

US Department of Labor, Mine Safety and Health Administration. The Mine Safety and Health Administration is part of the US Department of Labor. Regulations for the control of the noise exposure of miners is covered in 30 CFR 62. The basic requirements are:

- The eight hour time-weighted, A-frequency-weighted sound pressure level shall not exceed 90 dB. Levels below 90 dB and above 140 dB are not included in the integration.
- A 5 dB exchange rate is used.
- Above an *action level* of 85 dB, hearing protection must be used, and the individual must be enrolled in a hearing conservation program.

Additional information on the policies of other government agencies vis à vis occupational noise may be found in a paper by *Bruce* and *Wood* [23.176].

Federal Highway Administration. The primary activity of the Federal Highway Administration is to coordinate state efforts with regard to the construction of highway noise barriers. Noise barrier design in discussed in Chap. 4. Additional information on noise barriers is in Sect. 23.3.1, in the section on state policies below, and in [23.120]. More recently, there have been efforts to design highways so that tire–road noise is reduced.

State Government Policies

Policies of the state governments can generally be divided into policies with respect to exposure to occupational noise, transportation noise, and noise emissions from industrial plants. In the first case, states may establish occupational noise policies that are at least as stringent as federal regulations (see the section on OSHA).

Highway Noise Barriers. Many State governments have established noise policies with regard to the erection of noise barriers along highways [23.120]. Noise barrier policy is based on a cooperative arrangement between the federal government and state governments. Federal policy is set by the Federal Highway Administration, an agency of the US Department of Transportation, and is

detailed in an FHWA policy document [23.177]. It is, however, the responsibility of each State Department of Transportation (SDoT) to determine the extent of noise abatement measures and to balance costs and environmental benefits in determining where noise barriers are to be erected.

Industrial Noise Emissions. The policy situation with regard to industrial noise immissions varies from state-to-state. The Internet site maintained by the Noise Pollution Clearing House [23.178] lists 12 states (with links to the requirements) with regulations on noise. One of the states not listed is the state of Maine – whose noise requirements have been described as the most complex in the United States [23.179]. These requirements show evidence of being carefully written. *Brooks* [23.180,181] has identified two other states, Illinois [23.182] and Connecticut [23.183] as two other states with carefully crafted environmental noise regulations.

The Maine text is in the Department of Environmental Protection regulations 375.10, and is approximately 6000 words in length. The requirements are written in terms of hourly A-weighed sound levels. Daytime levels are between 7 a.m. and 7 p.m., and nighttime levels are between 7 p.m. and 7 a.m. The key elements are:

- In protected locations that are not predominantly commercial, transportation, or industrial, 60 dB daytime and 50 dB nighttime.
- In other areas, the required levels are 10 dB higher.
- Where pre-development levels are less than 45 dB in the daytime and 35 dB at night, the required levels are 5 dB lower.
- There are penalties for repetitive sounds and requirements on blast noise.
- Maximum levels are specified for construction activities.

Local Noise Regulations and Policies. A large number of cities and towns in the United States have ordinances and building codes to deal with local noise issues. For example, noise ordinances from cities and towns in 31 states have been posted on the Internet by the Noise Pollution Clearing House [23.177]. A model noise ordinance published by the EPA and dating from 1975 September has also been posted [23.184]. However, there is no consistency in how local noise ordinances are structured. Some use subjective noise exposure criteria, while others use objective, quantitative criteria. As described by *Finegold* and *Brooks* [23.185], an American National Standards Institute (ANSI) working group is currently developing a new ANSI standard with an updated model community noise ordinance for use by local jurisdictions to provide the needed guidance. There is a strong preference for objective noise standards as opposed to subjective standards. For example, a requirement for the prohibition of *excessive and unreasonable noises* without objective limits is difficult to enforce.

As one example of the purpose of local noise ordinances, the noise policy statement in the March 1998 New York City noise code [23.186] is reproduced below. This noise code is being revised.

24-202 Declaration of policy. It is hereby declared to be the public policy of the city to reduce the ambient noise level in the city, so as to preserve, protect and promote the public health, safety and welfare, and the peace and quiet of the inhabitants of the city, prevent injury to human, plant and animal life and property, foster the convenience and comfort of its inhabitants, and facilitate the enjoyment of the natural attractions of the city. It is the public policy of the city that every person is entitled to ambient noise levels that are not detrimental to life, health and enjoyment of his or her property. It is hereby declared that the making, creation or maintenance of excessive and unreasonable noises within the city affects and is a menace to public health, comfort, convenience, safety, welfare and the prosperity of the people of the city. For the purpose of controlling and reducing such noises, it is hereby declared to be the policy of the city to set the unreasonable noise standards and decibel levels contained herein and to consolidate certain of its noise control legislation into this code. The necessity for legislation by enactment of the provisions of this chapter is hereby declared as matter of legislative determination.

Noise Policies in Other Countries. Most industrialized countries have published noise regulations for a variety of sources. *Gottlob* [23.187] as well as *Flindell* and *McKenzie* [23.188] have presented information on community noise regulations in a large number of countries, and have listed the noise descriptors in use. More recently, technical study group 3 of the International Institute of Noise Control Engineering (I-INCE) prepared a comprehensive draft report on noise policies and regulations worldwide [23.189]. This report documents the results of an international survey on current environmental noise policies and regulations, and describes some similarities and differences in noise policies that exist at the global level. It also

provides recommendations for a follow-on project to estimate national noise exposures in the I-INCE participating member countries as a next step towards the long-term goal of assessing the effectiveness of noise policies.

23.5.2 European Noise Policy and Regulations

Early European noise policy emphasized *old approach* directives that covered specific noise sources such as motor vehicles, construction equipment, lawnmowers, aircraft, and other equipment. The original safety directive, 89/392/EC, contained requirements on emission sound pressure level (Sect. 23.2.3). This document was superseded by directive 98/37/EC [23.190], but with the same acoustical requirements. This directive has been implemented throughout the European Union – the details being in European standards (EN). There are now several hundred of these standards covering a wide variety of machine types [23.191].

More recently, *new approach* directives give requirements, but are much more general in their approach to regulation of noise. There are still specific requirements on machines – as discussed in Sect. 23.2.5. These approaches have been summarized by *Higginson* et al. [23.192] in 1996, the European Union published a green paper that recognized the fact that in spite of limits on the noise emissions of individual machines, the noise to which persons are exposed has been increasing, and that more emphasis should be placed on noise in communities. A summary of the future noise policy as presented in the green paper is available [23.193], as is the green paper itself [23.194] and an edited version [23.195]. This activity led to directive 2002/49EC [23.196] designed to understand noise problems in communities through noise mapping and other activities, and to prepare action plans. The directive instructs the member states to develop a long-range plan to establish common assessment methods, to develop noise maps, to develop action plans to combat noise, to keep the public informed about noise issues. It also requires that the European Commission make regular evaluations of the implementation of the directive.

Some key action items and implementation dates in the directive are:

1. Common noise assessment methods will be established by the European Commission.
2. By 2005 July 18, the European Commission will be informed of limit values in force by the member states.
3. By 2005 June 30 and every five years thereafter, the member states will inform the European Commission of the major roads that have more than six million vehicle passages per year, major railways that have more than 60 000 train passages per year, and airports and the agglomerations with more than 250 000 inhabitants within their territories.
4. By 2007 June 30, the member states will ensure that strategic noise maps showing the situation in the previous year have been made and approved by competent authorities. By 2008 June 30, all agglomerations, major roads, and major railways shall be identified and by 2012 June 30, noise maps for these areas will be prepared and updated every five years.
5. By 2008 July 18, competent authorities shall draw up action plans to manage noise issues in areas defined by item 3 above.
6. By 2013 July 18, action plans for those areas defined by item 4 above shall be developed.
7. Action plans shall be reviewed whenever the existing noise situation changes, and at least every five years.
8. The public will be kept informed about noise maps and action plans.
9. By 2004 January 18, the European Commission will submit a report to the European parliament which reviews existing measures related to sources of environmental noise. A summary report of strategic noise maps and action plans will be prepared by 2009 July 18 and every five years thereafter. By this date, a report on the implementation of the directive will also be submitted.

Six annexes to the directive cover noise indicators, assessment methods for the noise indicators, assessment methods for harmful effects, minimum requirements for strategic noise mapping, minimum requirements for action plans, and definitions of data to be sent to the European Commission.

There are a number of ongoing projects related to this directive. Further information on EU noise policies can be found at http://europa.eu.int/comm/environment/noise/home.htm.

Amazon EX1014 Page 1013

23.6 Other Information Resources

The following information will be helpful in locating many of the references below.

American National Standards are available from the Acoustical Society of America, asa.aip.org.

International Standards on electroacoustics (sound level meters, etc.) are published by the International Electrotechnical Commission (IEC), www.iec.ch.

International Standards on noise are published by the International Organization for Standardization (ISO), www.iso.ch.

The sponsor of the INTER-NOISE series of international congresses on noise control engineering is the International Institute of Noise Control Engineering, www.i-ince.org.

A technical journal, Noise Control Engineering Journal, has been published by INCE/USA since 1973, and all technical papers from that journal are now available on CD-ROM.

The organizer of the INTER-NOISE series when the congresses are held in North America is the Institute of Noise Control Engineering of the USA (www.inceusa.org). The institute also sponsors the NOISE-CON series of national conferences on noise control engineering. Technical papers on CD-ROM for both of these series are available from the institute (www.atlasbooks.com/marktplc/00726.htm).

References

23.1 R.H. Bolt, K.U. Ingard: System considerations in noise-control problems (Chap. 22). In: *Handbook of Noise Control*, ed. by C.M. Harris (McGraw-Hill, New York 1957)

23.2 Oxford English Dictionary, 2nd ed., Volume VII, Immission: The action of immitting; insertion, injection, admission, introduction. 1578 BANNISTER Hist.Man VIII 102, ...under judgement, as touchying emission and immission...

23.3 M.J. Lighthill: On sound generated aerodynamically, Proc. R. Soc. London **A 211**, 564–587 (1952)

23.4 E.A.G. Shaw: Noise pollution – what can be done?, Phys. Today **28**(1), 46 (1975)

23.5 P.L.Burgé: The power of public participation. In: *Proc. INTER-NOISE 02*, ed. by A. R. G.C. SelametSinghMaling (Int. Inst. Noise Control Eng., West Lafayette 2002), paper in02_501

23.6 K.U. Ingard, G.C. Maling: Physical principles of noise reduction: Properties of sound sources and their fields, Noise Control Eng. J. **2**, 37–48 (1974)

23.7 N.P. Miller: Transportation noise and recreational lands, Noise News Int. **11**, 9–21 (2003)

23.8 IEC: *IEC 61672-1:2002, Electroacoustics – Sound Level Meters – Part 1: Specifications* (IEC, Geneva 2002)

23.9 IEC: *IEC 60942:2003 Electroacoustics – Sound calibrators* (IEC, Geneva 2003)

23.10 ANSI: *ANSI S1.17-2004-Part 1. American National Standard microphone windscreens – Part 1, Measurement and Specification of Insertion Loss in Still or Slightly Moving Air* (Acoust. Soc. Am., Melville 2004)

23.11 IEC: *IEC 61043:1993 Electroacoustics – Instruments for measurement of sound intensity-measurements with pairs of pressure sensing microphones* (IEC, Geneva 1993)

23.12 ANSI: *ANSI S1.9-1996 (R2001) American National Standard instruments for the measurement of sound intensity* (Acoust. Soc. Am., Melville 2001)

23.13 I.L. Vér, L.L. Beranek: *Noise and Vibration Control Engineering*, 2nd edn. (Wiley, New York 2005), Chap. 4

23.14 ISO: *ISO 6926:1999 Acoustics – Requirements for the performance and calibration of reference sound sources used for the determination of sound power levels* (ISO, Geneva 1999)

23.15 L.L. Beranek: *Acoustical Measurements* (Acoust. Soc. Am., Woodbury 1988)

23.16 W.W. Lang, G.C. Maling, M.A. Nobile, J. Tichy: In: *Noise and Vibration Control Engineering*, 2nd edn., ed. by I.L. Vér, L.L. Beranek (Wiley, New York to be published), Chap. 4

23.17 ISO: ISO 3740:2000 Acoustics – Determination of sound power levels of noise sources – Guidelines for the use of basic standards (ISO, Geneva 2000)
ISO: ISO 3741:1999 Acoustics – Determination of sound power levels of noise sources using sound pressure – Precision methods for reverberation rooms (ISO, Geneva 1999)
ISO: ISO 3741:1999/Cor 1:2001 (ISO, Geneva 2001)
ISO: ISO 3743-1:1994 Acoustics – Determination of sound power levels of noise sources – Engineering methods for small, movable sources in reverberant fields – Part 1: Comparison method for hard-walled test rooms (ISO, Geneva 1994)
ISO: ISO 3743-2:1994 Acoustics – Determination of sound power levels of noise sources using sound pressure – Engineering methods for small, movable sources in reverberant fields – Part 2: Methods for special reverberation test rooms (ISO, Geneva 1994)
ISO: ISO 3744:1994 Acoustics – Determination of

Amazon EX1014 Page 1014

sound power levels of noise sources using sound pressure – Engineering method in an essentially free field over a reflecting plane (ISO, Geneva 1994)
ISO: ISO 3745:2003 Acoustics – Determination of sound power levels of noise sources using sound pressure – Precision methods for anechoic and hemi-anechoic rooms (ISO, Geneva 2003)
ISO: ISO 3746:1995 Acoustics – Determination of sound power levels of noise sources using sound pressure – Survey method using an enveloping measurement surface over a reflecting plane (ISO, Geneva 1995)
ISO: ISO 3746:1995/Cor 1:1995 (ISO, Geneva 1995)
ISO: ISO 3747:2000 Acoustics – Determination of sound power levels of noise sources using sound pressure – Comparison method in situ (ISO, Geneva 2000)

23.18 M.A. Nobile, B. Donald, J.A. Shaw: *The cylindrical microphone array: A proposal for use in international standards for sound power measurements, Proc. NOISE-CON 2000 (CD-ROM)* (Int. Inst. Noise Control Eng., West Lafayette 2000), paper 1pNSc2

23.19 M.A. Nobile, J.A. Shaw, R.A. Boyes: *The cylindrical microphone array for the measurement of sound power level: Number and arrangement of microphones, Proc. INTER-NOISE 2002 (CD-ROM)* (Bookmaster, Mansfield 2002), paper N318

23.20 ISO: *ISO 9614: Determination of sound power levels of noise sources using sound intensity Part 1: Measurement at discrete points* (ISO, Geneva 1993)

23.21 ISO: *ISO 9614: Determination of sound power levels of noise sources using sound intensity Part 2: Measurement by scanning* (ISO, Geneva 1994)

23.22 ISO: *ISO 9614: Determination of sound power levels of noise sources using sound intensity Part 3: Precision method for measurement by scanning* (ISO, Geneva 2000)

23.23 ECMA: *ECMA-160: Determination of Sound Power Levels of Computer and Business Equipment using Sound Intensity Measurements; Scanning Method in Controlled Rooms*, 2nd edn. (ECMA International, Geneva 1992), A free download is available from www.ecma-international.org

23.24 F. Jacobsen: Sound field indicators, useful tools, Noise Control Eng. J. **35**, 37–46 (1990)

23.25 A.C. Balant, G.C. Maling, D.M. Yeager: Measurement of blower and fan noise using sound intensity techniques, Noise Control Eng. J. **33**, 77–88 (1989)

23.26 ISO: *ISO 5136:2003, Acoustics – Determination of sound power radiated into a duct by fans and other air moving devices – Induct method* (ISO, Geneva 2003)

23.27 ISO: *ISO 5136:2003, Acoustics – Determination of sound power radiated into a duct by fans and other air moving devices – Induct method* (ISO, Geneva 2003), Section 6.2

23.28 P.K. Baade: Effects of acoustic loading on axial flow fan noise generation, Noise Control Eng. J. **8**, 5–15 (1977)

23.29 ISO: *ISO 11200:1995 Acoustics – Noise emitted by machinery and equipment – Guidelines for the use of basic standards for the determination of emission sound pressure levels at a work station and at other specified positions. ISO 11200:1995/Cor 1:1997* (ISO, Geneva 1995)

23.30 ISO: *ISO 11201:1995 Acoustics – Noise emitted by machinery and equipment – Measurement of emission sound pressure levels at a work station and at other specified positions – Engineering method in an essentially free field over a reflecting plane. ISO 11201:1995/Cor 1:1997* (ISO, Geneva 1995)

23.31 ISO: *ISO 11202:1995 Acoustics – Noise emitted by machinery and equipment – Measurement of emission sound pressure levels at a work station and at other specified positions – Survey method in situ. ISO 11202:1995/Cor 1:1997* (ISO, Geneva 1995), Applies to French version only

23.32 ISO: *ISO 11203:1995 Acoustics – Noise emitted by machinery and equipment – Determination of emission sound pressure levels at a work station and at other specified positions from the sound power level* (ISO, Geneva 1995)

23.33 ISO: *ISO 11204:1995 Acoustics – Noise emitted by machinery and equipment – Measurement of emission sound pressure levels at a work station and at other specified positions – Method requiring environmental corrections. ISO 11204:1995/Cor 1:1997* (ISO, Geneva 1995)

23.34 ISO: *ISO 11205:2003 Acoustics – Noise emitted by machinery and equipment – Engineering method for the determination of emission sound pressure levels in situ at the work station and at other specified positions using sound intensity* (ISO, Geneva 2003)

23.35 ISO: *ISO 362:1998 Acoustics – Measurement of noise emitted by accelerating road vehicles – Engineering method* (ISO, Geneva 1998)

23.36 ISO: *ISO 5128:1980 Acoustics – Measurement of noise inside motor vehicles* (ISO, Geneva 1980)

23.37 ISO: *ISO 5130:1982 Acoustics – Measurement of noise emitted by stationary road vehicles – Survey method* (ISO, Geneva 1982)

23.38 ISO: *ISO 7188:1994 Acoustics – Measurement of noise emitted by passenger cars under conditions representative of urban driving* (ISO, Geneva 1994)

23.39 ISO: *ISO 9645:1990 Acoustics – Measurement of noise emitted by two wheeled mopeds in motion – Engineering method* (ISO, Geneva 1990)

23.40 ISO: *ISO 10844:1994 Acoustics – Specification of test tracks for the purpose of measuring noise emitted by road vehicles* (ISO, Geneva 1994)

23.41 ISO: *ISO 11819-1:1997 Acoustics – Measurement of the influence of road surfaces on traffic noise – Part 1: Statistical Pass-By method* (ISO, Geneva 1997)

Amazon EX1014 Page 1015

23.42 ISO: *ISO 7779:1999 Acoustics – Measurement of airborne noise emitted by information technology and telecommunications equipment ISO 7779:1999/Amd 1:2003 Noise measurement specification for CD/DVD-ROM drives* (ISO, Geneva 1999)

23.43 ISO 9295: *1988 Acoustics – Measurement of high-frequency noise emitted by computer and business equipment* (ISO, Geneva 1988)

23.44 ISO: *ISO 9296:1988 Acoustics – Declared noise emission values of computer and business equipment* (ISO, Geneva 1988)

23.45 ISO: *ISO 1680:1999 Acoustics – Test code for the measurement of airborne noise emitted by rotating electrical machines* (ISO, Geneva 1999)

23.46 ISO: *ISO 2922:2000 Acoustics – Measurement of airborne sound emitted by vessels on inland waterways and harbours* (ISO, Geneva 2000)

23.47 ISO: *ISO 2923:1996 Acoustics – Measurement of noise on board vessels* (ISO, Geneva 1996), ISO 2923:1996/Cor 1:1997

23.48 ISO: *ISO 3891:1978 Acoustics – Procedure for describing aircraft noise heard on the ground* (ISO, Geneva 1978)

23.49 ISO: *ISO 5129:2001 Acoustics – Measurement of sound pressure levels in the interior of aircraft during flight* (ISO, Geneva 2001)

23.50 ISO: *ISO 8297:1994 Acoustics – Determination of sound power levels of multisource industrial plants for evaluation of sound pressure levels in the environment – Engineering method* (ISO, Geneva 1994)

23.51 ISO: *ISO 15664:2001 Acoustics – Noise control design procedures for open plant* (ISO, Geneva 2001)

23.52 ISO: *ISO 4872:1978 Acoustics – Measurement of airborne noise emitted by construction equipment intended for outdoor use – Method for determining compliance with noise limits* (ISO, Geneva 1978)

23.53 ISO: *ISO 5131:1996 Acoustics – Tractors and machinery for agriculture and forestry – Measurement of noise at the operator's position – Survey method* (ISO, Geneva 1996)

23.54 ISO: *ISO 7216:1992 Acoustics – Agricultural and forestry wheeled tractors and self-propelled machines – Measurement of noise emitted when in motion* (ISO, Geneva 1992)

23.55 ISO: *ISO 6393:1998 Acoustics – Measurement of exterior noise emitted by earth-moving machinery – Stationary test conditions* (ISO, Geneva 1998)

23.56 ISO: *ISO 6394:1998 Acoustics – Measurement at the operator's position of noise emitted by earth-moving machinery – Stationary test conditions* (ISO, Geneva 1998)

23.57 ISO: *ISO 6395:1988 Acoustics – Measurement of exterior noise emitted by earth-moving machinery – Dynamic test conditions ISO 6395:1988/Amd 1:1996* (ISO, Geneva 1988)

23.58 ISO: *ISO 6396:1992 Acoustics – Measurement at the operator's position of noise emitted by earth-moving machinery – Dynamic test conditions* (ISO, Geneva 1992)

23.59 ISO: *ISO 11094:1991 Acoustics – Test code for the measurement of airborne noise emitted by power lawn mowers, lawn tractors, lawn and garden tractors, professional mowers, and lawn and garden tractors with mowing attachments* (ISO, Geneva 1991)

23.60 ISO: *ISO 5135:1997 Acoustics – Determination of sound power levels of noise from air-terminal devices, air-terminal units, dampers and valves by measurement in a reverberation room* (ISO, Geneva 1997)

23.61 ISO: *ISO 15665:2003 Acoustics – Acoustic insulation for pipes, valves and flanges. ISO 15665:2003/Cor 1:2004* (ISO, Geneva 2003)

23.62 ISO: *ISO 7917:1987 Acoustics – Measurement at the operator's position of airborne noise emitted by brush saws* (ISO, Geneva 1987)

23.63 ISO: *ISO 12001:1996 Acoustics – Noise emitted by machinery and equipment – Rules for the drafting and presentation of a noise test code* (ISO, Geneva 1996)

23.64 ANSI: *ANSI S12.15-1992 (R2002), American National Standard for Acoustics – Portable electric power tools, stationary and fixed electric power tools, and gardening appliances – measurement of sound emitted* (Acoust. Soc. Am., Melville 1992)

23.65 ANSI: *ANSI S12.16-1992 (R2002), American National Standard guidelines for the specification of noise of new machinery* (Acoust. Soc. Am., Melville 1992)

23.66 ISO: ISO 7574-1:1985 Acoustics – Statistical methods for determining and verifying stated noise emission values of machinery and equipment – Part 1: General considerations and definitions (ISO, Geneva 1985)
ISO:ISO 7574-2:1985 Acoustics – Statistical methods for determining and verifying stated noise emission values of machinery and equipment – Part 2: Methods for stated values for individual machines. (ISO, Geneva 1985)
ISO:ISO 7574-3:1985 Acoustics – Statistical methods for determining and verifying stated noise emission values of machinery and equipment – Part 3: Simple transition method for stated values for batches of machines (ISO, Geneva 1985)
ISO:ISO 7574-4:1985 Acoustics – Statistical methods for determining and verifying stated noise emission values of machinery and equipment – Part 4: Methods for stated values for batches of machines.(ISO, Geneva 1985)

23.67 ISO: *ISO 4871:1996 Acoustics – Declaration and verification of noise emission values of machinery and equipment* (ISO, Geneva 1996)

Amazon EX1014 Page 1016

23.68 ISO: *ISO 9296:1988 Acoustics – Declared noise emission values of computer and business equipment* (ISO, Geneva 1988)

23.69 Swedish Agency for Public Management: *Acoustical Noise Emission of Information Technology Equipment, Statskontoret*, Statskontoret Technical Standard, Vol. 26.5 (Swedish Agency for Public Management, Stockholm 2002)

23.70 EU Official: Directive 2000/14/EC of the European Parliament and of the Council of 8 May, 2000 on the approximation of the laws of the Member States relating to the noise emission in the environment by equipment for use outdoors, Official J. Eur. Communities **L162/1** (2000)

23.71 Blauer Engel: Umwelt Bundesamt, Dessau Germany, www.blauer-engel.de

23.72 V. Irmer, E.F.-S. Ali: Reduction of noise emission of construction machines due to the "Blue Angel" award, Noise News Int. **7**, 73–80 (1999)

23.73 www.europe.eu.int/comm/environment/ecolabel

23.74 EU Official: Commission decision of 22 August 2001 establishing the ecological criteria for the award of the Community eco-label to personal computers, Official J. Eur. Communities **L242/4** (2001)

23.75 EU Official: Commission decision of 28 August 2001 establishing the ecological criteria for the award of the Community eco-label to portable computers, Official J. Eur. Communities **L242/11** (2001)

23.76 S. Ingemansson: *Noise and Vibration Control – Principles and Applications* (Ingemansson Technology AB, Gothenburg 2000), The URL is www.ingemansson.com. The booklet is a set of principles of noise control accompanied by illustrations and an example of the application of each principle. The booklet was jointly published by Ingemansson AB and the INCE Foundation

23.77 R.V. Waterhouse: Output of a sound source in a reverberation chamber and other reflecting environments, J. Acoust. Soc. Am. **30**, 4–12 (1958)

23.78 R.D. Madison: *Fan Engineering*, 5th edn. (Buffalo Forge Company, Buffalo 1949)

23.79 ISO: *ISO 10302 :1996. Acoustics – Measurement of airborne noise emitted by small air moving devices* (ISO, Geneva 1996)

23.80 ANSI: *ANSI S12.11-2003/Part 1 ; ISO 10302 :1996 (MOD). American National Standard/Acoustics – Measurement of noise and vibration of small air moving devices. Part 1. Airborne noise emission* (Acoust. Soc. Am., Melville 2003)

23.81 G.C. Maling Jr.: Measurements of the noise generated by centrifugal blowers , J.Acoust. Soc. Am. **35**, 1913(A) (1963)

23.82 ANSI: *ANSI S12.11-2003/Part 2. Acoustics – Measurement of noise and vibration of small air moving devices. Part 2: Structure-borne vibration* (Acoust. Soc. Am., Melville 2003)

23.83 G.C. Maling: Historical developments in the control of noise generated by small air-moving devices, Noise Control Eng. J. **42**, 159–169 (1994)

23.84 G.C. Maling, D.M. Yeager: Acoustical noise measurement and control in electronic systems. In: *Thermal Measurements in Electronics Cooling*, ed. by K. Azar (CRC, Boca Raton 1997) pp. 425–467

23.85 K.B. Washburn, G.C. Lauchle: Inlet flow conditions and tonal sound radiation from a subsonic fan, Noise Control Eng. J. **31**, 101–110 (1988)

23.86 H.F. Olson, E.G. May: Electronic sound absorber, J. Acoust. Soc. Am. **25**, 1130–1136 (1953)

23.87 P.A. Nelson, S.J. Elliott: *Active Control of Sound* (Academic, San Diego 1992)

23.88 C.H. Hansen, S.D. Snyder: *Active Control of Noise and Vibration* (E &FN Spon, Florence 1997)

23.89 P.A. Nelson, S.J. Elliott: Active noise control, Noise News Int. **2**, 75–98 (1994)

23.90 J. Tichy: Applications for active control of sound and vibration, Noise News Int. **4**, 73–86 (1996)

23.91 C.R. Fuller: *Active control of sound radiation from structures, progress and future directions, Proc. ACTIVE 02* (Institute of Sound and Vibration Research, Southampton 2002), paper P236

23.92 C.H. Hansen: *Current and future applications of active noise control, Proc. ACTIVE 04* (Institute of Noise Control Engineering USA, Williamsburg 2004), paper a04_053

23.93 J. Scheuren: *Engineering applications of active sound and vibration control, Proc. ACTIVE 04* (Institute of Noise Control Engineering USA, Williamsburg 2004), paper A04_100

23.94 B.B. Monson, S.D. Sommerfeldt: *Active control of tonal noise from small cooling fans, Proc ACTIVE 04* (Institute of Noise Control Engineering USA, Williamsburg 2004), paper A04_040

23.95 A.J. Brammer, R.B. Crabtree, D.R. Peterson, M.G. Cherniack, S. Gullapappi: *Active headsets: Influence of control structure on communication signals and noise reduction, Proc. ACTIVE 04* (Institute of Noise Control Engineering USA, Williamsburg 2004), paper A094_095

23.96 Institute of Noise Control Engineering of the USA: *Technical papers from the ACTIVE symposia in 1995, 1997, 1999, 2002, and 2004* (Institute of Noise Control Engineering of the USA, Ames 2004), Collected papers from the ACTIVE series on CD-ROM, see the URL www.atlasbooks.com/marktplc/00726.htm

23.97 U. Sandberg, Convenor: International INCE Final Report 01-1, Noise Emissions of Road Vehicles: Effects of regulations, Noise News Int. **9**, 147–206 (2001)

23.98 ISO: *ISO 362:1998 Acoustics – Measurement of noise emitted by accelerating road vehicles* (ISO, Geneva 1998)

Amazon EX1014 Page 1017

23.99 U. Sandberg, J.A. Ejsmont: *Tyre/Road Reference Book* (Informex, Kisa 2002)

23.100 Y.-J. Kim, J.S. Bolton: *Modeling tire treadband vibration, Proc. INTER-NOISE 01* (Int. Inst. Noise Control Eng., The Hague 2001), paper in01_716

23.101 A. Kuijpers, G. van Blokland: *Tyre/road noise models in the last two decades: a critical evaluation, Proc. INTER-NOISE 01* (Int. Inst. Noise Control Eng., The Hague 2001), paper in01_706

23.102 W. Kropp, K. Larsson, F. Wullens, P. Andersson, F.-X. Bécot, T. Beckenbauer: *The modeling of tyre/road noise – A quasi three-dimensional model, Proc. INTER-NOISE 01* (Int. Inst. Noise Control Eng., The Hague 2001), paper in01_657

23.103 F. de Roo, E. Gerretsen, E.H. Mulder: *Predictive performance of the tyre-road noise model TRIAS, Proc. INTER-NOISE 01* (Int. Inst. Noise Control Eng., The Hague 2001), paper in01_706

23.104 R. Bernhard, N. Franchek, V. Drnevich: *Tire/pavement interaction noise research activities of the Institute for Safe, Quiet, and Durable Highways, Proc. INTER-NOISE 00* (Int. Inst. Noise Control Eng., Nice 2000), paper in2000/543

23.105 U. Sandberg, H. Ohnishi, N. Kondo, S. Meiarashi: *Poroelastic road surfaces – state-of-the-art review, Proc INTER-NOISE 00* (French Acoustical Society, Nice 2000), paper in2002/772

23.106 W.D. Thornton, R.J. Bernhard, D.I. Hanson, L. Scofield: *Acoustical variability of existing pavements, Proc. NOISE-CON 04* (Int. Inst. Noise Control Eng., Baltimore 2004), paper nc040275

23.107 P.R. Donavan, L. Scofield: *Proc. NOISE-CON 04* (Int. Inst. Noise Control Eng., Baltimore 2004), paper nc040448

23.108 U.S. Code of Federal Regulations, 14CFR Part 36, Noise Standards, Aircraft Type and Airworthiness Certification, as amended (Federal Register, Vol. 67, No. 130, 45193-45237, July 08, 2002)

23.109 International Standards and Recommended Practices, Environmental Protection, Annex 16 to the Convention on International Civil Aviation, Volume 1: Aircraft Noise, 3rd edn., (July 1993), International Civil Aviation Organization, Montreal, Canada, including Amendments 1 through 7 as of 2002 March 21

23.110 W.L. Willshire Jr., D.G. Stephens: *Aircraft noise technology for the 21st century, Proc. NOISE-CON 98* (Int. Inst. Noise Control Eng., Ypsilanti 1998), paper NC980007.pdf

23.111 P. Condit: Performance, Process and Value: Commercial aircraft design in the 21st century. 1996 Wright Brothers Lectureshipin Aeronautics, World Aviation Congress and Exposition, Los Angeles,California, October 22, 1996

23.112 H.H. Hubbard (Ed.): *NASA Reference Publication 1258, Vols. 1 and 2* (National Aeronautics and Space Administration, Hampton 1991)

23.113 A.H. Marsh: *Noise control for in-service jet transports, Proc. INTER-NOISE 94, 1, 199-204* (Int. Noise Control Eng. Japan, Yokohama 1994)

23.114 A.H. Marsh: *ISO 5129:2001 – The international standard for measurement of noise in the interior of aircraft, Proc. INTER-NOISE 2004* (Czech Acoustical Society, Prague 2004), paper 218

23.115 ISO 5129: *2001, Acoustics – Measurement of sound pressure levels in the interior of aircraft during flight* (ISO, Geneva 2001)

23.116 T.F.W. Embleton: Tutorial on sound propagation outdoors, J. Acoust. Soc. Am. **100**, 31–48 (1996)

23.117 G.A. Daigle, Convenor: International INCE Technical Report 99-1, Technical assessment of the effectiveness of noise walls, Noise News Int. **7**, 137–161 (1999)

23.118 ANSI: *American National Standard S12.8-1988, Methods for determining the insertion loss of outdoor noise barriers* (Acoust. Soc. Am., Melville 1988)

23.119 FHWA Internet Home Page, http://www.fhwa.gov. Search for "noise barriers"

23.120 K.D. Polcak: Highway traffic noise barriers in the U.S. – construction trends and cost analysis, Noise News Int. **11**, 96–108 (2003)

23.121 U.S. Federal Highway Administration: *FHWA Traffic Noise Model*, Version 2.5 (U.S. Department of Transportation, Washington 2004)

23.122 C.W. Menge, G.S. Anderson, D.E. Barrett: *Experiences with USDOTs Traffic Noise Model (TNM), Proc. NOISE-CON 01* (Int. Inst. Noise Control Eng., Portland 2001), paper nc01_083

23.123 J.L. Rochat: *Highway traffic noise measurements at acoustically hard ground sites compared to predictions from FHWA's Traffic Noise Model, Proc. NOISE-CON 01* (Int. Inst.Noise Control Eng., Portland 2001), paper nc01_082

23.124 ECMA: *Technical Report TR/27, Method for the prediction of installation noise levels* (ECMA, Geneva 1995), Available for download at www.ecma.ch. ECMA was formerly the European Computer Manufacturers Association

23.125 K.U. Ingard: www.ingard.com. The program used was AbsMtl, Version 2.0

23.126 A.G. Galaitsis: Predicted sound interaction with a cascade of porous resistive layers in a duct, Noise Control Eng. J. **26**, 62–67 (1986)

23.127 K.U. Ingard: Notes on Sound Absorbers-N3 1999. (www.ingard.com)

23.128 K.U. Ingard: Notes on Sound Absorbers-N3 1999. (www.ingard.com, 1999) CD-ROM. See program AbsFlxSP

23.129 ISO: *ISO 10534-1: 1996. Acoustics – Determination of sound absorption coefficient and impedance in impedance tubes – Part 1: Method using standing wave ratio* (ISO, Geneva 1996)

23.130 ISO: *ISO 10534-2: 1998. Acoustics – Determination of sound absorption coefficient and impedance*

Amazon EX1014 Page 1018

in impedance tubes – Part 2: Transfer function method (ISO, Geneva 1998)

23.131 ASTM E 1050-98:2003: *Standard test method for impedance and absorption of acoustical materials using a tube, two microphones, and a digital analyzer system* (Am. Soc. Testing and Materials, Philadelphia 2003)

23.132 ISO: *ISO 354:2003. Acoustics – Measurement of sound absorption in a reverberation room* (ISO, Geneva 2003)

23.133 M.A. Nobile: *Measurement of the spherical wave absorption coefficient at oblique incidence using the two-microphone transfer function method, Proc. INTER-NOISE 89* (Int. Inst. Noise Control Eng., Newport Beach 1989) pp. 1067–1072

23.134 K.U. Ingard: Notes on duct attenuators-N4 (www.ingard.com, 1999) CD-ROM

23.135 ISO: *ISO 7235:2003 Acoustics – Laboratory measurement procedures, for ducted silencers and air-terminal units – Insertion loss, flow noise and total pressure loss* (ISO, Geneva 2003)

23.136 ISO: *ISO 11691:1995 Acoustics – Measurement of insertion loss of ducted silencers without flow – Laboratory survey method* (ISO, Geneva 1995)

23.137 ISO: *ISO 11820:1996 Acoustics – Measurements on silencers in situ* (ISO, Geneva 1996)

23.138 ISO: *ISO 14163:1998 Acoustics – Guidelines for noise control by silencers* (ISO, Geneva 1998)

23.139 ASTM E477-99: *Standard test method for measuring acoustical and airflow performance of duct liner materials and prefabricated silencers* (Am. Soc. Testing and Materials, Philadelphia 1999)

23.140 M. Hirschorn: The aeroacoustic rating of silencers for "forward" and "reverse" flow of air and sound, Noise Control Eng. **2**, 25–29 (1974)

23.141 ANSI: *ANSI S12.19-1996 (R2001). American National Standard measurement of occupational noise exposure* (Acoust. Soc. Am., Melville 1996)

23.142 ANSI: *ANSI S1.13-1995 (R1998). American National Standard measurement of sound pressure levels in air* (Acoust. Soc. Am., Melville 1996)

23.143 ANSI: *ANSI S12.9-1998 (R2003). Quantities and procedures for description and measurement of environmental sound, Part 1* (Acoust. Soc. Am., Melville 1998)

23.144 ANSI: *ANSI S12.9-1992 (R2003). Quantities and procedures for description and measurement of environmental sound. Part 2, measurement of long-term, wide area sound* (Acoust. Soc. Am., Melville 1992)

23.145 ANSI: *ANSI S12.9-1993 (R2003). Quantities and procedures for description and measurement of environmental sound. Part 3, short term measurements with an observer present* (Acoust. Soc. Am., Melville 1993)

23.146 ANSI: *ANSI S12.9-1996 (R2001), Quantities and procedures for description and measurement of environmental sound. Part 4, noise assessment and prediction of long term community response* (Acoust. Soc. Am., Melville 1996)

23.147 ANSI: *ANSI S12.9-1998, Quantities and procedures for description and measurement of environmental sound. Part 5, sound level descriptors for determination of compatible land use* (Acoust. Soc. Am., Melville 1998)

23.148 ANSI: *ANSI S12.9-1998 (R2003), Quantities and procedures for description and measurement of environmental sound. Part 6, methods for estimation of awakenings associated with aircraft noise events heard in homes* (Acoust. Soc. Am., Melville 1998)

23.149 A.H. Suter: *Hearing Conservation Manual*, 4th edn. (Council for Accreditation in Occupational Hearing Conservation, Milwaukee 1993)

23.150 T.F.W. Embleton, Convenor: I-INCE Publication 97-1, Technical Assessment of Upper Limits of Noise in the Workplace, Noise News Int. **5**, 203–216 (1997)

23.151 ISO: *ISO 1999:1990(E). Acoustics – Determination of occupational noise exposure and estimation of noise induced hearing impairment* (ISO, Geneva 1990)

23.152 ANSI: *ANSI S3.44-1996 (R2001) American National Standard determination of occupational noise exposure and estimation of noise induced hearing impairment* (Acoust. Soc. Am., Melville 1998)

23.153 J.M. Fields: Reporting guidelines for community noise reaction surveys, Noise News Int. **6**, 139–144 (1998)

23.154 T.J. Schultz: Synthesis of social surveys on noise annoyance, J. Acoust. Soc. Am. **64**, 377–405 (1978)

23.155 L.S. Finegold, C.S. Harris, H.E. von Gierke: Community annoyance and sleep disturbance: Updated criteria for assessing the impacts of general transportation noise on people, Noise Control Eng. J. **42**, 25–30 (1994)

23.156 S. Fidell, D.S. Barber, T.J. Schultz: Updating a dosage-effect relationship for the prevalence of annoyance due to general transportation noise, J. Acoust. Soc. Am. **89**, 221–233 (1991)

23.157 H.M.E. Miedema: *Noise & Health: How does noise affect us? Proc. INTER-NOISE 01* (Int. Inst. Noise Control Eng., The Hague 2001), paper in01_740

23.158 H.M.E. Miedema, C.G.M.Oudshoorn: Annoyance from transportation noise: Relationships with exposure metrics DNL and DENL and their confidence intervals, Environmental Health **109**, 409–416 (2001)

23.159 S. Fidell: *Reliable prediction of community response to noise: Why you can't get there from here, Proc. INTER-NOISE 02* (Int. Inst. Noise Control Eng., Dearborn 2002), paper N500

23.160 S. Fidell: The Schultz curve 25 years later: A research perspective, J. Acoust. Soc. Am. **114**, 3007–3015 (2003)

Amazon EX1014 Page 1019

23.161 P.D. Schomer: *Criteria for assessment of noise annoyance, Proc. NOISE-CON 01* (Int. Inst. Noise Control Eng., Portland 2001), paper nc01_018

23.162 R.H. Lyon: *Designing for product sound quality* (Marcel Dekker, New York 2000)

23.163 R.H. Lyon: *Product sound quality – from design to perception, Proc. INTER-NOISE 04* (Int. Inst. Noise Control Eng., Prague 2004), keynote paper

23.164 Special issue on Global Noise Policy, Noise Control Engineering Journal **49**(4) (2001), The papers were reprinted on the CD-ROM prepared for INTER-NOISE 2002, Dearborn, Michigan, USA, 2002 August 19-21

23.165 L.L. Beranek, W.W. Lang: America needs a new national noise policy, Noise Control Eng. J. **51**(3), 123–130 (2003)

23.166 L.L. Beranek, W.W. Lang: *The need for a unified national noise policy, Proc. NOISE-CON 01* (Int. Inst. Noise Control Eng., Portland 2001), paper NC01_002

23.167 L.L. Beranek, W.W. Lang: *U.S. noise policy on the 30th anniversary of INCE/USA, Proc. NOISE-CON 01* (Int. Inst. Noise Control Eng., Portland 2001), paper NC01_001

23.168 L.S. Finegold, M.S. Finegold, G.C. Maling: An overview of U.S. national noise policy, Noise News Int. **10**(2), 51–63 (2002)

23.169 L.S. Finegold, M.S. Finegold, G.C. Maling: An overview of U.S. national noise policy, Noise Control Eng. J. **51**(3), 162–165 (2003)

23.170 M.S. Finegold, L.S. Finegold: Proc. INTER-NOISE 2002 on CD-ROM, Dearborn, Michigan, USA, 2002 August 19-21. The Excel database may be found at x:\policy\database\policy.xls, where x: is the designation of the CD-ROM drive.

23.171 U.S. Code of Federal Regulations, 14 CFR 36, 1969 (FAR 36)

23.172 G.C. Maling: An editor's view of the EPA noise program, Noise Control Eng. J. **51**(3), 143–150 (2003)

23.173 S.A. Shapiro: The Dormant Noise Control Act and Options to Abate Noise Pollution. In: *Noise and its Effects, Administrative Conference of the United States*, ed. by A.H. Suter (Washington 1991)

23.174 Council for Accreditation in Occupational Hearing Conservation: *Hearing Conservation Manual, 4th edn.* (Council for Accreditation in Occupational Hearing Conservation, Milwaukee 1993)

23.175 R.D. Bruce, E.W. Wood: The USA needs a new national policy for occupational noise, Noise Control Eng. J. **51**(3), 162–165 (2003)

23.176 U.S. Department of Transportation, Office of Environment and Planning, Noise and Air Quality Branch: *Highway traffic noise analysis and abatement policy and guidance* (U.S. Department of Transportation, Washington 1995), see also 23 CFR 772

23.177 Noise Pollution Clearing House: http://www.nonoise.org/lawlib/cities/cities.htm

23.178 T. Doyle: Twelve years with the most complex noise regulations in the United States. In: *Proc. NOISE-CON 01* (Int. Inst. Noise Control Eng., Portland 2001), paper NC01_067

23.179 B.M. Brooks: The need for a unified community noise policy. In: *Proc. NOISE-CON 01* (Int. Inst. Noise Control Eng., Portland 2001), paper NC01_016

23.180 B.M. Brooks: The need for a unified community noise policy, Noise Control Eng. J. **51**(3), 160–161 (2003)

23.181 State of Illinois Rules and Regulations, Title 35: Environmental Protection, Subtitle H: Noise, Chapter 1: Pollution Control Board, Parts 900 and 901 (1991)

23.182 State of Connecticut Department of Environmental Protection (DEP) regulations Title 22a, Environmental Protection, "Control of Noise", Connecticut General Statues Sections 22a-69-1 to 22a-69-7.4 (1978)

23.183 Noise Pollution Clearing House: www.nonoise.org/epa/roll2/roll2doc7blp7.pdf

23.184 L.S. Finegold, B.M. Brooks: Progress on Developing a Model Community Noise Ordinance as a National Standard in the US. In: *Proceedings of INTER-NOISE 2003*, ed. by S. Lee (Seogwipo, Jeju Island, Korea 2003), CD-ROM, paper N589

23.185 Noise Pollution Clearing House: www.nonoise.org/lawlib/cities/ny/newyork.htm

23.186 D. Gottlob: Regulations for Community Noise, Noise News Int. **3**, 223–236 (1995)

23.187 I.H. Flindell, A.R. McKenzie: *Technical Report: An inventory of current European methodologies and procedures for environmental noise management* (European Environmental Agency, Copenhagen 2000)

23.188 H. Tachibana, Convenor: International INCE Technical Study Group 3, Assessing the effectiveness of noise policies and regulations: Phase I, Noise Policies and Regulations, Draft Report dated 31 July (2004)

23.189 Directive 98/37/EC of the European Parliament and of the Council of 22 June 1998 on the approximation of the laws of the Member States relating to machinery

23.190 R. F. Higginson, personal communication, 2004 November 22

23.191 R.F. Higginson, J. Jacques, W.W. Lang: Directives, standards, and European noise requirements, Noise News Int. **2**, 156–184 (1994)

23.192 C. Grimwood, M. Ling: The EC Green Paper on future noise policy – A need for change, Acoustics Bulletin **1**, 5–8 (1997)

23.193 Commission of the European Communities: *Future Noise Policy*, European Commission Green Paper, Vol. COM(96) 540 (Commission of the European Communities, Brussels 1996)

Amazon EX1014 Page 1020

23.194 Commission of the European Communities: Future noise policy – European Commission Green Paper, Noise News Int. **5**, 77–98 (1997)
23.195 EU Official: Directive 2002/49/EC of the European Parliament and of the Council of 25 June, 2002 relative to the assessment and management of environmental noise, Official J. Eur. Communities **L189**(12) (2002)
23.196 International Electrotechnical Commission, Geneva, Switzerland: www.iec.ch

Amazon EX1014 Page 1021

Part H Engineering Acoustics

24 Microphones and Their Calibration
George S. K. Wong, Ottawa, Canada

25 Sound Intensity
Finn Jacobsen, Lyngby, Denmark

26 Acoustic Holography
Yang-Hann Kim, Daejeon, Korea

27 Optical Methods for Acoustics and Vibration Measurements
Nils-Erik Molin, Luleå, Sweden

28 Modal Analysis
Thomas D. Rossing, Stanford, USA

Amazon EX1014 Page 1022

24. Microphones and Their Calibration

The condenser microphone continues to be the standard against which other microphones are calibrated. A brief discussion of the theory of the condenser microphone, including its open-circuit voltage, electrical transfer impedance, and mechanical response, is given. The most precise method of calibration, the reciprocity pressure calibration method for laboratory standard microphones is discussed in detail, beginning with the principles of the reciprocity method. Corrections for heat conduction, equivalent volume, capillary tube, wave motion, barometric pressure and temperature are necessary to achieve the most accurate open-circuit sensitivity of condenser microphones.

Free-field calibration is discussed briefly, and in view of the difficulties in obtaining more accurate results than those provided by the reciprocity method, references are given for more detailed consideration. Secondary microphone calibration methods by comparison are described. These methods include interchange microphone comparison, comparison with a calibrator, comparison pressure and free-field, and comparison with a precision attenuator. These secondary calibration methods, which are adequate for most industrial applications, are economically attractive and less time consuming.

The electrostatic actuator method for frequency response measurement of working standard microphones is discussed with some pros and cons presented. An example to demonstrate the stability of laboratory standard microphones and the stability of a laboratory calibration system is described.

Appendix A discusses acoustic transfer impedance evaluation, while appendix B contains physical properties of air, which are necessary for microphone calibration.

24.1 **Historic References on Condenser Microphones and Calibration** 1024

24.2 **Theory** 1024
24.2.1 Diaphragm Deflection 1024
24.2.2 Open-Circuit Voltage and Electrical Transfer Impedance 1024
24.2.3 Mechanical Response 1025

24.3 **Reciprocity Pressure Calibration** 1026
24.3.1 Introduction 1026
24.3.2 Theoretical Considerations 1026
24.3.3 Practical Considerations 1027

24.4 **Corrections** 1029
24.4.1 Heat Conduction Correction 1029
24.4.2 Equivalent Volume 1031
24.4.3 Capillary Tube Correction 1032
24.4.4 Cylindrical Couplers and Wave-Motion Correction 1034
24.4.5 Barometric Pressure Correction 1035
24.4.6 Temperature Correction 1037
24.4.7 Microphone Sensitivity Equations 1038
24.4.8 Uncertainty on Pressure Sensitivity Level 1038

24.5 **Free-Field Microphone Calibration** 1039

24.6 **Comparison Methods for Microphone Calibration** 1039
24.6.1 Interchange Microphone Method of Comparison 1039
24.6.2 Comparison Method with a Calibrator 1040
24.6.3 Comparison Pressure and Free-Field Calibrations 1042
24.6.4 Comparison Method with a Precision Attenuator 1042

24.7 **Frequency Response Measurement with Electrostatic Actuators** 1043

24.8 **Overall View on Microphone Calibration** 1043

24.A **Acoustic Transfer Impedance Evaluation** 1045

24.B **Physical Properties of Air** 1045
24.B.1 Density of Humid Air 1045
24.B.2 Computation of the Speed of Sound in Air 1046
24.B.3 Ratio of Specific Heats of Air 1047
24.B.4 Viscosity and Thermal Diffusivity of Air for Capillary Correction 1047

References 1048

Amazon EX1014 Page 1023

Nomenclature

A'_1	numerical coefficient
$\tilde{A}_1$, $\tilde{A}_2$	complex quantities
a	the radius of the capillary tube (m)
a_0 to a_{12}	coefficients
$B = (\eta/\rho\alpha_t)^{\frac{1}{2}}$	coefficient
B'_1	numerical coefficient
C	fixed capacitance (F)
C'_1	shunt capacitance (F)
C_p	specific heat capacity at constant pressure ($kJ\,kg^{-1}\,K^{-1}$)
C_r	reference capacitance (F)
C_v	specific heat capacity at constant volume ($kJ\,kg^{-1}\,K^{-1}$)
C_t	shunt capacitance (F)
c_c	large shunt capacitance (F)
c	sound speed (m/s)
c_0	reference dry air sound speed at 0 °C, 101.325 kPa and 400 ppm CO_2 content (m/s)
c_i	input capacitance of the preamplifier (F)
c_{stat}	static capacitance (F)
c_s	stray capacitance (F)
$c_t(t)$	variable capacitance (F)
Δ_c	capillary correction ($\Delta_{c(AB)}$, $\Delta_{c(BC)}$, and $\Delta_{c(CA)}$ are the capillary corrections for the microphone pairs)
D	complex function
D_1	function for computation of R'
D'_1	numerical coefficient
D_2	function for computation of R'
d	diameter of microphone cavity (m)
E	voltage across the microphone (V)
E_0	polarizing voltage (V)
E_v	complex temperature transfer function
e_A, e_B, e_C	open-circuit voltage (V)
e_o	output voltage (V)
e_{oc}	output voltage as function of the varying capacitor c_t (V)
$e_{i(B)}$	sinusoidal insert voltage (V)
$e(t)$	time-varying voltage (V)
e'_B	microphone output voltage with microphone shunting capacitance
e_{Bref}, e_{Aref}	open-circuit voltage and the source driving voltage when the reference microphone is in position
e_{Bx}, e_{Ax}	open-circuit voltage and the source driving voltage when the test microphone is in position
e_1	driving voltage across Z_x (V)
e_2	preamplifier output voltage (V)
f	frequency (Hz)
f_e	$= 1.00062 + p_s(3.14\times10^{-8}) + t^2(5.6\times10^{-7})$, enhancement factor
f_0	resonance frequency (Hz)
g_1	gain of the preamplifier
H	relative humidity, %
h_0	static deflection of diaphragm (m)
h_a	air gap between the diaphragm and the backplate when the polarizing voltage is applied (m)
$h_s = \frac{p_{sv}}{p_0}\frac{H}{100}$	fractional molar concentration of moisture
h_c	CO_2 content (%)
$h = H/100$	humidity (dimensionless)
ΔH	humidity correction (dB/100%)
Δ_H	complex correction factor
I	input current (A)
i_t	time varying current generated by the microphone (A)
K	wave number of sound in the membrane (m^{-1})
k	$= i\omega Z_x/(\gamma P_s)$
k_0	constant
k_c	$= (-i\omega\rho/\eta)^{1/2}$ complex wave number (m^{-1})
L_r	level reading of the reference microphone (dB)
L_t	level reading of the test microphone (dB)
ℓ	volume to surface ratio of the coupler (m)
ℓ_c	length of the capillary tube (m)
l_0	length of the cavity, i. e. distance between the two diaphragms (m)
M	microphone sensitivity
M_A, M_B, M_C	open-circuit sensitivity of microphone A,B,C (V/Pa)
M_m	mechanical response (m/Pa)
M_e	electrical transfer impedance
M'_A, M'_B, M'_C	modified microphone A, B, C sensitivity (V/Pa)
M_t	open-circuit sensitivity of the test microphone (dB re 1 V/Pa)
M_r	open-circuit sensitivity of the reference microphone (dB re 1 V/Pa)
M_{dB}	microphone sensitivity (dB re 1 V/Pa)
M_{corr}	microphone sensitivity with correction (V/Pa)
M_{com}	combined level sensitivity of microphone and preamplifier (dB)
n	number of capillary tubes

P_s	barometric pressure (Pa)
p	alternating pressure inside the cavity (Pa)
p_i	incident sound pressure (Pa)
p_0	reference pressure = 101.325 kPa
p_{sv}	saturation water vapor pressure (Pa)
p_s	static pressure (during calibration) (Pa)
ΔP_c	capacitance correction (dB)
ΔP_v	microphone sensitivity level pressure correction (dB)
Δ_P	$= (p_s - p_0)$ pressure difference (kPa)
R	Universal gas constant, 8.314 51 J mol^{-1} K^{-1}. For dry air, 0 °C, 400 ppm CO_2 content and 101 325 Pa
R'	parameter for computation of heat conduction correction
R_p	impedance parallel with R_c and R_i (Ω)
R_c	high resistance (Ω)
R_i	input resistance of the preamplifier (Ω)
r_a	radius of microphone diaphragm (m)
r_b	radius of microphone backplate (Ω)
r_c	capillary tube radius (m)
S	parameter for computation of heat conduction correction
S_0	cross-sectional area of the cavity (m^2)
S_w	switch
T	$= (273.15 + t)$, thermodynamic temperature (K)
T_m	membrane tension (N/m)
T_0	= 273.15 K
t	temperature (°C)
ΔT	microphone sensitivity temperature correction (db)
Δt	$(T - 273.15)$, temperature difference (K)
u	volume velocity (m^3/s)
V	equivalent volumes of the cavity (m^3)
V_{eA}, V_{eB}, V_{eC}	equivalent volumes of the microphones A, B, C (m^3)
V_{AB}	$= (V + V_{eA} + V_{eB})$ (m^3)
V_{BC}	$= (V + V_{eB} + V_{eC})$ (m^3)
V_{CA}	$= (V + V_{eC} + V_{eA})$ (m^3)
ΔV_0	small change of volume (m^3)
V'_{AB},V'_{BC},V'_{CA}	equivalent volume including capillary tubes (m^3)
W	wave-motion correction (dB)
X'	parameter for computation of heat conduction correction
$x = f/f_0$	frequency normalized by the resonance frequency f_0 of the individual microphone
$x_w = \frac{p_{sv}}{p_s} f_e h$	mole fraction of water vapor in air
x_c	mole fraction of carbon dioxide in air
Δx	variation in depth of the cavity (m)
y_0	initial deflection of diaphragm (m)
y_r	diaphragm deflection (m)
Z_{AB}	acoustic impedance of a cavity with a pair of microphones A and B (N s m^{-5})
Z_{AC}	acoustic impedance of a cavity with a pair of microphones A and C (N s m^{-5})
Z_{CA}	acoustic impedance of a cavity with a pair of microphones C and A (N s m^{-5})
Z'_{AB}	acoustic impedance of a cavity with a pair of microphones A and B with assumptions (N s m^{-5})
Z'_{AC}	acoustic impedance of a cavity with a pair of microphones A and C with assumptions (N s m^{-5})
Z'_{CA}	acoustic impedance of a cavity with a pair of microphones C and A with assumptions (N s m^{-5})
Z_x	electrical impedance (Ω)
Z	$= \rho c S_0^{-1}$
$\underline{Z}$	compressibility factor for humid air
$\underline{Z}_{a,c}$	impedance of an open capillary tube (N s m^{-5})
$\underline{Z}_{a,t}$	complex acoustic wave impedance of an infinite tube (Pa s m^{-3})
$\underline{Z}'_{a,12}$	acoustic transfer impedance of a pair of microphones
α_t	thermal diffusivity of the gas media (m^2 s^{-1})
α_1, α_2	attenuator reading
β_{AB}	voltage ratio with microphone pair A and B
β_{BC}	voltage ratio with microphone pair B and C
β_{CA}	voltage ratio with microphone pair C and A
β_0, β_1, β_2	attenuator reading
β	voltage ratio reading
γ	ratio of specific heats
γ_0	ratio of specific heats of dry air at 0 °C, 101.325 kPa and 314 ppm CO_2 content (dimensionless)
η	viscosity of air (Pa s)
θ	phase angle (deg)
λ	wavelength (m)
ξ	complex propagation coefficient (m^{-1})
ρ	density of the gas enclosed (kg/m^3)
ρ_0	= 1.29295 (dry air, 0 °C, 101.325 kPa and 400 ppm CO_2 content) (kg/m^3)

Amazon EX1014 Page 1025

σ_M	membrane surface mass density (k_g/m^2)
Δ	compensation for dispersion (dB)
$\Delta_{c(AB)}$	capillary tube correction factor for microphones A and B
$\Delta_{c(BC)}$	capillary tube correction factor for microphones B and C
$\Delta_{c(CA)}$	capillary tube correction factor for microphones C and A
ω	$= 2\pi f$, angular frequency (rad/s)
$J_0()$ and $J_1()$	zero- and first-order cylindrical Bessel functions of the first kind for complex argument
i	$\sqrt{-1}$

24.1 Historic References on Condenser Microphones and Calibration

In 1917, *Wente* [24.1] described a microphone close to what we find today as the modern condenser microphone. The theory of absolute pressure calibration for condenser microphones and some of the modern analyses and implementations including the early implementation of the Western Electric 640AA condenser microphone have been described [24.2–30]. In 1995, a comprehensive discussion on the history of condenser microphone development and calibration was published [24.29].

24.2 Theory

The theory of condenser microphone operation has been investigated [24.1–30], and a brief summary is discussed in the following.

24.2.1 Diaphragm Deflection

The basic condenser microphone consists of a stretched diaphragm (Fig. 24.1) over a backplate that is polarized with a voltage E_0, usually 200 V. Due to the small air gap h_a (approximately 20 µm for a 25 mm diameter microphone) between the backplate and the thin (approximately 1–5 µm) metallic diaphragm, the latter is deflected by electrostatic charge of the backplate. With the diameter of the planar (flat) backplate ($2r_b$) smaller than that of the diameter ($2r_a$) of the diaphragm, the relatively complex initial deflection (y_0) of the diaphragm shape was analyzed by *Hawley* et al. ([24.29], Chap. 2). It has been shown by *Fletcher* and *Thwaites* [24.30] that it is an advantage to modify the backplate to have a parabolic profile to accommodate the curvature of the diaphragm and, according to their analysis, this eliminates distortion and increases the microphone sensitivity. Until this idea is further developed, the following will concentrate on condenser microphones with planar backplates.

24.2.2 Open-Circuit Voltage and Electrical Transfer Impedance

For functional implementation of a condenser microphone, *Zuckerwar* gave a detailed analysis ([24.29], Chap. 3), and the electrical circuit is shown in Fig. 24.2. A microphone is represented by a variable capacitance c_t with a static value of c_{stat}, and a stray capacitance of c_s. The polarizing voltage E_0 is applied to the microphone backplate via a high resistance R_c. The preamplifier is represented by an input impedance consisting of a capacitance c_i and a resistance R_i; c_c is a large blocking capacitor to prevent the polarizing voltage from overloading the preamplifier.

When a time-varying sound pressure is applied to the diaphragm, the diaphragm vibrates and the microphone capacitance c_t and the voltage E across the microphone

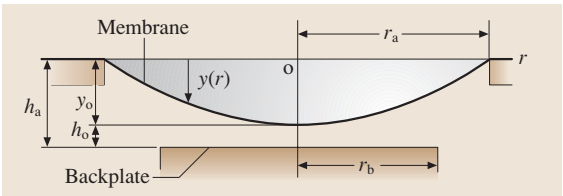


Fig. 24.1 Schematic diagram of a condenser microphone

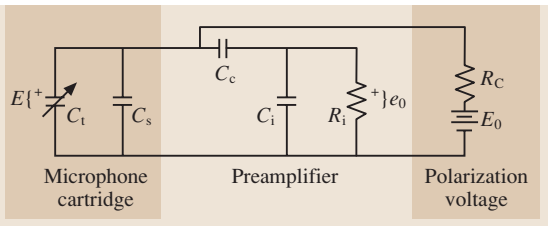


Fig. 24.2 Electrical circuit of a condenser microphone

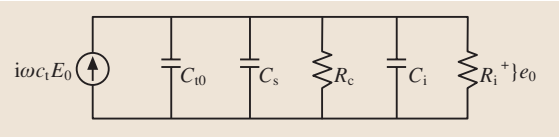


Fig. 24.3 Equivalent small-signal circuit

are represented by their corresponding static and time-varying components

$$c_t = c_{stat} + c_t(t)\,, \tag{24.1}$$

$$E = E_0 + e(t)\,. \tag{24.2}$$

The time-varying current i_t generated by the microphone is

$$i_t = E_0 \frac{dc_t}{dt} + c_{stat} \frac{de}{dt}\,. \tag{24.3}$$

For small electrical signals, Fig. 24.2 can be represented by an equivalent circuit shown in Fig. 24.3 and for small time-varying (ω) pressure at the diaphragm, the microphone can be represented by a fixed capacitance C and a current source i_t, and the output voltage e_o is:

$$e_o = E_0 \frac{c_t}{C} \frac{i\omega C R_p}{1 + i\omega C R_p}\,, \tag{24.4}$$

where R_p is the impedance of R_c in parallel with R_i, and C is the sum of c_{stat}, c_i and c_s. The microphone open-circuit voltage e_{oc} as a function of the varying capacitance c_t is

$$e_{oc} = E_0 \frac{c_t}{c_{stat}} \left(1 + \frac{c_i + c_s}{c_{stat}}\right)^{-1}\,. \tag{24.5}$$

Based on an approximate equation derived by *Hawley* ([24.29], Chap. 2, Eq. 5.8) for the capacitance of a microphone under the influence of the polarizing voltage, and assuming that the diaphragm can be modeled as a piston-like displacement, *Zuckerwar* ([24.29], Chap. 3, Eq. 2.23) has shown that the electrical transfer impedance M_e is

$$M_e = \frac{E_0}{h_0} \left(1 + \frac{r_b^2}{2r_a^2}\right) \left(1 + \frac{c_i + c_s}{c_{stat}}\right)^{-1}\,, \tag{24.6}$$

where r_a and r_b are the radii of the diaphragm and the backplate, respectively.

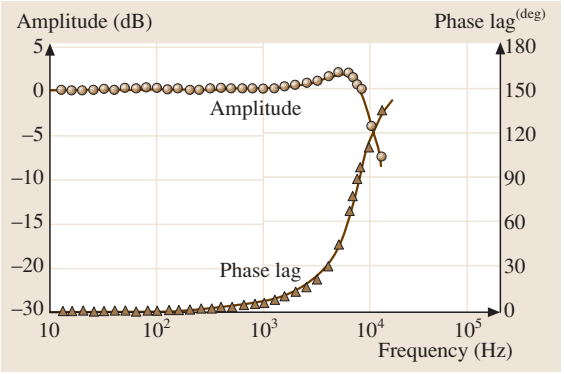


Fig. 24.4 Sample amplitude and phase response of a one-inch microphone (Brüel Kjær 4146) *Solid lines*: theoretical. *Symbols*: experimental (after *Zuckerwar* [24.29], Chap. 3)

Both *Hawley* et al. ([24.29], Chap. 2) and *Zuckerwar* ([24.29], Chap. 3) arrived at the conclusion that the optimum backplate size is

$$r_a/r_b = (2/3)^{1/2} = 0.8165\,. \tag{24.7}$$

24.2.3 Mechanical Response

The membrane motion is coupled to the air between the diaphragm and the backplate. The system exhibits damping due to the damping holes in the backplate. *Zuckerwar* ([24.29], Chap. 3, Eq. 3.51) arrived at a solution for the mechanical response as

$$M_m = \frac{[y(r)]}{p_i} = \frac{1}{TK^2} \frac{J_2(K_a)}{J_0(K_a) + D}\,, \tag{24.8}$$

where K is the wave number of sound in the membrane, given by

$$K = \omega \left(\frac{\sigma_M}{T_m}\right)^{1/2}\,, \tag{24.9}$$

ω is angular frequency, σ_M is the membrane surface mass density, and T_m is the membrane tension. D is a complex function ([24.29], Chap. 3, Eq. 3.50). With (24.8) the amplitude and phase response can be realized; some examples ([24.29], Chap. 3, Fig. 3.8) are shown in Fig. 24.4.

Amazon EX1014 Page 1027

24.3 Reciprocity Pressure Calibration

24.3.1 Introduction

High precision in acoustical measurements is needed even though the human ear cannot discern a change in sound level much smaller than 1 dB. For example, to certify aircraft for regulations, it is necessary to obtain measurements with a known uncertainty, usually 0.1–0.2 dB (Unless otherwise stated, the uncertainties referred to in this chapter, may be taken as better than two standard deviations. However, in most cases, the quoted statements on uncertainty are unclear in the source documents. Further complications are introduced when the original data are converted to decibels. For a more rigorous treatment of uncertainties, one should consult [24.31]). It is reasonable to assume that laboratory standard microphones (working standards) should be approximately an order of magnitude better than this, say with an uncertainty ranging from 0.01 to better than 0.1 dB. For research and development purposes, including the study of microphones and monitoring their stability, the primary calibration of condenser microphones should have an uncertainty no larger than several thousandths of a decibel.

One of the most accurate techniques to calibrate a primary standard condenser microphone is the absolute method of reciprocity pressure calibration (sometimes called the coupler method), which currently has a best uncertainty of less than 0.01 dB at 250 Hz, under a fully controlled environment under reference conditions [24.20]. If the calibration were to be performed on a laboratory bench without any control on the environment, such as barometric pressure, temperature and humidity, the estimated uncertainty of the coupler method is approximately 0.05 dB at lower and middle frequencies.

The theory of absolute pressure calibration methods for condenser microphones and some of the relatively modern implementations have been described in [24.1–29].

24.3.2 Theoretical Considerations

The reciprocity method measures the product of the sensitivities of each pair of a set of three microphones in terms of related electrical and mechanical quantities, from which the absolute sensitivity of each microphone can be deduced.

The acoustic impedance Z_{AB}, of a cavity with a pair of microphones A and B, as shown in Fig. 24.5 is

$$Z_{AB} = \gamma P_s [i\omega(V + V_{eA} + V_{eB})]^{-1} , \qquad (24.10)$$

where γ is the ratio of specific heats of the gas in the coupler, P_s is the barometric pressure, ω equals $2\pi f$, where f is the frequency of the driving sinusoidal signal, and V, V_{eA} and V_{eB} are the equivalent volumes of the cavity and of microphone A and microphone B, respectively. Equivalent volumes, as the name implies, are volumetric measures that represent the physical volumes of the cavity and of the coupled microphones modified by thermal and finite impedance factors.

The relationship between the alternating pressure p inside the cavity and the volume velocity u is

$$p = uZ_{AB} = u\gamma P_s (i\omega V_{AB})^{-1} , \qquad (24.11)$$

where the equivalent volume of the cavity with microphones A and B is

$$V_{AB} = (V + V_{eA} + V_{eB}) . \qquad (24.12)$$

The reciprocity theorem states that, in a passive linear reversible (reciprocal) transducer, the ratio of the volume velocity u in the cavity to the input current I when used as a sound source is equal to the ratio of the open-circuit voltage e_A across the electrical terminals to the sound pressure p acting on the diaphragm when used as a receiver. The theorem enables one to write the

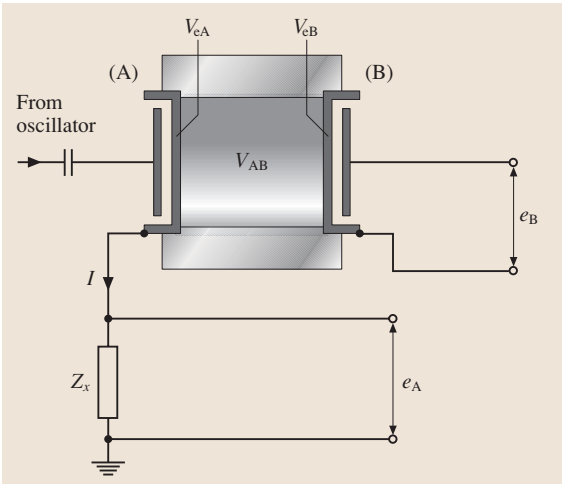


Fig. 24.5 Calibrating condenser microphones by the reciprocity method (after *Wong*, [24.29], Chap. 4)

following equations:

$$M_A = u/I = e_A/p\,, \tag{24.13}$$
$$M_B = e_B/p\,, \tag{24.14}$$
$$M_C = e_C/p\,, \tag{24.15}$$

where M_A, M_B and M_C are the open-circuit sensitivities of the microphones.

Multiplying (24.13) and (24.14), and substituting p from (24.11) gives

$$M_A M_B = e_B \mathrm{i}\omega V_{AB}/(I\gamma P_s)\,. \tag{24.16}$$

Since

$$I = e_A/Z_x \tag{24.17}$$

and Z_x is an electrical impedance, substitution of (24.17) into (24.16) gives

$$M_A M_B = V_{AB} k \beta_{AB}\,, \tag{24.18}$$

where

$$k = \mathrm{i}\omega Z_x/(\gamma P_s) \tag{24.19}$$

and

$$\beta_{AB} = e_B/e_A\,. \tag{24.20}$$

By using the microphones A, B and C, configured in pairs to give equivalent volumes V_{AB}, V_{BC} and V_{CA}, and by measuring the corresponding voltage ratios β_{AB}, β_{BC}, and β_{CA}, respectively, the sensitivity product of three pairs of microphones can be obtained:

$$\begin{aligned} M_A M_B &= k\beta_{AB} V_{AB}\,,\\ M_B M_C &= k\beta_{BC} V_{BC}\,,\\ M_C M_A &= k\beta_{CA} V_{CA}\,. \end{aligned} \tag{24.21}$$

From (24.21), the open-circuit sensitivities of the individual microphones can be derived

$$\begin{aligned} M_A &= [(V_{CA}V_{AB}/V_{BC})(\beta_{CA}\beta_{AB}/\beta_{BC})k]^{1/2}\,,\\ M_B &= [(V_{AB}V_{BC}/V_{CA})(\beta_{AB}\beta_{BC}/\beta_{CA})k]^{1/2}\\ M_C &= [(V_{BC}V_{CA}/V_{AB})(\beta_{BC}\beta_{CA}/\beta_{AB})k]^{1/2}\,. \end{aligned} \tag{24.22}$$

It can be seen from (24.22) that the sensitivity of each microphone can be deduced by measuring the voltage ratios if the equivalent volumes for each of the three pairs of microphones and the numerical value of the constant k are known.

Similarly, the open-circuit sensitivity shown in (24.22) can be expressed in terms of the acoustic impedance of the cavity (24.10):

$$\begin{aligned} M_A &= \{[Z_{BC}/(Z_{CA}Z_{AB})](\beta_{CA}\beta_{AB}/\beta_{BC})Z_x\}^{1/2}\,,\\ M_B &= \{[Z_{CA}/(Z_{AB}Z_{BC})](\beta_{AB}\beta_{BC}/\beta_{CA})Z_x\}^{1/2}\,,\\ M_C &= \{[Z_{AB}/(Z_{BC}Z_{CA})](\beta_{BC}\beta_{CA}/\beta_{AB})Z_x\}^{1/2}\,, \end{aligned} \tag{24.23}$$

where Z_{AB}, Z_{BC} and Z_{CA} are the acoustic impedances of the cavities.

An equation for calculating the acoustic impedance of a coupler is given in Appendix 24.A.

24.3.3 Practical Considerations

The general arrangement for implementation of pressure reciprocity calibration of condenser microphones is shown in Fig. 24.6. To simplify electrical measurements, it is necessary that the driving microphone A should be isolated electrically from the receiving microphone B. The preamplifier has a gain of g_1 and an input capacitance of C_i. Since the receiving microphone is shunted by C_i the microphone output voltage is modified to e'_B. When the switch S_w is at position 2, an insert voltage can be applied in order to obtain the open-circuit voltage. For both microphones, a polarization voltage (usually 200 V) is applied via a high resistance. A small shunt capacitor C_t, which closely approximates C_i, modifies the driving voltage e_A to e_1.

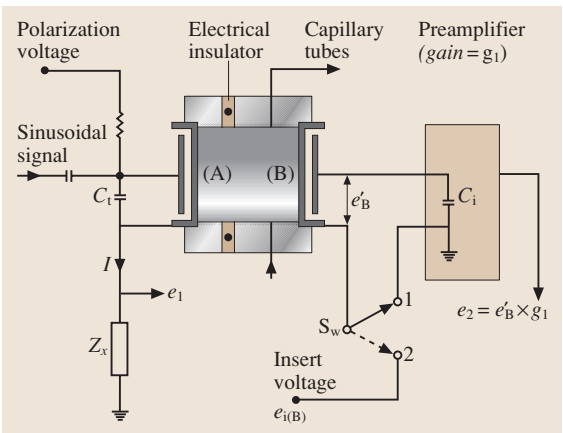


Fig. 24.6 Pressure reciprocity calibration method with provision for insert voltage (after *Wong* [24.29], Chap. 4)

The cavity usually has two capillary tubes for atmospheric pressure equalization and for the insertion of gases other than air. Hence the sensitivities of the microphones shown in (24.22) are modified to

$$M'_{\mathrm{A}} = [(V'_{\mathrm{CA}} V'_{\mathrm{AB}}/V'_{\mathrm{BC}})(\beta_{\mathrm{CA}}\beta_{\mathrm{AB}}/\beta_{\mathrm{BC}})k]^{1/2} ,$$
$$M'_{\mathrm{B}} = [(V'_{\mathrm{AB}} V'_{\mathrm{BC}}/V'_{\mathrm{CA}})(\beta_{\mathrm{AB}}\beta_{BC/}\beta_{\mathrm{CA}})k]^{1/2} ,$$
$$M'_{\mathrm{C}} = [(V'_{\mathrm{BC}} V'_{\mathrm{CA}}/V'_{\mathrm{AB}})(\beta_{\mathrm{BC}}\beta_{CA/}\beta_{\mathrm{AB}})k]^{1/2} , \quad (24.24)$$

where the cavity equivalent volume is marked with a prime to indicate the inclusion of the equivalent volume of the capillary tubes. The voltage ratio $e_{\mathrm{B}}/e_{\mathrm{A}}$ becomes e_2/e_1 and it is represented by β_{AB} in (24.24). The next section discusses the parameters shown in (24.24).

Open-Circuit Sensitivity

The open-circuit sensitivity of the microphones is obtained with the insert voltage method [24.8]. From Fig. 24.6, the measurement procedure is as follows.

With the switch S_{w} at position 1, measure the output voltage e_2 from the preamplifier. Next, remove the drive sinusoidal signal from microphone A, and with the switch at position 2, apply a sinusoidal insert voltage $e_{\mathrm{i(B)}}$ to drive the diaphragm of microphone B. The magnitude of $e_{\mathrm{i(B)}}$ is adjusted such that the voltage e_2 is repeated at the output of the preamplifier. As the circuit shows, the insert voltage is identical to the desired open-circuit voltage of microphone B if the loading of the preamplifier's input impedance were to be removed. The open-circuit sensitivity of the microphones can be obtained from (24.24) with the voltage ratio $e_{\mathrm{i(B)}}/e_1$, for each pair of microphones, substituted into (24.20). Alternatively, the insert voltage can be computed from an injected voltage when the switch is at position 2, and then measuring the corresponding output voltage e_2 to obtain the overall gain that enables the computation of the proper insert voltage.

Electrical Circuit for Measurement

The basic electrical measurement for pressure reciprocity calibration is that of the amplitude ratio of two sinusoidal signals (e_1 and e_2 in Fig. 24.6) that may not be in phase. The uncertainty of direct measurement of each of the two signals is limited by the uncertainty of the alternating-current (AC) voltmeter. Several practical circuits for this purpose have been described [24.27]. A higher accuracy can be achieved with voltage ratio measurements. Two examples are described below to give some insight into the diversity of the methods of implementation.

Rectified Signal Null Method

In this method, used in commercial reciprocity calibration apparatus, one of the AC signals is applied to both inputs (Fig. 24.7). With the attenuator removed but with the bypass connection in place, the signal is balanced at the amplifier–rectifier circuit, such that a null reading is indicated by the null-meter. With the two sinusoidal signals connected to the inputs, the attenuator is adjusted for a null reading. The attenuator reading gives the voltage ratio. The uncertainty of the voltage ratio is theoretically dependent on the uncertainty of the precision attenuator. However, the linearity and matching of the amplifiers, amplifier–rectifiers (with RC time constants, not shown) together with the amplitude difference of the two signals, also affect the uncertainty of the circuit. Even with good design, the uncertainty of the voltage ratio measured is approximately 0.003 dB. With some modifications, the user of the apparatus may reduce the uncertainty of measurements by exchanging the signals at the input, and by shifting the attenuator from positions A and B to positions C and D, then taking the mean of the ratio readings for the two attenuator positions.

Variations on this method have been used; for example, the insert voltage (Fig. 24.6) can be derived from a precision attenuator driven by the same source as the driving microphone [24.25].

Interchange Reference Method

The amplitude ratio R and the phase θ of two sinusoidal signals can be measured very precisely with the interchange reference method [24.32] (Fig. 24.8). Signals e_1 and e_2 are presented to the differential inputs of a lock-in amplifier via the switch S_w and the attenuators. When the switch is in position 1, e_1 is selected to be the reference signal for the lock-in amplifier. The attenuator readings β_1 and α_1 are adjusted for a null condition. Using the vector diagram in Fig. 24.9,

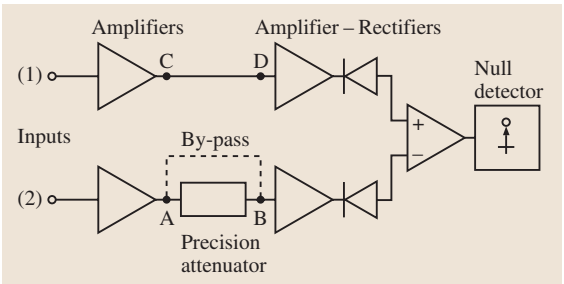


Fig. 24.7 Rectified signal null circuit (after *Wong* [24.29], Chap. 4)

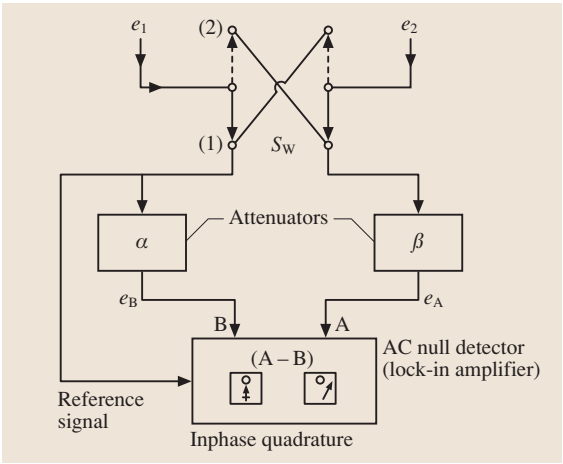


Fig. 24.8 Interchange reference method (after *Wong* [24.29], Chap. 4)

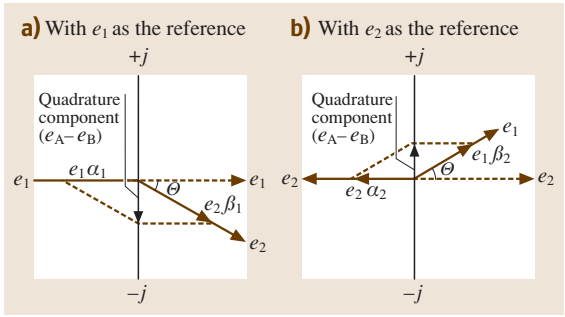


Fig. 24.9 Vector diagram for the in-phase null condition (after *Wong* [24.29], Chap. 4)

we have

$$e_2\beta_1\cos\theta - e_1\alpha_1 = 0\,. \tag{24.25}$$

Similarly, when e_2 is selected as the reference by the switch at position 2, the null condition with attenuator readings β_2 and α_2 provides the following:

$$e_1\beta_2\cos\theta - e_2\alpha_2 = 0\,. \tag{24.26}$$

From (24.5) and (24.6), the general equations for the amplitude ratio $R = e_2/e_1$ and $\cos\theta$ are found

$$R = [(\alpha_1/\alpha_2)(\beta_2/\beta_1)]^{1/2}\,, \tag{24.27}$$

$$\cos\theta = [(\alpha_1\alpha_2)/(\beta_1\beta_2)]^{1/2}\,. \tag{24.28}$$

Although for symmetry, Fig. 24.8 shows two attenuators, in practice only one attenuator is required. For the condition in Fig. 24.9, where $e_2 > e_1$, $\alpha_1 = \beta_2 = 1$. The uncertainty of the attenuator that can be a seven-decade ratio transformer (inductive voltage dividers) is of the order of 0.1 ppm. The uncertainty of the measured amplitude ratio is of the order of 1 ppm. Other circuits employing inductive voltage dividers for voltage ratio measurements are given in [24.17, 23].

Reference Impedance Selection

The reference impedance Z_x shown in Fig. 24.6 needs to be carefully selected. The nature of the impedance, either purely resistive or purely capacitive, or a combination of electrical impedances, dictates the mode of evaluation of the factor k, which is required for the computation of microphone sensitivity in (24.24). If Z_x is a resistance, the angular frequency ω, shown in (24.19), has to be measured. When the impedance is a capacitance C_r the term $Z_x = 1/(i\omega C_r)$, and the frequency terms are canceled. The numerical value of Z_x is chosen such that the magnitudes of e_1 and e_2 are nearly equal in order to enhance the measurement of voltage ratios using null measurement techniques. For precise measurement of Z_x, the capacitance of the connecting cables to the impedance should be taken into consideration.

24.4 Corrections

24.4.1 Heat Conduction Correction

The alternating sound pressure induces compression and expansion in the gas medium inside the closed cavity. At sufficiently low frequencies, the induced temperature changes occur isothermally, and the heat exchange at the walls of the cavity has to be included when computing the acoustic impedance of the cavity. As the frequency increases, heat conduction between the gas and the walls decreases. Gradually, isothermal conditions change to adiabatic conditions, at which virtually no heat is exchanged with the walls.

Classical analytical approaches to calculate heat conduction in cavities are given by *Ballantine* [24.2] and *Daniels* [24.33]. Correction factors for heat conduction were obtained by *Biagi* and *Cook* [24.34]. Theoretical and experimental data, based on thermal diffusion, on the acoustic impedance of the cavity, are given by *Ger-*

Table 24.1 Tabulated values of E_v for the heat conduction correction (ANSI S1.15: 2005, and IEC 61094-2:1992-03)

Real part of E_v			X'	Imaginary part of E_v		
$R' = 0.2$	$R' = 0.5$	$R' = 1$		$R' = 0.2$	$R' = 0.5$	$R' = 1$
0.72127	0.71996	0.72003	1.0	0.24038	0.22323	0.22146
0.80092	0.80122	0.80128	2.0	0.17722	0.16986	0.16885
0.83727	0.83751	0.83754	3.0	0.14818	0.14304	0.14236
0.85907	0.85920	0.85922	4.0	0.13003	0.12614	0.12563
0.87393	0.87402	0.87403	5.0	0.11732	0.11421	0.11380
0.89343	0.89348	0.89349	7.0	0.10030	0.09807	0.09777
0.91082	0.91086	0.91086	10.0	0.08477	0.08321	0.08300
0.93693	0.93694	0.93694	20.0	0.06086	0.06007	0.05997
0.94850	0.94851	0.94851	30.0	0.05002	0.04950	0.04942
0.95540	0.95541	0.95541	40.0	0.04349	0.04310	0.04304
0.96358	0.96359	0.96359	60.0	0.03568	0.03541	0.03538
0.96846	0.96846	0.96846	80.0	0.03098	0.03078	0.03076
0.97179	0.97179	0.97179	100.0	0.02776	0.02761	0.02758
0.98005	0.98005	0.98005	200.0	0.01972	0.01964	0.01963
0.98590	0.98590	0.98590	400.0	0.01399	0.01395	0.01395
0.99003	0.99003	0.99003	800.0	0.00992	0.00990	0.00989

The numerical values given are considered accurate to 0.00001

ber [24.35]. *Ballagh* [24.36] took into consideration heat loss effects due to the microphone diaphragms at the ends of the cavity. *Jarvis* [24.37] pointed out the need to include the impedance of the driver microphone during computation of the heat conduction correction. It is difficult to decide accurately at which middle frequencies the isothermal–adiabatic transition occurs, and which portions of the cavity to include in the impedance of the microphone. The exact nature of this transition depends upon the frequency of the calibration and the dimensions of the coupler. The sound pressure generated by the transmitter microphone, i. e. a constant-volume displacement source, will change accordingly. The effect can be considered as an apparent increase in the coupler volume expressed by a complex correction factor Δ_H to the geometrical volume V in Sect. 24.A or to the cross-sectional area S_0 defined in $Z = \rho c S_0^{-1}$ in Sect. 24.B.

The heat conduction correction factor is given by:

$$\Delta_H = \frac{\gamma}{1 + (\gamma - 1)E_v} , \qquad (24.29)$$

where E_v is the complex temperature transfer function defined as the ratio of the space average of the sinusoidal temperature variation associated with the sound pressure to the sinusoidal temperature variation that would be generated if the walls of the coupler were perfectly nonconducting (24.30), and γ is the ratio of specific heats of the gas inside the coupler. Tabulated values for E_v can be found in Table 24.1 [24.35] as a function of the parameters R' and X', where $R'$is the length-to-diameter ratio of the coupler, $X' = f\ell^2/(\gamma\alpha_t)$, f is the frequency, ℓ is the volume-to-surface ratio of the coupler and α_t is the thermal diffusivity of the gas enclosed.

For finite cylindrical couplers as described in [24.38], annex C, the approximation described below for the complex quantity E_v will be satisfactory

$$E_v = 1 - S + D_1 S^2 + (3/4)\sqrt{\pi} D_2 S^3 , \qquad (24.30)$$

where

$$S = \left(-i\frac{1}{2\pi X'}\right)^{1/2} = \frac{1 - i}{2\sqrt{\pi X'}} ,$$

$$D_1 = \frac{\pi R'^2 + 8R'}{\pi(2R' + 1)^2} ,$$

$$D_2 = \frac{R'^3 - 6R'^2}{3\sqrt{\pi}(2R' + 1)^3} .$$

The modulus of E_v, as calculated from (24.30), is accurate to 0.01% within the range $0.125 < R' < 8$ and for $X' > 5$. The first two terms in (24.30) constitute an approximation that may be used for couplers that are not right circular cylinders.

24.4.2 Equivalent Volume

The equivalent volume without heat conduction correction, as defined in (24.12), consists of the volume of the cavity plus the equivalent volumes of the microphones. The volume of the cavity is usually measured with traditional methods offered by mechanical metrology. The equivalent volume of a standard microphone, which includes a small volume occupied by a screw thread and an effective volume caused by the non-rigidity of the microphone diaphragm, is very difficult to measure precisely with conventional mechanical means. Various methods for the measurement of the equivalent volume of microphones are available [24.39]. Optical techniques, such as the traveling microscope, have been used to measure the cavity length [24.25]. For higher precision, interferometric procedures can be applied.

An acoustical resonance method can be used to determine the front cavity volume of a standard microphone. A three-port coupler accommodates two smaller microphones (e.g. 1/4 inch microphones), and the standard microphone. The smaller microphones are used as a driver–receiver combination to give the electrical transfer impedance including the cavity volume with the standard microphone in place. The standard microphone is replaced with a movable plunger; the displacement of the plunger is calibrated to indicate volumetric changes covering the range of actual microphone volumes. The equivalent front volume of the test microphone can be deduced from the calibrated position of the plunger at which the two smaller microphones indicate the same electrical transfer impedance as when the test microphone is in place. See [24.12] for a similar three-port procedure and [24.16] for precise measurement of volumetric changes.

Wong and *Embleton* [24.20] developed a very precise method that assesses the equivalent volume with the heat conduction correction and includes the impedance of the capillary tubes for the coupler and two microphones in one procedure. The length of the cavity can be varied with a removable spacer to replace the electrical insulation, and the voltage ratio $\beta = e_2/e_1$, as shown in Fig. 24.6, is assessed at the frequency of interest with the interchange reference method [24.32]. From (24.10) and (24.11), the equivalent volume of the cavity can be expressed in terms of the volume velocity u and the alternating pressure p

$$V = (\gamma P_s/\mathrm{i}\omega)(u/p)\,. \tag{24.31}$$

Since the voltage ratio β is inversely proportional to the pressure p inside the cavity (an increase of signal magnitude requires a decrease in ratio reading to maintain a null condition), (24.31) can be modified to

$$V = k_0\beta\,, \tag{24.32}$$

where k_0 is a constant.

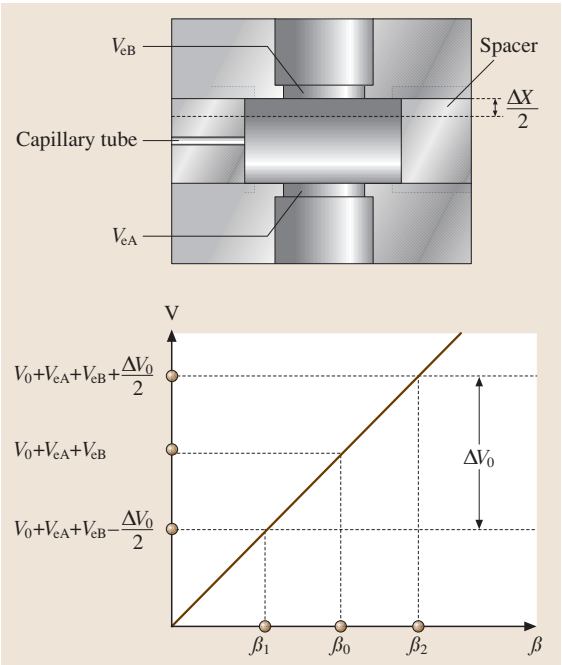


Fig. 24.10 Arrangement for determining the equivalent volume, including corrections for capillary tubes, and heat conduction (after [24.20])

Three readings, β_0, β_1 and β_2 corresponding to cavity volume $(V_0 + V_{eA} + V_{eB})$, volume $(V_0 + V_{eA} + V_{eB} - \Delta V_0/2)$ and volume $(V_0 + V_{eA} + V_{eB} + \Delta V_0/2)$, are obtained. Here ΔV_0 is a small variation in volume corresponding to a small variation Δx in spacer thickness. Figure 24.10 illustrates the relationship between changes in volume and the ratio readings. The equivalent volume of the cavity is

$$V = (V_0 + V_{eA} + V_{eB}) = \Delta V_0[\beta_0/(\beta_2 - \beta_1)]\,. \tag{24.33}$$

From Fig. 24.10,

$$V = [\beta_0/(\beta_2 - \beta_1)]d^2\Delta x\pi/4\,, \tag{24.34}$$

where d and Δx are the diameter and the variation in depth of the cavity.

For highly accurate measurements, the spacers are implemented with optical flats whose thicknesses are

measured by interferometry. The cavity is manufactured with precision optical fabrication. The uncertainty in the equivalent volume of such a cavity is estimated to be approximately 20 ppm. For less stringent applications the three optical flats can be replaced with adaptor rings [24.25] or with three cavities of known volumes. The equivalent volume of the cavity can then be determined by interpolation. This method has been commercialized with a similar procedure that relied on two couplers (long and short couplers) in the Brüel and Kjær 5998 reciprocity apparatus. With the sensitivities of the microphone pairs obtained with the two couplers, the microphone cavity depths are then adjusted numerically until the final microphone sensitivities obtained with the two couplers are nearly identical or very close.

24.4.3 Capillary Tube Correction

For microphone calibration, the preferred expression [24.38,40] adopted for the acoustic input impedance of an open capillary tube is:

$$Z_c = Z_t \tanh(\zeta L_c) \,, \tag{24.35}$$

where Z_t is the complex characteristic impedance of a capillary tube with infinite length, L_c is the length of the capillary tube, ζ is the complex propagation coefficient for plane waves in a tube, and

$$Z_t = \left(\tilde{A}_1/\tilde{A}_2\right)^{1/2} \,, \tag{24.36}$$

$$\zeta = \left(\tilde{A}_1\tilde{A}_2\right)^{1/2} \,. \tag{24.37}$$

$\tilde{A}_1$ and $\tilde{A}_2$ are complex quantities; $\tilde{A}_1$ represents viscosity loss at the walls and inertia of the gas medium, and $\tilde{A}_2$ represents heat conduction loss at the walls and the compliance of the gas medium, where

$$\tilde{A}_1 = \mathrm{i}\frac{\omega\rho}{\pi r_c^2}\left(1 - \frac{2J_1(k_c r_c)}{k_c r_c J_0(k_c r_c)}\right)^{-1} \,, \tag{24.38}$$

$$\tilde{A}_2 = \mathrm{i}\omega\frac{\pi r_c^2}{\rho c^2}\left(1 + \frac{2}{Bk_c r_c}(\gamma - 1)\frac{j_1(Bk_c r_c)}{j_0(Bk_c r_c)}\right) \,, \tag{24.39}$$

J_0 and J_1 are, respectively, the zeroth- and first-order cylindrical Bessel functions of the first kind for complex arguments, r_c is tube radius (m), $k_c = (-\mathrm{i}\omega\rho/\eta)^{1/2}$ is the complex wave number (m^{-1}), $B = [\eta/(\rho\alpha_t)]^{1/2}$, α_t is the thermal diffusivity of the gas media (m^2/s).

Table 24.2 Real part of Z_c in GPa s/m^3 (ANSI S1.15: 2005, and IEC 61094-2:1992-03), tube dimensions in millimeters

$\ell_C = 50$			Frequency	$\ell_C = 100$		
$r_c = 0.1667$	$r_c = 0.20$	$r_c = 0.25$	(Hz)	$r_c = 0.1667$	$r_c = 0.20$	$r_c = 0.25$
3.018	1.457	0.597	20	6.041	2.916	1.195
3.019	1.457	0.597	25	6.044	2.919	1.196
3.020	1.458	0.597	31.5	6.049	2.922	1.198
3.022	1.459	0.598	40	6.059	2.928	1.201
3.025	1.460	0.599	50	6.072	2.937	1.205
3.029	1.463	0.600	63	6.094	2.951	1.212
3.036	1.467	0.602	80	6.130	2.975	1.225
3.047	1.473	0.605	100	6.185	3.011	1.243
3.063	1.482	0.610	125	6.270	3.069	1.272
3.093	1.499	0.620	160	6.422	3.173	1.326
3.137	1.524	0.633	200	6.643	3.331	1.408
3.207	1.564	0.654	250	6.989	3.595	1.550
3.326	1.631	0.689	315	7.542	4.066	1.817
3.534	1.750	0.750	400	8.353	4.944	2.381
3.871	1.943	0.849	500	9.068	6.288	3.535
4.504	2.314	1.034	630	8.670	7.336	5.631
5.807	3.113	1.435	800	6.375	5.311	4.375
8.332	4.890	2.378	1000	4.353	3.005	1.925
12.120	9.008	5.385	1250	3.545	2.127	1.146

The data used for this table are: $c = 345.7$ m/s, $\gamma = 1.40$, $\rho = 1.186$ kg/m^3, $\eta = 18.3 \times 10^{-6}$ Pa s, $\alpha_t = 21 \times 10^{-6}$ m^2/s
The values given in this table are valid at the reference environmental conditions: 23 °C, 101.325 kPa and 50% RH

Table 24.2 (continued)

$\ell_C = 50$			Frequency	$\ell_C = 100$		
$r_c = 0.1667$	$r_c = 0.20$	$r_c = 0.25$	(Hz)	$r_c = 0.1667$	$r_c = 0.20$	$r_c = 0.25$
9.191	7.926	6.740	1600	4.171	2.410	1.196
4.326	3.021	1.951	2000	6.325	4.409	2.527
2.694	1.637	0.893	2500	4.979	3.717	2.768
2.807	1.580	0.783	3150	4.411	2.661	1.392
5.923	3.536	1.749	4000	5.238	4.019	3.075
5.946	4.825	3.903	5000	5.059	3.262	1.770
3.306	1.939	1.011	6300	4.578	2.920	1.672
6.571	5.375	4.137	8000	4.695	3.034	1.749
4.184	2.465	1.258	10 000	4.977	3.363	1.952
3.902	2.539	1.540	12 500	4.760	3.331	2.271
4.043	2.590	1.534	16 000	4.753	3.263	2.137
4.535	2.813	1.517	20 000	4.844	3.324	2.023
0.097	0.074	0.049	20	0.096	0.114	0.090
0.122	0.092	0.061	25	0.120	0.143	0.112
0.153	0.116	0.077	31.5	0.151	0.180	0.141
0.195	0.147	0.098	40	0.191	0.228	0.180
0.244	0.184	0.123	50	0.238	0.285	0.225
0.307	0.232	0.155	63	0.299	0.359	0.283
0.390	0.295	0.197	80	0.376	0.455	0.360
0.488	0.369	0.246	100	0.465	0.569	0.452
0.610	0.461	0.308	125	0.569	0.710	0.567
0.782	0.592	0.396	160	0.701	0.905	0.731
0.980	0.743	0.496	200	0.824	1.123	0.923
1.228	0.933	0.623	250	0.916	1.380	1.170
1.556	1.186	0.792	315	0.888	1.664	1.500
1.990	1.527	1.021	400	0.479	1.842	1.922
2.511	1.948	1.306	500	–0.684	1.11	2.200
3.189	2.532	1.711	630	–2.739	–0.777	0.926
3.987	3.353	2.325	800	–3.890	–3.152	–2.510
4.280	4.213	3.186	1000	–3.031	–2.595	–2.130
1.338	3.162	3.730	1250	–1.382	–1.157	–0.944
–5.333	–4.384	–3.281	1600	0.429	0.456	0.282
–4.500	–3.768	–2.956	2000	0.260	0.971	1.221
–1.996	–1.663	–1.280	2500	–1.702	–1.552	–1.344
0.491	0.244	0.051	3150	0.205	0.199	0.053
2.428	2.283	1.692	4000	–1.074	–0.864	–0.524
–2.803	–2.434	–1.954	5000	0.208	0.438	0.406
0.186	–0.037	–0.190	6300	–0.070	–0.095	–0.219
–1.245	–0.607	0.209	8000	–0.041	–0.027	–0.138
0.872	0.643	0.336	10 000	–0.056	0.152	0.212
–0.542	–0.699	–0.764	12 500	–0.281	–0.295	–0.281
–0.210	–0.399	–0.532	16 000	–0.174	–0.187	–0.228
0.430	0.349	0.142	20 000	–0.109	–0.001	0.035

The data used for this table are: $c = 345.7\,\mathrm{m/s}$, $\gamma = 1.40$, $\rho = 1.186\,\mathrm{kg/m^3}$, $\eta = 18.3 \times 10^{-6}\,\mathrm{Pa\,s}$, $\alpha_t = 21 \times 10^{-6}\,\mathrm{m^2/s}$
The values given in this table are valid at the reference environmental conditions: 23 °C, 101.325 kPa and 50% RH

Amazon EX1014 Page 1035

For n capillary tubes the correction factors $\Delta_{c(AB)}$, $\Delta_{c(BC)}$ and $\Delta_{c(CA)}$ for the respective cavity impedances in (24.23) are

$$\Delta_{c(AB)} = 1 + n(Z_{AB}/Z_c)\,,$$
$$\Delta_{c(BC)} = 1 + n(Z_{BC}/Z_c)\,,$$
$$\Delta_{c(CA)} = 1 + n(Z_{CA}/Z_c)\,. \qquad (24.40)$$

Equation (24.40) assumes that the heat conduction correction (Sect. 24.4.1) has been applied.

At a temperature of 23 °C, a relative humidity of 50% and a static pressure of 101.325 kPa, for a typical range of parameters and frequencies, the real and imaginary parts of Z_c are as shown in Table 24.2, respectively. The computation of the air density ρ, sound speed c in humid air and other physical quantities are discussed in Sect. 24.B.3.

It should be noted that the numerical values given in these tables are relatively sensitive to the change in the viscosity of air η. For example, when η deviates by 0.5%, the numerical values changes by approximately 1% in the real part of Z_c and approximately 8% in the corresponding imaginary part. Since the original data for the computation of η (Sect. 24.B.4) may have an uncertainty of several percent, the Table 24.2a,b should be used with caution.

24.4.4 Cylindrical Couplers and Wave-Motion Correction

Two types of couplers (cavities) are used for microphone calibration: plane-wave couplers, where the diameter of the cavity equals the diameter of the microphone diaphragm; and large-volume couplers, where the cavity diameter is larger than that of the diameter of the microphone diaphragm and the cavity volume is much larger than the sum of the equivalent volume and front volumes of the microphones. In reciprocity calibration, the dimensions of the large-volume coupler are chosen such that the pressure increase at the diaphragm of the receiving microphone, due to the first longitudinal mode, is partially canceled by the pressure decrease due to the lowest radial mode, whose maximum pressures occur at the side walls of the cavity and hence are removed from the vicinity of the microphone diaphragm. A generally accepted rule to ensure that the pressure is sufficiently uniform over the microphone diaphragm is that the maximum dimension of the cavity should not exceed $\lambda/20$, where λ is the wavelength in the gas. With a large-volume coupler there is less influence from the equivalent volumes of the capillary tubes and the microphones. However, with larger dimensions, the coupler is restricted to lower-frequency applications. In a plane-wave coupler with relatively dimensions there are smaller wave-motion effects, and the coupler can be used at higher frequencies. To extend the range of calibration frequency, a gas with a higher sound speed should be used. Theoretical and experimental data [24.38, 42–44] on wave motion in couplers have been published. In practice, it is difficult to obtain a precise theoretical expression for wave-motion correction. However, for experimental determination, the following method [24.44] has been used.

Assuming that the sensitivity of the microphones remains constant, the microphone sensitivity is measured with air as the gas at relatively high frequencies for which the pressure distribution in the cavity is nonuniform. The measurements are repeated with hydrogen or helium, which have higher sound speeds and for which the wave motion correction is correspondingly smaller.

Table 24.3 Experimental data on wave-motion corrections for the air-filled large-volume coupler used with type LS1P microphones (ANSI S1.15: 2005, IEC 61094-2:1992-03). LS1P: type designation [24.41] for laboratory standard (LS) microphones, where the last letter P or F represents pressure or free-field microphones, and the number 1 or 2 represent mechanical configuration for one-inch and half-inch microphones, respectively

Frequency (Hz)	Correction (dB)
800 and below	0.000
1000	–0.002
1250	–0.013
1600	–0.034
2000	–0.060
2500	–0.087

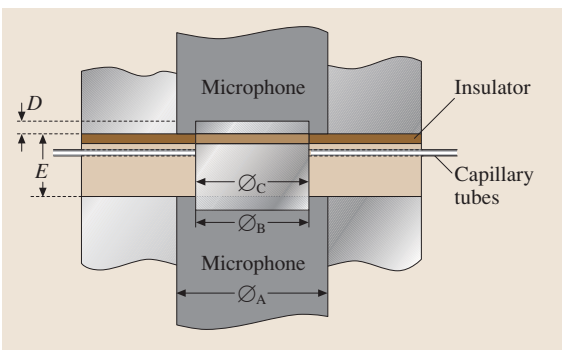


Fig. 24.11 Mechanical configuration of plane-wave couplers (ANSI S1.15: 2005, and IEC 61094-2:1992-03)

Table 24.4 Nominal dimensions for plane-wave couplers (ANSI S1.15: 2005, and IEC 61094-2:1992-03)

Dimensions (mm)	Laboratory standard microphones		
Symbol	Type LS1P	Type LS2aP	Type LS2bP
$\varnothing_A$	23.77	13.2	12.15
$\varnothing_B$	18.6	9.3	9.8
$\varnothing_C$	18.6	9.3	9.8
D	1.95	0.5	0.7
E	6.5–8.5	3.5–6	3.5–6

Table 24.5 Nominal dimensions and tolerances for large-volume couplers (ANSI S1.15: 2005, and IEC 61094-2:1992-03)

Dimensions (mm)	Laboratory standard microphones		
Symbol	Type LS1P	Type LS2aP	Type LS2bP
$\varnothing_A$	23.77	13.2	12.15
$\varnothing_B$	18.6	9.3	9.8
$\varnothing_C$	42.88 ± 0.03	18.30 ± 0.03	18.30 ± 0.03
D	1.95	0.5	0.7
E	12.55 ± 0.03	3.50 ± 0.03	3.50 ± 0.03
F	0.80 ± 0.03	0.40 ± 0.03	0.40 ± 0.03

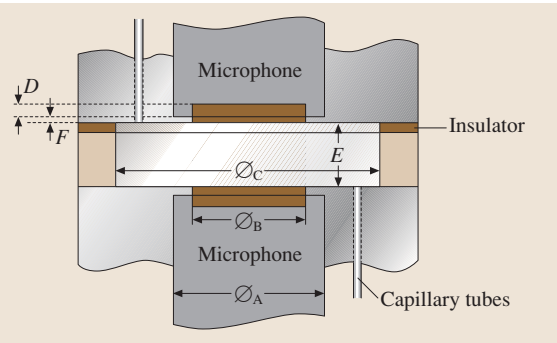


Fig. 24.12 Mechanical configuration of large-volume couplers (ANSI S1.15: 2005, and IEC 61094-2:1992-03)

Changes in the apparent sensitivity of the microphones give the wave-motion correction W for microphones calibrated in air.

Recommended [24.38] dimensions for the plane-wave and large-volume couplers are shown in Fig. 24.11, Table 24.4 and Fig. 24.12, Table 24.5, respectively. Representative wave-motion corrections [24.38] for both couplers used with LS1P (one-inch) microphones are shown in Table 24.3. These corrections should be added to the pressure sensitivity level measured with the coupler filled with air. When the coupler is filled with a gas other than air, the same correction can be used when the frequency scale is multiplied by a factor equal to the ratio of the velocity of sound in the gas to the corresponding velocity in air.

For LS1P microphones, the following empirical equation [24.25] for the wave-motion correction W, in decibels, may be used

$$W = -0.2242F^2 + 1.2145F - 1.6473\,, \qquad (24.41)$$

where F equals $\log f$, and W should be added to the pressure sensitivity level of the microphone.

24.4.5 Barometric Pressure Correction

The sensitivity of a condenser microphone ([24.38], annex D) is inversely proportional to the acoustic impedance of the microphone. In a lumped parameter representation, the impedance is given by a serial connection of the impedance of the diaphragm (due primarily to its mass and compliance) and the impedance of the air behind the diaphragm is mainly determined by the following: (a) the thin air film between the diaphragm and the backplate, introducing loss and mass; (b) the air in slots or holes in the backplate, introducing loss and mass; and (c) the air in the cavity behind the backplate, acting at low frequencies as a compliance but at high frequencies as a mass due to wave motion in the cavity.

The density and the viscosity of air are considered linear functions of temperature and/or static pressure. Consequently the acoustic impedance of the microphone also depends upon the static pressure and the temperature. The resulting static pressure and temperature coefficients of the microphone are then considered to be determined by the ratio of the acoustic impedance

Table 24.6 Coefficients of the polynomial for calculating the microphone sensitivity pressure corrections using (24.42) or (24.43), and temperature corrections using (24.44) for specific LS1P and LS2P microphones (ANSI S1.15: 2005)

Coefficients	Pressure correction (24.42) [24.45,46]			Pressure correction (24.43) [24.47]		Temperature correction (24.44) [24.47]	
	Brüel & Kjær Type 4160 LS1P	Brüel & Kjær Type 4180 LS2P	G.R.A.S. Type 40AG LS2P	Brüel & Kjær Type 4160 LS1P	Brüel & Kjær Type 4180 LS2P	Brüel & Kjær Type 4160 LS1P	Brüel & Kjær Type 4180 LS2P
a_0	-1.625×10^{-2}	$-4.446\,13\times10^{-3}$	$-3.934\,58\times10^{-3}$	−0.0152	−0.00519	−0.0020	−0.0012
a_1	-1.152×10^{-6}	$-8.343\,14\times10^{-7}$	$-5.687\,14\times10^{-7}$	−0.00584	−0.0304	0.00913	0.00633
a_2	1.816×10^{-9}	$-3.516\,08\times10^{-10}$	$-3.006\,41\times10^{-10}$	0.132	0.5976	−0.245	−0.242
a_3	-7.111×10^{-13}	$-1.602\,78\times10^{-14}$	$-1.439\,14\times10^{-14}$	−0.596	−3.912	1.673	1.656
a_4	2.056×10^{-16}			1.763	14.139	−6.058	−6.1833
a_5	-2.721×10^{-20}			−2.491	−27.561	11.766	11.81
a_6	1.188×10^{-24}			1.581	29.574	−13.11	−12.1366
a_7				−0.358	−17.6325	8.5138	6.875
a_8				−0.0364	5.4997	−3.0016	−2.0324
a_9				0.01894	−0.7017	0.4426	0.2457

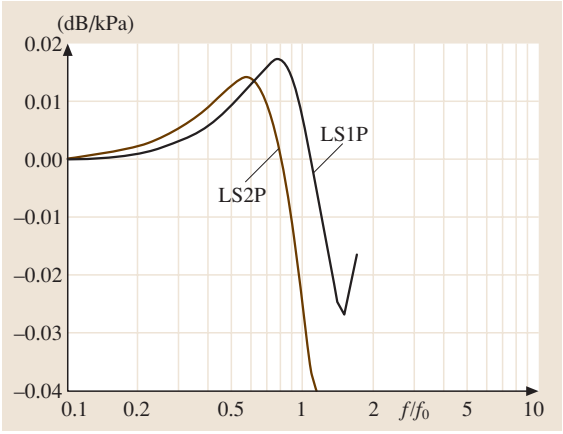


Fig. 24.13 Examples of static pressure coefficient of LS1P and LS2P microphones relative to the low-frequency value as a function of the relative frequency f/f_0 (ANSI S1.15: 2005, and IEC 61094-2:1992-03)

at reference conditions to the acoustic impedance at the relevant static pressure and temperature, respectively.

Both the mass and the compliance of the enclosed air depend on the static pressure, while the resistance can be considered independent of static pressure. The static pressure coefficient generally varies with frequency as shown in Fig. 24.13. For frequencies higher than about $0.5\,f_0$ (f_0 being the resonance frequency of the microphone), the frequency variation depends strongly upon the wave motion in the cavity behind the backplate. In general, the pressure coefficient depends on constructional details in the shape of the backplate and back volume, and the actual values may differ considerably for two microphones of different manufacture although the microphones may belong to the same type, say LS1P. Consequently the pressure coefficients shown in Fig. 24.13 should not be applied to individual microphones.

The low-frequency values of the static pressure coefficient generally lie between −0.01 and −0.02 dB/kPa for LS1P microphones, and between −0.003 and −0.008 dB/kPa for LS2P microphones.

For the Brüel and Kjær type 4160 LS1P microphones, an empirical equation based on precise measurement of the microphone sensitivity [24.45] at various static pressures to derive the pressure coefficient, may be used to correct for microphone sensitivity variation with static pressure:

$$\Delta P = \left(a_0 + a_1 f + a_2 f^2 + a_3 f^3 + a_4 f^4 + a_5 f^5 + a_6 f^6\right) \Delta_\mathrm{p}\,, \qquad (24.42)$$

where ΔP is the microphone sensitivity level pressure correction (dB), (to be added to the sensitivity level of a microphone), a_0–a_6 are constant coefficients listed in Table 24.6, f is the frequency (Hz), $\Delta_\mathrm{p} = (p_\mathrm{s} - p_0)$ is the pressure difference (kPa), p_s is the static pressure during calibration (kPa), and p_0 is 101.325 kPa.

The variation of the pressure sensitivity correction with frequency is shown in Fig. 24.14. At a particular frequency, if the difference between the standard pressure and the barometric pressure during calibration is known, the sensitivity pressure correction can be obtained from the above equation. Over a pressure range 94–106 kPa, if (24.42) is used for sensitivity level pressure correction for a type 4160 microphone, the maximum deviation between the corrected microphone sensitivity level and the corresponding measured microphone sensitivities level is within 0.0085 dB over the frequency range 250–8000 Hz. For a wider frequency range of 63–10 000 Hz, the corresponding deviation is within 0.013 dB. Similar corrections can be obtained for LS2P (half-inch) microphones by applying the coefficients [24.46] given in Table 24.6.

Users of condenser microphones, particularly for very precise measurements such as during aircraft certification that involves huge resources, should be fully aware of the fact that the sensitivities of condenser microphones change with frequencies (frequency response) and these changes are functions of barometric pressure ([24.45], Fig. 3). Therefore for two sets of measurements at different barometric pressures, pressure corrections, such as with (24.43), can be applied at each frequency to arrive at more-precise measurements.

For LS2P microphones Brüel and Kjær type 4180 and GRAS-type 40AG, the pressure correction curves similar to that shown in Fig. 24.14 have been published [24.46]. With (24.42) their corrections can be computed from the coefficients shown in Table 24.6.

Alternatively, a similar equation for pressure correction developed at a later date also based on measurement [24.47], may be used

$$\delta_p = a_0 + a_1 x + a_2 x^2 + \ldots + a_9 x^9 \,, \qquad (24.43)$$

where δ_p is the microphone sensitivity pressure correction (dB/kPa), a_0–a_9 are the constants listed in Table 24.6, $x = f/f_0$ is the frequency normalized to the resonance frequency f_0 of the individual microphone, and f is the frequency (Hz).

With (24.43), it is necessary to determine the resonant frequency f_0 of the microphones. With the assumption of a mean value for f_0, the numerical values obtained with (24.43) and (24.42) differ by a few thousandths of a decibel per kPa.

24.4.6 Temperature Correction

Both the mass and the resistance of the enclosed air depend on the temperature, while the compliance can be considered independent of temperature. The dependence on temperature is of secondary when compared with the pressure dependence. The resulting frequency dependence of the temperature coefficient is shown in Fig. 24.15.

In addition to the influence on the enclosed air, temperature variations also affect the mechanical parts of the microphone. The main effect will generally be a change in the tension of the diaphragm and thus a change in its

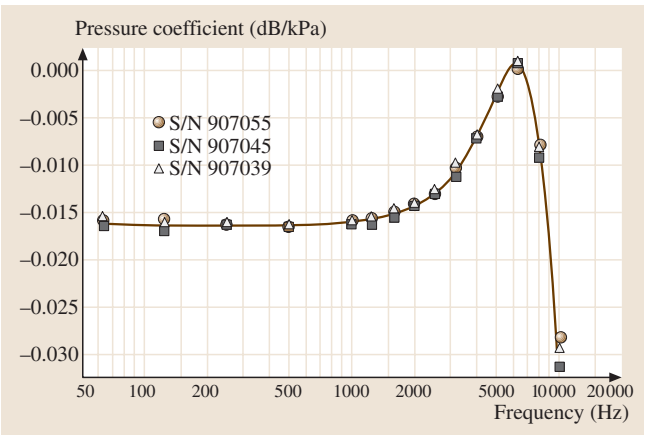


Fig. 24.14 Variation of the slopes of sensitivity correction curves with frequency for three Brüel and Kjær type 4160 microphones. The curve is obtained with an empirical equation for the computation of microphone sensitivity pressure correction. See (24.42). Similar corrections can be obtained for Brüel and Kjær Type 4180 and GRAS 40AG microphones with the coefficients shown in Table 24.6 (after [24.48])

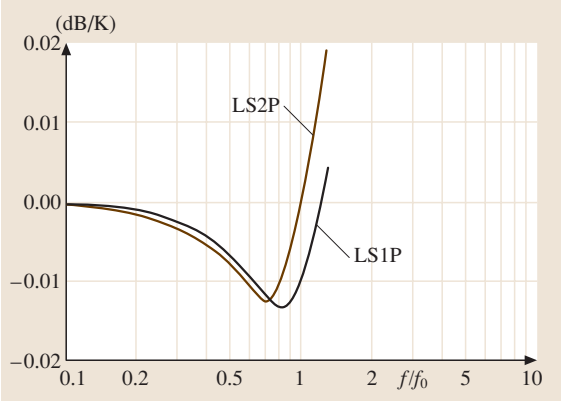


Fig. 24.15 General frequency dependence of the part of the temperature coefficient for LS1P and LS2P microphones caused by the variation in the impedance of the enclosed air (ANSI S1.15: 2005, and IEC 61094-2:1992-03)

Table 24.7 A numerical example for the calculation of estimated expanded uncertainty of microphone sensitivity level with a particular microphone calibration arrangement at 250 Hz (ANSI S1.15: 2005)

Source	Type	Estimated contribution (dB)	Distribution	Sensitivity coefficient	Standard uncertainty (dB)
Acoustic transfer impedance	B	0.025	Rectangular	1	0.0144
Voltage ratio	B	0.01	Rectangular	1	0.0058
Reference impedance	B	0.0042	Rectangular	1	0.0024
Specific heat ratio	B	0.005	Rectangular	1	0.0029
Density of air	B	0.001	Rectangular	1	0.0006
Barometric pressure	B	0.004	Rectangular	1	0.0023
Heat conduction correction	B	0.02	Rectangular	1	0.00115
Wave motion etc.	B	0.006	Rectangular	1	0.0035
Insert voltage	B	0.001	Rectangular	1	0.0006
Polarizing voltage	B	0.001	Rectangular	1	0.0006
Pressure coefficient	B	0.002	Rectangular	1	0.0012
Temperature coefficient	B	0.001	Rectangular	1	0.0006
Humidity coefficient	B	0.001	Rectangular	1	0.0006
Repeatability	A	0.004	Normal	1	0.0040
Combined uncertainty					0.0206
Expanded uncertainty ($k = 2$)					0.0412
Rounded expanded uncertainty					**0.042**

compliance. This results in a constant change in sensitivity in the stiffness-controlled range and a slight change in the resonance frequency.

The low-frequency values of temperature coefficient generally lie close to +0.005 dB/K for both LS1P and LS2P microphones.

An equation developed for the normalized temperature coefficient based on measurements of LS1P and LS2P microphones [24.47, 49], may be used

$$\Delta T = (a_0 + a_1 x + a_2 x^2 + \ldots + a_9 x^9)\Delta t\,, \qquad (24.44)$$

where ΔT is the microphone sensitivity temperature correction (dB), a_0–a_9 are the constants listed in Table 24.6, $x = f/f_0$ is the frequency normalized by the resonance frequency f_0 of the individual microphone, f is the frequency (Hz), $\Delta t = (T - 273.15)$, the temperature difference from the reference condition (K).

24.4.7 Microphone Sensitivity Equations

In general, based on (24.22) or (24.23), the open-circuit sensitivity of a microphone expressed in decibels relative to 1 V/Pa is

$$M_{\mathrm{dB}} = 20\log M + 10\log \Delta_{\mathrm{c}} + 10\log \Delta_{\mathrm{H}} + 10\log \Delta P_{\mathrm{v}} + 10\log \Delta T + 10\log \Delta h + W, \qquad (24.45)$$

where M is the microphone sensitivity, and Δ_{c}, Δ_{H}, ΔP, ΔT, Δh and W are the corrections for capillary, heat conduction, pressure, temperature, humidity and wave motion, respectively. For LS1P and LS2P microphones, the humidity corrections of the order of 0.0025 dB/100% RH may be ignored.

When expressed in the format of volts per pascal, and including corrections, the microphone sensitivity is:

$$M_{\mathrm{corr}} = 10^{M_{\mathrm{dB}}/20}\,. \qquad (24.46)$$

24.4.8 Uncertainty on Pressure Sensitivity Level

The uncertainty of the pressure sensitivity level, expressed as a function of frequency, should be stated as the expanded uncertainty of measurement obtained by multiplying the derived standard uncertainty by a coverage factor of two.

It should be noted that not all of the contributing uncertainty components are known. Some of the uncertainty components that may be necessary for consideration for a given calibration arrangement are: (a) the electrical transfer impedance: series impedance, voltage ratio, cross-talk and noise, distortion etc., (b) the acoustic transfer impedance related to the coupler: coupler dimensions and surface area, capillary tube parameters

and environmental conditions, and (c) the microphone parameters, such as loss factor, diaphragm: mass, compliance, resistance and heat conduction related to front cavity etc. Details of some of these uncertainties have been published [24.50].

For the determination of the pressure sensitivity level, it is estimated [24.33, 39] that a reciprocity calibration carried out under laboratory conditions can achieve an uncertainty of approximately 0.05 dB at low and middle frequencies. The uncertainty increases to about 0.1 dB at 10 kHz and 20 kHz for LS1P and LS2P laboratory standard microphones, respectively.

In order to clarify the computation process, a numerical example is given in Table 24.7 for the calculation of estimated expanded uncertainty of the microphone sensitivity level with a particular microphone calibration arrangement at 250 Hz.

24.5 Free-Field Microphone Calibration

The theory and procedure for free-field calibration have been discussed in detail [24.51, 52]. Similarly to pressure reciprocity calibration, one microphone is driven as a sound source and the microphone pair faces each other in a free field at a fixed distance. One of the major uncertainties in free-field calibration is to measure the positions of the acoustic centers of the microphones accurately so that the distance between them can be deduced. Procedures for measuring and estimating values of the positions of the acoustic centers for laboratory standard microphones have been published ([24.52], annex A). For free-field calibration of half-inch microphones, over a frequency range from about 1.25 kHz to more than 20 kHz the uncertainty (three standard deviations) [24.51] is approximately 0.1–0.2 dB.

The manufacturers of the microphones usually supply free-field corrections for their microphones, to be added to the pressure reciprocity measurements, for free-field applications.

24.6 Comparison Methods for Microphone Calibration

Reciprocity microphone calibration discussed in Sect. 24.3 is a primary method that provides high accuracy but requires stringent procedures and is relatively time consuming. A more economical approach to microphone calibration is by means of comparison methods with which the performance of the test microphone is compared with that of a standard microphone that has been calibrated with a primary method. Secondary methods, such as using comparison, have higher uncertainties but offer several advantages, such as simplicity in procedure, are less time consuming and, depending on the method, require little or no correction, and are very economically attractive.

24.6.1 Interchange Microphone Method of Comparison

This economically attractive method was developed to compare microphones in a cavity or in a small anechoic box (*Wong* and *Embleton* [24.53] and *Wong* and *Wu* [24.54]). The technique can be applied to microphone phase comparison calibration (*Wong* [24.55]). The method has been standardized in an international standard [24.56].

When two microphones with their diaphragms facing in close proximity to each other are excited in a sound field, the difference of level readings, L_{C12} between the two channels, where microphone 1 is connected to preamplifier 1, and microphone 2 is connected to preamplifier 2, is

$$L_{C12} = (L_1 + L_{m1} + L_d + L_{WA}) - (L_2 + L_{m2} + L_d + L_{WB}) , \quad (24.47)$$

where L_1 and L_2 are the sensitivity levels of the microphones 1 and 2, respectively, L_{m1} and L_{m2} are the gain sensitivity levels of the measuring systems 1 and 2, respectively, L_d is the level of the sound excitation, and L_{WA} and L_{WB} are the wave pattern effects at the microphone positions A and B, respectively.

When the microphones are interchanged so that microphone 1 is now connected to preamplifier 2 and microphone 2 is now connected to preamplifier 1, the difference of level readings between the two channels

becomes

$$L_{C21} = (L_2 + L_{m1} + L_d + L_{WA}) - (L_1 + L_{m2} + L_d + L_{WB}) . \quad (24.48)$$

Subtracting (24.48) from (24.47), the difference in level between the two microphones is

$$(L_1 - L_2) = 1/2(L_{C12} - L_{C21}) . \quad (24.49)$$

If either L_1or L_2 is the sensitivity level of a calibrated reference microphone, then the sensitivity level of the other microphone (the test microphone) can be deduced. It is interesting to point out that with this method, the level L_d of the driving sound need not have a flat response or known levels.

The above relatively simple theoretical consideration has assumed that the input capacitances of the two microphones are identical, i. e. the same model of microphones, and the same model of preamplifiers used for both channels such that their input capacitances have the same value.

If the input capacitances C_m of the preamplifiers are the same but the two models of microphones are different, then a correction L_{corr} should be added to the right-hand side of (24.49), where

$$L_{corr} = 20\log[C_2/(C_m + C_2)] - 20\log[C_1/(C_m + C_1)] . \quad (24.50)$$

The two terms in (24.50) are the capacitance corrections for the two microphones; and C_1 and C_2 are the capacitances of microphone 1 and microphone 2, respectively.

It is important to realize that the physical positions of the reference microphone should be repeated accurately before and after the microphones are interchanged such that the sound field at the reference microphone is unchanged. The difference in level readings shown in (24.47) and (24.48) can be measured with the ratio provision of a precision AC voltmeter.

Uncertainties

The uncertainty for the above method depends on the reference microphone uncertainty that may be of the order of 0.05 dB. With very sophisticated measuring methods such as phase-lock amplifiers the uncertainty introduced by this comparison method to be added to the uncertainty of the reference microphone [24.57] is estimated to be less than 0.1 dB.

24.6.2 Comparison Method with a Calibrator

In general, there are five components and three basic steps in this comparison method [24.57]. The components are the reference microphone, the test microphone, a stable sound source, which is usually an acoustical calibrator that generates a constant sound pressure level, a microphone preamplifier and an acoustical level indicator such as a measuring amplifier or a voltmeter. Since the calibrator is used as a transfer standard, its sound pressure level need not be known.

The three basic steps are as follows

1. The reference microphone which is connected to the preamplifier is inserted into the acoustical calibrator and a level reading L_r is noted.
2. The reference microphone is replaced with the test microphone. With the same acoustical calibrator, a second level reading L_t is noted.
3. The test microphone is removed, and again with the reference microphone, step 1 is repeated to give a third level reading.

The agreement between the first and third level readings with the reference microphone is a confirmation of the validity of the second level reading obtained with the test microphone, that is, to assure that nothing has changed after the first level reading is taken. The difference between the level readings, $(L_t - L_r)$ is the difference in open-circuit sensitivities (expressed in decibels) between the two microphones if the following conditions are satisfied:

1. The equivalent volumes of the two microphones are identical, or the equivalent volume of the sound calibrator is much larger than that of the microphones, such that any difference in the front volumes of the microphones does not produce a significant change in the sound pressure levels measured in steps 1 and 2 above.
2. The capacitances of the two microphones are identical. Since the preamplifier has a finite input impedance (a very high resistance in parallel with a small known capacitance), the loading on the microphone will be different if the microphone capacitances were to be different, and this will produce a small change in the overall combined sensitivity of the microphone and preamplifier.
3. The environmental conditions remain constant during the measurements.

Amazon EX1014 Page 1042

Corrections

When it is not possible to satisfy all of the above conditions during the implementation of the comparison procedure, the following corrections can be applied.

Equivalent Volume Correction

Depending on the type of microphones, the equivalent volume of the test microphone, as specified by the manufacturer, can differ substantially from that of the reference microphone. The following correction can be applied.

$$\Delta P_{\mathrm{v}} = 20\log[V/(V+\Delta V)]\mathrm{dB}\,, \qquad (24.51)$$

where ΔP_{v} is the volume correction to be added to the calibrated sensitivity of the microphone, V is the effective coupler volume of the acoustical calibrator, ΔV is the difference between the equivalent volumes of the microphones, i. e., the equivalent volume of the reference microphone minus the equivalent volume of the test microphone.

When the combined volume of the calibrator and the equivalent volume of the microphone increases, the sound pressure level inside the acoustical calibrator decreases. For example, if ΔV is negative, i. e., the equivalent volume of the test microphone is larger than that of the reference microphone the volume correction ΔP_{v} has a positive sign in order to compensate for the decrease in sound pressure level when the test microphone is measured. When the correction is added to the microphone sensitivity (24.45), the apparent sensitivity of the test microphone increases.

Depending on the frequency of the acoustical calibrator, the effective coupler volume V should include the additional volume due to heat conduction (Sect. 24.4.1). For example at a frequency of 250 Hz, the additional volume to account for heat conduction for the Brüel and Kjær type 4220 pistonphone is 0.16 cm^3. There are other acoustical calibrators that have relatively large cavity volumes, such as the Brüel and Kjær model 4230 (94 dB at 1 kHz, with an equivalent volume of $> 100\,\mathrm{cm}^3$ between 10 and 40 °C); and the Larson–Davis model CA250. In these cases, from (24.51), the correction is negligible since V is much larger than ΔV. Most calibrators are supplied with adaptors to accommodate microphones of various diameters, and these adaptors are designed to include the volume correction for the particular types of microphones when used with the calibrator. If the adaptors and the calibrator are from different manufacturers, the instruction manual of the calibrator should be consulted to ensure proper usage.

Capacitance Correction

The combined level sensitivity of the microphone and preamplifier is:

$$M_{\mathrm{com}} = M_{\mathrm{o}} + g_1 + 20\log[C/(C+C_{\mathrm{i}})]\,, \qquad (24.52)$$

where M_{o} is the open-circuit sensitivity of the microphone (dB re 1 V/PA), g_1 is the gain of the preamplifier (dB), C is the capacitance of the microphone, C_{i} is the input capacitance of the preamplifier. The input capacitance of the preamplifier would load the microphone and the overall sensitivity decreases. With this comparison method, if the capacitances of the two microphones are different, the capacitance correction is

$$\Delta P_{\mathrm{c}} = 20\log[C_{\mathrm{r}}/(C_{\mathrm{r}}+c_{\mathrm{i}})] - 20\log[C_{\mathrm{t}}/(C_{\mathrm{t}}+c_{\mathrm{i}})]\,, \qquad (24.53)$$

where ΔP_{c} is the capacitance correction to be added to the calibrated sensitivity of the microphone (dB), C_{r} is the capacitance of the reference microphone, c_{i} is the input capacitance of the preamplifier, and C_{t} is the capacitance of the test microphone.

The first and the second term on the right-hand side of (24.53) are the capacitance corrections for the reference microphone and the test microphone, respectively.

Environmental Conditions

One of the advantages of a comparison method is that environmental effects usually remain constant during measurements outlined in the above three basic steps. Changes in temperature and humidity affect both microphones. A rapid variation in barometric pressure may affect some acoustical calibrators, and precaution should be taken to avoid opening or closing the doors of the calibration laboratory during measurements.

Uncertainties

From the above discussion, the open-circuit sensitivity of the test microphone is

$$M_{\mathrm{t}} = M_{\mathrm{r}} + (L_{\mathrm{t}} - L_{\mathrm{r}}) + \Delta P_{\mathrm{v}} + \Delta P_{\mathrm{c}}\,, \qquad (24.54)$$

where M_{r} is the open circuit sensitivity of the reference microphone (dB re 1 V/Pa), L_{t} is the level reading obtained with the test microphone (dB), and L_{r} is the level reading obtained with the reference microphone (dB).

The uncertainty of M_{r} depends on the primary reciprocity procedure that calibrates the reference microphone (Sect. 24.3). If the environmental conditions are controlled [24.20], the uncertainty of the open-circuit sensitivity can be less than 0.005 dB. The uncertainty

expectation for reciprocity calibrations based on international standard [24.38, 40] is approximately 0.05 dB.

If the magnitudes of the levels L_t and L_r are nearly identical, the uncertainty can be much less than 0.05 dB. However, if it is necessary for the level-measuring device, such as a measuring amplifier, to engage different instrument ranges during the measurement of the above levels, the uncertainties can be up to ± 0.1 dB. The uncertainties of ΔP_v and ΔP_c are estimated to be approximately 0.01 dB each, and the overall uncertainty of calibrator comparison method is estimated to be 0.05–0.2 dB.

For this comparison method, the preamplifier should have very high input impedance, usually in the order of gigaohms with a parallel capacitance of a fraction of a picofarad.

24.6.3 Comparison Pressure and Free-Field Calibrations

The coupler method described in Sect. 24.3 for primary reciprocity microphone calibration can be utilized to implement comparison pressure calibration. A laboratory standard microphone of unknown pressure response can be calibrated against a reference microphone with a known pressure response. One example of the coupler arrangement shown in Fig. 24.6 with which microphone A is the driver that serves as a sound source. The reference microphone and the test microphone replace microphone B in succession on the right-hand side of the coupler. The ratio of the driving voltage e_A applied to the driver microphone to the open-circuit output voltage of the receiving microphones e_B, is measured as described in Sect. 24.3.3. The sensitivity of the test microphone can be calculated as follows

$$M_t = M_r - 20\log(e_{Bref}/e_{Aref}) + 20\log(e_{Bx}/e_{Ax})\,, \tag{24.55}$$

where M_t and M_r are the sensitivities of the test and the reference microphones, respectively, e_{Bref} and e_{Aref} are the open-circuit voltage and the source driving voltage when the reference microphone is in position, e_{Bx} and e_{Ax} are the open-circuit voltage and the source driving voltage when the test microphone is in position.

With (24.55), unless the equivalent volume of the coupler is large compared to those of the reference microphone and the test microphone, and the equivalent volumes of the reference microphone and the test microphone are similar, suitable volume correction should be applied such that the equivalent sound pressure levels are identical for both the reference and the test microphones.

Uncertainties

The uncertainties of the coupler pressure comparison method are very similar to those described in Sect. 24.6.2 with the exception that the open-circuit voltage measurements with the insert voltage method, capacitance corrections are unnecessary. The uncertainty of the coupler comparison method may approach approximately two times the uncertainty of the reference microphone plus the uncertainty involved with the equivalent volume corrections; assuming that the reference microphone has been calibrated with a similar method for open-circuit voltage measurement.

The uncertainty for free-field comparison method is higher and is due to electrical and mechanical air-transmitted interferences. Even with narrow-band filtering, the overall uncertainty for free-field comparison is of the order of 0.5 dB.

24.6.4 Comparison Method with a Precision Attenuator

A more precise method than that described in Sect. 24.6.2, comparison with a calibrator, is comparison with an attenuator. The acoustical level indicator is replaced with a calibrated attenuator [24.58]. Over the usable range of 5–100 mV/Pa of the open-circuit sensitivity of a microphone, the attenuator, i. e., a precision ten-turn potentiometer, is calibrated with a resolution of better than 0.05 mV/Pa. The comparison procedure is as follows:

1. The reference microphone is inserted into a calibrator. The sensitivity of the reference microphone is entered into the calibrated attenuator, say 50 mV/Pa. An indicator reading is taken.
2. The reference microphone is replaced with the test microphone, and the calibrated attenuator is adjusted until the indicator gives the same reading. The new attenuator reading gives the sensitivity of the test microphone.

With this method, it is still necessary to correct for capacitances and equivalent volumes of the microphones. However, the uncertainty is reduced by the precision of the attenuator, which may have an uncertainty of a few thousandths of a decibel. If the test microphone is of the same type and model as the reference microphones, the uncertainty of this method is the uncertainty of the reference microphone plus a few thousandths of a decibel, if the indicator has a resolution of a thousandth of a decibel.

Amazon EX1014 Page 1044

24.7 Frequency Response Measurement with Electrostatic Actuators

Electrostatic actuators were used by *Ballantine* [24.2] to investigate microphone calibration and *Koidan* [24.59] gave a comprehensive discussion of the uncertainties between measurements obtained with electrostatic actuators compared with those measured with the coupler pressure reciprocity method. The description and analyses of some commercially available electrostatic actuators for microphone calibration have been published [24.60–62] and standardized [24.63] for frequency response measurement for working standard (WS) microphones. The electrostatic actuator method, Fig. 24.16, consists of a metal grid polarized with a high voltage direct-current (DC) supply (usually 800 V). An AC time-varying sweep signal provides the electrostatic pressure on the microphone diaphragm. With the usual amplification and a recorder, the frequency response is displayed graphically.

Madella [24.64] and *Nedzelnitsky* [24.65] pointed out that with electrostatic actuator measurements the effective mechanical radiation impedance loading of the microphone diaphragm in the presence of the electrostatic actuator is different from that of those used in a coupler or in a free field. Consequently, at higher frequencies the absolute values of the difference between the actuator-determined response of type L microphones and pressure calibrations determined in couplers by reciprocity can be as large as about 1.5 dB [24.65]. In practice, the design of the metal grid can be optimized for a particular microphone type. According to the IEC standard [24.63], the expanded uncertainty of the method is 0.1–0.2 dB for frequencies up to 10 kHz for WS1 (1-inch) and WS2 (half-inch) type microphones. Since the air gap between the metal grid and the microphone diaphragm is very small (nominally approximately 0.5 mm) the use of electrostatic actuators for models of microphones other than those specified is not recommended. Since the motion of the microphone diaphragm, caused by electrostatic pressure produce by the actuator, creates a sound pressure on the outer surface of the diaphragm that adds to the electrostatic pressure and influences the measure response, precautions should be taken to avoid blocking the actuator space that opens to the atmosphere.

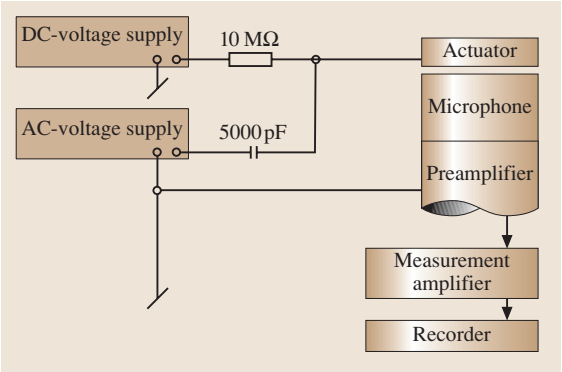


Fig. 24.16 Frequency response measurement with an electrostatic actuator (after *Frederiksen* [24.29], Chap. 15)

Apart from being economically attractive, there are some salient features to the electrostatic actuator method.

1. The method is ideal for comparing the frequency responses of microphones, such as those in a production line, at which only changes from a nominal value is important.
2. Since the actuator method is unaffected by atmospheric pressure, humidity and temperature (assuming the air gap remains constant) [24.63], the method may be used to measure the change in microphone responses with respect to variations in the environment.

Given the fact that the international standard [24.63] only discusses type WS1 and WS2 working standard microphones and not the laboratory types LS1 and LS2 microphones, it is obvious that the electrostatic actuator method still requires further development to reduce uncertainties.

24.8 Overall View on Microphone Calibration

Primary microphone calibrations, such as those performed with the reciprocity method, provide uncertainty estimations. One may wonder what is the contribution to the calibration uncertainty from two major sources: (a) the stability of the microphones and (b) the stability of the calibration system that performed the microphone calibration. It is very difficult to separate these two sources of uncertainties.

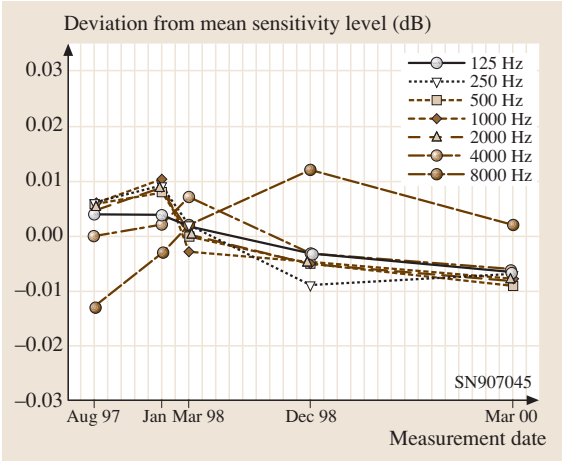


Fig. 24.17 Deviation from the mean sensitivity level of a transfer standard microphone s/n 907045 (after [24.67])

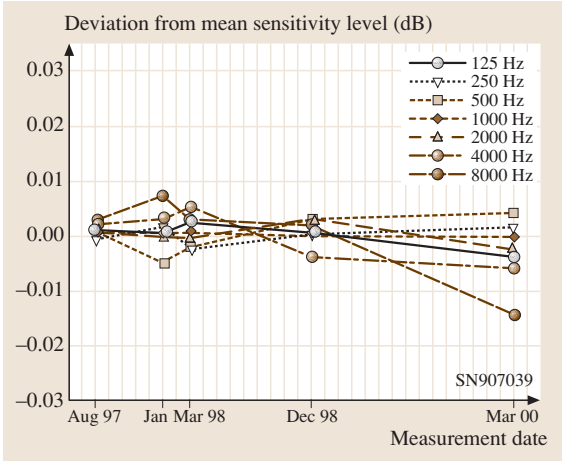


Fig. 24.19 Deviation from the mean sensitivity level of a transfer standard microphone s/n 907039 (after [24.67])

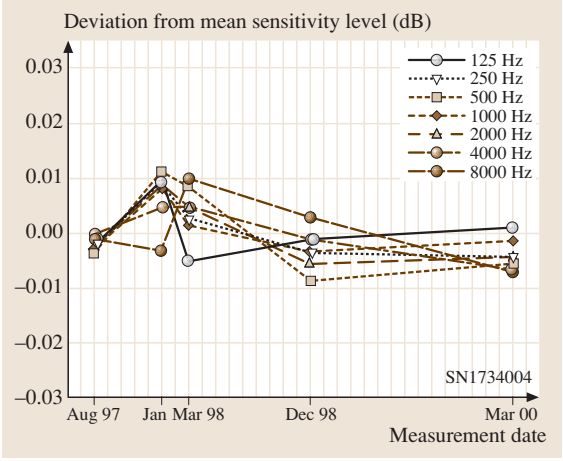


Fig. 24.18 Deviation from the mean sensitivity level of a transfer standard microphone s/n 1734004 (after [24.67])

In connection with an international microphone calibration comparison [24.66] that involved five National Metrology Institutes (NMIs), the pilot laboratory (Canada) had the opportunity to calibrate the same set of three laboratory standard LS1P microphones five times over a period of 31 months. The calibrations were made in a chamber with a controlled environment [24.45] at the reference condition of 23 °C, 101.325 kPa and 50% RH. The microphone sensitivity levels were measured at seven frequencies from 125 Hz to 8 kHz. Two of the microphones (the transfer standards) were *hand carried* to and from the pilot laboratory in a *star* configuration, i. e., the microphones were calibration by the pilot laboratory before and after delivery to each of the participating NMIs. The average of five sets of readings obtained by the pilot laboratory was taken as the mean sensitivity level. The deviation from the mean sensitivity level of the transfer standard microphones (LS1P Brüel and Kjær type 4160 microphones, s/n 907045 and s/n 1734004) are shown in Fig. 24.17 and Fig. 24.18, and are within approximately 0.011 dB. It is interesting to show that, for the above reciprocity calibration, the third type 4160 LS1P microphone s/n 907039 which remained at the pilot laboratory without the need to endure air transportation to and from the participating laboratories over the test period, the deviations shown in Fig. 24.19 were significantly smaller for frequencies below 8000 Hz, and are within +0.007 and −0.006 dB. It should be noted that the deviations shown for the three microphones are the combined contributions from the sensitivity level stability of the microphones and the stability of the primary calibration system. Since the specifications for laboratory standard microphones [24.41] states that the type 4160 LSIP microphone has a long-term stability coefficient of < 0.02 dB per year from 250 Hz to 1000 Hz, and the manufacturer Brüel and Kjær indicated the stability of their LS1P microphones may have a stability coefficient of approximately 0.01 dB per year, one may conclude that the primary microphones and the calibration system of the pilot laboratory have an excellent stability of approximately 0.01 dB over the period of 31 months.

24.A Acoustic Transfer Impedance Evaluation

Assume the sound pressure to be the same at any point inside the coupler (this will take place when the physical dimensions of the coupler are very small compared to the wavelength) the acoustic transfer impedance can be evaluated theoretically [24.38]. The air in the coupler then behaves as a pure compliance and assuming adiabatic compression and expansion of the gas:

$$\frac{1}{Z'_{\mathrm{AB}}} = \mathrm{i}\omega\left(\frac{V}{\gamma p_{\mathrm{s}}} + \frac{V_{\mathrm{eA}}}{\gamma_0 p_0} + \frac{V_{\mathrm{eB}}}{\gamma_0 p_0}\right) , \qquad (24.A1)$$

where values for γ and γ_0 can be derived from the equations given in Sect. 24.B.

The computation of the acoustic transfer impedance becomes complicated at high frequencies when the dimensions of the coupler are not small compared with the wavelength. When the shape of the coupler is cylindrical and the cavity diameter is the same as that of the microphone diaphragm [24.38], and at frequencies where plane-wave transmission and adiabatic conditions can be assumed, the acoustic transfer impedance is

$$\frac{1}{Z'_{\mathrm{AB}}} = \frac{1}{Z}\left[\left(\frac{Z}{Z_{\mathrm{A}}} + \frac{Z}{Z_{\mathrm{B}}}\right)\cosh(\xi\ell_0) + \left(1 + \frac{Z}{Z_{\mathrm{A}}}\frac{Z}{Z_{\mathrm{B}}}\right)\sinh(\xi\ell_0)\right] , \qquad (24.A2)$$

where ξ is the complex propagation coefficient (m^{-1}), and $\xi = \mathrm{i}(\omega/c)$, approximately.

Allowance should be made for the air volume associated with the microphones that is not enclosed by the circumference of the coupler and the two diaphragms.

24.B Physical Properties of Air

Certain physical properties, characterizing the enclosed gas in the coupler, enter into the expressions for calculating the sensitivity of the microphones, see (24.A1) and Sects. 24.4.1 and 24.4.3. These properties are: the speed of sound in the gas; the density of the gas; the ratio of the specific heats of the gas; the viscosity of the gas; and the thermal diffusivity of the gas. These properties depend on one or more of the variables: temperature, static pressure and humidity.

A large number of investigations have been published in the literature where reference values for the physical properties can be found for specified environmental conditions, i. e. for standard dry air [24.68] at 0 °C and at a static pressure of 101.325 kPa. In the following, unless otherwise stated, the recommended calculation procedures with the corresponding estimated uncertainties are valid over the temperature range 0–30 °C; barometric pressure of 60–110 kPa, and relative humidity from 10% to 90%.

24.B.1 Density of Humid Air

An equation for the determination of the density of moist air was first published by *Giacomo* [24.69] and some constants were modified by *Davies* [24.70]. The following equation may be used to compute the density of humid air ρ based on a CO_2 content of 400 ppm, which is slightly higher than the 314 ppm specified for the ISO standard air [24.68] constituents.

$$\rho = [3.48349 + 1.44\,(x_{\mathrm{c}} - 0.0004)] \times 10^{-3}\,\frac{p_{\mathrm{s}}}{ZT}\,(1 - 0.3780 x_{\mathrm{w}}) , \qquad (24.B1)$$

where x_{c} and x_{w} are the mole fractions of carbon dioxide and water vapor in air, respectively; p_{s} is the static pressure, Z is the compressibility factor for humid air, T is the thermodynamic temperature, and

$$Z = 1 - \frac{p_{\mathrm{s}}}{T}\left[a_0 + a_1 t + a_2 t^2 + (a_3 + a_4 t)\,x_{\mathrm{w}} + (a_5 + a_6 t)\,x_{\mathrm{w}}^2\right] + \frac{p_{\mathrm{s}}^2}{T^2}\left(a_7 + a_8 x_{\mathrm{w}}^2\right) ,$$

$$x_{\mathrm{w}} = \frac{p_{\mathrm{sv}}}{p_{\mathrm{s}}} f_{\mathrm{e}} h ,$$

$$p_{\mathrm{sv}} = \exp\left(A'_1 T^2 + B'_1 T + C'_1 + D'_1 T^{-1}\right) ,$$

$$f_{\mathrm{e}} = 1.00062 + p_{\mathrm{s}}(3.14 \times 10^{-8}) + t^2(5.6 \times 10^{-7}) .$$

For Z the numerical coefficients are:

$$a_0 = 1.581\,23 \times 10^{-6} , \quad a_1 = -2.9331 \times 10^{-8} ,$$
$$a_2 = 1.1043 \times 10^{-10} , \quad a_3 = 5.707 \times 10^{-6} ,$$
$$a_4 = -2.051 \times 10^{-8} , \quad a_5 = 1.9898 \times 10^{-4} ,$$
$$a_6 = -2.376 \times 10^{-6} , \quad a_7 = 1.83 \times 10^{-11} ,$$
$$a_8 = -0.765 \times 10^{-8} .$$

For p_{sv} the numerical coefficients are:

$$A_1' = 1.237\,8847 \times 10^{-5}\,,$$
$$B_1' = -1.912\,1316 \times 10^{-2}\,,$$
$$C_1' = 33.93711047\,,$$
$$D_1' = -6.343\,1645 \times 10^{3}\,.$$

Within the normal range of environmental conditions during calibrations, the following simplified equation for the density of humid air may be used

$$\rho = \rho_0 \frac{p_s}{p_0} \frac{T_0}{T}(1 - 0.378 h_s)\,, \qquad (24.B2)$$

where ρ and ρ_0 are the densities of air, p_0 and p_s are the reference and static pressure, respectively; T_0 and T are the temperatures in Kelvin and h_s is the fractional molar concentration of moisture.

Uncertainties in ρ

The uncertainty in ρ obtained with (24.B1) has been estimated [24.69, 70] at approximated 100 ppm. At the reference conditions of 101.325 kPa and 50% relative humidity, ρ obtained with (24.B2) are 239 ppm and 293 ppm larger than those obtained with (24.B1) at 23 °C and 30 °C, respectively.

24.B.2 Computation of the Speed of Sound in Air

Method 1

The speed of sound in air varies with temperature, carbon dioxide content, relative humidity and barometric pressure. The sequence of the above parameters is listed roughly in decreasing order of their influence on the speed of sound with respect to the day-to-day encounter of environmental conditions. A large number of investigations related to the speed of sound [24.50, 71–80] had been published, detailed references have been given [24.75], and an updated and comprehensive bibliography ([24.80], Chap. 17, pp. 265–284 and references therein) on publications relating to sound speed in air is included at the end of this appendix. It can be shown that the speed of sound remains relatively constant with barometric pressure [24.72]: at 23 °C and 50% RH, over the barometric pressure range 60–110 kPa, the sound speed varies by less than 76 ppm. In view of this, the following equation has a relatively small overall uncertainty, is based on a steady barometric pressure of 101.325 kPa and may be used to compute the variation of the speed of sound with temperature, carbon dioxide content and relative humidity.

A general empirical equation has been obtained [24.71] for calculation of the variation of c/c_0 with relative humidity h, temperature t and carbon dioxide content h_c:

$$c/c_0 = a_0 + a_1 t + a_2 t^2 + a_3 h_c + a_4 h_c t + a_5 h_c t^2 + a_6 h + a_7 h t + a_8 h t^2 + a_9 h t^3 + a_{10}(h_c)^2 + a_{11} h^2 + a_{12} h t h_c\,, \qquad (24.B3)$$

where c and c_0 are the sound speed and the reference dry-air sound speed, respectively; a_0–a_{12} are coefficient constants listed in Table 24.8. With Table 24.8, the sound speed can be deduced by multiplying c/c_0 with the corresponding reference dry-air sound speed c_0.

For h_c values from 0% to 1%, and for t from 0 °C to 30 °C, for h from 0 to 1 (relative humidity 0% to 100%), and at a barometric pressure of 101.325 kPa, the sound speed computed using the numerical coefficients in Table 24.8 fits the theoretical data with a standard uncertainty of ±48 ppm.

Uncertainties in c_0

Over the temperature range 0–30 °C, (24.B3) is fitted to a computation [24.71] for a real gas at 101.325 kPa at which the value $C_p - C_v$ is not greatly different from the universal constant R [24.75]. Based on this approximate assumption, the dry-air sound speed c_0 is 331.29 m/s, with an uncertainty of approximately 200 ppm [24.75], which encompasses sound speeds from 331.224 to 331.356 m/s [24.50].

Table 24.8 Coefficient constants for the computation of c/c_0 and γ/γ_0 (after [24.71])

Coefficient constants	c/c_0 (24.B3)	γ/γ_0 (24.B5)
a_0	1.000100	1.000034
a_1	1.8286×10^{-3}	-2.8100×10^{-6}
a_2	-1.6925×10^{-6}	-2.1210×10^{-7}
a_3	-3.1066×10^{-3}	$-1.012\,23 \times 10^{-3}$
a_4	-7.9762×10^{-6}	-5.2500×10^{-6}
a_5	3.4000×10^{-9}	1.1290×10^{-8}
a_6	8.9180×10^{-4}	-3.4920×10^{-4}
a_7	7.7893×10^{-5}	-2.8560×10^{-5}
a_8	1.3795×10^{-6}	-5.9000×10^{-7}
a_9	9.5330×10^{-8}	-2.9710×10^{-8}
a_{10}	1.2990×10^{-5}	$4.234\,27 \times 10^{-6}$
a_{11}	4.8016×10^{-5}	8.0000×10^{-7}
a_{12}	-1.4660×10^{-6}	5.1000×10^{-7}

Amazon EX1014 Page 1048

Method 2

Alternatively, over the temperature range 0–30 °C, with a computation [24.72–74] that is based on the derivation of real-gas sound speed from virial coefficients, the dry-air sound speed c_0 calculated with 16 coefficients similar to those shown in Table 24.8, is 331.46 m/s. The uncertainty is approximately 545 ppm [24.73, 74], which encompasses sound speeds c_0 from 331.279 to 331.641 m/s. It should be noted that the sound speed of 331.29 m/s obtained with the first method is within the uncertainty range of the second method [24.50].

Within the normal range of environmental conditions during calibration, the following simplified equation [24.38, 40, 50] for the sound speed in humid air may be used:

$$c = c_0 \left(\frac{T}{T_0}\right)^{1/2} (1 + 0.165 h_s)\Delta \,, \qquad (24.B4)$$

where h_s is the fractional molar concentration of moisture, and Δ is a factor to compensate for dispersion. Values of $\Delta = 0.99935$ and $\Delta = 0.99965$ are found in [24.81] and [24.82], respectively. A value of 1.0001 has also been obtained [24.72].

Over a frequency range of 10 Hz to 10 kHz, by ignoring the dispersion factor Δ, the uncertainty in the sound speeds obtained with methods 1 and 2 increases by approximately 300 ppm.

By ignoring dispersion, at the reference conditions of 23 °C, 101.325 kPa and 50% relative humidity, the sound speed obtained with (24.B4) is 196 ppm higher than that obtained with (24.B3).

24.B.3 Ratio of Specific Heats of Air

There have been several experimental [24.83, 84] and theoretical [24.71–74,85,86] investigations into the variation of the ratio of specific heats of air with temperature, humidity, pressure and carbon dioxide content [24.75] ([24.86], pp. 36–39). A general empirical equation has been obtained [24.71] for the calculation of the variation of γ/γ_0 with relative humidity h, temperature t and carbon dioxide content h_c

$$\begin{aligned}\gamma/\gamma_0 = {} & a_0 + a_1 t + a_2 t^2 + a_3 h_c + a_4 h_c t + a_5 h_c t^2 \\ & + a_6 h + a_7 h t + a_8 h t^2 + a_9 h t^3 + a_{10} (h_c)^2 \\ & + a_{11} h^2 + a_{12} h t h_c \,, \end{aligned} \qquad (24.B5)$$

where a_0–a_{12} are coefficient constants listed in Table 24.8. With (24.B5), the above normalized ratio of specific heats can be deduced by multiplying γ/γ_0 by the corresponding reference dry-air ratio of specific heats γ_0. For CO_2 content h_c values from 0% to 1%, and for temperatures of 0–30 °C, humidity from 0 to 1 (relative humidity 0% to 100%), and at a barometric pressure of 101.325 kPa, the ratio of specific heats computed using the numerical coefficients in Table 24.8, fit the theoretical data with a standard uncertainty of ±17 ppm.

Uncertainties in γ_0

Based on method 1 above [24.71], the dry-air specific heat ratio γ_0 is 1.3998. The standard uncertainty in γ_0 is approximately 400 ppm.

Similarly, based on method 2 [24.72–74], the dry-air specific heat ratio γ_0 is 1.4029; the standard uncertainty in γ_0 is over 760 ppm.

24.B.4 Viscosity and Thermal Diffusivity of Air for Capillary Correction

The viscosity η of air, in the parameters in (24.39) of Sect. 24.4.3, is a function of temperature t. An empirical equation which is based on a least-squares fit to published data [24.87] is

$$\begin{aligned}\eta = {} & [17.26797 + (5.0756 \times 10^{-2}) t \\ & - (4.4028 \times 10^{-5}) t^2 + (5.0000 \times 10^{-8}) t^3] \\ & \times 10^{-6} \text{ Pa s} \end{aligned} \qquad (24.B6)$$

The equation for the thermal diffusivity α_t of air [24.38, 40] is

$$\alpha_t = \eta(9\kappa - 5)/(4\kappa\rho) \text{m}^2/\text{s} \,. \qquad (24.B7)$$

Uncertainties in η

Over the temperature range from −80 °C to 100 °C, when compared with the published data [24.87], the maximum deviation in η obtained with (24.B6) is ±1 ppm from the data points. However, the data point uncertainty may be several percent [24.87].

For standard dry air at a pressure of 101.325 kPa, the numerical values calculated with the above equations for the viscosity are 1.7268×10^{-5} Pa s and 1.8413×10^{-5} Pa s, at 0 and 23 °C, respectively; and the corresponding values for the thermal diffusivity are $1.812\,34 \times 10^{-5}$ m^2/s and $2.095\,49 \times 10^{-5}$ m^2/s, respectively.

Examples. Aiming at the highest accuracies (method 1), Table 24.9 gives the recommended values of the quantities given in (24.B2)–(24.B4) for the reference

Table 24.9 Recommended values for some physical quantities in (24.A1)–(24.B5) (ANSI S1.15: 2005)

Environmental conditions	Density of air ρ (kg/m^3)	Speed of sound c (m/s)	Ratio of specific heats γ	Viscosity of air η (Pa s)	Thermal diffusivity of air α_t (m^2/s)
$T = 23\,^\circ$C					
$p_s = 101325$ Pa	1.1859997	345.677519	1.39836198	1.841268×10^{-5}	2.105344×10^{-5}
$H = 50\%$					

Table 24.10 Recommended reference values applicable to dry air at 0 °C and 101.325 kPa. (ANSI S1.15: 2005)

Environmental conditions	Density of air ρ (kg/m^3)	Speed of sound c (m/s)	Ratio of specific heats γ	Viscosity of air η (Pa s)	Thermal diffusivity of air α_t (m^2/s)
$T = 0\,^\circ$C					
$p_0 = 101325$ Pa	1.29296	331.28	1.3998	1.7268×10^{-5}	1.8123×10^{-5}

conditions. The values in Table 24.9 are shown with more decimals than necessary and are intended for testing computation programs that are used to calculate these quantities.

Again, aiming at the highest accuracies (method 1) and in view of the need to have reference values c_0 and γ_0 in (24.B3), (24.B4) and (24.B5), Table 24.10 gives the recommended values for dry air.

References

24.1 E.C. Wente: A condenser transmitter as a uniformly sensitive instrument for the absolute measurement of sound intensity, Phys. Rev. **10**(1), 39–63 (1917)

24.2 S. Ballantine: Technique of microphone calibration, J. Acoust. Soc. Am. **3**, 319–360 (1932)

24.3 W.R. MacLean: Absolute measurement of sound without a primary standard, J. Acoust. Soc. Am. **12**, 140–146 (1940)

24.4 R.K. Cook: Absolute pressure calibration of microphones, Res. Nat. Bur. Standard. **25**, 489–555 (1940)

24.5 R.K. Cook: Absolute pressure calibration of microphones, J. Acoust. Soc. Am. **12**, 415–420 (1941), published in abbreviated form

24.6 M.S. Hawley: The condenser microphone as an acoustical standard, Bell Lab. Rec. **22**, 6–10 (1943)

24.7 A.L. DiMattia, F.M. Wiener: On the absolute pressure calibration of condenser microphones by the reciprocity method, J. Acoust. Soc Am. **18**(2), 341–344 (1946)

24.8 M.S. Hawley: The substitution method of measuring the open circuit voltage generated by a microphone, J. Acoust. Soc. Am. **21**(3), 183–189 (1949)

24.9 B.D. Simmons, F. Biagi: Pressure calibration of condenser microphones above 10 000 cps, J. Acoust. Soc. Am. **26**(5), 693–695 (1954)

24.10 T. Hayasaka, M. Suzuki, T. Akatsuka: New method of absolute pressure calibration of microphone sensitivity, Inst. Electr. Commun. Eng. Jpn. **33**, 674–680 (1955)

24.11 H.G. Diestel: Zur Bestimmung der Druckempfindlichkeit von Mikrophonen, Acustica **9**, 398–402 (1959), (in German)

24.12 T.F.W. Embleton, I.R. Dagg: Accurate coupler pressure calibration of condenser microphones at middle frequencies, J. Acoust. Soc. Am. **32**, 320–326 (1960)

24.13 W. Koidan: Method for measurement of $[E'/I']$ in the reciprocity calibration of microphones, J. Acoust. Soc. Am. **32**, 611 (1960)

24.14 A.N. Rivin, V.A. Cherpak: Pressure calibration of measuring microphones by the reciprocity method, Sov. Phys. Acoust. **6**, 246–253 (1960)

24.15 P.V. Brüel: *Accuracy of Condenser Microphone Calibration Methods, Part II*, Tech. Rev. **1** (Brüel Kjær, Nœrum 1965)

24.16 P. Riety, M. Lecollinet: Le dispositif d'etalonnage primaire des microphones de laboratoire de l'Institut National de Metrologie, Metrologia **10**, 17–34 (1974)

24.17 A.C. Corney: Capacitor microphone reciprocity calibration, Metrologia **11**, 25–32 (1975)

24.18 H. Miura, T. Takahashi, S. Sato: Correction for 1/2 inch laboratory standard condenser microphones, Trans. IECE Japan **EA77-41**, 15–22 (1977)

24.19 A. Suzuki, S. Yoshikawa: Simplified method for pressure calibration of condenser microphones us-

ing active couplers, Trans. IECE Japan **EA77-40**, 9–14 (1977)
24.20 G.S.K. Wong, T.F.W. Embleton: Arrangement for precision reciprocity calibration of condenser microphones, J. Acoust. Soc. Am. **66**(5), 1275–1280 (1979)
24.21 V. Nedzelnitsky, E. D. Burnett, W. B. Penzes: Calibration of laboratory condenser microphones. In: *Proc. 10th Transducer Workshop, Transducer Committee, Telemetry Group, Range Commanders Council* (DTIC, Colorado Springs 1979)
24.22 A. Suzuki, S. Yoshikawa: On the estimated error for pressure calibration of standard condenser microphones, Electr. Commun. Lab. J. (Jpn) **29**(7), 1251–1262 (1980)
24.23 D.L.H. Gibbings, A.V. Gibson: Contributions to the reciprocity calibration of microphones, Metrologia **17**, 7–15 (1981)
24.24 T. Takahashi, H. Miura: Corrections for the reciprocity calibration of laboratory standard condenser microphones, Bull. Electrotech. Lab. (Jpn) **46**(3-4), 78–81 (1982)
24.25 M.E. Delany, E.N. Bazley: *Uncertainties in Realizing the Standard of Sound Pressure by Closed-Coupler Reciprocity Technique*, Acoust. Rep. **99** (National Physical Laboratory, Teddington 1980), (see also 2nd ed. 1982)
24.26 D.L.H. Gibbings, A.V. Gibson: Wide-band calibration of capacitor microphones, Metrologia **20**, 95–99 (1984)
24.27 L. L. Beranek: *Acoustical Measurements* (Acoust. Soc. Am./AIP, Melville 1988), (**4**, 133-134)
24.28 K.O. Ballagh, A.C. Corney: Some developments in automated microphone reciprocity calibration, Acustica **71**, 200–209 (1990)
24.29 G. S. K. Wong, T. F. W. Embleton: *AIP Handbook of Condenser Microphones. Theory, Calibration, and Measurements* (American Institute of Physics, New York 1995)
24.30 N.H. Fletcher, S. Thwaites: Electrode surface profile and the performance of condenser microphones, J. Acoust. Soc. Am. **112**(6), 2779–2785 (2002)
24.31 BIPM: *Guide to the Expression of Uncertainties in Measurement* (BIPM, Paris 1995)
24.32 G.S.K. Wong: Precise measurement of phase difference and amplitude ratio of two coherent sinusoidal signals, J. Acoust. Soc. Am. **75**(3), 967–972 (1984)
24.33 B. Daniels: Acoustic impedance of enclosures, J. Acoust. Soc. Am. **19**, 569–571 (1947)
24.34 F. Biagi, R.K. Cook: Acoustic impedance of a right circular cylindrical enclosure, J. Acoust. Soc. Am. **26**, 506–509 (1954)
24.35 H. Gerber: Acoustic properties of fluid-filled chambers at infrasonic frequencies in the absence of convection, J. Acoust. Soc. Am. **36**, 1427–1434 (1964)
24.36 K.O. Ballagh: Acoustical admittance of cylindrical cavities, J. Sound Vibrat. **112**(3), 567–569 (1987)
24.37 D.R. Jarvis: Acoustical admittance of cylindrical cavities, J. Sound Vibrat. **117**(2), 390–392 (1987)
24.38 ANSI: ANSI S1.15 – 2005. American National Standard Measurement Microphones – Part 2: Primary Method for Pressure Calibration of Laboratory Standard Microphones by Reciprocity Technique, (NIST, Gaithersburg 2005)
24.39 T. Salava: *Measurement of the Acoustic Impedance of Standard Laboratory Microphones*, The Acoustics Laboratory, Report, Vol. 18 (Technical University of Denmark, Lyngby 1976)
24.40 IEC: IEC 61094-2:1992-03 Measurement Microphones - Part 2: Primary Method for Pressure Calibration of Laboratory Standard Microphones by the Reciprocity Technique (IEC, Geneva 1992)
24.41 ANSI S1.15-1997/Part 1 (R2001) American National Standard Measurement Microphones – Part 1: Specifications for Laboratory Standard Microphones. See also: IEC International Standard 61094-11992-05: Measurement Microphones Part 1: Specifications for Laboratory Standard Microphones (NIST, Gaithersburg 1997)
24.42 K. Rasmussen: *Acoustical behaviour of cylindrical couplers*, The Acoustics Laboratory Report, Vol. 1 (Technical University of Denmark, Lyngby 1969)
24.43 H. Miura, E. Matsui: On the analysis of the wave motion in a coupler for the pressure calibration of laboratory standard microphones, J. Acoust. Soc. Jpn. **30**, 639–646 (1974)
24.44 F. Jacobsen: An improvement of the 20 cm^3 coupler for reciprocity calibration of microphones, Acustica **38**, 151–153 (1977)
24.45 G.S.K. Wong, L. Wu: Controlled environment for reciprocity calibration of laboratory standard microphone and measurement of sensitivity pressure correction, Metrologia **36**, 275–280 (1999)
24.46 L. Wu, G.S.K. Wong, P. Hanes, W. Ohm: Measurement of sensitivity level pressure corrections for LS2P laboratory standard microphones, Metrologia **42**, 45–48 (2005)
24.47 K. Rasmussen: *The Influence of Environmental Conditions on the Pressure Sensitivity of Measurement Microphones*, Brüel Kjær Tech. Rev. **1** (Brüel Kjær, Nœrum 2001)
24.48 G.S.K. Wong, L. Wu: Controlled environment for reciprocity callibration of laboratory standard miccrophones and measurement of sensitivity pressure correction, Metrologica **36**, 275–280 (1999)
24.49 K. Rasmussen: The static pressure and temperature coefficients of laboratory standard microphones, Metrologia **36**(4), 265–273 (1999)
24.50 G.S.K. Wong: Primary pressure calibration by reciprocity. In: *AIP Handbook of Condenser Microphones. Theory, Calibration, and Measurements, Chap.4*, ed. by G.S.K. Wong, T.F.W. Embleton. (American Institute of Physics, New York 1995) p. 99
24.51 V. Nedzelnitsky: Primary method for calibrating free-field response. In: *AIP Handbook of Condenser*

Amazon EX1014 Page 1051

Microphones. Theory, Calibration, and Measurements, ed. by G.S.K. Wong, T.F.W. Embleton (American Institute of Physics, New York 1995) pp. 103–119, Chap. 5

24.52 IEC: IEC 61094-3 Ed. 1.0 b: 1995 Measurement Microphones – Part 3: Primary Method for Free-Field Calibration of Laboratory Standard Microphones by the Reciprocity Technique. (IEC, Geneva 1995)

24.53 G.S.K. Wong, T.F.W. Embleton: Three-port two-microphone cavity for acoustical calibrations, J. Acoust. Soc. Am. **71**(5), 1276–1277 (1982)

24.54 G.S.K. Wong, L. Wu: *Interchange microphone method for calibration by comparison*, Congress on Noise Control Engineering, Christchurch (Institute of Noise Control Engineering, Ames 1998), paper #15

24.55 G.S.K. Wong: Precision method for phase match of microphones, J. Acoust. Soc. Am. **90**(3), 1253–1255 (1991)

24.56 IEC: IEC 61094-5: 2001 Measurement Microphones Part 5: Method for Pressure Calibration of Working Standard Microphones by Comparison (IEC, Geneva 2001)

24.57 G.S.K. Wong: Comparison methods for microphone calibration. In: *AIP Handbook of Condenser Microphones. Theory, Calibration, and Measurements*, ed. by G.S.K. Wong, T.F.W. Embleton (American Institute of Physics, New York 1995) pp. 215–222, Chap. 13

24.58 G.S.K. Wong: Precision A.C. voltage-level measuring system for acoustics, J. Acoust. Soc. Am. **65**(3), 830–837 (1979)

24.59 W. Koidan: Calibration of standard condenser microphones: Coupler versus electrostatic actuator, J. Acoust. Soc. Am. **44**(5), 1451–1453 (1968)

24.60 E. Frederiksen: Electrostatic Actuator. In: *AIP Handbook of Condenser Microphones. Theory, Calibration, and Measurements*, ed. by G.S.K. Wong, T.F.W. Embleton. (American Institute of Physics, New York 1995) pp. 231–246, Chap. 15

24.61 P.V. Brüel: *The accuracy of microphone calibration methods Part II*, Brüel and Kjær Tech. Rev. **1**, 3–26 (Brüel and Kjær, Nœrum 1965)

24.62 G. Rasmussen: *Free-Field and Pressure Calibration of Condenser Microphones Using Electrostatic Actuator*, Proc. 6th Int. Congress on Acoustics (Elsevier, New York 1968) pp. 25–28

24.63 IEC: *IEC 61094-6: 2004 Measurement Microphones – Part 6: Electrostatic Actuators for Determination of Frequency Response* (IEC, Geneva 2004)

24.64 G.B. Madella: Substitution method for calibrating a microphone, J. Acoust. Soc. Am. **20**(4), 550–551 (1948)

24.65 V. Nedzelnitsky: Laboratory microphone calibration methods at the National Institute of Standards and Technology U.S.A.. In: *AIP Handbook of Condenser Microphones. Theory, Calibration, and Measurements*, ed. by G.S.K. Wong, T.F.W. Embleton. (American Institute of Physics, New York 1995) pp. 145–161, Chap. 8

24.66 G.S.K. Wong, L. Wu: Interlaboratory comparison of microphone calibration, J. Acoust. Soc. Am. **115**(2), 680–682 (2004)

24.67 G.S.K. Wong, L. Wu: Primary microphone calibration system stability, J. Acoust. Soc. Am. **114**(2), 577–579 (2003)

24.68 ISO: ISO 2533-1975(E), 1975 Standard Atmosphere, International Organization for Standardization (ISO, Geneva 1975)

24.69 P. Giacomo: Equation for the determination of the density of moist air (1981), Metrologia **18**, 33–40 (1982)

24.70 R.S. Davis: Equation for the determination of the density of moist air (1981/91), Metrologia **29**, 67–70 (1992)

24.71 G.S.K. Wong: Approximate equations for some acoustical and thermodynamic properties of standard air, J. Acoust. Soc. Jpn. E **11**, 145–155 (1990)

24.72 O. Cramer: The variation of the specific heat ratio and the speed of sound in air with temperature, pressure, humidity, and CO_2 concentration, J. Acoust. Soc. Am. **93**, 2510–2516 (1993)

24.73 G.S.K. Wong: Comments on The variation of the specific heat ratio and the speed of sound in air with temperature, pressure, humidity, and CO_2 concentration, J. Acoust. Soc. Am. **93**, 2510–2516 (1993)

24.74 G.S.K. Wong: Comments on The variation of the specific heat ratio and the speed of sound in air with temperature, pressure, humidity, and CO_2 concentration, J. Acoust. Soc. Am. **97**(5), 3177–3179 (1995)

24.75 G.S.K. Wong: Speed of sound in standard air, J. Acoust. Soc. Am. **79**, 1359–1366 (1986)

24.76 M. Greenspan: Comments on Speed of sound in standard air, J. Acoust. Soc. Am. **79**, 1359–1366 (1986)

24.77 M. Greenspan: Comments on Speed of sound in standard air, J. Acoust. Soc. Am. **82**, 370–372 (1987)

24.78 G.S.K. Wong: Response to Comments on 'Speed of sound in standard air', J. Acoust. Soc. Am. **82**, 370–372 (1987)

24.79 G.S.K. Wong: Response to Comments on 'Speed of sound in standard air', J. Acoust. Soc. Am. **83**, 373–374 (1987)

24.80 G.S.K. Wong: Air sound speed measurement and computation, A historical review. In: *Handbook of the Speed of Sound in Real Gases: Speed of Sound in Air*, Vol. III, ed. by A.J. Zuckerwar (Academic, New York 2002) pp. 265–284, Chap. 17, and references therein

24.81 C.M. Harris: Effects of humidity on the velocity of sound in air, J. Acoust. Soc. Am. **49**, 890–893 (1971)

24.82 G.P. Howell, C.L. Morfey: Frequency dependence of the speed of sound in air, J. Acoust. Soc. Am. **82**, 375–376 (1987)

Amazon EX1014 Page 1052

24.83 G.S.K. Wong, T.F.W. Embleton: Experimental determination of the variation of specific heat ratio in air with humidity, J. Acoust. Soc. Am. **77**, 402–407 (1985)
24.84 J.R. Partington, W.G. Shilling: *The Specific Heats of Gases* (Ernest Benn, London 1924)
24.85 G.S.K. Wong, T.F.W. Embleton: Variation of specific heats and of specific heat ratios in air with humidity, J. Acoust. Soc. Am. **76**, 555–559 (1984)
24.86 A.J. Zuckerwar (Ed.): *Speed of Sound in Air*, Handbook of the Speed of Sound in real Gases, Vol. III (Academic, New York 2002)
24.87 E. Lide (Ed.): *CRC Handbook of Chemistry and Physics*, 83rd edn. (CRC, Boca Raton 2002–2003) pp. 6–182

Amazon EX1014 Page 1053

25. Sound Intensity

Sound intensity is a vector that describes the flow of acoustic energy in a sound field. The idea of measuring this quantity directly, instead of deducing it from the sound pressure on the assumption of some idealized conditions, goes back to the early 1930s, but it took about 50 years before sound intensity probes and analyzers came on the market. The introduction of such instruments has had a significant influence on noise control engineering.

This chapter presents the *energy corollary*, which is the basis for sound power determination using sound intensity. The concept of reactive intensity is introduced, and relations between fundamental sound field characteristics and active and reactive intensity are presented and discussed.

Measurement of sound intensity involves the determination of the sound pressure and the particle velocity at the same position simultaneously. The established method of measuring sound intensity employs two closely spaced pressure microphones. An alternative method is based on the combination of a pressure microphone and a particle velocity transducer. Both methods are described, and their limitations are analyzed. Methods of calibrating and testing the two different measurement systems are also described. Finally the state of the art in the various areas of practical application of sound intensity measurement is summarized. These applications include the determination of the sound power of sources, identification and rank ordering of sources, and the measurement of the transmission of sound energy through partitions.

25.1 **Conservation of Sound Energy** 1054
25.2 **Active and Reactive Sound Fields** 1055
25.3 **Measurement of Sound Intensity** 1058
25.3.1 The p–p Measurement Principle .. 1058
25.3.2 The p–u Measurement Principle .. 1066
25.3.3 Sound Field Indicators 1068
25.4 **Applications of Sound Intensity** 1068
25.4.1 Noise Source Identification 1068
25.4.2 Sound Power Determination 1070
25.4.3 Radiation Efficiency of Structures 1071
25.4.4 Transmission Loss of Structures and Partitions 1071
25.4.5 Other Applications 1072
References 1072

Sound waves are compressional oscillatory disturbances that propagate in a fluid. Moving fluid elements have kinetic energy, and changes in the pressure imply potential energy. Thus, there is a flow of energy involved in the phenomenon of sound; sources of sound emit sound power, and sound waves carry energy. In most cases the oscillatory changes undergone by the fluid are very small compared with the equilibrium values, from which it follows that typical values of the sound power emitted by sources of sound, which is an acoustic second-order quantity, are extremely small. The radiated sound power is a negligible part of the energy conversion of almost any source. However, energy considerations are nevertheless of great practical importance in acoustics. Their usefulness is mainly due to the fact that a statistical approach where the energy of the sound field is considered turns out to give extremely useful approximations in room acoustics and in noise control. In fact determining the sound power of sources is a central point in noise control engineering. The value and relevance of knowing the sound power radiated by a source is due to the fact that this quantity is largely independent of the surroundings of the source in the audible frequency range.

Sound intensity is a measure of the flow of acoustic energy in a sound field. More precisely, the sound intensity is a vector that describes the time average of the net flow of sound energy per unit area. The units of this quantity are power per unit area (W/m^2).

The advent of sound intensity measurement systems in the early 1980s had a significant influence on noise control engineering. One of the most important

Amazon EX1014 Page 1054

advantages of this measurement technique is that sound intensity measurements make it possible to determine the sound power of sources in situ without the use of costly special facilities such as anechoic and reverberation rooms, and sound intensity measurements are now routinely used in the determination of the sound power of machinery and other sources of noise in situ. Other important applications of sound intensity include the identification and rank ordering of partial noise sources, the determination of the transmission losses of partitions, and the determination of the radiation efficiencies of vibrating surfaces. Because the intensity is a vector it is also more suitable for visualization of sound fields than, for instance, the sound pressure.

25.1 Conservation of Sound Energy

In the absence of mean flow the instantaneous sound intensity is the product of the sound pressure $p(t)$ and the particle velocity $\boldsymbol{u}(t)$

$$\boldsymbol{I}(t) = p(t)\boldsymbol{u}(t)\,. \tag{25.1}$$

By combining the fundamental equations that govern a sound field, the equation of conservation of mass, the adiabatic relation between changes in the sound pressure and in the density, and Euler's equation of motion, one can show that the divergence of the instantaneous intensity equals the (negative) rate of change of the sum of the potential and kinetic energy density $w(t)$,

$$\nabla \cdot \boldsymbol{I}(t) = -\frac{\partial w(t)}{\partial t}\,. \tag{25.2}$$

This is the equation of conservation of sound energy [25.1, 2], expressing the simple fact that if there is net flow of energy away from a point in a sound field then the sound energy density at that point is reduced at a corresponding rate. Integrating this equation over a volume V enclosed by the surface S gives, with Gauss's divergence theorem,

$$\begin{aligned}\int_S \boldsymbol{I}(t)\cdot \mathrm{d}\boldsymbol{S} &= -\frac{\partial}{\partial t}\left(\int_V w(t)\,\mathrm{d}V\right)\\ &= -\frac{\partial E(t)}{\partial t}\,,\end{aligned} \tag{25.3}$$

in which $E(t)$ is the total sound energy in the volume as a function of time. The left-hand term is the total net outflow of sound energy through the surface, and the right-hand term is the rate of change of the total sound energy in the volume. In other words, the net flow of sound energy out of a closed surface equals the (negative) rate of change of the sound energy in the volume enclosed by the surface because energy is conserved.

In practice we are often concerned with stationary sound fields and the time-averaged sound intensity rather than the instantaneous intensity, that is,

$$\langle \boldsymbol{I}(t)\rangle_\mathrm{t} = \langle p(t)\boldsymbol{u}(t)\rangle_\mathrm{t}\,. \tag{25.4}$$

For simplicity the symbol $\boldsymbol{I}$ is used for this quantity in what follows rather than the more precise notation $\langle \boldsymbol{I}(t)\rangle_\mathrm{t}$. If the sound field is harmonic with angular frequency $\omega = 2\pi f$ the complex representation of the sound pressure and the particle velocity can be used, which leads to the expression

$$\boldsymbol{I} = 1/2\,\mathrm{Re}(p\boldsymbol{u}^*)\,, \tag{25.5}$$

where $\boldsymbol{u}^*$ denotes the complex conjugate of $\boldsymbol{u}$.

A consequence of (25.3) is that the integral of the normal component of the time-averaged sound intensity over a closed surface is zero,

$$\int_S \boldsymbol{I}\cdot \mathrm{d}\boldsymbol{S} = 0\,, \tag{25.6}$$

when there is neither generation nor dissipation of sound energy in the volume enclosed by the surface, irrespective of the presence of steady sources *outside* the surface. If the surface encloses a steady source then the surface integral of the time-averaged intensity equals the sound power emitted by the source P_a, that is,

$$\int_S \boldsymbol{I}\cdot \mathrm{d}\boldsymbol{S} = P_a, \tag{25.7}$$

irrespective of the presence of other steady sources outside the surface. This important equation is the basis for sound power determination using sound intensity.

In a plane wave propagating in the r-direction the sound pressure p and the particle velocity u_r are in phase and related by the characteristic impedance of air ρc, where ρ is the density of air and c is the speed of sound,

$$u_\mathrm{r}(t) = \frac{p(t)}{\rho c}\,. \tag{25.8}$$

Amazon EX1014 Page 1055

Under such conditions the intensity is

$$I_r = \langle p(t)u_r(t)\rangle_t = \langle p^2(t)\rangle_t / \rho c = p_{rms}^2 / \rho c = \frac{|p|^2}{2\rho c} , \quad (25.9)$$

where p_{rms}^2 is the mean square pressure (the square of the root-mean-square pressure) and p in the rightmost expression is the complex amplitude of the pressure in a harmonic plane wave. In the particular case of a plane propagating wave the sound intensity is seen to be simply related to the rms sound pressure, which can be measured with a single microphone. Under free-field conditions the sound field generated by any source of finite extent is *locally plane* sufficiently far from the source. This is the basis for the free-field method of sound power determination (which requires an anechoic room); the sound pressure is measured at a number of points on a sphere that encloses the source [25.3].

A practical consequence of (25.9) is the following extremely simple relation between the sound intensity level ($I_{ref} = 1\,pW/m^2$) and the sound pressure level ($p_{ref} = 20\,\mu Pa$),

$$L_I \simeq L_p . \quad (25.10)$$

This is due to the fortuitous fact that

$$\rho c \simeq \frac{p_{ref}^2}{I_{ref}} = 400\,kg/m^2 s \quad (25.11)$$

in air under normal ambient conditions. At a static pressure of 101.3 kPa and a temperature of 23 °C the error of (25.10) is about 0.1 dB.

However, it should be emphasized that in the general case there is *no* simple relation between the sound intensity and the sound pressure, and both the sound pressure and the particle velocity must be measured simultaneously and their instantaneous product time-averaged as indicated by (25.4). This requires the use of a more complicated device than a single microphone.

25.2 Active and Reactive Sound Fields

Some typical sound field characteristics can be identified. For example, the sound field far from a source under free-field conditions has certain well-known properties (dealt with above); the sound field near a source has other characteristics, and some characteristics are typical of a reverberant sound field. One of the characteristics of the sound field near a source is that the sound pressure and the particle velocity are partly out of phase. To describe such a phenomenon one may introduce the concepts of *active* and *reactive* sound fields.

It takes four second-order quantities to describe the distributions and fluxes of sound energy in a stationary sound field completely [25.4–6]: potential energy density, kinetic energy density, active intensity (the quantity given by (25.4) and (25.5), usually simply referred to as the intensity), and the reactive intensity. The last of these quantities represents the non-propagating, oscillatory sound energy flux that is characteristic of a sound field in which the sound pressure and the particle velocity are in quadrature (90° out of phase), as for instance in the near field of a small source. The reactive intensity is a vector defined as the imaginary part of the product of the complex pressure and the complex conjugate of the particle velocity,

$$\boldsymbol{J} = 1/2\,\mathrm{Im}\left(p\boldsymbol{u}^*\right) \quad (25.12)$$

with the $e^{i\omega t}$ sign convention [cf. (25.5)]. Units: power per unit area (W/m^2). More-general time-domain formulations based on the Hilbert transform are also available [25.7]. Unlike the usual active intensity, the reactive intensity remains a somewhat controversial issue although the quantity was introduced more than half a century ago [25.8], perhaps because the vector $\boldsymbol{J}$ has no obvious physical meaning [25.9], or perhaps because describing an oscillatory flux by a time-averaged vector seems peculiar to some. However, even though the reactive intensity is of no obvious direct practical use it is nevertheless quite convenient that we have a quantity that makes it possible to describe and quantify the particular sound field conditions in the near field of sources in a precise manner. This will become apparent in Sect. 25.3.2.

It can be shown from (25.5) that the active intensity is proportional to the gradient of the phase of the sound pressure [25.10],

$$\boldsymbol{I} = -\frac{|p|^2}{2\rho c}\frac{\nabla\varphi}{k} , \quad (25.13)$$

where $k = \omega/c$ is the wavenumber. Thus the active intensity is orthogonal to surfaces of equal phase, that is, the wavefronts [25.5]. Likewise it can be shown from (25.12) that the reactive intensity is proportional to the

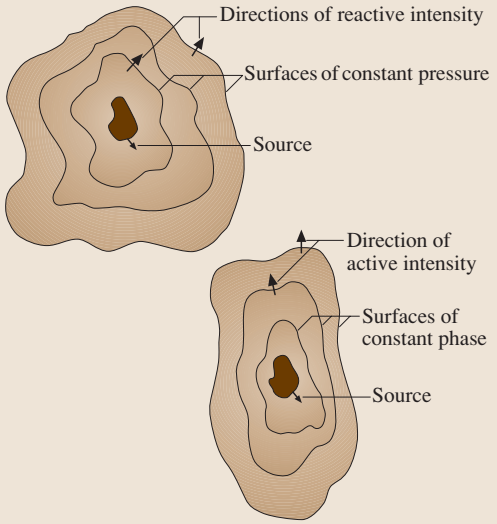


Fig. 25.1 Surfaces of constant phase and surfaces of constant pressure (After [25.5])

gradient of the mean square pressure [25.11],

$$\boldsymbol{J} = -\frac{\nabla\left(|p|^2\right)}{4\rho c k}\,, \tag{25.14}$$

and thus is orthogonal to surfaces of equal pressure [25.5]. See Fig. 25.1

Very near a sound source the reactive field is often stronger than the active field at low frequencies. However, the reactive field dies out rapidly with increasing distance to the source. Therefore, even at a fairly moderate distance from the source, the sound field is dominated by the active field. The extent of the reactive field depends on the frequency and the radiation characteristics of the sound source. In practice, the reactive field may usually be assumed to be negligible at a distance greater than, say, half a wavelength from the source.

The fact that $\boldsymbol{I}$ is the real part and $\boldsymbol{J}$ is the imaginary part of the product of the pressure and the complex conjugate of the particle velocity has led to the concept of complex sound intensity [25.4, 10],

$$\boldsymbol{I} + \mathrm{i}\boldsymbol{J} = 1/2 p \boldsymbol{u}^* \,. \tag{25.15}$$

Note that

$$\frac{I_\mathrm{r} + \mathrm{i}J_\mathrm{r}}{1/2\,|u_\mathrm{r}|^2} = \frac{1/2\,|p|^2}{I_\mathrm{r} - \mathrm{i}J_\mathrm{r}} = \frac{p}{u_\mathrm{r}} = Z_\mathrm{s}\,, \tag{25.16}$$

which shows that there is a simple relation between the complex intensity and the wave impedance of the sound field Z_s [25.6, 10]. It is also worth noting that

$$\frac{I_\mathrm{r}^2 + J_\mathrm{r}^2}{1/4\,|p|^2\,|u_\mathrm{r}|^2} = 1\,. \tag{25.17}$$

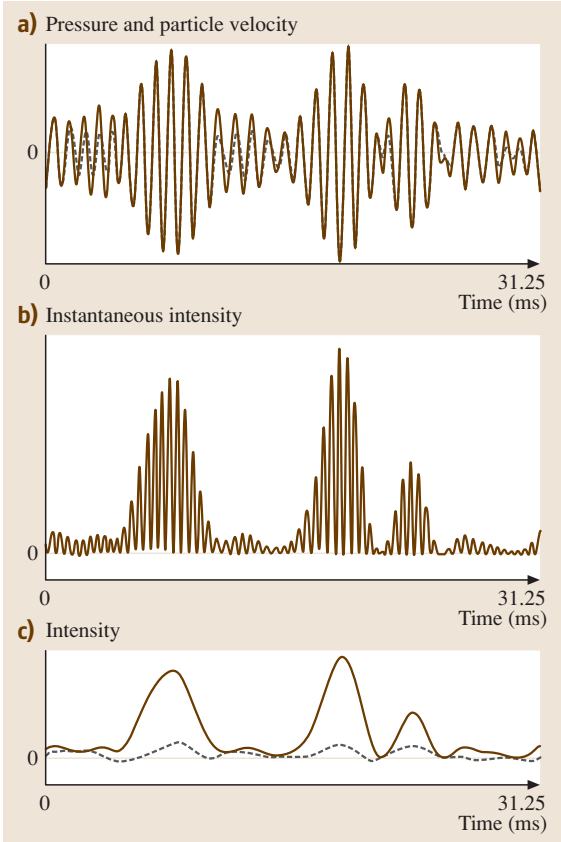


Fig. 25.2a–c Measurement 30 cm from a loudspeaker driven with one-third octave noise with a center frequency of 1 kHz. **(a)** Instantaneous sound pressure (*solid line*); instantaneous particle velocity multiplied by ρc (*dashed line*); **(b)** instantaneous sound intensity; **(c)** the real part of the complex instantaneous intensity (*solid line*); the imaginary part of the complex instantaneous intensity (*dashed line*) (After [25.7])

Figures 25.1–25.4 demonstrate the physical significance of the active and reactive intensities. The figures show the sound pressure and a component of the particle velocity as functions of time, the corresponding instantaneous sound intensity, and the real and imaginary part of the *complex instantaneous intensity*, that is, the quantity

$$\boldsymbol{I}_\mathrm{c}(t) = 1/2\,(p(t) + \mathrm{i}\tilde{p}(t))\,(\boldsymbol{u}(t) - \mathrm{i}\tilde{\boldsymbol{u}}(t))\,, \tag{25.18}$$

Amazon EX1014 Page 1057

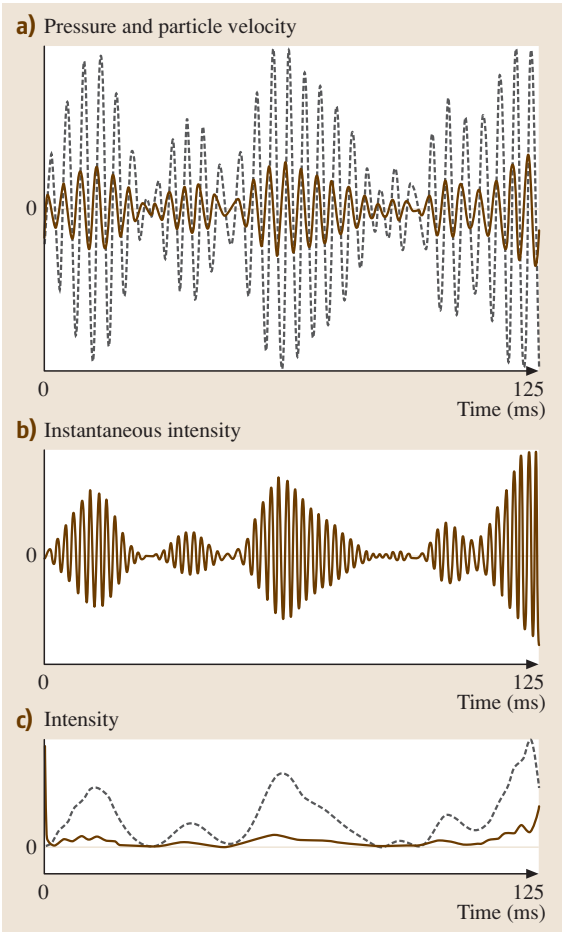


Fig. 25.3 Measurement in the near field of a loudspeaker driven with one-third octave noise with a center frequency of 250 Hz. *Key* as in Fig. 25.2 (After [25.7])

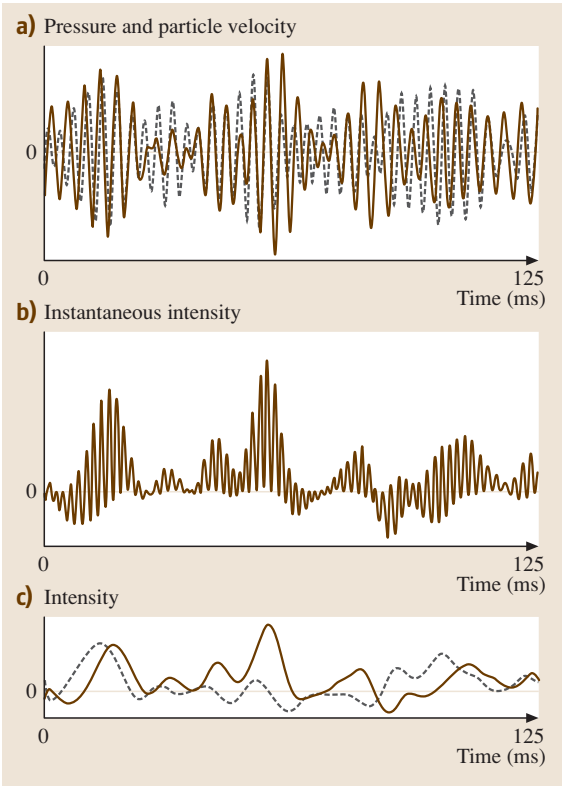


Fig. 25.4 Measurement 30 cm from a vibrating steel box driven with one-third octave noise with a center frequency of 250 Hz. *Key* as in Fig. 25.2 (After [25.7])

where $\tilde{p}(t)$ and $\tilde{\boldsymbol{u}}(t)$ are the Hilbert transforms of the pressure and the particle velocity [25.12]. The time average of this quantity in a steady sound field is the complex intensity given by (25.15).

In a narrow-band sound field the real and imaginary parts of the complex instantaneous intensity are low-pass signals that represent short-time average values of the two components of (25.15) [25.7].

Figure 25.2 shows the result of a measurement at a position 30 cm (about one wavelength) from a small loudspeaker driven with a band of one-third octave noise. The sound pressure and the particle velocity (multiplied by ρc) are almost identical; therefore the instantaneous intensity is always positive, and the real part of the complex instantaneous intensity is much larger than the imaginary part. This is an active sound field. Figure 25.3 shows the result of a similar measurement at a distance of a few centimeters (less than one tenth of a wavelength) from the loudspeaker cone. In this case the sound pressure and the particle velocity are almost in quadrature, and as a result the instantaneous intensity fluctuates about zero, that is, sound energy flows back and forth, out of and into the loudspeaker, and the imaginary part of the complex instantaneous intensity is much larger than the real part. This is an example of a strongly reactive sound field. Figure 25.4 shows data measured about 30 cm from a vibrating box made of 3 mm steel plates. It is apparent that the vibrating structure generates a much more complicated sound field than a loudspeaker does. And finally Fig. 25.5 shows the result of a measurement in a reverberant room several meters from the loudspeaker generating the sound field. Here the sound pressure and the particle velocity appear to be uncorrelated signals; this is neither an active nor a reactive sound field; this is a diffuse sound field.

Amazon EX1014 Page 1058

25.3 Measurement of Sound Intensity

Acousticians have attempted to measure sound intensity since the early 1930s, but measurement of sound intensity is more difficult than measurement of the sound pressure, and it took almost 50 years before sound intensity measurement systems came on the market. The first international standards for measurements using sound intensity and for instruments for such measurements were issued in the middle of the 1990s. A description of the history of the development of sound intensity measurement up to the middle of the 1990s is given in *Fahy*'s monograph *Sound Intensity* [25.2].

Measurement of sound intensity involves determination of the sound pressure and the particle velocity at the same position simultaneously. In the general case at least two transducers are required. There are three possible measurement principles: (i) one can determine the particle velocity from a finite-difference approximation of the pressure gradient using two closely spaced pressure microphones and use the average of the two microphone signals as the pressure [25.2, 13] (the *two-microphone* or *p–p* method); (ii) one can combine a pressure microphone with a particle velocity transducer [25.2] (the *p–u* method); and (iii) one can determine the pressure from a finite-difference approximation of the divergence of the particle velocity [25.14] (the *u–u* method). The first of these methods is well established. The second method has been hampered by the absence of reliable particle velocity transducers, but with the recent advent of the Microflown particle velocity sensor [25.15, 16] it seems to have potential [25.17]. The third method, which involves three matched pairs of particle velocity transducers, has never been used in air and is mentioned here for the sake of completeness.

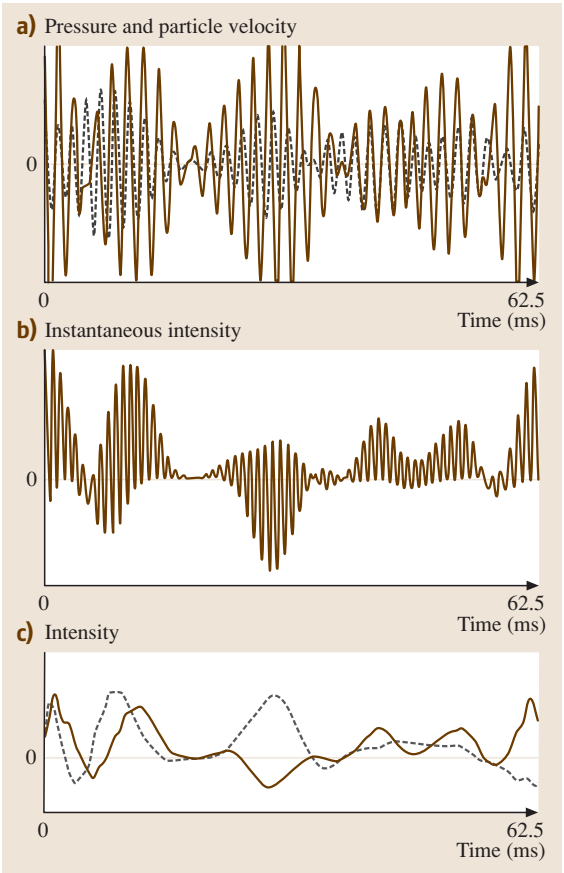


Fig. 25.5 Measurement in a reverberation room driven with one-third octave noise with a center frequency of 500 Hz. *Key* as in Fig. 25.2 (After [25.7])

25.3.1 The *p–p* Measurement Principle

For more than 25 years the *p–p* method based on two closely spaced pressure microphones (or hydrophones) has dominated sound intensity measurement. This method relies on a finite-difference approximation to the sound pressure gradient. Both the International Electrotechnical Commission (IEC) standard on instruments for the measurement of sound intensity and the corresponding American National Standards Institute (ANSI) standard deal exclusively with *p–p* measurement systems [25.18, 19]. The success of this method is related to the fact that condenser microphones are more stable and reliable than any other acoustic transducer.

Two pressure microphones are placed close together. The particle velocity component in the direction of the axis through the two microphones r is obtained from Euler's equation of motion

$$\frac{\partial p(t)}{\partial r} + \rho \frac{\partial u_r(t)}{\partial t} = 0 \,, \tag{25.19}$$

where the gradient of the pressure is approximated by a finite difference. Thus the particle velocity is determined as

$$\hat{u}_r(t) = -\frac{1}{\rho} \int_{-\infty}^{t} \frac{p_2(\tau) - p_1(\tau)}{\Delta r} \, \mathrm{d}\tau \,, \tag{25.20}$$

where p_1 and p_2 are the signals from the two microphones, Δr is the microphone separation distance, and

Amazon EX1014 Page 1059

τ is a dummy time variable. The caret indicates that the result is an estimate, which of course is an approximation to the true particle velocity. The sound pressure at the center of the probe is estimated as

$$\hat{p}(t) = \frac{p_1(t) + p_2(t)}{2}, \tag{25.21}$$

and the time-averaged intensity component in the r-direction is

$$\hat{I}_r = \left\langle \hat{p}(t)\hat{u}_r(t) \right\rangle_t = \left\langle \frac{p_1(t) + p_2(t)}{2} \int_{-\infty}^{t} \frac{p_1(\tau) - p_2(\tau)}{\rho \Delta r} \, d\tau \right\rangle_t . \tag{25.22}$$

Some sound intensity analyzers use (25.22) to measure the intensity in frequency bands (usually one-third octave bands). Another type calculates the intensity from the imaginary part of the cross spectrum of the two microphone signals $S_{12}(\omega)$,

$$\hat{I}_r(\omega) = -\frac{1}{\omega \rho \Delta r} \mathrm{Im}\left[S_{12}(\omega)\right] . \tag{25.23}$$

The frequency-domain formulation is equivalent to the time-domain formulation, and (25.23) gives exactly the same result as (25.22) when the intensity spectrum is integrated over the frequency band of concern [25.20, 21]. The frequency-domain formulation makes it possible to determine sound intensity with a dual-channel fast Fourier transform (FFT) analyzer.

The most common microphone arrangement is known as *face-to-face*, but another called *side-by-side* is occasionally used. The latter arrangement has the advantage that the diaphragms of the microphones can be placed very near a radiating surface, but the disadvantage that the microphones disturb each other acoustically more than they do in the other configuration. Figure 25.6 shows a three-dimensional (3-D) intensity probe produced by Ono-Sokki with yet another configuration. At high frequencies the face-to-face configuration with a solid plug between the microphones is superior [25.22]. Such a sound intensity probe produced by Brüel & Kjær is shown in Fig. 25.7. The *spacer* between the microphones tends to stabilize the *acoustic distance* between them.

Sources of Error in Measurement of Sound Intensity with p–p Measurement Systems

It is far more difficult to measure sound intensity than to measure sound pressure, and a surprisingly large part of the literature on sound intensity is concerned with identifying and studying the sources of error. One confusing problem is that the accuracy of any sound intensity measurement system depends strongly on the sound field under study; sometimes such measurements are not very difficult, but under certain conditions even very small imperfections of the measuring equipment can have a significant influence on the results. Another complication is that small local errors are sometimes amplified into large global errors when the intensity is integrated over a closed surface [25.23]. The opposite may also happen. Yet another problem is that the distribution of the sound intensity in the near field of a source of sound often is far more complicated than the distribution of the

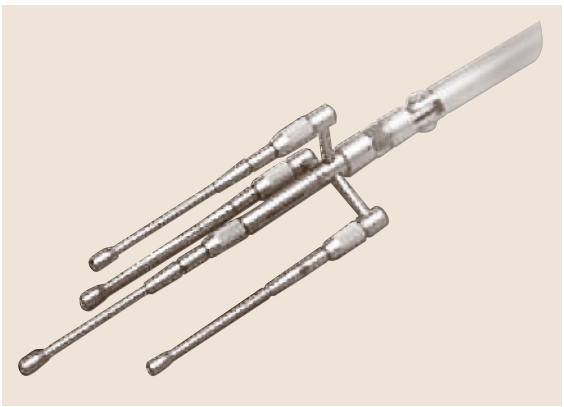


Fig. 25.6 Three-dimensional sound intensity probe for vector measurements (Ono Sokki, Japan)



Fig. 25.7 Sound intensity probe with the microphones in the *face-to-face* configuration (Brüel & Kjær, Denmark)

Amazon EX1014 Page 1060

sound pressure, indicating that sound fields can be much more complicated than earlier realized [25.2]. The problems are reflected in the fairly complicated international and national standards for sound power determination using sound intensity, ISO 9614-1, ISO 9614-2, ISO 9614-3, and ANSI S12.12 [25.24–27].

The most important limitations of sound intensity measurement systems based on the p–p approach are caused by the finite-difference approximation, scattering and diffraction, and instrumentation phase mismatch.

The Finite-Difference Error

The accuracy of the finite-difference approximation obviously depends on the separation distance and the wavelength. For a plane wave of axial incidence the finite-difference error can be shown to be [25.22]

$$\hat{I}_r / I_r = \frac{\sin k\Delta r}{k\Delta r} , \qquad (25.24)$$

This expression is shown in Fig. 25.8 for various values of the microphone separation distance. More complicated expressions for other sound field conditions are available in the literature [25.30]. The upper frequency limit of p–p intensity probes has generally been considered to be the frequency at which the finite-difference error for axial plane-wave incidence is acceptably small. With 12 mm between the microphones (a typical value) this gives an upper limiting frequency of about 5 kHz.

Scattering and Diffraction

It is evident that the effect of scattering and diffraction depends on the geometry of the microphone arrangement. Several configurations are possible, but in the early 1980s it was shown experimentally that the face-to-face configuration with a solid spacer between the two microphones is particularly favorable [25.22]. About 15 years later it was discovered that the effect of scattering and diffraction in combination with the resonance of the small cavity between the spacer and the diaphragm of each microphone not only tends to counterbalance the finite-difference error but in fact for a certain length of the spacer cancels it almost perfectly over a wide frequency range under fairly general sound field conditions [25.28]. (This finding had been anticipated much earlier [25.31].) 25.9 shows the increase of the pressure on two 1/2 inch microphones in the face-to-face configuration for axial sound incidence, and Fig. 25.10, which corresponds to Fig. 25.8, shows the error of the resulting sound intensity estimate. A practical consequence is that the upper frequency limit of a sound intensity probe based on two 1/2 inch microphones separated by a 12 mm spacer in the face-to-face arrangement is about 10 kHz, which is an octave higher than the frequency limit determined by the finite-difference

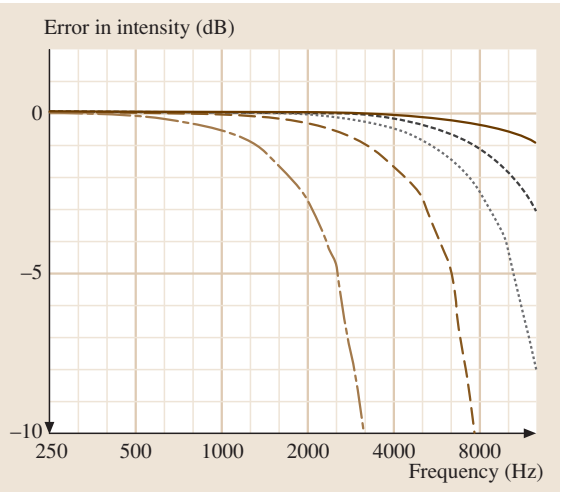


Fig. 25.8 Finite-difference error of an ideal p–p sound intensity probe in a plane wave of axial incidence for different values of the separation distance: 5 mm (*solid line*); 8.5 mm (*dashed line*); 12 mm (*dotted line*); 20 mm (*long dashes*); 50 mm (*dash-dotted line*) (After [25.28])

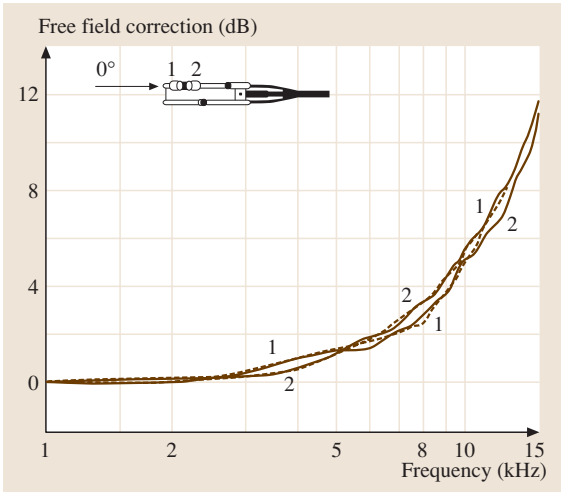


Fig. 25.9 Pressure increase on the two microphones of a sound intensity probe with 1/2 inch microphones separated by a 12 mm spacer for axial sound incidence. Experimental results (*solid line*); numerical results (*dashed line*) (After [25.29])

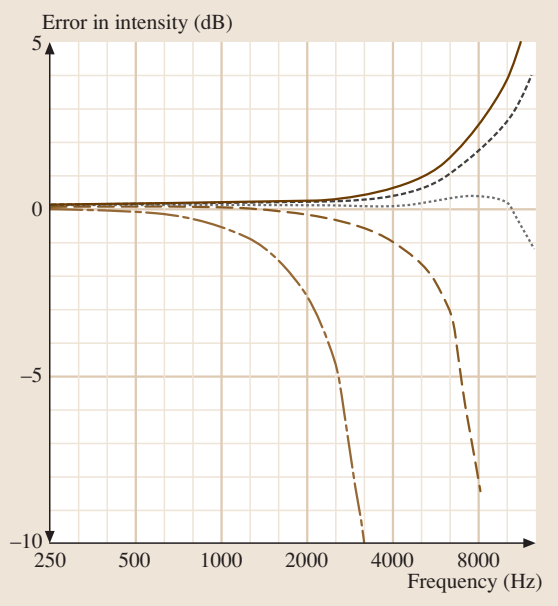


Fig. 25.10 Error of a sound intensity probe with 1/2 inch microphones in the face-to-face configuration in a plane wave of axial incidence for different spacer lengths: 5 mm (*solid line*); 8.5 mm (*dashed line*); 12 mm (*dotted line*); 20 mm (*long dashes*); 50 mm (*dash-dotted line*) (After [25.28])

approximation. The combination of 1/2 inch microphones and a 12 mm spacer is now regarded as optimal, and longer spacers are only used when the focus is exclusively on low frequencies. With a longer spacer between 1/2 inch microphones the resonance occurs at too high a frequency to be of any help and the finite-difference error will dominate; thus an intensity probe with a 50 mm spacer has an upper frequency limit of about 1.2 kHz.

Phase Mismatch

Unless the measurement is compensated for phase mismatch the microphones for measurement of sound intensity with the p–p method have to be phase-matched extremely well, and state-of-the-art sound intensity microphones are matched to a maximum phase response difference of 0.05° below 250 Hz and a phase difference proportional to the frequency above 250 Hz (say, 0.2° at 1 kHz) [25.33] The proportionality to the frequency is a consequence of the fact that phase mismatch in this frequency range is caused by differences between the resonance frequencies and the damping of the two microphones [25.34].

Phase mismatch between the two measurement channels is the most serious source of error in measurement of sound intensity with p–p measurement systems, even with the best equipment that is available today. It can be shown that a small (positive or negative) phase mismatch error φ_{pe} gives rise to a bias error that can be approximated by the following expression,

$$\hat{I}_r \simeq I_r - \frac{\varphi_{pe}}{k\Delta r}\frac{p_{rms}^2}{\rho c} = I_r\left(1 - \frac{\varphi_{pe}}{k\Delta r}\frac{p_{rms}^2/\rho c}{I_r}\right), \quad (25.25)$$

where I_r is the true intensity (unaffected by phase mismatch) [25.35]. This expression shows that the effect of a given phase error is inversely proportional to the frequency and the microphone separation distance and is proportional to the ratio of the mean square sound pressure to the sound intensity. If this ratio (which in logarithmic form is known as the *pressure-intensity index*) is large, say, more than 10 dB, then the true phase difference between the two pressure signals in the sound field is small and even the small phase errors mentioned above will give rise to significant bias errors. Because of phase mismatch it will rarely be possible to make reliable measurements below, say, 80 Hz unless a longer spacer than the usual 12 mm spacer is used.

Figure 25.11 shows the effect of a positive phase error of 0.3° in a plane wave of axial incidence, calcu-

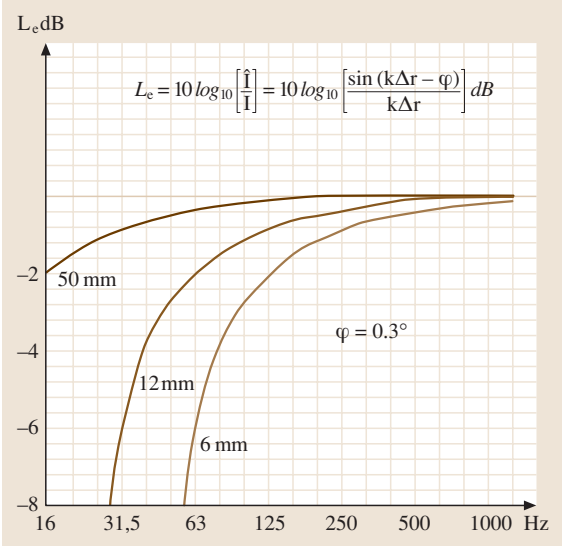


Fig. 25.11 Error due to a phase error of 0.3° in a plane propagating wave (After [25.32])

lated for different values of the microphone separation distance Δr. It is apparent that large underestimation errors occur at low frequencies. Note, however, that still larger errors will occur when the ratio of the mean square pressure to the sound intensity takes a larger value than unity, which is likely to happen unless the measurement takes place in an anechoic room. It should also be noted that a frequency-independent value of the phase error φ_{pe} is very unlikely [25.34]. Finally it is worth mentioning again that state-of-the-art microphone pairs for sound intensity measurements are much better matched now than within 0.3°.

Inspection of (25.25) shows that the simple expedient of reversing a p–p probe makes it possible to eliminate the influence of p–p phase mismatch; the intensity changes sign but the error does not [25.20, 36]. Unfortunately, most p–p intensity probes are not symmetrical and are therefore not suitable for real measurements with the probe reversed.

The ratio of the phase error to the product of the frequency and the microphone separation distance can be measured (usually in the form of the so-called *pressure-residual intensity index*) by exposing the two pressure microphones to the same pressure. The residual intensity is the *false* sound intensity indicated by the instrument when the two microphones are exposed to the same pressure p_0, for instance in a small cavity driven by a wide-band source. A commercial example of such a device is shown in Fig. 25.12. When

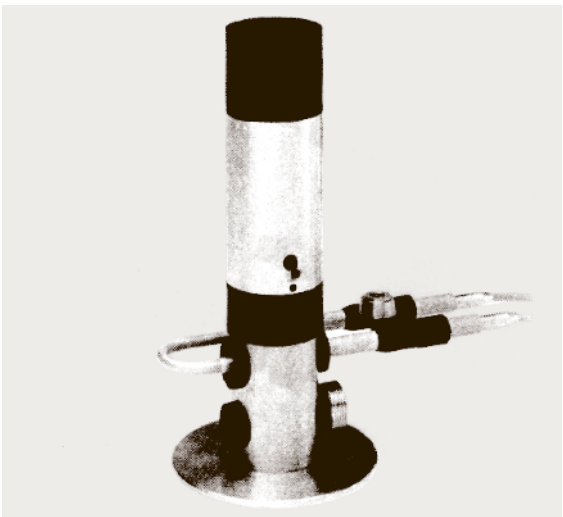


Fig. 25.12 Coupler for measurement of the pressure-residual intensity index of p–p sound intensity probes (Brüel & Kjær, Denmark)

the pressure on the two microphones is the same (in amplitude as well as in phase) the true intensity is zero, and the magnitude of the indicated, residual intensity,

$$I_0 = -\frac{\varphi_{pe}}{k\Delta r}\frac{p_0^2}{\rho c}\,, \tag{25.26}$$

should obviously be as small as possible. Expressed in terms of this quantity (25.25) takes the form

$$\begin{aligned}\hat{I}_r &= I_r + \left(\frac{I_0}{p_0^2}\right) p_{rms}^2 \\ &= I_r\left(1 + \frac{I_0}{p_0^2/\rho c}\,\frac{p_{rms}^2/\rho c}{I_r}\right)\,.\end{aligned} \tag{25.27}$$

An alternative form that follows directly from (25.27) has the advantage of expressing the error in terms of the available, biased intensity estimate [25.37],

$$\hat{I}_r = I_r\left(1 - \frac{I_0}{p_0^2/\rho c}\,\frac{p_{rms}^2/\rho c}{\hat{I}_r}\right)^{-1}\,. \tag{25.28}$$

The pressure-residual intensity index of the measurement system can be measured once (and should be checked occasionally). Combined with the pressure-intensity index of the actual measurement it makes it possible to estimate the error. Some analyzers can give warnings when the error due to phase mismatch as predicted by (25.28) exceeds a specified level. The bias error predicted by (25.28) is less than $\pm 10\log(1 \pm 10^{-K/10})$dB if the pressure-intensity index of the measurement, δ_{pI}, is less than the pressure-residual intensity index, δ_{pIo}, minus the *bias error index* K, that is

$$\begin{aligned}\delta_{pI} &= 10\log\left(\frac{p_{rms}^2/\rho c}{|I_r|}\right) < \delta_{pIo} - K \\ &= 10\log\left(\frac{p_0^2/\rho c}{|I_0|}\right) - K\,.\end{aligned} \tag{25.29}$$

The larger the value of K the smaller the maximum error that can occur and the stronger and more restrictive on the range of measurement is the requirement, as demonstrated by Fig. 25.13. Note that a negative residual intensity (which leads to underestimation of a positive intensity component) gives larger errors (in decibels) than a corresponding positive residual intensity (which leads to overestimation of a positive intensity component) unless the error is small. A bias error index of 7 dB corresponds to the error due to phase mismatch being

Amazon EX1014 Page 1063

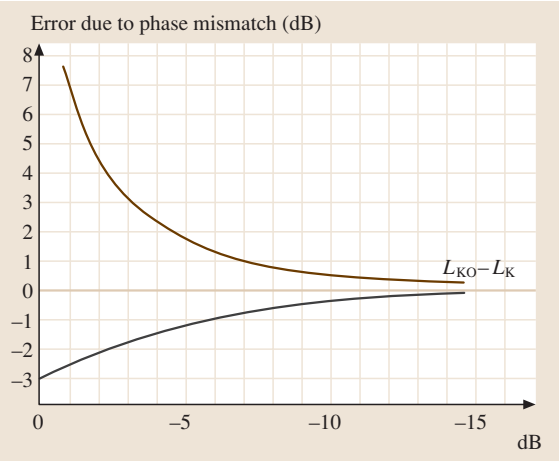


Fig. 25.13 Maximum error due to phase mismatch as a function of the bias error index K for negative residual intensity (*upper curve*) and for positive residual intensity (*lower curve*) (After [25.38])

less than 1 dB (*survey accuracy* [25.25]), and a bias error index of 10 dB corresponds to the error being less than 0.5 dB (*engineering accuracy* [25.25]). These values correspond to the phase error of the equipment being five and ten times less than the actual phase angle in the sound field, respectively. The quantity $\delta_{pIo} - K$ is known as the *dynamic capability* of the measurement system.

Many applications of sound intensity measurements involve integrating the normal component of the intensity over a surface. The global versions of (25.27) and (25.28) are found by integrating the normal component over a surface that encloses a source. The result is the expressions

$$\begin{aligned}\hat{P}_a &= \int_S \hat{\boldsymbol{I}} \cdot \mathrm{d}\boldsymbol{S} \\ &\simeq P_a \left(1 - \frac{\varphi_{pe}}{k\Delta r} \frac{\int_S \left(p_{rms}^2 / \rho c \right) \mathrm{d}S}{\int_S \boldsymbol{I} \cdot \mathrm{d}\boldsymbol{S}} \right) \\ &= P_a \left(1 + \frac{I_0 \rho c}{p_0^2} \frac{\int_S \left(p_{rms}^2 / \rho c \right) \mathrm{d}S}{\int_S \boldsymbol{I} \cdot \mathrm{d}\boldsymbol{S}} \right) \\ &= P_a \left(1 - \frac{I_0 \rho c}{p_0^2} \frac{\int_S \left(p_{rms}^2 / \rho c \right) \mathrm{d}S}{\int_S \hat{\boldsymbol{I}} \cdot \mathrm{d}\boldsymbol{S}} \right)^{-1} , \end{aligned} \quad (25.30)$$

where P_a is the true sound power of the source within the surface [25.35]. The condition expressed by (25.29) still applies, although the pressure-intensity index now involves averaging over the measurement surface.

Sources outside the measurement surface do not contribute to the surface integral of the true intensity [the denominator of the second term on the right-hand side of (25.30)], but they invariantly increase the surface integral of the mean square pressure (the numerator of the second term), as demonstrated by the results shown in Fig. 25.14. It follows that even a very small phase error imposes restrictions on the amount of extraneous noise that can be tolerated in sound power measurement with a p–p sound intensity measurement system.

Other Sources of Error

It can be difficult to avoid that the intensity probe is exposed to airflow, for example in measurements near air-cooled machinery. Strictly speaking the p–p measurement principle is simply not valid in such circumstances [25.40]. However, practice shows that the resulting fundamental error is insignificant in airflows of moderate velocities (say, up to 10 m/s), and that the false, low-frequency intensity signals produced by turbulence are a more serious problem under such conditions. Turbulence generates pressure fluctuations (flow noise, unrelated to the sound field) that contaminate the signals from the two microphones, and at low frequencies these signals are correlated and thus interpreted by the measurement system as intensity. The resulting false intensity is unpredictable and can be positive or negative. This is mainly a problem below 200 Hz [25.41]. A longer spacer helps reducing the problem, but the most

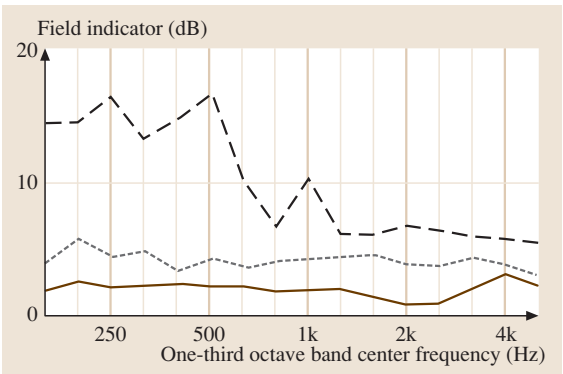


Fig. 25.14 Pressure-intensity index on a surface enclosing a noise source determined under three different conditions: measurement using a reasonable surface (*solid line*); measurement using an eccentric surface (*dashed line*); measurement with strong background noise at low frequencies (*long dashes*) (After [25.39])

Amazon EX1014 Page 1064

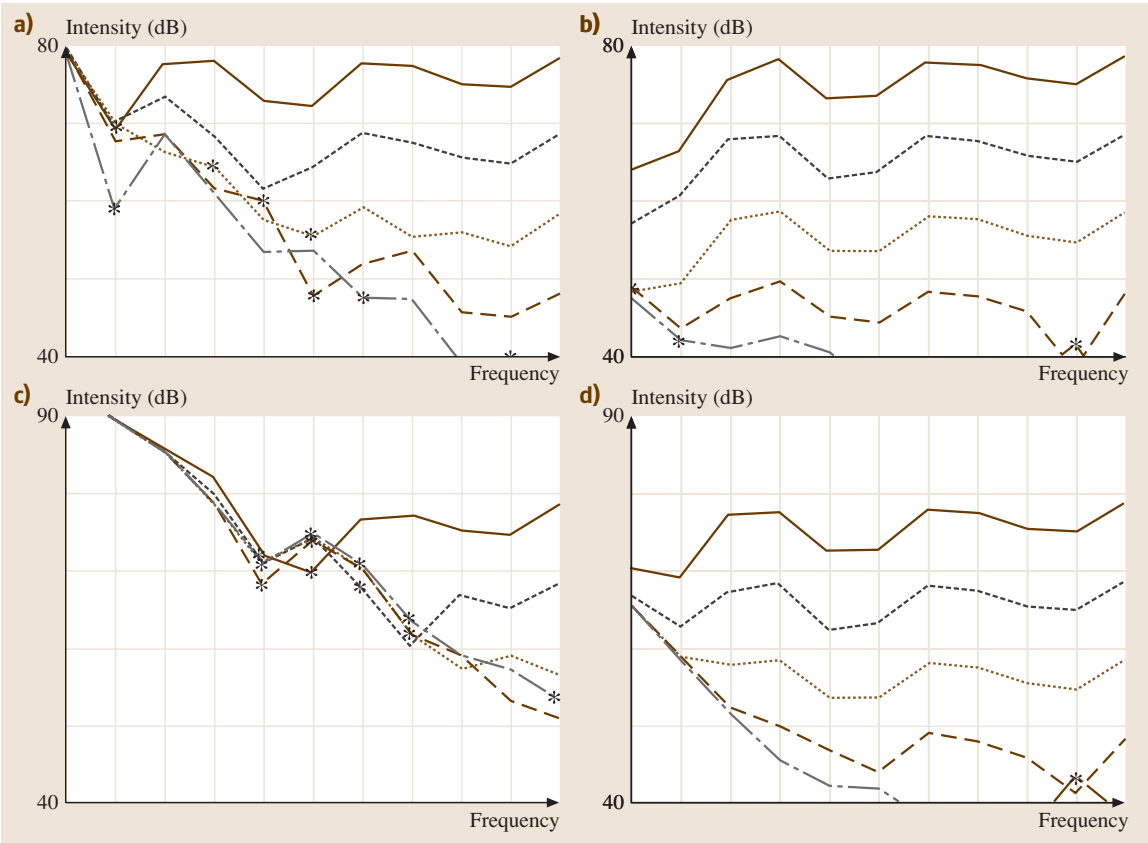


Fig. 25.15 Measurement 60 cm from a loudspeaker and a fan producing airflow of about 4 m/s at the measurement position. *Top figures*: 50 mm spacer; *bottom figures*: 12 mm spacer; *left figures*: no windscreen; *right figures*: windscreen. Asterisk: negative intensity estimate. Nominal sound power level of source: 100 dB (*solid line*); 90 dB (*dashed line*); 80 dB (*dotted line*); 70 dB (*long dashes*); 60 dB (*dash-dotted line*) (After [25.41])

efficient expedient is to use a windscreen of porous foam, as demonstrated by the results shown in Fig. 25.15. However, windscreens give rise to errors at low frequencies in highly reactive sound fields, because the losses of the foam modify Euler's equation of motion (25.19) [25.42, 43]. Thus measurements with windscreened probes very near sources should be avoided.

The finite averaging time used in any measurement results in a random error, and this random error is usually larger in sound intensity measurements than in sound pressure measurements – sometimes much larger [25.44–46]. Thus to maintain the same random error as in measurement of the sound pressure one will usually have to average over a longer time. However, most applications of sound intensity involve integrating over a measurement surface, and since it can be shown that it is the total averaging time that matters [25.47], the problem is less serious in practice than one might expect from observations at discrete positions.

Yet another source of error is the electrical self-noise from the microphones and preamplifier circuits. Although the level of such noise is very low in modern 1/2 inch condenser microphones it can have a serious influence on sound intensity measurement at low levels. The noise increases the random error associated with a finite averaging time at low frequencies, in particular if the pressure-intensity index takes a large value. The problem reveals itself by poor or nonexistent repeatability [25.48].

Calibration of p–p Sound Intensity Measurement Systems

Calibration of p–p sound intensity measurement systems is fairly straightforward: the two pressure mi-

crophones are calibrated with a pistonphone in the usual manner. However, because of the serious influence of phase mismatch the pressure-residual intensity index should also be determined. The IEC standard for sound intensity instruments and its North American counterpart [25.18, 19] specify minimum values of the acceptable pressure-residual intensity index for the probe as well as for the processor; according to the results of a test the instruments are classified as being of class 1 or class 2. The test involves subjecting the two microphones of the probe to identical pressures in a small cavity driven with wide-band noise. A similar test of the processor involves feeding the same signal to the two channels. The pressure and intensity response of the probe should also be tested in a plane propagating wave as a function of the frequency, and the directional response of the probe is required to follow the ideal cosine law within a specified tolerance.

According to the two standards a special test is required in the frequency range below 400 Hz: the intensity probe should be exposed to the sound field in a standing-wave tube with a specified standing wave ratio (24 dB for probes of class 1). When the sound intensity probe is drawn through this interference field the sound intensity indicated by the measurement system should be within a certain tolerance.

Figure 25.16a illustrates how the sound pressure, the particle velocity and the sound intensity vary with

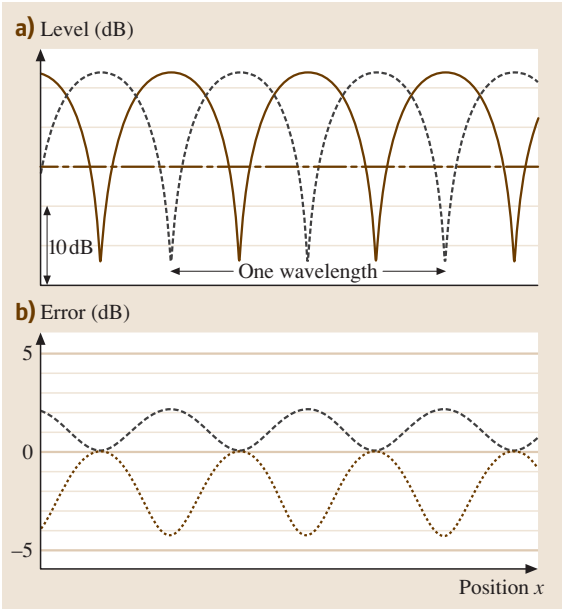


Fig. 25.16 (a) Sound pressure level (*solid line*), particle velocity level (*dashed line*), and sound intensity level (*dash-dotted line*) in a standing wave with a standing-wave ratio of 24 dB (b) Estimation error of a sound intensity measurement system with a residual pressure-intensity index of 14 dB (positive and negative residual intensity) (After [25.49])

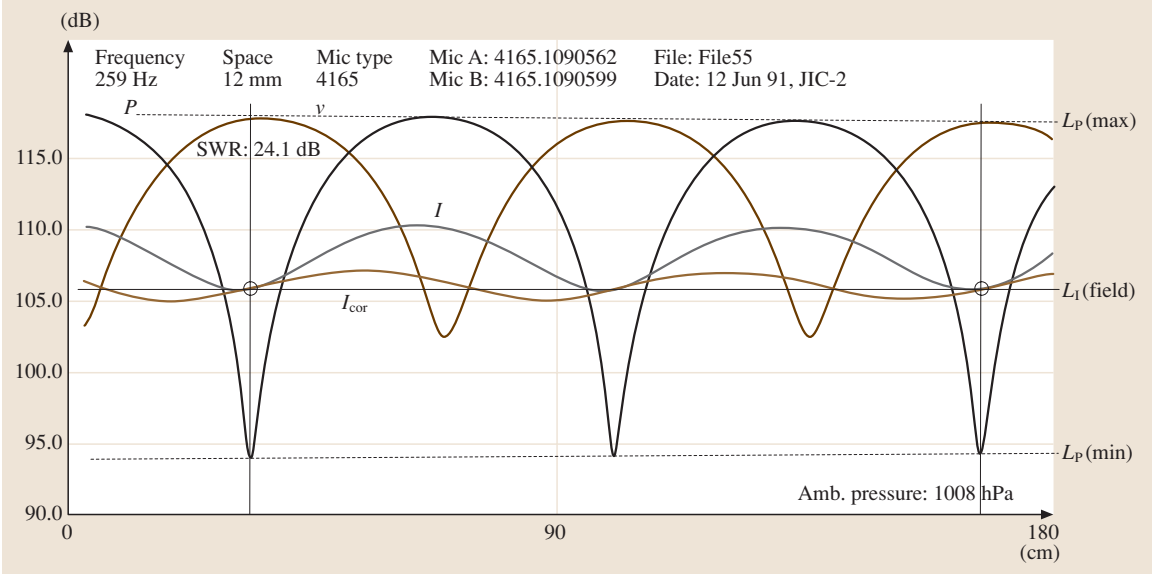


Fig. 25.17 Response of a sound intensity probe exposed to a standing wave: sound pressure, particle velocity, intensity, and phase-corrected intensity (After [25.50])

position in a one-dimensional interference field with a standing-wave ratio of 24 dB. It is apparent that the pressure-intensity index varies strongly with the position in such a sound field. Accordingly, the influence of a given phase error depends on the position, as shown in the calculations presented in Fig. 25.16b. Figure 25.17 shows an example of measurements with an intensity probe drawn through a standing-wave tube. The standing-wave test will also reveal other sources of error than phase mismatch, for example, the influence of an unacceptably high vent sensitivity of the microphones [25.51].

25.3.2 The *p–u* Measurement Principle

A *p–u* sound intensity measurement system combines two fundamentally different transducers, a pressure microphone and a particle velocity transducer. The sound intensity is simply the time average of the instantaneous product of the pressure and particle velocity signal,

$$I_\mathrm{r} = \langle p(t)u_\mathrm{r}(t)\rangle_\mathrm{t} = 1/2\,\mathrm{Re}\left(pu_\mathrm{r}^*\right)\ , \qquad (25.31)$$

where the latter expression is based on the complex exponential representation. In the frequency domain the expression takes the form

$$I_\mathrm{r}(\omega) = S_\mathrm{pu}(\omega). \qquad (25.32)$$

Equation (25.32) gives the same result as (25.31) when the intensity spectrum is integrated over the frequency band of concern.

A *p–u* sound intensity probe that combined a pressure microphone with a transducer based on the convection of an ultrasonic beam by the particle velocity flow was produced by Norwegian Electronics for some years [25.2, 52], but the device was somewhat bulky, very sensitive to airflow, and difficult to calibrate, and production was stopped in the middle of the 1990s. More recently, a micromachined transducer called the *Microflown* has become available for measurement of the particle velocity [25.15], and an intensity probe based on this device in combination with a small pressure microphone is now in commercial production [25.16]; see Fig. 25.18. The Microflown particle velocity transducer consists of two short, thin, closely spaced wires, heated to about 300 °C [25.15]. Their resistance depends on the temperature. A particle velocity signal in the perpendicular direction changes the temperature distribution instantaneously, because one of the wires will be cooled more than the other by the airflow. The frequency response of this device is relatively flat up to a corner



Fig. 25.18 A *p–u* sound intensity probe (by Microflown Technologies, The Netherlands)

frequency of the order of 1 kHz caused by diffusion effects related to the distance between the two wires. A second corner frequency at about 10 kHz is caused by the thermal heat capacity of the wires. Between 1 and 10 kHz there is a roll-off of 6 dB per octave. The particle velocity transducer is combined with a small electret condenser microphone in the 1/2 inch sound intensity probe shown in Fig. 25.18. The velocity transducer is mounted on a small, solid cylinder, and the condenser microphone is mounted inside another, hollow cylinder. The geometry of this arrangement increases the sensitivity of the velocity transducer. Unlike Norwegian Electronics' intensity probe the Microflown probe is very small – in fact much smaller than a standard *p–p* probe. Thus it is possible to measure very close to a vibrating surface with this device. At the time of writing there is still relatively little experimental evidence of the practical utility of the Microflown intensity probe, but it seems to be promising [25.17]. Figure 25.19 shows the results of sound power measurements with a Microflown intensity probe in comparison with similar results made with a Brüel & Kjær *p–p* sound intensity probe.

A variant of the *p–u* method, the *surface intensity method*, combines a pressure microphone with a transducer that measures the vibrational displacement, velocity or acceleration of a solid surface, for example with an accelerometer or a laser vibrometer [25.53–55]; see Fig. 25.20. Obviously, this method can only give the normal component of the sound intensity near vibrating surfaces. A disadvantage of the surface intensity method is that sound fields near complex sources are often very

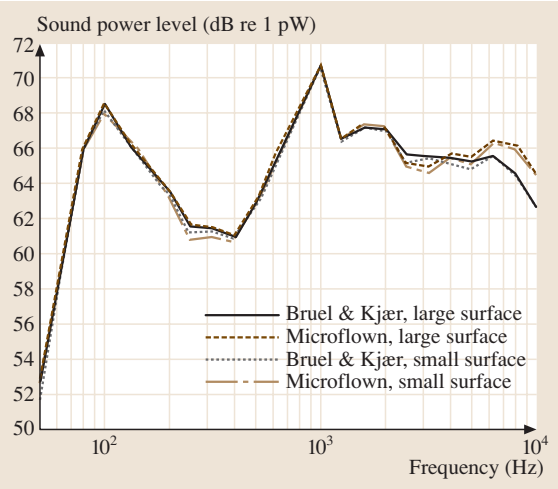


Fig. 25.19 Sound power of a source measured using a *p–u* intensity probe produced by Microflown and *p–p* intensity probe produced by Brüel & Kjær. Brüel & Kjær probe on large measurement surface (*solid line*); Microflown probe on large measurement surface (*dashed line*); Microflown probe on small measurement surface (*dotted line*) (After [25.17])

complicated, which makes it necessary to measure at many points.

Sources of Error in Measurement of Sound Intensity with *p–u* Measurement Systems

Evidently, some of the limitations of any *p–u* intensity probe must depend on the particulars of the particle velocity transducer. However, some general problems are described in the following.

Phase Mismatch

Irrespective of the measurement principle used in determining the particle velocity there is one fundamental problem: the pressure and the particle velocity transducer will invariably have different phase responses. One must compensate for this *p–u* phase mismatch, otherwise the result may well be meaningless. In fact even a small residual *p–u* mismatch error can have serious consequences under certain conditions. This can be seen by introducing such a small phase error, φ_{ue}, in (25.31). The result is

$$\begin{aligned}\hat{I}_r &= 1/2\,\mathrm{Re}\left(pu_r^*\,\mathrm{e}^{-\mathrm{i}\varphi_{ue}}\right)\\ &= \mathrm{Re}\left[(I_r+\mathrm{i}J_r)\,(\cos\varphi_{ue}-\mathrm{i}\sin\varphi_{ue})\right]\\ &\simeq I_r+\varphi_{ue}J_r\,,\end{aligned}\qquad (25.33)$$

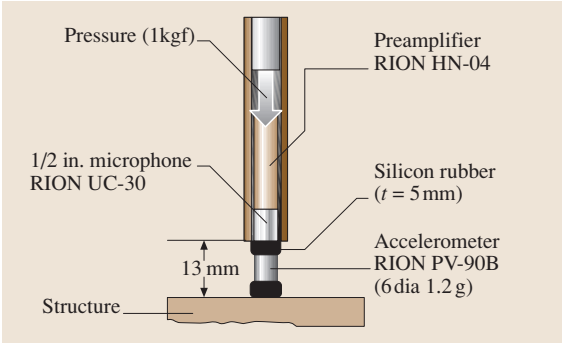


Fig. 25.20 Hand-held probe for surface intensity measurement (After [25.53])

where J_r is the reactive intensity, cf. (25.12). Equation (25.33) demonstrates that even a small uncompensated *p–u* phase mismatch error will give rise to a significant bias error when $J_r \gg I_r$. On the other hand it also shows that substantial *p–u* phase errors can be tolerated if $J_r \ll I_r$. For example, even a phase mismatch of 35° gives a bias error of less than 1 dB under such conditions. In other words, phase calibration is critical when measurements are carried out under near-field conditions, but not at all critical if the measurements are carried out in the far field of a source. The *reactivity* (the ratio of the reactive to the active intensity) indicates whether this source of error is of concern or not.

Whereas phase-mismatching of a *p–p* sound intensity measurement system can in principle be eliminated simply by reversing the probe and measuring again, it can be seen from (25.33) that reversing a *p–u* probe simply changes the sign of the result, including the bias error. In other words, probe reversal does not provide any new information.

The global version of (25.33) is found by integrating over a surface that encloses a source,

$$\begin{aligned}\hat{P}_a &= \int_S \mathrm{Re}\left[(\boldsymbol{I}+\mathrm{i}\boldsymbol{J})\,(\cos\varphi_{ue}-\mathrm{i}\sin\varphi_{ue})\right]\cdot\mathrm{d}\boldsymbol{S}\\ &\simeq P_a+\varphi_{ue}\int_S \boldsymbol{J}\cdot\mathrm{d}\boldsymbol{S}\\ &= P_a\left(1+\varphi_{ue}\frac{\int_S \boldsymbol{J}\cdot\mathrm{d}\boldsymbol{S}}{\int_S \boldsymbol{I}\cdot\mathrm{d}\boldsymbol{S}}\right)\\ &= P_a\left(1-\varphi_{ue}\frac{\int_S \boldsymbol{J}\cdot\mathrm{d}\boldsymbol{S}}{\int_S \hat{\boldsymbol{I}}\cdot\mathrm{d}\boldsymbol{S}}\right)^{-1}\,,\end{aligned}\qquad (25.34)$$

and this shows that uncompensated p–u phase mismatch is a potential source of error when the reactivity (which in the global case is the ratio of the surface integral of the reactive intensity to the surface integral of the active intensity) is large. This will typically occur at low frequencies when the measurement surface is close to the source. Thus the reactivity is an important error indicator for p–u probes [25.17]. In contrast the pressure-intensity index is not relevant for p–u probes.

Sources outside the measurement surface do not in general increase the reactivity, and thus they do not in general increase the error due to p–u phase mismatch.

Other Sources of Error

Airflow, and in particular unsteady flow, is a more serious problem for p–u than for p–p sound intensity measurement systems, irrespective of the particulars of the particle velocity transducer, since the resulting velocity cannot be distinguished from the velocity associated with the sound waves. Windscreens of porous foam reduce the problem.

Calibration of p–u Sound Intensity Measurement Systems

Calibration of p–u sound intensity measurement systems involves exposing the probe to a sound field with a known relation between the pressure and the particle velocity, for example a plane propagating wave, a simple spherical wave or a standing wave [25.15, 16]. One cannot calibrate a particle velocity transducer in a coupler. There are no standardized calibration procedures and no standards for testing such instruments. However, recent experimental results seem to indicate the possibility of calibrating the particle velocity channel of the Microflown intensity probe in the far field of a loudspeaker in an anechoic room, in the near field of a very small source (sound emitted from a small hole in a plane or spherical baffle), and in a rigidly terminated standing wave tube [25.17, 56].

25.3.3 Sound Field Indicators

A sound field indicator may be defined as a normalized, energy-related quantity that describes a local or global property of the sound field [25.39]. The pressure-intensity index defined by (25.29) is an example. The concept of sound field indicators is closely related to sound intensity. The idea is that useful information about the nature of the sound field might be derived from the signals from an intensity probe. The purpose can be to derive information that may be helpful in interpreting experimental data, with a view, for example, to improving measurement accuracy in intensity-based sound power estimation by choosing another measurement surface, by shielding the surface from extraneous sources, etc. The international standards on sound power determination using sound intensity [25.24–26] prescribe initial measurements of a number of indicators and specify corrective actions on the basis of the values of these quantities. The corresponding ANSI standard [25.27] is more pragmatic; no less than 26 indicators are described, but their use is optional and it is left to the user to interpret the data and decide what to do.

It is clear from the considerations in Sect. 25.3.1 that the (global) pressure-intensity index reflects the amount of extraneous noise in sound power measurements and, combined with the pressure-residual intensity index of a p–p sound intensity measurement system, makes it possible to predict the bias error due to p–p phase mismatch. Likewise, the considerations in Sect. 25.3.2 show that the reactivity reflects whether the measurement takes place in the near field of the source under test or not and, combined with knowledge about the residual phase mismatch of a p–u sound intensity measurement system, makes it possible to predict the bias error due to the mismatch. In comparison, most of the many quantities suggested in [25.27] are, as shown in [25.57], difficult to interpret and only vaguely related to the measurement accuracy.

25.4 Applications of Sound Intensity

Some of the most important practical applications of sound intensity measurements are now briefly discussed. In view of the relative lack of experimental evidence of the performance of p–u sound intensity measurement systems it is assumed in the following that p–p measurement systems are used unless otherwise mentioned.

25.4.1 Noise Source Identification

A noise reduction project usually starts with the identification and ranking of noise sources and transmission paths. Before sound intensity measurement systems became available this was often a difficult task, but now

Amazon EX1014 Page 1069

it is relatively straightforward since intensity measurements make it possible to determine the sound power contribution of the various components separately. Plots of the sound intensity normal to a measurement surface can be used in locating noise sources. Figure 25.21 shows the results of 3-D sound intensity measurements near a chain saw, and Fig. 25.22 shows an example of intensity measurements near a ship window. It should be mentioned, though, that sound intensity measurement can give misleading results; for example, the intensity vector will point to a position between two uncorrelated sources where no source actually exists.

Visualization of sound fields contributes to our understanding of the sound radiation of complicated sources, and sound intensity is more suitable for visualizing sound fields than sound pressure, which is a scalar. Figure 25.23 shows a map of the sound intensity in the sound field generated by a rectangular plate driven in a certain mode, measured with a microphone array using near-field acoustic holography. It is apparent that the generated sound field is fairly complicated. Note in particular the recirculation of sound energy; a region of the plate acts as a sink. This phe-

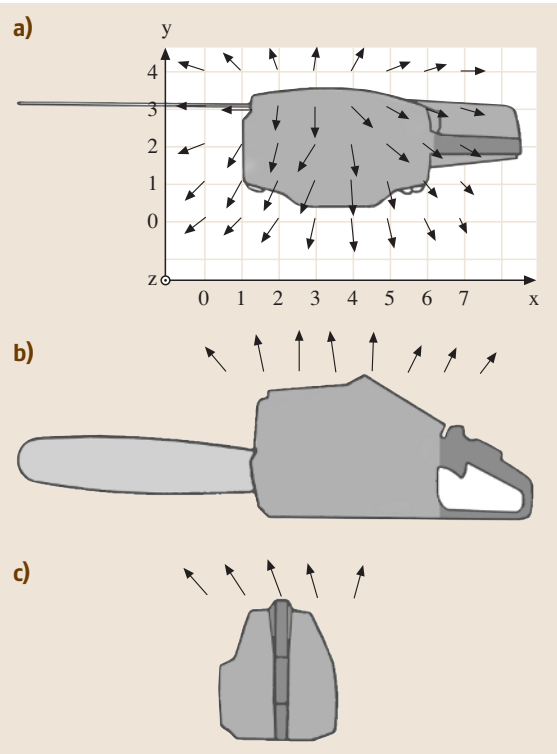


Fig. 25.21a–c Noise radiation from a chain saw in the 1600 Hz one-third octave band. **(a)** Sound intensity vector in the x–y plane; **(b)** sound intensity vector in the x–z plane; **(c)** sound intensity vector in the y–z plane (After [25.58])

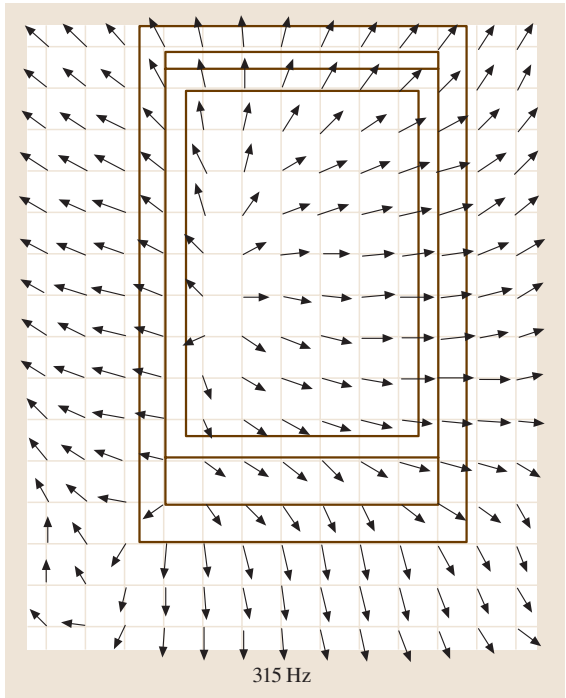


Fig. 25.22 Sound intensity distribution (tangential component) near a single cabin window (After [25.59])

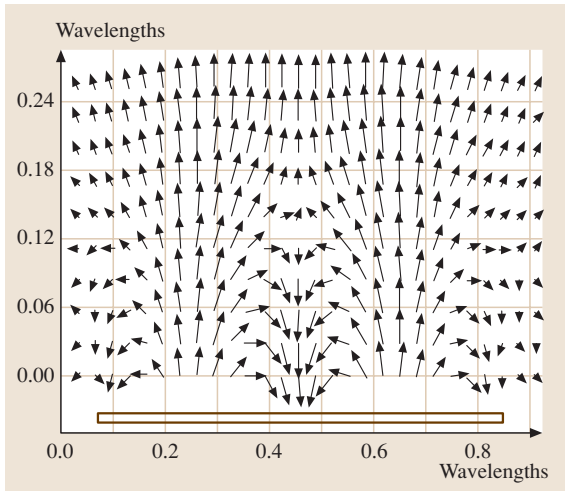


Fig. 25.23 Intensity vector map of the sound field generated by a rectangular plate excited in its (4, 2) mode (After [25.60])

nomenon is typical of vibrating panels of low radiation efficiency and demonstrates that spatial averaging of the sound intensity very near such sources is problematic. The circulation of sound energy, which implies that some regions act as sources without actually radiating to the far field, has led Williams to introduce the concept of *supersonic intensity*, which is the part of the sound intensity associated with wavenumber components within the *radiation circle*, in other words, the part of the intensity associated with radiation to the far field [25.61]. One cannot determine the supersonic intensity with an ordinary sound intensity probe, though; wavenumber processing of near-field holographic data is require.

25.4.2 Sound Power Determination

One of the most important applications of sound intensity measurement is the determination of the sound power of operating machinery in situ. Sound power determination using intensity measurements is based on (25.7), which shows that the sound power of a source is given by the integral of the normal component of the intensity over a surface that encloses the source, also in the presence of other sources outside the measurement surface. The analysis of errors and limitations presented in Sect. 25.3.1 leads to the conclusion that the sound intensity method is suitable for determining the sound power of stationary sources in stationary background noise provided that the pressure-intensity index is within the dynamic capability of the measurement system. On the other hand, the method is *not* suitable in nonstationary background noise (because the sound field will change during the measurement); it cannot be used for determining the sound power of very weak sources of low-frequency noise (because of large random errors caused by electrical noise in the microphone signals); and the absorption of the source under test should be negligible compared with the total absorption in the room where the measurement takes place (otherwise the sound power will be underestimated because the measurement gives the *net* sound power).

The surface integral can be approximated either by sampling at discrete points or by scanning manually or with a robot over the surface. With the scanning approach, the intensity probe is moved continuously over the measurement surface. A typical scanning path is shown in Fig. 25.24. The scanning procedure, which was introduced by Chung in the late 1970s on a purely empirical basis, was regarded with much skepticism for more than a decade [25.63], but is now generally regarded as more accurate and very much faster and more convenient than the procedure based on fixed points [25.62, 64, 65]. A moderate scanning rate, say 0.5 m/s, and a reasonable scan line density should be used, say 5 cm between adjacent lines if the surface is very close to the source, 20 cm if it is further away. However, whereas it may be possible to use the method based on discrete positions if the source is operating in cycles (simply by measuring over a full cycle at each position) one cannot use the scanning method under such conditions; both the source under test and possible extraneous noise sources must be perfectly stationary.

Usually the measurement surface is divided into a number of segments that are convenient to scan. The pressure-intensity index of each segment and the accuracy of each partial sound power estimate depends on whether (25.29) is satisfied or not, but it follows from (25.30) that it is the global pressure-intensity index associated with the entire measurement surface that determines the accuracy of the estimate of the (total) radiated sound power. It may be impossible to satisfy (25.29) on a certain segment, for example because the net sound power passing through the segment takes a very small value because of extraneous noise, but if the global criterion is satisfied then the total sound power estimate will nevertheless be accurate.

Theoretical considerations seem to indicate the existence of an optimum measurement surface that minimizes measurement errors [25.66]. In practice one uses a surface with a simple shape at some distance, say 25–50 cm, from the source. If there is a strong reverberant field or significant ambient noise from other sources, the measurement surface should be chosen to be somewhat closer to the source under study. One particular problem is that one might be tempted to forget to close a measurement surface that is very close to, say, a panel or a window by measuring only the component of the

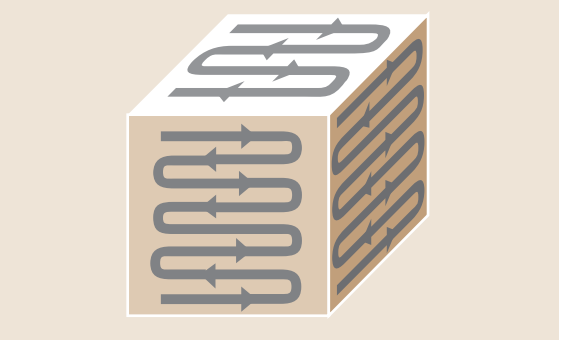


Fig. 25.24 Typical scanning path on a measurement surface (After [25.62])

intensity normal to the source. This can lead to serious errors in cases where the panel radiates very weakly, because the radiation will be nearly parallel to the source plane.

The three ISO standards for sound power determination using intensity measurement have been designed for sources of noise in their normal operating conditions, which may be very unfavorable [25.24–26]. In order to ensure accurate results under such general conditions the user must determine a number of field indicators and check whether various conditions are satisfied, as mentioned in Sect. 25.3.3. Fahy, who was the convener of the working group that developed ISO 9614-1 and 9614-2, has described the rationale, background, and principles of the procedures specified in these standards [25.65].

25.4.3 Radiation Efficiency of Structures

The radiation efficiency of a structure is a measure of how effectively it radiates sound. This dimensionless quantity is defined as

$$\sigma = \frac{P_a}{\rho c \left\langle v_n^2 \right\rangle S}\,, \qquad (25.35)$$

where P_a is the sound power radiated by the structure, S is its surface area, v_n is normal velocity of the surface, and the angular brackets indicate averaging over time as well as space. Comparing with (25.16) shows the close relation between this quantity and the real part of the specific impedance, which can be measured directly with a sound intensity probe if it can be placed sufficiently close to the structure [25.68]. The Microflown p–u probe has an advantage in this respect. However, measurements very near weak radiators of sound are difficult because of the circulating energy flow mentioned in Sect. 25.4.1.

25.4.4 Transmission Loss of Structures and Partitions

The transmission loss of a partition is the ratio of incident to transmitted sound power in logarithmic form. The traditional method of measuring this quantity requires a transmission suite consisting of two vibration-isolated reverberation rooms. The sound power incident on the partition under test in the source room is deduced from the spatial average of the mean square sound pressure in the room on the assumption that the sound field is diffuse, and the transmitted sound power is determined from a similar measurement in the receiving room where, in addition, the reverberation time must be deter-

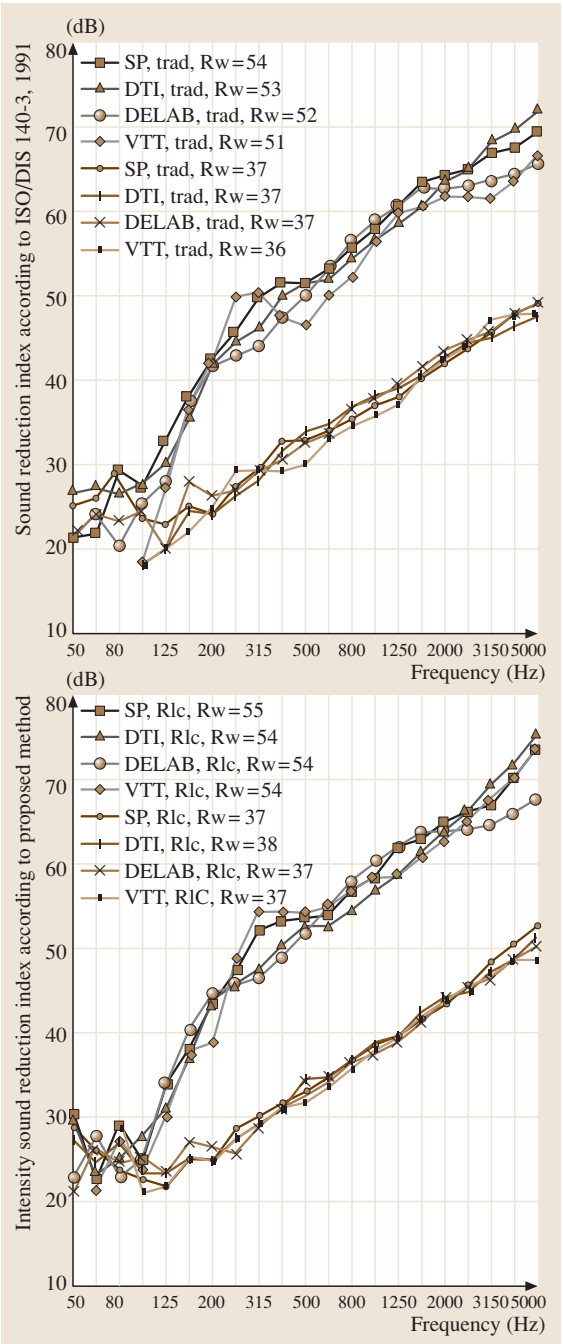


Fig. 25.25 Inter-laboratory comparison of measured transmission loss of a single metal leaf window (*lower curves*) and a double metal leaf window (*upper curves*). *Top panel*: Conventional method; *bottom panel*: intensity method (After [25.67])

mined. The sound intensity method makes it possible to measure the transmitted sound power directly. In contrast one cannot measure the incident sound power in the source room using sound intensity, since the method gives the *net* sound intensity. If the intensity method is used for determining the transmitted sound power it is not necessary that the sound field in the receiving room is diffuse, from which it follows that only one reverberation room is necessary. Thus sound intensity is suitable for field measurements of transmission loss. There are international standards both for laboratory and field measurements of transmission loss based on sound intensity [25.69, 70].

Figure 25.25 shows the results of a *round robin* investigation in which a single-leaf and a double-leaf construction were tested by four different laboratories using the conventional method and the intensity-based method. Apart from the fact that only one reverberation room is needed the main advantage of the intensity method is that it makes it possible to evaluate the transmission loss of individual parts of the partition. However, to be reliable each sound power measurement must obviously satisfy the condition expressed by (25.29). There are other sources of error than phase mismatch. If a significant part of the absorption in the receiving room is due to the partition under test then the net power is less than the transmitted power because a part of the transmitted sound energy is absorbed or retransmitted by the partition itself [25.71]. Under such conditions one must increase the absorption of the receiving room; otherwise the intensity method will overestimate the transmission loss because the transmitted sound power is underestimated. In contrast, the conventional method measures the transmitted sound power irrespective of the distribution of absorption in the receiving room.

Deviations between results determined using the traditional method and the intensity method led several authors to reanalyze the traditional method in the 1980s [25.72] and point out that the Waterhouse correction [25.73], well established in sound power determination using the reverberation room method [25.74], had been overlooked in the standards for conventional measurement of transmission loss. Recent results imply that the Waterhouse correction should be used not only for the receiving room but also for the source room [25.75].

25.4.5 Other Applications

The fact that the sound intensity level is considerably lower than the sound pressure level in a diffuse, reverberant sound field has led to the idea of replacing a measurement of the *emission sound pressure level* generated by machinery at the operator's position by a measurement of the sound intensity level, because the latter is less affected by diffuse background noise [25.76]. This method, which involves measuring three components of the intensity at a specified position near the source, has recently been standardized [25.77].

In principle, sound intensity may be used for measuring sound absorption in situ. As in measurement of transmission losses the incident sound power must be deduced from a spatial average of the mean square pressure in the room on the assumption that the sound field is diffuse, and the absorbed sound power is measured by integrating the normal component of the intensity over a surface that encloses the specimen under test [25.2]. In practice, however, this is one of the least successful applications of sound intensity, partly because of the assumption of diffuse sound incidence and partly because estimation errors in the absorbed power will be translated to relatively large fractional errors in the resulting absorption coefficients.

References

25.1 A.D. Pierce: *Acoustics: An Introduction to Its Physical Principles and Applications*, 2nd edn. (Acoustical Society of America, New York 1989)

25.2 F.J. Fahy: *Sound Intensity*, 2nd edn. (E & FN Spon, London 1995)

25.3 ISO: *ISO 3745 Acoustics – Determination of sound power levels of noise sources using sound pressure – Precision methods for anechoic and hemianechoic rooms* (ISO, Geneva 2003)

25.4 J.-C. Pascal: *Mesure de l'intensité active et réactive dans differents champs acoustiques, Proc. Rec. Devel. Acoust. Intens* (CETIM, Senlis 1981) pp. 11–19

25.5 J.A. Mann III, J. Tichy, A.J. Romano: Instantaneous and time-averaged energy transfer in acoustic fields, J. Acoust. Soc. Am. **82**, 17–30 (1987)

25.6 F. Jacobsen: Active and reactive, coherent and incoherent sound fields, J. Sound Vib. **130**, 493–507 (1989)

25.7 F. Jacobsen: A note on instantaneous and time-averaged active and reactive sound intensity, J. Sound Vib. **147**, 489–496 (1991)

25.8 P.J. Westervelt: Acoustical impedance in terms of energy functions, J. Acoust. Soc. Am. **23**, 347–348 (1951)

25.9 W. Maysenhölder: *The reactive intensity of general time-harmonic structure-borne sound fields. Proc. Fourth Int. Congr. Intens. Tech.* (CETIM, Senlis 1993) pp. 63–70

25.10 U. Kurze: Zur Entwicklung eines Gerätes für komplexe Schallfeldmessungen, Acustica **20**, 308–310 (1968)

25.11 J.C. Pascal, C. Carles: Systematic measurement errors with two microphone sound intensity meters, J. Sound Vib. **83**, 53–65 (1982)

25.12 R.C. Heyser: Instantaneous intensity. Preprint 2399, 81st Conv. Audio Eng. Soc. (1986)

25.13 M.P. Waser, M.J. Crocker: Introduction to the two-microphone cross-spectral method of determining sound intensity, Noise Control Eng. J. **22**, 76–85 (1984)

25.14 K.J. Bastyr, G.C. Lauchle, J.A. McConnell: Development of a velocity gradient underwater acoustic intensity sensor, J. Acoust. Soc. Am. **106**, 3178–3188 (1999)

25.15 H.-E. de Bree: The Microflown: An acoustic particle velocity sensor, Acoust. Australia **31**, 91–94 (2003)

25.16 R. Raangs, W.F. Druyvesteyn, H.E. de Bree: A low-cost intensity probe, J. Audio Eng. Soc. **51**, 344–357 (2003)

25.17 F. Jacobsen, H.-E. de Bree: A comparison of two different sound intensity measurement principles, J. Acoust. Soc. Am. **118**, 1510–1517 (2005)

25.18 IEC: *IEC (International Electrotechnical Commission) 1043 Electroacoustics – Instruments for the Measurement of Sound Intensity – Measurements with Pairs of Pressure Sensing Microphones* (IEC, Geneva 1993)

25.19 ANSI: *ANSI (American National Standards Institute) S1.9-1996 Instruments for the Measurement of Sound Intensity* (ANSI, Washington 1996)

25.20 J.Y. Chung: Cross-spectral method of measuring acoustic intensity without error caused by instrument phase mismatch, J. Acoust. Soc. Am. **64**, 1613–1616 (1978)

25.21 F.J. Fahy: Measurement of acoustic intensity using the cross-spectral density of two microphone signals, J. Acoust. Soc. Am. **62**, 1057–1059 (1977)

25.22 G. Rasmussen, M. Brock: *Acoustic intensity measurement probe, Proc. Rec. Devel. Acoust. Intens.* (CETIM, Senlis 1981) pp. 81–88

25.23 J. Pope: *Qualifying intensity measurements for sound power determination, Proc. Inter-Noise 89* (Int. Inst. Noise Control Eng., West Lafayette 1989) pp. 1041–1046

25.24 ISO: *International Organization for Standardization) 9614-1 Acoustics – Determination of Sound Power Levels of Noise Sources Using Sound Intensity – Part 1: Measurement at Discrete Points* (ISO, Geneva 1993)

25.25 ISO: *International Organization for Standardization) 9614-2 Acoustics – Determination of Sound Power Levels of Noise Sources Using Sound Intensity – Part 2: Measurement by Scanning* (ISO, Geneva 1996)

25.26 ISO: *International Organization for Standardization) 9614-3 Acoustics – Determination of Sound Power Levels of Noise Sources Using Sound Intensity – Part 3: Precision Method for Measurement by Scanning* (ISO, Geneva 2002)

25.27 ANSI: *ANSI (American National Standards Institute) S12.12-1992 Engineering Method for the Determination of Sound Power Levels of Noise Sources Using Sound Intensity* (ANSI, Washington 1992)

25.28 F. Jacobsen, V. Cutanda, P.M. Juhl: A numerical and experimental investigation of the performance of sound intensity probes at high frequencies, J. Acoust. Soc. Am. **103**, 953–961 (1998)

25.29 P. Juhl, F. Jacobsen: A note on measurement of sound pressure with intensity probes, J. Acoust. Soc. Am. **116**, 1614–1620 (2004)

25.30 S. Shirahatti, M.J. Crocker: Two-microphone finite difference approximation errors in the interference fields of point dipole sources, J. Acoust. Soc. Am. **92**, 258–267 (1992)

25.31 P.S. Watkinson, F.J. Fahy: Characteristics of microphone arrangements for sound intensity measurement, J. Sound Vib. **94**, 299–306 (1984)

25.32 S. Gade: Sound intensity (Theory), Brüel, Kjær Tech. Rev. **3**, 3–39 (1982)

25.33 Anonymous: *Product data, sound intensity pair – type 4197* (Brüel, Kjær, Nærum 2000)

25.34 E. Frederiksen, O. Schultz: Pressure microphones for intensity measurements with significantly improved phase properties, Brüel, Kjær Tech. Rev. **4**, 11–12 (1986)

25.35 F. Jacobsen: A simple and effective correction for phase mismatch in intensity probes, Appl. Acoust. **33**, 165–180 (1991)

25.36 S.J. Elliott: Errors in acoustic intensity measurements, J. Sound Vib. **78**, 439–445 (1981)

25.37 M. Ren, F. Jacobsen: Phase mismatch errors and related indicators in sound intensity measurement, J. Sound Vib. **149**, 341–347 (1991)

25.38 S. Gade: Validity of intensity measurements in partially diffuse sound field, Brüel, Kjær Tech. Rev. **4**, 3–31 (1985)

25.39 F. Jacobsen: Sound field indicators: Useful tools, Noise Control Eng. J. **35**, 37–46 (1990)

25.40 D.H. Munro, K.U. Ingard: On acoustic intensity measurements in the presence of mean flow, J. Acoust. Soc. Am. **65**, 1402–1406 (1979)

25.41 F. Jacobsen: *Intensity measurements in the presence of moderate airflow, Proc. Inter-Noise 94* (Int. Inst. Noise Control Eng., Yokohama 1994) pp. 1737–1742

25.42 F. Jacobsen: A note on measurement of sound intensity with windscreened probes, Appl. Acoust. **42**, 41–53 (1994)

25.43 P. Juhl, F. Jacobsen: A numerical investigation of the influence of windscreens on measurement of

Amazon EX1014 Page 1074

sound intensity, J. Acoust. Soc. Am. **119**, 937–942 (2006)
25.44 A.F. Seybert: Statistical errors in acoustic intensity measurements, J. Sound Vib. **75**, 519–526 (1981)
25.45 O. Dyrlund: A note on statistical errors in acoustic intensity measurements, J. Sound Vib. **90**, 585–589 (1983)
25.46 F. Jacobsen: Random errors in sound intensity estimation, J. Sound Vib. **128**, 247–257 (1989)
25.47 F. Jacobsen: Random errors in sound power determination based on intensity measurement, J. Sound Vib. **131**, 475–487 (1989)
25.48 F. Jacobsen: Sound intensity measurement at low levels, J. Sound Vib. **166**, 195–207 (1993)
25.49 F. Jacobsen, E.S. Olsen: Testing sound intensity probes in interference fields, Acustica **80**, 115–126 (1994)
25.50 E. Frederiksen: *BCR-report, Sound intensity measurement instruments. Free-field intensity sensitivity calibration and standing wave testing* (Brüel, Kjær, Nærum 1992)
25.51 F. Jacobsen, E.S. Olsen: The influence of microphone vents on the performance of sound intensity probes, Appl. Acoust. **41**, 25–45 (1993)
25.52 S.A. Nordby, O.H. Bjor: *Measurement of sound intensity by use of a dual channel real-time analyzer and a special sound intensity microphone, Proc. Inter-Noise 84* (Int. Inst. Noise Control Eng., Honolulu 1984) pp. 1107–1110
25.53 J.A. Macadam: The measurement of sound radiation from room surfaces in lightweight buildings, Appl. Acoust. **9**, 103–118 (1976)
25.54 M.C. McGary, M.J. Crocker: Surface intensity measurements on a diesel engine, Noise Control Eng. J. **16**, 27–36 (1981)
25.55 Y. Hirao, K. Yamamoto, K. Nakamura, S. Ueha: Development of a hand-held sensor probe for detection of sound components radiated from a specific device using surface intensity measurements, Appl. Acoust. **65**, 719–735 (2004)
25.56 F. Jacobsen, V. Jaud: A note on the calibration of pressure-velocity sound intensity probes, J. Acoust. Soc. Am. **120**, 830–837 (2006)
25.57 F. Jacobsen: *A critical examination of some of the field indicators proposed in connection with sound power determination using the intensity technique, Proc. Fourth Internat. Congr. Sound Vib.* (IIAV, St. Petersburg 1996) pp. 1889–1896
25.58 T. Astrup: Measurement of sound power using the acoustic intensity method –A consultant's viewpoint, Appl. Acoust. **50**, 111–123 (1997)
25.59 S. Weyna: The application of sound intensity technique in research on noise abatement in ships, Appl. Acoust. **44**, 341–351 (1995)
25.60 E.G. Williams, J.D. Maynard: *Intensity vector field mapping with nearfield holography, Proc. Rec. Devel. Acoust. Intens* (CETIM, Senlis 1981) pp. 31–36
25.61 E.G. Williams: Supersonic acoustic intensity on planar sources, J. Acoust. Soc. Am. **104**, 2845–2850 (1998)
25.62 U.S. Shirahatti, M.J. Crocker: Studies of the sound power estimation of a noise source using the two-microphone sound intensity technique, Acustica **80**, 378–387 (1994)
25.63 M.J. Crocker: Sound power determination from sound intensity – To scan or not to scan, Noise Contr. Eng. J. **27**, 67 (1986)
25.64 O.K.Ø. Pettersen, H. Olsen: On spatial sampling using the scanning intensity technique, Appl. Acoust. **50**, 141–153 (1997)
25.65 F.J. Fahy: International standards for the determination of sound power levels of sources using sound intensity measurement: An exposition, Appl. Acoust. **50**, 97–109 (1997)
25.66 F. Jacobsen: Sound power determination using the intensity technique in the presence of diffuse background noise, J. Sound Vib. **159**, 353–371 (1992)
25.67 H.G. Jonasson: Sound intensity and sound reduction index, Appl. Acoust. **40**, 281–293 (1993)
25.68 B. Forssen, M.J. Crocker: Estimation of acoustic velocity, surface velocity, and radiation efficiency by use of the two-microphone technique, J. Acoust. Soc. Am. **73**, 1047–1053 (1983)
25.69 ISO: *ISO 15186-1 Acoustics – Measurement of sound insulation in buildings and of building elements using sound intensity – Part 1: Laboratory measurements* (ISO, Geneva 2000)
25.70 ISO: *ISO 15186-2 Acoustics – Measurement of sound insulation in buildings and of building elements using sound intensity – Part 2: Field measurements* (ISO, Geneva 2003)
25.71 J. Roland, C. Martin, M. Villot: *Room to room transmission: What is really measured by intensity? Proc. 2nd Intern. Congr. Acoust. Intens.* (CETIM, Senlis 1985) pp. 539–546
25.72 E. Halliwell, A.C.C. Warnock: Sound transmission loss: Comparison of conventional techniques with sound intensity techniques, J. Acoust. Soc. Am. **77**, 2094–2103 (1985)
25.73 R.V. Waterhouse: Interference patters in reverberant sound fields, J. Acoust. Soc. Am. **27**, 247–258 (1955)
25.74 ISO: *ISO 3741:1999 Acoustics – Determination of sound power levels of noise sources using sound pressure – Precision methods for reverberation rooms* (ISO, Geneva 1999)
25.75 A. Ismai: On the application of the Waterhouse correction in sound insulation measurement. In: *Proc. Inter-Noise 2006* (Int. Inst. Noise Control. Eng., Honolulu 2006)
25.76 H.G. Jonasson: *Determination of emission sound pressure level and sound power level in situ, SP Rep. 18* (Swedish National Testing and Research Institute, Borås 1999)

Amazon EX1014 Page 1075

25.77 ISO: *ISO 11205 Acoustics – Noise emitted by machinery and equipment – Engineering method for the determination of emission sound pressure levels in situ at the work station and at other specified positions using sound intensity* (ISO, Geneva 2003)

Amazon EX1014 Page 1076

26. Acoustic Holography

One of the subtle problems that make noise control difficult for engineers is the invisibility of noise or sound. A visual image of noise often helps to determine an appropriate means for noise control. There have been many attempts to fulfill this rather challenging objective. Theoretical (or numerical) means for visualizing the sound field have been attempted, and as a result, a great deal of progress has been made. However, most of these numerical methods are not quite ready for practical applications to noise control problems. In the meantime, rapid progress with instrumentation has made it possible to use multiple microphones and fast signal-processing systems. Although these systems are not perfect, they are useful. A state-of-the-art system has recently become available, but it still has many problematic issues; for example, how can one implement the visualized noise field. The constructed noise or sound picture always consists of bias and random errors, and consequently, it is often difficult to determine the origin of the noise and the spatial distribution of the noise field. Section 26.2 of this chapter introduces a brief history, which is associated with "sound visualization," acoustic source identification methods and what has been accomplished with a line or surface array. Section 26.2.3 introduces difficulties and recent studies, including de-Dopplerization and de-reverberation methods, both essential for visualizing a moving noise source, such as occurs for cars or trains. This section also addresses what produces ambiguity in realizing real sound sources in a room or closed space. Another major issue associated with sound/noise visualization is whether or not we can distinguish between mutual dependencies of noise in space (Sect. 26.2.4); for example, we are asked to answer the question, "Can we see two birds singing or one bird with two beaks?"

26.1 **The Methodology of Acoustic Source Identification** 1077

26.2 **Acoustic Holography: Measurement, Prediction and Analysis** 1079
26.2.1 Introduction and Problem Definitions 1079
26.2.2 Prediction Process 1080
26.2.3 Measurement 1083
26.2.4 Analysis of Acoustic Holography .. 1089

26.3 **Summary** 1092

26.A **Mathematical Derivations of Three Acoustic Holography Methods and Their Discrete Forms** 1092
26.A.1 Planar Acoustic Holography 1092
26.A.2 Cylindrical Acoustic Holography ... 1094
26.A.3 Spherical Acoustic Holography 1095

References 1095

26.1 The Methodology of Acoustic Source Identification

The famous article written by *Kac* [26.1], "Can one hear the shape of the drum?" clearly addresses the essence of the inverse problem. It can be regarded as an attempt to obtain what is *not* available, using what *is* available, using the example of the relationship between sound generation by membrane vibration and its reception in space. One can find many other examples of inverse problems [26.2–8]. Often, in the inverse problem, it is hard to predict or describe data that are not measured because the available data are insufficient. This circumstance is commonly referred to as an *ill-posed problem* in the literature (for examples, see [26.1–19]). Figure 26.1 demonstrates what might happen in practice; the prediction depends on how well the basis function (the elephants or dogs in Fig. 26.1) mimics what happens in reality. When we try to see the shape of noise/sound sources, how well we see the shape of a noise source completely depends on this basis function, because we predict what is not available by using this selected basis function.

One of the common methods of classifying methods used in noise/sound source identification, is by the type of basis function. According to this classification,

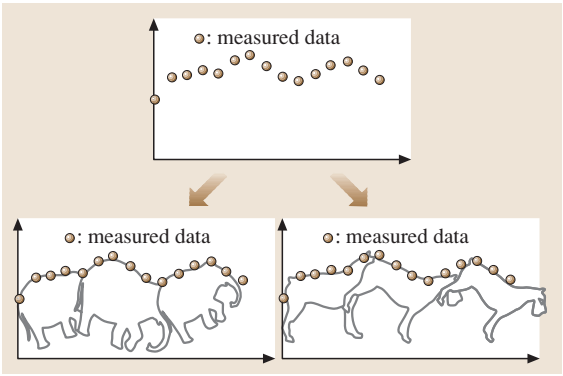


Fig. 26.1 The inverse problem and basis function. Are the measured data the parts of elephants or dogs?

one approach is the nonparametric method, which uses basis functions that do not model the signal. In other words, the basis functions do not map the unmeasured sound field; all orthogonal functions fall into this category. One of the typical methods of this kind uses Fourier transforms. Acoustic holography uses this type of basis function, mapping the sound field of interest with regard to every measured frequency; it therefore sees the sound field in the frequency domain. In fact, the ideas of acoustic holography originated from optics [26.20–30]. Acoustic holography was simply extended or modified from the basic idea of optical holography. Near-field acoustic holography [26.31,32] has been recognized as a very useful means of predicting the true appearance of the source Fig. 26.2. (The near-field effect on resolution was first introduced in the field of microwaves [26.33].) The basis of this method is to include or measure exponentially decaying waves as they propagate from the sound source so that the sources can be completely reconstructed.

Another class of approaches are based on the parametric method, which derives its name from the fact that the signal is modeled using certain parameters. In other words, the basis function is chosen depending upon the prediction of the sound source. A typical method of this kind is the so-called *beam-forming method*. Different types of basis functions can be chosen for this method, entirely depending on the sound field that the basis function is trying to map [26.34,35]. In Fig. 26.1, we can select either the elephants or dogs (or another choice), depending on what we want to predict. This type of mapping gives information about the source location. As illustrated in Fig. 26.1, the basis function maps the signal by changing its parameter; in the case of forming a plane-wave beam, the incident angle of the plane wave can be regarded as a parameter. The main issues that have been discussed for this kind of mapping method are directly related to the structure of the correlation matrix that comes from the measured acoustic pressure vector and its complex conjugate (see Fig. 26.3 for the details). In this method, each scan vector has a multiplicative parameter; for the plane wave in Fig. 26.3 it is the angle of arrival. The correlation matrix is given as illustrated in Fig. 26.3. The scan vector is a basis function in this case. As one can see immediately, this problem is directly related

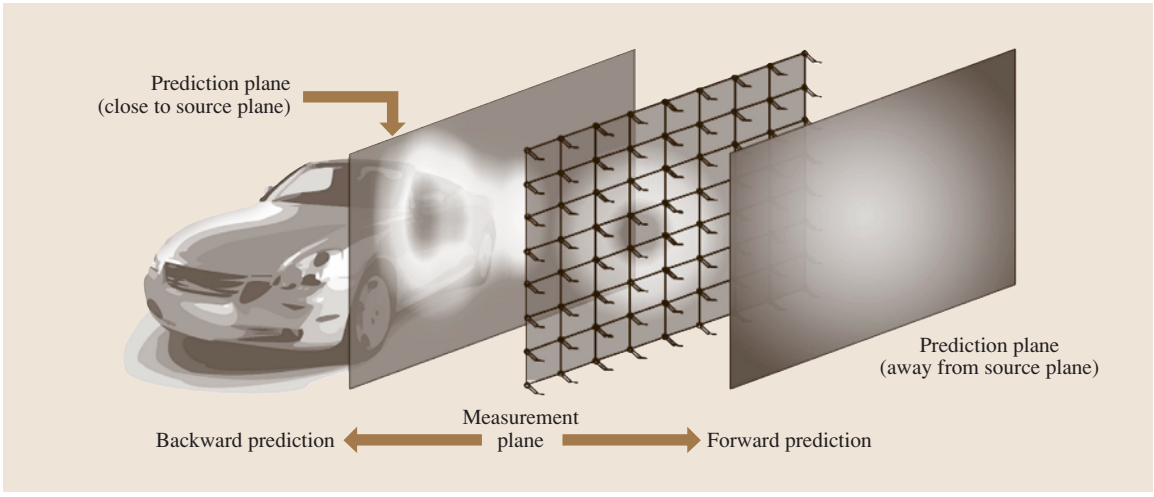


Fig. 26.2 Illustration of acoustic holography. Near-field acoustic holography measures evanescent waves on the measurement plane. The measurement plane is always finite, i.e. there is always a finite aperture. Therefore, we only get limited data)

Amazon EX1014 Page 1078

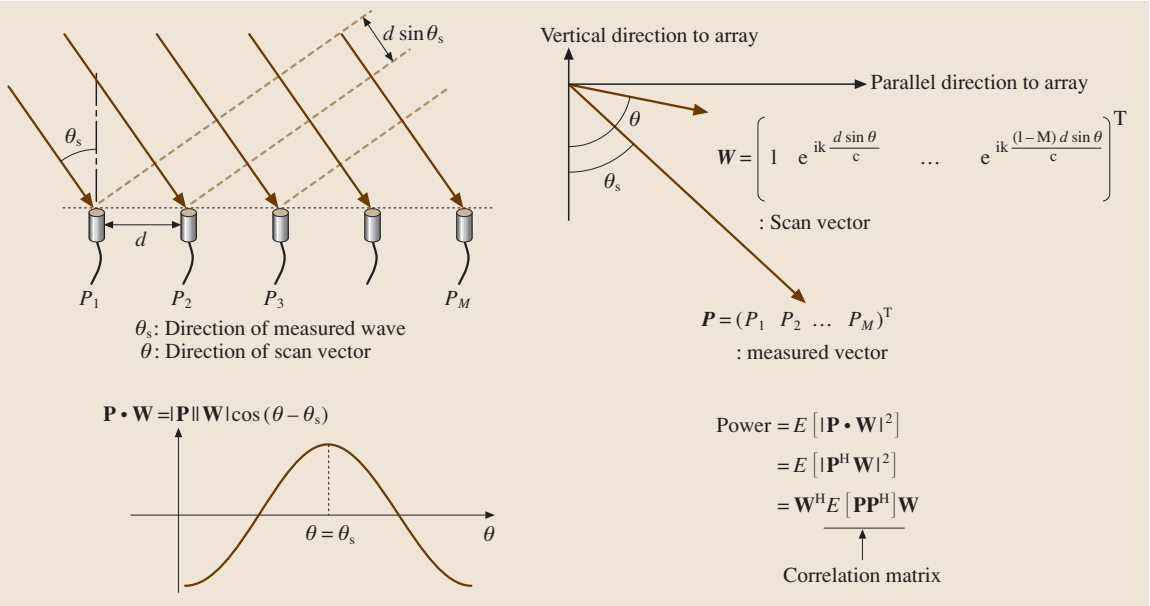


Fig. 26.3 The beam-forming method

to the structure of the correlation matrix and the basis function used. The signal-to-noise (S/N) ratio of the measured correlation matrix determines the effectiveness of the estimation. There have been many attempts to improve the estimator's performance with regard to the signal-to-noise ratio [26.35,36]. These methods have mainly been developed for applications in the radar and underwater communities [26.37]. This technique has also been applied to a noise source location finding problem; high-speed-train noise source estimation [26.38–40] is one such example. Various shapes of arrays have been tried to improve the spatial resolution [26.41–43]. However, it is obvious that these methods cannot sense the shape of the sound or noise source; they only provide its location. Therefore, we will not discuss the beam-forming method in this chapter. In the next section, the problems that we have discussed will be defined.

26.2 Acoustic Holography: Measurement, Prediction and Analysis

26.2.1 Introduction and Problem Definitions

Acoustic holography consists of three components: measurement, which consists of measuring the sound pressure on the hologram plane, prediction of the acoustic variables, including the velocity distribution, on the plane of interest, and analysis of the holographic reconstruction. This last component was not recognized as important as the others in the past. However, it yields the real meaning of the sound picture: visualization.

The issues associated with measurement are all related to the hologram measurement configuration; we measure the sound pressure at discrete measurement points over a finite measurement area (finite aperture), as illustrated in Fig. 26.2. References [26.44–52] explain the necessary steps to avoid spatial aliasing, wrap-around errors, and the effect of including evanescent waves on the resolution (near-field acoustic holography). If sensors are incorrectly located on the hologram surface, errors result in the prediction results. Similar errors can be produced when there is a magnitude and phase mismatch between sensors. This is well summarized in [26.53]. There have been many attempts to reduce the aperture effect. One method is to extrapolate the pressure data based on the measurements taken [26.50,52]. Another method allows the measurement of sound pressure in a sequence and interprets the measured sound pressures with respect to reference signals, assuming that the measured sound pressure field is stationary dur-

Amazon EX1014 Page 1079

ing the measurement and the number of independent sources is smaller than the number of reference microphones [26.54–61]. Another method allows scanning or moving of the microphone array, thereby extending the aperture size as much as possible [26.62–65]. This also allows one to measure the sound pressure generated by moving sound sources, such as a vehicle's exterior noise.

The prediction problem is rather well defined and relatively straightforward. Basically, the solution of the acoustic wave equation usually results in the sound pressure distribution on the measurement plane. Prediction can be attempted using a Green's function, an example of which may be found in the Kirchhoff–Helmholtz integral equation. It is noteworthy, however, that the prediction depends on the shape of the measurement and prediction surfaces, and also on the presence of sound reflections [26.54, 66–87].

The acoustic holography analysis problem was introduced rather recently. As mentioned earlier in this section, this is one of the essential issues connected to the general inverse problem. One basic question is whether what we see and imagine is related to what happens in reality. There are two different sound/noise sources, one of which is really radiating the sound, and the another that is reflecting the sound. The former is often called *active sound/noise*, while the latter is called *passive sound/noise*. This is an important practical concept for establishing noise control strategies; we want to eliminate the active noise source. Another concern is whether the sources are independently or dependently correlated (Fig. 26.23). The concept of an independent and dependent source has to be addressed properly to understand the issues.

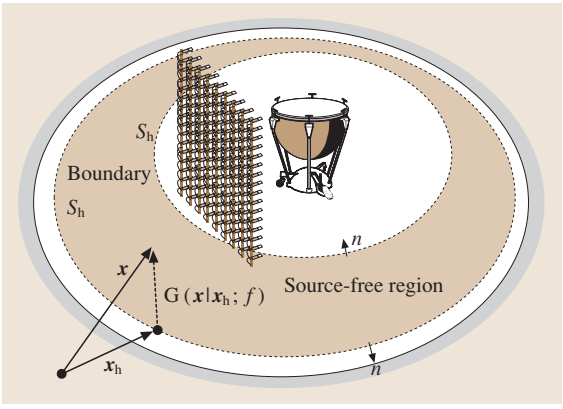


Fig. 26.4 The geometry and nomenclature for the Kirchhoff–Helmholtz integral (26.1)

26.2.2 Prediction Process

The prediction process is related to how we predict the unmeasured sound pressure or other acoustic variables based on the measured sound pressure information. The following equation relates the unmeasured and measured pressure:

$$P(\boldsymbol{x};\, f) = \int_{S_h} \left[G(\boldsymbol{x}|\boldsymbol{x}_h;\, f)\, \frac{\partial P}{\partial n}\bigg|_{(\boldsymbol{x}=\boldsymbol{x}_h;\, f)} - P(\boldsymbol{x}_h;\, f) \frac{\partial G(\boldsymbol{x}|\boldsymbol{x}_h;\, f)}{\partial n} \right] \mathrm{d}S_h \,. \qquad (26.1)$$

Equation (26.1) is the well-known Kirchhoff–Helmholtz integral equation, where $G(\boldsymbol{x}|\boldsymbol{x}_h;\, f)$ is the free-space Green's function. This equation essentially says that we can predict the sound pressure anywhere if we know the sound pressures and velocities on the boundary Fig. 26.4. However, it is noteworthy that measuring the velocity on the boundary is more difficult than measuring the sound pressure. This rather practical difficulty can be solved by introducing a Green's function that satisfies the Dirichlet boundary condition: $G_D(\boldsymbol{x}|\boldsymbol{x}_h;\, f)$. Then, (26.1) becomes

$$P(\boldsymbol{x}; f) = \int_{S_h} \left[-P(\boldsymbol{x}_h;\, f) \frac{\partial G_D(\boldsymbol{x}|\boldsymbol{x}_h; f)}{\partial n} \right] \mathrm{d}S_h \,. \qquad (26.2)$$

This equation allows us to predict the sound pressure on any surface of interest. It is noteworthy that we can choose a Green's function as long as it satisfies the

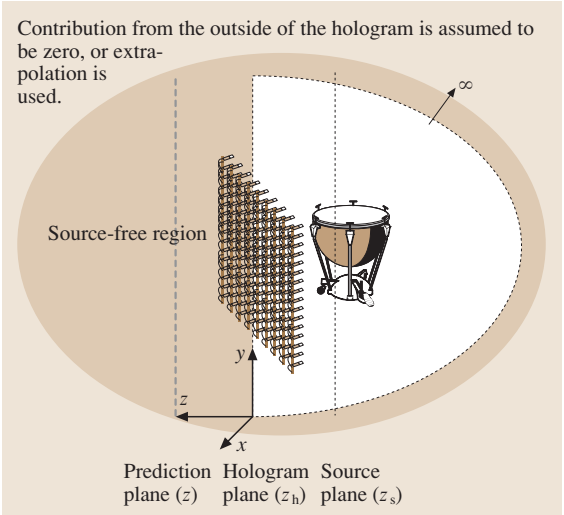


Fig. 26.5 Illustration of the planar acoustic holography

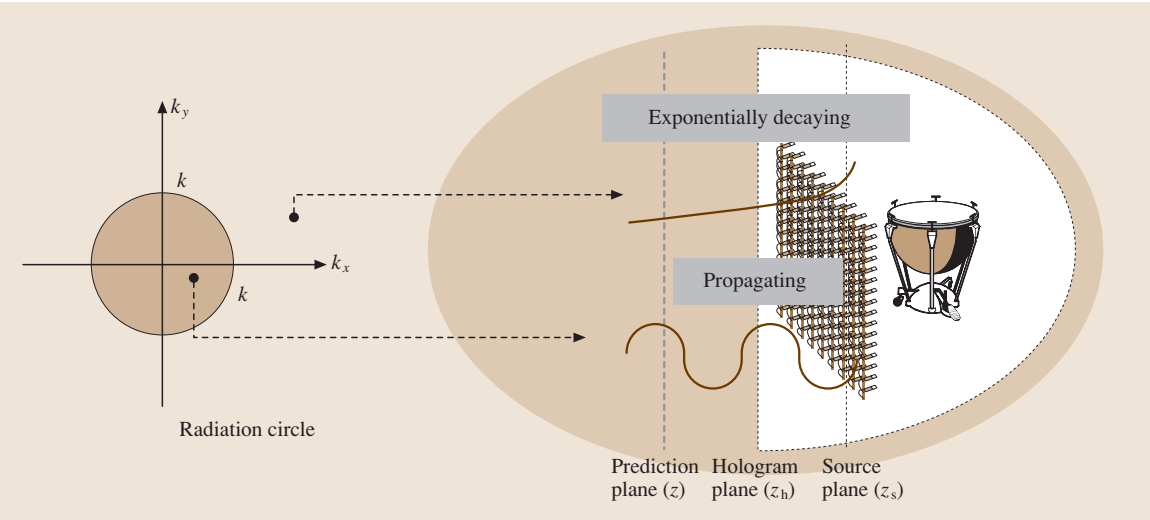


Fig. 26.6 Propagating and exponentially waves in acoustic holography

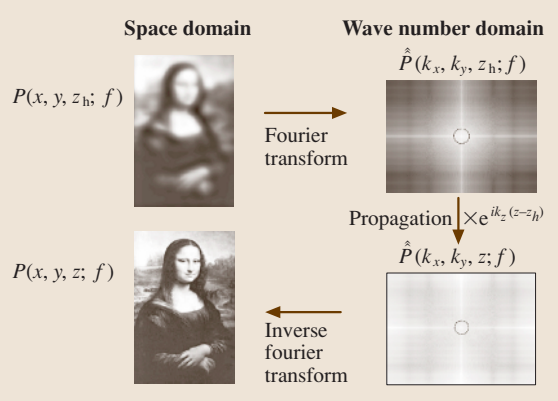


Fig. 26.7 The data-processing procedure for acoustic holography

linear inhomogeneous wave equation, or the inhomogeneous Helmholtz equation in the frequency domain. That is,

$$\nabla^2 G(\boldsymbol{x}\,|\boldsymbol{x}_\mathrm{h};\, f) + k^2 G(\boldsymbol{x}\,|\boldsymbol{x}_\mathrm{h};\, f) = -\delta(\boldsymbol{x}-\boldsymbol{x}_\mathrm{h})\,. \tag{26.3}$$

Therefore, we can select a Green's function in such a way that we can eliminate one of the terms on the right-hand side of (26.1); (26.2) is one such case.

To see what essentially happens in the prediction process, let us consider (26.2) when the measurement and prediction plane are both planar. Planar acoustic holography assumes that the sound field is free from reflection (Fig. 26.5); then we can write (26.2) as

$$P(x, y, z;\, f) = \int_{S_\mathrm{h}} P(x_\mathrm{h}, y_\mathrm{h}, z_\mathrm{h};\, f) \times K_\mathrm{PP}(x-x_\mathrm{h}, y-y_\mathrm{h}, z-z_\mathrm{h};\, f)\,\mathrm{d}S_\mathrm{h}\,, \tag{26.4}$$

$$K_\mathrm{PP}(x, y, z;\, f) = \frac{1}{2\pi}\frac{z}{r^3}(1-\mathrm{i}kr)\exp(\mathrm{i}kr)\,, \tag{26.5}$$

where $r = \sqrt{x^2+y^2+z^2}\,,$

$k = \dfrac{2\pi f}{c}\,,$

$\boldsymbol{x} = (x, y, z)\,,$

$\boldsymbol{x}_\mathrm{h} = (x_\mathrm{h}, y_\mathrm{h}, z_\mathrm{h})\,.$

K_PP can be readily obtained by using two free-field Green's functions that are located at z_h and $-z_\mathrm{h}$, so that it satisfies the Dirichlet boundary condition.

This is a convolution integral, and therefore we can write this in the wave-number domain as

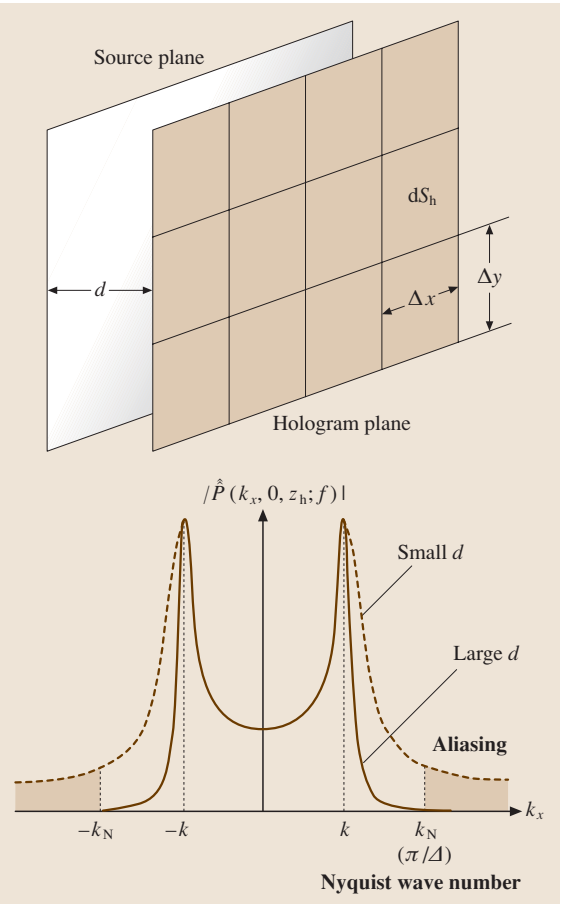
$$\hat{\hat{P}}(k_x, k_y, z;\, f) = \hat{\hat{P}}(k_x, k_y, z_\mathrm{h};\, f)\exp[\mathrm{i}k_z(z-z_\mathrm{h})]\,, \tag{26.6}$$

where

$$\hat{\hat{P}}(k_x, k_y, z;\, f) = \int_{-\infty}^{\infty}\int_{-\infty}^{\infty} P(x, y, z;\, f)\,\mathrm{e}^{-\mathrm{i}(k_x x + k_y y)}\,\mathrm{d}x\,\mathrm{d}y\,, \tag{26.7}$$

$k_z = \sqrt{k^2 - k_x^2 - k_y^2}\,.$

Amazon EX1014 Page 1081



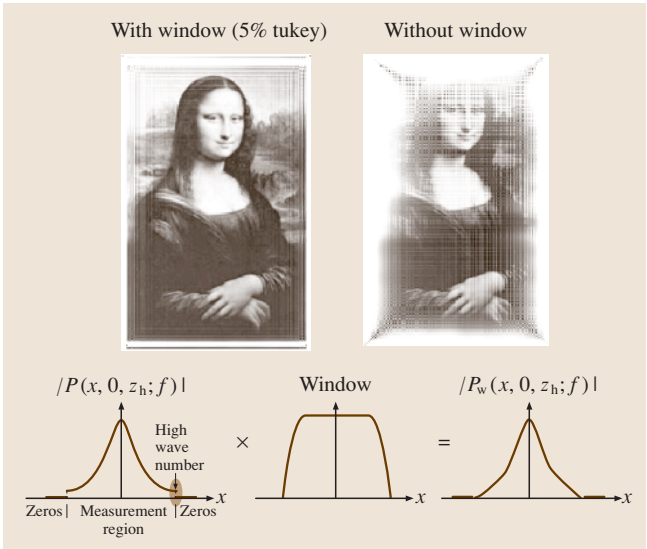


Fig. 26.8 The error due to discrete measurement: the spatial aliasing problem. The microphone spacing determines the Nyquist wave number. This wave number has to be smaller than the maximum wave number of the acoustic pressure distribution on the hologram plane. The microphone spacing, therefore, has to get smaller as the distance between the hologram (the measurement plane) and source decrease. The rule of thumb is $\delta < d$)

This equation essentially predicts the sound pressure with respect to the wave number (k_x, k_y). If $k^2 \geqslant k_x^2 + k_y^2$, the wave in z-direction (k_z) is propagating in space. Otherwise, the z-direction wave decays exponentially, i.e. it is an evanescent wave (Fig. 26.6).

We have derived the formulas that can predict what we did not measure based on what we measured, by using a Green's function. It is noteworthy that we can get the same results if we use the characteristic solutions of the Helmholtz equation; the Appendix describes the details. The Appendix also includes discrete expressions for the formula, which are normally used in the computation.

Equation (26.6) also allows us to predict the sound pressure on the source plane, when $z = z_s$. This is an inverse problem because it predicts the pressure distribution on the source plane based on the hologram pressure (see Figs. 26.3 and 26.6).

Figure 26.7 essentially illustrates how we can process the data for predicting what we did not measure based on what we measure. There are four major areas that cause errors in acoustic holography prediction. One is related to the integration of (26.4). Equation (26.4) has to be implemented on the discretized surface Fig. 26.8. This surface, therefore, has to be spatially sampled according to the selected surface. This spatial sampling can produce spatial aliasing, depending on the spatial distribution of the sound source: the sampling wave number must be larger than twice the maximum wave number of interest. It is noteworthy that, as illustrated in Fig. 26.8, the distance between the hologram and source planes is usually related to the sampling distance d. The closer one is to the source, the smaller the sampling distance needs to be. We must also note that the size of the aperture determines the wave-number resolution of acoustic holography. The finite aperture inevitably produces very sharp data truncation, as illustrated in Fig. 26.9. This produces unrealistic high-wave-number noise (see "without window" in Fig. 26.9). Therefore, it is often required that

Fig. 26.9 The effect of a finite aperture: the rapid change at the aperture edges produces high-wave-number noise

Amazon EX1014 Page 1082

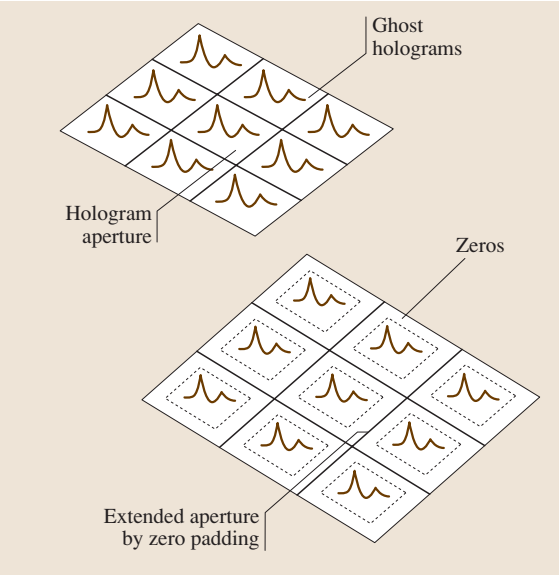


Fig. 26.10 The effect of the finite spatial Fourier transform on acoustic holography: the ghost image is due to the finite Fourier transform; circular convolution can be eliminated by adding zeros

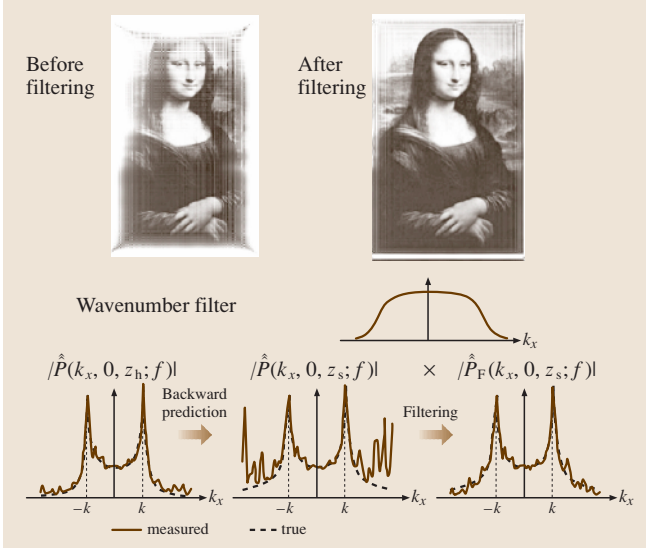


Fig. 26.11 Wave-number filtering in backward prediction. Evanescent wave components are magnified without filtering [26.47]

we use a window, which can result in a smoother data transition from what is on the measurement plane to what is not measured (Fig. 26.9).

The spatial Fourier transform that has to be done in the prediction process (26.6) has to be carried out in the domain for which data is available, i.e. a finite Fourier transform. It therefore produces a ghost hologram, as illustrated in Fig. 26.10 [26.46, 50]. This effect can be effectively removed by adding zeros to the hologram data (Fig. 26.11). The last thing to note is what can happen when we do backward propagation. As we can see in (26.6), when we predict the sound pressure distribution on a plane close to the sound source [$z < z_h$ (Fig. 26.5)] and k_z has an imaginary value (evanescent wave), then the sound pressure distribution of the exponentially decaying part will be unrealistically magnified (Fig. 26.11) [26.47]. Figure 26.12 graphically summarizes the entire processing steps of acoustic holography.

The issues related with the evanescent wave and its measurement are well addressed in the literature (for example, see [26.88]). The measurement of evanescent waves essentially allows us to achieve higher resolution than conventional acoustic holography [26.89–94]. However, it is noteworthy that the evanescent-wave component is substantially smaller than the other propagating components. Therefore, it is easy to produce errors that are associated with sensor or position mismatch [26.53]; in other words, it is very sensitive to the signal-to-noise ratio. Errors due to position and sensor mismatch are bias errors and random errors, respectively. It has been shown [26.53] that the bias error due to the mismatches is negligible, but the random error is significant in backward prediction. This is related to the measurement spacing on the hologram plane (Δ_h), prediction plane (Δ_z), and the distance between the hologram plane and the prediction plane (d). It is approximately proportional to $24.9(d/\Delta_z) + 20\log_{10}(\Delta_h/\Delta_z)$ in a dB scale. The signal-to-noise ratio can be amplified when we try to reconstruct the source field: a typical ill-posed phenomena. There have been many attempts to reduce this effect by using a spatial filter [26.47, 95–99], which is often called the *regularization* of acoustic holography [26.100–115].

Depending on the separable coordinates that we use for acoustic holography, we can construct cylindrical or spherical coordinates [26.54, 67, 69] (Figs. 26.13 and 26.14). These methods predict the sound field in exactly the same manner as in planar holography but with respect to different coordinates. As expected, however, these methods have some advantages. For example, the wrap-around error is negligible – in fact, there is no such error in spherical acoustic holography – and there is no aperture-related error [26.54]. Recently, the advantage

Amazon EX1014 Page 1083

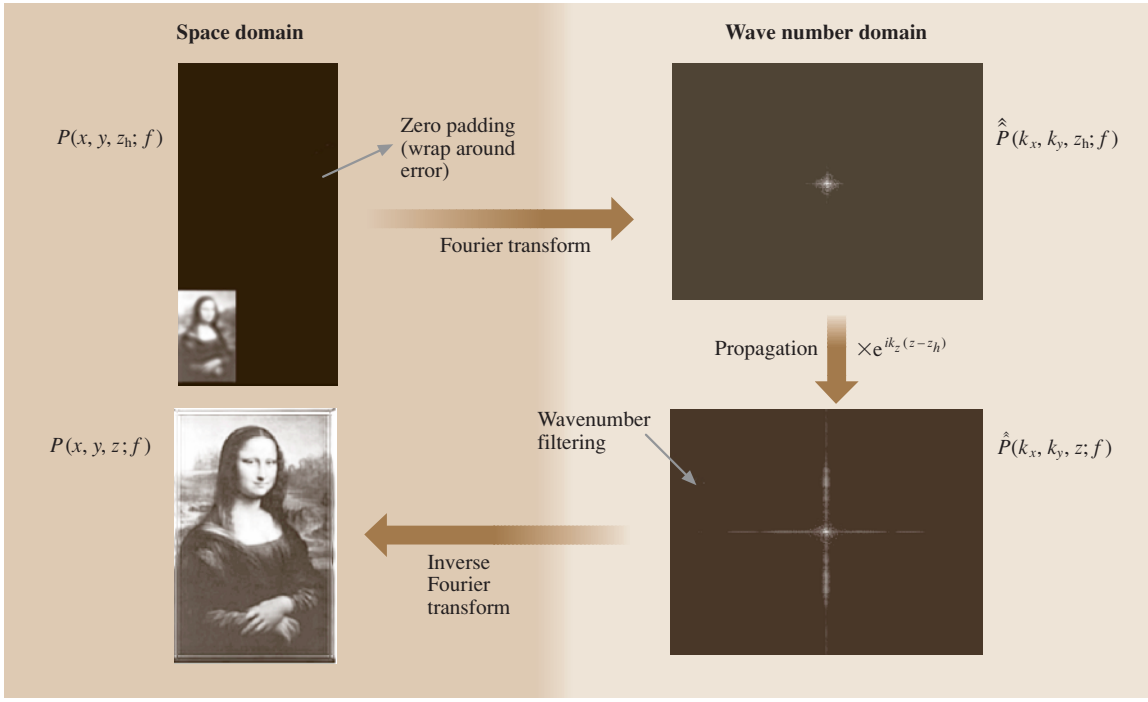


Fig. 26.12 Summary of the acoustic holography prediction process

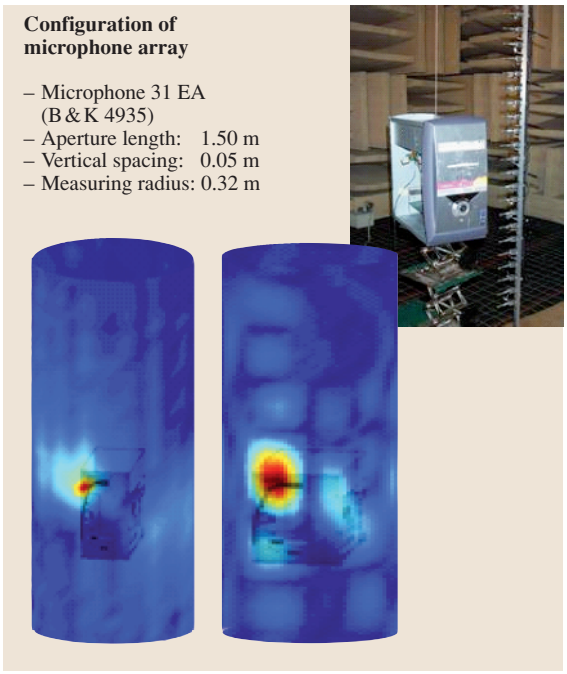


Fig. 26.13 Cylindrical holography

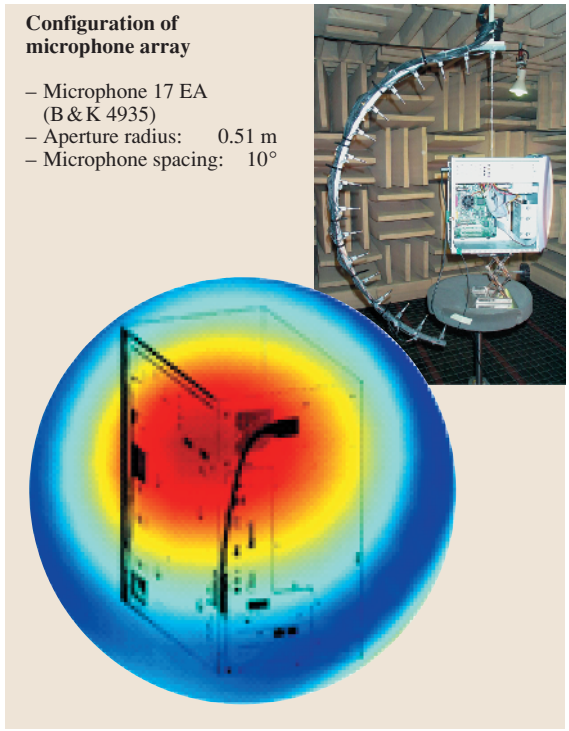


Fig. 26.14 Spherical holography

Amazon EX1014 Page 1084

of using spherical functions has also been noted [26.79, 81, 86, 87, 113].

26.2.3 Measurement

To construct a hologram, we commonly measure the sound pressure at discrete positions, as illustrated in Fig. 26.2. However, if the sound generated by the source, and therefore the sound field, can be assumed to be stationary, then we do not have to measure them at the same time.

Figure 26.15 illustrates one way to accomplish this measurement. This method normally measures the sound pressure field using a stepped line array (Fig. 26.15a). To understand the issues associated with this measurement system for the sake of its simplicity, let us see how we process a signal of frequency f when there is a single source. The relationship between the sound source and sound pressure in the field, or measurement position ($\boldsymbol{x}_\mathrm{h}$), can be written as

$$P(\boldsymbol{x}_\mathrm{h};\, f) = H(\boldsymbol{x}_\mathrm{h};\, f)Q(f)\,, \tag{26.8}$$

where $Q(f)$ is the source input signal and $H(\boldsymbol{x}_\mathrm{h};\, f)$ is the transfer function between the source input and the measured pressure. This means that, if we know the transfer function and the input, we can find the magnitude and phase between the measured positions. Because it is usually not practical to measure the input, we normally use reference signals (Fig. 26.15a). By using a reference signal, the pressure can be written as

$$P(\boldsymbol{x}_\mathrm{h};\, f) = H'(\boldsymbol{x}_\mathrm{h};\, f)R(f)\,, \tag{26.9}$$

where $R(f)$ is the reference signal. We can obtain $H'(\boldsymbol{x}_\mathrm{h};\, f)$ by

$$H'(\boldsymbol{x}_\mathrm{h};\, f) = \frac{P(\boldsymbol{x}_\mathrm{h};\, f)}{R(f)}\,. \tag{26.10}$$

The input and reference are related through:

$$R(f) = H_\mathrm{R}(f)Q(f)\,, \tag{26.11}$$

where $H_\mathrm{R}(f)$ is the transfer function between the input and the reference. As a result, we can see that (26.9) has the same form as (26.8).

It is noteworthy that (26.8) holds for the case that we have only one sound source and the sound field is stationary and random. However, if there are two sound sources, then (26.8) becomes

$$P(\boldsymbol{x}_\mathrm{h};\, f) = H_1(\boldsymbol{x}_\mathrm{h};\, f)Q_1(f) + H_2(\boldsymbol{x}_\mathrm{h};\, f)Q_2(f)\,, \tag{26.12}$$

where $Q_i(f)$ is the i-th input and $H_i(\boldsymbol{x}_\mathrm{h};\, f)$ is its transfer function. There are now two independent sound fields. This requires, of course, two independent reference signals. It has been well accepted that the number of reference microphones has to be greater than the number of independent sources [26.57]. However, if this is strictly true, then it means that we have to somehow know the number of sources, and this, in some degree, contradicts the the acoustic holography approach.

A recent study [26.61] demonstrated that the measured information, the location of the sources, and the number of independent sources converge to their true values as the number of reference microphones increases. This study also showed that high-power sources

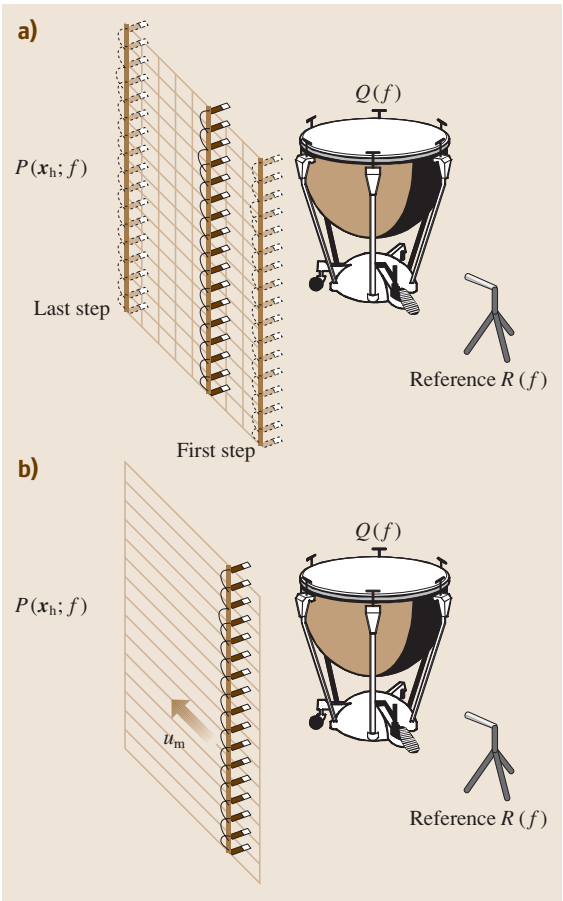


Fig. 26.15a,b Two measurement methods for the pressure on the hologram plane: **(a)** step-by-step scanning **(b)** continuous scanning

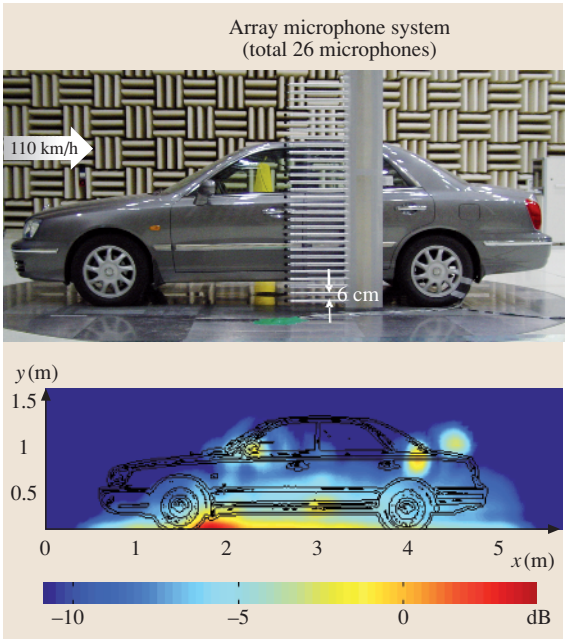


Fig. 26.16 Application result of the step-by-step scanning method to the wind noise of a car. This figure is the pressure distribution at 710 ~ 900 Hz in a source plane when the flow velocity is 110 km/h. In this experiment, 17 reference microphones are randomly located in the car, to see the coherence between interior noise and what are measured by the array microphone system. The array microphone system was initially located at 3 m forward from the middle point of a car, and moved 6 cm in step until it reached at 3 m backward from the middle point

are likely to be identified even if the number of reference microphones is less than the number of sources. Figure 26.16 shows an example of this method when there are many independent sound fields. On the other hand, one study showed that we can even continuously scan the sound field by using a line array of microphones (Fig. 26.15b) [26.62–65]. This method essentially allows us to extend the aperture size without any limit as long as the sound field is stationary. In fact, [26.65] also showed that this method can be used for a slowly varying (quasi-stationary) sound field.

This method has to deal with the Doppler shift. For example, let us consider a plane wave in the $(k_{x_0}, k_{y_0}, k_{z_0})$ direction and a pure tone of frequency f_{h_0}. Then the pressure on the hologram plane can be written as

$$p(x_h, y_h, z_h; t) = P_0 \exp\left[i(k_{x_0}x_h + k_{y_0}y_h + k_{z_0}z_h)\right] \exp(-i, f_{h_0}t) , \quad (26.13)$$

where P_0 denotes the complex magnitude of the plane wave. Spatial information about the plane wave with respect to the x-direction can be represented by a wave-number spectrum, and can be described as

$$\begin{aligned}\hat{P}(k_x, y_h, z_h; t) &= \int_{-\infty}^{\infty} p(x_h, y_h, z_h; t)\, e^{-ik_x x_h}\, dx_h \\ &= P_0 \exp\left[i(k_{y_0}y_h + k_{z_0}z_h)\right] \\ &\quad \times \delta(k_x - k_{x_0}) \exp(-i2\pi f_{h_0}t) \\ &= P(k_{x_0}, y_h, z_h)\delta(k_x - k_{x_0}) \\ &\quad \times \exp(-i2\pi f_{h_0}t) , \end{aligned} \quad (26.14)$$

where $P(k_{x_0}, y_h, z_h) = P_0 \exp[i(k_{y_0}y_h + k_{z_0}z_h)]$ is the wave-number spectrum of the plane wave at $k_x = k_{x_0}$.

If a microphone is moving at an x-velocity u_m, the measured signal $p_m(x_h, y_h, z_h; t)$ is

$$p_m(x_h, y_h, z_h; t) = p(u_m t, y_h, z_h; t) . \quad (26.15)$$

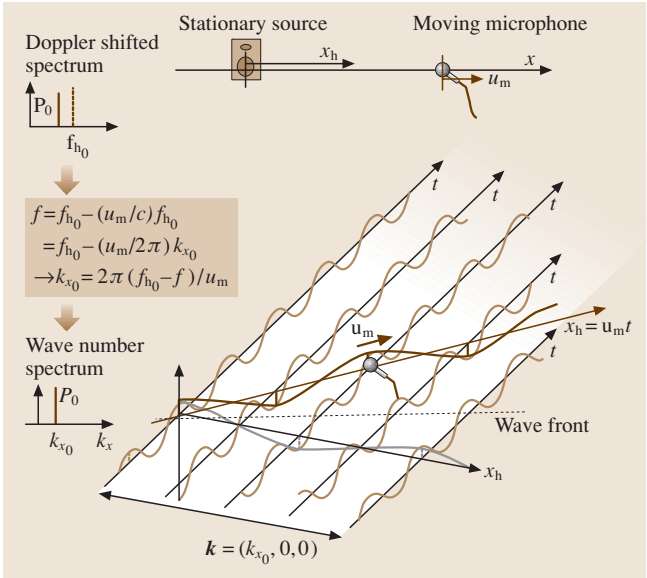


Fig. 26.17 The continuous scanning method for a plane wave and a pure tone (one-dimensional illustration). f_{h_0} is the source frequency, f is the measured frequency, u_m is the microphone velocity, c is the wave speed, k_{k_0} is the x-direction wave number, and P_0 is the complex amplitude of a plane wave

Amazon EX1014 Page 1086

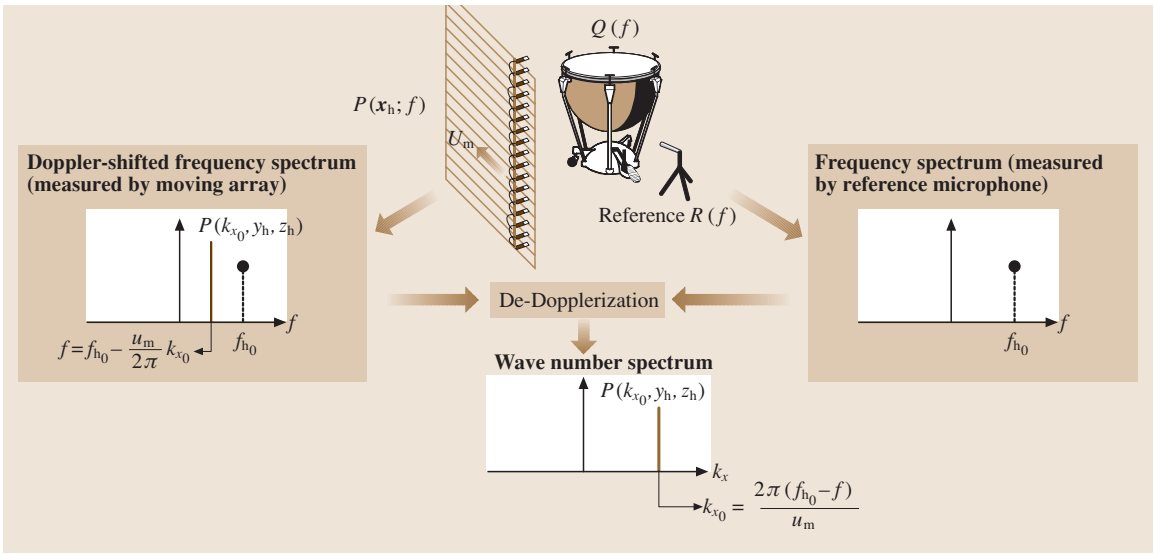


Fig. 26.18 De-Dopplerization procedure for a line spectrum

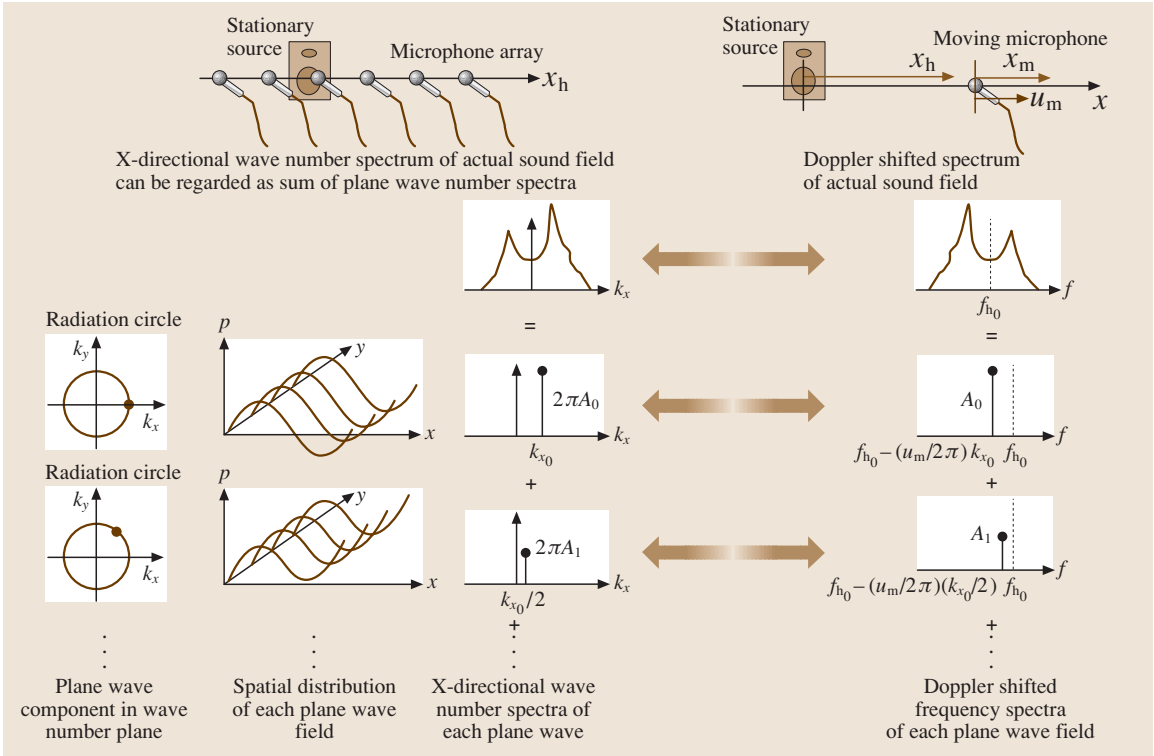


Fig. 26.19 The continuous scanning method for a more general case (one-dimensional illustration)

Amazon EX1014 Page 1087

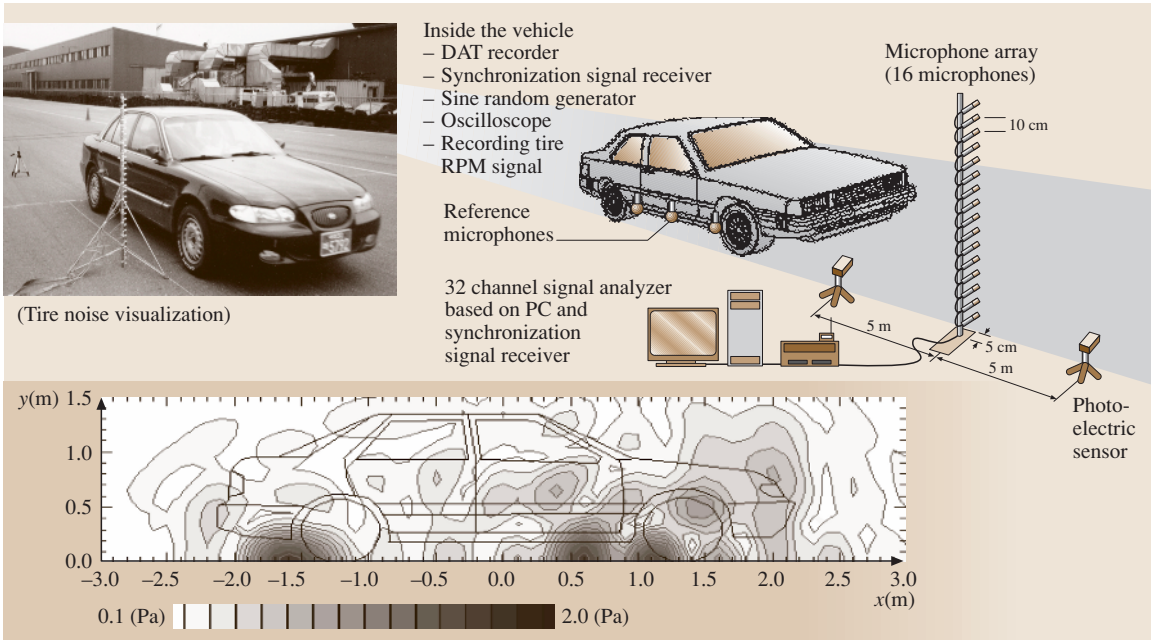


Fig. 26.20 Experimental configuration and result of the continuous scanning method to vehicle pass-by noise. The tire pattern noise distribution (pressure) on the source plane is shown when the car passed the microphone array with constant speed of 50 km/h

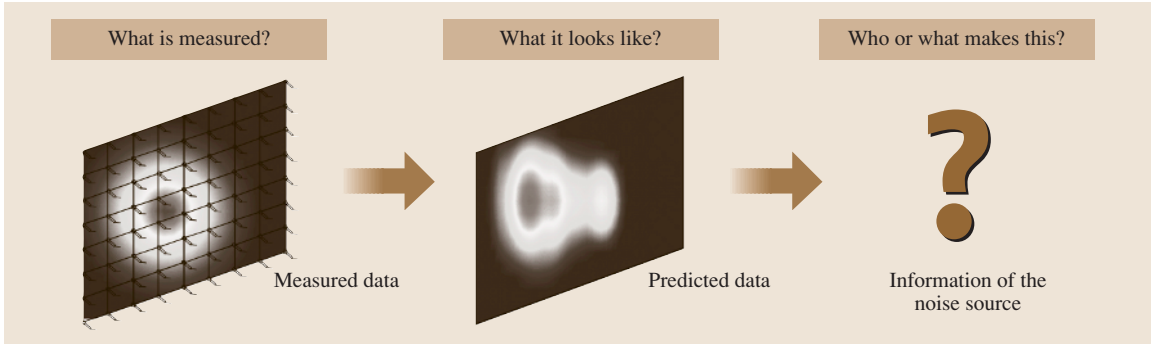


Fig. 26.21 Illustration of analysis problem in acoustic holography

The Fourier transform of (26.15) with respect to time F_T, using (26.13), can be expressed as

$$
\begin{aligned}
&F_T[p_m(u_m t, y_h, z_h; t)] \\
&= \int_{-\infty}^{\infty} p_m(u_m t, y_m, z_h; t)\, e^{i2\pi f t}\, dt \\
&= P_0 \exp\left[i(k_{y_0} y_h + k_{z_0} z_h)\right] \delta\left(\frac{u_m}{2\pi} k_{x_0} - f_{h_0} + f\right) \\
&= P(k_{x_0}, y_h, z_h)\delta\left(\frac{u_m}{2\pi} k_{x_0} - f_{h_0} + f\right) . \qquad (26.16)
\end{aligned}
$$

Equation (26.16) means that the complex amplitude of the plane wave is located at the shifted frequency $f_{h_0} - u_m k_{x_0}/2\pi$, as shown in Fig. 26.17. In general, the relation between the shifted frequency f and x-direction wave number k_x is expressed as Fig. 26.18

$$
k_x = \frac{2\pi(f_{h_0} - f)}{u_m} . \qquad (26.17)
$$

We can measure the original frequency f_{h_0} by a fixed reference microphone. Using the Doppler

shift, we can therefore obtain the wave-number components from the frequency components of the moving microphone signal. Figure 26.19 illustrates how we obtain the wave-number spectrum.

This method essentially uses the relative coordinate between the hologram and microphone. Therefore, it can be used for measuring a hologram of moving noise sources (Fig. 26.20), which is one of the major contributions of this method [26.62–65].

26.2.4 Analysis of Acoustic Holography

Once we have a picture of the sound (acoustic holography), w questions about its meaning are the next topic of interest. What we have is usually a contour plot of the sound pressure distribution or a vector plot of the sound intensity on a plane of interest. This plot may help us to imagine where the sound source is and how it radiates into space with respect to a frequency of interest. However, in the strict sense, the only thing we can do from the two-dimensional expression of sound pressure or intensity distribution is to guess what was really there. We do not know, precisely, where the sound sources are (Fig. 26.21).

As mentioned earlier, there are two types of sound sources: active and passive sound source. The former is the source that radiates sound itself, while the latter only radiates reflected sound. These two different types of sound sources can be distinguished by eliminating reflected sound [26.116]. This is directly related to the way boundary conditions are treated in the analysis.

The boundary condition for a locally reacting surface can be written as [26.116–118]

$$V(\boldsymbol{x}_s;\, f) = A(\boldsymbol{x}_s;\, f)P(\boldsymbol{x}_s;\, f) + S(\boldsymbol{x}_s;\, f)\,, \qquad (26.18)$$

where $V(\boldsymbol{x}_s;\, f)$ and $P(\boldsymbol{x}_s;\, f)$ are the velocity and pressure on the wall. $A(\boldsymbol{x}_s;\, f)$ is the wall admittance and $S(\boldsymbol{x}_s;\, f)$ is the source strength on the wall. The active sound source is located at a position such that the source strength is not zero. This equation says that we can estimate the source strength if we measure the wall admittance. To do this, it is necessary to first turn off the source or sources, and then measure the wall admittance by putting a known source in the desired position (Fig. 26.22a). The next step is to turn on the sources and obtain the sound pressure and velocity distribution on the wall, using the admittance information (Fig. 26.22b). This provides us with the location

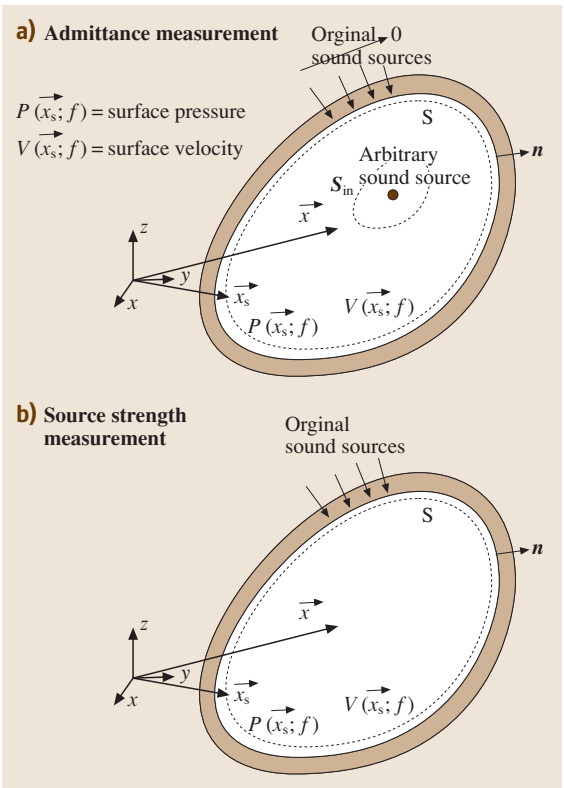


Fig. 26.22 Two steps to separate the active and passive source



Fig. 26.23 Spatially independent or dependent sources

and strength of the source (i.e. the source power; for example, see Fig. 26.24).

Another very important problem is whether or not we can distinguish between independent or dependent sources, i.e. two birds singing versus one bird with two beaks (Fig. 26.23). This has a rather significant practical application. For example, to control noise sources effectively, we only need to control independent noise sources. This can be achieved by using the statistical

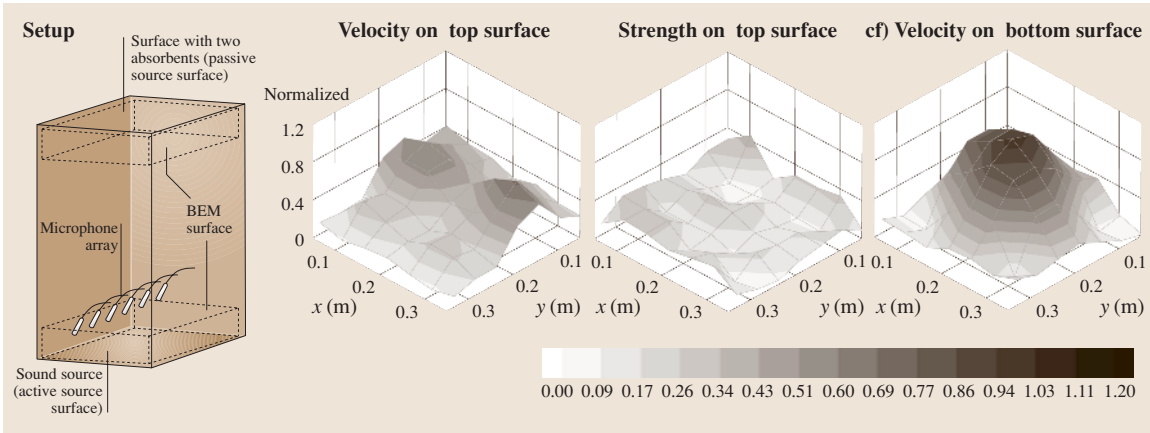


Fig. 26.24 Experiment results that separate the active and passive sources. The top surface is made by the sound absorption material. The speaker on the bottom surface, which is reflecting sound, is eliminated by this separation

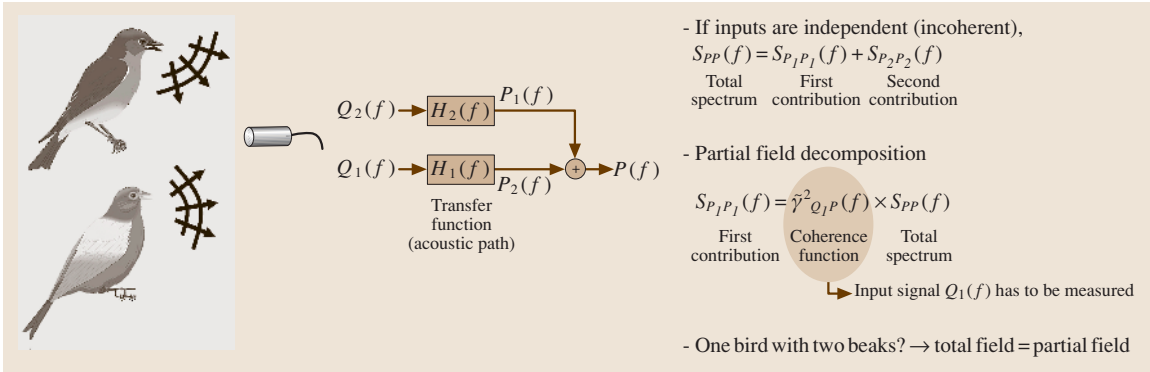


Fig. 26.25 A two-input single-output system and its partial field

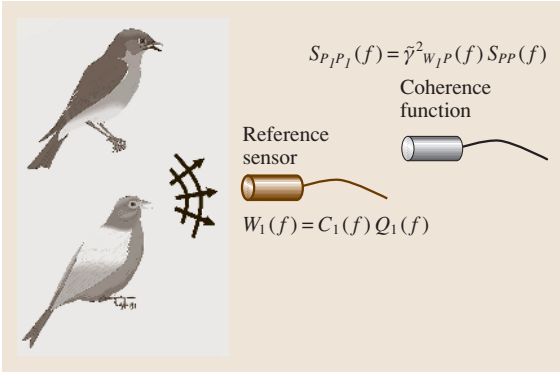


Fig. 26.26 The conventional method to obtain the partial field

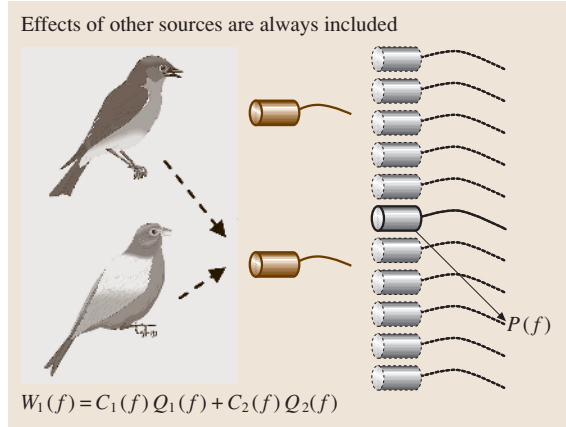


Fig. 26.27 Acoustic holography and partial field decomposition

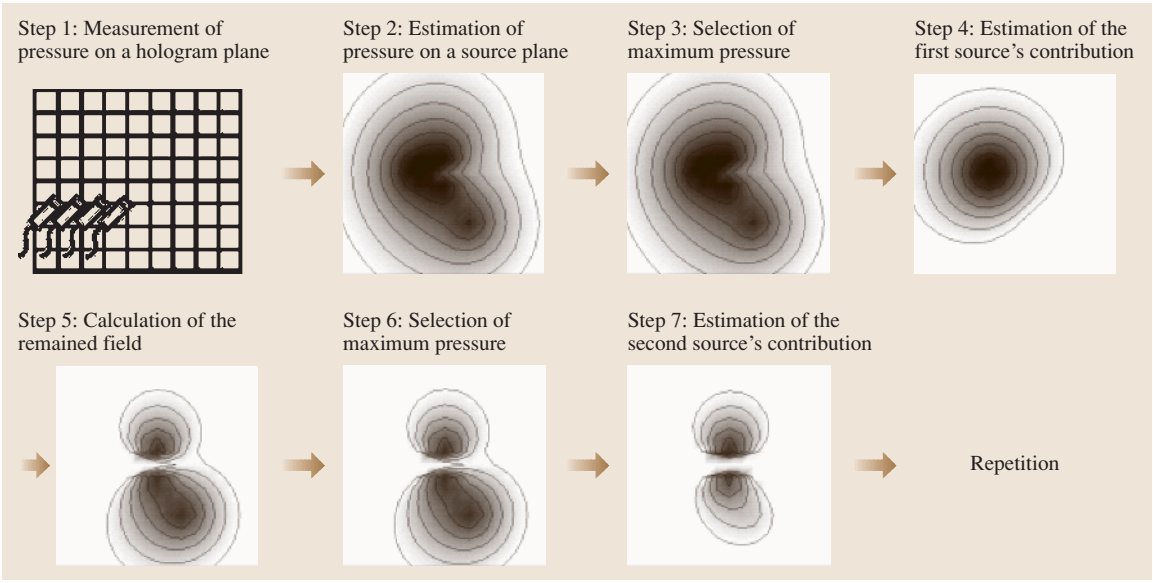


Fig. 26.28 The procedure to separate the independent and dependent sources

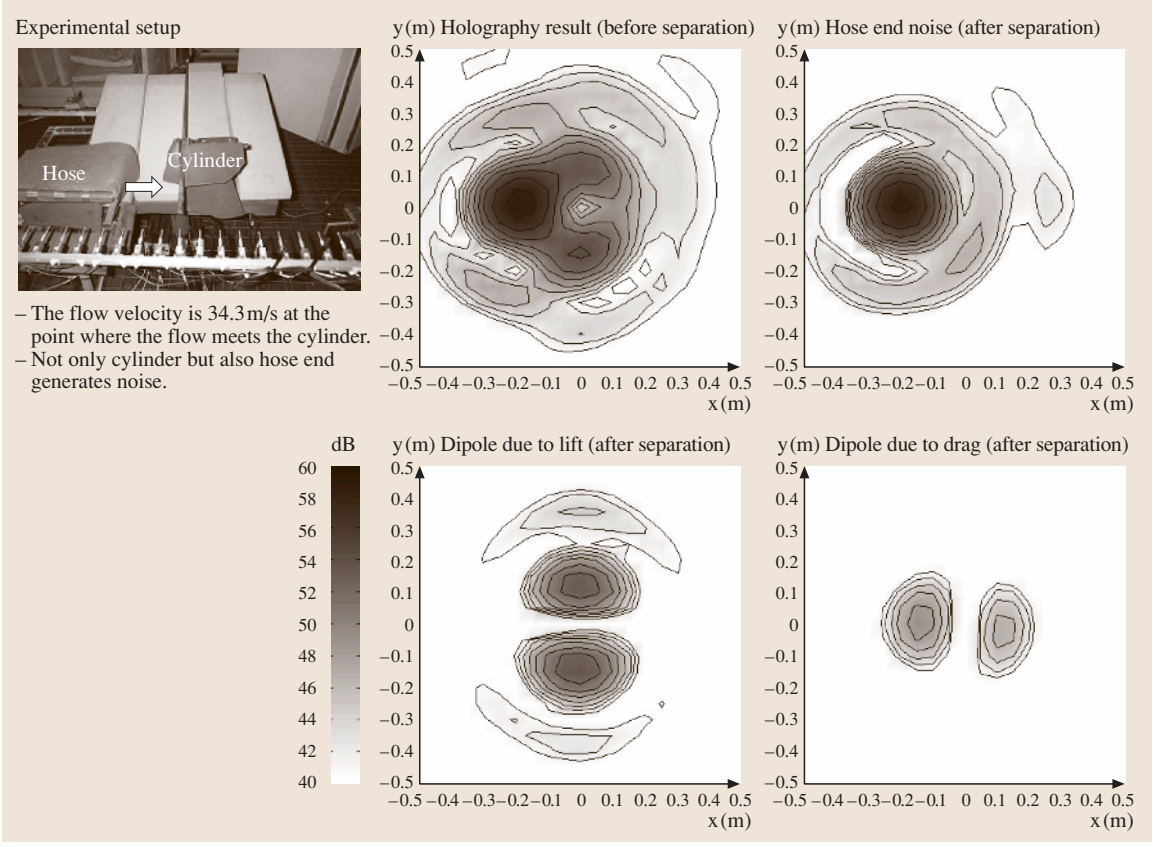


Fig. 26.29 The separation method applied to a vortex experiment

Amazon EX1014 Page 1091

differences between signals that are induced by independent and dependent sound sources.

For example, let us consider a two-input single-output system (Fig. 26.25). If the two inputs are independent, the spectrum $S_{PP}(f)$ of the output $P(f)$ can be expressed as

$$S_{PP}(f) = |H_1(f)|^2 S_{Q_1Q_1}(f) + |H_2(f)|^2 S_{Q_2Q_2}(f) , \quad (26.19)$$

where $S_{Q_iQ_i}(f)$ is the spectrum of the i-th input $Q_i(f)$, and $H_i(f)$ is its transfer function. The first and second terms represent the contributions of the first and second input to the output spectrum, respectively. If we can obtain a signal as

$$W_1(f) = C(f)Q_1(f) , \quad (26.20)$$

then we can estimate the contribution of the first source as [26.119]

$$S_{P_1P_1}(f) = |H_1(f)|^2 S_{Q_1Q_1}(f) = \gamma^2_{W1P}(f) S_{PP}(f) , \quad (26.21)$$

where $\gamma^2_{W1P}(f)$ is the coherence function between $W_1(f)$ and $Q_1(f)$ (Fig. 26.26).

We can simply extend (26.21) to the case of multiple outputs, as in the case of acoustic holography (Fig. 26.27). The main problem is how to obtain a signal that satisfies (26.20). We can generally say that, by putting sensors closer to the source or sources [26.57, 58, 120–123], we may have a better signal that can be used to distinguish between independent or dependent sources. However, this is neither well proven nor practical, as it is not always easy to put the sensors close to the sources. Very recently, a method that does not require this [26.124, 125] was developed. Figure 26.28 explains the method's procedures. The first and second steps are the same as in acoustic holography: measurement and prediction. The third step is to search for the maximum pressure on the source plane. This method assumes that the maximum pressure satisfies (26.20). The fourth step is to estimate the contribution of the first source by using the coherence functions between the maximum pressure and other points, as in (26.21). The fifth step is to calculate the remaining spectrum by subtracting the first contribution from the output spectrum. These steps are repeated until the contributions of the other sources are estimated (for example, see Fig. 26.29).

26.3 Summary

As expected, it is not simple to answer the question of whether we can see the sound field. However, it is now understood that the analysis of what we obtained, acoustic holography, needs to be properly addressed, although little attention was given to this problem in the past. We now understand better how to obtain information from the sound picture. Making a picture is the job of acoustic holography, but the interpretation of this picture is the responsibility of the observer. This paper has reviewed some useful guidelines for better interpretation of the sound field to deduce the right impression or information from the picture.

26.A Mathematical Derivations of Three Acoustic Holography Methods and Their Discrete Forms

We often use the Kirchhoff–Helmholtz integral equation to explain how we predict what we do not measure based on what we do measure. It is noteworthy, however, that the same result can be obtained by using the characteristic solutions of the Helmholtz equation. The following sections address how these can be obtained. Planar, cylindrical, and spherical acoustic holography are derived using characteristic equations in terms of a corresponding coordinate system. The equations for holography are also expressed in a discrete form.

26.A.1 Planar Acoustic Holography

If we see solutions of the Helmholtz equation

$$\nabla^2 P + k^2 P = 0 , \quad (26.A1)$$

in terms of Cartesian coordinate, then we can write them as

$$P(x, y, z; f) = X(x)\, Y(y)\, Z(z) , \quad (26.A2)$$

where $k = \frac{\omega}{c} = \frac{2\pi f}{c}$. We assume then P is separable with respect to X, Y and Z. Equations (26.A1) and (26.A2)

yield the characteristic equation

$$\psi(x, y, z; k_x, k_y, k_z) = \begin{pmatrix} e^{ik_x x} \\ e^{-ik_x x} \end{pmatrix} \begin{pmatrix} e^{ik_y y} \\ e^{-ik_y y} \end{pmatrix} \begin{pmatrix} e^{ik_z z} \\ e^{-ik_z z} \end{pmatrix}, \quad (26.A3)$$

where

$$k^2 = k_x^2 + k_y^2 + k_z^2 . \quad (26.A4)$$

Now we can write

$$P(x, y, z; f) = \int \hat{P}(\boldsymbol{k})\psi(x, y, z; k_x, k_y, k_z)\,d\boldsymbol{k} , \quad (26.A5)$$

where

$$\boldsymbol{k} = (k_x, k_y, k_z) . \quad (26.A6)$$

Let us assume that the sound sources are all located at $z < z_s$ and we measure at $z = z_h > z_s$. Then we can write (26.A5) as

$$P(x, y, z; f) = \int_{-\infty}^{\infty}\int_{-\infty}^{\infty} \hat{\hat{P}}(k_x, k_y) e^{i(k_x x + k_y y + k_z z)}\,dk_x\,dk_y . \quad (26.A7)$$

It is noteworthy that we selected only $+ik_z z$. This is because of the assumptions we made ($z < z_s$ and $z = z_h > z_s$). The k_x and k_y can be either positive or negative. Therefore it is not necessary to include $-ik_x x$ or $-ik_y y$ in (26.A3).

In (26.7),

$$k_z = \begin{cases} \sqrt{k^2 - k_x^2 - k_y^2}, & \text{when} \quad k^2 > k_x^2 + k_y^2 \\ i\sqrt{k_x^2 + k_y^2 - k^2}, & \text{when} \quad k^2 < k_x^2 + k_y^2 . \end{cases} \quad (26.A8)$$

Figure 26.6 illustrates what these two different k_z values essentially mean. We measure $P(x, y, z = z_h; f)$, therefore we have data of the sound pressure data on $z = z_h$. A Fourier transform of (26.A7) leads to

$$\hat{\hat{P}}(k_x, k_y) = \int_{-\infty}^{\infty}\int_{-\infty}^{\infty} P(x, y, z; f) e^{-i(k_x x + k_y y + k_z z)}\,dx\,dy . \quad (26.A9)$$

Using (26.A9) and (26.A7), we can always estimate the sound pressure on z, which is away from the source.

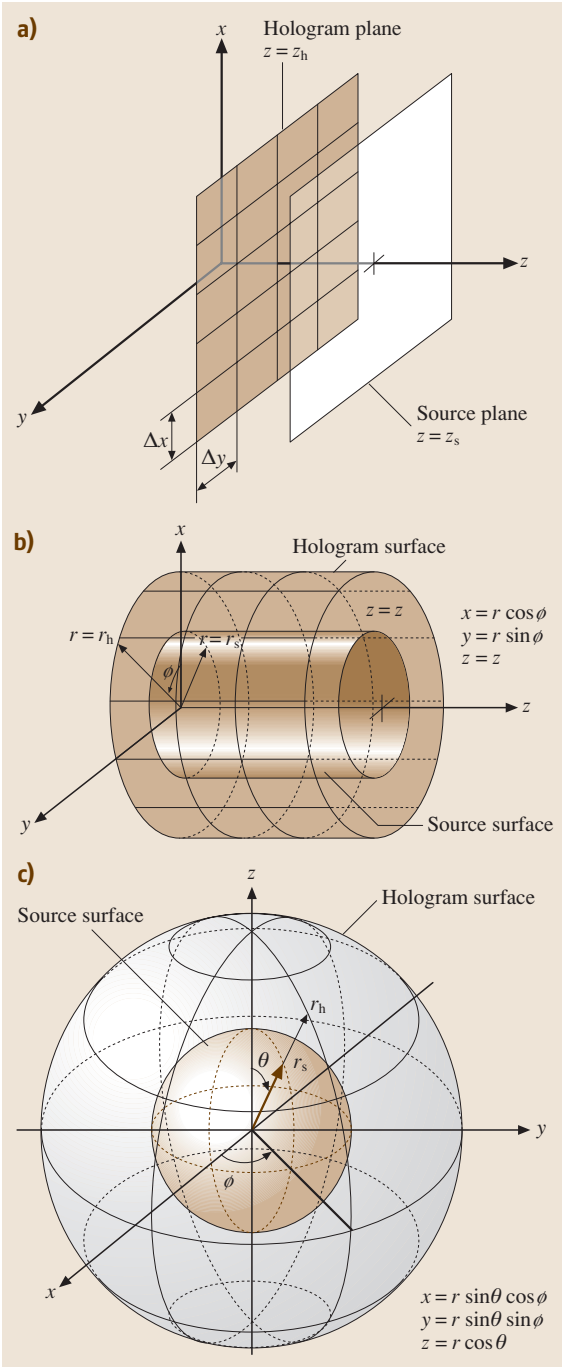


Fig. 26.30a–c Coordinates system for acoustic holography: **(a)** planar acoustic holography **(b)** cylindrical Acoustic holography **(c)** spherical acoustic holography

Amazon EX1014 Page 1093

It is noteworthy that (26.A9) has to be preformed in the discrete domain. In other words, we have to use a finite rectangular aperture, which is spatially sampled (26.8 and 26.30a). If the number of measurement points along the x-and y-directions are M and N, respectively, and the corresponding sampling distances are Δx and Δy, then (26.A9) can be rewritten as

$$\hat{\hat{P}}(k_x, k_y) = \frac{1}{(2\pi)^2} \mathrm{e}^{-\mathrm{i}k_z z_\mathrm{h}} \Delta x \Delta y \sum_{m=0}^{M-1} \sum_{n=0}^{N-1} P(x_m, y_n, z_\mathrm{h}) \mathrm{e}^{-\mathrm{i}k_x x_m} \mathrm{e}^{-\mathrm{i}k_y y_n} \,. \tag{26.A10}$$

where

$$x_m = \left(m + \frac{1-M}{2}\right) \Delta x,$$
$$y_n = \left(n + \frac{1-N}{2}\right) \Delta y \,. \tag{26.A11}$$

M and N are the number of data points in the x- and y-directions, respectively.

26.A.2 Cylindrical Acoustic Holography

A solution can also found in cylindrical coordinate, that is

$$P(r, \phi, z) = R(r)\Phi(\phi)Z(z) \,. \tag{26.A12}$$

Figure 26.1 shows the coordinate systems. Then, its characteristic solutions are

$$\psi(r, \phi, z; k_r, k_z) = \begin{pmatrix} H_m^{(1)}(k_r r) \\ H_m^{(2)}(k_r r) \end{pmatrix} \begin{bmatrix} \mathrm{e}^{\mathrm{i}m\phi} \\ \mathrm{e}^{-\mathrm{i}m\phi} \end{bmatrix} \begin{bmatrix} \mathrm{e}^{\mathrm{i}k_z z} \\ \mathrm{e}^{-\mathrm{i}k_z z} \end{bmatrix} \,, \tag{26.A13}$$

where

$$k^2 = k_r^2 + k_z^2 \,. \tag{26.A14}$$

It is noteworthy that m is a nonnegative integer. $H_m^{(1)}$ and $H_m^{(2)}$ are first and second cylindrical Hankel functions, respectively. $\mathrm{e}^{\mathrm{i}m\phi}$ and $\mathrm{e}^{-\mathrm{i}m\phi}$ express the mode shapes in the ϕ-direction.

Using the characteristic function (26.A6), we can write a solution of the Helmholtz equation with respect to cylindrical coordinate as

$$P(r, \phi, z; f) = \int \hat{P}_m(\boldsymbol{k}) \psi_m(r, \phi, z; k_r, k_z) \mathrm{d}\boldsymbol{k} \,, \tag{26.A15}$$

where

$$\boldsymbol{k} = (k_r, k_z) \,. \tag{26.A16}$$

Assuming that the sound sources are all located at $r < r_\mathrm{s}$ and that the hologram surface is situated on the surface $r = r_\mathrm{h}$, and that $r_\mathrm{h} > r_\mathrm{s}$, then no waves propagate into the negative r-direction, in other words, toward the sources. Then (26.A15) can be rewritten as

$$P(r, \phi, z; f) = \sum_{m=-\infty}^{\infty} \int_{-\infty}^{\infty} \hat{P}_m(k_z) \mathrm{e}^{\mathrm{i}m\phi} \mathrm{e}^{\mathrm{i}k_z z} H_m^{(1)}(k_r r) \mathrm{d}k_z \,, \tag{26.A17}$$

and k_r has to be

$$k_r = \begin{cases} \sqrt{k^2 - k_z^2} \,, & \text{when } k^2 > k_z^2 \\ \mathrm{i}\sqrt{k_z^2 - k^2} \,, & \text{when } k^2 < k_z^2 \,. \end{cases} \tag{26.A18}$$

We measure the acoustic pressure at $r = r_\mathrm{h}$, therefore $P(r_\mathrm{h}, \phi, z)$ is available. $\hat{P}_m(k_z)$ can then be readily obtained.

That is

$$\hat{P}_m(k_z) = \frac{1}{(2\pi)^2} \int_0^{2\pi} \int_{-\infty}^{\infty} P(r_\mathrm{h}, \phi, z) \mathrm{e}^{-m\phi} \mathrm{e}^{-\mathrm{i}k_z z} \left\{H_m^{(1)}(k_r r_\mathrm{h})\right\}^{-1} \mathrm{d}z \, \mathrm{d}\phi \,. \tag{26.A19}$$

Inserting (26.A19) into (26.A17) provides us with the acoustic pressure at the unmeasured surface at r.

Discretization of (26.A19) leads to a formula that can be used in practical calculations:

$$\hat{P}_m(k_z) = \frac{1}{(2\pi)^2 H_m^{(1)}(k_r r_\mathrm{h})} \frac{2\pi}{L} \Delta z \sum_{l=0}^{L-1} \sum_{n=0}^{N-1} P(r_\mathrm{h}, \phi_l, z_n) \mathrm{e}^{-\mathrm{i}m\phi_l} \mathrm{e}^{-\mathrm{i}k_z z_n} \,, \tag{26.A20}$$

where

$$\phi_l = \frac{(2l+1)\pi}{L} \,,$$
$$z_n = \left(n + \frac{1-N}{2}\right) \Delta z \,. \tag{26.A21}$$

L and N are the number of data points in the ϕ- and z-directions, respectively.

Amazon EX1014 Page 1094

26.A.3 Spherical Acoustic Holography

The Helmholtz equation can also be expressed in spherical coordinate (Fig. 26.30c). Assuming again that the separation of variable also holds in this case, we can write:

$$P(r,\theta,\phi) = R(r)\Theta(\theta)\Phi(\phi)\,. \tag{26.A22}$$

Substituting this into (26.A1) gives the characteristic equation

$$\psi_{mn}(r,\theta,\phi;k) = \begin{pmatrix} h_m^{(1)}(kr) \\ h_m^{(2)}(kr) \end{pmatrix} \begin{pmatrix} P_m^n \cos\theta \\ Q_m^n \cos\theta \end{pmatrix} \begin{pmatrix} \mathrm{e}^{\mathrm{i}n\phi} \\ \mathrm{e}^{-\mathrm{i}n\phi} \end{pmatrix}\,. \tag{26.A23}$$

m is a nonnegative integer and n can be any integer between 0 and m. $h_m^{(1)}$ and $h_m^{(2)}$ are first and second spherical Hankel functions. It is also noteworthy that P_m^n and Q_m^n are first and second Legendre polynomials.

Then we can write the solution of the Helmholtz equation as

$$P(r,\theta,\phi) = \sum_{m=0}^{\infty} \sum_{n=-m}^{m} \hat{P}_{mn}\psi_{mn}(r,\theta,\phi;k)\,. \tag{26.A24}$$

Suppose that we have sound sources at $r < r_\mathrm{s}$ and the hologram is on the surface $r = r_\mathrm{h} > r_\mathrm{s}$; then (26.A24) can be simplified to:

$$P(r,\theta,\phi) = \sum_{m=0}^{\infty} \sum_{n=-m}^{m} \hat{P}_{mn} Y_{mn}(\theta,\phi) h_m^{(1)}(kr)\,, \tag{26.A25}$$

where

$$Y_{mn}(\theta,\phi) = P_m^{|n|}(\cos\theta)\mathrm{e}^{\mathrm{i}n\phi}\,. \tag{26.A26}$$

This is a spherical harmonic function. It is noteworthy that we only have first spherical harmonic functions because all waves propagate away from the sources. The second Legendre function was discarded because it would have finite acoustic pressure at $\theta = 0$ or π.

Similarly, as previously stated, the sound pressure data on the hologram is available, therefore we can obtain P_{mn} in (26.A25) by

$$\hat{P}_{mn} = \frac{2m+1}{4\pi h_m^{(1)}(kr_\mathrm{h})} \frac{(m-|n|)!}{(m+|n|)!} \int_0^{\pi}\int_0^{2\pi} P(r_\mathrm{h},\theta,\phi) Y_{mn}^*(\theta,\phi)\sin\theta\,\mathrm{d}\phi\,\mathrm{d}\theta\,, \tag{26.A27}$$

where we have used the orthogonality property of Y_{mn}. The $*$ represents the complex conjugate. Using (26.A27) and (26.A25), we can estimate the acoustic pressure anywhere away from the sources.

The discrete form of (26.A27) can be written as

$$\hat{P}_{mn} = A_{mn}\frac{2\pi^2}{LQ}\sum_{l=0}^{L-1}\sum_{q=0}^{Q-1} P(r_\mathrm{h},\theta_l,\phi_q) P_m^{|n|}(\cos\theta_l)(\sin\theta_l)\mathrm{e}^{-\mathrm{i}n\phi_q}\,, \tag{26.A28}$$

where

$$\theta_l = \frac{(2l+1)\pi}{2L}\,, \qquad \phi_q = \frac{(2q+1)\pi}{Q}\,. \tag{26.A29}$$

where L is the number of data points in θ and Q is what is in ϕ-direction.

References

26.1 M. Kac: Can one hear the shape of the drum?, Am. Math. Mon. **73**, 1–23 (1966)

26.2 G.T. Herman, H.K. Tuy, K.J. Langenberg: *Basic methods of tomography and inverse problems* (Malvern, Philadelphia 1987)

26.3 H.D. Bui: *Inverse Problems in the Mechanics of Materials: An Introduction* (CRC, Boca Raton 1994)

26.4 K. Kurpisz, A.J. Nowak: *Inverse Thermal Problems* (Computational Mechanics Publ., Southampton 1995)

26.5 A. Kirsch: *An Introduction to the Mathematical Theory of Inverse Problems* (Springer, Berlin Heidelberg New York 1996)

26.6 M. Bertero, P. Boccacci: *Introduction to Inverse Problems in Imaging* (IOP, Bristol 1998)

26.7 V. Isakov: *Inverse Problems for Partial Differential Equations* (Springer, New York 1998)

26.8 D.N. Ghosh Roy, L.S. Couchman: *Inverse Problems and Inverse Scattering of Plane Waves* (Academic, New York 2002)

26.9 J. Hardamard: *Lectures on Cauchy's Problem in Linear Partial Differential Equations* (Yale Univ. Press, New Haven 1923)

26.10 L. Landweber: An iteration formula for Fredholm integral equations of the first kind, Am. J. Math. **73**, 615–624 (1951)

Amazon EX1014 Page 1095

26.11 A.M. Cormack: Representation of a function by its line integrals, with some radiological applications, J. App. Phys. **34**, 2722–2727 (1963)
26.12 A.M. Cormack: Representation of a function by its line integrals, with some radiological applications II, J. App. Phys. **35**, 2908–2913 (1964)
26.13 A.N. Tikhonov, V.Y. Arsenin: *Solutions of Ill-Posed Problems* (Winston, Washington 1977)
26.14 S.R. Deans: *The Radon Transform and Some of its Applications* (Wiley, New York 1983)
26.15 A.K. Louis: Mathematical problems of computerized tomography, Proc. IEEE **71**, 379–389 (1983)
26.16 M.H. Protter: Can one hear the shape of a drum? Revisited, SIAM Rev. **29**, 185–197 (1987)
26.17 K. Chadan, P.C. Sabatier: *Inverse Problems in Quantum Scattering Theory*, 2nd edn. (Springer, New York 1989)
26.18 A.K. Louis: Medical imaging: state of the art and future development, Inv. Probl. **8**, 709–738 (1992)
26.19 D. Colton, R. Kress: *Inverse Acoustic and Electromagnetic Scattering Theory*, 2nd edn. (Springer, New York 1998)
26.20 D. Gabor: A new microscopic principle, Nature **161**, 777 (1948)
26.21 B.P. Hilderbrand, B.B. Brenden: *An Introduction to Acoustical Holography* (Plenum, New York 1972)
26.22 E.N. Leith, J. Upatnieks: Reconstructed wavefronts and communication theory, J. Opt. Soc. Am. **52**, 1123–1130 (1962)
26.23 W.E. Kock: Hologram television, Proc. IEEE **54**, 331 (1966)
26.24 G. Tricoles, E.L. Rope: Reconstructions of visible images from reduced-scale replicas of microwave holograms, J. Opt. Soc. Am. **57**, 97–99 (1967)
26.25 G.C. Sherman: Reconstructed wave forms with large diffraction angles, J. Opt. Soc. Am. **57**, 1160–1161 (1967)
26.26 J.W. Goodman, R.W. Lawrence: Digital image formation from electronically detected holograms, Appl. Phys. Lett. **11**, 77–79 (1967)
26.27 Y. Aoki: Microwave holograms and optical reconstruction, Appl. Opt. **6**, 1943–1946 (1967)
26.28 R.P. Porter: Diffraction-limited, scalar image formation with holograms of arbitrary shape, J. Opt. Soc. Am. **60**, 1051–1059 (1970)
26.29 E. Wolf: Determination of the amplitude and the phase of scattered fields by holography, J. Opt. Soc. Am. **60**, 18–20 (1970)
26.30 W.H. Carter: Computational reconstruction of scattering objects from holograms, J. Opt. Soc. Am. **60**, 306–314 (1970)
26.31 E.G. Williams, J.D. Maynard, E. Skudrzyk: Sound source reconstruction using a microphone array, J. Acoust. Soc. Am. **68**, 340–344 (1980)
26.32 E.G. Williams, J.D. Maynard: Holographic imaging without the wavelength resolution limit, Phys. Rev. Lett. **45**, 554–557 (1980)
26.33 E.A. Ash, G. Nichols: Super-resolution aperture scanning microscope, Nature **237**, 510–512 (1972)
26.34 S.U. Pillai: *Array Signal Processing* (Springer, New York 1989)
26.35 D.H. Johnson, D.E. Dudgeon: *Array Signal Processing Concepts and Techniques* (Prentice–Hall, Upper Saddle River 1993)
26.36 M. Kaveh, A.J. Barabell: The statistical performance of the MUSIC and the minimum-Norm algorithms in resolving plane waves in noise, IEEE Trans. Acoust. Speech Signal Process. **34**, 331–341 (1986)
26.37 M. Lasky: Review of undersea acoustics to 1950, J. Acoust. Soc. Am. **61**, 283–297 (1977)
26.38 B. Barskow, W.F. King, E. Pfizenmaier: Wheel/rail noise generated by a high-speed train investigated with a line array of microphones, J. Sound Vib. **118**, 99–122 (1987)
26.39 J. Hald, J.J. Christensen: *A class of optimal broadband phased array geometries designed for easy construction*, Proc. Inter-Noise 2002 (Int. Inst. Noise Control Eng., West Lafayette 2002)
26.40 Y. Takano: *Development of visualization system for high-speed noise sources with a microphone array and a visual sensor*, Proc. Inter-Noise 2003 (Int. Inst. Noise Control Eng., West Lafayette 2003)
26.41 G. Elias: *Source localization with a two-dimensional focused array: Optimal Signal processing for a cross-shaped array*, Proc. Inter-Noise 95 (Int. Inst. Noise Control Eng., West Lafayette 1995) pp. 1175–1178
26.42 A. Nordborg, A. Martens, J. Wedemann, L. Wellenbrink: *Wheel/rail noise separation with microphone array measurements*, Proc. Inter-Noise 2001 (Int. Inst. Noise Control Eng., West Lafayette 2001) pp. 2083–2088
26.43 A. Nordborg, J. Wedemann, L. Wellenbrink: *Optimum array microphone configuration*, Proc. Inter-Noise 2000 (Int. Inst. Noise Control Eng., West Lafayette 2000)
26.44 P.R. Stepanishen, K.C. Benjamin: Forward and backward prediction of acoustic fields using FFT methods, J. Acoust. Soc. Am. **71**, 803–812 (1982)
26.45 E.G. Williams, J.D. Maynard: Numerical evaluation of the Rayleigh integral for planar radiators using the FFT, J. Acoust. Soc. Am. **72**, 2020–2030 (1982)
26.46 J.D. Maynard, E.G. Williams, Y. Lee: Nearfield acoustic holography (NAH): I. Theory of generalized holography and the development of NAH, J. Acoust. Soc. Am. **78**, 1395–1413 (1985)
26.47 W.A. Veronesi, J.D. Maynard: Nearfield acoustic holography (NAH) II. Holographic reconstruction algorithms and computer implementation, J. Acoust. Soc. Am. **81**, 1307–1322 (1987)
26.48 S.I. Hayek, T.W. Luce: Aperture effects in planar nearfield acoustical imaging, ASME J. Vib. Acoust. Stress Reliab. Des. **110**, 91–96 (1988)
26.49 A. Sarkissian, C.F. Gaumond, E.G. Williams, B.H. Houston: Reconstruction of the acoustic field

Amazon EX1014 Page 1096

over a limited surface area on a vibrating cylinder, J. Acoust. Soc. Am. **93**, 48–54 (1993)
26.50 J. Hald: *Reduction of spatial windowing effects in acoustical holography*, Proc. Inter-Noise 94 (Int. Inst. Noise Control Eng., West Lafayette 1994) pp. 1887–1890
26.51 H.-S. Kwon, Y.-H. Kim: Minimization of bias error due to windows in planar acoustic holography using a minimum error window, J. Acoust. Soc. Am. **98**, 2104–2111 (1995)
26.52 K. Saijou, S. Yoshikawa: Reduction methods of the reconstruction error for large-scale implementation of near-field acoustical holography, J. Acoust. Soc. Am. **110**, 2007–2023 (2001)
26.53 K.-U. Nam, Y.-H. Kim: Errors due to sensor and position mismatch in planar acoustic holography, J. Acoust. Soc. Am. **106**, 1655–1665 (1999)
26.54 G. Weinreich, E.B. Arnold: Method for measuring acoustic radiation fields, J. Acoust. Soc. Am. **68**, 404–411 (1980)
26.55 E.G. Williams, H.D. Dardy, R.G. Fink: Nearfield acoustical holography using an underwater, automated scanner, J. Acoust. Soc. Am. **78**, 789–798 (1985)
26.56 D. Blacodon, S.M. Candel, G. Elias: Radial extrapolation of wave fields from synthetic measurements of the nearfield, J. Acoust. Soc. Am. **82**, 1060–1072 (1987)
26.57 J. Hald: *STSF – a unique technique for scan-based near-field acoustic holography without restrictions on coherence*, Bruel Kjær Tech. Rev. 1 (Bruel Kjær, Noerum 1989)
26.58 K.B. Ginn, J. Hald: *STSF – practical instrumentation and applications*, Bruel Kjær Tech. Rev. 2 (Bruel Kjær, Noerum 1989)
26.59 S.H. Yoon, P.A. Nelson: A method for the efficient construction of acoustic pressure cross-spectral matrices, J. Sound Vib. **233**, 897–920 (2000)
26.60 H.-S. Kwon, Y.-J. Kim, J.S. Bolton: Compensation for source nonstationarity in multireference, scan-based near-field acoustical holography, J. Acoust. Soc. Am. **113**, 360–368 (2003)
26.61 K.-U. Nam, Y.-H. Kim: *Low coherence acoustic holography*, Proc. Inter-Noise 2003 (Int. Inst. Noise Control Eng., West Lafayette 2003)
26.62 H.-S. Kwon, Y.-H. Kim: Moving frame technique for planar acoustic holography, J. Acoust. Soc. Am. **103**, 1734–1741 (1998)
26.63 S.-H. Park, Y.-H. Kim: An improved moving frame acoustic holography for coherent band-limited noise, J. Acoust. Soc. Am. **104**, 3179–3189 (1998)
26.64 S.-H. Park, Y.-H. Kim: Effects of the speed of moving noise sources on the sound visualization by means of moving frame acoustic holography, J. Acoust. Soc. Am. **108**, 2719–2728 (2000)
26.65 S.-H. Park, Y.-H. Kim: Visualization of pass-by noise by means of moving frame acoustic holography, J. Acoust. Soc. Am. **110**, 2326–2339 (2001)
26.66 S.M. Candel, C. Chassaignon: Radial extrapolation of wave fields by spectral methods, J. Acoust. Soc. Am. **76**, 1823–1828 (1984)
26.67 E.G. Williams, H.D. Dardy, K.B. Washburn: Generalized nearfield acoustical holography for cylindrical geometry: Theory and experiment, J. Acoust. Soc. Am. **81**, 389–407 (1987)
26.68 B.K. Gardner, R.J. Bernhard: A noise source identification technique using an inverse Helmholtz integral equation method, ASME J. Vib. Acoust. Stress Reliab. Des. **110**, 84–90 (1988)
26.69 E.G. Williams, B.H. Houston, J.A. Bucaro: Broadband nearfield acoustical holography for vibrating cylinders, J. Acoust. Soc. Am. **86**, 674–679 (1989)
26.70 G.H. Koopmann, L. Song, J.B. Fahnline: A method for computing acoustic fields based on the principle of wave superposition, J. Acoust. Soc. Am. **86**, 2433–2438 (1989)
26.71 A. Sarkissan: Near-field acoustic holography for an axisymmetric geometry: A new formulation, J. Acoust. Soc. Am. **88**, 961–966 (1990)
26.72 M. Tamura: Spatial Fourier transform method of measuring reflection coefficients at oblique incidence. I: Theory and numerical examples, J. Acoust. Soc. Am. **88**, 2259–2264 (1990)
26.73 L. Song, G.H. Koopmann, J.B. Fahnline: Numerical errors associated with the method of superposition for computing acoustic fields, J. Acoust. Soc. Am. **89**, 2625–2633 (1991)
26.74 M. Villot, G. Chaveriat, J. Ronald: Phonoscopy: An acoustical holography technique for plane structures radiating in enclosed spaces, J. Acoust. Soc. Am. **91**, 187–195 (1992)
26.75 D.L. Hallman, J.S. Bolton: *Multi-reference nearfield acoustical holography in reflective environments*, Proc. Inter-Noise 93 (Int. Inst. Noise Control Eng., West Lafayette 1993) pp. 1307–1310
26.76 M.-T. Cheng, J.A. Mann III, A. Pate: Wave-number domain separation of the incident and scattered sound field in Cartesian and cylindrical coordinates, J. Acoust. Soc. Am. **97**, 2293–2303 (1995)
26.77 M. Tamura, J.F. Allard, D. Lafarge: Spatial Fourier-transform method for measuring reflection coefficients at oblique incidence. II. Experimental results, J. Acoust. Soc. Am. **97**, 2255–2262 (1995)
26.78 Z. Wang, S.F. Wu: Helmholtz equation – least-squares method for reconstructing the acoustic pressure field, J. Acoust. Soc. Am. **102**, 2020–2032 (1997)
26.79 S.F. Wu, J. Yu: Reconstructing interior acoustic pressure fields via Helmholtz equation least-squares method, J. Acoust. Soc. Am. **104**, 2054–2060 (1998)
26.80 S.-C. Kang, J.-G. Ih: The use of partially measured source data in near-field acoustical holography based on the BEM, J. Acoust. Soc. Am. **107**, 2472–2479 (2000)

Amazon EX1014 Page 1097

26.81 S.F. Wu: On reconstruction of acoustic pressure fields using the Helmholtz equation least squares method, J. Acoust. Soc. Am. **107**, 2511–2522 (2000)

26.82 N. Rayess, S.F. Wu: Experimental validation of the HELS method for reconstructing acoustic radiation from a complex vibrating structure, J. Acoust. Soc. Am. **107**, 2955–2964 (2000)

26.83 Z. Zhang, N. Vlahopoulos, S.T. Raveendra, T. Allen, K.Y. Zhang: A computational acoustic field reconstruction process based on an indirect boundary element formulation, J. Acoust. Soc. Am. **108**, 2167–2178 (2000)

26.84 S.-C. Kang, J.-G. Ih: On the accuracy of nearfield pressure predicted by the acoustic boundary element method, J. Sound Vib. **233**, 353–358 (2000)

26.85 S.-C. Kang, J.-G. Ih: Use of nonsingular boundary integral formulation for reducing errors due to near-field measurements in the boundary element method based near-field acoustic holography, J. Acoust. Soc. Am. **109**, 1320–1328 (2001)

26.86 S.F. Wu, N. Rayess, X. Zhao: Visualization of acoustic radiation from a vibrating bowling ball, J. Acoust. Soc. Am. **109**, 2771–2779 (2001)

26.87 J.D. Maynard: *A new technique combining eigenfunction expansions and boundary elements to solve acoustic radiation problems*, Proc. Inter-Noise 2003 (Int. Inst. Noise Control Eng., West Lafayette 2003)

26.88 E.G. Williams: *Fourier Acoustics: Sound Radiation and Near Field Acoustical Holography* (Academic, London 1999)

26.89 F.L. Thurstone: Ultrasound holography and visual reconstruction, Proc. Symp. Biomed. Eng. **1**, 12–15 (1966)

26.90 A.L. Boyer, J.A. Jordan Jr., D.L. van Rooy, P.M. Hirsch, L.B. Lesem: *Computer reconstruction of images from ultrasonic holograms*, Proc. Second International Symposium on Acoustical Holography (Plenum, New York 1969)

26.91 A.F. Metilerell, H.M.A. El-Sum, J.J. Dreher, L. Larmore: Introduction to acoustical holography, J. Acoust. Soc. Am. **42**, 733–742 (1967)

26.92 L.A. Cram, K.O. Rossiter: *Long-wavelength holography and visual reproduction methods*, Proc. Second International Symposium on Acoustical Holography (Plenum, New York 1969)

26.93 T.S. Graham: *A new method for studying acoustic radiation using long-wavelength acoustical holography*, Proc. Second International Symposium on Acoustical Holography (Plenum, New York 1969)

26.94 E.E. Watson: Detection of acoustic sources using long-wavelength acoustical holography, J. Acoust. Soc. Am. **54**, 685–691 (1973)

26.95 H. Fleischer, V. Axelrad: Restoring an acoustic source from pressure data using Wiener filtering, Acustica **60**, 172–175 (1986)

26.96 E.G. Williams: Supersonic acoustic intensity, J. Acoust. Soc. Am. **97**, 121–127 (1995)

26.97 M.R. Bai: Acoustical source characterization by using recursive Wiener filtering, J. Acoust. Soc. Am. **97**, 2657–2663 (1995)

26.98 J.C. Lee: Spherical acoustical holography of low-frequency noise sources, Appl. Acoust. **48**, 85–95 (1996)

26.99 G.P. Carroll: The effect of sensor placement errors on cylindrical near-field acoustic holography, J. Acoust. Soc. Am. **105**, 2269–2276 (1999)

26.100 W.A. Veronesi, J.D. Maynard: Digital holographic reconstruction of sources with arbitrarily shaped surfaces, J. Acoust. Soc. Am. **85**, 588–598 (1989)

26.101 G.V. Borgiotti, A. Sarkissan, E.G. Williams, L. Schuetz: Conformal generalized near-field acoustic holography for axisymmetric geometries, J. Acoust. Soc. Am. **88**, 199–209 (1990)

26.102 D.M. Photiadis: The relationship of singular value decomposition to wave-vector filtering in sound radiation problems, J. Acoust. Soc. Am. **88**, 1152–1159 (1990)

26.103 G.-T. Kim, B.-H. Lee: 3-D sound source reconstruction and field reprediction using the Helmholtz integral equation, J. Sound Vib. **136**, 245–261 (1990)

26.104 A. Sarkissan: Acoustic radiation from finite structures, J. Acoust. Soc. Am. **90**, 574–578 (1991)

26.105 J.B. Fahnline, G.H. Koopmann: A numerical solution for the general radiation problem based on the combined methods of superposition and singular value decomposition, J. Acoust. Soc. Am. **90**, 2808–2819 (1991)

26.106 M.R. Bai: Application of BEM (boundary element method)-based acoustic holography to radiation analysis of sound sources with arbitrarily shaped geometries, J. Acoust. Soc. Am. **92**, 533–549 (1992)

26.107 G.V. Borgiotti, E.M. Rosen: The determination of the far field of an acoustic radiator from sparse measurement samples in the near field, J. Acoust. Soc. Am. **92**, 807–818 (1992)

26.108 B.-K. Kim, J.-G. Ih: On the reconstruction of the vibro-acoustic field over the surface enclosing an interior space using the boundary element method, J. Acoust. Soc. Am. **100**, 3003–3016 (1996)

26.109 B.-K. Kim, J.-G. Ih: Design of an optimal wave-vector filter for enhancing the resolution of reconstructed source field by near-field acoustical holography (NAH), J. Acoust. Soc. Am. **107**, 3289–3297 (2000)

26.110 P.A. Nelson, S.H. Yoon: Estimation of acoustic source strength by inverse methods: Part I, conditioning of the inverse problem, J. Sound Vib. **233**, 643–668 (2000)

26.111 S.H. Yoon, P.A. Nelson: Estimation of acoustic source strength by inverse methods: Part II, experimental investigation of methods for choosing regularization parameters, J. Sound Vib. **233**, 669–705 (2000)

Amazon EX1014 Page 1098

26.112 E.G. Williams: Regularization methods for near-field acoustical holography, J. Acoust. Soc. Am. **110**, 1976–1988 (2001)
26.113 S.F. Wu, X. Zhao: Combined Helmholtz equation – least squares method for reconstructing acoustic radiation from arbitrarily shaped objects, J. Acoust. Soc. Am. **112**, 179–188 (2002)
26.114 A. Schuhmacher, J. Hald, K.B. Rasmussen, P.C. Hansen: Sound source reconstruction using inverse boundary element calculations, J. Acoust. Soc. Am. **113**, 114–127 (2003)
26.115 Y. Kim, P.A. Nelson: Spatial resolution limits for the reconstruction of acoustic source strength by inverse methods, J. Sound Vib. **265**, 583–608 (2003)
26.116 Y.-K. Kim, Y.-H. Kim: Holographic reconstruction of active sources and surface admittance in an enclosure, J. Acoust. Soc. Am. **105**, 2377–2383 (1999)
26.117 P.M. Morse, H. Feshbach: *Methods of Theoretical Physics, Part I* (McGraw–Hill, New York 1992)
26.118 L.L. Beranek, I.L. Ver: *Noise and Vibration Control Engineering* (Wiley, New York 1992)
26.119 J.S. Bendat, A.G. Piersol: *Random Data: Analysis and Measurement Procedures*, 2nd edn. (Wiley, New York 1986)
26.120 D. Hallman, J.S. Bolton: *Multi-reference nearfield acoustical holography*, Proc. Inter-Noise 92 (Int. Inst. Noise Control Eng., West Lafayette 1992) pp. 1165–1170
26.121 R.J. Ruhala, C.B. Burroughs: *Separation of leading edge, trailing edge, and sidewall noise sources from rolling tires*, Proc. Noise-Con 98 (Noise Control Foundation, Poughkeepsie 1998) pp. 109–114
26.122 H.-S. Kwon, J.S. Bolton: *Partial field decomposition in nearfield acoustical holography by the use of singular value decomposition and partial coherence procedures*, Proc. Noise-Con 98 (Noise Control Foundation, Poughkeepsie 1998) pp. 649–654
26.123 M.A. Tomlinson: Partial source discrimination in near field acoustic holography, Appl. Acoust. **57**, 243–261 (1999)
26.124 K.-U. Nam, Y.-H. Kim: Visualization of multiple incoherent sources by the backward prediction of near-field acoustic holography, J. Acoust. Soc. Am. **109**, 1808–1816 (2001)
26.125 K.-U. Nam, Y.-H. Kim, Y.-C. Choi, D.-W. Kim, O.-J. Kwon, K.-T. Kang, S.-G. Jung: *Visualization of speaker, vortex shedding, engine, and wind noise of a car by partial field decomposition*, Proc. Inter-Noise 2002 (Int. Inst. Noise Control Eng., West Lafayette 2002)

Amazon EX1014 Page 1099

27. Optical Methods for Acoustics and Vibration Measurements

Modern optical methods applicable to vibration analysis, monitoring bending-wave propagation in plates and shells as well as propagating acoustic waves in transparent media such as air and water are described. Field methods, which capture the whole object field in one recording, and point measuring (scanning) methods, which measure at one point (small area) at a time (but in that point as a function of time), will be addressed. Temporally, harmonic vibrations, multi-frequency repetitive motions and transient or dynamic motions are included.

Interferometric methods, such as time-average and real-time holographic interferometry, speckle interferometry methods such as television (TV) holography, pulsed TV holography and laser vibrometry, are addressed. Intensity methods such as speckle photography or speckle correlation methods and particle image velocimetry (PIV) will also be treated.

27.1 **Introduction** 1101
27.1.1 Chladni Patterns, Phase-Contrast Methods, Schlieren, Shadowgraph 1101
27.1.2 Holographic Interferometry, Acoustical Holography 1102
27.1.3 Speckle Metrology: Speckle Interferometry and Speckle Photography 1102
27.1.4 Moiré Techniques 1104
27.1.5 Some Pros and Cons of Optical Metrology 1104

27.2 **Measurement Principles and Some Applications** 1105
27.2.1 Holographic Interferometry for the Study of Vibrations 1105
27.2.2 Speckle Interferometry – TV Holography, DSPI and ESPI for Vibration Analysis and for Studies of Acoustic Waves 1108
27.2.3 Reciprocity and TV Holography 1113
27.2.4 Pulsed TV Holography – Pulsed Lasers Freeze Propagating Bending Waves, Sound Fields and Other Transient Events 1114
27.2.5 Scanning Vibrometry – for Vibration Analysis and for the Study of Acoustic Waves 1116
27.2.6 Digital Speckle Photography (DSP), Correlation Methods and Particle Image Velocimetry (PIV) 1119

27.3 **Summary** 1122

References 1123

27.1 Introduction

27.1.1 Chladni Patterns, Phase-Contrast Methods, Schlieren, Shadowgraph

Visualization of vibration patterns in strings, plates and shells and propagating acoustic waves in transparent objects such as air and water have been of great importance for the understanding and description of different phenomena in acoustics. *Chladni* [27.1] (1756–1824) sprinkled sand on vibrating plates to show the nodal lines. His beautiful figures challenged the research community for a theoretical description and Napoleon provided a prize of 3000 francs for someone that could give a satisfactory explanation; historical introduction by Lindsay in Lord Rayleigh's, *Theory of Sound* [27.2]. Chladni patterns are in some applications a simple, cost-effective way to visualize vibration patterns, often competitive to and an alternative to modern optical methods. In certain cases, such as for curved surfaces, the Chladni patterns may however, give completely misleading results.

Amazon EX1014 Page 1100

Transparent or semitransparent objects such as cells and bacteria in microscopy, air flow and pressure fields in fluid mechanics, sound fields in acoustics etc. are objects that was not readily observed with the unaided eye. *Zernike* [27.3] developed phase-contrast microscopy, one of many optical, spatial-filtering techniques that operate in the Fourier-transform plane of imaging systems, to obtain images of such normally invisible objects. These techniques became very important in medicine and biology and are today used both in routine investigations and in research. In *Atlas de phénomènes d'optique* (Atlas of optical phenomena) [27.4] a collection of beautiful photographs of interference, diffraction, polarization and phase-contrast experiments are found. In *An Album of Fluid Motion* [27.5] different kinds of fluid flows are visualized. Classical optical filtering methods such as shadowgraph and Schlieren [27.6] are, together with interferometric methods, used to illustrate phenomena in turbulence, convection, subsonic and supersonic flow, shock waves, etc. Some of them, such as shock waves in air and water, certainly also generate sound fields. Still, most of those more classical methods only find limited application in acoustics since they mostly give qualitative pictures only. Practical optical methods with higher sensitivity, higher spatial resolution and that also give quantitative data have therefore been developed.

27.1.2 Holographic Interferometry, Acoustical Holography

In 1965 *Horman* [27.7], *Burch* [27.8], *Powell* and *Stetson* [27.9, 10] proposed to use holography [27.11] for optical interferometry. With holography a method was invented by which a wavefront, including phase and amplitude information, could be recorded and stored in a hologram. Subsequently a copy of the recorded wavefront could be reconstructed from the hologram for later use. At that time most holograms were recorded on special, high-resolution photographic plates. In ordinary photography it is the intensity (the irradiance distribution) that is recorded and displayed. This quantity is proportional to the amplitude squared. In that operation the phase is lost. And it is the phase that carries the information of the optical path: that is the distance to the object, or the direction, for light passing through a transparent medium. Now, assume for instance that a hologram was exposed twice in the same setup (a double-exposed hologram) of an object in two different states, for instance with a small deformation introduced between the exposures. Then in the reconstruction both these two fields were reconstructed and displayed simultaneously. The total reconstruction then showed the object covered with a set of interference fringes (dark and bright bands) that display the difference in phase. A measure of the deformation field was thus obtained by letting an object interfere with itself. The techniques were called holographic interferometry or just hologram interferometry. Three sub-techniques evolved: two-exposure (or double exposure), time-average and real-time holographic interferometry. The research area evolved rapidly. A thorough, self-contained description of holographic interferometry of that time, including pulsed (two-exposure) holographic interferometry, is found in *Vest* [27.12]. For the first time diffusely scattering objects and transparent objects could be subjected to interferometric analysis. Holograms were, however, mostly recorded on photographic plates or film. The reconstruction of the recorded field was done optically and to evaluate data often a new set of photographs had to be made. All together, this was a quite time-consuming and complicated task and this fact stopped or hindered many attempts for industrial use of the technique. Holographic interferometry methods were also applied in acoustics quite early on [27.13], in what was called acoustical holography (see also Chap. 26).

27.1.3 Speckle Metrology: Speckle Interferometry and Speckle Photography

Speckle Interferometry and Shearography

The use of video systems to record holograms and speckle patterns was proposed by several groups in the early 1970s [27.14–17]. Several different names for such systems were proposed, among them, electronic speckle-pattern interferometry (ESPI). But these new holographic techniques also had quite limited commercial success. One drawback was the rather poor quality of the interferograms (poor resolution, noisy images); furthermore quantitative evaluation of deformation and vibration fields was still difficult to obtain. Any diffuse object that is illuminated by coherent laser light will normally appear very grainy (speckled) to an observer. These randomly distributed spots are called speckles. They carry information about the fine structure of the objects micro-surface and of the optical system (the illumination and the observation system) used. The smaller aperture of the imaging system is set, the larger the speckles are. Speckles are of

Amazon EX1014 Page 1101

course also present in ordinary holographic interferometry but, as the apertures used here normally are much larger, the effects of speckles are not too severe. However, sometimes the speckles lowered the quality of the interferograms significantly, especially in early speckle interferometry. Vibration analysis using speckle interferometry was, however, developed quite far by a group in Trondheim [27.18–21]. With the improved capabilities during the 1980s of computers, sophisticated high-resolution charge-coupled device (CCD) cameras, fiber optics and ingenious piezoelectric devices, quantitative fringe interpretation became feasible. ESPI became digital and was renamed digital speckle-pattern interferometry (DSPI). Other names are electro-optic holography (EOH) and television (TV) holography. These methods are *all electronic* and they capture images at TV rate (25 pictures/s). Interferograms are also updated at such a rate that, for the human eye, they seem to be displayed in real time even if they are really time-average interferograms displayed at high rate, all in one system. Such systems work well both for sinusoidal vibrations and two-step motions. The quality of the interferograms was improved with the introduction of phase stepping [27.22–25] and speckle averaging methods [27.18, 19], which largely eliminated the noisy, speckled background.

Pulsed TV holography [27.12, 26–28] has a pulsed laser as a light source instead of continuous laser as in the ordinary TV holography system. It was used mainly for the study of transient and dynamic events both for solids and transparent objects.

Shearography or speckle shearing interferometry [27.29–31] is another branch of speckle metrology that can directly measure derivatives of surface displacements (without numerical differentiation of deformation fields) of surfaces undergoing a deformation. It is, for instance, used for nondestructive testing (NDT) of parts for the airplane industry and for tire testing. It is a much more robust technique than DSPI or TV holography. The laser-illuminated object is imaged twice, usually before and after some load or deformation is introduced, in such a way that two nearby object points in the image plane will overlap and interfere. This shearing effect can, for instance, be accomplished by letting the camera look at the object through a Michelson interferometer setup with the two mirrors slightly tilted with respect to each other, thus forming two overlapping sheared images. A more traditional method is to cover one half of the imaging aperture (the camera lens) with a thin prism so that two sheared images will overlap each other in the image plane. Since both these sheared fields have traveled almost along the same path from the object to the image plane, they will both be submitted to about equal disturbances caused by the surroundings. In the sheared interferogram, these two fields are subtracted and therefore such equal disturbances will disappear and not affect the final interferogram. If, however, local disturbances exist, for instance an opening crack causing large in-plane, local deformations, such events will show up in the interferogram. The setup is thus quite robust and can be used in the workshop. Another advantage is that the measuring sensitivity can easily be changed by changing the amount of shear (tilt of mirrors in the Michelson setup) that is introduced. Even very large deformations or vibration amplitudes can be measured but since the instrument measures slope change (surface derivatives) the measured result has to be integrated to give deformation or vibration amplitudes. In [27.31–33] shearography is compared to TV holography and applied to measure vibration fields.

Several different kinds of speckle interferometry systems manufactured in Germany, US, Norway etc. are available on the market.

Laser Doppler Anemometry (LDA) Velocimetry and Vibrometry (LDV)

Parallel to full-field methods, point-measuring, interferometric methods were developed quite early. Laser Doppler anemometry (LDA, also named LDV where V stands for velocimetry) is a technique that measures flow velocities in seeded fluids such as air or water. It can also be used to measure the in-plane motion of solid surfaces. It was proposed as early as 1964 [27.34, 35]. A single laser beam is split into two beams. The beams are focused at an angle to each other into a common small volume in the flow, where they interfere so an interference pattern is formed in this small volume. Particles moving through this striped interference pattern scatter light with varying intensities when moving through it. The frequency of this intensity variation is measured. The distance between the interference stripes is given by the angle between the interfering beams and the laser wavelength. A measure of the velocity component of the flow at a right angle to the striped pattern is therefore obtained. With several crossing beams at different wavelengths in one point, it is possible to obtain several velocity components. Another explanation of the same phenomenon states that laser-illuminated, moving particles will scatter light with a shifted frequency, a Doppler shift, relative to particles that have zero veloc-

ity. The frequency of this intensity variation is detected despite the very large difference in frequency between this Doppler signal and the frequency of undisturbed light by combining interferometry with heterodyne detection. It can be shown that this frequency shift is proportional to the flow-velocity component at a right angle to the interference pattern.

Laser Doppler vibrometry or just vibrometry [27.36] is a related interferometric point-measuring method that also uses a heterodyne technique. It is used to measure vibration amplitudes, or rather vibration velocities of vibrating surfaces instead of flow velocities. Here it is the Doppler shift that laser light experiences when it is reflected from a moving surface that is detected. It gives a measure of the out-of-plane velocity component of the moving object point if it is illuminated also at a right angle. Both LDA and vibrometry systems can be equipped with scanning facilities that allow whole-field measurements. To preserve relative phase information in the signals when moving from one measuring point to the next, some kind of reference signal from a microphone, accelerometer or other transducer is necessary. Hardware and software of point-measuring techniques are sold by several manufacturers and the equipment is today quite user-friendly but also rather expensive.

Digital Speckle Photography (DSP) Speckle Correlation, Particle Image Velocimetry (PIV)

Another branch of speckle metrology [27.37–40] in addition to speckle interferometry, is speckle photography or speckle correlation methods. Speckle photography measures the bulk motion of the speckle pattern, the random noisy pattern that is present. This random pattern is either created artificially (i.e. sprayed dots of paint), present naturally (i.e. as fibers in a wood sample) or caused by laser-light illumination of diffuse objects. In speckle interferometry it is the phase coded in intensity of the speckles (assumed more or less stationary in space) and in speckle photography it is the position of the speckles that is detected. Speckle photography is based upon the fact that, if the laser-illuminated object is moved or deformed, then the speckles in the image plane will also move. So speckle photography in its simplest form gives a measure of the in-plane motion of the object surface. In particle image velocimetry (PIV) a sheet of light illuminates a flow seeded with suitable scattering particles [27.41]. These particles follow the flow. They are imaged twice with a CCD camera at a known time interval. The distance the particles have moved is determined with a correlation technique. In this way a measure of the flow velocity field is obtained [27.42].

27.1.4 Moiré Techniques

The Moiré effect, sometimes also named mechanical interference, shows up in many practical viewing situations. It is called mechanical interference since it is not optical interference between light fields that is studied; instead two or more striped, meshed, physical intensity patterns are overlaid and imaged most often in white light illumination. Folded fine-meshed curtains, suits of people appearing on TV, netting along roads etc. sometimes become modulated by a coarse pattern overlapping the finer mesh itself; in many cases this finer mesh is not resolved at all only the coarse, so-called Moiré patterns remain. Moiré as a measuring technique is quite old [27.43, 44]. It is related to the more modern speckle photography technique with the great difference that, instead of a random pattern, a regular pattern, a grating or a mesh, is used. If two identical gratings are overlapped and imaged a regular pattern of so called Moiré fringes will show up. If one of the gratings is glued onto an object and this object is deformed a modulation of the Moiré fringes will appear when this grating is compared to the stationary grating. This exemplifies an in-plane measuring technique using the Moiré effect. Combined with high-speed photography this technique has been used for the study of very fast events in engineering mechanics [27.45].

Techniques to measure out-of-plane deformations, vibrations, shape (contouring) are also in use as well as shadow Moiré, projected fringe techniques etc. These techniques are also named triangulation techniques since they rely on the fact that, if a regular striped pattern is projected onto a curved object surface, initially straight fringes will appear curved. A viewer will record different curved fringe patterns from different positions in the room. Knowing the geometrical parameters it is then possible to determine, e.g., the shape of a body illuminated by the projected fringes. One great advantage of Moiré methods is that the sensitivity can be chosen at will by proper selection of the line separation of the grating lines. This distance can be compared to the wavelength in optical interferometry. Quite small up to very large deformation fields can therefore be studied. A good overview of Moiré techniques can be found in [27.46], a book in which many other different phenomena and methods in optical metrology are described.

Amazon EX1014 Page 1103

27.1.5 Some Pros and Cons of Optical Metrology

In the following, measuring principles for holographic interferometry, speckle metrology, vibrometry, pulsed TV holography, Moiré methods and PIV are discussed together with some applications. The main advantages of these methods are:

- There are no contact probes. They are non-disturbing.
- Most of them are whole-field, all-electronic methods. They give pictures.
- They give not only qualitative but also quantitative measures.
- The (digital) processing is often very fast, sometimes as if in real time.
- Pulsed lasers give very short light pulses (exposure times ≈ 10 ns), that *freezes* propagating sound fields and vibrations as if stationary.

Some disadvantages are:

- Optical equipment and lasers are, in many cases, still quite expensive.
- Trained personnel are needed to get full use of high-technology equipment.
- Speckle interferometry methods such as TV holography (DSPI, ESPI) most often need auxiliary equipment such as vibration-isolated optical tables placed in rooms that are not too dusty or noisy. Others, such as pulsed TV holography and vibrometry instruments, work well in more hostile environments without vibration isolation.
- Lasers are used and must be handled in a safe way.

27.2 Measurement Principles and Some Applications

27.2.1 Holographic Interferometry for the Study of Vibrations

With the introduction of holographic interferometry in 1965, amplitude fields of vibrating, diffusely reflecting surfaces could be mapped. Earlier only mirror-like, polished objects were used in interferometry but now suddenly all kinds of objects could be studied. The interest in holographic methods increased dramatically. The most often used technique for vibration studies was time-average holographic interferometry [27.9, 10]. A hologram of the vibrating object was recorded while the object was vibrating. The exposure time of the photographic plates was quite long, often about one second. This time was long compared to the period time of the object vibration so light fields from many cycles contributed to the total exposure of the photographic plate. After development this plate is called a hologram. In the optical reconstruction of the hologram, these object fields were reconstructed simultaneously. Now, a sinusoidally vibrating object spends most of its time in each cycle at the turning points, where the velocity is momentarily zero. These parts (at a distance of twice the amplitude of vibration) therefore contribute the most (spend the longest time) to the total exposure and therefore these parts will also dominate the reconstructed fields. A time-average field is therefore reconstructed, and essentially light beams from the turning points interfere with each other. Iso-amplitude fringes that cover the object surface are mapped using this technique. The intensity of the reconstructed image of a sinusoidally vibrating surface can be described by

$$I(x, y) = I_0(x, y) J_0^2(\Omega) , \tag{27.1}$$

where $I_0(x, y)$ is the intensity of the object at rest and J_0 is the zero-order Bessel function of the first kind. The exposure does not have to span many cycles to get the J_0^2 function in time-average techniques. It is also possible to record time-average interferograms of low-frequency vibrations.

The argument

$$\Omega = \boldsymbol{K} \cdot \boldsymbol{L} , \tag{27.2}$$

where $\boldsymbol{K}$ is a sensitivity vector defined as

$$\boldsymbol{K} = \boldsymbol{k}_1 - \boldsymbol{k}_2 , \tag{27.3}$$

and $\boldsymbol{L}(x, y)$ is the vibration amplitude field. $\boldsymbol{k}_1$ and $\boldsymbol{k}_2$ are the illumination and observation directions, respectively, measured relative to the normal of the object surface. With normal illumination and observation directions the maximum sensitivity becomes

$$|\boldsymbol{K}| = 4\pi/\lambda , \tag{27.4}$$

where λ is the laser wavelength used.

A deformation field or a vibration field $\boldsymbol{L}(x, y)$ is however vectorial, that is, it has three components.

Equation (27.2) implies that it is the projected component of $\boldsymbol{L}(x, y)$ along the sensitivity vector $\boldsymbol{K}$ that is measured. With normal illumination and observation directions only the out-of-plane component is therefore measured. To obtain the in-plane components the measurements can be performed with two or more inclined illumination and observation directions. Several reference beams may also be used; see for instance [27.12, 47, 48]. With two symmetrically placed and inclined illumination directions and with observation along the object normal, the sensitivity will be zero for the out-of-plane component and optimal for one in-plane component [27.49]. A device for planning and evaluation of holographic interferometry measurements is called a holo-diagram [27.50], proposed by Abramson and in [27.23], Kreis presents computer methods to optimize holographic arrangements for different purposes.

For a two-step (double-exposure or double-pulsed) motion the squared zero-order Bessel function in (27.1) is replaced by a squared-cosine function with half the argument, that is, $\cos^2(\Omega/2)$. $\boldsymbol{L}(x, y)$ is now the displacement of the object field that has taken place between the two recordings (pulses).

Most studies of vibrating objects, however, involve a combination of the time-average and real-time holographic interferometry technique [27.10]. Real-time observation of the vibration field gives very useful information to the experimentalist. A search for resonant modes can be made in real time to find the settings of frequency, amplitude and position of exciters etc. The vibration pattern is then recorded by the time-average technique, which often gives very nice interferograms that allow a more detailed analysis of the vibration field. Vibration modes of a violin recorded at different steps in making the violin [27.51–53] used this combined technique.

To illustrate these combined traditional techniques, the following experiment is sketched. The setup used is pictured in Fig. 27.1.

The laser, optical and mechanical components and the object are placed on a vibration isolated optical table in an off-axes holographic setup. In the off-axes technique there is an angle at the hologram plate between the object-observation direction and the reference-beam direction so that the object appears against a dark background. This way an observer does not have to look into the bright laser light from the reference beam to see the object. Beautiful reconstructions are thus obtained [27.54]. First a hologram is recorded of the object at rest, in this case the bottom of a herring can. The hologram is recorded on a high-resolution photographic plate in a special holder, a liquid gate hologram plate

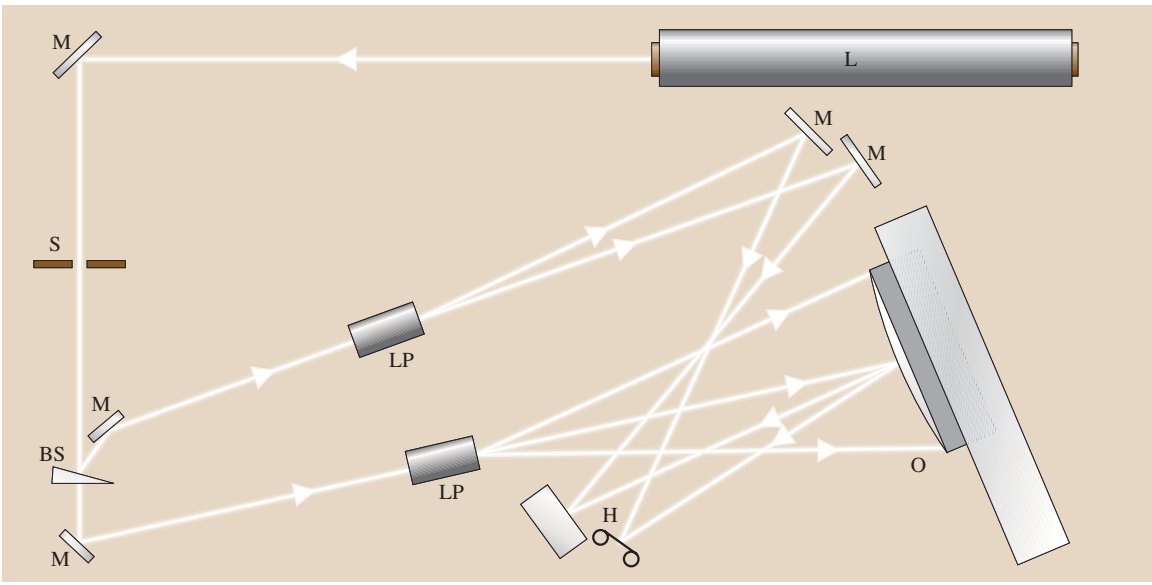


Fig. 27.1 A combined real-time and time-average hologram interferometry setup. Abbreviations: laser (L), front surface mirrors (M), glass wedge beam splitter (BS), beam expander lens–pinhole system (LP), shutter (S), a liquid gate hologram plate holder and a holder for 35 mm film (H) and an object (O), for instance a herring can or a guitar clamped to a rigid, heavy jig (J)

Amazon EX1014 Page 1105

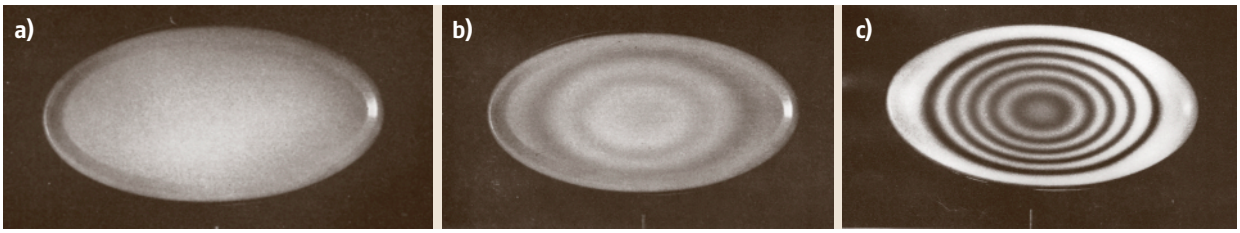


Fig. 27.2 **(a)** The test object, the bottom of a white-painted herring can, observed in its rest position in the real-time hologram interferometer using the liquid gate hologram holder (H) in Fig. 27.1, [27.55]. The object field emanating from the herring can is transmitted through the hologram and interferes with the field reconstructed by the hologram. These fields are so similar that no interference fringes are seen (actually it is the same broad white fringe that is covering the whole object). **(b)** Real-time interferogram obtained by taking a photo through the liquid gate when the herring can is vibrating in its fundamental mode. **(c)** Time-average interferogram obtained from a time-average hologram recording (using the film holder at H in Fig. 27.1) of the same vibration pattern as in Fig. 27.2b. (Permission to reproduce the Figs. 26.2a–c is given by IOP Publishing Ltd. 21/10/04)

holder [27.55]. It is exposed to the interfering light from the reference and object beam. The object field at rest is reconstructed by illuminating the hologram with the former reference wave or a laser wave proportional to it, in the same setup as before. The reconstructed stationary object field is then observed by looking through the hologram by eye or with a camera. Compare Fig. 27.2a which shows the bottom of the elliptical herring can at rest.

Now, if the original object is also illuminated by laser light in the same setup as before and observed through the hologram, the observer will see two images of the same object through the hologram, one as it is in real time and one as it was when the hologram was recorded. As both fields are coherent (the same laser reconstructs and illuminates the object), they will interfere. If the two fields are identical, no fringes will appear. To be more correct, since a negative hologram plate [a high irradiation gives a high exposure of a photographic plate, which is dark (high absorbing) and not bright] is used for the real-time holographic reconstruction and this field is added to the direct field observed through the hologram, the total object field should appear dark since the two fields are identical but out of phase (one field is negative and the other positive). If however the hologram plate holder or the object itself is moved slightly so that the first white cosine fringe covers the whole object, then the whole field will appear bright. Actually Fig. 27.2a is such a recording. The object is at rest but slightly translated from its initial position. When the object is vibrating it will become covered with interference fringes – compare Fig. 27.2b. The contrast of such real-time fringes are, however, quite low. It is also difficult, without special techniques, to avoid spurious fringes caused by rigid-body motions, emulsion shrinkage etc. of the real-time interferogram. Therefore a time-average hologram of interesting patterns is recorded; compare the time-average interferogram of the same vibrating herring can in Fig. 27.2c. This time-average hologram is recorded on 35 mm holographic film in a hologram film holder (a camera house without lenses), at H in Fig. 27.1. It is placed close to the real-time hologram liquid gate on the hologram table. The time-average interferogram contains twice as many fringes with higher contrast than the corresponding real-time one. The distance from peak to peak in a sinusoidal vibration is also twice as great as the distance from the peaks to the average (the amplitude) value. This is why the number of fringes is doubled. This combined real-time and time-average technique has been applied to many different structures, such as musical instruments, turbine blades, aircraft and car structures etc. Figure 27.3 shows an example of a time-average recording of a vibration mode of a guitar front plate identified using the real-time technique



Fig. 27.3 Time-average interferogram of a guitar top plate vibrating at 505 Hz (Bolin guitar from 1969).

Amazon EX1014 Page 1106

and recorded by time-average hologram interferometry. This picture was used as a Christmas card interferogram and it appeared in a number of physics textbooks, see also [27.56, 57]. It may be pointed out that the quality of interferograms as well as the spatial resolution, obtained in this way was high but it was a time-consuming task to obtain them compared to today's methods.

Practical resolution of vibration modes by visual observation in real time is often better than 100 nm ($\lambda/10$) – compare Fig. 27.2b. Practical maximum measurement range for time-average recordings as in Fig. 27.2c is about 4 μm, otherwise the fringe density might be too high to be resolved. The maximum possible object size in width and depth depends very much upon the laser used, both its output energy and its coherence length. The coherence length of the laser determines how big a difference in path length between the reference wave and the object beam is allowed if recording high-quality holograms. The difference in path length between the reference beam, from the laser via mirrors to the hologram, and the object beam, from the laser via the object to the hologram, should therefore not exceed the coherence length. This is easily determined with a soft string fastened at the laser and at the hologram. The power of the laser and the object reflectivity determines the width of the object and the coherence length, and thus the depth of the object volume. Objects that absorb light might be dusted with chalk or painted white. In difficult cases retro-reflective paint or tape might be used. The guitar interferogram shown in Fig. 27.3 was recorded using a 20 mW HeNe laser having a wavelength of 633 nm and a coherence length of about 25 cm, the guitar shown in Fig. 27.3 was recorded. Remember that a holographic setup is sensitive to disturbances; an optical vibration-isolated table is recommended. Powerful lasers shorten the exposure time and lower the requirements for vibration isolation.

Holographic interferometry has been further developed using pulsed or stroboscopic techniques, temporal phase modulation as well as for studies of transparent objects such as flames, pressure waves in air and water. The books by *Vest* [27.12], *Kreis* [27.23] and *Hariharan* [27.48] are recommended. In practice today, all electronic, digital speckle interferometry methods have more or less replaced wet-processing photographic holographic interferometry, at least for industrial use. The fundamental ideas are, however, still the same.

27.2.2 Speckle Interferometry – TV Holography, DSPI and ESPI for Vibration Analysis and for Studies of Acoustic Waves

Speckles [27.32–35, 46, 47] are the granular, speckled appearance that a laser-illuminated diffusely reflecting object gets, when imaged by an optical system such as the eye or a camera. The speckles can be viewed as a fingerprint that is as a unique, random pattern generated by

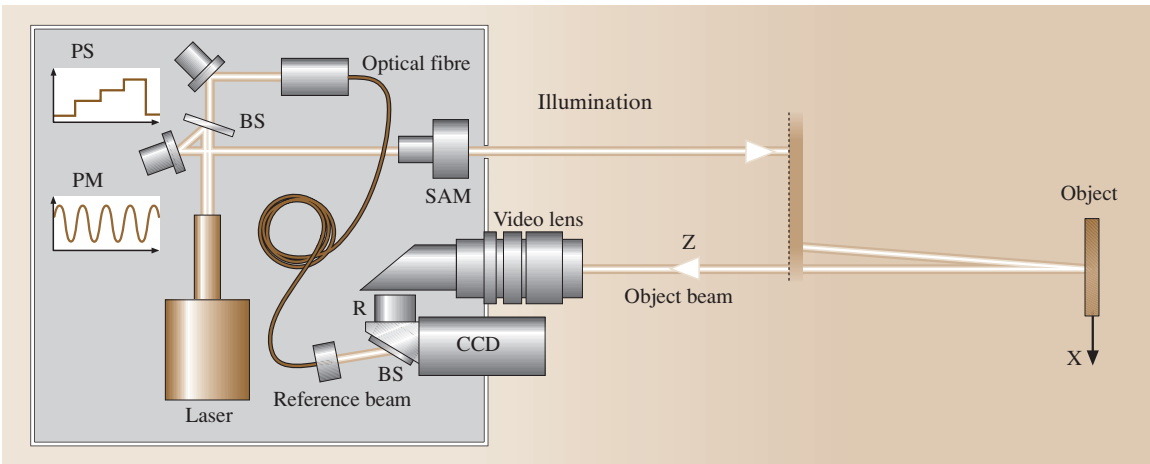


Fig. 27.4 The optical unit of TV holography (electro-optic holography, DSPI). Abbreviations: beam splitter (BS), speckle average mechanism (SAM), mirrors on piezoelectric devices used for phase stepping (PS) and sinusoidal phase modulation (PM), relay lenses (R). The distance between the optical head to the left and the object to the right can vary considerably depending of object size, magnification etc.

the fine structure of the object surface. One technically important property of the speckles is that the speckles seem to move as if glued to the object surface when the object is moved or deformed. A change in illumination or observation directions of the object will however also change the speckle pattern. Two different observers both see speckles but with different distributions. The speckles were earlier looked upon as unwanted noise but as they also carry information; they also form the basis for techniques such as speckle photography (SP) and speckle interferometry (SI). They both belong to a group of methods named speckle metrology [27.32–34]. In SP the in-plane motion of the speckles themselves is measured, and in SI the change in intensity of the speckles (i. e. the phase change of interfering beams) are used. Hologram interferometry is also based on recording the information of the same speckles.

The optical arrangement of a speckle interferometer setup called TV holography or electro-optic holography [27.25] (also named DSPI or ESPI) is shown in Fig. 27.4. A special computer board is developed that allows real-time presentations of phase-stepped interferograms.

Laser light is divided by a beam splitter (BS) into an object illumination part and a reference wave part. The object space, situated to the right, is illuminated and imaged almost along the z-axis of the object. The measuring sensitivity of this configuration therefore also becomes highest along the same direction and consequently zero along the x–y-axes. The object light amplitude field, E_{obj}, is imaged by a video lens and some transferring optics onto the photosensitive surface of the CCD chip, where the smooth reference beam, E_{ref}, also emanating from the end of an optical reference fiber is added. Each pixel of the CCD camera pictures a small area in the object space, i. e. this can be described as an in-line, image-plane holographic setup. Via a special personal computer (PC) image-processor board, results are presented at the rate allowed by the digital camera (25 or 30 Hz) on a monitor, which is a highly valuable feature in many experimental situations. In the setup there are mirrors mounted on piezoelectric crystals, allowing phase modulation (PM) and phase stepping (PS). These options are used to determine the relative phase of vibration fields and to extract quantitative data from the interferograms.

The optical detectors are so-called quadratic detectors. They measure intensity or irradiance which in turn is proportional to the square of the sum of the two interfering electromagnetic amplitude fields. The instantaneous intensity $I(x, y)$ at a pixel of the CCD detector can therefore be written:

$$I(x, y) = |(E_{\text{obj}} + E_{\text{ref}})|^2 = I_0 + I_{\text{A}} \cos(\Delta\Phi) , \tag{27.5}$$

where I_0 is the background intensity and I_{A} the modulating intensity. The desired information however, is found in $\Delta\Phi$, the relative optical phase difference between the (constant) reference and the object field in each pixel. A difficulty exists since there are three unknowns in (27.5); $\Delta\Phi$, I_0 and I_{A} but only one equation. This can be solved by Fourier-filtering methods or phase-stepping (shifting) techniques [27.22–24]. In the phase-stepping technique, PS in Fig. 27.3 is used to shift the phase with, for instance, $\pi/2$ in steps between consecutive recorded frames to obtain four equations. With four equations and three unknowns, $\Delta\Phi$ can be calculated with good accuracy. In double-exposure and pulsed TV holography two series of recordings are made, one before and one after some deformation or change is introduced to the object. The corresponding phase changes $\Delta\Phi(x, y)$ for each of the two states are determined as above and then subtracted. Since the same reference beam is used in the recording of both states, ideally only the difference in object phase will remain after subtraction. The change in object phase, $\Omega = \Delta\Phi_1 - \Delta\Phi_2$, between the two objects fields are thus obtained. This quantity, Ω in turn is defined as the change (Δ) of the product of refractive index n, the geometrical path length l and the laser wave number k. That is, the measured change in optical phase between two object states can be written as:

$$\Omega = \Delta(knl) = k(n\Delta l + l\Delta n) . \tag{27.6}$$

The wave number, $k = 2\pi/\lambda$, is (most often) a constant since λ, the laser wavelength, is the same in all recordings. Equation (27.6) illustrates two main application areas: one where the optical phase change is proportional to the change in path length (i. e. vibration amplitudes, deformation fields etc.) and one where it is proportional to the change in refractive index (caused by, for instance, wave propagation in fluids, flames etc.).

The TV holography system, shown in Fig. 27.4, illuminating and observing the object along its normal, is highly sensitive to out-of-plane vibrations or object motions and insensitive to in-plane motions. A frequency doubled, continuous-wave Nd:YAG laser with a wavelength of 532 nm, is often used. Such lasers often have a higher output power and a longer coherence length than most comparable He–Ne lasers, say 50 mW and a few meters in coherence length. The object size can now vary from a few mm up to meter-sized objects both

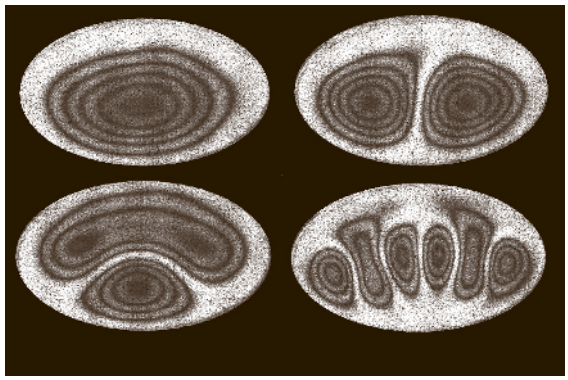


Fig. 27.5 Interferograms of four modes of vibration of the bottom of the same herring can as in Fig. 27.2, now recorded using TV holography. Both real-time observation to find the settings and time-average recordings are made at once

in width and depth. With visual observation of the monitor in real time, the resolution of the vibration amplitude is often better than 100 nm and, if the phase-stepping technique is used, the resolution limit is of the order of 20 nm, compare Fig. 27.5. The practical maximum amplitude range for vibration modes is about 2.5 μm. To be able to unwrap (numerically evaluate) fringe patterns automatically without problems, fringe densities should be kept low; not less than 15–20 pixels/fringe is recommendable. For example, a CCD camera may have 512×512 pixels or more. If the imaged object covers all 512 pixels this would allow about 25 fringes or more over the whole object field to be analyzed automatically. So it is preferable that as much as possible of the CCD chip is used to image the object. This is favorable both for the unwrapping and also for the spatial resolution of the imaged object. It is also a great advantage if a vibration-isolated optical table is used for the experiments.

The TV holography system, like many other commercial systems can also be arranged for maximum sensitivity for motion in the plane or in some other direction. Dual-beam, symmetric illumination directions about the object normal and normal object observation direction are used to achieve maximum in-plane motion sensitivity and no sensitivity to out-of-plane motions [27.47–49]. Practical resolution (adjusted for noise) is now about 30 nm with phase-stepped interferograms. The maximum measurement range for the vibration mode is about 2.5 μm. The object size in this case is often limited by the size of the illuminating lenses if equal sensitivity (with collimated light) over the whole object area is important. So, object diameters smaller than 5–10 cm are often the case, but much larger objects can be studied if varying sensitivity over the object field is allowed. Other 2-D and 3-D arrangements that measure two or three vibration components are also commercially available.

Interferograms of Vibration Modes Using TV Holography

In normal use the TV holography setup is used for sinusoidally vibrating, diffusely reflecting objects, such as the bottom of the elliptical herring can in Fig. 27.5. This is the same can that was used in Fig. 27.2, 35 years earlier. Since then the ravage of time has changed the can somewhat. It has been dropped from the shelf etc. and despite its rigid construction the mechanical shape and behavior has changed somewhat during the years. It is not as symmetrical as before. This experiment is also an example of nondestructive testing of components, which is a large application area of TV holography where vibration analysis is used.

In Fig. 27.5 the setup is arranged so that the change in index of refraction can be neglected; only the first part, $\Omega = kn\Delta l$, of (27.6) remains. In this way we get a measure of the change in geometrical path length, Δl. A complication with sinusoidally vibrating objects such as the herring can is that the modulation of the interference fringes is, as in time-average holographic interferometry, not cosinusoidal as with two-step motions (i. e. double exposure, double-pulsed holographic and pulsed speckle interferometry) but instead modulated by a zero-order Bessel function squared $J_0^2(\Omega)$, (27.1). As before, this has to do with the integrated exposure during several cycles that the detector gets when the period time of the sinusoidally vibrating object is much shorter than the exposure time of the detector (about 1/25 s at a video rate of 25 frames per second). It is, however, also possible to record time-average interferograms of low-frequency vibrations. It is only at the start that the fringe function is somewhat dependent on which part of the vibration the integration spans — after 2–3 periods the difference between the recorded fringe function and the theoretical is negligible. The white closed line (fringe) along the rim of the can, in some higher modes connected to vertical white fringes, indicates zero amplitude, i. e. a nodal line. The bright and the dark closed loop fringes connect points with equal vibration amplitude, increasing towards the center towards a hill or a valley. Measurements such as this are quite simple to perform since the equipment works well in real time. Quantitative values of the vibration amplitude and phase in each pixel is also possible using the modulation options in the setup. This is exempli-

Amazon EX1014 Page 1109

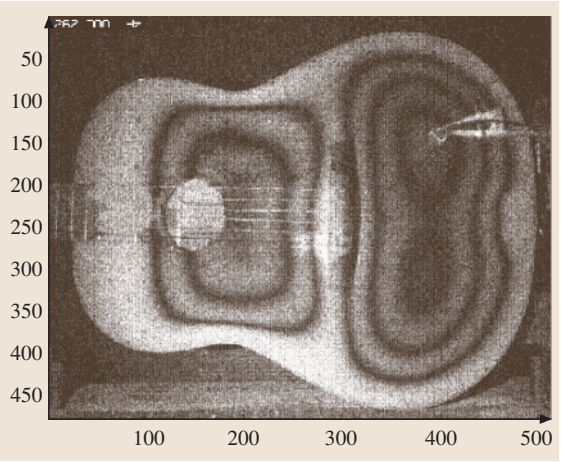


Fig. 27.6 TV holography interferogram of a baritone guitar showing a top-plate mode at 262 Hz [27.58]

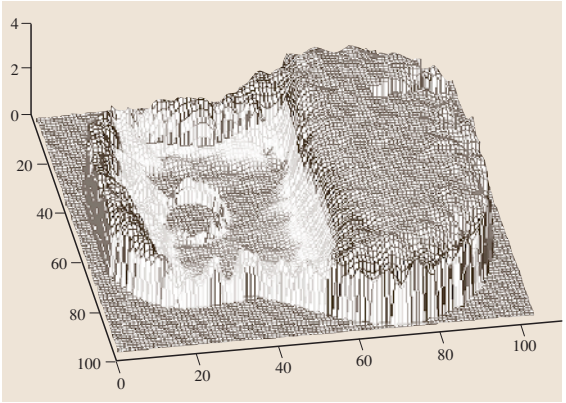


Fig. 27.7 A phase map of the same guitar mode as in Fig. 27.6 measured by phase-modulated TV holography. The units for the phase values at the z-axis are radians [27.58]

fied in Figs. 27.6 and 27.7 [27.58]. Figure 27.6 shows an ordinary TV holography recording of a mode shape of a baritone guitar mode at 262 Hz. Since this is a normal vibration mode of the front plate, the phase on each side of the vertical nodal line at the bridge should be in anti-phase.

It must, however, be stressed that, in many practical vibration situations, normal modes are often replaced by combinations or superpositions of a number of different modes. A loudspeaker, for instance, often only shows uniform, normal-mode behavior at the lowest modes. At higher frequencies the phase may vary quite a lot over the field of view; not only object areas vibrating in anti-phase are present but there is a continuous change of phase over the loudspeaker membrane. A simple test to see if mode combinations are present is to observe if nodal lines are stationary when the driving amplitude is increased from zero upwards or when the frequency is varied slightly about an amplitude resonance peak. If the nodal lines start to move sideways or twist, or so that nodal points or other peculiar phenomena occur, then mode combinations can be the source. If the experimentalist is not sure that it is a real normal mode that he has detected, i.e. one that does not have neighboring vibrating areas vibrating in anti-phase, he often calls it an operation deflection shape (ODS). So, there is a need for the experimentalist to measure not only the amplitude distribution but also the phase variation over the field of view to be sure. One technique is to set the mirror (PM in Fig. 27.4) in vibration at the same frequency and in phase with one of the vibrating areas of the object. If the amplitude of the mirror is then increased from zero, the white nodal line will start to move to new object points where the difference between the object amplitude and the mirror amplitude is zero. If, as in Fig. 27.6, a normal mode is studied, one vibrating area gets smaller (that is, there are fewer fringes in the area which is in phase with the mirror) and one area gets larger as the nodal line moves. Another technique is to use a small frequency difference, a *beat*, between the object frequency and the mirror frequency. By visual inspection, moving nodal lines are seen. A review of a number of different measurement techniques of mechanical vibrations is given by *Vest* in [27.12], by *Kreis* in [27.47] and by *Stetson* in [27.59].

The vibration phase can also be determined quantitatively using phase modulated TV holography (again using PM in Fig. 27.4). The phase difference between the upper and lower bouts, as shown in Fig. 27.7, was measured as π with such a method. Phase modulated TV holography is a technique used to measure phase and amplitude of small vibrations [27.21]. The method uses Bessel-slope evaluation of small amplitudes. Here the vibrating mirror and the object itself are given such small amplitudes such that the total maximum amplitude is kept within the linear part of the J_0^2 fringe function at low arguments. The vibrating reference wave is given such amplitude that it forms a working point, where the slope of the fringe function is the largest and around which the object amplitude may vary. By changing the phase in steps of the reference wave relative to the object wave a number of recordings are made with a known phase difference. From this the phase and amplitude distribution can be estimated. A review of such

recent developments in speckle interferometry is given by *Lökberg* as one chapter in [27.37]. Visual use of the phase-modulated techniques works in near real time, but calculations based on phase-modulation take a short time.

Visualization of Aerial Waves Using TV Holography

To get a measure of the sound field, the geometrical path length l in (27.6), is kept constant so that the first part $kn\Delta l$, equals zero. Then only the $kl\Delta n$ part remains. Since an increased air density or air pressure gives an increase to the refractive index Δn the way to see the sound is simply to let the index of refraction vary along the probing length l in a measuring volume. This distance l has to be kept constant to be able to quantify the results. Figure 27.8 illustrates the measuring principle.

Inside the box a standing aerial wave is generated by a loudspeaker. The incident plane light wave is modulated by the aerial pressure and density field in the box. A curved wavefront is generated to the right of the box. This phase change may also be measured by the TV holography system in Fig. 27.4.

Projections of the box are shown in Figs. 27.9 and 27.10. Laser light travels through the measuring volume, in the simplest case a rather flat, two-dimensional (2-D), transparent box. The light field is phase modulated by a standing aerial wave inside the box. To increase the modulation the field is reflected back again by a rigid diffuse wall (not seen in Fig. 27.8) to pass through the box twice and then pass on into the interferometer (Fig. 27.4) as the object beam. The instantaneous phase shift compared to the undisturbed air (no standing wave) with index of refraction n_0 can then be written as

$$\Omega(t, y) = \frac{4\pi}{\lambda} \int_L [n(t, x, y) - n_0]\,\mathrm{d}x$$
$$\cong 2k[n(t, y) - n_0]L\,. \qquad (27.7)$$

Since L can be measured, the integrated product of L and $\Delta n = n - n_0$ in (27.3) is known. The refractive index n is related to the air density ρ by the Gladstone–Dale equation, $n - 1 = K\rho$, where K is the Gladstone–Dale constant [27.12]. If, for instance, adiabatic conditions are assumed $(p/p_0) = (\rho/\rho_0)^\gamma$, then the relations between air density ρ and pressure p are also known. By combining these equations, a quantitative measure of the sound pressure $p(x, y, t)$ at all points in the projected field of view can be obtained. Observe that it is the integrated field that is measured; thus when we have a 2-D distribution of the sound field like the one in Fig. 27.8, it can be assumed that the integral in (27.3) is reduced to the sim-

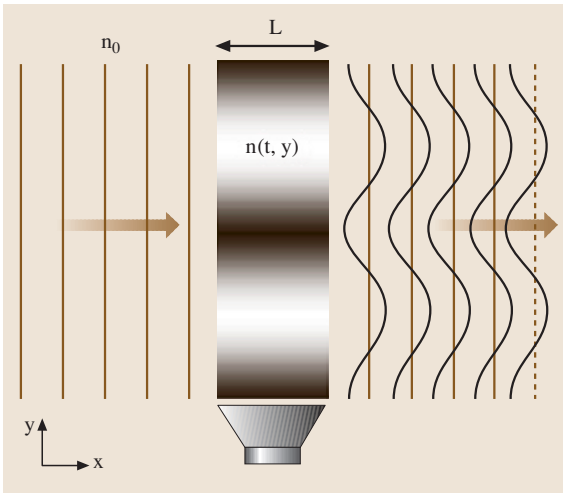


Fig. 27.8 A plane laser wave is traveling through a transparent box with dimensions 10 cm × 30 cm × 50 cm; the geometrical path length L is 10 cm [27.60]. (Reprint from S. Hirzel Verlag, Stuttgart 2004)

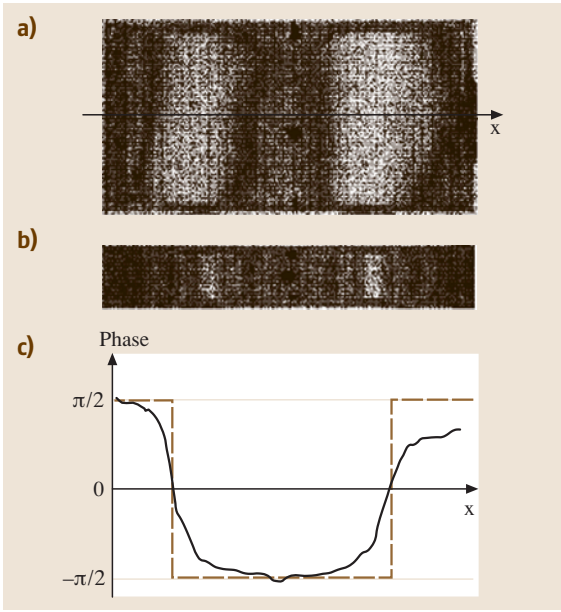


Fig. 27.9a–c Air mode (2, 0, 0) in the rectangular transparent box in Fig. 27.8 [27.60]. **(a)** view along the shortest side (1 dm); **(b)** View along the next shortest side (3 dm); **(c)** phase along the x-axis in **(a)** measured by phase-modulated TV holography. (Reprint by S. Hirzel Verlag, Stuttgart)

Amazon EX1014 Page 1111